

University of Southampton Research Repository ePrints Soton

Copyright © and Moral Rights for this thesis are retained by the author and/or other copyright owners. A copy can be downloaded for personal non-commercial research or study, without prior permission or charge. This thesis cannot be reproduced or quoted extensively from without first obtaining permission in writing from the copyright holder/s. The content must not be changed in any way or sold commercially in any format or medium without the formal permission of the copyright holders.

When referring to this work, full bibliographic details including the author, title, awarding institution and date of the thesis must be given e.g.

AUTHOR (year of submission) "Full thesis title", University of Southampton, name of the University School or Department, PhD Thesis, pagination

UNIVERSITY OF SOUTHAMPTON

FACULTY OF MEDICINE

BONE & JOINT RESEARCH GROUP

High-Throughput Skeletal Stem Cell
Separation using Magnetic Labelling and
Microfluidic Sorting

Marco Peca

Thesis for the degree of Doctor of Philosophy

September 2014

Academic Thesis: Declaration Of Authorship

I,Marco Peca.....

declare that this thesis and the work presented in it are my own and has been generated by me as the result of my own original research.

High-Throughput Skeletal Stem Cell Separation using Magnetic Labelling and Microfluidic Sorting.....

I confirm that:

1. This work was done wholly or mainly while in candidature for a research degree at this University;
2. Where any part of this thesis has previously been submitted for a degree or any other qualification at this University or any other institution, this has been clearly stated;
3. Where I have consulted the published work of others, this is always clearly attributed;
4. Where I have quoted from the work of others, the source is always given. With the exception of such quotations, this thesis is entirely my own work;
5. I have acknowledged all main sources of help;
6. Where the thesis is based on work done by myself jointly with others, I have made clear exactly what was done by others and what I have contributed myself;
7. Either none of this work has been published before submission, or parts of this work have been published as: [please list references below]:

Signed:

Date:

ABSTRACT

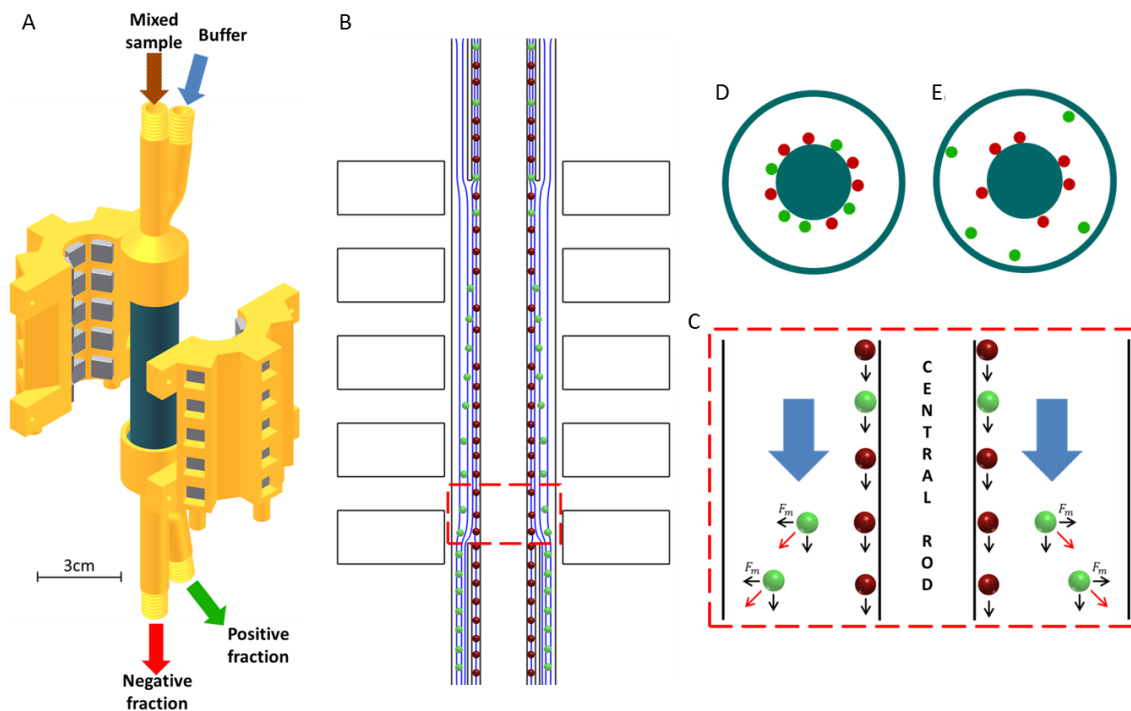
UNIVERSITY OF SOUTHAMPTON
FACULTY OF MEDICINE
BONE & JOINT RESEARCH GROUP
DOCTOR OF PHILOSOPHY

HIGH-THROUGHPUT SKELETAL STEM CELL SEPARATION USING MAGNETIC LABELLING AND MICROFLUIDIC SORTING

BY MARCO PECA

Medical advances have led to a welcome increase in life expectancy. However, this progress presents its own new challenges; an increase in age-related diseases, and associated reductions in quality of life. An increasingly aged population suffers from a range of degenerative diseases such as arthritis and osteoporosis. The most common form of arthritis worldwide is Osteoarthritis (OA). In severe cases, joint replacement may be necessary using non-biological prostheses such as hip replacement surgery. Hip replacement surgeries are on the increase, with accompanying significant socio-economic costs. According to the National Joint Registry for England, Wales and Northern Ireland, 89,945 hip replacement procedures were conducted in 2013 with an increment of 4% from 2012. The increase was even more evident considering that hip replacement procedures conducted in 2010 were only 76,759 [1].

A major limitation in the use of prostheses is the risk of infection, dislocation, mechanical mismatch and functional failure; all leading to revised implants and further surgery. Cell-based therapies are currently some of the most exciting and promising areas for treatment of bone disease and reparative medicine. Skeletal stem cells (SSCs) present in bone marrow (BM) contribute to the regeneration of mesenchymal tissues such as bone, muscle, ligament, tendon and stroma. However, despite intensive research interest, there are currently no reliable methods to isolate (or sufficiently enrich) homogeneous SSC populations needed for these strategies given their rarity (<0.01%, human BM stromal cells (HBMSCs)). This research seeks to develop SSC isolation techniques using unique microfluidic strategies. Traditional immunological sorting methods such as fluorescence/magnetic activated cell sorting (FACS/MACS) can be used to isolate SSCs according to surface marker expression. Both techniques have limitations with regards to purity (~70%), running cost, mechanical complexity and the need for trained dedicated technicians, especially FACS. A microfluidic-based approach offers reduced running costs and enhanced homogeneous stem cell and progenitor enrichment.



(A) 3D models of the CFMS. (B) Diagrams showing the working principle of the CFMS. (C) The mixed cell population (non-target cells in red, target cells in green) start in the inner stream. Under the influence of a magnetic field the target cells experienced a magnetic force (\vec{F}_m) and were pulled into the outer stream. (D, E) Diagrams showing the device working principle on a horizontal section

Here, we describe an innovative approach to isolate, sort and characterise SSCs from HBMSCs using a developed microfluidic device. Functionalised super-paramagnetic beads with adsorbed STRO-1 antibody were used to target the SSC population. The STRO-1+ cell fraction of HBM is heterogeneous, exhibiting variable proliferation and differentiation potentials. Immunomagnetically labelled cells experience a drag force due to a magnetic field generated by thirty permanent neodymium magnets. The system, called continuous flow magnetic sorter (CFMS), designed using the same principles as conventional MACS has the added advantage of continuous flow enabling labelled cell separation.

The device's sorting performance was investigated, using both human cell lines and HBMSCs. Sorting capacity was compared with that of conventional MACS. The sorting device achieved a greater than two fold increased recovery efficiency compared to sorting achieved by MACS. The newly developed microfluidic device was able to correctly sort double the number of STRO-1+ cells within a sample at comparable purity. The STRO-1+ cell population sorted with the developed device had the same differentiation capability of the ones isolated with conventional MACS. The developed device allows cell isolation with

contained running costs. Moreover, due to its mechanical simplicity, the device did not need trained personnel to be operated. For these reasons, the developed device would be beneficial for research purposes, representing a functional, easy to use and to maintain sorting platform for researchers' everyday uses.

Contents

List of Figures	xv
List of Table.....	xxxi
List of Abbreviations.....	xxxv
List of Symbols	xli
Acknowledgements	xliii
1 Introduction	1
1.1 Skeletal Stem Cells.....	4
1.1.1 Mesenchymal stem cells	4
1.1.2 Skeletal Stem Cells	4
1.1.3 SSCs in bone regeneration	6
1.1.3.1 Clinical applications	7
1.1.4 Summary	8
2 Literature Review.....	9
2.1 Traditional Sorting Techniques: MACS & FACS.....	9
2.2 Microfluidic Techniques	13
2.3 Classifications of Microfluidic Devices.....	13
2.3.1 Affinity based isolation	13
2.3.2 Size-based separation.....	20
2.3.2.1 Selective size amplification (SSA)	20

2.3.2.2 Size-based separations: Hydrodynamics	20
2.3.2.3 Size-based separations: Filtration and Centrifugation.....	24
2.3.2.4 Size-based separations: Dielectrophoresis	27
2.3.2.5 Size-based separations: Acustophoresis and Deformability.....	28
2.3.3 Immunomagnetic cell sorting	30
2.4 Summary of Sorting Techniques	37
3 Background Theory.....	43
3.1 Magnetic flux density	43
3.2 Flow regime	45
3.3 Balance of forces	46
3.3.1 Balance of forces within the sorting device.....	48
4 Immunomagnetic separations: device design and fabrication	51
4.1 Inspiration	51
4.2 Device	52
4.3 Sorting Device version 1	52
4.3.1 Cylinder and the Rod.....	53
4.3.2 Manifold	54
4.3.3 Assembled Device	56
4.4 Device Support.....	57
4.4.1 Top and Bottom Support.....	59
4.4.2 Magnet Holders	60
4.3.3 Column and Base	61

4.5	Assembly and final setup.....	61
4.6	Sorting Device version 2	62
4.6.1	Material analysis.....	63
4.7	Sorting Device Third Generation.....	63
4.7.1	Sorting Device ver. 3.....	65
4.7.2	Sorting Devices ver. 3.2 to 3.5.....	67
4.8	Summary.....	68
5	Device working principle, magnetic systems and numerical simulations	71
5.1	Device working principle	71
5.2	Quadrupole magnetic system version 1.....	74
5.2.1	Numerical simulation of magnetic flux density	76
5.2.2	Magnetic flux density measurements	79
5.3	Quadrupole magnetic system version 2.....	84
5.3.1	Magnetic system support: design and construction	86
5.3.2	Numerical simulation of the magnetic flux density.....	86
5.4	Hexapole magnetic system	90
5.4.1	Magnetic system support: design and manufacturing.....	92
5.4.2	Numerical simulation of the magnetic flux density.....	94
5.5	Summary.....	96
6	Cell Magnetisation.....	99
6.1	Magnetic bead	99
6.1.1	Experimental estimation of bead magnetic susceptibility	101
6.2	Cell labelling.....	102

6.2.1 Superparamagnetic bead functionalisation	102
6.2.1.1 Negative and positive controls	102
6.2.1.2 STRO-1 antibody titration	103
6.2.2 Cell labelling protocol.....	106
6.3 Experimental estimation of labelled cells magnetic susceptibility.....	108
6.3.1 Microfluidic device for magnetic susceptibility estimation.....	108
6.3.2 Labelled cell magnetic susceptibility calculation.....	108
6.4 Sample and buffer input flow rates ratio modelling	111
6.5 Particle tracking: 2D numerical simulation.....	113
6.5.1 Unlabelled cells	113
6.5.2 Labelled cells.....	114
6.6 Particle tracking: 3D numerical simulation.....	115
6.7 Summary	121
7 Sorting Device Testing.....	123
7.1 Experimental setup and protocol	123
7.2 Preliminary experiments	125
7.2.1 Cross-contamination.....	125
7.2.1.1 Cross-contamination and sample concentration relationship.....	130
7.2.2 Missing cells.....	131
7.2.2.1 Missing cell fraction and surface treatments.....	133
7.3 Sorting experiments: device ver.3.4 + QMS ver.1.....	135
7.3.1 Bead mobility	135
7.3.2 Bead sorting.....	137

7.3.3 MG63 cell sorting.....	140
7.3.3.1 Experimental setup	140
7.3.3.2 Results	141
7.4 MG63 cell sorting: device ver.3.4 + QMS ver.2	145
7.5 MG63 cell sorting: device ver.3.4 + HMS.....	149
7.6 MG63 cell sorting: device ver.3.5 + HMS.....	154
7.7 Comparison among magnetic systems and analysis.....	158
7.8 Sorting device ver.3.5 + HMS vs MACS	162
7.8.1 Experiment design.....	162
7.8.2 Results.....	162
7.8.2.1 Purity.....	163
7.8.2.2 Cell recovery efficiency.....	164
7.8.2.3 Summary.....	166
7.9 Summary and considerations.....	167
8 Human Bone Marrow Stromal Cell Characterisation	169
8.1 Materials and Methods.....	169
8.1.1 Bone marrow sample.....	169
8.1.2 Cultures conditions.....	170
8.2 Alkaline Phosphatase Activity.....	170
8.2.1 Histological analysis.....	170
8.2.2 Biochemical analysis	171
8.2.3 Biochemical analysis	171
8.2.4 Biochemical analysis	171

8.3 Results.....	173
8.3.1 Histological and Biochemical Analysis.....	173
8.3.2 Molecular Analysis.....	176
8.4 STRO-1 positive cells characterisation.....	177
8.5 Conclusion	181
9 Device characterisation and comparison with MACS	183
9.1 Experimental design.....	183
9.1.1 STRO-1 positive cells sorting.....	183
9.1.2 Negative and positive fraction analysis.....	185
9.1.3 Cell differentiation and characterisation.....	187
9.2 Results.....	189
9.2.1 Negative and positive fraction analysis: results	189
9.2.1.1 Purity.....	191
9.2.1.2 Recovery Efficiency	192
9.2.2 Cell differentiation and characterisation: results	197
9.3 Conclusion	201
10 Device characterisation and comparison with MACS.....	205
10.1 Discussion.....	207
10.2 Further work	211
References.....	213

LIST OF APPENDICES.....	224
APPENDIX A – QMS ver.1	225
APPENDIX B – Magnetic field measurements	227
APPENDIX C – QMS ver.2	233
APPENDIX D – HMS	237
APPENDIX E – Superparamagnetic bead susceptibility calculation.....	239
APPENDIX F – Superparamagnetic beads funtionalisation protocol.....	241
APPENDIX G – Cell magnetic susceptibility calculation	243
APPENDIX H – Particle tracing simulation details.....	245
APPENDIX I – Surface treatments	249
APPENDIX L – Carboxyl polystyrene beads coating protocol.....	253
APPENDIX M – Sorting device threshold.....	255
APPENDIX N – Protocols	259
APPENDIX O – ALP staining.....	265
APPENDIX P – Technical Drawings.....	267

List of Figures

Figure 1.1: Diagrams showing the working principle of the sorting device. The mixed cell population (non-target cells in red, target cells in green) start in the inner stream. Under the influence of a magnetic field the target cells experienced a magnetic force (\vec{F}_m) and were pulled into the outer stream. (A) Overview of the device working principle on a vertical mid-section (B) and detail. (C, D) Diagrams showing the device working principle on a horizontal section.....2

Figure 1.2: Cell-based strategy for bone regeneration. A bone marrow sample was collected from patient (typically aspirated from the iliac crest). SSCs were isolated from HBMSCs population. This plastic adherent cell population was subjected to *in vitro* expansion and differentiation. Afterwards, the SSCs were seeded (seeding density $\sim 3 \times 10^5$ cells/mm³) onto three dimensional biomaterial scaffolds to be implanted into the site of injury [2]5

Figure 2.1: Schematic diagram of the MACS procedure. (A) Two step immunostaining consisting of labelling mixed cell population with STRO-1 primary antibody labelling and MACS beads. (B) Green and red spheres represented target and non-target cells, respectively. (C) Mixed cell population loaded in a MACS column surrounded by the magnet. (D) Particular of the ferromagnetic spheres within the column trapping immunomagnetically labelled cells (green spheres). (E) MACS protocol. Mixed cell population loaded in a MACS column. (F) Washing step. Non-target cells were washed away and collected (negative fraction) while the target cells remained within the column. (G) Recovery step. Target cells were removed from the column (positive fraction)..... 10

Figure 2.2: Schematics of the equipment used for FACS procedure. Target cells were labelled with a fluorescent dye using a specific antibody and pumped into a flow chamber. The sample was divided into droplets by a vibrator nozzle, each droplet was illuminated by one or more laser beams and the emitted fluorescent signals detected by optical sensors. According to these signals, the polarity of the high-voltage deflection plates was switched and the droplets were directed to collection or waste chambers [3] 12

Figure 2.3: (A) Overview of the experimental setup (Nagrath <i>et al.</i>); (B) the dimensions of the CTC-chip were 25 mm x 66 mm, with the capture area of 19 mm x 51 mm; (C) device fulfil with blood; (D) SEM image of a captured cancer cell (NCI-H1650) [4]	15
Figure 2.4: (A) The Herringbone chip (HB-chip) (Stott <i>et al.</i>) glass slide (25 mm x 75 mm) serving as a substrate for the microchannels with herringbones feature on the upper wall. The device had a single inlet and outlet; (B) Illustration of the interaction between cells and microfluidic pattern [5]	16
Figure 2.5: (A) Picture of the affinity based capture microfluidic device (Yoon <i>et al.</i>); (B) Schematic of the graphene oxide chip; (C) SEM image of the flower-shaped gold patterns and magnified SEM image of adsorbed graphene oxide nanosheet [6].....	17
Figure 2.6: (A) Microfluidic device from Sheng <i>et al.</i> comprising a glass substrate (25 mm x 75 mm) and a layer of PDMS that create 8 channels with posts on the bottom. The device had a single inlet and outlet; (B) array of posts (C) and scanning electron microscope (SEM) image; (D) capturing cell mechanism within the device; (E) cancer cell captured on the functionalized post surface [7]	18
Figure 2.7: Schematic of the microfluidic device and the separation principle (Lee <i>et al.</i>). The CTCs and the blood cells experienced both inertial lift and Dean drag forces and the cell trajectory depends on the balance of the two forces. Cells within the device were separated via two outlets according to dimensions [8]	21
Figure 2.8: (A) Schematic of the p-MOFF device (Hyun <i>et al.</i>). Within each channel the CTCs were focused at the centre and collected in the target outlet; (B) picture of the device, consisting of one inlet, four MOFF channels and six outlet (just one of them was the target outlet); (C) the channels were preceded by a filter [9]	22
Figure 2.9: (A) Diagram of a single channel with focusing and sorting ridges (Choi <i>et al.</i>). Target cells roll on the functionalized surfaces following the trench, while non-target cells flow above the ridges; (B) picture of the microfluidic device comprising 20 channels on two layer [10]	23
Figure 2.10: (A) Schematic of the device (Zheng <i>et al.</i>). Filtration mechanism and forces acting on a trapped cells (F_s : supporting force, F_L : force due to the applied pressure, F_T : tension stress force); (B) schematics of a microfilter patch; (C) picture of the device; (D) single capture area; (E) one microfilter patch [11].....	25

- Figure 2.11: Diagram of the microfluidic device (Hou *et al.*) and separation mechanism within the channel. Sample and PBS were pumped into the device through the outer and inner inlets respectively. Led by the Dean drag (F_D) blood cells travel towards the inner flow and back to the original position, while the CTCs experienced a strong inertial lift force (F_L) that keeps them in the outer stream where they were collected [12] 26
- Figure 2.12: (A) Schematic representation of DEP-FFF device (Shim *et al.*). The cell suspension was injected into the device through an inlet in the channel bottom; (B) the sample flow was constrained in a thin layer adjacent to the channel floor by the shear flow; (C) in the separation region target and background cells were influenced by DEP forces and arranged in two vertical levels; (D) cancer cells were collected, while background cells were discarded [13] 27
- Figure 2.13: (A) Schematics of the rare cell isolation device (Kang *et al.*), consisting in a single inlet, a main channel, a double collection channel and one outlet. Both main and double channels had side chambers for magnetically labelled cells trapping; (B) picture of the device showing capture of magnetic beads in both channels. The beads not trapped from the chambers in the main channel were collected in the double channel [14] 31
- Figure 2.14: Schematics of the microfluidic CTC-iChip (Ozkumur *et al.*). The device consisted of three stages using different techniques. The first stage used deterministic lateral displacement to discard RBSs, free beads and platelets; the second stage focuses the nucleated cells through inertial forces and the final separate labelled target cells from background cells applying an external magnetic field [15] 32
- Figure 2.15: Quadrupole magnetic sorter (QMS). (A) Diagram of the QMS device (Hoyos *et al.*); (B) working principle where “a” and “b” were the inner stream (carrying the mixed cell sample) and the outer stream (shear flow), respectively. Black and white spots represented cells labelled and unlabelled respectively. (C) Cross-sectional view of the four magnets. Magnets placed in adjacent positions had opposite magnetisation direction (M). This configuration generated a magnetic force (\vec{F}_m) with a radial disposition. (D) The mixed cell population was injected in the inner stream through a pulse (50 μ l) injection system. Both, target cells and waste, outputs were connected to two UV detectors, which recorder light attenuation due to the presence of cells in suspension. The detectors’ signals were recorded and analysed through a data acquisition system, which allowed to determine the number of cells recovered from each output [16]..... 33

Figure 3.1: Two-dimensional schematic of the forces acting on a magnetic particle within the sorting device. The gravitational force \vec{F}_g has opposite direction compared to the buoyancy force \vec{F}_B . The magnetic force \vec{F}_m pulled the magnetic particle towards the magnet with the opposition of the hydrodynamic force \vec{F}_h	47
Figure 4.1: 3D model of the sorting device final version (ver. 3.5). Overall aspect of the assembled device consisting of cylinder, rod and manifolds and longitudinal section of the device. Measurements in millimetres.....	52
Figure 4.2: (A) 3D image showing prototype of the central rod and cylinder and (B) their relative positions.....	53
Figure 4.3: (A) 3D drawing of the manifold external part, the body structure was made of FullCure 720 (in yellow); (B) the contact points with the internal part and the cylinder were printed using TangoBlack 85 (in black), together with the outer O-ring.....	54
Figure 4.4: (A) 3D model of the internal part of the manifold. The external fins (highlighted in blue) keep the cup equidistant from the cylinder, defining the channel gap between them; (B) the internal fins (highlighted in blue) keep the rod in position, confining the flow near the rod surface.....	55
Figure 4.5: (A) 3D model of the assembled manifold; (B) inner view of the manifold internal/external part interface.....	56
Figure 4.6: (A) 3D model of the assembled device, consisting of two manifolds, the cylinder and the central rod; (B) the manifold internal part matches the rod tip geometry, providing a stable support for the rod; (C) device cross section showing the inner stream (in red) carrying the mixed cell sample and the buffer outer stream (in green)	57
Figure 4.7: 3D models of the bottom (and top) supports. (A) Part fixed to the column and (B) semi-transparent model of the same part showing a number of holes and threads. (C) The sliding part presenting several holes (D) in addition to the two screws housing fastening this part to the fixed one.	58
Figure 4.8: (A) 3D models of the bottom support handling the device, (B) and section of the support showing the fixing mechanism.....	58
Figure 4.9: (A) 3D models of the magnet holder from different angles; (B) column and base assembled in support of the entire structure (Image not in scale)	59

- Figure 4.10: (A) Device support with one magnet; (B) the sliding parts of the top and bottom support slide on the four screws allowing the device to fit in. (C) Device assembled into the support with one (D) and two magnets around it. (E) Experimental setup (F) and 3D model of the fully assembled system 60
- Figure 4.11: (A) 3D model of the manifold external part (ver. 2), the body structure was made in FullCure 720; (B) assembled manifold: the internal part and the points of contact between the two parts were shown in transparency..... 61
- Figure 4.12: (A) Model of the ver. 1 (B) and ver. 2 internal part of the manifold, with six respectively small fins and three larger fins grounded on the bottom..... 62
- Figure 4.13: SEM images of the device components. (A) 3D model of the tube; (B,C) SEM images of the internal surface of the tube (scale bar 400 μm and 100 μm) at different magnifications. (D) 3D model of the central rod; (E,F) SEM images of the internal surface of the central rod (scale bar 100 μm and 20 μm) at different magnifications. (G) 3D model of the manifold ver.2; (H,I) SEM images of the internal surface of the manifold ver.2 (scale bar 300 μm) at different angles..... 64
- Figure 4.14: SEM images of the device components. (A) 3D model of the tube ver.3; (B,C) SEM images of the internal surface of the tube ver.3 (scale bar 200 μm and 60 μm) at different magnifications. (D) 3D model of the central rod ver.3; (E,F) SEM images of the internal surface of the central rod ver.3 (scale bar 100 μm and 20 μm) at different magnifications 65
- Figure 4.15: (A) SEM images of the internal surface of the manifold ver.3 built using stereolithography at different (B) magnifications (scale bar 400 μm and 40 μm). (C) Photomicroscopy of a sample from the manifold ver.3 (scale bar 45 μm). (D) 3D model of the manifold used in the sorting device ver. 3 66
- Figure 4.16: 3D model of the sorting device ver. 3.4. (A) Overall aspect of the assembled device; (B) exploded view of the device, with the push-in fasten mechanism using O-rings at the ends of the tube; (C) longitudinal section of the device and detail of the fasten mechanism 67
- Figure 4.17: 3D model of the sorting device ver. 3.5. (A) The tube was the only component changed from the previous version and had a thickness of 750 μm ($\pm 3 \mu\text{m}$); (B) overall aspect of the ultimate version of the device..... 68

Figure 4.18: 3D models of the sorting devices developed in this study. (A) Versions 1 (B) and 2 used common building techniques and materials, while the geometries of few components were subjected to changes. (C) The third series of devices consisted of several versions: version 3 was the first to use different materials and building methods compared with the previous version, leading to sealing problems (no multiple-materials printing). (D) The two following versions solved those problems using different kinds of threads, (E) while version 3.4 achieved a watertight using O-rings on the tube ends. (F) The 3.5 was the ultimate version of the sorting device, featuring a reduced tube thickness ($750 \mu\text{m} \pm 3 \mu\text{m}$).
 69

Figure 5.1: (A) 3D models of the sorting device (ver. 3.5) and the hexapole magnetic system (HMS). (B) Sample and buffer were merged in two concentric streams: inner stream and outer stream respectively. (C) Picture of the experimental setup in a laminar flow hood 72

Figure 5.2: Diagrams showing the working principle of the sorting device. The mixed cell population (non-target cells in red, target cells in green) start in the inner stream. Under the influence of a magnetic field the target cells experienced a magnetic force (\vec{F}_m) and were pulled into the outer stream. (A) Overview of the device working principle on a vertical mid-section (B) and detail. (C, D) Diagrams showing the device working principle on a horizontal section..... 73

Figure 5.3: (A) 3D model of the arc segment of the neodymium magnet used. All measurements were in millimetres except the arc angle which was in degrees. (B) The north pole (in red) can be on the outside face (C) or on the inside face of the arc magnet. Magnets with both magnetization directions were used 74

Figure 5.4: (A) 3D model of QMS ver.1. The 12 arc magnets were arranged on three levels. All measurements were in millimetres. (B) Magnets with the same polarity were placed in opposite positions. (C) Red arrows represented the magnetization direction of each magnet. (D) Top view (xy plane) of the magnetic system, (E) magnet polarity arrangement (F) and magnetization directions 75

Figure 5.5: (A) 3D model of QMS ver. 1 including the magnet holders and the device support. (B) The sorting device was the middle of the magnetic system, held in place by the device support 76

Figure 5.6: Numerical simulation of the magnetic flux density generated by the QMS ver.1. (A) Magnetic system horizontal mid-plane; (B) magnet arrangement and polarity. (C) Red

- arrows (normalised vectors) show the direction of \vec{B} and (D) colour map was the value of $|\vec{B}|$ (in Tesla) over the mid-plane. (E) Line across the system along mid-plane; central point of the magnetic system represented in blue; (F) plot of $|\vec{B}|$ on the horizontal line (simulation details in Appendix A – Figure A.1)..... 77
- Figure 5.7: Numerical simulation of $|\vec{B}|$ and $|(\vec{B} \cdot \nabla)\vec{B}|$ generated by QMS ver.1. (A) Horizontal mid-plane; (B) line drawn between the centre point and the magnet surface; (C) plot of $|\vec{B}|$ along line. (D) Plot of $|(\vec{B} \cdot \nabla)\vec{B}|$ along the line. Simulation details in Appendix A – Figure A.1. 78
- Figure 5.8: (A) 3D model of the simplified magnetic system used for the experimental measurements of magnetic field. All the measurements were in millimetres. (B) The 4 arc magnets were arranged so that magnets with the same polarity were placed in opposition (North pole in red, South pole in blue)..... 79
- Figure 5.9: (A) Schematics of the home made Gaussmeter (voltage regulator: SparkFun Electronics, USA - COM-00107); (B) 3D model of the linear Hall effect probe (4.09 x 1.52 x 3.02 mm) used and (C) picture of the home-made Gaussmeter 80
- Figure 5.10: (A) Picture of the setup used to measure the field generated by the magnetic system consisting of a home-made Gaussmeter and a 2D micromanipulator which was used to move the magnetic system and perform measurements of B_x and B_y over (B) 80 points within an area of 20 mm x 20 mm at the centre of the system. (C) Vertical plane where measurements were made 81
- Figure 5.11: (A) Colour map of $|\vec{B}|$ obtained from experimental measurements of B_x and B_y after cubic interpolation. (B) 3D shaded surface representing $|\vec{B}|$ over the area of interest. (C) Plane representing the Z level of the measurements and the modelled data. (D) Segment D and (E) segment E drawn on the plane. (F) Plot of $|\vec{B}|$ over segment D and (G) segment E of modelled data (red line) and laboratory measurements (black line) 82
- Figure 5.12: (A) Arrangement of the magnets in system and (B) magnetization directions. (C) Red arrows (normalised vectors) representing the direction of \vec{B} according to the modelled data and (E) experimental measurements (blue proportional vectors). (D) The experimental measurements covered just the central area that included the sorting device (section visible in black). Red arrows (normalised vectors) representing the direction of

$(\vec{B} \cdot \nabla)\vec{B}$ according to the modelled data and (F) to the experimental measurements (blue proportional vectors - details in Appendix B).....	83
Figure 5.13: (A) 3D model of the block neodymium magnet. All measurements were in millimetres. The magnets were magnetized across their thin section. (B) North pole in red and South pole in blue. (C) Red arrow representing the magnetization direction of the magnet. (D) Half rod shaped pieces made from mild steel. (E) 3D model of QMS ver.2; magnets with the same polarity placed in opposite positions. (F) Top view of the magnetic system and (G) magnetization directions.....	85
Figure 5.14: (A) 3D model of the support for the QMS ver.2. It consisted of a stainless steel frame and 8 3D printed holders (in yellow). One side of the support was movable. (B) QMS ver.2 in its support.....	86
Figure 5.15: (A) 3D models of QMS ver.2 and the sorting device. (B) Once the sorting device was in position, the magnetic system slides into the device support. (C) The hinged side allows magnetic system to be closed and (D) secured in position.....	87
Figure 5.16: Numerical simulation of the magnetic flux density generated by the QMS ver.2. (A) Position of the horizontal plane; (B) magnet arrangement and polarity. (C) Red arrows (normalised vectors) show the direction of \vec{B} and (D) colour map was the value of $ \vec{B} $ (in mT) over the plane. (E) Line across the system along mid-plane; central point of the system represented in blue; (F) plot of $ \vec{B} $ on the horizontal line (simulation details in Appendix C – Figure C.1).....	88
Figure 5.17: (A) Numerical simulation of $ \vec{B} $ and $ (\vec{B} \cdot \nabla)\vec{B} $ generated by the QMS ver.2. Horizontal mid-plane; (B) cut line drawn between the centre point and the half rod piece surface; (C) plot of $ \vec{B} $ along the line. (D) Plot of $ (\vec{B} \cdot \nabla)\vec{B} $ along the line. Simulation details in Appendix C – Figure C.1.....	89
Figure 5.18: (A) 3D model of the cubic neodymium magnet used. (B) North pole in red and South pole in blue. (C) 3D model of the block magnets created by two cubic magnets. (D) Magnets polarity. All the measurements were in millimetres	90
Figure 5.19: (A) 3D model of the HMS. (B) Each level consisted of 6 block magnets organised in a hexapole configuration. (C) Top view (xy plane) of the magnetic system and (D) magnetization directions	91

- Figure 5.20: (A) 3D model of the support for the HMS. (B) Block magnets placed into one part of the support. (C) Picture of one half of the support..... 92
- Figure 5.21: (A) 3D models of the HMS and the sorting device. (B) Magnetic system slid into the device support once the sorting device was placed in position. (C) The two halves of the magnetic system in place around the sorting device. (D) Picture of the HMS and the sorting device..... 94
- Figure 5.22: Numerical simulation of the magnetic flux density generated by the HMS. (A) Position of the horizontal mid-plane; (B) magnet arrangement and polarity. (C) Red arrows (normalised vectors) show the direction of \vec{B} and (D) colour map was the value of $|\vec{B}|$ (in mT) over the plane. (E) Line across the system along mid-plane; central point of the system represented in blue; (F) plot of $|\vec{B}|$ on the horizontal line (simulation details in Appendix D – Figure D.1) 94
- Figure 5.23: Numerical simulation of $|\vec{B}|$ and $|(\vec{B} \cdot \nabla)\vec{B}|$ generated by the QMS ver.2. (A) Horizontal mid-plane; (B) line drawn between the centre point and the magnet surface; (C) plot of $|\vec{B}|$ along the line. (D) Plot of $|(\vec{B} \cdot \nabla)\vec{B}|$ along the line. Simulation details in Appendix D – Figure D.1) 95
- Figure 5.24: Comparison among magnetic systems. (A, B, C) Cut lines drawn between the centre of the magnetic systems ($X=0$) and the surface of the magnetic element on the horizontal mid-planes of the magnetic systems. Drawings not in scale. (D) $|\vec{B}|$ and (E) $|(\vec{B} \cdot \nabla)\vec{B}|$ generated by the QMS ver.1, the QMS ver.2 and the HMS represented by red, green and black lines respectively. The plots stop after the region of interest delimited by blue vertical lines 96
- Figure 6.1: 3D model of the experimental setup used to estimate χ_p ; PDMS channel and arc segment neodymium magnet. All measurements were in millimetres100
- Figure 6.2: Diagram of bead functionalisation procedure. (A) Carboxyl superparamagnetic bead. (B) Carboxyl superparamagnetic activated bead. (C) Superparamagnetic functionalised (STRO-1) bead. The chemical reactions on the beads surface were described in Appendix F (Figure F.1).....101
- Figure 6.3: Diagrams of the negative controls and the experiment. (A) Fluorescent antibodies (Alexa 488) were incubated with bare bead, (B) activated bead and (C) functionalised bead respectively. (D,E) Flow cytometry histograms showing no

fluorescence activity for the controls and (F) fluorescence signal for the experiment. (G,H,I) Bright field photomicroscopy of the three samples. (L,M) Fluorescence microscopy (FITC; Ex/Em (nm): 495/519) revealed no signals of fluorescence in the negative controls, (N) while signals of fluorescent bead were registered in the experiment. Scale bars represented 30 μm 104

Figure 6.4: (A) Fluorescent antibodies (Alexa 488) were incubated with six bead samples functionalised using different STRO-1 antibodies dilutions. (B) Flow cytometry histograms and percentages of fluorescent bead for samples functionalised using 1:1, (C) 1:10, (D) 1:100, (E) 1:200, (F) 1:500 and (G) 1:1000 dilutions of the STRO-1 antibodies (threshold set accordingly to negative control).....105

Figure 6.5: (A) Diagram of the cell labelling protocol; MG63 cells (fixed with Ethanol) were incubated with functionalised bead. (B, C and D, E) Bright field photomicroscopy of labelled cells at different focal planes. Scale bars represented 30 μm 97

Figure 6.6: (A) Diagram of the control experiment; labelled MG63 cells were incubated with fluorescent antibodies (Alexa 488). (B) Fluorescence microscopy (FITC; Ex/Em (nm): 495/519) of labelled cells; all the beads were fluorescent. (C) Overlying bright field photomicroscopy. Scale bars represented 30 μm107

Figure 6.7: (A) 3D models of the microfluidic device used to estimate χ_c ; (B) exploded view. (C) Stereolithography built support and (D) experimental setup. All the measurements were in millimetres.....109

Figure 6.8: (A,B) Frames extracted from the videos recorded during the χ_c estimation experiments at different magnifications. (C) Photomicroscopy of MG63 cells in the channel and in the input hole. (D) Horizontal mid-plane and (E) cut line along which \vec{B} and $(\vec{B} \cdot \nabla)\vec{B}$ were modelled. (F) Plot of $\vec{B}(B_x, B_y, B_z)$ and (G) $|\vec{B}|$ along the cut line. (H) Plot of $(\vec{B} \cdot \nabla)\vec{B}$ and (I) $|(\vec{B} \cdot \nabla)\vec{B}|$ along the cut line.....110

Figure 6.9: (A) Vertical mid-plane. (B) Section of the sorting device (without manifolds) and magnetic system. (C) Due to the geometrical symmetry, just half of the system was modelled (sample flow in red, buffer flow in blue): outputs unregulated, (D) equal flow rates for the two outputs. (E - L) Velocity field streamlines representing a parameter sweep for different flow rate ratios (simulation details in Appendix H – Figure H.1).....112

Figure 6.10: (A) Velocity field streamlines of the flow within the sorting device using a ratio between the two flow rates of 1:4. The lines in red and blues represented the sample

flow and buffer flow, respectively. (B) Details of the flow at the beginning of the outlet manifold (C) and in correspondence to the separate outputs (simulation details in Appendix H – Figure H.2).....	113
Figure 6.11: Particle trajectories for unlabelled cells (ratio between the two flow rate of 1:4) (simulation details in Appendix H – Figure H.3).....	114
Figure 6.12: (A) Vertical mid-plane. (B, C, D) Trajectory of a single labelled cell modelled using a range of Q_T with a fixed ratio between Q_S and Q_B of 1:4. The labelled cell in the sample input and collected in the non-target output or (E, F) in the target output according to the Q_T used (simulation details in Appendix H – Figure H.4)	115
Figure 6.13: (A) Magnitude of the flow velocity. (B) Trajectory of labelled cell within the sorting device ($Q_T = 4.5$ ml/min). (C) Table summarizing the simulation parameters. (D) Plot of the cell velocity along the sorting device	116
Figure 6.14: (A) Plane where the cells final positions ($t=150$ s) were projected. (B) Summarizing table of the percentages of cells recovered in each output for the values of Q_T investigated. (C – H) Projections on the plane of the cells positions at $t=150$ s under several Q_T values. All the cells had identical magnetic susceptibility χ_c . The Matlab script allowed to represent the cells collected into the target and non-target outputs by red and blue dots respectively.....	117
Figure 6.15: (A - F) Projections on the plane (Figure 6.14A) of the cells positions at different time points, between $t=0$ s and $t=150$ s (residence time), at a fixed flow rate ($Q_T = 2.5$ ml/min – $Q_S:Q_B = 1:4$). The Matlab script allowed to represent the cells collected into the target and non-target outputs by red and blue dots respectively.....	118
Figure 6.16: (A) Final positions of the labelled cells, $t=150$ s and (B) trajectories of the labelled cells within the sorting device (simulation details in Appendix H – Figure H.5) .	119
Figure 6.17: (A) Final positions of the labelled cells within the sorting device. (B) Detail of cells trapped onto the internal surface of the input manifold. (C) Detail of cells trapped onto the internal surface of the tube (highlighted by green arrows) and the internal surface of the output manifold (highlighted by blue arrows)	120
Figure 6.18: Flow velocity magnitude within the sorting device ($Q_T = 2.5$ ml/min); table summarising parameters used and cells velocity values obtained	121

Figure 7.1: (A) Picture of the experimental setup in a laminar flow hood. (B) The setup consisted of: two syringe pumps (Harvard Apparatus – 11 Plus, USA), plastic syringes, tubing (Omnifit No:12946291), valves (Omnifit No:001101), the magnetic system and the sorting device.....	124
Figure 7.2: (A) 3D models of the sorting device ver.1 and (B) ver.2. (C) Horizontal section of the input/output manifolds ver.1 and (D) ver.2. All measurements were in millimetres	127
Figure 7.3: Plots of the cross-contamination percentages (mean values $n=3 \pm SD$) recorded using the sorting device ver.1 (blue line) and the sorting device ver.2 (red line) across the range of $Q_S:Q_B$ ratios investigated	129
Figure 7.4: 3D bar chart of the cross-contamination percentages (mean values $n=3$) recorded using the sorting device ver.2 across the range of $Q_S:Q_B$ ratios investigated using different sample concentrations	130
Figure 7.5: Missing cell fraction percentages (mean values $n=3$) recorded using the sorting device ver.1 (blue line) and the sorting device ver.2 (red line) across the range of $Q_S:Q_B$ ratios investigated	131
Figure 7.6: (A) 3D models of the sorting device ver.3.4. (B) Horizontal section of the sorting device ver.3.4. All measurements were in millimetres.....	132
Figure 7.7: Missing cell fraction recorded (mean values $n=3$) using the sorting device ver.1 (blue line), the sorting device ver.2 (red line) and the sorting device ver.3.4 (green line) across the range of $Q_S:Q_B$ ratios investigated	133
Figure 7.8: Missing cell fraction recorded (mean values $n=3$) using the sorting device ver.3.4 (green line) and the sorting device ver.3.4 coated with PLL-g-PEG (black line) across the range of $Q_S:Q_B$ ratios investigated	134
Figure 7.9: (A) 3D models of the QMS ver.1 and (B) the experimental setup with the sorting device ver.3.4 surrounded by the QMS ver.1	135
Figure 7.10: Plots of the percentages (mean values $n=3$) of magnetically labelled beads recovered in the target output using the sorting device ver.3.4 + QMS ver.1.....	136
Figure 7.11: (A) Photomicroscopy of a target and non-target bead in bright field and (B) in fluorescence light (FITC filter – bright bead was the target bead).....	139

Figure 7.12: Purity increases (defined as the difference between the percentage of STRO-1+ cells in the positive fraction and percentage of STRO-1+ cells in the original sample) in the cell population recovered from the positive fraction of the device ver.3.4 PEG coated + QMS ver.1 across the range of $Q_S:Q_B$ ratios tested (mean values $n=9 \pm SD$)	143
Figure 7.13: STRO-1+ cells recovery efficiency in the positive fraction of the device ver.3.4 PEG coated + QMS ver.1 across the range of $Q_S:Q_B$ ratios tested. Percentages of the initial STRO-1+ cells number collected in the positive fraction were plotted (mean values $n=9 \pm SD$).....	144
Figure 7.14: (A) 3D models of the QMS ver.2 and (B) the experimental setup with the sorting device ver.3.4 (PEG coated) surrounded by the QMS ver.2	149
Figure 7.15: Purity increases (defined as the difference between the percentage of STRO-1+ cells in the positive fraction and percentage of STRO-1+ cells in the original sample) in the cell population recovered from the positive fraction of the device ver.3.4 PEG coated + QMS ver.2 across the range of $Q_S:Q_B$ ratios tested (mean values $n=9 \pm SD$)	147
Figure 7.16: STRO-1+ cells recovery efficiency in the positive fraction of the device ver.3.4 PEG coated + QMS ver.2 across the range of $Q_S:Q_B$ ratios tested. Percentages of the initial STRO-1+ cells number collected in the positive fraction were plotted (mean values $n=9 \pm SD$).....	148
Figure 7.17: (A) 3D models of the HMS and (B) the experimental setup with the sorting device ver.3.4 (PEG coated) surrounded by the HMS	149
Figure 7.18: Purity increases in the cell population recovered from the positive fraction of the device ver.3.4 PEG coated + HMS across the range of $Q_S:Q_B$ ratios tested (mean values $n=9 \pm SD$).....	152
Figure 7.19: STRO-1+ cells recovery efficiency in the positive fraction of the device ver.3.4 PEG coated + HMS across the range of $Q_S:Q_B$ ratios tested. Percentages of the initial STRO-1+ cells number collected in the positive fraction were plotted (mean values $n=9 \pm SD$)..	153
Figure 7.20: (A) 3D models of the tube used in (B) the sorting device ver.3.4. (C) 3D models of the tube (D) used in the sorting device ver.3.5. (E) Horizontal mid-plane of the HMS; (F) cut line drawn between the centre point and the magnet surface. (G) Plot of $ \vec{B} $ generated by the device ver.3.4 + HMS (red line) and the device ver.3.5 + HMS (black line) along the cut line. (H) Plot of $ (\vec{B} \cdot \nabla)\vec{B} $ generated by the device ver.3.4 + HMS (red line) and the device ver.3.5 + HMS (black line) along the cut line.....	154

- Figure 7.21: Purity increases in the cell population recovered from the positive fraction of the device ver.3.5 PEG coated + HMS across the range of $Q_S:Q_B$ ratios tested (mean values $n=9 \pm SD$).157
- Figure 7.22: STRO-1+ cells recovery efficiency in the positive fraction of the device ver.3.5 PEG coated + HMS across the range of $Q_S:Q_B$ ratios tested. Percentages of the initial STRO-1+ cells collected in the positive fraction were plotted (mean values $n=9 \pm SD$).....158
- Figure 7.23: Purity increases the cell population recovered from the positive fractions of all the sorting device + magnetic system combinations across the range of $Q_S:Q_B$ ratios tested (mean values $n=9$)159
- Figure 7.24: STRO-1+ cells recovery efficiency in the positive fractions of all the sorting device + magnetic system combinations across the range of $Q_S:Q_B$ ratios tested. Percentages of the initial STRO-1+ cells number collected in the positive fractions were plotted (mean values $n=9 \pm SD$).....160
- Figure 7.25: (A) The cell sample was divided in two. (B) Half was processed with a one-step immunostaining and (C) processed with the sorting device. (D) The second part was processed with a two-step immunostaining and (E) processed with traditional MACS....161
- Figure 7.26: (A) Bar chart reporting the composition of the original sample, negative fraction and positive fraction recovered from MACS and (B) final device. Results expressed as mean \pm SD, $n = 9$ 163
- Figure 7.27: (A)Bar charts reporting the total number of cells in the original sample, negative fraction and positive fraction recovered from MACS and sorting device. (B) Number of STRO-1+ cells recovered from each fraction of the two techniques and (C) percentages these numbers represented compared with the original number. Results expressed as mean \pm SD and $n = 9$ 165
- Figure 8.1: Photomicroscopy of HBMSCs in basal and osteogenic media at day 0, day 7 and day 14 from the start of differentiation (11 days after seeding). Scale bars represented 500 μ m172
- Figure 8.2: (A) ALP staining at day 7 and (E) day 14 for Basal and Osteogenic samples. (B) Photomicroscopy of HBMSCs under basal condition a day 7. (C) Photomicroscopy of HBMSCs maintained in osteogenic conditions at day 7 and (D) through a H/DIC (Differential Interference Contrast) filter. Samples were run in triplicate. Scale bars represented 20 mm and 200 μ m174

- Figure 8.3: ALP assay performed for HBMSCs after 7 days and 14 days of differentiation under basal and osteogenic conditions. Results expressed as mean \pm SD and $n = 3$. * $P < 0.05$ calculated using t -test.....175
- Figure 8.4: ALP Specific Activity for HBMSCs after 7 days and 14 days of differentiation under basal and osteogenic condition (incubation time 40 min). Results expressed as mean \pm SD and $n = 3$. * $P < 0.05$ calculated using t -test175
- Figure 8.5: Real time PCR quantification for HBMSCs cultured under basal and osteogenic conditions for 14 days ($n=2$). The values were normalised for the basal condition for each gene. Results expressed as average \pm SD and $n = 2$176
- Figure 8.6: Photomicroscopy of P1 STRO-1+ cells in basal and osteogenic media at day 7, day 14 and day 21 from the start of differentiation (10 days from the seeding operation). Scale bars represented 500 μm 178
- Figure 8.7: (A) ALP staining at day 7, (B) day 14 and (C) day 21 for Basal and Osteogenic samples. Samples were run in triplicate.....179
- Figure 8.8: RT-PCR quantification for STRO-1+ cells cultured under basal and osteogenic conditions for 21 days. The values were normalised for the condition basal at day 7 for each gene. Results expressed as average \pm SD and $n = 2$ 180
- Figure 9.1: (A) Bone marrow sample. (B) HBMSCs were isolated using density gradient centrifugation. (C) HBMSC populations were divided in two to enable processing with the sort device and MACS. (D) HBMSCs were labelled with functionalised beads and (F) processed through the device. (E) HBMSCs labelled with MACS beads (two-step process) and (G) treated with MACS.....184
- Figure 9.2: (A) Samples collected from each fraction. (B) Sample for immunostaining (STRO-1 + Alexa Fluor 488). (C) Bright field and (D) fluorescence microscopy of HBMSCs collected from the positive fraction (DEVICE). (E) Flow cytometry scatter plot and (F) histogram of HBMSCs immunostained for STRO-1 expression; only the monocytes (red circle) were gated to derive the histogram plots. Scale bars represented 30 μm 185
- Figure 9.3: (A) The positive fraction (DEVICE) and (B) the positive fraction (MACS) were cultured in basal media for 10 days and then each cell populations was seeded (P0 \rightarrow P1) in six wells plates and flasks as illustrated in C and D188

- Figure 9.4: (A) Bar chart illustrating the composition of the original sample, negative fraction and positive fraction recovered from MACS and (B) sorting device. Results expressed as mean \pm SD and from $n = 9$ 190
- Figure 9.5: (A) Bar charts illustrating the total number of cells in the original sample, negative fraction and positive fraction recovered from MACS and (B) sorting device. The device collected more than twice the amount of cells in the positive fraction (in red) compared to the MACS with equal purity. Results expressed as mean \pm SD and $n = 9$194
- Figure 9.6: (A) The number of STRO-1+ cells in the original sample, negative fraction and positive fraction recovered from MACS and sorting device. (B) Percentages of STRO-1+ cells in negative and positive fractions recovered with MACS and sorting device. Results expressed as mean \pm SD and $n = 9$. * $P < 0.05$ calculated using *t*-test.....196
- Figure 9.7: Photomicroscopy of P1 STRO-1+ cells sorted with the MACS and the sorting device under basal and osteogenic conditions at day 7 and day 14 from the start of differentiation (10 days from the seeding operation)197
- Figure 9.8: ALP staining of the STRO-1+ cell populations sorted with MACS and sorting device cultured under basal and osteogenic conditions. (A, B) ALP staining performed after 7 days. (C, F) Photomicroscopy of the cell populations cultured under basal conditions at day 7. (D, G) Photomicroscopy of the cell populations cultured under osteogenic condition at day 7 and (E, H) through a H/DIC (Differential Interference Contrast) filter. The procedure was implemented in triplicate (incubation time 30 min).....198
- Figure 9.9: RT-PCR quantification for STRO-1+ cells isolated with MACS (blue bars) and sorting device (red bars) cultured under basal and osteogenic conditions for 14 days. The values were normalised against the condition basal 7 (MACS) sample for each gene. Results expressed as mean \pm SD and $n = 9$. * $P < 0.05$; ** $P < 0.005$; *** $P < 0.001$ calculated using Mann-Whitney test.....200

List of Tables

Table 2.1: Affinity based isolation. Keys parameters for each paper were reported, including: the author, year, discrimination parameters, sorting methods the devices used, purity, recovery, flow rate, throughput and the kind of cells used. The papers in red were widely discussed in the chapter with data from the papers. The devices tested with whole blood from cancer patients present two lines in the recovery and particle columns. The cells highlighted in bold represented the results from cancer blood analysis (number of cancer samples in which CTCs were identified). The paper in blue was the most effective work within the category 39

Table 2.2: Size-based separation. Keys parameters for each paper were reported, including: the author, year, discrimination parameters, sorting methods the devices used, purity, recovery, flow rate, throughput and the kind of cells used. The papers in red were widely discussed in the chapter with data from the papers. The devices tested with whole blood from cancer patients present two lines in the recovery and particle columns. The cells highlighted in bold represented the results from cancer blood analysis (number of cancer samples in which CTCs were identified). The paper in blue was the most effective work within the category 40

Table 2.3: Immunomagnetic separation. Keys parameters for each paper were reported, including: the author, year, discrimination parameters, sorting methods the devices used, purity, recovery, flow rate, throughput and the kind of cells used. The papers in red were widely discussed in the chapter with data from the papers. The devices tested with whole blood from cancer patients present two lines in the recovery and particle columns. The cells highlighted in bold represented the results from cancer blood analysis (number of cancer samples in which CTCs were identified). The paper in blue was the most effective work within the category. The paper highlighted in yellow impressed the author for the achievements reached and contribution to the field 41

Table 5.1: Summary table reporting the values of $|\vec{B}|$ and $|(\vec{B} \cdot \nabla)\vec{B}|$ at the beginning ($X=3.5$) and the end ($X=6.5$) of the segment of interest (within the device); and the $|\nabla\vec{B}|$ along the same segment 97

Table 7.1: Table summarising the cross-contamination experiments (mean values $n=3 \pm$ SD) performed with the sorting device ver.1	126
Table 7.2: Table summarising the cross-contamination experiments (mean values $n=3$) performed with the sorting device ver.2.....	127
Table 7.3: Comparative table of the cross-contamination experiments performed with the sorting device ver.1 and the sorting device ver.2	128
Table 7.4: Table summarising the beads sorting experiments (mean values $n=3 \pm$ SD) performed with the sorting device ver.3.4+QMS ver.1. Target beads (in orange) and non-target beads (in blue) percentages of the original bead population recovered from the negative and positive fraction of the sorting device.....	138
Table 7.5: Percentages (mean values $n=9 \pm$ SD) of STRO-1+ cells (in orange) and the STRO-1- cells (in blue) recovered from the negative and positive fraction of the sorting device (device ver.3.4 PEG coated + QMS ver.1). The sorting experiments were performed using MG63 cells across the entire range of $Q_S:Q_B$ ratios.....	142
Table 7.6: Table summarising MG63 cell sorting experiments (mean values $n=9 \pm$ SD). Total numbers of cells and numbers of STRO-1+ cells in the original sample, positive and negative fractions (after sorting with device ver.3.4 PEG coated + QMS ver.1) were reported. Percentages of the initial STRO-1+ cells number collected in the negative and positive fractions reported in red	142
Table 7.7: Percentages (mean values $n=9 \pm$ SD) of STRO-1+ cells (in orange) and the STRO-1- cells (in blue) recovered from the negative and positive fraction of the sorting device (device ver.3.4 PEG coated + QMS ver.2). The sorting experiments were performed using MG63 cells across the entire range of $Q_S:Q_B$ ratios.....	146
Table 7.8: Table summarising the MG63 cell sorting experiments (mean values $n=9 \pm$ SD). Total numbers of cells and numbers of STRO-1+ cells in the original sample, positive and negative fractions (after sorting with device ver.3.4 PEG coated + QMS ver.2) were reported. Moreover, the percentages of the initial STRO-1+ cells number collected in the negative and positive fractions were reported (in red).....	146
Table 7.9: Percentages (mean values $n=9 \pm$ SD) of STRO-1+ cells (in orange) and the STRO-1- cells (in blue) recovered from the negative and positive fraction of the sorting device (device ver.3.4 PEG coated + HMS). The sorting experiments were performed using MG63 cells across the entire range of $Q_S:Q_B$ ratios	151

Table 7.10: Table summarising MG63 cell sorting experiments (mean values $n=9 \pm SD$). Total numbers of cells and numbers of STRO-1+ cells in the original sample, positive and negative fractions (after sorting with device ver.3.4 PEG coated + HMS) were reported. Percentages of the initial STRO-1+ cells number collected in the negative and positive fractions were reported (in red).....	151
Table 7.11: Percentages (mean values $n=9 \pm SD$) of STRO-1+ cells (in orange) and the STRO-1- cells (in blue) recovered from the negative and positive fraction of the sorting device (device ver.3.5 PEG coated + HMS). The sorting experiments were performed using MG63 cells across the entire range of $Q_S:Q_B$ ratios.....	156
Table 7.12: Table summarising MG63 cell sorting experiments (mean values $n=9 \pm SD$). Total numbers of cells and numbers of STRO-1+ cells in the original sample, positive and negative fractions (after sorting with device ver.3.5 PEG coated + HMS) were reported. Percentages of initial STRO-1+ cells number collected in the negative and positive fractions reported in red.....	156
Table 8.1: List of real time primers used in this study with sequences (Developed by Dr Rahul Tare, Bone and Joint Research Group)	173
Table 9.1: List of real time primers used in this study and corresponding sequence (Developed by Dr Rahul Tare, Bone and Joint Research Group.....	189
Table 9.2: Summary of purity achieved by MACS and the sorting device. The first row indicates the composition of the original samples (orange STRO-1+ cells; blues STRO-1- cells); the following rows the composition of the negative and positive fractions collected from MACS and sorting device after the sorting protocol.....	192
Table 9.3: Summary table of recovery efficiency for MACS and sorting device (mean values $n=3 \pm SD$). In red the total number (in million) of cells recovered from the positive fractions of the two techniques. In blue the percentages of STRO-1+ cells contained in the original samples recovered from the positive fractions of the two techniques.....	195
Table 10.1: Table comparing the performances of the most efficient microfluidic cell sorting devices with the CFMS developed in this study. The sorting devices were divided in three main categories: affinity-based (in blue), size-based (in red) and immunomagnetic (in black). The values in bold referred to experiments with primary cells (in the case of CFMS, HBMSCs from patients). The highlighted row reported the details form CFMS tests	208

List of Abbreviations

ABG	Autologous bone grafting
4T1	Murine breast cancer cells
ADSC	Adipose-derived stem cell
ADSC	Adipose-derived stem cell
AG01522	Human fibroblast
ALP	Alkaline phosphatase
BM	Bone marrow
BM	Bone marrow
BMA	Bone marrow aspirate
BM-MNC	Bone marrow mononuclear cell
BMSC	Bone marrow stromal cell
BSA	Bovine serum albumin
BT-474	Human breast cancer cell
C166-GFP	Mouse endothelial cell
CCRF-CEM	Human T cell lymphoblast-like cell line
CFMS	Continuous flow magnetic sorter
cDNA	Complementary Deoxyribonucleic Acid
CFU-F	colony-forming unit-fibroblastic
Colo205	Human colon cell line

COOH	Carboxylic acid group
CTC	Circulating tumour cell
DEP	Dielectrophoresis
DEP-FFF	Dielectrophoresis field-flow-fractioning
DGM	Density gradient medium
DLD	Deterministic lateral displacement
DNA	Deoxyribonucleic Acid
dsDNA	Double-Stranded Deoxyribonucleic Acid
DU145	Human prostate cancer cell line
EC	Endothelial cell
EDC	N-(3-Dimethylaminopropyl)-N'-ethylcarbodiimide hydrochloride
EDTA	Ethylenediaminetetraacetic acid
EPC	Endothelial progenitor cell
EpCAM	Epithelial cell adhesion molecule
FACS	Fluorescence activated cell sorting
FB	Fibroblast
FCS	Fetal calf serum
FDA	Food and drug administration
GAENE	Glycolic acid ethoxylate 4-nonylphenyl ether
Gd-DTPA	Paramagnetic salt
GEDI	Geometrically enhanced differential immunocapture
HB-chip	Herringbone chip

HBMSC	Human bone marrow stromal cell
HCT116	Colorectal carcinoma cell
HeLa	Human carcinoma cell
HEPES	4-(2-hydroxyethyl)-1-piperazineethanesulfonic acid
HL-60	Leukemia cell line
HMS	Hexapole magnetic system
HT29	Colorectal cancer cell line
HuT 78	Human T lymphocyte
ICS	Immunomagnetic Cell Separation
ITO	Indium tin oxide
K562	Leukemia cell line
KG1-a	White blood cell line
LNCaP	Human prostate cancer cell
MACS	Magnetic activated cell sorting
MC6	Mouse metastatic breast cancer cell
MCF-7	Breast cancer cell line
MDA-MB-231	Human mammary gland adenocarcinoma
MDA-MB-435	Breast cancer cell line
MDA-MB-436	Metastatic breast cancer cell line
MG63	Human osteosarcoma cell line
MG63	Human osteosarcoma cell line
MLC	Mouse lymphoma cell
MOA	Multi-obstacle architecture

MSC	Mesenchymal stem cell
NB-4	Human promyelocytic leukemia cell line
NCI-H1650	Lung cancer cell line
nDEP	Negative dielectrophoresis
NdFeB	Neodymium magnet
NHSS	N-Hydroxysulfosuccinimide sodium salt
OA	Osteoarthritis
OPC	Oligodendrocyte progenitor cell
P/S	Penicillin and Streptomycin
PBL	Peripheral blood lymphocytes
PBMN	Peripheral blood mononuclear cell
PBS	Phosphate buffered saline
PC3	Prostate cancer cell
PDMS	Polydimethylsiloxane
PLL-g-PEG	Poly(L-lysine)-graft-poly(ethylene glycol)
PMMA	Poly(methyl methacrylate)
p-MOFF	Parallel multi-orifice flow fractionation
PP-R	Polypropylene random copolymer
PSMA	Prostate-specific membrane antigen
PTFE	Polytetrafluoroethylene
PVC	Polyvinyl chloride
QMS	Quadrupole magnetic sorter
RBC	Red blood cell

RCL-2583	Mouse endothelial cell line
RNA	Ribonucleic acid
RT-PCR	Real time polymerase chain reaction
Runx2	Runt-related transcription factor 2
SEM	Scanning electron microscope
SKBR3	Human breast cancer cell
SKOV3	Ovarian carcinoma cell
SMC	Smooth muscle cell
SOG	Silicon-on-glass
SSA	Selective size amplification
SSC	Skeletal stem cells
ssDNA	single-stranded DNA
STRO-1-	STRO-1 negative
STRO-1+	STRO-1 positive
SW620	Colorectal cancer cell line
TCP	Tissue culture plastic
U937	Human histolytic lymphoma monocyte
WBC	White blood cell

List of Symbols

\vec{B}	Magnetic flux density [T]
f	Friction coefficient [$\text{N}^2\text{m}/\text{A}^2$]
\vec{f}	External force acting on the fluid [N]
\vec{F}_B	Buoyancy force [N]
\vec{F}_g	Gravitational force [N]
\vec{F}_h	Hydrodynamic force [N]
\vec{F}_m	Magnetic force [N]
\vec{F}_{mb}	Magnetic force experienced by a magnetic bead [N]
\vec{F}_{mc}	Magnetic force experienced by a labelled cell [N]
g	Gravitational constant [m/s^2]
\vec{H}	Magnetic field strength [A/m]
l	Characteristic length of the system [m]
m	Particle mass [g]
\vec{m}	Magnetic moment [A m^2]
\vec{M}	Magnetization [A/m]
p	Pressure [Pa]
r_b	Superparamagnetic bead radius [m]
r_c	Cell radius [m]
r_p	Radius of the magnetic particle [m]

Re	Reynolds number [unitless]
U	Magnetostatic potential energy [Nm]
\vec{v}	Velocity of the fluid [m/s]
v_b	Superparamagnetic bead average velocity [m/s]
v_c	Cell average velocity [m/s]
\vec{v}_f	Fluid velocity [m/s]
\vec{v}_p	Magnetic particle velocity [m/s]
V_b	Superparamagnetic bead volume [m ³]
V_c	Cell volume [m ³]
V_m	Volume of the magnetic material [m ³]
V_p	Volume of the magnetic particle [m ³]
η	Dynamic fluid viscosity [Ns/m ²]
μ_0	Magnetic permeability in free space [N/A ²]
μ_m	Magnetic permeability of the material [N/A ²]
μ_r	Relative magnetic permeability [unitless]
ρ_f	Density of the suspending fluid [kg/m ³]
ρ_m	Density of the fluid [kg/m ³]
ρ_p	Density of the particle [kg/m ³]
χ_b	Superparamagnetic bead magnetic susceptibility [unitless]
χ_c	Magnetic susceptibility of a labelled cells [unitless]
χ_f	Magnetic susceptibility of the suspending fluid [unitless]
χ_m	Magnetic susceptibility of the material [unitless]
$\Delta\chi$	Difference between χ_m and χ_f [unitless]

Acknowledgements

I would like to thank my supervisors Professor Richard Oreffo (Bone & Joint Research Group, Faculty of Medicine) and Professor Hywel Morgan (Electronics and Computer Science, Faculty of Physical Sciences and Engineering) for their support and guidance throughout this work. I would like to thank all my colleagues in the centre for hybrid biodevices and bone and joint group. A special mention goes to Dr David Gothard for his constant help over the years and to Dr Ambra Milani for her precious support. Finally, I would like to express my gratitude to my friends and parents for their never ending support through this project.

Chapter 1

Introduction

An increasingly aged population suffers from a range of degenerative diseases such as arthritis and osteoporosis. Osteoarthritis (OA) was the most common (91% of patients that underwent a hip replacement surgery have been diagnosed with OA) form of arthritis worldwide and the sixth leading cause of disability [17]. In severe cases, joint replacement may be necessary using non-biological prostheses such as hip replacement surgery.

Hip replacement surgeries are on the increase, with accompanying significant socio-economic costs. According to the National Joint Registry for England, Wales and Northern Ireland, 89,945 hip replacement procedures were conducted in 2013 with an increment of 4% from 2012. The increase was even more evident considering that hip replacement procedures conducted in 2010 were only 76,759 [1].

Despite the high number of hip replacement surgeries conducted every year, there are still risks related to the implantation of non-biological prostheses including dislocation, mechanical mismatch and functional failure. In these cases, a revision procedure is needed.

An alternative treatment, currently under research is the use of bone stem cells. Stem cell biology is a major component within the field of regenerative medicine and tissue regeneration [18]. In relation to the treatment of orthopaedic diseases, skeletal regeneration utilising skeletal stem cells (SSCs) is an area of intense research activity. SSCs can be derived from bone marrow (BM) and contribute to the regeneration of mesenchymal tissues such as bone, muscle, ligament, tendon and stroma. Their isolation and subsequent homogeneity affects their differentiation potential and therefore their clinical application. Conventional immunological methods such as fluorescence/magnetic activated cell sorting (FACS/MACS) are used to sort SSCs according to surface marker expression. Both techniques have limitations in terms of purity, running cost, mechanical complexity and the need for trained dedicated technicians, especially FACS.

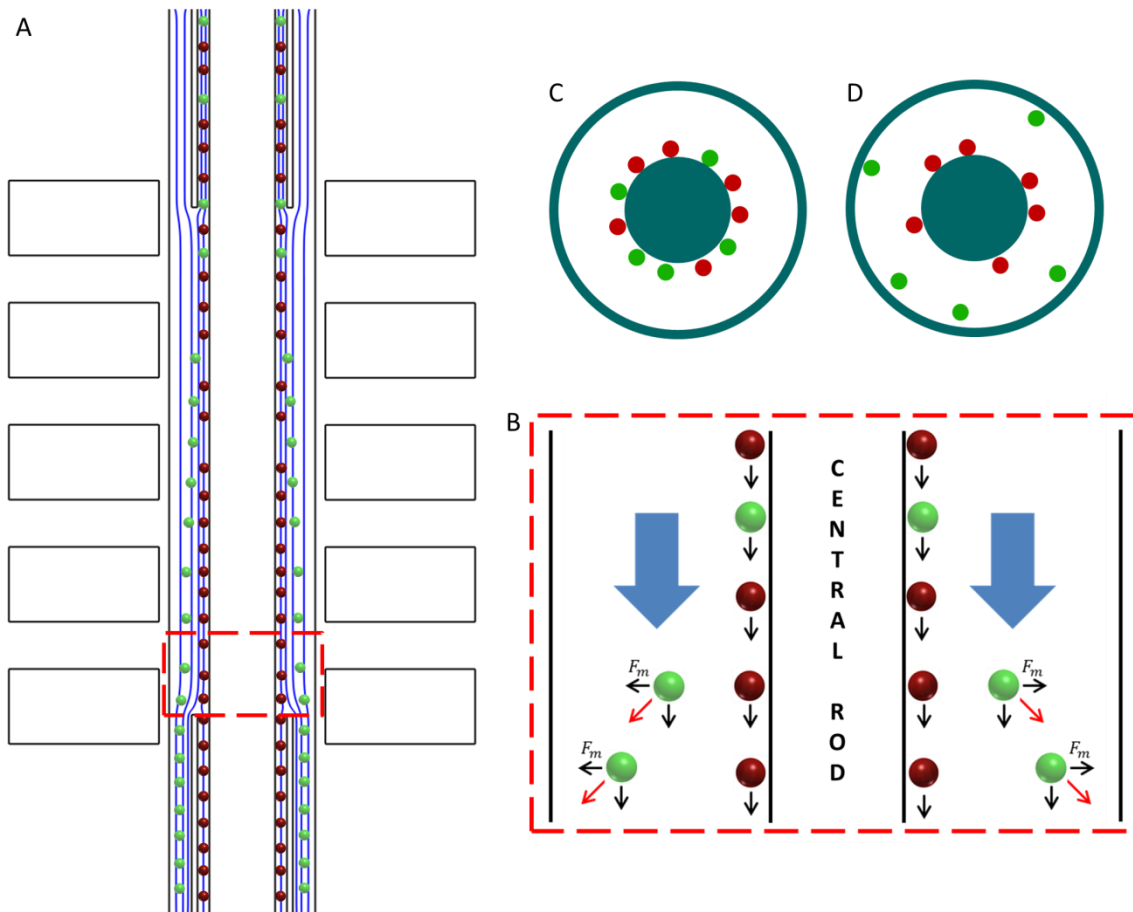


Figure 1.1: Diagrams showing the working principle of the sorting device. The mixed cell population (non-target cells in red, target cells in green) start in the inner stream. Under the influence of a magnetic field the target cells experienced a magnetic force (\vec{F}_m) and were pulled into the outer stream. (A) Overview of the device working principle on a vertical mid-section (B) and detail. (C, D) Diagrams showing the device working principle on a horizontal section.

A novel approach to resolve some of these issues involves the application of microfluidics, which offers the promise of reduced purification costs and enhanced stem cell enrichment. There are a number of microfluidic devices available, which use different sorting methods such as dielectrophoresis (DEP) [13], hydrodynamic forces [8], acoustophoresis [19] and immunomagnetic labelling [15]. Microfluidic devices allow for facile integration of several types of standard analytical operations. In addition, reagent consumption is dramatically reduced and therefore running costs. However, in some cases, an issue in the use of microfluidics is low throughput due to the small dimensions of the device and the sorting methods involved ($\mu\text{l}/\text{min}$ flow rate for optimum working conditions). Furthermore, microfluidic devices have reasonably expensive setup costs due to the essential peripheral

equipment typically required, including lasers, waveform generator, flow controllers and imaging apparatus (particularly in the sorting device using DEP - see Section 2.2).

The aim of this study was to develop a sorting device to isolate and characterise SSCs from human BM stromal cells (HBMSCs).

In brief, the study involves the use of a device to sort target cells by immunomagnetic cell separation (ICS). Superparamagnetic beads were functionalized with primary monoclonal antibodies raised against a specific cell surface marker. Target cells were labelled with superparamagnetic beads through primary antibody adhesion, enabling cell sorting within a magnetic field. In the interest of developing a rapid and simple continuous process of cell separation a magnetic cell separation system was utilised. The device consisted of a cylinder and concentric rod in which a stream can be generated to carry a mixed sample near the central rod, surrounded by a sheath flow. Immunomagnetically labelled cells experienced a drag force toward the outer stream due to a magnetic field generated by permanent neodymium magnets in a hexapole configuration. The device components were designed using 3D CAD software and built with rapid prototype techniques (3D printer, stereolithography). The aim of this study was to isolate SSCs according to expression of the surface marker STRO-1. The STRO-1+ cell fraction of BM was heterogeneous, exhibiting variable proliferative and differentiation potentials. BM mononuclear cells sorted according to STRO-1 expression were capable of establishing an adherent proliferative cell layer *in vitro* with colony-forming unit-fibroblastic (CFU-F) potential, a prerequisite of SSCs. STRO-1+ SSCs also demonstrate multi-lineage differentiation towards osteoblasts, chondrocytes and adipocytes [20].

The device sorting performances were investigated, using both human cell lines and HBMSCs. The sorting capacity of the developed device was compared to conventional MACS.

1.1 Skeletal Stem Cells

The term stem cell refers to a wide group for cells with the ability to self-renewal under controlled conditions and the capacity to differentiate into various cell types. SSCs represented the stem cell population within bone marrow stroma and are responsible for the innate regenerative ability of bones [21].

1.1.1 Mesenchymal stem cells

Over the years several definitions and names have been used to define the stem cell present in bone. More than 40 years ago, Alexander Friedenstein first discovered a population of tissue culture plastic-adherent cells within BM capable of differentiation towards osteoblasts, adipocytes, and chondrocytes [22,23]. These multipotential cells have various names, including: marrow stromal fibroblastic cells, SSCs, mesenchymal stem cells (MSCs), BMSCs, stromal precursor cells and osteogenic stem cells.

For several years, MSCs have been the preferred and commonly accepted term [21]. However, until 2005 there was a lack of a universally accepted set of criteria to define MSCs, which hindered comparison between studies from different research groups. In 2005 the 'Mesenchymal and Tissue Stem Cell Committee of the International Society for Cellular Therapy' proposed a minimum criteria to define human MSCs [24]:

- Ability to adhere to culture plastic;
- Expression of human MSC-specific antigen markers including: CD105, CD73 and CD90;
- Lack of expression of hematopoietic/endothelial markers including: CD34, CD45, CD14, CD11b and CD79 α ;
- Differentiation into osteoblasts, adipocytes and chondrocytes *in vitro*;
- Unlimited self-renewal under controlled conditions.

The term MSC referred to a common progenitor of a wide range of mesenchymal tissue, with a broad spectrum of lineage potentialities.

1.1.2 Skeletal stem cells

The idea of MSCs with wide differentiation potential was more recently replaced with the concept of a more specific group of stem cells, called SSCs. In this thesis, SSCs are defined as the self-renewing stem cell of bone marrow stroma. SSCs are responsible for the formation of bone, cartilage and fat [21].

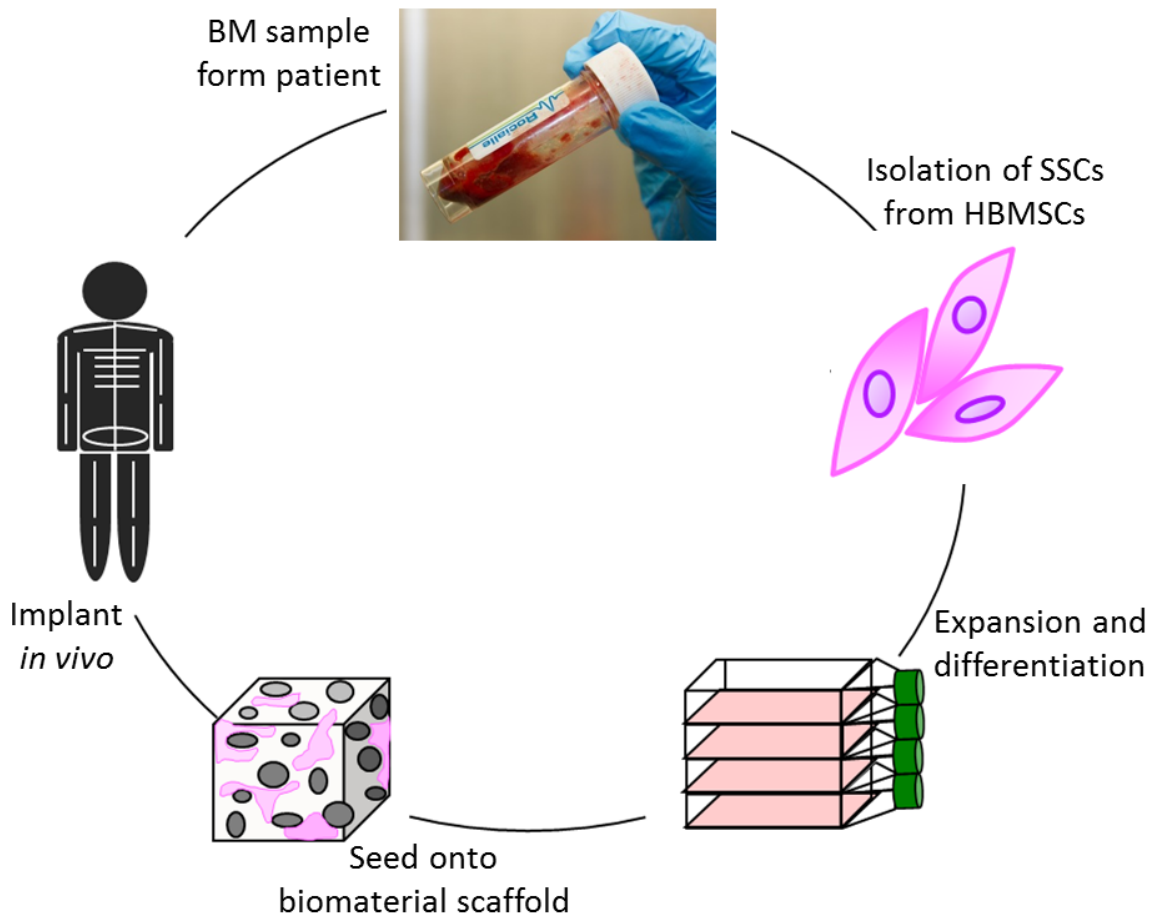


Figure 1.2: Cell-based strategy for bone regeneration. A bone marrow sample was collected from patient (typically aspirated from the iliac crest). SSCs were isolated from HBMSCs population. This plastic adherent cell population was subjected to *in vitro* expansion and differentiation. Afterwards, the SSCs were seeded (seeding density $\sim 3 \times 10^5$ cells/mm³) onto three dimensional biomaterial scaffolds to be implanted into the site of injury [2].

SSCs display all the characteristic properties of stem cells; capacity of unlimited self-renewal and differentiation potential. In addition, these tissue culture plastic (TCP) adherent non-haematopoietic cells have been isolated (with variable homogeneity) according to the expression of single or multiple antigens including CD105, CD73, CD90, CD29, STRO-1, CD106, CD146, CD166, CD271 and CD44. Furthermore, SSCs have been sorted by negative selection using CD19, CD45, CD34, CD14, CD11b and CD79 α . These antigens are haematopoietic markers and were used to deplete the non-target cell population [25].

1.1.3 SSCs in bone regeneration

In most cases, the regenerative capacity of bones was sufficient to repair bone fractures. However, in presence of large bone defects the healing could be partial. Regenerative medicine exploits the unique *in vivo* capacity of SSCs to repair or replace damaged tissue. SSCs were utilised in a number of clinical applications such as autologous bone grafting (ABG), which repairs complex fractures by implanting bone segments harvested from the patient. In this method, SSCs were transplanted alongside other cell populations within a pre-existing structure. However, this strategy is limited by source material, which drives research into alternative therapies [26].

Bone marrow aspirate (BMA) (typically from the iliac crest) is an acknowledged source of SSCs. Bone fractures have been treated with this technique with satisfying results [27]. Typically, the red blood cells population (present in the BM aspirated from the iliac crest) were depleted and the remaining mononuclear cells were injected, within 2 hours from the BM collection, to the site of injury [28]. However, BMA would not be sufficient to ensure skeletal regeneration in the conditions ideal for ABG

Limitations with these techniques (ABG and BMA), drove the research towards a cell-based strategy able to enhance bone regeneration. This strategy included isolation of SSCs from HBMSCs, their expansion and differentiation. Afterwards, cultured cells were seeded (seeding density $\sim 3 \times 10^5$ cells/mm³) in tissue engineered scaffolds, which functioned as three dimensional support structure, and implanted into the site of injury with local bone regeneration as final aim (Figure 1.2) [2].

One of the challenges faced by cell-based strategies was the isolation of homogeneous SSCs from the heterogeneous HBMSC population. The gold-standard approach was the use of conventional MACS to isolate SSCs based on expression of one or more SSC-surface markers.

Once isolated, SSCs needed to be expanded *in vitro* to achieve sufficient numbers for clinical application [2]. This process involved cell culture under controlled conditions, whilst preserving cell phenotype. However, expansion of SSCs was a complex process due to limited cell proliferation capacity, following successive culture. Furthermore, senescence have been reported in BMSCs obtained from elderly human patients as consequence of *in vitro* culture [29]. The use of SSCs in bone regeneration depended significantly on the cell expansion process, which was the most challenging aspect in cell-based strategies. Consequently, several approaches have been investigated to optimise this procedure, including the use of growth factors and dynamic culture environments.

An approach employed by Mizukami *et al.*, involved the application of a disposable fixed bed culture system capable of efficient expansion of human cord blood-derived MSCs

(hCBMSCs) while maintaining their differentiation potential. The system consisted of an immobilized scaffold (Fibra-Cell disks, New Brunswick Scientific) in a disposable sterile bottle. The system automatically raised or lowered the medium level in the bottle where the cells were seeded, ensuring correct diffusion of oxygen and nutrients, key to successful cell expansion [30]. Moreover, for the cell expansion process, a high initial SSCs cell number would be beneficial to *in vitro* expansion given the ability to thus reduce both culture period and passage number prior to utilisation. Reduced passage number was especially important as serial *in vitro* passage have been shown repeatedly to result in the emergence of a dominating fibroblastic phenotype [31].

The differentiation step consisted in leading the differentiation of human SSCs into osteoblast cells. This procedure was based on the addition of growth factors and hormones to the cell culture media (dexamethasone, calcitriol).

The use of SSCs for local bone regeneration usually depends on the efficiency of the osteoinductive scaffold. Several materials were used to manufacture these structures, including synthetic polymers, ceramics and materials based on hydroxyapatite .

For years, tissue engineered scaffolds were implemented purely as culture supports offering minimal osteoconductivity and osteoinductivity. More recently, scaffolds had evolved with the use of biomaterials which offer osteoconductive properties and can be tailored to deliver osteoinductive signals through controlled distribution of biochemical cues influencing cellular metabolism and differentiation [32,33].

1.1.3.1 Clinical applications

To translate SSC-based bone regeneration to the clinic, it was imperative that reproducible methods for cell growth and differentiation were developed. To date, clinical use of SSCs had typically been limited to patient specific application.

The most abundant cell-based strategy for bone regeneration was direct transplantation of HBMSCs to damaged tissue. However, the need for high numbers of osteoprogenitor cells within these strategies was prevalent. Therefore, cell enrichment and *in vitro* culture expansion were important factors to be considered.

The majority of reported studies had utilised autologous bone marrow mononuclear cells (BM-MNC) isolated from iliac crest BMA alone or within scaffolds [21]. The BM-MNC population remain heterogeneous, containing HBMSCs as well as other kinds of cells (endothelial and haematopoietic). Nevertheless, BM-MNC-based therapies had achieved good results in some studies in the treatment of non-union fractures [34]. A restricted number of studies has been conducted with autologous *in vitro* expanded HBMSCs.

One example was the study conducted by Kitoh *et al.* [35], which used autologous *in vitro* expanded HBMSCs in the treatment of tibial osteotomies with good outcomes.

Studies based on SSC-based (autologous and allogeneic) tissue regeneration are ongoing, however, the efficacy of the SSC-based strategy needs to be compared to standard therapies. To do that, reproducible and standardised methods to isolate, expand and differentiate SSCs are needed [21].

1.1.4 Summary

An increase in life expectancy had also led to an increase in age-related diseases including osteoarthritis and osteoporosis. In severe cases, joint replacement was required (e.g. hip replacement surgery). These surgeries had significant socio-economic impact, and several limitations. An alternative strategy was the application of cell-based therapies. In the area of orthopaedic diseases, skeletal regeneration utilising SSCs was currently under intense investigation. SSC-based bone regeneration therapy requires high cell numbers for clinical application, with a homogeneous cell population. The homogeneity of the SSC population affects their differentiation potential and therefore their clinical application.

The device developed in this study intended to improve the cell sorting capabilities of conventional MACS in both purity of sorted cells and recovery efficiency. A more homogeneous SSCs cells population would be beneficial for any tissue engineering strategies. Moreover, increasing the recovery efficiency would facilitate the *in vitro* cell expansion, which was the most challenging aspect of cell-based strategies. In addition, reducing the culturing period and passage number prior to utilisation would be beneficial to preserve the cell differentiation capability, thus as serial *in vitro* passages have been shown to result in the emergence of a dominating fibroblastic phenotype [31].

Chapter 2

Literature Review

Magnetic activated cell separation (MACS) and fluorescence-activated cell sorting (FACS) represented two of the most commonly used immunological methods for sorting cell populations. Critical for each process was an appropriate, specific antigen present on the cell surface. Each process used comparable separation times and sample sizes and has been employed across the biological spectrum [36]. Current MACS and FACS applications for cell separation, as well as alternative microfluidic strategies for cell isolation were discussed here. Most published work investigated sorting methodology for circulating tumour cells (CTCs), however the principles could be easily adapted for SSC sorting.

2.1 Traditional Sorting Techniques: MACS & FACS

MACS was a well-established laboratory (bench) technique used to purify a range of cell types including the enrichment of SSCs from bone marrow. This method was often referred to as “bulk technique” due to the fact that it was applied to all the cells of the sample at the same time. In the case of SSCs isolation, STRO-1 antibody, was added to a mixed population of BM cells. After incubation for a few minutes at 4°C, magnetic beads, (\varnothing 50 nm) labelled with Anti-mouse secondary antibodies were added (Figure 2.1).

The primary antibody bound to a specific antigen on the target cell surface, and bound to magnetic beads through secondary antibody interaction. Labelled cells can be isolated from non-target cells by passing the cell suspension through a column between magnets. The column contains ferromagnetic spheres forming a matrix maximizing the contact surface and the effect of the external magnetic field on labelled cells. MACS can be used as positive or negative sorting method and was viewed as an efficient and economical process, with a total throughput in the range of 10^7 cells per second [37].

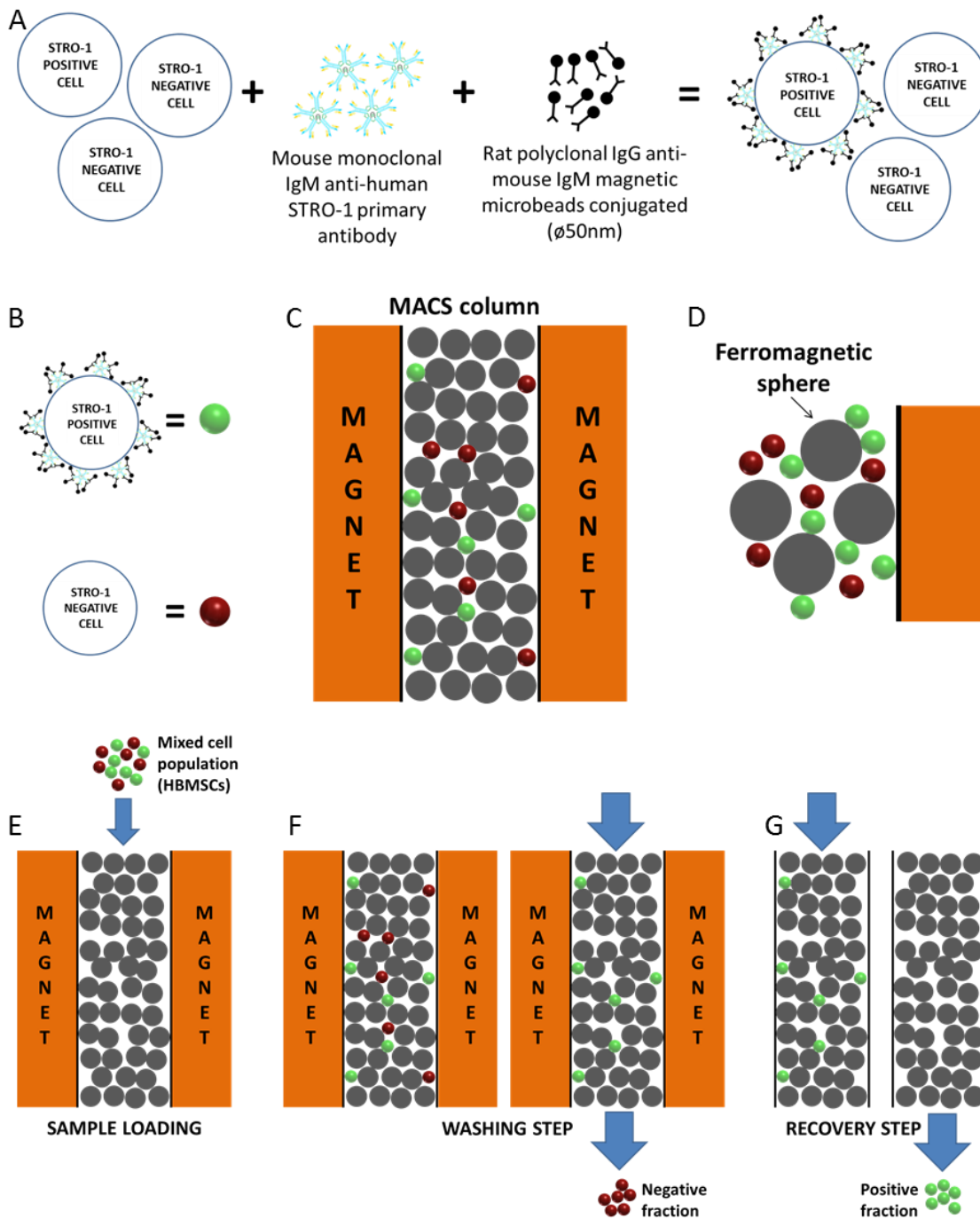


Figure 2.1: Schematic diagram of the MACS procedure. (A) Two step immunostaining consisting of labelling mixed cell population with STRO-1 primary antibody labelling and MACS beads. (B) Green and red spheres represented target and non-target cells, respectively. (C) Mixed cell population loaded in a MACS column surrounded by the magnet. (D) Particular of the ferromagnetic spheres within the column trapping immunomagnetically labelled cells (green spheres). (E) MACS protocol. Mixed cell population loaded in a MACS column. (F) Washing step. Non-target cells were washed away and collected (negative fraction) while the target cells remained within the column. (G) Recovery step. Target cells were removed from the column (positive fraction).

However, the purity of the sorted cells was typically 70% or less when target cells were a minority of the cell population. This occurred as a consequence of non-specific adhesion between unlabelled cells and the matrix within the MACS column. This was the case for SSCs in a BM sample which, typically represented 1 in 10-40,000 of the total cell population [38].

FACS was developed by Herzenberg et al.[3], to enable single cell sorting and was useful when the target cells represented a minority of the total amount of cells in the sample. The target cells were labelled with a fluorescent dye using a specific antibody and pumped into a flow chamber. The sample was divided into droplets by a vibrator nozzle, each droplet was illuminated by one or more laser beams and the emitted fluorescent signals detected by optical sensors [39]. According to these signals, the polarity of the high-voltage deflection plates was switched and the droplets were directed to collection or waste chambers (Figure 2.2). The flow rate was controlled to minimize the possibility of multiple particles being narrowed in the same droplet. This method had a sorting rate in the region of 70,000 cells per second and the potential to detect a number of different target cells, simultaneously through application of 12 colour labelling strategies each with a different emission wavelength [40]. However, it should be noted 12 lasers approaches had significant associated costs and related mechanical complexity [41].

Traditional immunological techniques such as FACS and MACS had limitations in the degree of purity of sorted cells and level of cell viability post-sorting that can be achieved [36,42]. Both methods typically produce a decrease in cell viability of 20-25% with a purity of around 90% for FACS and 80% for MACS.

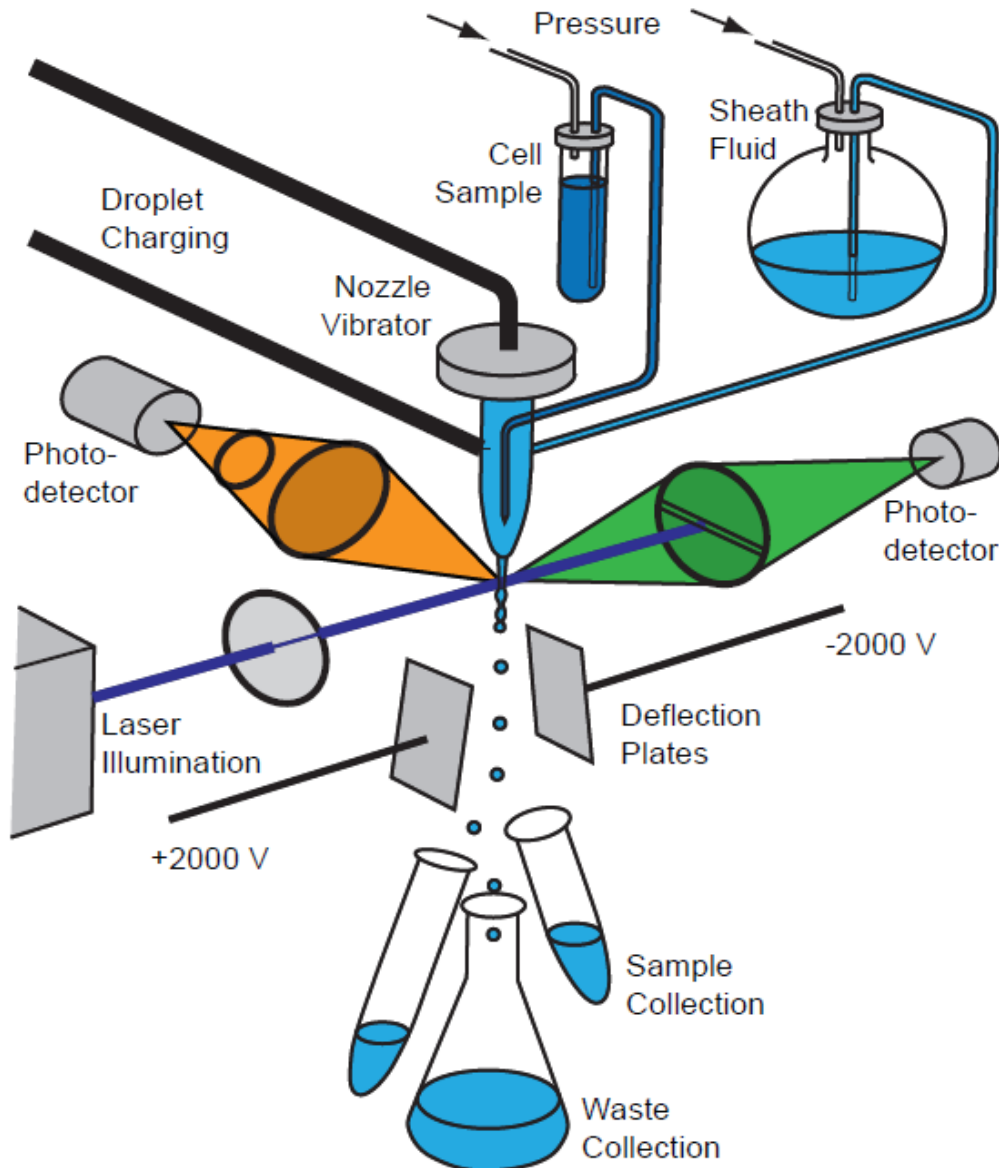


Figure 2.2: Schematics of the equipment used for FACS procedure. Target cells were labelled with a fluorescent dye using a specific antibody and pumped into a flow chamber. The sample was divided into droplets by a vibrator nozzle, each droplet was illuminated by one or more laser beams and the emitted fluorescent signals detected by optical sensors. According to these signals, the polarity of the high-voltage deflection plates was switched and the droplets were directed to collection or waste chambers [3].

2.2 Microfluidic Techniques

To address the limitations of MACS and FACS, microfluidics had come to the fore as an approach to enhance the purity and throughput of isolated cell populations. Microfluidic devices offer facile integration of a number of analytical standard operations and offer the promise of reduced reagent and running costs. Critically microfluidic devices had dimensions comparable to the intrinsic cell dimensions, which imply the possibility to manipulate single cell and thus enhance cell

isolation purity in combination with exquisite fluid flow control. However, the sorting rate was typically slower than observed with classical methods [43,44,45].

2.3 Classification of Microfluidic Devices

Microfluidic devices can be classified according to the discrimination parameters employed: i) affinity based, ii) size based and iii) immunomagnetic based cell separation.

Affinity based separation and immunomagnetic cell sorting rely on the biological characteristics of the cells of interest, in particular on the expression of specific surface markers. Affinity based approaches used functionalized surfaces to trap label-free cells, taking advantage of ligand-cell bonding within the microfluidic device.

Size based techniques utilise physical properties of the desired target cells to isolate the cells from the background cell population. Devices using this method employed a label-free cell separation approach and examples include: hydrodynamics, filtration, dielectrophoresis, acoustophoresis and cell deformability.

Immunomagnetic approaches rely on external magnetic field to manipulate target cells labelled with functionalized magnetic particles. Magnetically labelled cells were separated from the background cells within the device, enabling continuous cell sorting.

The following details each approach with a final summary table detailing state of the art devices for rare cell isolation.

2.3.1 Affinity based isolation

Affinity based isolation utilised the advantages of non-covalent bonds between molecules immobilized on a surface and an antigen expressed on the target cell membrane. The blend of this technique with microfluidics allowed for the generation of a device with high surface area. The features within a microfluidic device were in the same dimension range as a cell, and allow for the design of devices using geometrically enhanced differential

immunocapture (GEDI) [46]. The application of specific geometries increased the possibility of contact and bonding between target cells and a functionalized surface.

When target cells interact with the capture surface, cells were held in place by the bonds formed against the shear force due to flow within the microfluidic device, while background cells were removed.

It was important that the flow rate was optimized to allow cell-surface interactions and to generate sufficient shear force to prevent non-specific capture [47]. Cell isolation approaches could employ negative or positive capture - in the first method background cells were retained in the device, and target cells were collected from the device output. An affinity ligand unique to the target cells of interest was required for positive selection techniques. Surface coating molecules for affinity-based isolation comprise aptamers, proteins and antibodies [48]. This approach have been extensively applied to the isolation of CTCs from whole blood. The detection of CTCs from peripheral blood was an indicator of metastasis (the mechanism through which tumour cells leave the primary tumour and cause secondary tumours at distant sites, travelling through the circulatory system). The detection and isolation of CTCs from peripheral blood was an important tool for cancer diagnosis and prognosis although the rarity of these cells was a significant challenge.

There can be just a few CTCs among 5 million white blood cells (WBCs) and 5 billion red blood cells (RBCs) in 1 ml of whole blood. Epithelial cell adhesion molecule (EpCAM), have been widely used as a biological parameter to isolate CTCs. EpCAM was frequently overexpressed by carcinomas of lung, colorectal, breast, prostate and was absent on hematologic cells surface, thus enabling the requisite to isolate CTCs [49].

The food and drug administration (FDA) had approved CellSearch™ an automated system to capture CTCs from blood samples for prognosis and treatment of a variety of cancer types. CellSearch used anti-EpCAM ferromagnetic nanoparticles to separate CTCs from background cells [11]. However, this technique needs preliminary centrifugation and dilution of the blood sample and, currently, can only identify CTCs in half of all cancer blood samples [49]. One of the microfluidic features adopted to isolate CTCs was the use of array of posts grounded on the bottom of the channel. This approach aims to increase the surface functionalized with a specific ligand.

Nagrath *et al.* in 2007, developed a microfluidic system, CTC-chip, consisting of a microfluidic chip engraved in silicon, a manifold and a pneumatic pump [4]. The device was composed of an array of 78,000 microposts (100 μm in diameter and 100 μm tall) functionalised with anti-EpCAM antibodies, with a total capture surface of 970 mm^2 (Figure 2.3). To evaluate the device capture performance, Nagrath *et al.* spiked the lung cancer cell line (NCI-H1650) in whole blood samples of healthy donors.

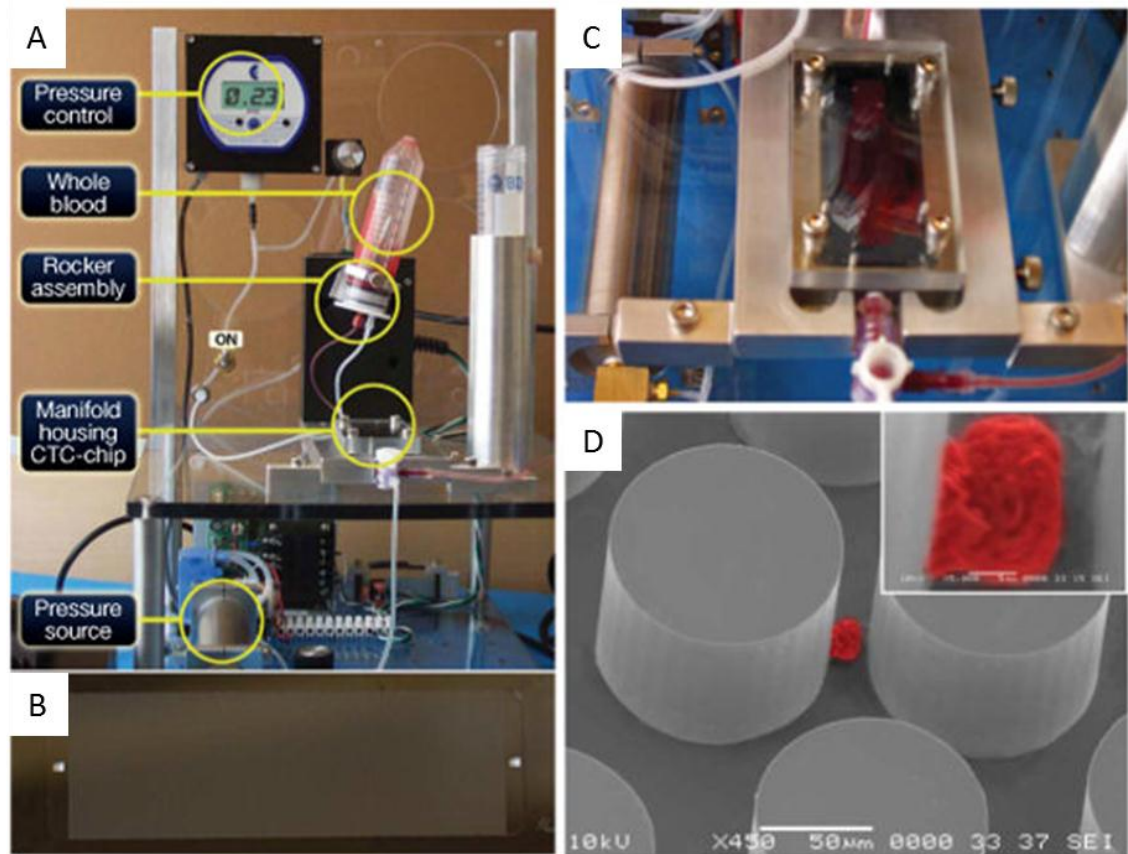


Figure 2.3: (A) Overview of the experimental setup (Nagrath *et al.*); (B) the dimensions of the CTC-chip were 25 mm x 66 mm, with the capture area of 19 mm x 51 mm; (C) device filled with blood; (D) SEM image of a captured cancer cell (NCI-H1650) [4].

Samples with concentrations from 50 to 50×10^3 of NCI-H1650 per ml of whole blood were examined using a flow rate of 1ml/h. The authors reported a 60% cancer cell recovery rate. To investigate the CTC capture ability of the device, Nagrath *et al.* tested the system using whole blood samples from cancer patients. Analysis of 116 samples from patients affected by different kinds of epithelial cancers, identified CTCs in 115 out of 116 samples. The number of cancer cells captured ranged from 5 to 1,281 CTCs per ml of blood, and the authors reported an average purity of 50%.

Stott *et al.* tried to improve the performance of the CTC-chip, creating a “Herringbone chip” (HB-chip), able to create a micro vortex within the microfluidic device, to increase the potential for collisions between target cells and functionalised walls [5]. The device comprised eight polydimethylsiloxane (PDMS) channels with a herringbone structure on the upper surface, bonded to a glass substrate using soft lithography (Figure 2.4). The internal surfaces of the device were functionalized with anti-EpCAM antibodies, and to investigate the capture ability of the system.

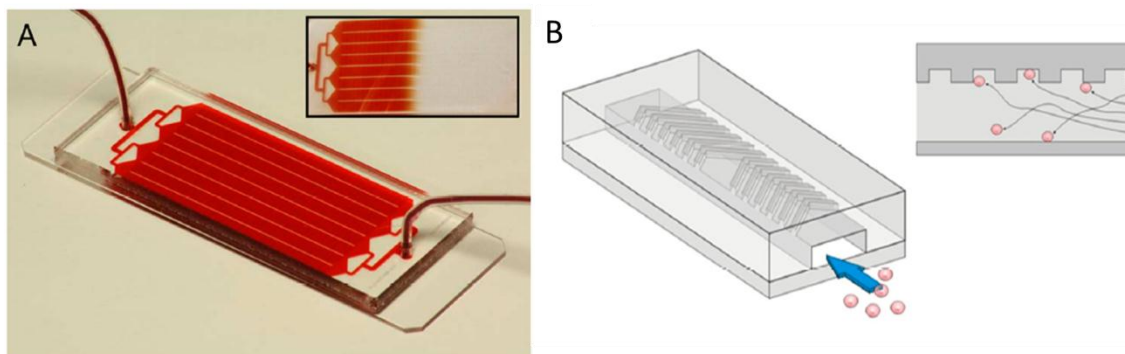


Figure 2.4: (A) The Herringbone chip (HB-chip) (Stott *et al.*) glass slide (25 mm x 75 mm) serving as a substrate for the microchannels with herringbones feature on the upper wall. The device had a single inlet and outlet; (B) Illustration of the interaction between cells and microfluidic pattern [5].

Prostate cancer cells (PC3) were spiked in whole blood of healthy donors. The authors observed a cancer cell recovery of 91.8% from whole blood samples using a flow rate of 1.2 ml/h. Moreover, the HB-chip was used to isolate CTCs from 15 cancer blood samples. Experiments performed with the same parameters optimized from tests using the PC-3 cell line, revealed the presence of CTCs in 14 of the 15 cancer blood samples investigated.

In 2013, Yoon *et al.* [6] published a study on the use of functionalized graphene oxide nanosheets on a patterned gold surface to isolate CTCs. The device comprised of a silicon substrate with thousands of flower-shaped gold patterns (100 μm x 100 μm). On the gold features, nanosheets of graphene oxide were adsorbed and functionalized with anti-EpCAM antibodies (Figure 2.5). A PDMS structure was bound on the affinity capture substrate to create a microfluidic chamber (height of 50 μm). Breast cancer cells (MCF-7) spiked in whole blood from healthy donors, were then used to characterize the device. Three concentrations of MCF-7 (3-5 cells, 10-20 cells, 100 cells) per ml of whole blood were investigated, and using a flow rate of 1ml/h, the device recovery yielded was 73%, 94.2% and 87.3% respectively. The graphene oxide chip was also used to isolate CTCs from 20 samples of whole blood obtained from patients affected by breast, lung and pancreatic cancer. The device captured cancer cells from each sample with a concentration ranging from 2 to 23 CTCs per ml of blood.

In 2012, Sheng *et al.* developed a microfluidic system for the isolation of CTCs from whole blood [7]. The device comprised more than 59,000 elliptical pillars (30 μm x 15 μm x 32 μm) grounded on a glass substrate (25 mm x 75 mm) and a PDMS layer bonded on the glass to create the microfluidic channels (Figure 2.6). The internal surfaces of the device were functionalized through physical adsorption of avidin on the glass substrate

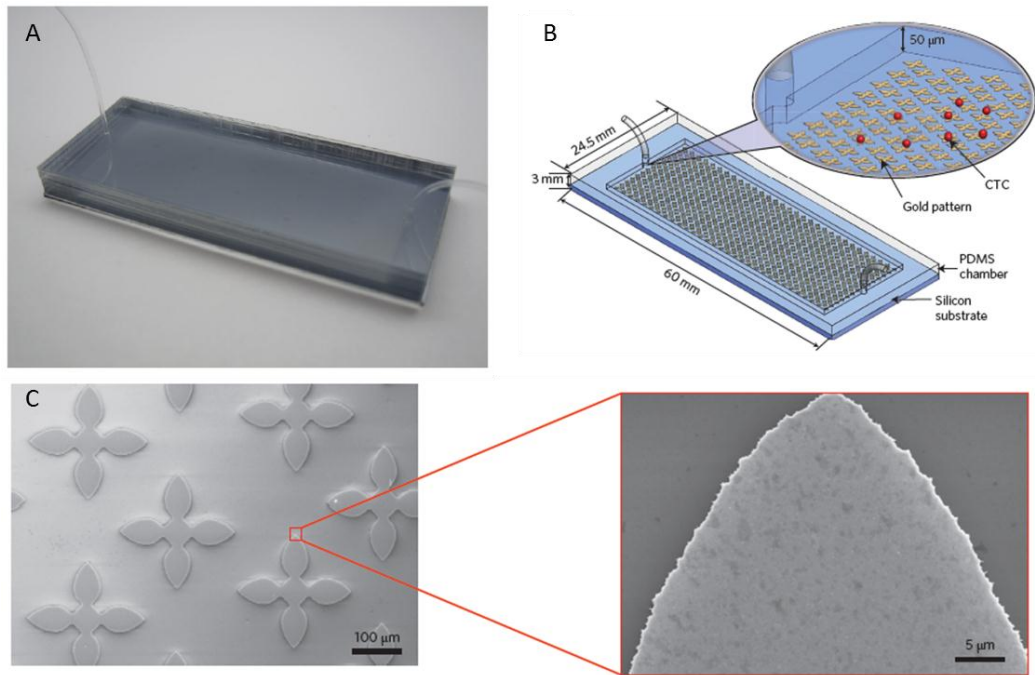


Figure 2.5: (A) Picture of the affinity based capture microfluidic device (Yoon *et al.*); (B) Schematic of the graphene oxide chip; (C) SEM image of the flower-shaped gold patterns and magnified SEM image of adsorbed graphene oxide nanosheet [6].

followed by the binding of biotinylated KCHA10 aptamers. To characterize the device isolation ability, the authors spiked colorectal carcinoma cells (HCT116) in whole blood from healthy donors at a concentration of 10 cells/ml. Exploiting the interaction among the cell surface receptors and the aptamers, positive selection experiments were performed. Using a flow rate of 2.16 ml/h, the device achieved a recovery efficiency of 95% with a purity of 81%.

Saliba *et al.* developed a device using self-assembled magnetic beads functionalized with anti-CD19 to form columns functioning as posts. The authors captured B-lymphoid cells (Raji cell line) suspended in a population of T-lymphoid cells (Jurka cell line) [50]. The device comprised a PDMS channel on a glass substrate. An array of magnetic ink dots was present on the channel bed. When a perpendicular magnetic field was applied, the beads re-arranged to form columns in alignment with the magnetic ink dots. Positive selection experiments were performed, achieving a capture efficiency of 97% with a flow rate of just 9 μ l/h. To increase the flow rate, the researchers developed a device using the same principles and included a microfluidic geometry for high flow rate, called a Diamond-tree [51]. The aim of this device was to increase the capture surface and the authors observed comparable capture efficiency with a flow rate of 2 ml/h.

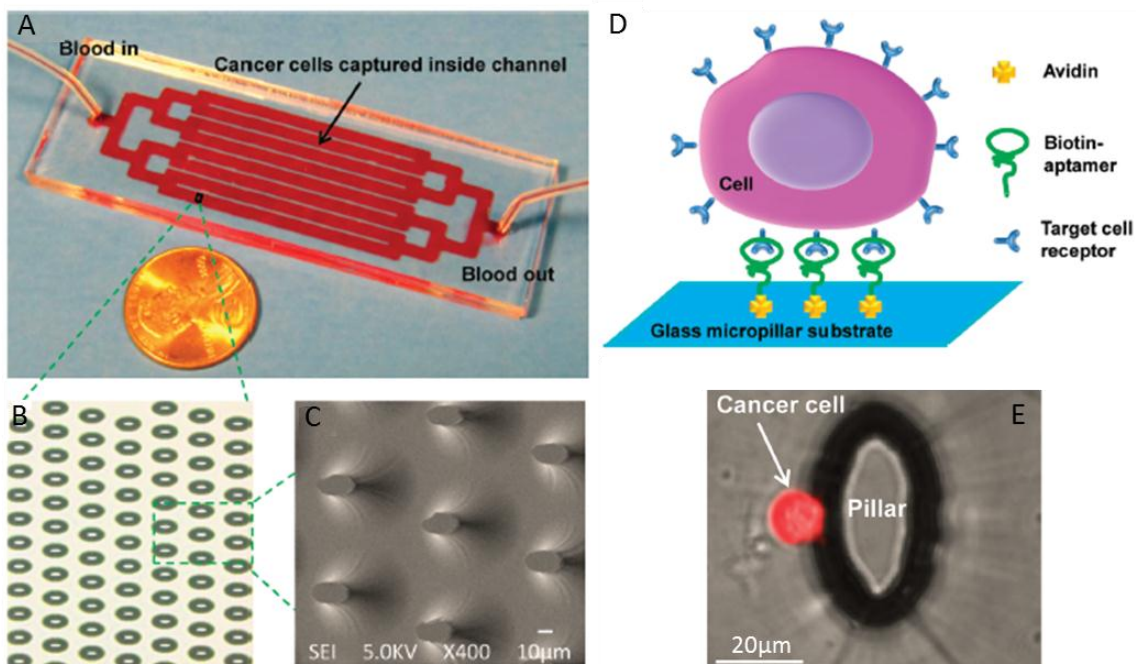


Figure 2.6: (A) Microfluidic device from Sheng *et al.* comprising a glass substrate (25 mm x 75 mm) and a layer of PDMS that create 8 channels with posts on the bottom. The device had a single inlet and outlet; (B) array of posts (C) and scanning electron microscope (SEM) image; (D) capturing cell mechanism within the device; (E) cancer cell captured on the functionalized post surface [7].

Affinity based capture techniques present advantages such as capture efficiency, in the range of 90%, and flow rate of 1-2 ml/h. Furthermore, these devices were able to detect few target cells suspended in high number of background cells (e.g. CTCs in whole blood), maximising the capture surface using geometrically enhanced patterns within the microfluidic device. However, when the dimensions of target and non-target cells were similar the possibility of non-specific binding was high, resulting in low purity of the captured cells. In addition, negative selection performed with this technique can cause the blockage of the device due to the large number of background cells compared with target cells. In this Section several affinity based devices were described, particularly interesting were the devices developed by Nagrath *et al.* [4] and Stott *et al.* [5]. Both devices used affinity based separation to isolate CTCs from whole blood. The samples used in these devices did not need any dilution or preparation; the devices were able to process more than 1 ml of whole blood per hour (1.2 ml/h Stott *et al.*) achieving high values of recovery. Moreover, the authors characterized the devices' performances using cancer cells, and

then isolated CTCs from whole cancer blood samples with good results (see Table 2.1). More recently Yoon *et al.* (2013) [6] published a study on the use of functionalized (anti-EpCAM) graphene oxide nanosheets to isolate CTCs. The authors tested the potential of the device to isolate CTCs from whole blood of cancer patients. The graphene oxide chip captured CTCs from each of the 20 samples analysed.

2.3.2 Size-based separation

Size-based separation used the size difference between target and background cells as the separation parameter. There were numerous methods to exploit the physical characteristics of target cells, including hydrodynamics, filtration, dielectrophoresis, acoustophoresis, magnetophoresis and deformability. The methods employed physical parameters to perform label-free cell sorting, with minimal sample preparation required. However, selective size amplification used biological and physical characteristics at the same time offering an intermediate strategy between affinity and sized based approaches.

2.3.2.1 Selective size amplification (SSA)

This technique used functionalized microbeads to enhance the size difference between target cells and background cells. A good example of this method was published in 2012 by Kim *et al.* whom developed a microfluidic device using a selective size amplification (SSA) technique to isolate CTCs from whole blood. The device used a multi-obstacle architecture (MOA) filter to capture target cells. The SSA technique utilised functionalised polymer microbeads with anti-EpCAM antibodies to target cancer cells over WBCs. The MOA chip was developed using a silicon-on-glass (SOG) technique and was made up of 3,900 obstacles arranged in a zigzag array providing a capture area of 38.88 mm². MCF-7 cells (used to mimic CTCs) were labelled with 3 µm anti-EpCAM functionalized beads and spiked in whole healthy blood at two different concentrations. Experiments were performed using a flow rate of 1.2 ml/h, and the device yielded a recovery efficiency of 99.1% and 89.7% using cancer cells concentration of 100 and 10 cells per ml of blood respectively [52].

Lin *et al.* conducted a study with a high throughput device, using 3 µm beads coated with anti-EpCAM antibodies, to label CTCs and amplify their size. The microfluidic system contained a number of wave ducts with sharp turns that acted as a micromixer to tag CTCs with anti-EpCAM beads, and a microfilter. MCF-7 cells were spiked into the buffy coat (diluted with PBS) of healthy blood to mimic the CTCs presence, and using a flow rate of 36 ml/h, 91.3% of cancer cells were recovered [53].

2.3.2.2 Size-based separation: Hydrodynamics

This method relied on the hydrodynamic forces experienced by particles in a laminar flow regime. Microfluidics was used to separate cells based on the behaviour of the cells to the force experienced which will vary depending on the size of the cell.

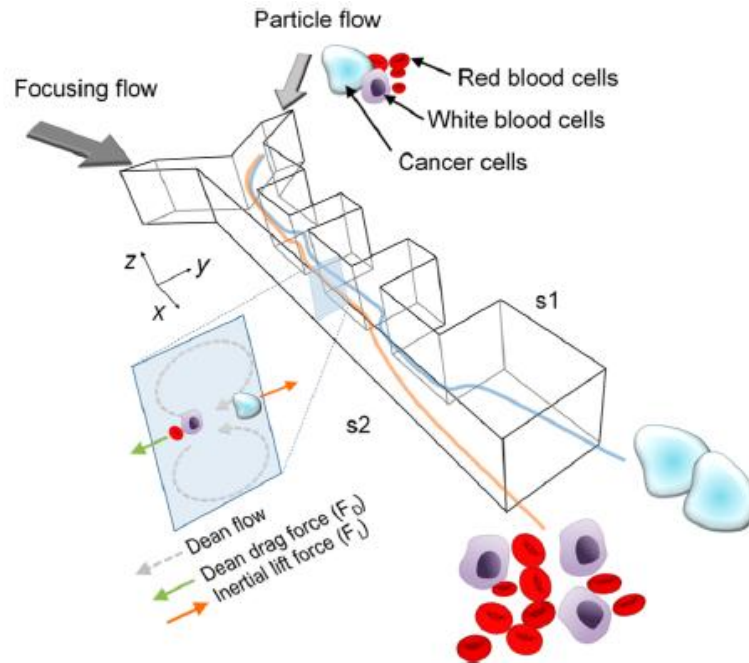


Figure 2.7: Schematic of the microfluidic device and the separation principle (Lee *et al.*). The CTCs and the blood cells experienced both inertial lift and Dean drag forces and the cell trajectory depends on the balance of the two forces. Cells within the device were separated via two outlets according to dimensions [8].

Lee *et al.* [8] developed a microfluidic device capable of isolating CTCs from whole blood using hydrodynamics field effect to perform label-free cell sorting. The device was made up of a PDMS channel (350 μm wide and 63 μm height) with six rectangular structures (50 μm wide and 1200 μm long) with intervals between them of 700 μm (Figure 2.7) and two inlets, for the focusing flow and particle suspension respectively. The parts of the channel free from any structures were called “expansion regions”, which were alternated with “contraction regions” in correspondence with the rectangular obstacles. The device used inertial effects like inertial lift force and Dean vortices to isolate CTCs (15-30 μm in diameter) from the background blood cells (2-15 μm in diameter). The Dean vortices usually arise in coiled pipe, in this circumstance the velocity differences in the tube cross-section caused the centrifugal forces to vary, forming vortices. Through the use of contraction and expansion regions, the authors promoted the formation of Dean vortices within the microfluidic device. When a fluid from an expansion region entered a contraction region, the flow streamlines experienced acceleration, following a curved trajectory producing the Dean vortices. Cells flowing within the device experienced both inertial lift and Dean drag forces from opposite directions. The magnitude of these forces depend on the cells dimensions. CTCs were predominantly subjected to inertial lift force,

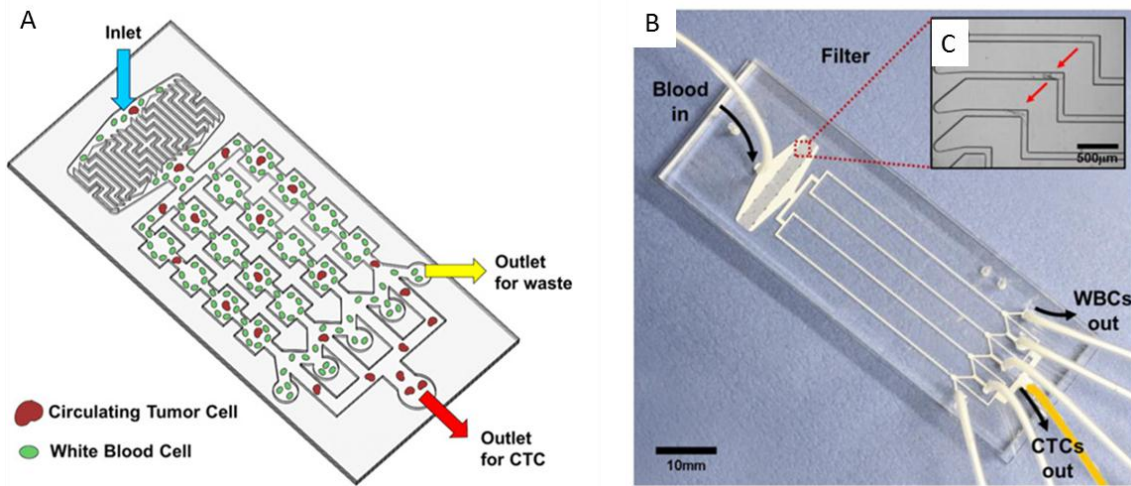


Figure 2.8: (A) Schematic of the p-MOFF device (Hyun *et al.*). Within each channel the CTCs were focused at the centre and collected in the target outlet; (B) picture of the device, consisting of one inlet, four MOFF channels and six outlet (just one of them was the target outlet); (C) the channels were preceded by a filter [9].

while blood cells (RBC and WBC) were mainly influenced by Dean flow. This phenomenon allows to sort and collect CTCs from two different outputs. To validate the separation performance of the microfluidic device, MCF-7 were spiked into whole blood samples to mimic the CTCs behaviour and then pumped through the device at a total flow rate of 6 ml/h (PBS plus blood). The cancer cell recovery efficiency yielded was 99.1% with a purity of 88.8% and a cell throughput of 1.8×10^6 cells/s. In addition, the purity increased when two devices were connected in series to 97.4%.

Hyun *et al.* [9] developed a PDMS parallel multi-orifice flow fractionation (p-MOFF) microfluidic device for size-based CTCs isolation. The device comprised four parallel channels each containing contraction and expansion chambers generating inertial hydrodynamic forces allowing label-free cell separation (Figure 2.8). Before the MOFF channel, a filter was placed to avoid device blockage due to the presence of debris. The filter consisted of a series of channels (60 µm wide) presenting sharp bends, and ensures a device life span of 1 hour (without filter the device running life would be 5 min).

To evaluate the device separation performance, human mammary gland adenocarcinoma (MDA-MB-231) and MCF-7 were added to buffy coat derived from blood of healthy volunteers.

The cancer cells were influenced by the inertial lift forces comparison to the smaller WBC, consequently the cancer cells were focused in the middle of the channel and collected in the central outlet. The cell suspension was pumped through the device at 36 ml/h,

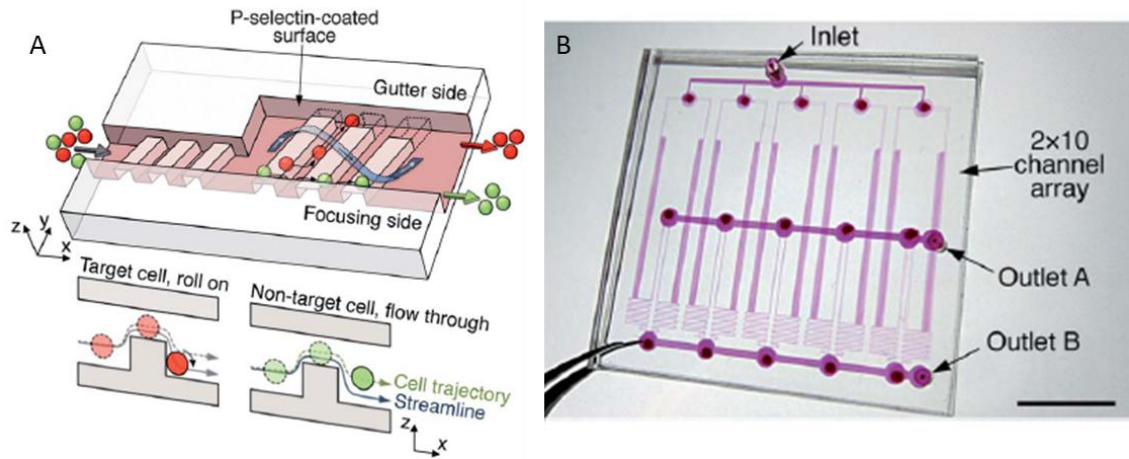


Figure 2.9: (A) Diagram of a single channel with focusing and sorting ridges (Choi *et al.*). Target cells roll on the functionalized surfaces following the trench, while non-target cells flow above the ridges; (B) picture of the microfluidic device comprising 20 channels on two layer [10].

resulting in a recovery efficiency of 91.6% and 92.7% for MDA-MB-231 and MCF-7 respectively. The device sorting ability was tested using blood samples from metastatic breast cancer patients. The authors examined 24 blood samples (7.5 ml each) and CTCs were isolated from 19 samples in a concentration ranging from 1 to 21 CTCs per sample.

Choi *et al.* [10] developed a microfluidic device capable of label-free cell separation using both cell-surface interaction and hydrodynamic forces. The phenomenon occurring within the device was called cell rolling and involves the formation and degradation of transitory cell-surface bonds. The device was made up of twenty PDMS channels arranged in two layers. Each channel comprised a narrow (100 μm) and a wide (670 μm) section, providing focusing and sorting ridges respectively (Figure 2.9). The internal surfaces of the device were functionalized with a specific ligand (P-selectin) and two leukemia cell lines, HL60 and K562, were used as target and background cells respectively.

Target cells in contact with a ridge, started rolling on the functionalized surface, following the ridge geometry and entering the trench between the ridges to the sorting outlet. Non-target cells failed to roll on the functionalized surfaces, flowing above the ridges without entering the trenches and were collected in the waste outlet. HL60 and K562 were suspended in PBS (in a ratio of 2:3) and pumped through the device at 4.2 ml/h. The device yielded a recovery efficiency of 80%, with a purity of 94% and a cell throughput of 277 cells/s.

Hydrodynamic force based devices for size-based cell separation offer a label-free process providing a simple low cost sample preparation procedure.

Moreover, these devices operate at high flow rate (in the order of tens ml per hour) with throughput in the order of thousands of cells per second. However, to perform the separation the hydrodynamic forces within the devices had to be finely controlled, involving the dilution of the samples in buffer with known properties. In addition the size overlapping of target and background cells was a limitation of all the devices relying on physical parameters to perform cell separation.

Given the high throughput and purity, the work of Lee *et al.* [8] stands out among the works carried out using hydrodynamics technique to perform size based label-free separation. The authors developed a system capable of separating rare cells from whole blood. MCF-7 cells were spiked into whole blood samples to mimic the CTCs behaviour and the device achieved a recovery efficiency of 99.1%, a cell throughput of 1.8×10^6 cells/s. The purity of the sorted cells was 88.8%. However, this value rose to 97.4% when two devices were connected in series. Not negligible was the work described by Hyun *et al.* [9] who isolated CTCs in 19 out of 24 buffy coat extracted from cancer blood samples (see Table 2.1)

2.3.2.3 Size-based separation: Filtration and Centrifugation

Microfluidic devices relying on filtration to perform cell separation implied membranes or filters to capture target cells using their size as discriminant parameter. One example was the isolation of CTCs from blood by flushing it through a filter. In this case, WBC should deform themselves to pass through the filter, smaller RBC should easily enter the pores, while CTCs (bigger and more rigid) would not pass through.

Zheng *et al.* [11] developed a three dimensional microfilter for the capture of CTCs from blood. The device used two overlapped parylene membranes, with arrays of pores. The microfluidic device consisted of nine capture areas, each composed of 99 hexagonal microfilter patches (Figure 2.10). Each patch consisted of a top membrane with 36 pores (9 μm in diameter) and a bottom membrane with 37 pores (8 μm in diameter). The chip was embedded in a PDMS chamber. The pores of the two membranes were shifted, in order to sustain cells trapped in the top membrane that experienced a supporting force from the bottom membrane. This arrangement reduces the tension stress applied by the pore edges on the cell membrane, which was a cause of cell damage. MCF-7 cells were spiked in whole blood samples from healthy donors with a concentration of 340 cells/ml. One ml of blood was diluted in 9 ml of PBS and pumped through the device that processed 1 ml of blood in 5 min, resulting in a flow rate of 12 ml/h The microfilter yielded a capture efficiency of 86.5%, capturing viable cancer cells.

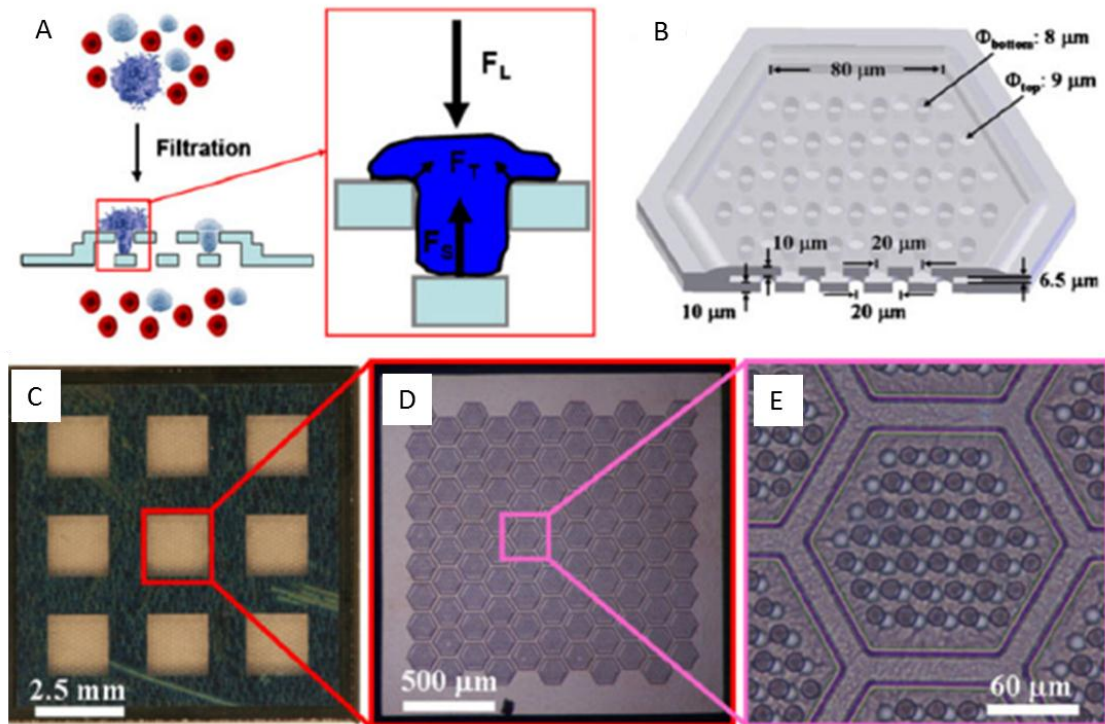


Figure 2.10: (A) Schematic of the device (Zheng *et al.*). Filtration mechanism and forces acting on a trapped cells (F_S : supporting force, F_L : force due to the applied pressure, F_T : tension stress force); (B) schematics of a microfilter patch; (C) picture of the device; (D) single capture area; (E) one microfilter patch [11].

Another technique used to isolate rare cells from background cells was centrifugation. This procedure was commonly used to fractionate blood into its constituent components. Density gradient centrifugation was used to isolate CTCs from blood cells. However, due to the partial overlap in size between CTCs and WBC and their comparable density, CTCs can be found in the same layer of WBC after density gradient centrifugation.

Hou *et al.* described a spiral channel with intrinsic centrifugation forces for label-free separation of CTCs from blood [12]. In a curved channel, centrifugal acceleration produces Dean vortices which were symmetrically counter-rotating across the channel cross-section. The device consisted of a single spiral PDMS channels on a glass substrate, two inlets and two outlets (Figure 2.11). To mimic the presence of CTCs, MCF-7 (10^5 cells/ml) were spiked in diluted blood samples (20% haematocrit) and pumped into the outer inlet whereas PBS were injected through the inner inlet. All the cells in the channel were driven by the Dean vortex towards the inner flow, where the larger cancer cells experienced strong inertial lift force that keep them into the inner stream, whereas blood cells were led back to the outer flow following the vortex streamlines.

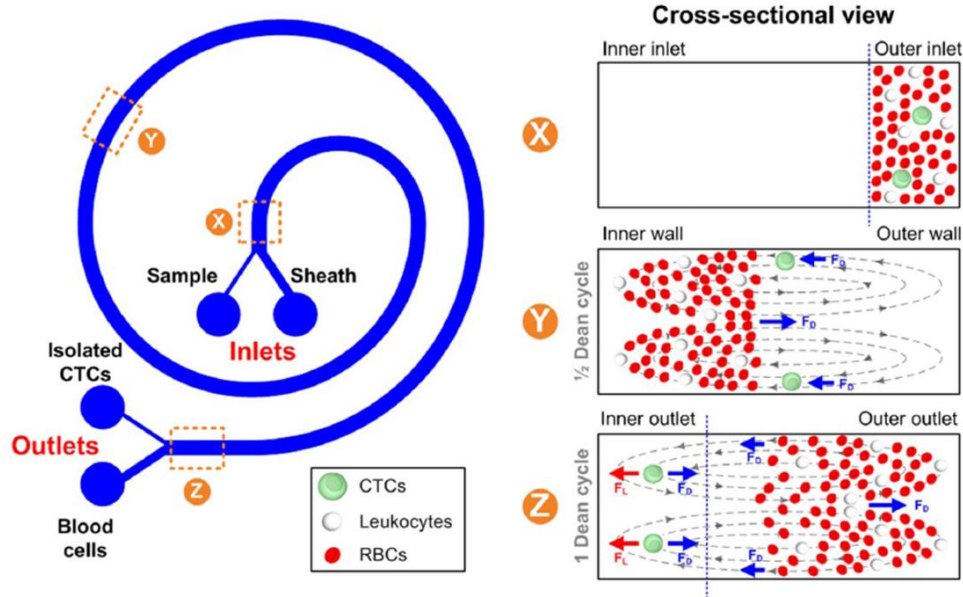


Figure 2.11: Diagram of the microfluidic device (Hou *et al.*) and separation mechanism within the channel. Sample and PBS were pumped into the device through the outer and inner inlets respectively. Led by the Dean drag (F_D) blood cells travel towards the inner flow and back to the original position, while the CTCs experienced a strong inertial lift force (F_L) that keeps them in the outer stream where they were collected [12].

The MCF-7 cells were recovered from the inner outlet with a recovery efficiency of 85% and the blood cells were collected and discarded from the outer outlet. The device processed 3 ml of diluted blood in one hour, allowing a continuous high-throughput cell separation. Moreover, the separation ability of the device was investigated with twenty blood samples from lung cancer patients. CTCs were detected in all the samples examined with cell concentrations ranging from 5 to 88 cells/ml.

Devices using filtration as a sorting method for rare cell isolation, showed interesting results in terms of recovery efficiency, and as an advantage they offer a label-free technique. However, this kind of devices was subjected to clogging due to the high concentration of background cells. In addition as for all physically based cell separation techniques, size overlap between target and non-target cells can be problematic. This aspect was partially solved by the use of the size-density amplification technique described above [54]. However, the separation achieved using size-density amplification was not label-free due to the need to selectively enhance the size of target cells using microbeads coated with a specific ligand.

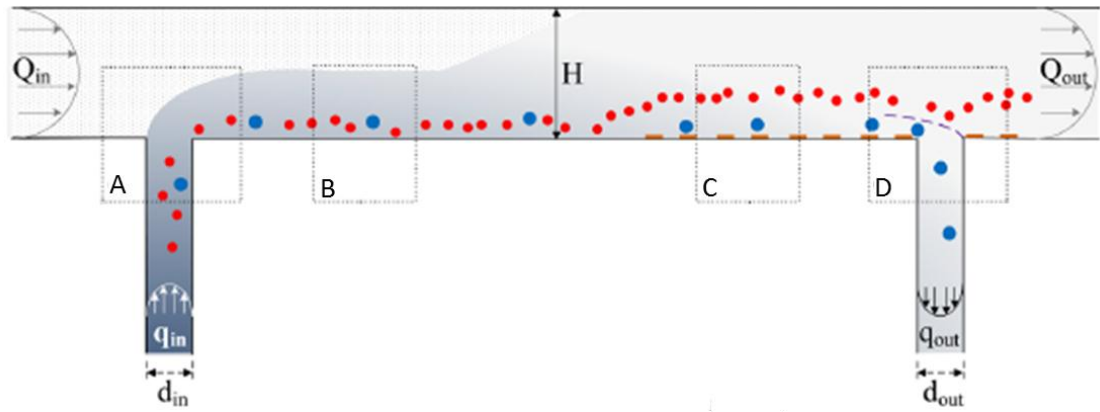


Figure 2.12: (A) Schematic representation of DEP-FFF device (Shim *et al.*). The cell suspension was injected into the device through an inlet in the channel bottom; (B) the sample flow was constrained in a thin layer adjacent to the channel floor by the shear flow; (C) in the separation region target and background cells were influenced by DEP forces and arranged in two vertical levels; (D) cancer cells were collected, while background cells were discarded [13].

2.3.2.4 Size-based separation: Dielectrophoresis

Dielectrophoresis (DEP) was a label-free method used in rare cells separation that employed the dielectric properties of a cell for separation. Membrane surface area and morphology influence the dielectric characteristics of the cell, making this techniques suitable for CTCs isolation from blood [49]. When a non-uniform electric field was applied to target cells, they become polarised experiencing a net electrical force dependent of their dielectric characteristics [47]. This phenomenon was typically used to deflect moving particles within a microfluidic channel, inducing different trajectories according to the cells sizes [55].

One example of this size-based separation technique was the dielectrophoresis field-flow-fractioning (DEP-FFF) microfluidic device developed in 2013 by Shim *et al.* [13]. The device used DEP forces to perform continuous flow separation of CTCs from peripheral blood mononuclear cells (PBMNs). The device consisted of a separation channel (200 mm long, 25 mm wide and 314 μm high) with gold-on-copper microelectrodes on the floor, two inlets and two outlets (Figure 2.12). To evaluate the device performances, breast cancer cells (MDA-MB-435) were spiked into PBMNs collected from healthy donor blood samples through density gradient. The cell suspension was injected into the device at 1.5 ml/h through the sample inlet and a low conductivity medium was pumped at 120 ml/h through the buffer inlet. Within the device the shear flow constrained the sample in a thin lamina contiguous to the channel floor. As the

heterogeneous cell suspension flowed above the microelectrodes (applied voltage 4 V p-p at 130 kHz), positive DEP forces dragged cancer cells towards the channel bed, whereas PBMNs were pushed away by negative DEP. Target cells and background cells reached an equilibrium position (on two different vertical levels) and were collected through the two outlets. The applied electric field frequency chosen was between the crossover frequency of the PBMNs and the cancer cells providing positive and negative DEP forces to two kinds of cells at the same time. The MDA-MB-435 cells were spiked into the PBMNs cell population at a range of physiological concentration, and the recovery efficiency yield was 75% with a throughput of around 12×10^4 cells/s. The device was also tested using PBMNs derived from cancer blood samples using the same the optimized voltage and it identified CTCs in the samples.

Devices using DEP forces to perform size-based label-free cell separation can often yield relatively high recovery efficiency, purity and in some case high cell throughput. However, DEP forces were typically weaker than the hydrodynamics forces induced by the liquid flow and at high flow rate device performances were compromised.

Furthermore, DEP devices typically used a working medium with known properties (low-conductivity) to perform the cell separation, involving the dilution of the sample. Lastly, the dielectric properties of the cells can vary depending on the stage of cell cycle, and this lack of consistency might affect the device sorting capability [55].

2.3.2.5 Size-based separation: Acoustophoresis and Deformability

Acoustophoresis was a technique used to perform label-free size-based cell separation. When a cell was put within an acoustic field, the cell experienced a force dependent on the difference in compressibility and density between the cell and the surrounding media. Cells with different size and density, would be subject to acoustic forces of different magnitudes [55].

The microfluidic device developed by Augustsson *et al.* [19] used ultrasound radiation forces to isolate CTCs from WBCs. Two piezo-ceramic transducers generated the acoustic forces acting on human prostate cancer cells (DU145) used to mimic the CTCs behaviour. DU145 cells were added to WBCs in PBS and pumped through the device at 4.2 ml/h, resulting in a recovery efficiency of 82.7%, and a purity of 93%. Microfluidic devices using magnetophoresis to perform label-free cell separation rely on the difference in the magnetic force magnitude acting on cells of a different size.

Cell deformability had also been used as a physical cell characteristic for cell sorting and isolation. Hur *et al.* [56] described a high-throughput passive label-free cell separation process using cell deformability and dimension as separation parameters. The device was made of a PDMS layer incorporating microfluidic structures, bonded to a slide glass substrate. The device relied on inertial focusing and deformability-induced migration to separate MCF-7 cells from WBCs. Cancer cells were spiked buffy coat, representing 1% of the total number of cells and injected into the device with a throughput of 366 cells/s. More deformable large cancer cells were observed to focus closer to the centre of the channel than the blood cells, allowing the cells collection in two different outlets. The device yielded a MCF-7 recovery efficiency of 96%.

2.3.3 Immunomagnetic cell sorting

Immunomagnetic cell sorting (ICS) used antibodies conjugated to magnetic nanoparticles in order to target specific cell membrane antigens. The coated magnetic particles were incubated with a heterogeneous cell population, labelling the cells expressing the specific surface marker, which could be manipulated by applying an external magnetic field. Microfluidic devices based on this methodology generate high field gradients at the microscale, manipulating soft particles contactless.

In 2013, Huang *et al.* developed a microfluidic device for immunomagnetic isolation of CTCs. The systems consisted of a PDMS microchannel bonded on a glass coverslip, placed under a permanent magnet. Anti-EpCAM functionalized magnetic particles (100 nm) were used in the study. When the cell suspension was injected in the channel, labelled cells were attracted towards the magnet and captured on the glass coverslip, while the background cells were flushed away. To determine the device performance, colon cell line (Colo205), prostate cell line (PC3) and breast cells line (SKBR3) were spiked in whole blood sample from healthy donors. The blood was pumped through the device at 2.5 ml/h and the average cancer cell recovery efficiency was 94%. In addition the system was used to capture CTCs from cancer blood samples, isolating CTCs with a range from 1 to 50 per sample [57].

Kang *et al.* described a PDMS microfluidic micromagnetic device made up of an angled inlet channel connected to a main channel followed by a double collection channel ending with a single outlet. To prevent cell clumps from clogging the device, an array of square posts (50 μm x 50 μm) was placed on the bottom of the inlet channel. On the side wall of the main and double channels, several side chambers (400 μm x 80 μm) found place. There magnetically labelled cells would be collected due to the magnetic field applied by a permanent magnet (Figure 2.13). Mouse metastatic breast cancer cells (M6C) were spiked into mice blood at a physiological concentration. The blood was subject to RBC lysis and, after incubation with anti-EpCAM coated magnetic beads, the cell suspension was injected through the device at 1.2 ml/h, resulting in a cancer cell recovery efficiency of 87% [14].

The two devices described above used magnetic forces to capture magnetically labelled cell. The following works describe flow-through microfluidic device, using the same principle for continuous rare cells separation.

Plouffe *et al.* developed a magnetophoretic microfluidic device able to separate MCF-7 cells from a whole blood sample. The device was made of a PDMS layer incorporating the microfluidics bonded on a glass coverslip and placed between an electromagnet wire array generating the magnetic field.

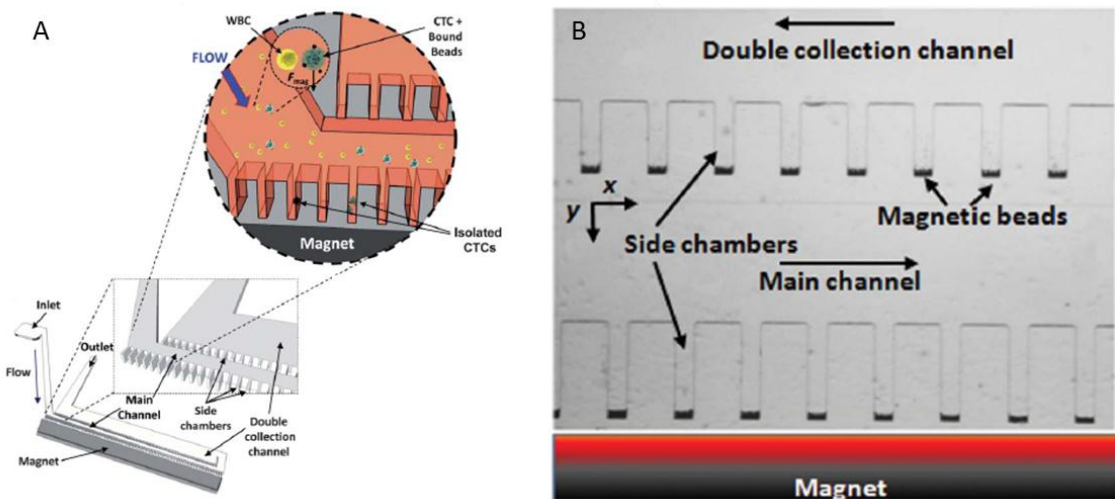


Figure 2.13: (A) Schematics of the rare cell isolation device (Kang *et al.*), consisting in a single inlet, a main channel, a double collection channel and one outlet. Both main and double channels had side chambers for magnetically labelled cells trapping; (B) picture of the device showing capture of magnetic beads in both channels. The beads not trapped from the chambers in the main channel were collected in the double channel [14].

MCF-7 cells and anti-EpCAM coated magnetic beads were spiked in healthy blood sample with a concentration of 50 cells/ml. Within the device, labelled cancer cells were deflected from the original flow to the target outlet and background cells discarded.

The cell suspension was pumped through the device at 14 ml/h, and cancer cells were recovered with a purity of 90% and 85% efficiency [58].

In 2013, Ozkumur *et al.* [15] described a CTCs separation microfluidic device from whole blood called “CTC-iChip”, that used three sequential microfluidic technologies: lateral displacement, inertial focusing and magnetic manipulation. The device was etched in a silicon substrate and bonded to a glass cover to create the microfluidic chamber. After incubation with anti-EpCAM functionalized magnetic beads (1 μm), blood sample was injected in the device, facing the first stage of separation where an array of microposts was used to drive size-dependent lateral displacement sorting, resulting in the removal of RBCs, free magnetic beads and platelets. Only CTCs and WBCs accessed the second stage, where the cells flowed through a microfluidic channel presenting a series of bends. Cells experienced inertial focusing within the channel, emerging from the second stage aligned in a tight line. In the final stage, CTCs and WBCs were immersed in a nonuniform magnetic field (generated by permanent magnets) perpendicular to the flow direction, able to separate cancer cells from background cells, deflecting the cells into the target output (Figure 2.14).

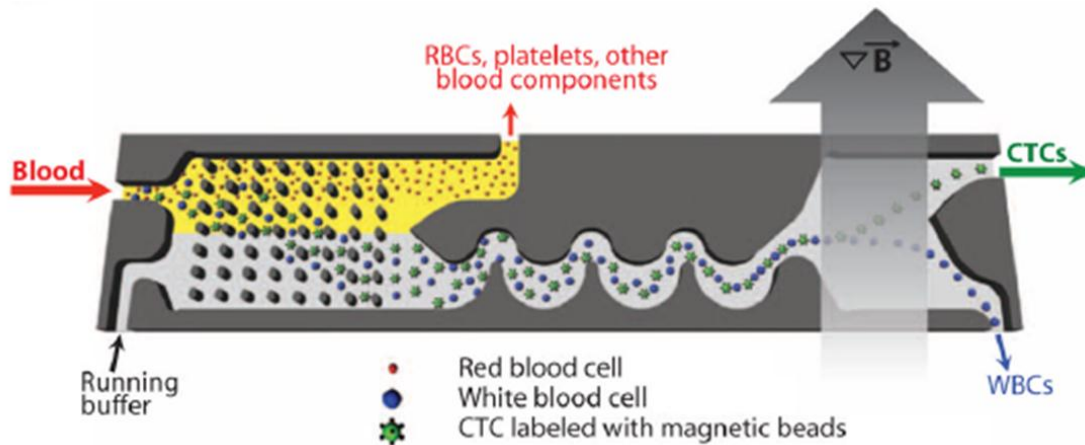


Figure 2.14: Schematics of the microfluidic CTC-iChip (Ozkumur *et al.*). The device consisted of three stages using different techniques. The first stage used deterministic lateral displacement to discard RBSs, free beads and platelets; the second stage focuses the nucleated cells through inertial forces and the final separate labelled target cells from background cells applying and external magnetic field [15].

In the final stage, CTCs and WBCs were immersed in a nonuniform magnetic field (generated by permanent magnets) perpendicular to the flow direction, able to separate cancer cells from background cells, deflecting the cells into the target output (Figure 2.14). To determine the separation performance of the device, SKBR3, human prostate cancer cells (PC3-9) and MDA-MB-231 were spiked into whole blood samples, and pumped through the device at 8 ml/h with a throughput of 10^7 cells/s. The device yielded a recovery efficiency of 98%, 89% and 77% for the three cell line respectively. The CTC-iChip was used to detect CTCs in blood samples (7.5 ml) obtained from patients with prostate, breast, pancreas and lung cancers. The device isolated CTCs in 36 of the 42 cancer blood samples, isolating a number of CTCs ranging from 1 to 4000 cells per sample.

Another device using an external magnetic field to isolate rare cells was the quadrupole magnetic sorter (QMS) developed by Chalmers and co-workers. This device was described in the Hoyos *et al.* [16] work and it was a flow-through system capable of process large volume of liquid. The QMS consisted of a cylinder (internal \varnothing 8.06 mm) and a concentric rod (\varnothing 4.76 mm), with inlet and outlet splitters to separate the sample inlet from the carrier injection site (Figure 2.15A). The inlet splitter arranged the inputs in two concentric streams. The inner stream (carrying the mixed cell sample) and the outer stream (shear flow). The column was surrounded by four permanent neodymium-iron-boron magnets, which generated a magnetic field with maximum strength of 1.37 T and a magnetic gradient of 179 mT/mm [59] (Figure 2.15C).

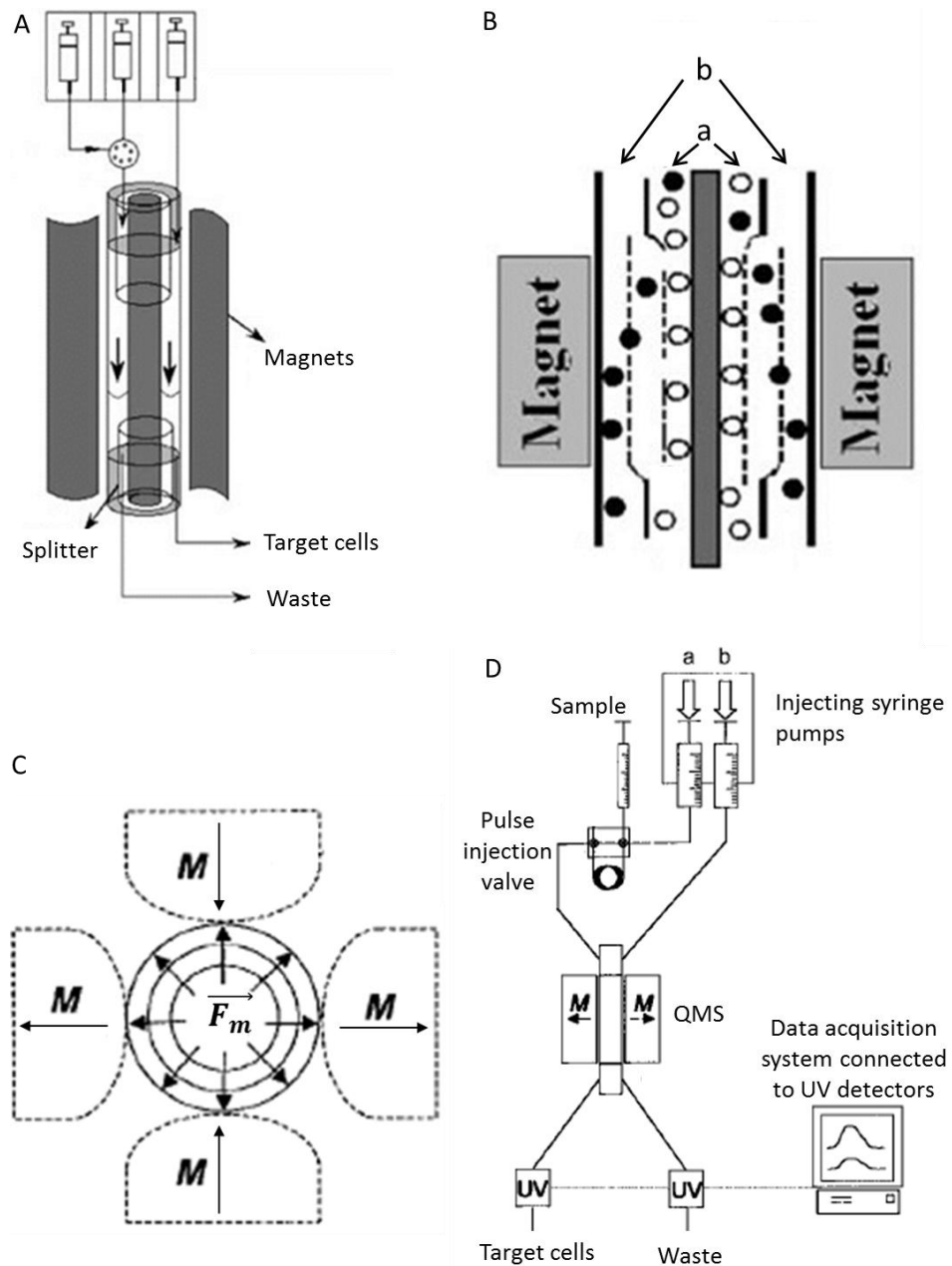


Figure 2.15: Quadrupole magnetic sorter (QMS). (A) Diagram of the QMS device (Hoyos *et al.*); (B) working principle where “a” and “b” were the inner stream (carrying the mixed cell sample) and the outer stream (shear flow), respectively. Black and white spots represented cells labelled and unlabelled respectively. (C) Cross-sectional view of the four magnets. Magnets placed in adjacent positions had opposite magnetisation direction (M). This configuration generated a magnetic force (\vec{F}_m) with a radial disposition. (D) The mixed cell population was injected in the inner stream through a pulse (50 μ l) injection system. Both, target cells and waste, outputs were connected to two UV detectors, which recorder light attenuation due to the presence of cells in suspension. The detectors’ signals were recorded and analysed through a data acquisition system, which allowed to determine the number of cells recovered from each output [16].

The quadrupole configuration consisted of place magnets with opposite magnetisation direction (M) in adjacent positions. This arrangement generated a magnetic force (\vec{F}_m) with a radial disposition, pointing towards the magnets' surface. Due to the magnetic field generated, cells previously labelled with antibody-conjugated magnetic beads experienced a magnetic force (\vec{F}_m), and were deflected into the outer stream (Figure 2.15B).

The outlet splitter allowed to recover the inner stream (carrying the non-target cells) and the outer stream (carrying the target cells) in two separate output. Both, target cells and waste, outputs were connected to two UV detectors, which recorder light attenuation due to the presence of cells in suspension. The detectors' signals were recorded and analysed through a data acquisition system, which allowed to determine the number of cells recovered from each output (Figure 2.15D).

Chalmers and colleagues published a number of papers using the QMS to isolate rare cells. In particular, they observed significant achievements in the enrichment of CTC in peripheral blood lymphocytes (PBL) population.

In 1997 Zborowski *et al.* [60] tested an early version of the QMS using human peripheral lymphocytes. Lymphocytes have been targeted using CD8 antibodies against T cytotoxic cells. A two steps immunostaining procedure was performed, using a primary antibody-fluorescein (FITC) conjugate and secondary antibody-magnetic beads conjugated (MACS microbeads, Miltenyi Biotec). Experiments with the QMS (producing a magnetic gradient of 100 mT/mm) were performed using cell suspensions of 16% to 27% CD8 cell purity. The QMS increased the CD8 cell purity to 54%, with a recovery efficiency ranging between 11% and 38%.

These results were improved in 1998 by Sun *et al.* [61], adjusting the working parameters of the QMS (flow rate was 0.1 – 0.75 ml/min and magnetic field of 174 mT/mm), the authors achieved purity of 99% (CD8 cells, initial purity 26%) and a recovery efficiency of 64%.

Several years later, in 2007, Tong *et al.* [62] used the QMS for negative selection. PBL cells were immunomagnetically labelled with anti-CD3 Dynabeads (M-450, Dynal Biotech) and spiked with KG1a cells. The aim of the authors was to deplete the leukocyte population using negative selection. The QMS recovered 99.4% of the KG1a cells spiked in the PBL population, with a cell sorting rate of 10^6 cells/sec.

The same strategy was used in 2009 by Yang *et al.* [63]. The authors, using negative selection (labelling non-target cells to deplete their population), achieved remarkable results. In this study 800 cancer cells were added to 80 million PBL cells (collected from healthy blood after RBC lysis) previously labelled with anti-CD45 magnetic beads (diameter ranging from 100 nm to 1 μ m). The mixed population was pumped through the

QMS resulting in the recovery of 670 cancer cells and 73,000 PBL cells to the insider outlet (farthest away from the magnet). The device was used to perform a negative selection, depleting the PBL population of 99.9%. The experiment was executed with a total flow rate of 300 ml/h. Moreover, the device sorting performances were investigated using blood samples (after RBC lysis) from cancer patients. In particular CTCs were isolated from 20 of the 26 samples analysed, with a recovery ranging from 0.53 to 282 cells/ml.

An alternative way to exploit a non-uniform magnetic field was investigated by Shen *et al.* in 2012. The authors developed a PDMS microfluidic device using magnetic repulsive forces to separate human histolytic lymphoma monocytes (U937) from deoxyhemoglobin RBCs suspended in a paramagnetic salt (Gd-DTPA) solution. The device performed a label-free cell sorting based on the non-target cells (RBCs) properties in response to an applied external magnetic field. The magnetic field was generated using permanent magnets placed above the microfluidic device. The cell suspension was injected into the device at 19.2 $\mu\text{l/h}$, and U937 cells were isolated with a purity of 90% with a throughput of 27 cells/s [64].

The same principle was used in 2013 by Moore *et al.* used the QMS to separate RBCs from the white blood cell line (KG1-a) population. The cell separation performed was label-free dependent on intrinsic RBC magnetophoretic mobility. In the absence of oxygen, RBCs were less diamagnetic than water, resulting in an attraction of the RBCs toward the magnets. The RBCs hemoglobin was converted in deoxyhemoglobin by exposure to nitrogen. RBCs and KG1-a were mixed in equal numbers, and the cell suspension was pumped through the device at 3 ml/h with a throughput of 550 cells/s. Deoxygenated RBCs were dragged towards the magnets, and were retained on the internal wall surface, while the KG1-a cells were flushed away. Increasing the flow rate the RBCs were recovered with a purity of 90%. The QMS was used to perform a label-free positive selection of RBC, generating a magnetic field gradient of 1620 T/m [65].

The company IKOTECH (USA) commercialised a device using the QMS technology, which allowed high speed cell sorting based on immunological biomarkers. As for the Chalmers and co-workers device, the throughput was really high (10^7 cells/sec) and the purity of sorted cells was in the range of 96% [66].

The QMS technology was used to isolate different types of cells, and could be a good candidate for the aim of this study. The sorting device developed in this work was based on the principle of the QMS used in Chalmers work, with several differences (Chapter 4).

Immunomagnetic cell sorting devices were characterized by high cell throughput, purity and recovery efficiency. These devices did not rely on physical cell characteristics, and

were ideal to separate target cells from background cells with comparable dimensions. The equipment needed for the experimental setup was generally reduced compared to the methods illustrated in previous sections; in particular when permanent magnets were used to generate the magnetic field. However, the cell separation selectivity relies on the specificity of the surface marker chosen. Given the high throughput and recovery efficiency, the work of Ozkumur *et al.* [15] stands out among immunomagnetic based separations carried out.

2.4 Summary of Sorting Techniques

Three main approaches to cell sorting were presented: i) affinity based, ii) size based and iii) immunomagnetic based separation.

Affinity based and immunomagnetic based separations rely on biological cell characteristics including specific surface markers expression.

Affinity based techniques used functionalized surfaces to capture label-free cells taking advantage of the ligand-cell bonding formation within the microfluidic device. Particularly interesting were the devices developed by Nagrath *et al.* [4] and Stott *et al.* [5]. Both devices used affinity based separation to isolate CTCs from whole blood.

The authors characterized the devices performances using cancer cells, and then isolated CTCs from whole cancer blood samples with good results.

More recently Yoon *et al.* (2013) [6] published a study on the use of functionalized (anti-EpCAM) graphene oxide nanosheets on a patterned gold surface to isolate CTCs (Figure 2.5). To mimic the CTCs behaviour, MCF-7 cells were spiked in whole blood with a concentration ranging from 3 to 100 cells/ml. Using a flow rate of 1 ml/h, the average device recovery efficiency was 85%. The authors tested the potential of the device to isolate CTCs from whole blood of 20 cancer patients. The graphene oxide chip captured CTCs from each sample with a concentration ranging from 2 to 23 CTCs per ml of blood.

Size based techniques, rely on the difference between the physical properties of target and background cells. These systems typically used different technologies to perform label-free cell separation, including hydrodynamics, filtration, dielectrophoresis, acoustophoresis, magnetophoresis and cell deformability. Generally size based methods present high recovery and purity performances, and reduced sample preparation due to the label-free cell separation performed. However, even partial size overlap between target and background cells can decrease device performance.

A good example of a microfluidic device using hydrodynamics to perform size based label-free separation was described by Hyun *et al.* [9] who separated CTCs from buffy coat extracted from blood of cancer patients. The device isolated CTCs in 19 samples out of 24, in a concentration ranging from 1 to 21 CTCs per sample.

In 2013 Lee *et al.* [8] developed a system capable of separating rare cells from whole blood samples with high purity, recovery and throughput. The PDMS device presented internal structures capable of generating hydrodynamics effects (Dean vortices) and performed label-free cell sorting according to cell size (Figure 2.6). The authors spiked MCF-7 cells into whole blood samples to mimic the CTCs behaviour. The cancer cell

recovery efficiency yielded was 99.1% with a purity of 88.8% and a cell throughput of 1.8×10^6 cells/s. In addition, the purity increased when two devices were connected in series to 97.4%.

Immunomagnetic based approaches used an external magnetic field to manipulate target cells labelled with functionalized magnetic particles. Magnetically labelled cells were separated from the background cells within the device, enabling continuous cell sorting.

Yang *et al.* [63] used the QMS to deplete 99.9% of the background cells from buffy coat and recovered 82.7% of the target cells. The device isolated CTCs from buffy coat of 20 cancer patients out of 26 analysed.

In 2013, Ozkumur *et al.* [15] developed a microfluidic system capable of continuous rare cells separation of CTCs from whole blood samples. The device included three sequential microfluidic technologies: lateral displacement, inertial focusing and magnetic manipulation (Figure 2.13). The device was tested spiking several cancer cell lines in whole blood samples. The samples were pumped through the device at 8 ml/h with a throughput of 10^7 cells/s. The device yielded a recovery efficiency ranging from 77% to 98%. The CTC-iChip was used to detect CTCs in blood samples (7.5 ml of blood analysed in one hour) obtained from 42 cancer patients. The device isolated CTCs in 36 of the 42 cancer blood samples, isolating a number of CTCs ranging from 1 to 4000 cells per sample.

In conclusion, the device developed by Lee *et al.* used physical properties to isolate target cells, recording good recovery of MCF-7 cells spiked in whole blood. However, the devices developed by Yoon *et al.* and Ozkumur *et al.* were both tested with whole blood of cancer patients. Yoon *et al.* used affinity based strategy to isolate CTCs from all the cancer blood samples tested (20 samples) with a flow rate of 1 ml/h. On the other hand, Ozkumur *et al.*, combined different techniques including: lateral displacement, inertial focusing and magnetic manipulation, managed to analyse 7.5 ml of whole cancer blood in less than one hour (flow rate 8 ml/h), identifying CTCs in 36 sample of the 42 tested (85.7%). According to these results, the CTC-iChip developed by Ozkumur *et al.* was one of the most efficient microfluidic devices for diagnostic purpose.

The immunomagnetic based cell sorting did not rely on physical cell characteristics and therefore can be used to separate target cells from background cells accordingly to the expression of a surface marker. This method was the best candidate for the aim of this study, and the device developed used this working principle to isolate SSCs from HBMSCs accordingly to the expression of the surface antigen STRO-1.

Table 2.1: **Affinity based isolation**. Keys parameters for each paper were reported, including: the author, year, discrimination parameters, sorting methods the devices used, purity, recovery, flow rate, throughput and the kind of cells used. The papers in red were widely discussed in the chapter with data from the papers. The devices tested with whole blood from cancer patients present two lines in the recovery and particle columns. The cells highlighted in bold represented the results from cancer blood analysis (number of cancer samples in which CTCs were identified). The paper in blue was the most effective work within the category.

AUTOR	YEAR	GROUP	METHOD	PURITY	RECOVERY	FLOW RATE	THROUGHPUT	PARTICLES	REF
Saliba et al.	2010	Affinity-based	Positive selection (CD19)	-	97%	9 µl/h	-	B-lymphoid cells from T-lymphoid cells	[50]
Lin et al.	2012	Affinity-based	Positive selection (EpCAM)	-	91.3%	36 ml/h	-	MCF-7 from WBC in PBS	[53]
Yoon et al.	2013	Affinity-based	Positive selection (EpCAM)	-	3-5cells→73% 10-20→94.2% 100→87.3%	1 ml/h	-	MCF-7 in whole blood CTCs from whole blood	[6]
Sheng et al.	2012	Affinity-based	Positive selection (KCHA10aptamer)	81%	96%	2.16 ml/h	-	HCT116 from whole blood	[7]
Nagrath et al.	2007	Affinity-based	Positive selection (EpCAM)	50%	60% 115 of 116 S	1 ml/h	-	NCI-H1650 from blood CTCs from whole blood	[4]
Stott et al.	2010	Affinity-based	Positive selection (EpCAM)	-	91% 14 of 15 S	1.2 ml/h	-	PC3 from whole blood CTCs from whole blood	[5]

Table 2.2: **Size-based separation**. Keys parameters for each paper were reported, including: the author, year, discrimination parameters, sorting methods the devices used, purity, recovery, flow rate, throughput and the kind of cells used. The papers in red were widely discussed in the chapter with data from the papers. The devices tested with whole blood from cancer patients present two lines in the recovery and particle columns. The cells highlighted in bold represented the results from cancer blood analysis (number of cancer samples in which CTCs were identified). The paper in blue was the most effective work within the category.

AUTOR	YEAR	GROUP	METHOD	PURITY	RECOVERY	FLOW RATE	THROUGHPUT	PARTICLES	REF
Choi et al.	2012	Size-based	Hydrodynamic (label-free)	94%	80%	4.2 ml/h	277.7 cells/s	HL60 from K562 in buffer	[10]
Lee et al.	2013	Size-based	Hydrodynamic (label-free)	88% 97.4%	99%	6 ml/h	1.8 x 10 ⁶ cells/s	MCF-7 from whole blood	[8]
Hyun et al.	2012	Size-based	Hydrodynamic (label-free)	-	93%	36 ml/h	-	MCF-7 from buffy coat	[9]
					19 of 24 S			CTCs from buffy coat	
Hou et al.	2013	Size-based	Hydrodynamic (label-free)	-	>85%	3 ml/h	-	MCF-7 in blood (20% hematocrit)	[12]
					20 of 20 S			CTCs from blood	
Zheng et al.	2011	Size-based	Filtration	-	86.5%	12 ml/h	-	MCF-7 in whole blood	[11]
Shim et al.	2013	Size-based	DEP-FFF(label-free)	-	75%	1.5 ml/h	12 x 10 ⁴ cells/s	MDA-MB-435 from PBMN in buffer	[13]
Augustsson et al.	2012	Size-based	Acoustophoresis	93%	82.7%	4.2 ml/h	-	DU145 from WBC in PBS	[19]
Hur et al.	2011	Deformability	Hydrodynamic (label-free)	-	96%	-	366 cells/s	MCF-7 from buffy coat	[56]

Table 2.3: **Immunomagnetic separation**. Keys parameters for each paper were reported. The papers in red were widely discussed in the chapter with data from the papers. The devices tested with whole blood from cancer patients present two lines in the recovery and particle columns. The cells highlighted in bold represented the results from cancer blood analysis (number of cancer samples in which CTCs were identified). The paper in blue was the most effective work within the category. The paper highlighted in yellow impressed the author for the achievements reached and contribution to the field.

AUTOR	YEAR	GROUP	METHOD	PURITY	RECOVERY	FLOW RATE	THROUGHPUT	PARTICLES	REF
Shen et al.	2012	Magnetophoresis	Negative selection (label-free)	>90%	-	19.2 µl/h	27.7 cells/s	U937 from deoxyhemoglobin RBC in buffer	[64]
Huang et al.	2013	Immunomagnetic	Positive selection (EpCAM)	-	94%	2.5 ml/h	-	SKBR3, PC3, Colo205, CTC in blood	[57]
Ozkumur et al.	2013	Immunomagnetic	Positive selection (EpCAM)	-	98% 89% 36 of 42 S	8 ml/h	10 ⁷ cells/s	SKBR3, PC3-9 in blood CTCs from whole blood	[15]
Kang et al.	2012	Immunomagnetic	Positive selection (EpCAM)	-	87%	1.2 ml/h	-	M6C from WBC in PBS	[14]
Plouffe et al.	2012	Immunomagnetic	Positive selection (EpCAM)	90%	85%	14 ml/h	-	MCF-7 in blood	[58]
Moore et al.	2013	Immunomagnetic	Positive selection (label-free)	90%	80%	3 ml/h	550 cell/s	Deoxygenated RBC from KG1-a (1:1)	[65]
Yang et al.	2009	Immunomagnetic	Negative selection (CD45)	-	82.7% 99.9% Depletion 20 of 26 S	-	10 ⁷ cells/s	Cancer cells from PBL CTCs from buffy coat	[63]

Chapter 3

Background Theory

Magnetic beads attached to desired cells through specific antibodies can be used to make target cells susceptible to an applied magnetic field. Consequently, when a magnetic field was applied, only the labelled cells experienced a magnetic force (\vec{F}_m) which caused them to move. In this chapter the force \vec{F}_m acting on a magnetic particle will be defined. Furthermore, the balance of forces acting on a magnetic particle within the sorting device developed in this study will be described.

3.1 Magnetic flux density

In free space the magnetic flux density \vec{B} was related to the magnetic field strength \vec{H} by the equation 3.1:

$$\vec{B} = \mu_0 \vec{H} \quad (3.1)$$

where μ_0 was the magnetic permeability in free space. The presence of matter in the magnetic fields modified the magnetic flux density at constant field strength. The magnetic properties of a material were described by the magnetization (or magnetic polarization) \vec{M} , which had the form:

$$\vec{M} = \frac{1}{\mu_0} \vec{B} - \vec{H} = \chi_m \vec{H} \quad (3.2)$$

where χ_m was the magnetic susceptibility characteristic of the material and was defined [67]:

$$\chi_m = \mu_r - 1 \quad (3.3)$$

μ_r was the relative magnetic permeability described as follow:

$$\mu_r = \frac{\mu_m}{\mu_0} \quad (3.4)$$

where μ_m was the magnetic permeability of the material.

Magnetization was a vector field and represented the quantity of magnetic moment \vec{m} per unit volume. Rearranging the equation (3.1), it was possible to write:

$$\vec{B} = \mu_0(\vec{M} + \vec{H}) = \mu_0(\chi_m \vec{H} + \vec{H}) = \mu_0(1 + \chi_m)\vec{H} = \mu_0 \mu_r \vec{H} \quad (3.5)$$

A magnetic moment \vec{m} in an external magnetic field had a magnetostatic potential energy defined by:

$$U = -V_m \vec{M} \cdot \vec{B} = -\vec{m} \cdot \vec{B} \quad (3.6)$$

where V_m was the volume of the magnetic material.

If the external magnetic field was non-uniform, there was a force, proportional to the magnetic field gradient, acting on the magnetic moment itself. This force described by:

$$\vec{F}_m = (\vec{m} \cdot \nabla) \vec{B} = (V_m \vec{M} \cdot \nabla) \vec{B} = V_m \Delta \chi (\vec{H} \cdot \nabla) \vec{B} = \frac{V_m \Delta \chi}{\mu_0} (\vec{B} \cdot \nabla) \vec{B} \quad (3.7)$$

where $\Delta \chi$ was the difference between the magnetic susceptibility of the material χ_m and the magnetic susceptibility of the suspending fluid χ_f ($\Delta \chi = \chi_m - \chi_f$).

Expanded to component form, the equation (3.7) can be written as [68]:

$$\vec{F}_m = \frac{V_m \Delta \chi}{\mu_0} (\vec{B} \cdot \nabla) \vec{B} = \frac{V_m \Delta \chi}{\mu_0} \begin{bmatrix} B_x \frac{\partial B_x}{\partial x} + B_y \frac{\partial B_x}{\partial y} + B_z \frac{\partial B_x}{\partial z} \\ B_x \frac{\partial B_y}{\partial x} + B_y \frac{\partial B_y}{\partial y} + B_z \frac{\partial B_y}{\partial z} \\ B_x \frac{\partial B_z}{\partial x} + B_y \frac{\partial B_z}{\partial y} + B_z \frac{\partial B_z}{\partial z} \end{bmatrix} \quad (3.8)$$

The equation (3.7) was often express in the following form:

$$\vec{F}_m = V_m \Delta \chi \frac{|\nabla \vec{B}^2|}{2\mu_0} \quad (3.9)$$

Under the hypothesis of time-independent fields with no electric currents, the equations (3.7) and (3.9) were equivalent according to the following identity:

$$\nabla \vec{B}^2 = \nabla(\vec{B} \cdot \vec{B}) = 2\vec{B} \times (\nabla \times \vec{B}) + 2(\vec{B} \cdot \nabla)\vec{B} = 2(\vec{B} \cdot \nabla)\vec{B} \quad (3.10)$$

The term $\nabla \times B$ was equal to zero because there were no sources of \vec{B} in the surrounding fluid (or carrier medium). The (3.10) was true in presence of magnetostatic fields [69].

3.2 Flow regime

In microfluidics the viscous force were dominant, while the inertial forces were negligible. The Reynolds number (Re) of a system defined the relationship between these forces. Re was a dimensionless number and its value describes the flow regime within a system, and was defined as follow:

$$Re = \frac{\rho_m v l}{\eta} \quad (3.11)$$

Where ρ_m was the density of the fluid, η represented the dynamic fluid viscosity, l was the characteristic length of the system (diameter in the case of a circular pipe) and v represented the mean fluid velocity.

For values of Re below 2300 the flow was considered laminar, otherwise non-laminar. In the case of laminar flow regime, the flow velocity exhibited a parabolic profile (along a cross-section through the channel), reaching the zero value in correspondence of the channel walls. If the flow regime was laminar, the flow velocity profile through a channel (with known boundary conditions) could be described using the Navier-Stokes equation [70]:

$$\rho_m \frac{d\vec{v}}{dt} + \rho_m (\vec{v} \cdot \nabla)\vec{v} = -\nabla p + \eta \nabla^2 \vec{v} + \vec{f} \quad (3.12)$$

Where \vec{v} was the velocity of the fluid, ∇p represented the pressure gradient, \vec{f} was an external force acting on the fluid. The Reynolds number calculated for the device developed in this study, defined the flow regime within the device as laminar.

3.3 Balance of forces

A magnetic particle suspended in a fluid within the sorting device, was subjected to several forces, including the hydrodynamic force \vec{F}_h expressed by:

$$\vec{F}_h = -6\pi\eta r_p (\vec{v}_p - \vec{v}_f) \quad (3.13)$$

the \vec{F}_h a cell within the device was subjected, was calculated in Appendix M. A magnetic particle experienced a magnetic force \vec{F}_m defined as follow:

$$\vec{F}_m = \frac{V_p \Delta\chi}{\mu_0} (\vec{B} \cdot \nabla) \vec{B} \quad (3.14)$$

where V_p was the volume of the magnetic particle. The mass of the particle caused it to experienced a gravitational force \vec{F}_g which was defined as follow:

$$\vec{F}_g = gV_p\rho_p \quad (3.15)$$

This was opposed by a buoyancy force \vec{F}_B equal to the weight of the fluid displaced:

$$\vec{F}_B = -gV_p\rho_f \quad (3.16)$$

Where:

\vec{F}_h the hydrodynamic force [N]

\vec{F}_B the buoyancy force [N]

\vec{F}_g the gravitational force [N]

\vec{F}_m the magnetic force [N]

\vec{v}_p the particle velocity [m/s]

\vec{v}_f the fluid velocity [m/s]

η was the dynamic viscosity of the carrier fluid [Ns/m²]

g the gravitational constant [m/s²]

ρ_p was the density of the particle [kg/m³]

ρ_f was the density of the suspending fluid [kg/m³]

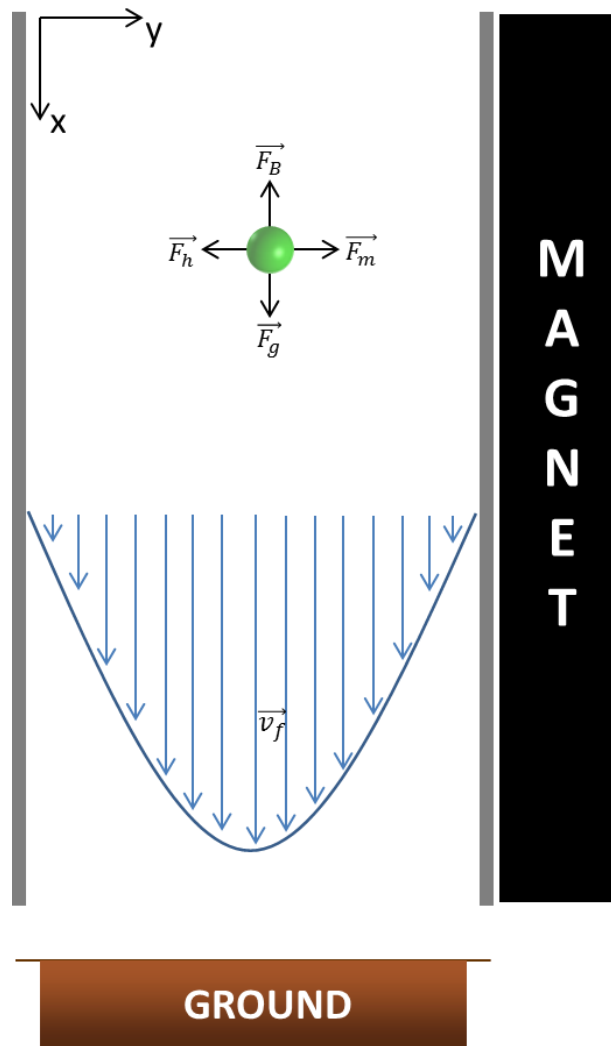


Figure 3.1: Two-dimensional schematic of the forces acting on a magnetic particle within the sorting device. The gravitational force \vec{F}_g has opposite direction compared to the buoyancy force \vec{F}_B . The magnetic force \vec{F}_m pulled the magnetic particle towards the magnet with the opposition of the hydrodynamic force \vec{F}_h .

r_p radius of the magnetic particle [m]

V_p the volume of the particle [m³]

According to the Newton's law, the mass acceleration of a body was related to the resultant of the external forces acting upon it [71].

$$m \frac{d\vec{v}_p}{dt} = \vec{F}_h + \vec{F}_m + \vec{F}_g + \vec{F}_B \quad (3.17)$$

Where m was the mass of the particle. Four forces were acting on a magnetic particle within the sorting device: hydrodynamic force, magnetic force, gravitational force and buoyancy force.

The particle experienced a gravitational force proportional to its mass. This force was opposed by the buoyancy force equal to the weight of the suspending fluid occupied by the particle. The net force acting on the particle was proportional to the difference between the densities of the particle and the suspending fluid.

Similarly, the hydrodynamic force opposes to the the magnetic force experienced by the magnetic particle. The hydrodynamic force opposed to any movement relative to the suspending fluid, proportionally to the particle velocity referred to the fluid.

3.3.1 Balance of forces within the sorting device

Figure 3.1 shows all the force acting on a magnetic particle suspended in a fluid within the sorting device developed in this study. In this particular case, few assumptions can be supposed. Considering the inertial forces negligible in this case it was possible to rewrite the (3.17) as follow:

$$0 = \vec{F}_h + \vec{F}_m + \vec{F}_g + \vec{F}_B \quad (3.18)$$

Considering the X and Y components of each force acting on the particle, we can write:

$$\begin{cases} F_{hx} + F_{mx} + F_{gx} + F_{Bx} = 0 \\ F_{hy} + F_{my} + F_{gy} + F_{By} = 0 \end{cases} \quad (3.19)$$

Assuming that the X component of \vec{F}_m was negligible, and the absence of Y components for the \vec{F}_g and the \vec{F}_B , it was possible to write:

$$\begin{cases} F_{hx} + F_{gx} + F_{Bx} = 0 \\ F_{hy} + F_{my} = 0 \end{cases} \quad (3.20)$$

During the tests conducted on the sorting device developed in this study, the suspending fluid used was a solution containing Dextran T70 (see Section 7.1).

Considering the difference between the densities of the particle and the suspending fluid negligible, it was possible to write the (3.20) as:

$$\begin{cases} F_{hx} = -6\pi\eta r_p(v_{px} - v_{fx}) = 0 \\ -6\pi\eta r_p(v_{py} - v_{fy}) + \frac{V_p\Delta\chi}{\mu_0} \left(B_x \frac{\partial B_y}{\partial x} + B_y \frac{\partial B_y}{\partial y} \right) = 0 \end{cases} \quad (3.21)$$

Where $\left(B_x \frac{\partial B_y}{\partial x} + B_y \frac{\partial B_y}{\partial y} \right)$ was the y component of $(\vec{B} \cdot \nabla)\vec{B}$ according to equation (3.8).

Considering the Y component of the fluid velocity zero ($v_{fy} = 0$), the particle velocity can be written as follow:

$$\begin{cases} v_{px} = v_{fx} \\ v_{py} = \frac{V_p\Delta\chi}{6\pi\eta r_p\mu_0} \left(B_x \frac{\partial B_y}{\partial x} + B_y \frac{\partial B_y}{\partial y} \right) \end{cases} \quad (3.22)$$

From equation (3.22), we can deduce that v_{px} was zero with reference to the flow velocity (v_{fx}) and that the particle assumes the flow velocity within the sorting device.

The Y component of the particle velocity depends on several parameters including: the magnetic flux density (\vec{B}) and its gradient ($\nabla\vec{B}$), the volume of the magnetic particle (V_p) and its magnetic susceptibility (compared to the one of the suspending fluid) (χ_m), the dynamic viscosity of the suspending fluid.

Chapter 4

Immunomagnetic separation: device design and fabrication

In this chapter, design and fabrication processes of the sorting device were described. Several versions of the sorting device were developed, using different building materials and techniques. The technical drawings with dimension and design of all the components developed were reported at the end of the thesis (see Appendix P).

4.1 Inspiration

In Chapter 2, several cell isolation techniques were described including: affinity based, size based and immunomagnetic based cell separation. This last method was characterized by high throughput and purity, and by a relatively simple setup. Immunomagnetic Cell Sorting (ICS) used antibodies conjugated to magnetic nanoparticles that bound to specific cell membrane antigens. This method does not rely on physical cell characteristics and therefore can be used to separate target cells from background cells. An external magnetic field was used to isolate labelled cells without physical contact, and ICS devices were now the major candidate for processing adherent cells such as BM cells. Chalmers and co-workers published some of the earliest papers concerning the enrichment of CTCs in PBL population using a quadrupole magnetic system (QMS) as a sorting device [63] [16].

The sorting device developed in this study was based on the working principle of the QMS developed by Chalmers and co-workers. All the versions of the sorting device were built using rapid prototyping techniques (3D printing and stereolithography), and the final aim was to develop a functional, compact, easy to use and to maintain sorting platform for reach uses. Moreover, several magnetic systems were developed using inexpensive permanent magnets, with the hexapole configuration elected to be the definitive magnets arrangement (Chapter 5).

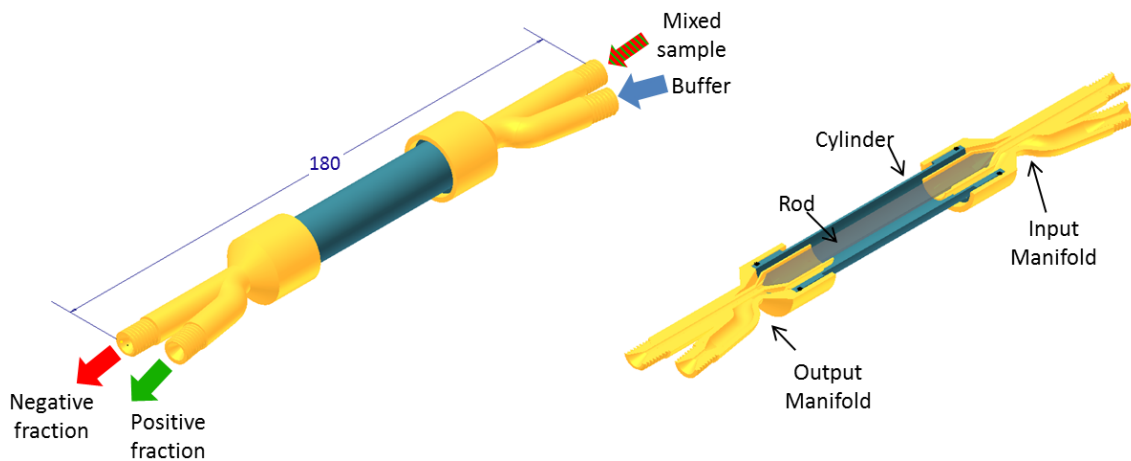


Figure 4.1: 3D model of the sorting device final version (ver. 3.5). Overall aspect of the assembled device consisting of cylinder, rod and manifolds and longitudinal section of the device. Measurements in millimetres.

4.2 Device

The sorting device consisted of a cylinder, a central rod and input/output manifolds. The manifolds were designed to combine two inlet flows in two concentric streams around the central rod and to return the streams in two distinct outlets. The mixed cell sample was carried in the inner stream, and the immunomagnetically labelled cells deflected into the external sheath flow using permanent magnets surrounding the sorting device. The two streams were retained in distinct outlets. All the device components underwent changes regarding design, building material and building technique. The various versions of the sorting device were described in the following Sections, while the final version was shown in Figure 4.1.

4.3 Sorting Device version 1

The QMS used in Chalmers work consisted of a cylinder and a concentric rod; a fluid stream carried the sample near the surface of the central rod. This stream was sheathed by a buffer flow. Immunomagnetically labelled cells experienced a drag force that pulled them towards the outer stream under the influence of an external magnetic field generated by four permanent neodymium magnets as described in section 2.3.3 (Figure 2.14).

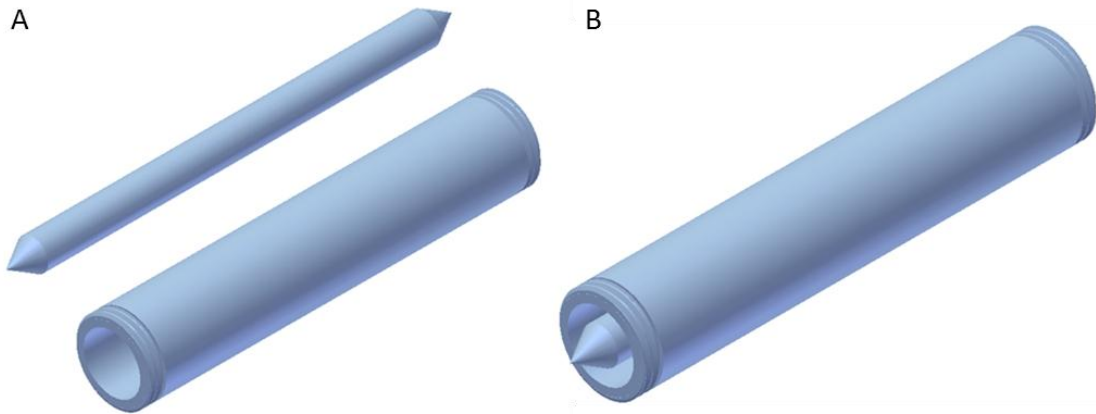


Figure 4.2: (A) 3D image showing prototype of the central rod and cylinder and (B) their relative positions.

The separation device was shown in Figure 4.1, and was designed with Autodesk Inventor Professional 2011 (3D mechanical solid modelling design software), and built at the mechanical workshop in the Mountbatten Building (University of Southampton).

4.3.1 Cylinder and the Rod

The cylinder (or tube) was the first component to be modelled. The internal surface of the cylinder was continuously in contact with cells, in particular with BM cells, which were known to have high adherence to the wall surface. Therefore, a non-adherent material was sourced. Tufset, an engineering plastic material, was a high quality rigid polyurethane with good mechanical strength, good stress cracking resistance and excellent fatigue resistance. Moreover, it was highly resistant to chemicals and it had a hard abrasion resistant surface with low friction. It could be processed to give a smooth surface which was indispensable for the correct use of the device. The cylinder was turned on a lathe, and a screw thread (20 TPI - threads per inch) was machined at each end of the tube (Figure 4.2A). The central rod was turned from a round Tufset bar. The rod had cone-shaped ends, processed to have a 60 degree cross-section angle (Figure 4.2A). The rod allowed the inner stream, carrying the mixed cell sample, to be in an area with high magnetic field gradient ($\nabla\vec{B}$) and magnetic field strength ($|\vec{B}|$).

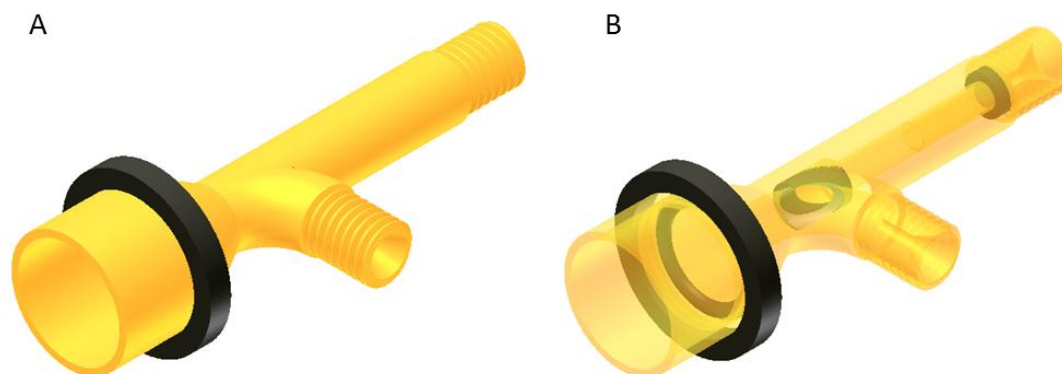


Figure 4.3: (A) 3D drawing of the manifold external part, the body structure was made of FullCure 720 (in yellow); (B) the contact points with the internal part and the cylinder were printed using TangoBlack 85 (in black), together with the outer O-ring.

Without this component, the inner stream would have been in the centre of the magnetic system, where the $|\vec{B}|$ and $\nabla\vec{B}$ were close to zero (see Section 5.2.1). In this area the magnetic force (\vec{F}_m) experienced by magnetically labelled cells would have been zero. The cylinder and the rod together formed an annulus 2.5 mm deep with a cross sectional area of 19.6 mm² (Figure 4.2B).

4.3.2 Manifold

A manifold able to arrange the two inlets (mixed sample and buffer) concentrically was developed. The same design was used to build an output manifold to collect the two concentric flows into separate outputs. It also maintained the relative positions of the cylinder and the rod. The manifolds were also used to combine the two inlets (mixed cell sample and buffer) and to separate the two outlets (target cells and unwanted cells both suspended in buffer). The manifold was built with a 3D printer (Object Connex 350, Stratasys, USA) from an acrylic-based photopolymer called FullCure 720 (Stratasys, USA), suitable for rigid model. The 3D printer creates objects by laying down successive layers of material; for the manifold a support material (FullCure 705, Stratasys, USA) was used to support the 3D structure. Due to the malleability and the elaborate geometry of the printed object this substance was difficult to remove after printing. Therefore it was necessary to divide the manifold into two components: an external and internal part.

The external part comprises two inlets/outlets with screw thread, with the internal shape designed to match the connector through which the tubing was linked to the manifold as shown in Figure 4.3A. The tube screws into an internal thread (20 TPI).

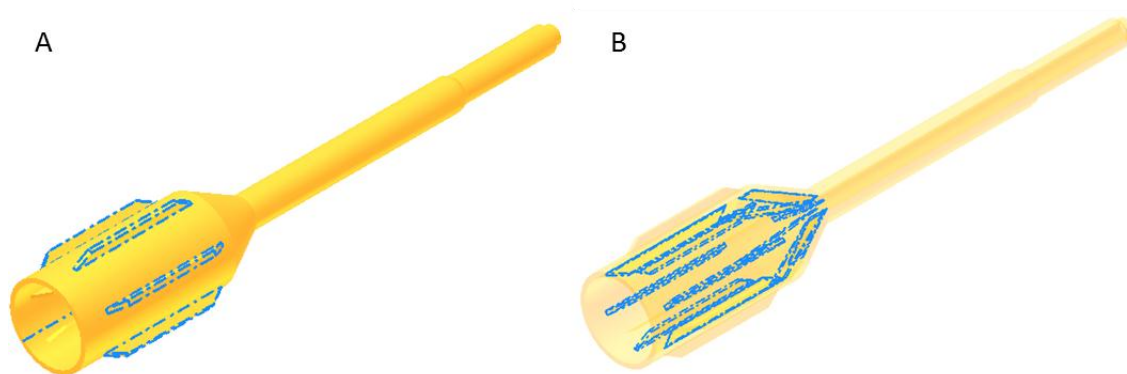


Figure 4.4: (A) 3D model of the internal part of the manifold. The external fins (highlighted in blue) keep the cup equidistant from the cylinder, defining the channel gap between them; (B) the internal fins (highlighted in blue) keep the rod in position, confining the flow near the rod surface.

An O-ring was printed at the bottom of the cylinder site to avoid leakage at the manifold-tube interface, as the boundaries between the internal and external components of the manifold could leak. Therefore, all contact points were printed using a rubber like material, TangoBlack 85 (Stratasys, USA), which was a blend of FullCure 720 and TangoBlack (Stratasys, USA). Figure 4.3 shows the external part with outer O-ring, placed to protect the manifold. This O-ring adjusts the external diameter of the manifold without changing the overall geometry, allowing the use of the same device support for different thicknesses. Figure 4.3B illustrates a semi-transparent 3D model of the external part, with elements built using TangoBlack 85.

The internal part of the manifold was designed to allow the mixed cell sample to flow in a stream near the rod. The cells flow through a channel (\varnothing 1.5 mm), which leads to the rod tip, which then generates a stream adjacent the rod surface. The manifold internal part was designed to keep the rod position a fixed distance from the internal wall. In order to create a cylindrical flow concentric with the rod with a well-defined depth, six 1 mm high 'fins' were fabricated on the inner surface, setting the flow depth (Figure 4.4). Fins were also made on the bottom of the cup to support the rod. Six more fins were made on the outer surface to keep the external wall side equidistant to the cylinder. To improve the structural stability, the external fins were rotated by 30 degrees with respect to the internal fins. Assembly of the manifold was undertaken ensuring that the two inlets (or outlets) were kept separate. To do this the internal part of the manifold was first inserted into the external part (Figure 4.5). There were two contact points between the components, both of which were printed in TangoBlack85 for better sealing.

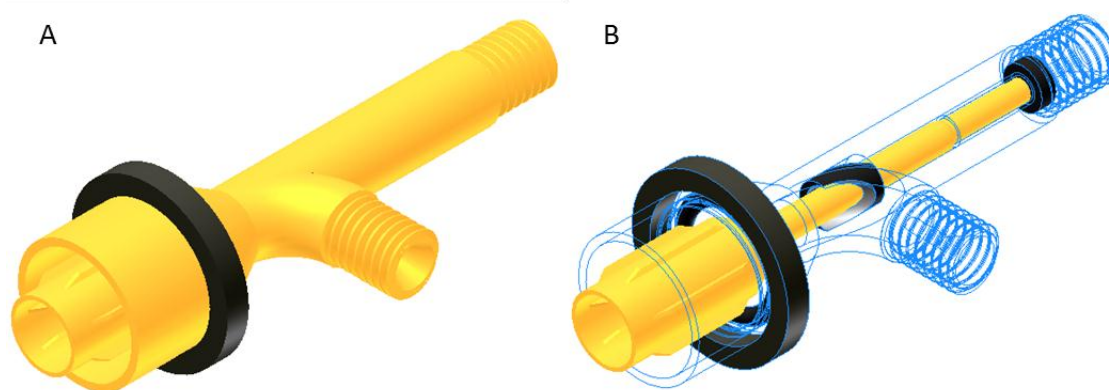


Figure 4.5: (A) 3D model of the assembled manifold; (B) inner view of the manifold internal/external part interface.

The first was placed at the interface between the narrow end of the internal part and the entrance of the mixed cell sample.

The second was located at the channel junction, making the internal part more stable and preventing buffer leakages (coming from the bent inlet). This component was crucial to keep the internal part in place, but it made assembly challenging. Due to its high grip, the use of a lubricant was required to drive one part of the manifold into the other.

4.3.3 Assembled Device

As described in section 4.3.2, the manifold separated the inlets and the outlets. The cylinder and the rod were kept in position through a thread cut on the internal wall of the manifold, and fins ground on the bottom of the manifold internal part (Figure 4.5B).

Figure 4.6A shows the entire device, consisting of two manifolds, the cylinder and the central rod. The combination of these components generated two concentric fluid streams at the entrance of the device, the buffer outer stream, and the inner flow carrying the suspended mixed cell sample. At the other end of the device, the manifold allowed the recovery of the unlabelled cells carried by the inner stream and the magnetically labelled cells, dragged into the outer stream by the magnetic field (Figure 4.6C).

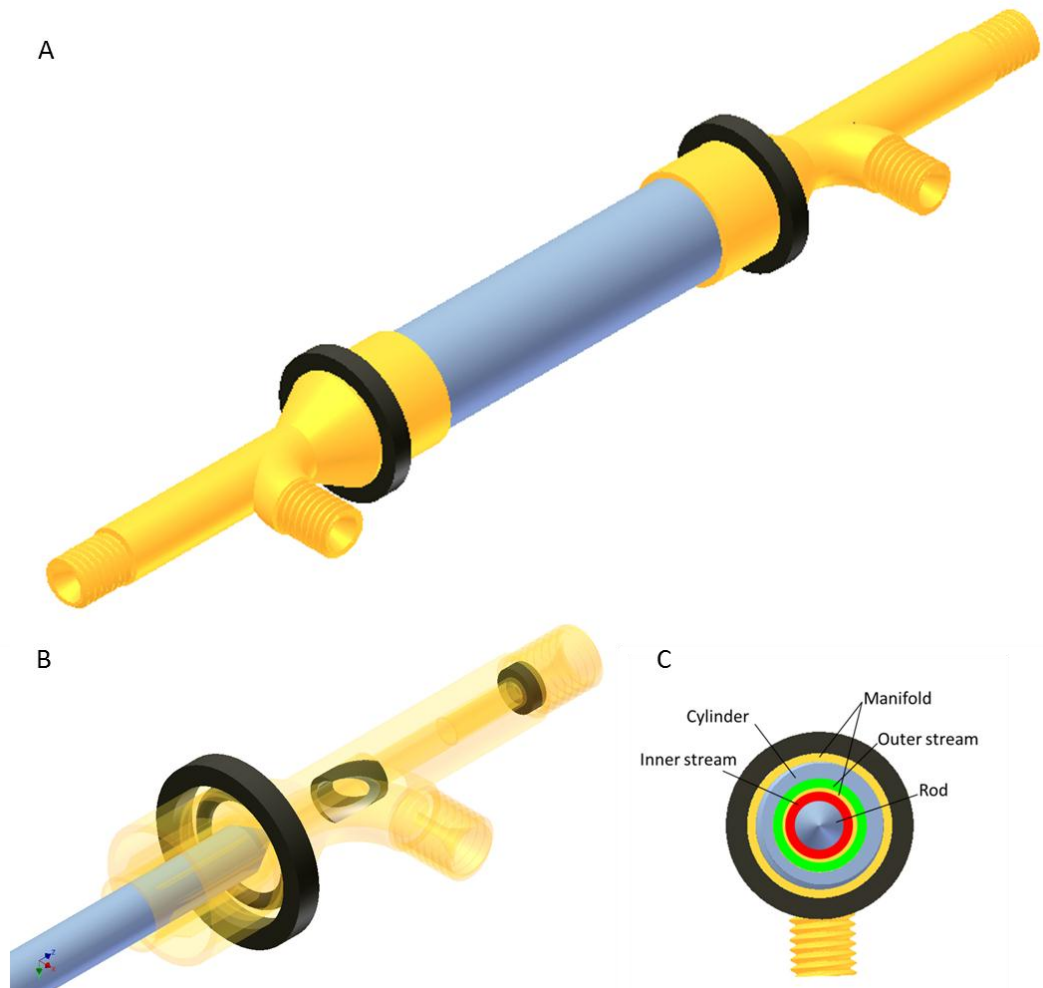


Figure 4.6: (A) 3D model of the assembled device, consisting of two manifolds, the cylinder and the central rod; (B) the manifold internal part matches the rod tip geometry, providing a stable support for the rod; (C) device cross section showing the inner stream (in red) carrying the mixed cell sample and the buffer outer stream (in green).

4.4 Device Support

As shown in Figure 4.6, the device had a unique shape; it was therefore necessary to design a support to hold it. Such a support also needed to keep the magnets in position, whilst allowing the distance between them and the device to be modified, in order to adjust the magnetic field strength and gradient. The main feature of the custom designed support was the adjustability, since it was designed to handle devices with different height and diameter and to control the position of the magnets. The device support consisted of several components including: top supports, bottom supports, magnets holders, a column and a base.

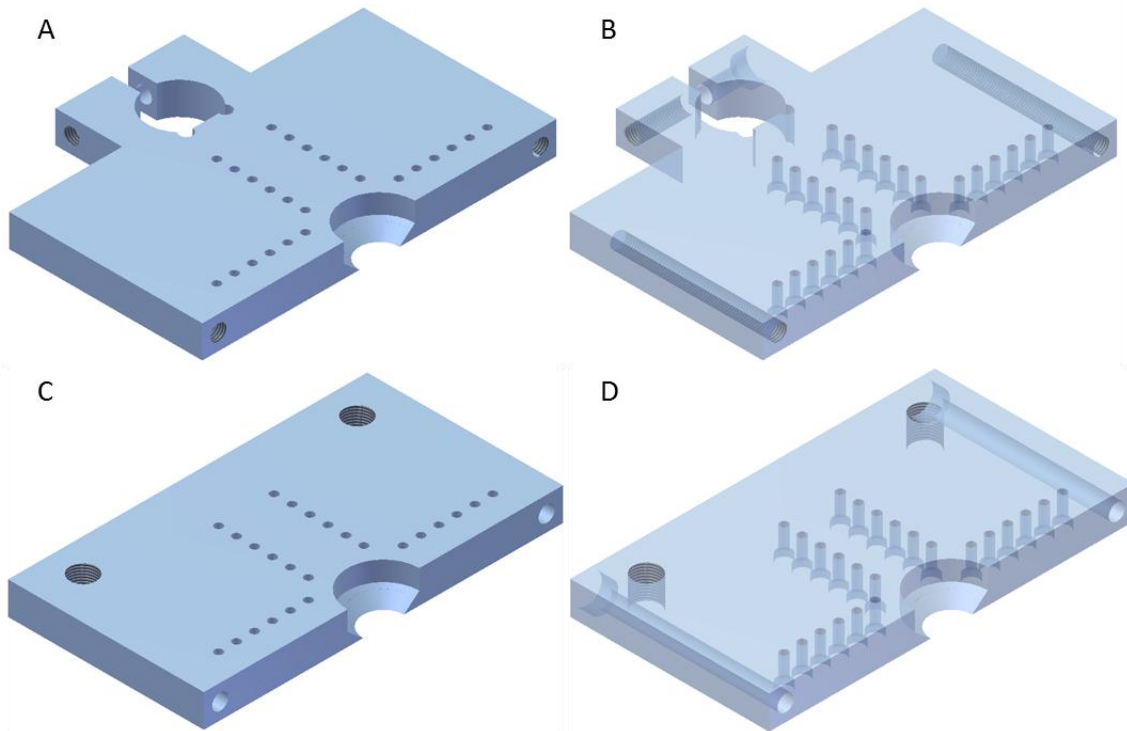


Figure 4.7: 3D models of the bottom (and top) supports. (A) Part fixed to the column and (B) semi-transparent model of the same part showing a number of holes and threads. (C) The sliding part presenting several holes (D) in addition to the two screws housing fastening this part to the fixed one.

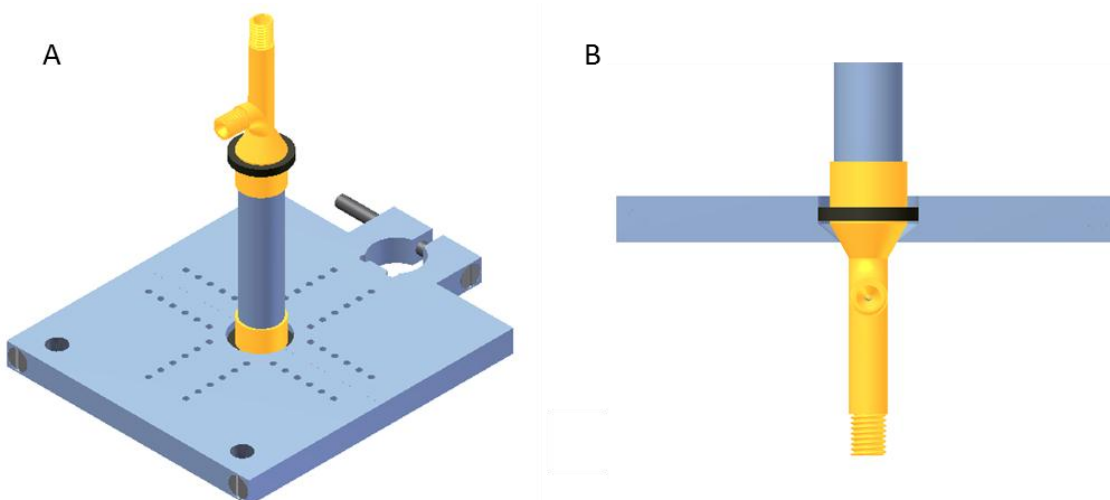


Figure 4.8: (A) 3D models of the bottom support handling the device, (B) and section of the support showing the fixing mechanism.

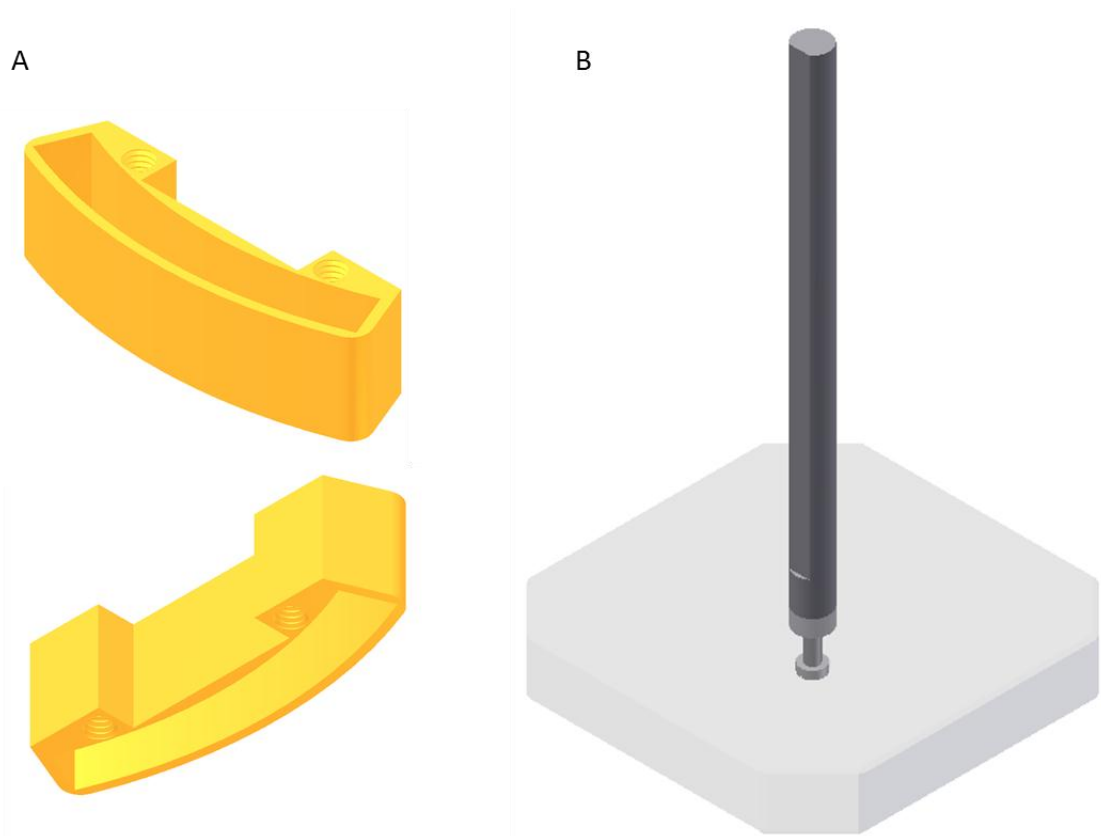


Figure 4.9: (A) 3D models of the magnet holder from different angles; (B) column and base assembled in support of the entire structure (Image not in scale).

4.4.1 Top and Bottom Supports

Tufset was used to build all top and bottom supports. It was an ideal material for cutting screw threads in, and it can be machined accurately.

The bottom support consisted of two parts: one part was designed to be fixed to a column; the other part was designed to slide onto two M5 threaded studs fastened to the fixed part (Figure 4.7C and D).

The fixed part had a through hole to allow the column to fit in, and two floating ends, tightened around the column by a screw. The walls of the hole matched the column shape to avoid rotation. The opposite side presented a recess characterised by a smooth slope, matching the manifold geometry (Figure 4.7A). On the top surface, a number of holes were created allowing six different magnet support configurations (Figure 4.7B).

The top support had the same design as the bottom support. Top and bottom supports kept the device firmly in position: the fixing mechanism was shown in Figure 4.8.

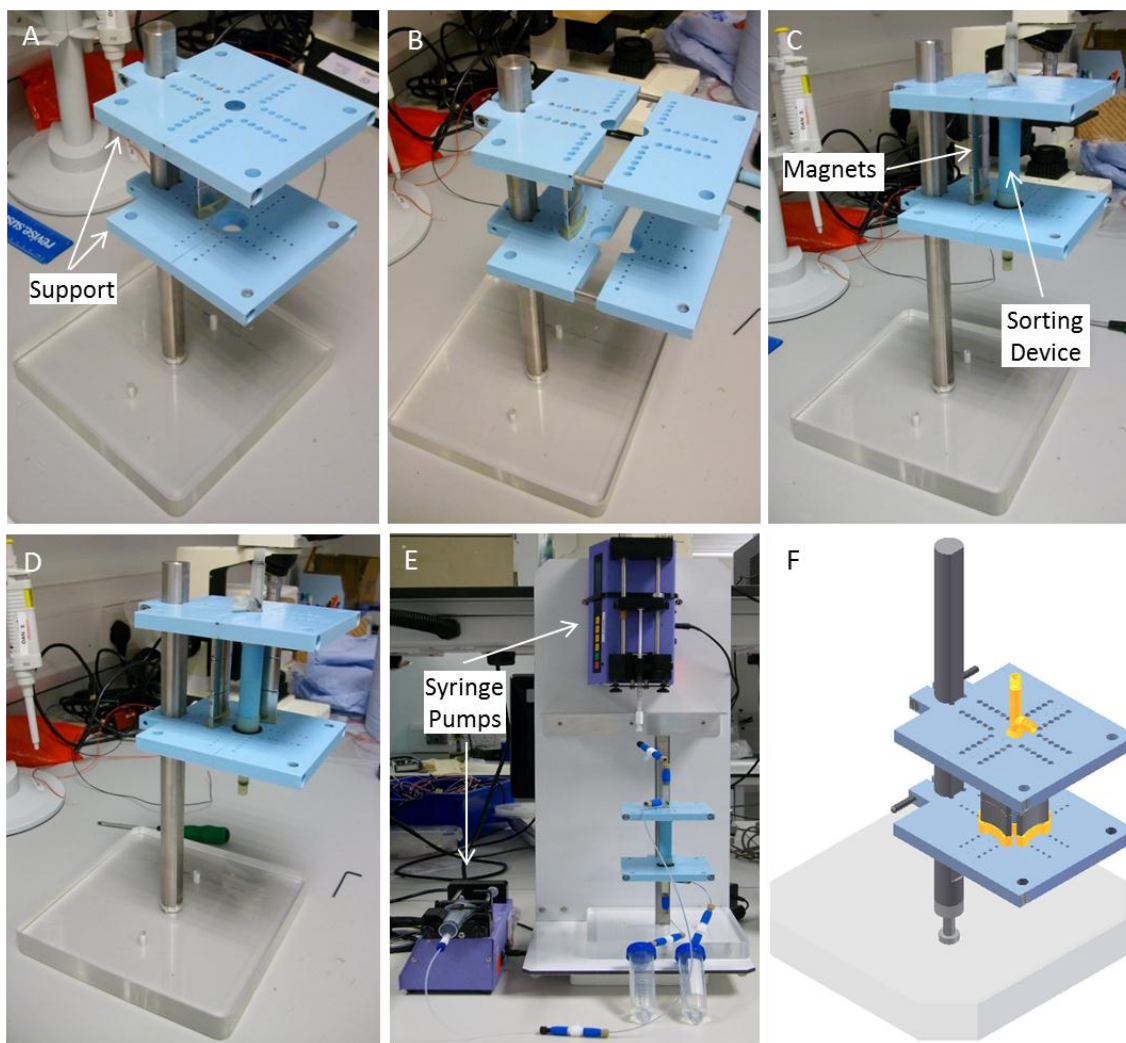


Figure 4.10: (A) Device support with one magnet; (B) the sliding parts of the top and bottom support slid on the four screws allowing the device to fit in. (C) Device assembled into the support with one (D) and two magnets around it. (E) Experimental setup (F) and 3D model of the fully assembled system.

4.4.2 Magnet Holders

In order to keep the magnets in position, it was necessary to design a holder capable of handling the magnetic force. A compromise between strength and width was achieved. The holder was printed using FullCure720, the same material used for the manifold. The two holes shown in Figure 4.9A were threaded to allow the holder to be fixed to the support by screws.

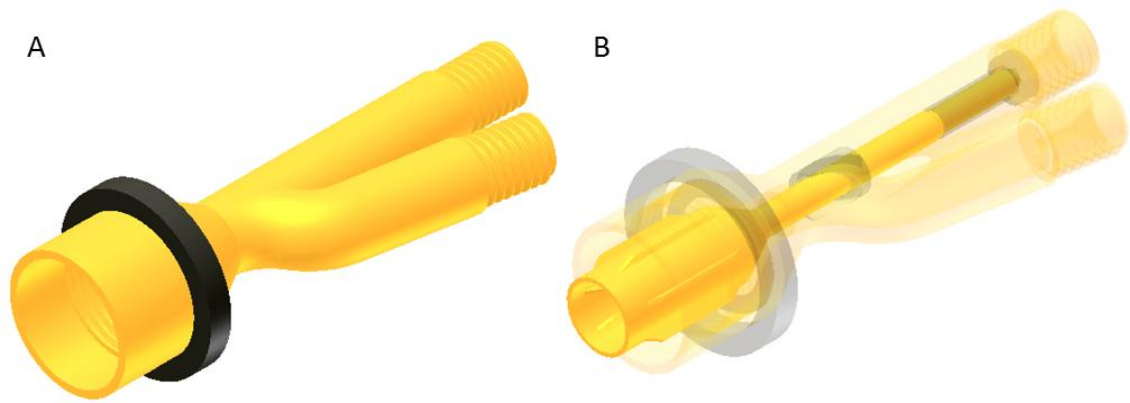


Figure 4.11: (A) 3D model of the manifold external part (ver. 2), the body structure was made in FullCure 720; (B) assembled manifold: the internal part and the points of contact between the two parts were shown in transparency.

4.4.3 Column and Base

The top and bottom supports were designed to be adjustable in height. A column, 300 mm high and 20 mm diameter, was designed to work as a runner. This component was built from a turned stainless steel bar. A flat groove was machined on one side in order to avoid any rotations and allow precise alignment. The column was fixed through a screw thread (cut into the column) and a screw to a 200 x 200 mm base built in transparent acrylic material, to prevent the device from falling (Figure 4.9B).

4.5 Assembly and final setup

The assembly operation consisted of fixing the device into the support and assembling the magnets around it; the entire operation took several minutes (Figure 4.10). Tubing connections, as well as two syringe pumps (one for the suspended mixed cells sample and one for the buffer) and the recovery reservoirs for target and non-target cells were needed to perform experiments. To avoid cell sedimentation inside the tubing, it was necessary to keep the dead volumes to a minimum and avoid sharp bends in the tubing. The syringe injecting the cell sample was placed vertically above the sample input to reduce the dead volume (Figure 4.10E). A vertical support for the syringe pump was designed and built.

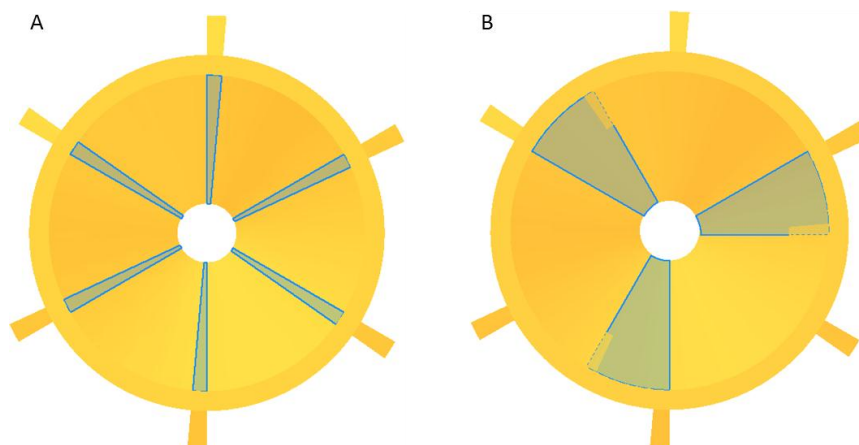


Figure 4.12: (A) Model of the ver. 1 (B) and ver. 2 internal part of the manifold, with six respectively small fins and three larger fins grounded on the bottom.

The material used was polyvinyl chloride (PVC) covered with a thin aluminium layer. This ensured a stable support for the syringe pump, held in a vertical position and fastened through a cable tie. The support could be sterilised and could be used in a laminar flow cabinet. The two liquid outputs were recovered into 50 ml falcon tubes. Holes were drilled in to the 50 ml falcon tube lids for insertion of the micro-sized tubes from the two outlets. Tubes were fixed in the holes with glue, creating an air-tight seal. Sterile Falcon tubes could then be attached to perform the experiment.

4.6 Sorting Device version 2

One of the problems observed during the testing of the sorting device ver.1 was particle cross-contamination (see Section 7.2.1). In particular during the experiments using non-magnetic polystyrene beads ($10\ \mu\text{m}$), in the absence of a magnetic field, a percentage of the beads were found in the target output (where ideally none should be found). This led to the conclusion that some particles moved from the original internal stream (close to the central rod) and ended in the output designed for the target particles.

To improve this problem, changes to the input/output manifolds were made; in particular to the buffer input (Figure 4.11), leading to the design of the sorting device version 2 (ver. 2) (see Section 7.2.1). With the exception of the manifolds, ver.2 shared all other components with the first version of the sorting device. This was tested with several combinations of flow rates and sample concentration to investigate the cross contamination, leading to a significant improvement.

Further issues arose with the internal part of the manifold. The six bottom fins appeared to be structurally weak and after around twenty experiments simply collapsed on one side. The device assembly procedure was also a source of mechanical stress for those fins, due to the lateral torque applied by the central rod during the assembly of the manifold. To solve this issue, the internal part of the manifold underwent design modification. The number of original bottom fins, each one forming an arc of a circle of 5° , were reduced to three fins, each one forming an arc of a circle of 30° (Figure 4.12). The design modification significantly improved the component durability.

4.6.1 Material analysis

The sorting device (both ver. 1 and ver. 2) consisted of three main parts including tube, central rod, and manifolds. The tube and the central rod were turned on a lathe from a bar of Tufset and the manifolds were 3D printed in FullCure720 using the Object Connex 350 machine.

To investigate the internal surfaces of the device, samples of all the components were imaged using a scanning electron microscope (SEM) (Figure 4.13). On the internal surface of the tube, large number of creases was found, indicative of a coarse surface. A similar situation was seen when observing the central rod surface: irregularities were found on the surface, which looked like melted material.

Both these results were compatible with the building technique used (machined on a lathe) for those components. A sample of the manifold was investigated as well, revealing an irregular internal surface with grooves and ridges due to the working principle of the 3D printer, which used a support material (FullCure 705) to support the internal geometry of the component during printing.

4.7 Sorting Device Third Generation

The third generation sorting devices were built using different materials and techniques compared with the first two versions. A few geometrical changes were made. The third generation sorting devices were all built with the same technique and material. In particular, the manifolds were built using stereolithography. This consists of curing a photopolymer layer with an ultraviolet laser, following a specific path. Adding one layer of photopolymer at the time, it was possible to create functional 3D parts.

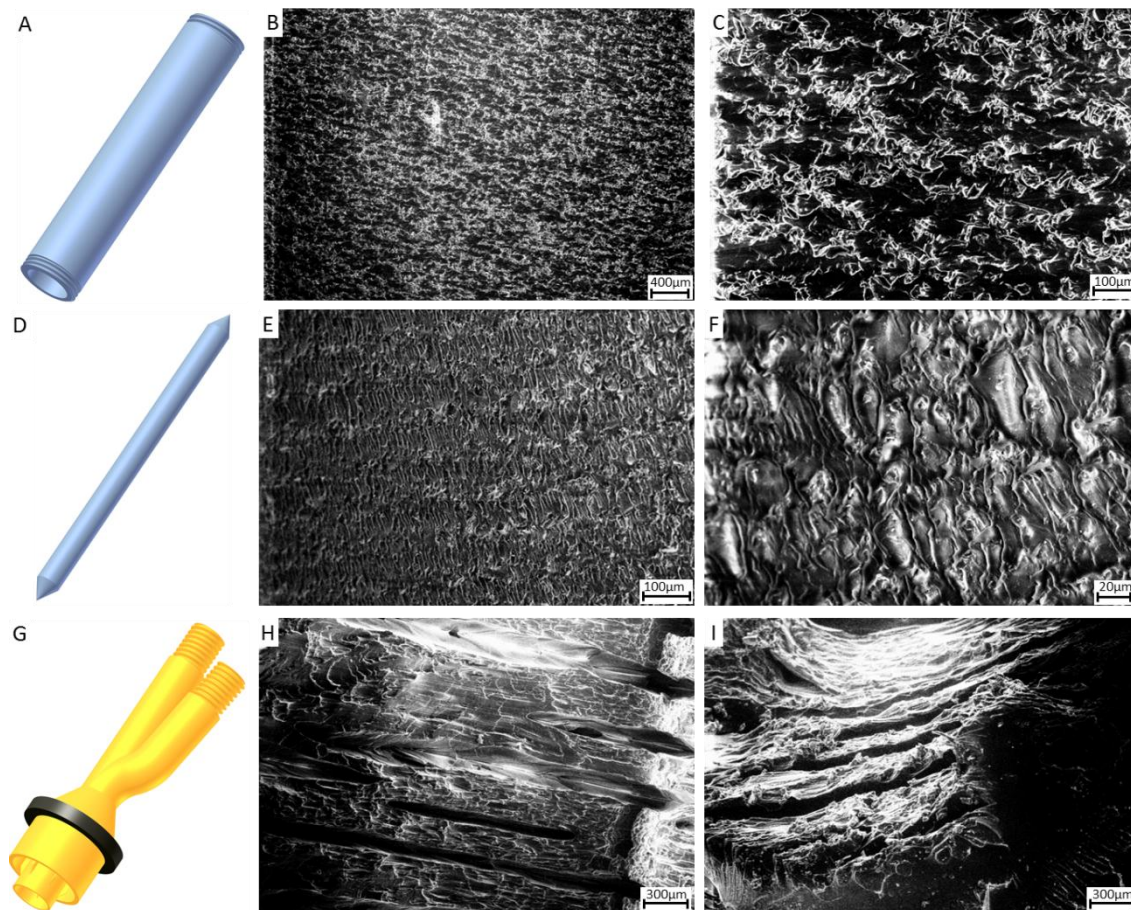


Figure 4.13: SEM images of the device components. (A) 3D model of the tube; (B,C) SEM images of the internal surface of the tube (scale bar 400 μm and 100 μm) at different magnifications. (D) 3D model of the central rod; (E,F) SEM images of the internal surface of the central rod (scale bar 100 μm and 20 μm) at different magnifications. (G) 3D model of the manifold ver.2; (H,I) SEM images of the internal surface of the manifold ver.2 (scale bar 300 μm) at different angles.

The machine (EnvisionTEC Ultra) used was in the Engineering Design and Manufacturing Centre (EDMC) at the University of Southampton and it used the photopolymer LS 600 as building material. The tube and the central rod were obtained from extruded plastic products.

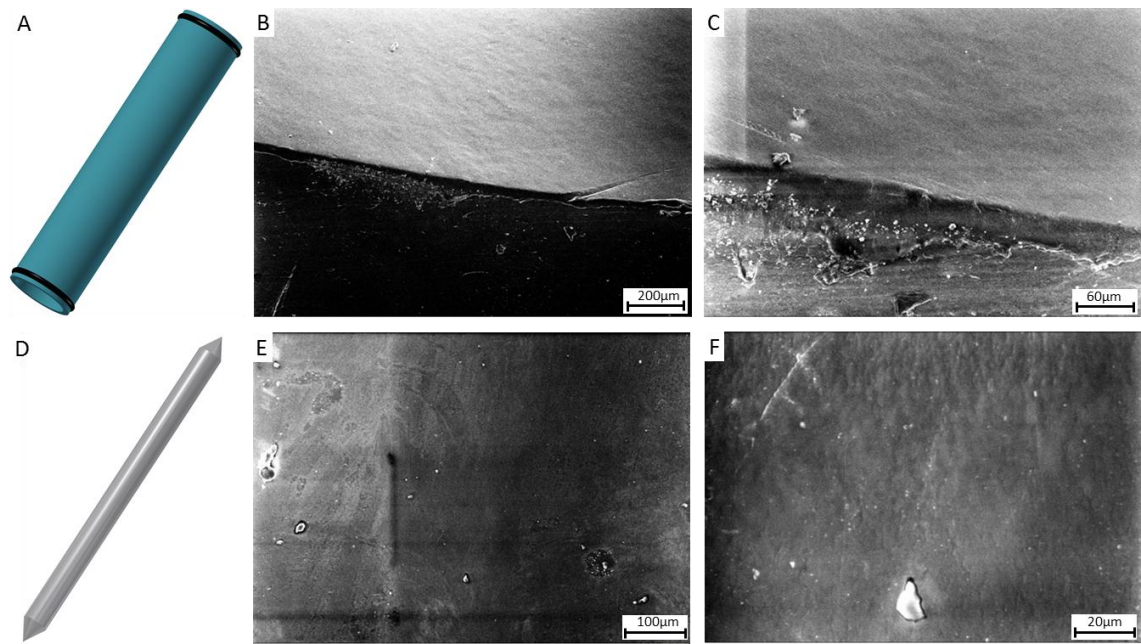


Figure 4.14: SEM images of the device components. (A) 3D model of the tube ver.3; (B,C) SEM images of the internal surface of the tube ver.3 (scale bar 200 μm and 60 μm) at different magnifications. (D) 3D model of the central rod ver.3; (E,F) SEM images of the internal surface of the central rod ver.3 (scale bar 100 μm and 20 μm) at different magnifications.

4.7.1 Sorting Device ver. 3

The components of sorting device ver. 3 differed from the previous versions with respect to the internal diameter of the tube, which was changed from 11 mm to 13 mm. This allowed to increase the working flow rate (and the throughput) without influence the cell residence time within the sorting device (see section 6.6). This component was manufactured from an extruded pipe of polypropylene random copolymer (PP-R). The pipe was machined on a lathe to reduce the external diameter and to give a thickness of 1.5 mm. The internal surface of the tube was not machined, preserving the original surface characteristics. The fixing mechanism between tube and manifolds remained the same (screwing), therefore threads were grooved on both ends of the tube. The central rod was obtained from an extruded acrylic bar, machined at both ends to achieved the desired length. These components were imaged using the SEM, indicating a regular surface and the absence of grooves or ridges (Figure 4.14). The manifolds used in sorting device ver. 3 were built using stereolithography, a method similar to the 3D printing technique used to build the manifolds in the previous versions.

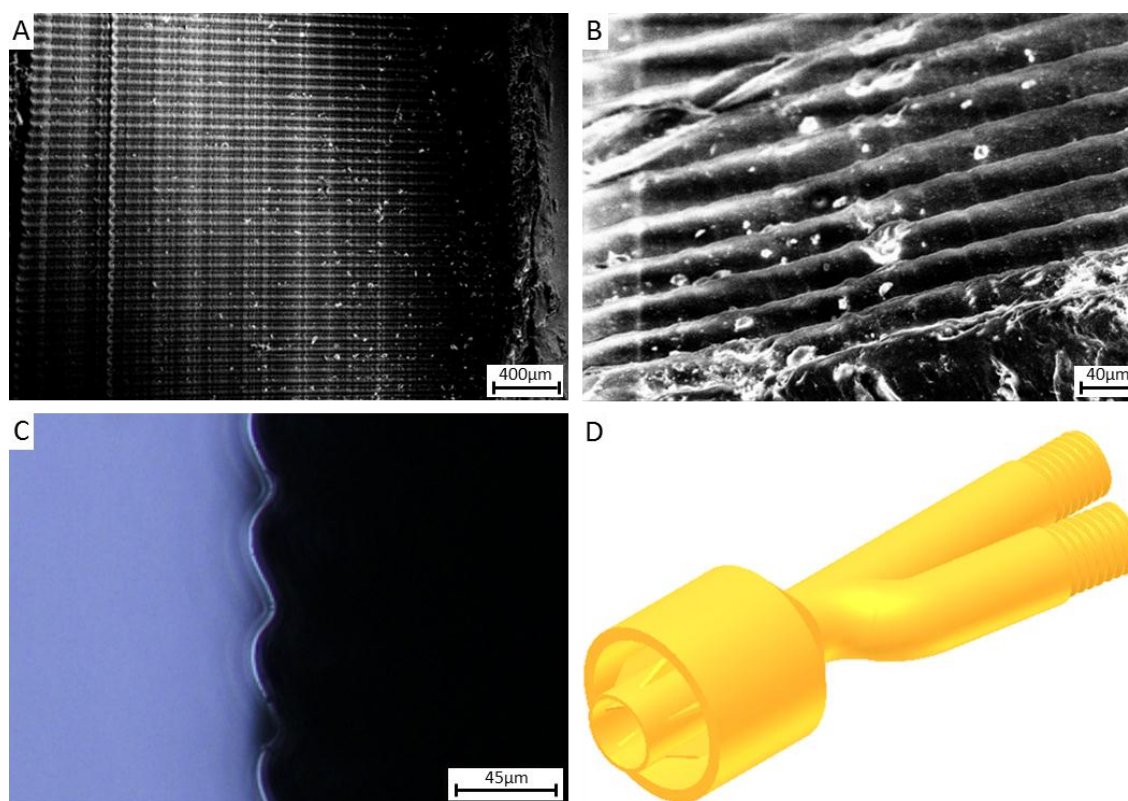


Figure 4.15: (A) SEM images of the internal surface of the manifold ver.3 built using stereolithography at different (B) magnifications (scale bar 400 μm and 40 μm). (C) Photomicroscopy of a sample from the manifold ver.3 (scale bar 45 μm). (D) 3D model of the manifold used in the sorting device ver. 3.

In particular, both methods were additive manufacturing techniques and need a support material during printing. Stereolithography used less support material, so that complex hollow geometries can be printed. In addition, the support material was arranged in a firm scaffold making it easier to remove than the malleable material used in 3D printing. It was therefore possible to build the manifold as a single part, avoiding the time consuming and challenging assembly procedure used in the second-generation device. Furthermore, the internal surface of the manifolds built with stereolithography had regular horizontal steps with a peak-to-peak distance of 50 μm and a depth of $\sim 15 \mu\text{m}$, resulting in a more even surface than the previous version. These steps were the layers of material added one at the time during the building process, and they represented the resolution of the machine (Figure 4.15). The stereolithography machine did not allow the printing of multi-material components. Due to the possibility of printing the manifold in one part, there was no need to add rubbery material at the contact points between the internal and external part as in the previous generation.

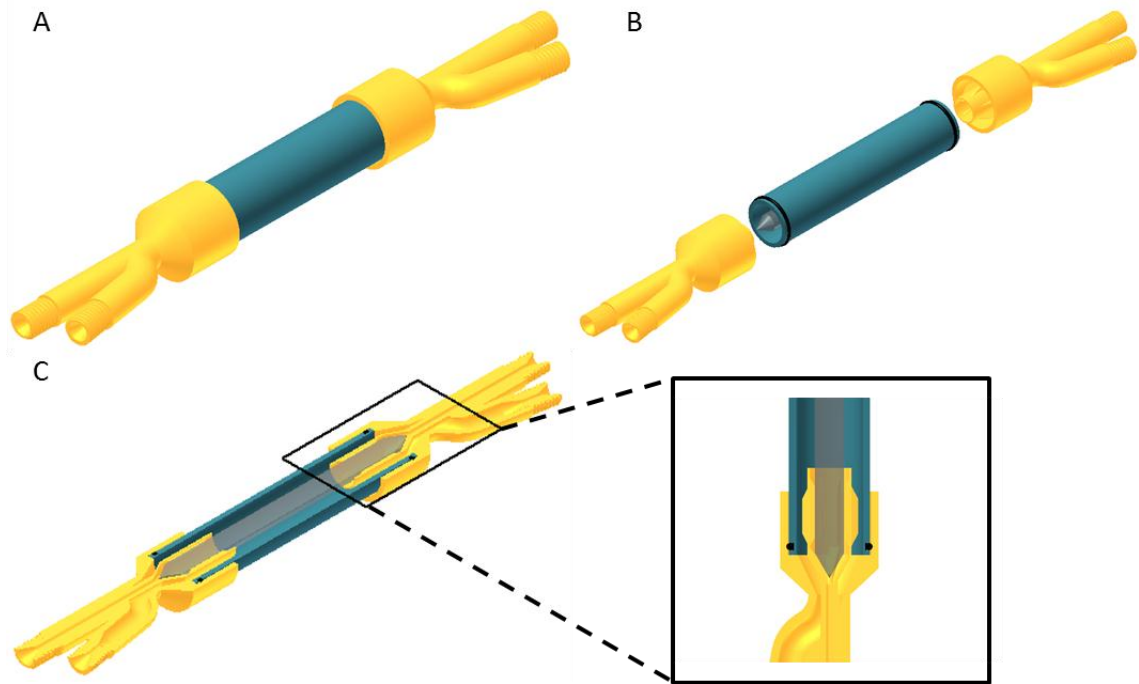


Figure 4.16: 3D model of the sorting device ver. 3.4. (A) Overall aspect of the assembled device; (B) exploded view of the device, with the push-in fasten mechanism using O-rings at the ends of the tube; (C) longitudinal section of the device and detail of the fasten mechanism.

However, the interface between the manifold and the tube led to several leakage problems, due to the fastening mechanism, as observed in the second generation manifold.

4.7.2 Sorting Devices ver. 3.2 to 3.5

To solve the sealing problems due to the interaction of manifold and tube in sorting device ver. 3, a series of fastening mechanisms were developed, leading to version 3.2, 3.3 and 3.4. The manifold ver. 3 had an internal thread of 20 TPI that did not improve the watertight properties. Version 3.2 and 3.3 investigated the manifold-tube fastening mechanism through the use of different threads: 8 TPI threads with $\frac{3}{4}$ and $1\frac{1}{2}$ revolutions respectively. Neither of these solutions ensured a watertight seal, even with the addition of polytetrafluoroethylene (PTFE) tape.

Sorting device ver. 3.4 was radically different from all others, using a completely different fastening mechanism. Both the manifolds and the tube had no threads; instead, the tube had a groove on each end and the manifolds had a clean internal surface. Two O-rings were placed in the groves at the tube ends, forming a push-fit mechanism with the manifolds, achieving a watertight seal when the device was assembled (Figure 4.16).

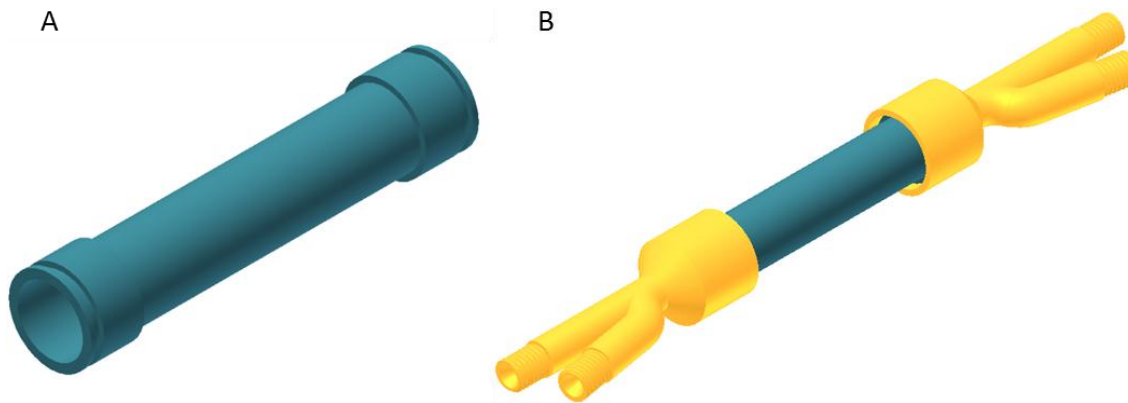


Figure 4.17: 3D model of the sorting device ver. 3.5. (A) The tube was the only component changed from the previous version and had a thickness of $750 \mu\text{m} (\pm 3 \mu\text{m})$; (B) overall aspect of the ultimate version of the device.

Tube thickness was an important parameter of the sorting device. It does not influence the magnetic flux density (\vec{B}) or the gradient ($\nabla\vec{B}$) (the material was magnetically transparent), but it determines the distance between the source of the magnetic field (permanent magnets in this study) and the sorting area within the device. Version one and two of the device, used a 2 mm thick tube.

The final version (3.5) of the sorting device had a tube thickness of $750 \mu\text{m} \pm 3 \mu\text{m}$. This was the only difference with the previous version, but it had significant effects on \vec{B} and $\nabla\vec{B}$ (see section 7.6). Figure 4.17 shows the tube used in sorting device ver. 3.5 and the final version of the device.

4.8 Summary

Three versions of the sorting device were developed in this study. The first and second versions shared materials and building techniques. In particular, the tube and the central rod were machined from a Tufset bar. The manifolds were built using a 3D printer and consisted of two parts assembled together. However, the design of some components required some optimisation. In the second version the manifold differed in both the internal and external parts. The third series of sorting devices consisted of five different versions: ver. 3 to 3.5. All the devices in this series shared building techniques and materials, which were different from those used in previous versions. The tube and the rod were made from an extruded pipe and an acrylic bar respectively. The machining was restricted to external surfaces (except the rod ends).

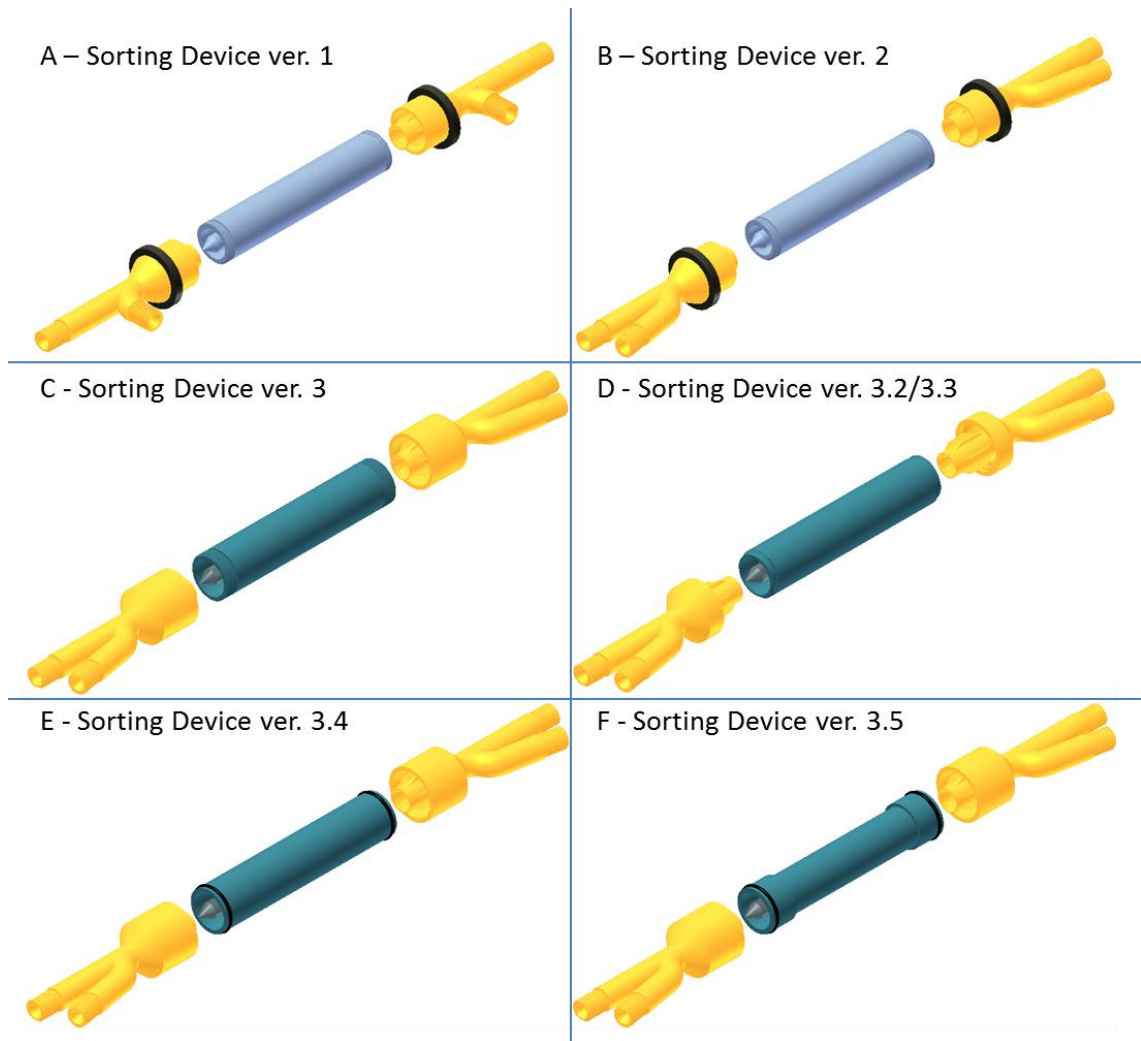


Figure 4.18: 3D models of the sorting devices developed in this study. (A) Versions 1 (B) and 2 used common building techniques and materials, while the geometries of few components were subjected to changes. (C) The third series of devices consisted of several versions: version 3 was the first to use different materials and building methods compared with the previous version, leading to sealing problems (no multiple-materials printing). (D) The two following versions solved those problems using different kinds of threads, (E) while version 3.4 achieved a watertight using O-rings on the tube ends. (F) The 3.5 was the ultimate version of the sorting device, featuring a reduced tube thickness ($750 \mu\text{m} \pm 3 \mu\text{m}$).

The manifolds were built using a stereolithography machine, which had advantages over 3D printing such as the possibility to build components in a single part, reduced use of support material (easy to detach) and a more regular surface finish. However, the inability to build multiple-material components using stereolithography led to leakage issues with the system. Versions 3.2 and 3.3 attempted to solve these problems. The solution was achieved in ver. 3.4. The final version of the device, ver. 3.5, reduced the tube thickness

from 1.5 mm to 750 μm ($\pm 3 \mu\text{m}$) in order to minimise the distance between the magnets and the sorting area within the device (Figure 4.17). Figure 4.18 shows 3D models of all the versions of the sorting devices developed in this study.

Chapter 5

Device working principle, magnetic systems and numerical simulations

To generate the magnetic force needed to perform cell sorting, three magnetic systems were developed: the quadrupole magnetic system version 1 (QMS ver.1), the quadrupole magnetic system version 2 (QMS ver.2) and the hexapole magnetic system (HMS). In this chapter the designs and building techniques of the magnetic systems were described. To model the magnetic flux density (\vec{B}) generated by the different magnetic systems used in this study, COMSOL Multiphysics 4.3b software was used.

To validate the data for \vec{B} obtained through numerical simulations, a set of experimental measurements were performed. The \vec{B} generated by a simplified magnetic system was measured with a Gaussmeter and compared with the modelled data for the same magnetic system. All the magnetic systems described in this chapter were tested in Chapter 7.

5.1 Device working principle

The aim of the study was to isolate and characterise SSCs from HBMSCs using a microfluidic device. The device consisted of a cylinder, concentric rod and two input/output manifolds (Figure 5.1A). The working principle involved creating a stream carrying the mixed cell sample near the central rod (inner stream) surrounded by a sheath flow (outer stream). This task was accomplished by the input manifold that merged two distinct inputs in two concentric streams (Figure 5.1B). The experimental setup consisted of: two syringe pumps (Harvard Apparatus – 11 Plus, USA), tubing, the magnetic system and the sorting device.

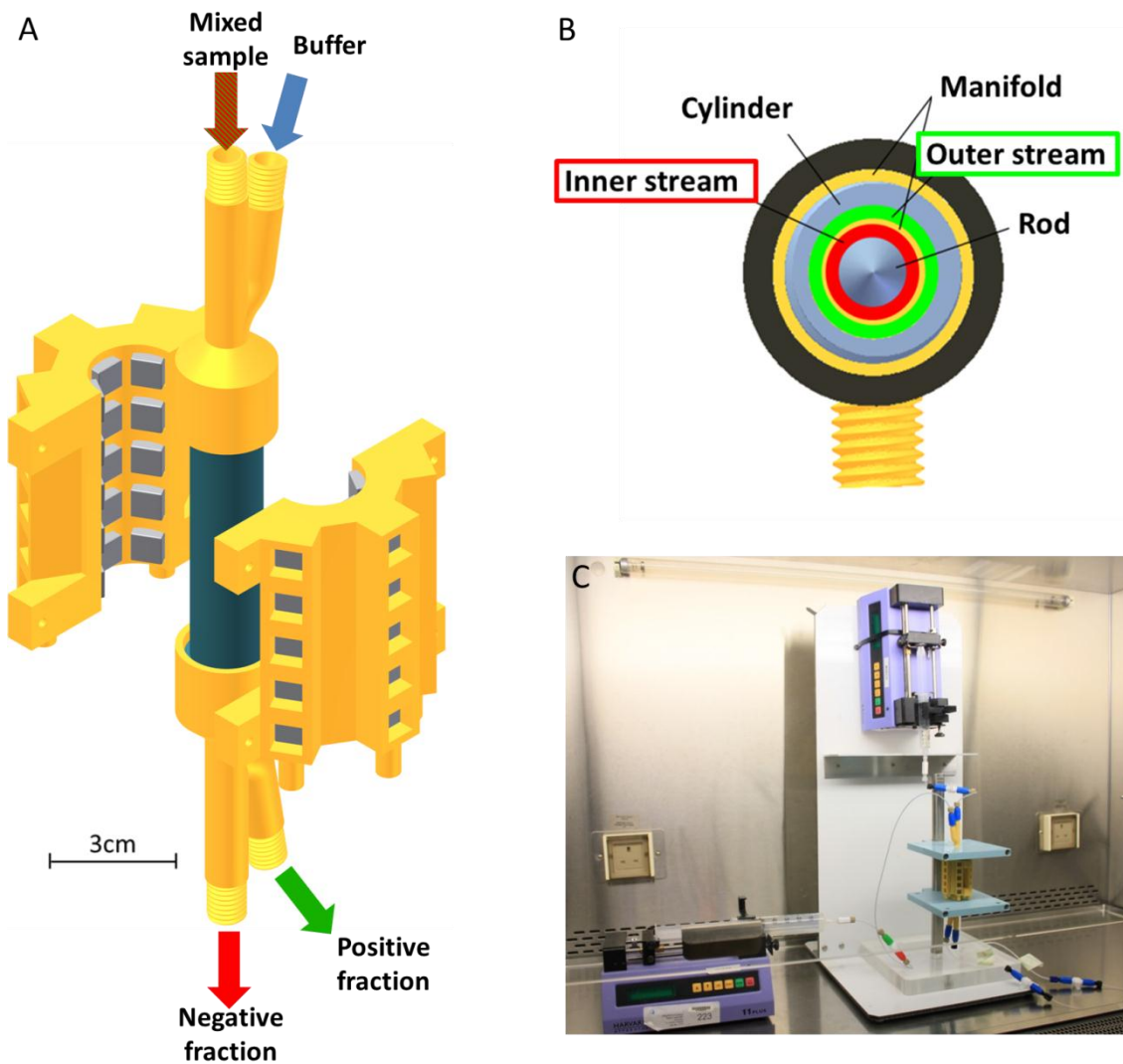


Figure 5.1: (A) 3D models of the sorting device (ver. 3.5) and the hexapole magnetic system (HMS). (B) Sample and buffer were merged in two concentric streams: inner stream and outer stream respectively. (C) Picture of the experimental setup in a laminar flow hood.

Due to its flexibility and reduced dimensions, the entire experimental setup was placed in a laminar flow hood, which provided a quasi-sterile experimental environment (Figure 5.1C).

The mixed cell sample included immunomagnetically labelled cells (target cells) and non-target cells. Immunomagnetically labelled cells experienced a magnetic force (\vec{F}_m), due to the magnetic field generated by the surrounding neodymium magnets, which pull them into the sheath flow. Figure 5.2A shows the working principle of the sorting device; the mixed cell population flowed through the input manifold and started in the inner stream. Immunomagnetically labelled cells were pulled into the outer stream by the magnetic force, while the non-target cells were constrained into the inner stream by the sheath flow.

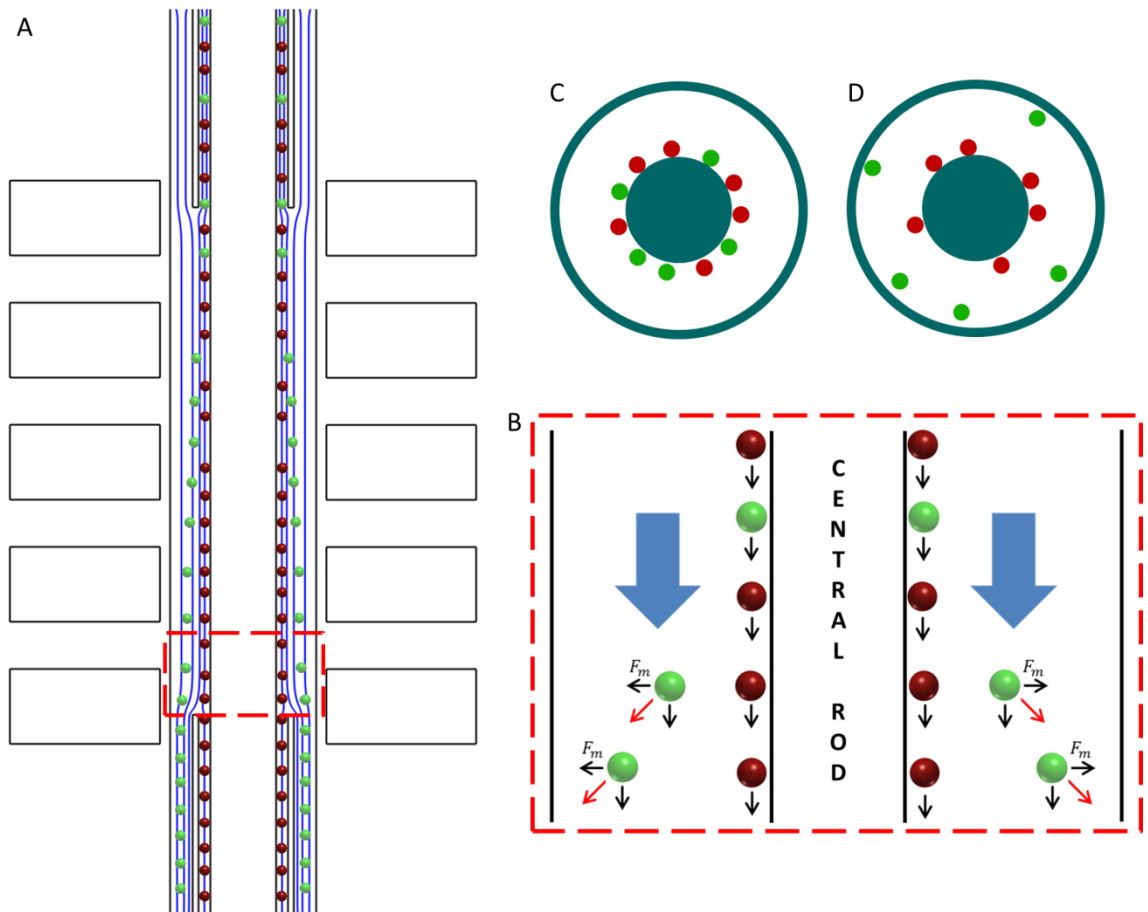


Figure 5.2: Diagrams showing the working principle of the sorting device. The mixed cell population (non-target cells in red, target cells in green) start in the inner stream. Under the influence of a magnetic field the target cells experienced a magnetic force (\vec{F}_m) and were pulled into the outer stream. (A) Overview of the device working principle on a vertical mid-section (B) and detail. (C, D) Diagrams showing the device working principle on a horizontal section.

Details of the sorting principle were shown in Figure 5.2B. Figure 5.2C and D shows the initial and final positions of target and non-target cells. The concentric flows carrying the two cell populations were collected via the output manifold. The non-target cells were collected in the negative fraction and the target cells in the positive fraction.

As from Chapter 3, the magnetic force acting on a labelled cell depends from \vec{B} and his gradient ($\nabla\vec{B}$). All the magnetic system described in this chapter were designed to obtain high values of \vec{B} and $\nabla\vec{B}$. The magnetic field gradient was a key aspect to address. Accordingly to the equation 3.8 (chapter 3), a labelled cell would experience a magnetic force \vec{F}_m if exposed to a non-uniform magnetic field.

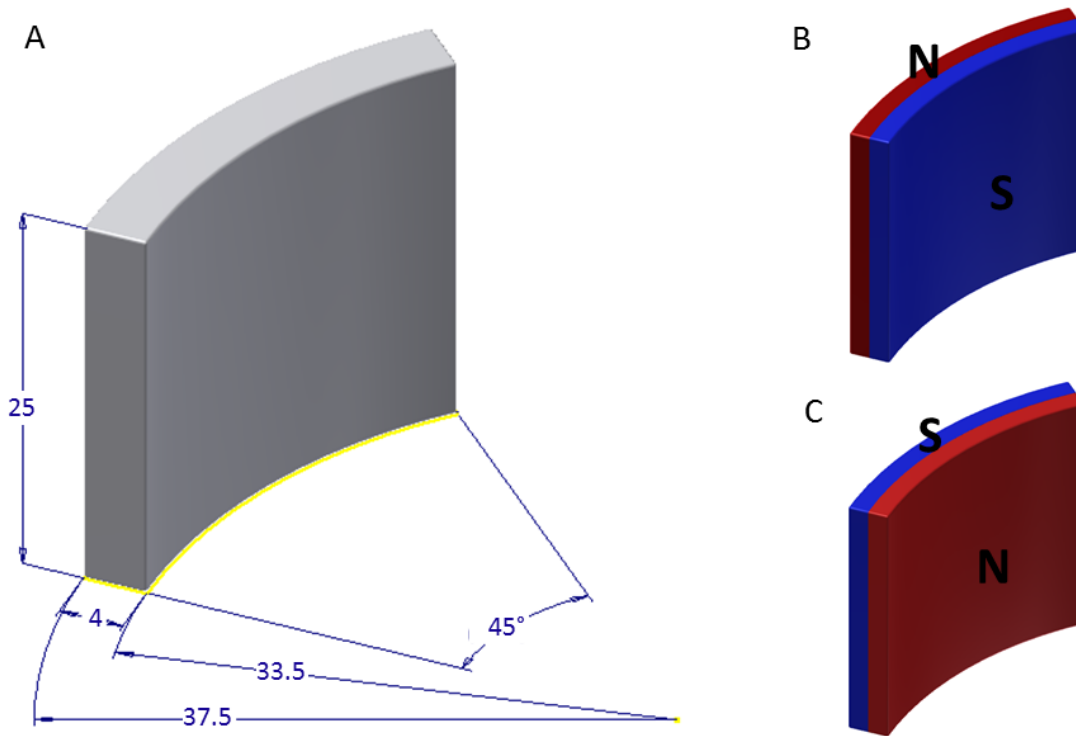


Figure 5.3: (A) 3D model of the arc segment of the neodymium magnet used. All measurements were in millimetres except the arc angle which was in degrees. (B) The north pole (in red) can be on the outside face (C) or on the inside face of the arc magnet. Magnets with both magnetization directions were used.

Magnets' geometry, strength and disposition around the sorting device, were designed to had the highest $\nabla \vec{B}$ possible in the area of interest (within the sorting device).

5.2 Quadrupole magnetic system version 1

The quadrupole magnetic system version 1 (QMS ver.1) consisted of 12 arc segment neodymium magnets (NdFeB) of grade N42 (the magnetic flux output per unit volume) purchased from first4magnets® (UK). Each arc magnet was 4 mm thick, 25 mm high, with an aperture of 45° (Figure 5.3A). The magnetic system shown in Figure 5.4 was created by alternating magnets with opposite magnetization directions (Figure 5.3B and C). The 12 arc magnets were placed on top of each other in groups of three (Figure 5.4A). At each level, magnets with the same magnetization direction occupied opposite positions (Figure 5.4B). The magnets were kept in place by 8 magnet holders screwed into the device support. The magnetic system configuration was shown in Figure 5.5A.

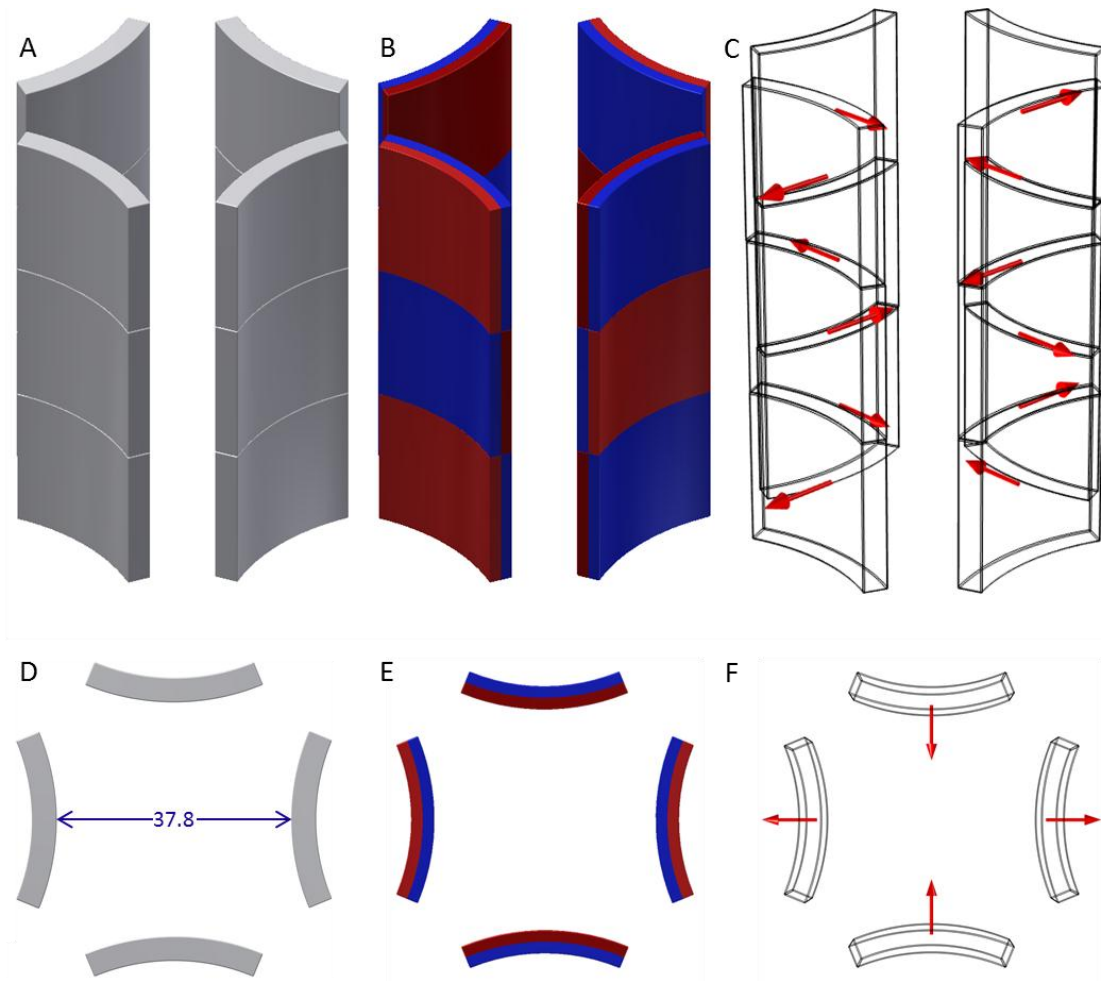


Figure 5.4: (A) 3D model of QMS ver.1. The 12 arc magnets were arranged on three levels. All measurements were in millimetres. (B) Magnets with the same polarity were placed in opposite positions. (C) Red arrows represented the magnetization direction of each magnet. (D) Top view (xy plane) of the magnetic system, (E) magnet polarity arrangement (F) and magnetization directions.

The device support had several holes to allow adjustment of the magnet position. The configuration shown in Figure 5.5 was the closest position to the device the magnets can assume. Due to the building technique and material used, the 3D printed magnet holders would not be able to sustain the attractive force between the magnets if these were positioned any closer to the device. Figure 5.5B shows the sorting device held in place by the device support. This device support was used throughout the whole project, and did not undergo any changes.

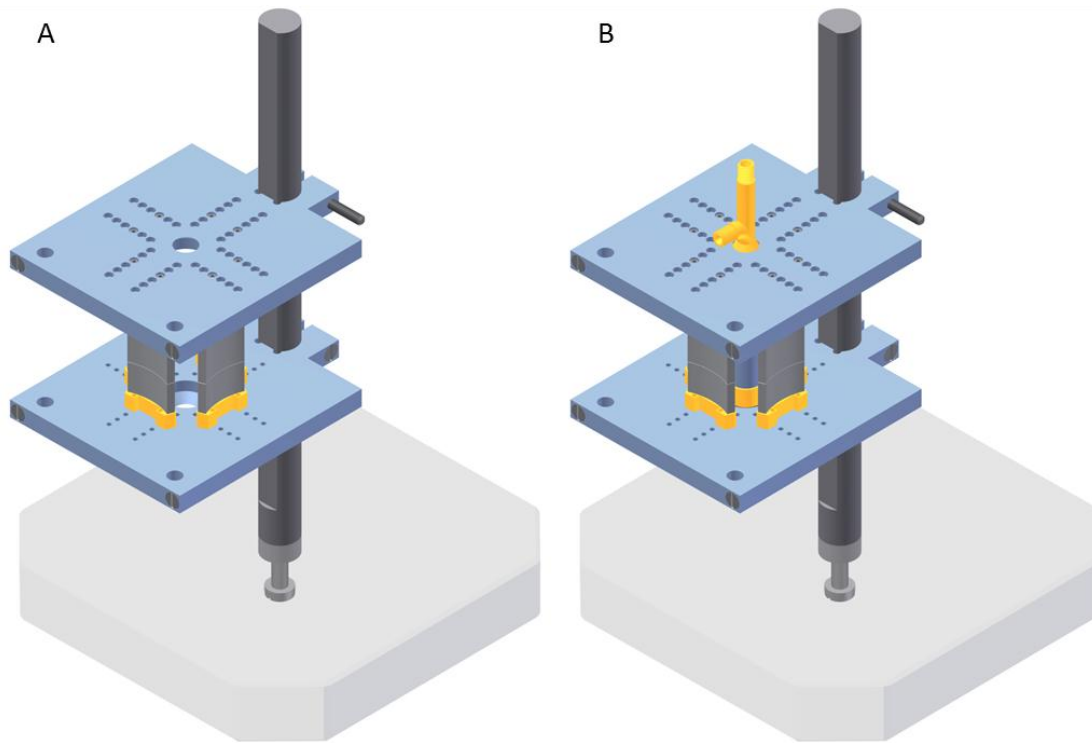


Figure 5.5: (A) 3D model of QMS ver. 1 including the magnet holders and the device support. (B) The sorting device was the middle of the magnetic system, held in place by the device support.

5.2.1 Numerical simulation of the magnetic flux density

Numerical simulation offers a useful tool to model and analyse the magnetic flux density (\vec{B}) within magnetic systems. To model the \vec{B} field generated by the different magnetic systems used in this study COMSOL Multiphysics 4.3b software was used (simulation details in Appendix A – Figure A.1). A horizontal mid-cut plane was used for the 3D simulation for QMS ver.1 (Figure 5.6A). The simulation showed the magnitude of \vec{B} ($|\vec{B}|$) and direction of \vec{B} (Figure 5.6D and C). \vec{B} was found to be completely symmetrical, due to the geometry of the system. To quantitatively estimate the $|\vec{B}|$ in the area within the magnetic system, a horizontal cut was drawn (Figure 5.6E), and $|\vec{B}|$ on this line was plotted (Figure 5.6F). On the magnet surface ($X=-19$) $|\vec{B}|$ was around 280 mT, dropping to 2 mT in the central part of the magnetic system ($X=0$). Due to the symmetry of the system, $|\vec{B}|$ increased to the initial value as it approached the surface of the opposite magnet. The symmetry of $|\vec{B}|$ along the horizontal means that only half of the path needs to be considered.

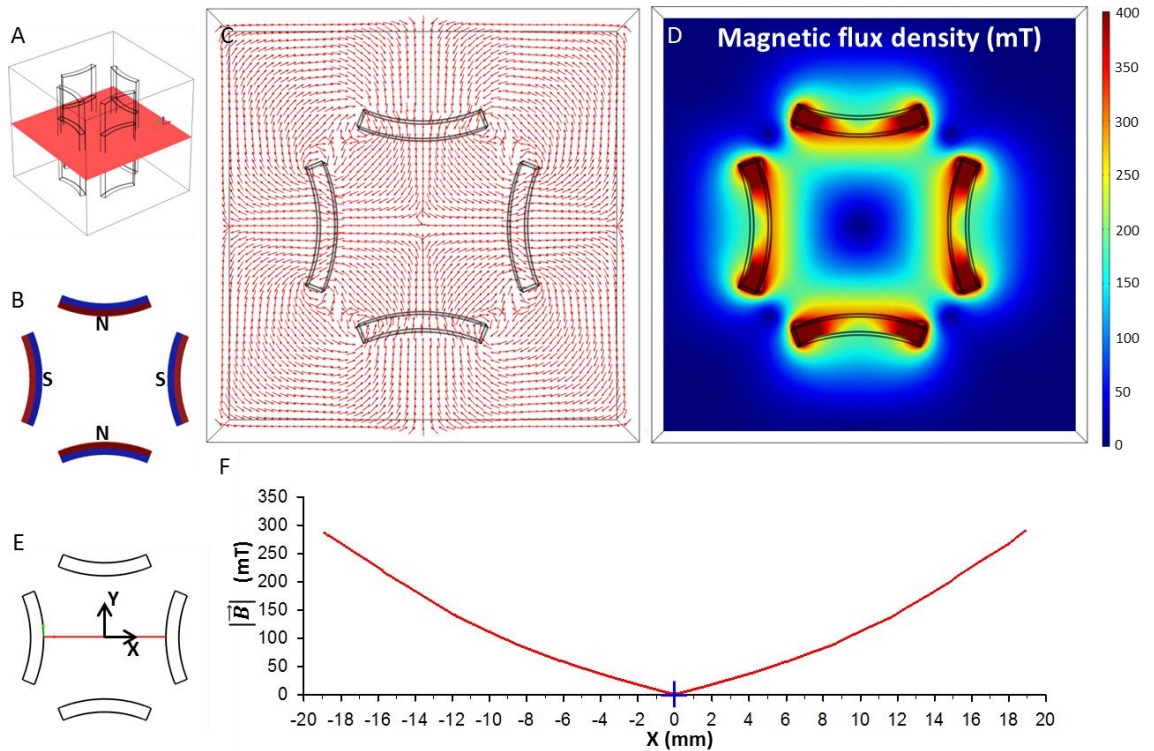


Figure 5.6: Numerical simulation of the magnetic flux density generated by the QMS ver.1. (A) Magnetic system horizontal mid-plane; (B) magnet arrangement and polarity. (C) Red arrows (normalised vectors) show the direction of \vec{B} and (D) colour map was the value of $|\vec{B}|$ (in Tesla) over the mid-plane. (E) Line across the system along mid-plane; central point of the magnetic system represented in blue; (F) plot of $|\vec{B}|$ on the horizontal line (simulation details in Appendix A – Figure A.1).

In view of the symmetry, the behaviour of $|\vec{B}|$ along a line starting from the centre point of the magnetic system and ending on the magnet surface was modelled (Figure 5.7B). Figure 5.7B shows the line along which $|\vec{B}|$ was quantified. The region of interest (within the sorting device) was indicated between the two vertical lines in Figure 5.7C. At the beginning of the region ($X=3$), $|\vec{B}|$ had a value of 27 mT, which increases to 64 mT ($X=6.5$). This change in $|\vec{B}|$ creates a gradient in magnetic flux density ($\nabla\vec{B}$) of 10 mT/mm. As discussed in Chapter 3 (see Section 3.1), $(\vec{B} \cdot \nabla)\vec{B}$ defined the magnetic force (\vec{F}_m) experienced by paramagnetic particles in the presence of the magnetic field.

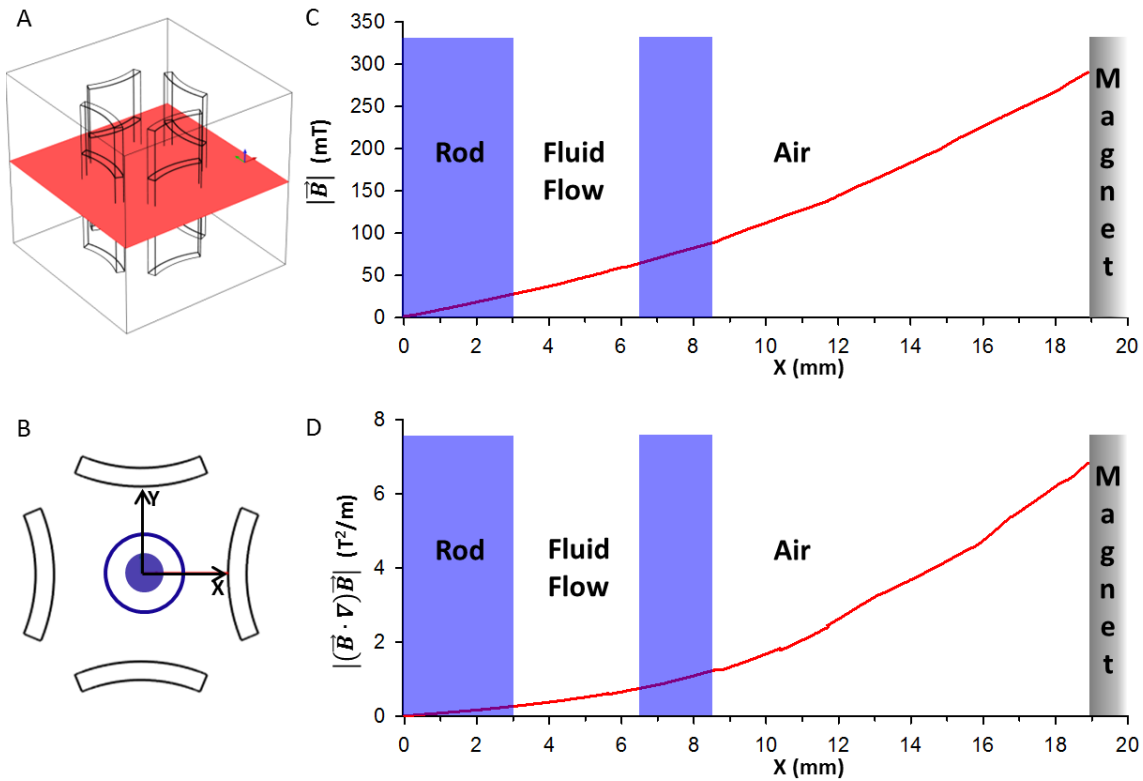


Figure 5.7: Numerical simulation of $|\vec{B}|$ and $|(\vec{B} \cdot \nabla)\vec{B}|$ generated by QMS ver.1. (A) Horizontal mid-plane; (B) line drawn between the centre point and the magnet surface; (C) plot of $|\vec{B}|$ along line. (D) Plot of $|(\vec{B} \cdot \nabla)\vec{B}|$ along the line. Simulation details in Appendix A – Figure A.1.

\vec{F}_m (see equation 5.3) was directly proportional to $(\vec{B} \cdot \nabla)\vec{B}$. The value of $|(\vec{B} \cdot \nabla)\vec{B}|$ along the cut line was plotted in Figure 5.7D; the region of interest was indicated between the two vertical lines. In this region, the values of $|(\vec{B} \cdot \nabla)\vec{B}|$ started from 0.26 T²/m and increased to maximum of 0.78 T²/m. In Appendix A (Figure A.2 / Figure A.3) the various components of \vec{B} and $(\vec{B} \cdot \nabla)\vec{B}$ along the lines analysed were plotted.

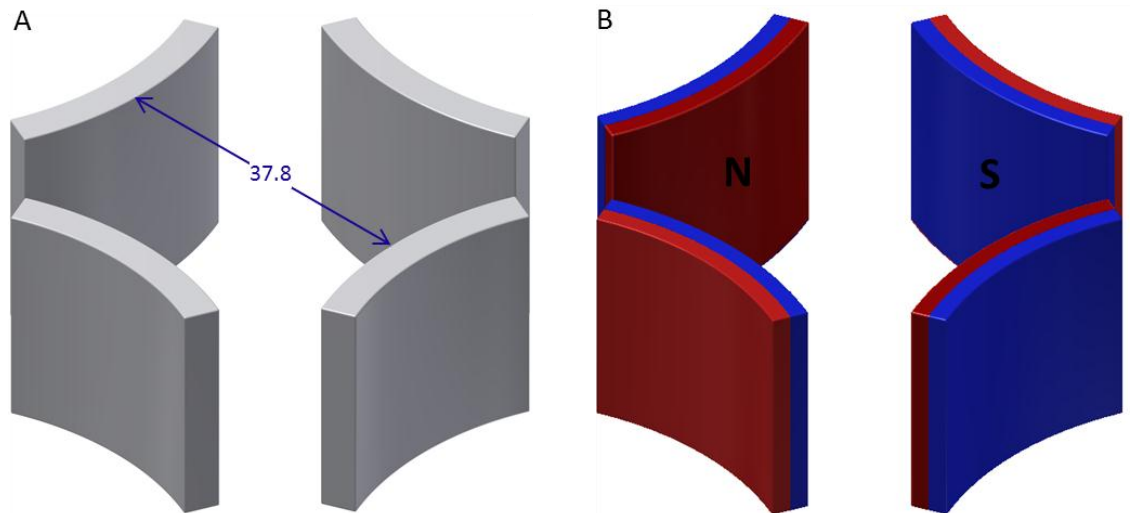


Figure 5.8: (A) 3D model of the simplified magnetic system used for the experimental measurements of magnetic field. All the measurements were in millimetres. (B) The 4 arc magnets were arranged so that magnets with the same polarity were placed in opposition (North pole in red, South pole in blue).

5.2.2 Magnetic flux density measurements

To validate the magnetic field values obtained through numerical simulation, a set of experimental measurements was performed. Due to difficulties in performing field measurements within QMS ver.1, a simplified magnetic system was assembled. It consisted of 4 arc segment neodymium magnets with the same specifications as those used in QMS ver.1. Arc magnets with the same magnetization sense were placed at opposite positions (Figure 5.8). A numerical simulation of this simplified magnetic system was performed and the results were compared with experimental measurements. These were taken using a home-made Gaussmeter made with a Hall effect linear probe (Allegro MicroSystem LLC, USA – A1321), see Figure 5.9. The linear Hall probe provided a voltage output proportional to the magnetic field. It was fixed to a rigid support and held in position by a stand clamp. The four neodymium magnets were fixed on a planar micromanipulator via the device supports (Figure 5.10A). A 20 mm x 20 mm area in the centre of the quadrupole system was mapped by adjustments of the micromanipulator. The sensor had a quiescent output voltage (voltage in the absence of magnetic flux density) equal to half the supply voltage, an output sensitivity of 5 mV/Gauss, and the maximum recordable value of \vec{B} was 500Gauss.

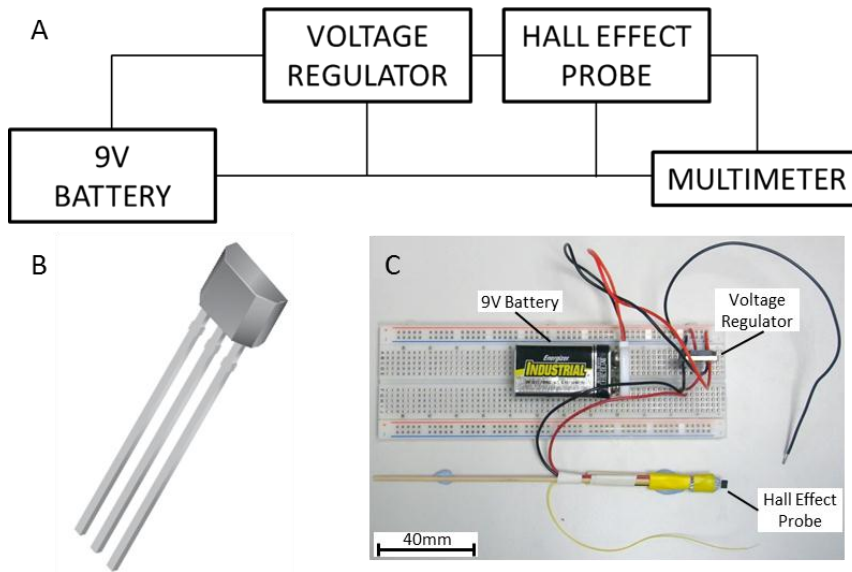


Figure 5.9: (A) Schematics of the home made Gaussmeter (voltage regulator: SparkFun Electronics, USA - COM-00107); (B) 3D model of the linear Hall effect probe (4.09 x 1.52 x 3.02 mm) used and (C) picture of the home-made Gaussmeter.

Measurements were made over 80 points (Figure 5.10B) within the analysed area. For each point the voltages corresponding to the X and Y component of the magnetic flux density (\vec{B}) were measured. To do so, the Hall probe was orientated perpendicularly to the X and Y axis of the system respectively. Voltages were then converted into the X and Y components of the magnetic flux density according to equation (5.1).

$$B_x = \frac{(V_0 - V_x)}{S} \quad (5.1)$$

$$B_y = \frac{(V_0 - V_y)}{S}$$

Where V_0 was the quiescent output voltage, V_x and V_y were the measured voltage corresponding to the X component (B_x) and Y component (B_y) of the magnetic flux density, and S was the output sensitivity of the Hall probe. Dimensionally (where [G] was gauss and [V] was volt):

$$[G] = \frac{[V]}{[V/G]} \quad (5.2)$$

Values B_x and B_y were processed in Matlab (MathWorks, Cambridge, UK) using cubic interpolation to obtain an array covering the entire analysed surface.

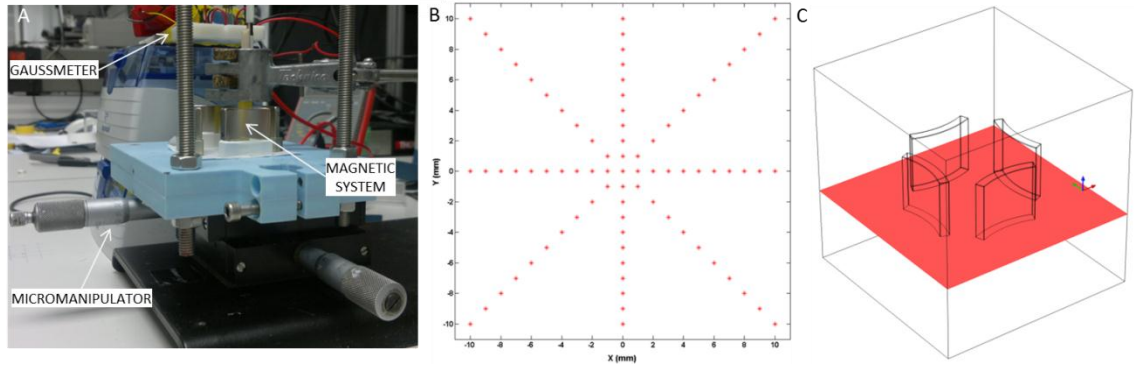


Figure 5.10: (A) Picture of the setup used to measure the field generated by the magnetic system consisting of a home-made Gaussmeter and a 2D micromanipulator which was used to move the magnetic system and perform measurements of B_x and B_y over (B) 80 points within an area of 20 mm x 20 mm at the centre of the system. (C) Vertical plane where measurements were made.

The $|\vec{B}|$ was obtained by calculating the Euclidean norm using B_x and B_y as components. The values were converted in Tesla. The calculated values of $|\vec{B}|$ were processed to obtain a 3D shaded surface. $|\vec{B}|$ ranged from 0 to 70 mT (where the Hall effect probe saturated). Figure 5.11A and Figure 5.11B show the variation in the field. Note the symmetry of $|\vec{B}|$ reflecting the geometry of the system. The values of $|\vec{B}|$ were represented by colours ranging from blue (10 mT) to red (70 mT) respectively.

To validate the numerical simulations, the experimental measurements of the simplified system were compared to data obtained from a numerical simulation of the same magnetic set up. The simulated experimental measurements were also performed over 80 points within an area of 20 mm x 20 mm at the centre of the magnetic system (Figure 5.10B). For an accurate comparison, the numerical simulation was performed on the same vertical plane (along the Z axis) as the measurements (Figure 5.11C). Due to the symmetry of the system, and following the path of the measurements points, only two segments (segment D and segment E) were drawn on the cut plane to characterize $|\vec{B}|$. Both segments start from the centre of the system ($X=0$) and cover a distance of 10 mm and 14 mm respectively (Figure 5.11D and E). $|\vec{B}|$ over these two segments was plotted for both experimental measurements and modelled data.

Figure 5.11F shows that the experimental measurements follow closely the modelled data up to 50 mT when the Hall probe saturated. The trend over segment E was similar; experimental and modelled data rise to reach a final value of around 70 mT (Figure 5.11G).

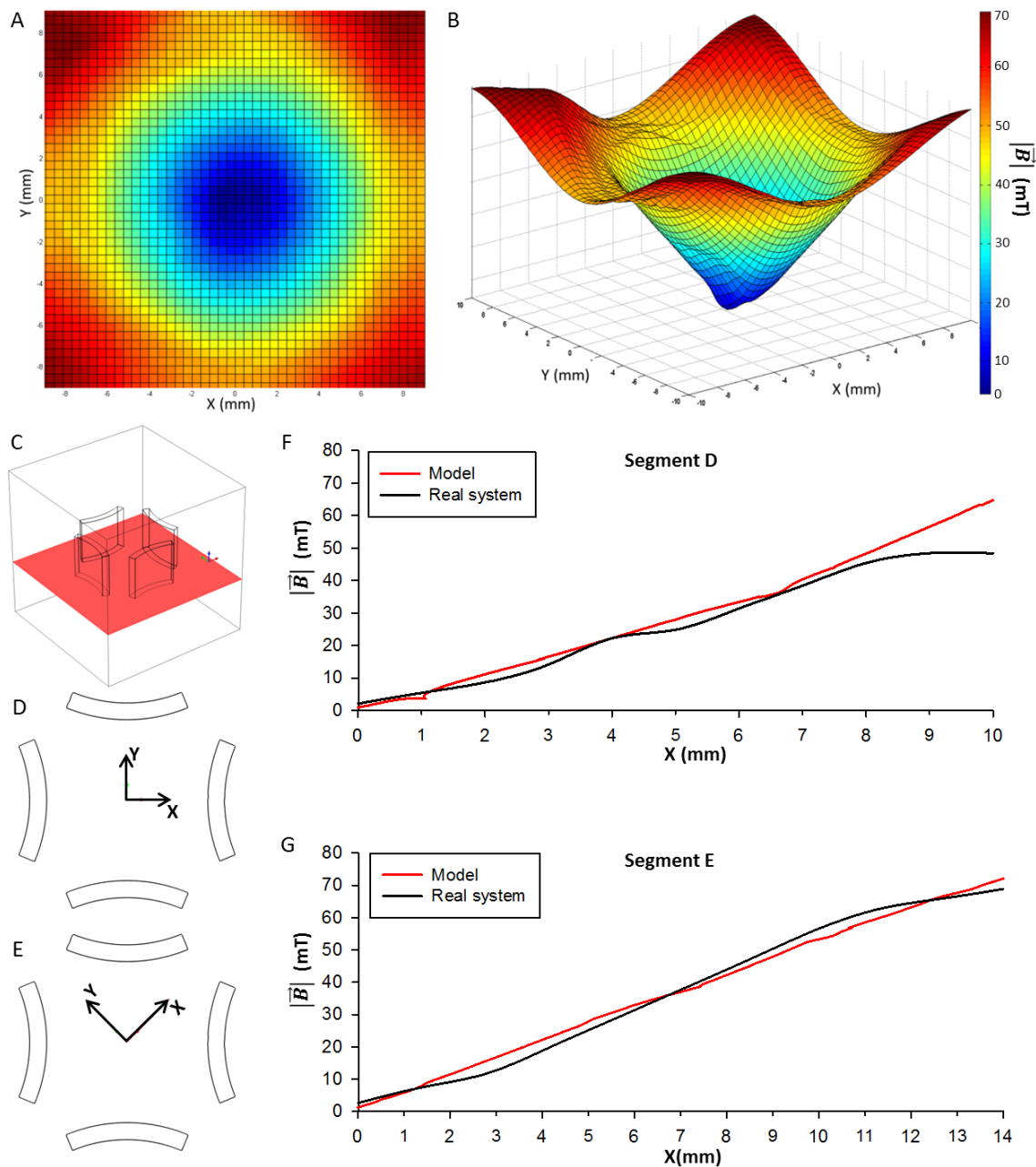


Figure 5.11: (A) Colour map of $|\vec{B}|$ obtained from experimental measurements of B_x and B_y after cubic interpolation. (B) 3D shaded surface representing $|\vec{B}|$ over the area of interest. (C) Plane representing the Z level of the measurements and the modelled data. (D) Segment D and (E) segment E drawn on the plane. (F) Plot of $|\vec{B}|$ over segment D and (G) segment E of modelled data (red line) and laboratory measurements (black line).

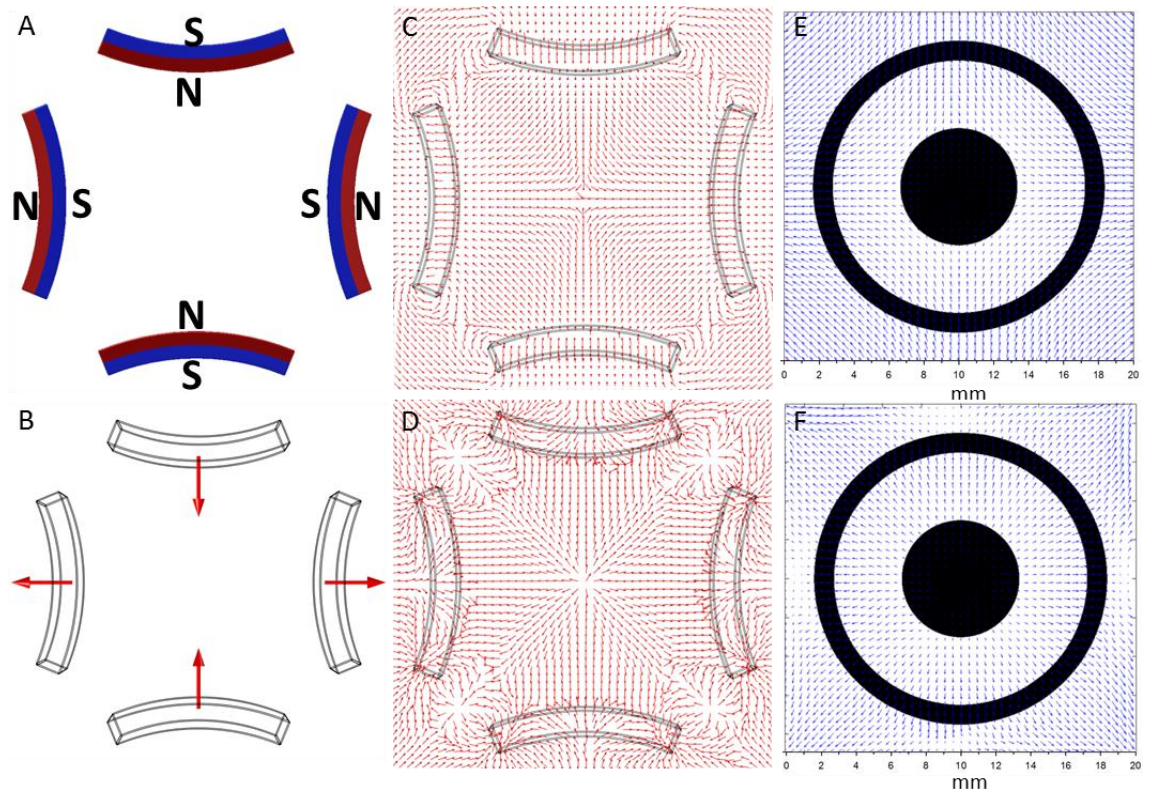


Figure 5.12: (A) Arrangement of the magnets in system and (B) magnetization directions. (C) Red arrows (normalised vectors) representing the direction of \vec{B} according to the modelled data and (E) experimental measurements (blue proportional vectors). (D) The experimental measurements covered just the central area that included the sorting device (section visible in black). Red arrows (normalised vectors) representing the direction of $(\vec{B} \cdot \nabla)\vec{B}$ according to the modelled data and (F) to the experimental measurements (blue proportional vectors - details in Appendix B).

The two final values of $|\vec{B}|$ (50 mT and 70 mT) obtained for the two different segments D and E can be explained by the different contributions in the calculation of the norm taken into account along the two paths. In segment D (parallel to the X axis) the B_y component was close to zero, and the only significant component was B_x which saturates the probe at 50 mT. This means that the maximum value of $|\vec{B}|$ would be 50 mT. On segment E, both components (B_x and B_y) can be measured up to 0.05T, which results in a maximum value of $|\vec{B}|$ equal to 7 mT (details in Appendix B). Comparison of the data with numerical simulation shows similarity between the two plots (Figure 5.12C and E). From the experimental data it was possible to calculate the direction of the force acting on a paramagnetic particle in a magnetic field, expressed by the following equation (see Section 3.2):

$$\vec{F}_m = (\vec{m} \cdot \nabla) \vec{B} = (V_p \vec{M} \cdot \nabla) \vec{B} = V_p \Delta \chi (\vec{H} \cdot \nabla) \vec{B} = \frac{V_p \Delta \chi}{\mu_0} (\vec{B} \cdot \nabla) \vec{B} \quad (5.3)$$

According to equation (5.3), the intensity and the direction of the force experienced by a paramagnetic particle depend on $(\vec{B} \cdot \nabla) \vec{B}$ (this element was the only spatial variable in the relationship), which was defined by:

$$(\vec{B} \cdot \nabla) \vec{B} = [\vec{B} \cdot \nabla B_x, \vec{B} \cdot \nabla B_y] = \left[B_x \frac{\partial B_x}{\partial x} + B_y \frac{\partial B_x}{\partial y}, B_x \frac{\partial B_y}{\partial x} + B_y \frac{\partial B_y}{\partial y} \right] \quad (5.4)$$

Using the experimental data, the direction of $(\vec{B} \cdot \nabla) \vec{B}$ was determined and represented as a vector field. The vector field was symmetric and radial from the center of the device. This suggests that the force \vec{F}_m drags a magnetic particle towards the magnets along the direction shown in Figure 5.12F. This result was compared with the numerical simulation (Figure 5.12D), which had the same radial symmetry.

The magnitude of \vec{B} ($|\vec{B}|$), its direction and the vector field showing the direction of $(\vec{B} \cdot \nabla) \vec{B}$ obtained through numerical simulation were compared to experimental measurements performed within the same magnetic system (Figure 5.11 and Figure 5.12), showing good agreement between model and data.

5.3 Quadrupole magnetic system version 2

Cell sorting experiments were performed with the QMS ver.1 (see Section 7.3.3). Issues with the practicality of this system were highlighted during experiments. In particular, the magnetic system had to be dismantled after each experiment, which was labour intensive requiring unscrewing the magnet holders, which was impractical for multiple experiments.

The quadrupole magnetic system version 2 (QMS ver.2) consisted of 4 block neodymium magnets (NdFeB), grade N52 purchased from K&J Magnetics, Inc.® (USA). Each block magnet was 12.5 mm thick, 50 mm high, 25 mm wide (Figure 5.13A). To generate a non-uniform magnetic field with a high value of $\nabla \vec{B}$ within the magnetic system, the block magnets were placed behind half rod shaped pieces made from mild steel. The half rod steel pieces were also used to hold the magnets in position.

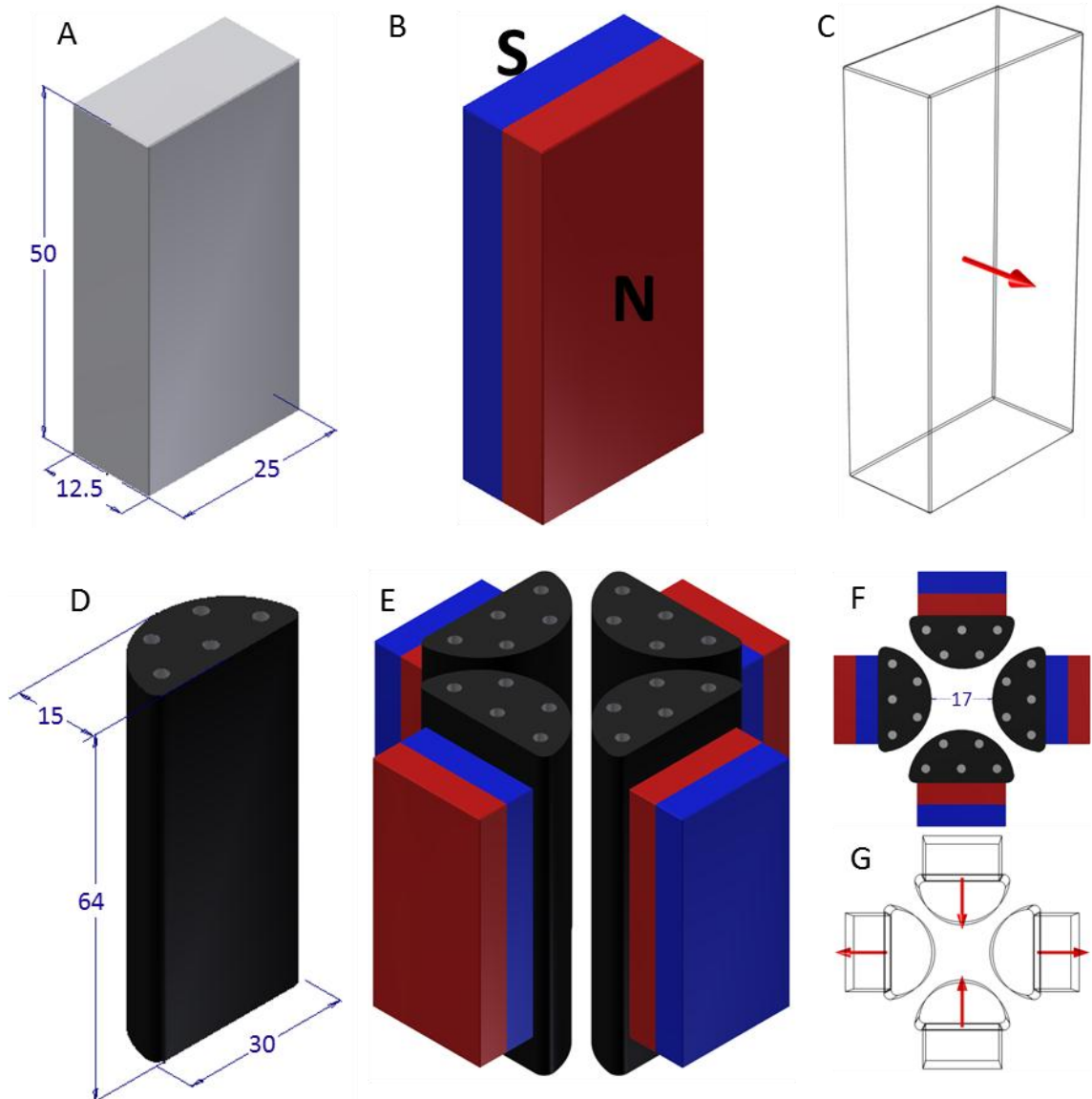


Figure 5.13: (A) 3D model of the block neodymium magnet. All measurements were in millimetres. The magnets were magnetized across their thin section. (B) North pole in red and South pole in blue. (C) Red arrow representing the magnetization direction of the magnet. (D) Half rod shaped pieces made from mild steel. (E) 3D model of QMS ver.2; magnets with the same polarity placed in opposite positions. (F) Top view of the magnetic system and (G) magnetization directions.

On the top and bottom surface of each piece 5 threaded holes were used to fasten the piece to a 3D printed holder (Figure 5.13D). Magnets with the same magnetization direction were placed in opposite positions within the magnetic system (Figure 5.13E).

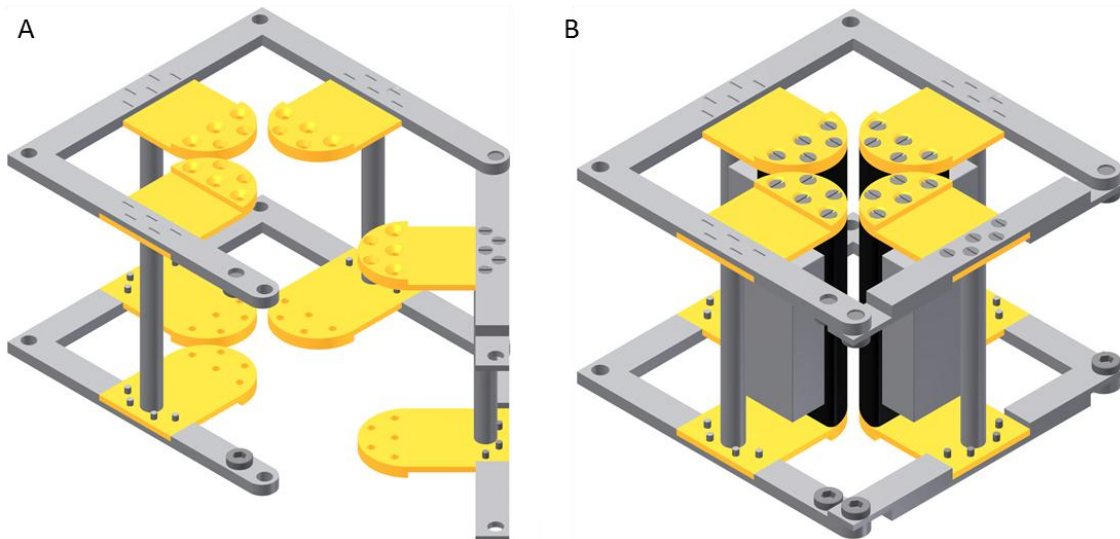


Figure 5.14: (A) 3D model of the support for the QMS ver.2. It consisted of a stainless steel frame and 8 3D printed holders (in yellow). One side of the support was movable. (B) QMS ver.2 in its support.

5.3.1 Magnetic system support: design and construction

To keep the magnets and the steel pieces in place, a support for the magnetic system was designed and built. It consisted of a stainless steel (Staybrite E.M.S. steel) frame and 3D printed holders. The holder sets the position of the steel pieces and magnets, and could be easily replaced with pieces of different length in order to change the magnet configuration. The holders were fastened to the frame through several screws. To increase the stability of the steel frame, 4 rods were added, as shown in Figure 5.14. One side of the support was hinged and could be opened to allow the placement of the QMS ver.2 around the sorting device in a simple and fast way. Figure 5.15 shows all the steps of the magnetic system setting up.

5.3.2 Numerical simulation of the magnetic flux density

As for QMS ver.1, the magnetic field generated by QMS ver.2 was modelled using COMSOL Multiphysics 4.3b. A horizontal mid-plane was used to plot the simulated field as shown in Figure 5.16A. The simulation shows the direction of \vec{B} and the values of $|\vec{B}|$ over the mid-plane (Figure 5.16C and D). As in the first magnetic system, the field generated by QMS ver.2 was completely symmetrical.

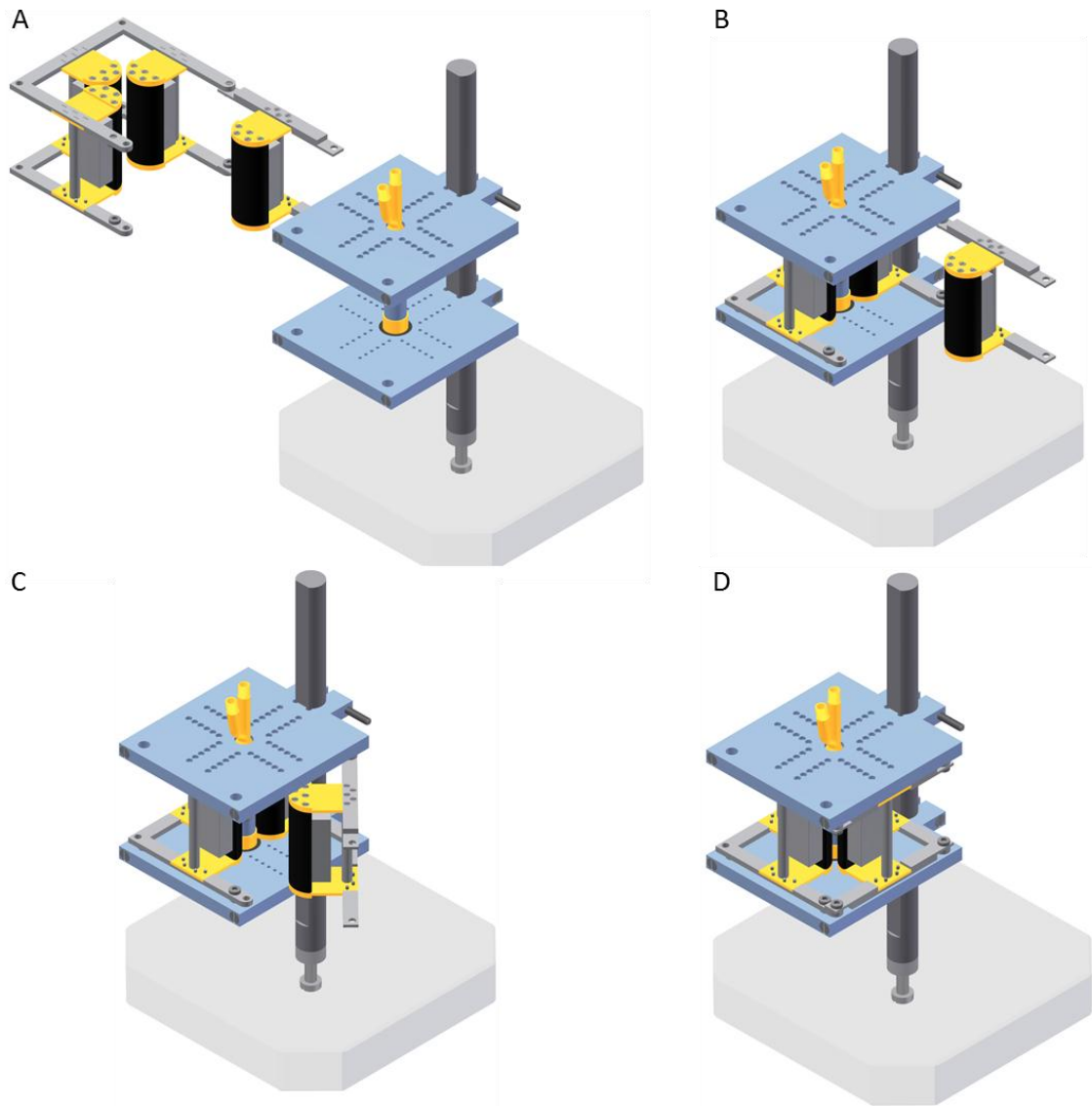


Figure 5.15: (A) 3D models of QMS ver.2 and the sorting device. (B) Once the sorting device was in position, the magnetic system slides into the device support. (C) The hinged side allows magnetic system to be closed and (D) secured in position.

To estimate $|\vec{B}|$ in the area within the magnetic system, a horizontal line was drawn (Figure 5.16E), and $|\vec{B}|$ along this line was plotted (Figure 5.16F). The graph shows that $|\vec{B}|$ decreases from 130 mT ($X=-8.5$) to 2 m T at the centre of the magnetic system ($X=0$). The initial value of the graph referred to the surface of the half rod mild steel piece.

The behaviour of $|\vec{B}|$ on a line starting from the centre point of the magnetic system and ending on the half rod piece was modelled. In Figure 5.17C, $|\vec{B}|$ was plotted and the device was indicated by two vertical blue lines.

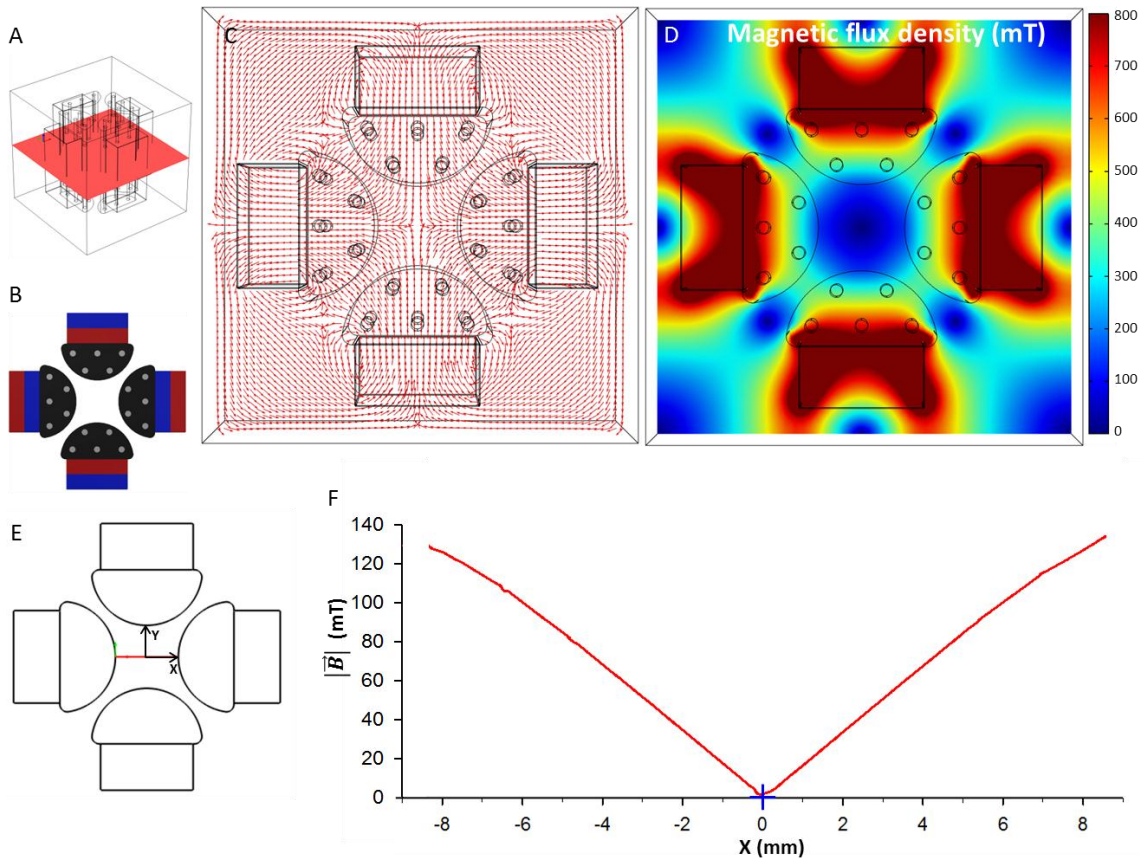


Figure 5.16: Numerical simulation of the magnetic flux density generated by the QMS ver.2. (A) Position of the horizontal plane; (B) magnet arrangement and polarity. (C) Red arrows (normalised vectors) show the direction of \vec{B} and (D) colour map was the value of $|\vec{B}|$ (in mT) over the plane. (E) Line across the system along mid-plane; central point of the system represented in blue; (F) plot of $|\vec{B}|$ on the horizontal line (simulation details in Appendix C – Figure C.1).

Within these lines, $|\vec{B}|$ increased from 52 mT to 110 mT over a distance of 3.5 mm creating a gradient in magnetic flux density $|\nabla\vec{B}|$ of 16 mT/mm. As in QMS ver.1, $(\vec{B} \cdot \nabla)\vec{B}$ was modelled along the same line, and $|(\vec{B} \cdot \nabla)\vec{B}|$ plotted (Figure 5.17D). $|(\vec{B} \cdot \nabla)\vec{B}|$ started from 0.88 T²/m and increased to a maximum of 1.7 T²/m. In Appendix C (Figure C.3 / Figure C.4) the various components of \vec{B} and $(\vec{B} \cdot \nabla)\vec{B}$ was plotted. Also, in Appendix C (Figure C.2) the effect of the half rod mild steel pieces on $|\vec{B}|$ was investigated.

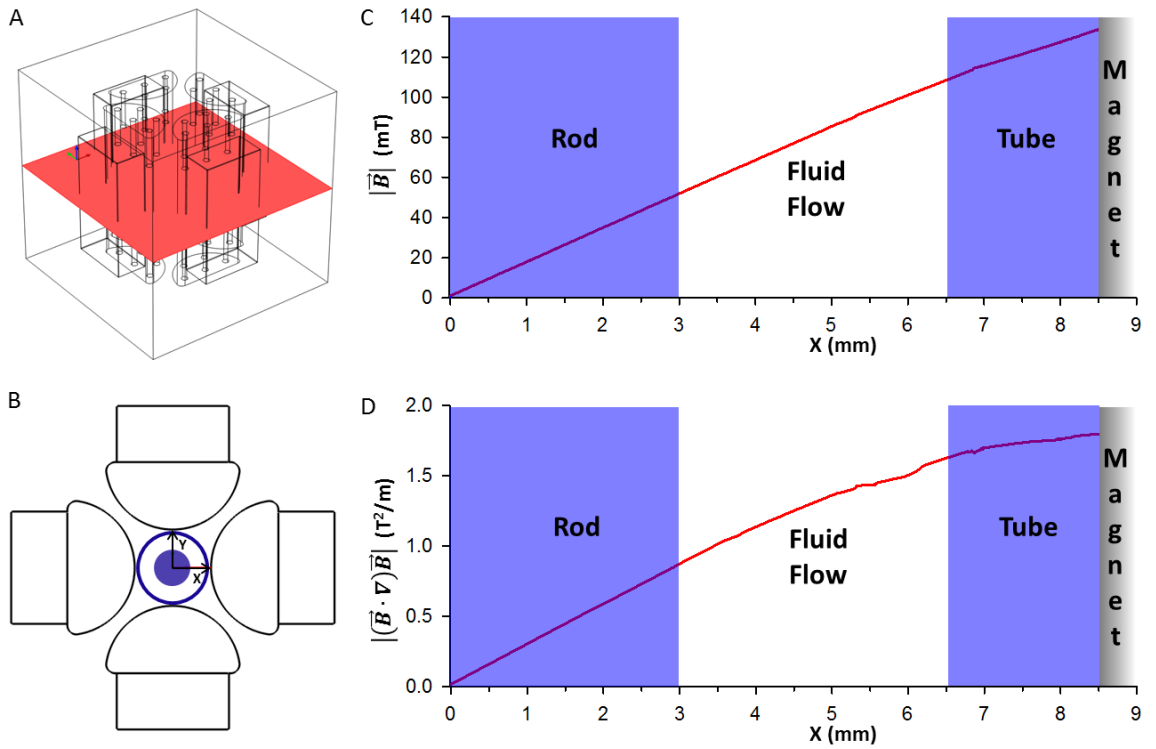


Figure 5.17: (A) Numerical simulation of $|\vec{B}|$ and $|(\vec{B} \cdot \nabla)\vec{B}|$ generated by the QMS ver.2. Horizontal mid-plane; (B) cut line drawn between the centre point and the half rod piece surface; (C) plot of $|\vec{B}|$ along the line. (D) Plot of $|(\vec{B} \cdot \nabla)\vec{B}|$ along the line. Simulation details in Appendix C – Figure C.1.

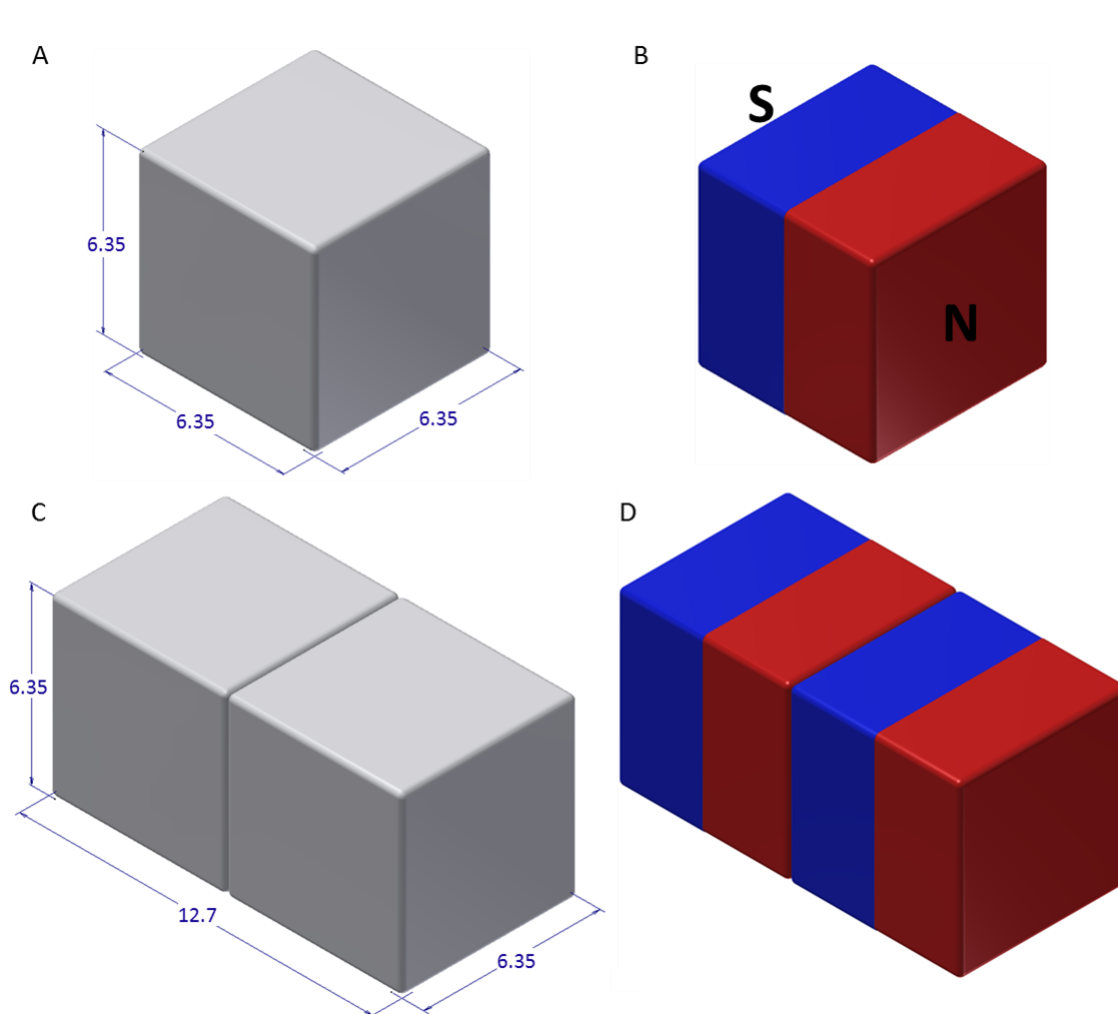


Figure 5.18: (A) 3D model of the cubic neodymium magnet used. (B) North pole in red and South pole in blue. (C) 3D model of the block magnets created by two cubic magnets. (D) Magnets polarity. All the measurements were in millimetres.

5.4 Hexapole magnetic system

The hexapole magnetic system (HMS) was the last magnetic system developed in this study. It consisted of 60 cubic neodymium magnets (NdFeB) of grade N52 purchased from K&J Magnetics, Inc.® (USA). The cubic magnets had a side length of 6.35 mm (Figure 5.18A). The cubic magnets were organised in groups of two, forming 30 block magnets 12.7 mm thick, 6.35 mm high and 6.35 mm wide (Figure 5.18C). The block magnets were organised on 5 levels (Figure 5.19A) and each level had 6 magnets arranged in a hexapole configuration (Figure 5.19C). Magnets placed in adjacent positions had opposite polarity, resulting in the configuration shown in Figure 5.19E. The magnetic system was designed to allow the magnets to be tangential to the sorting device exterior surface.

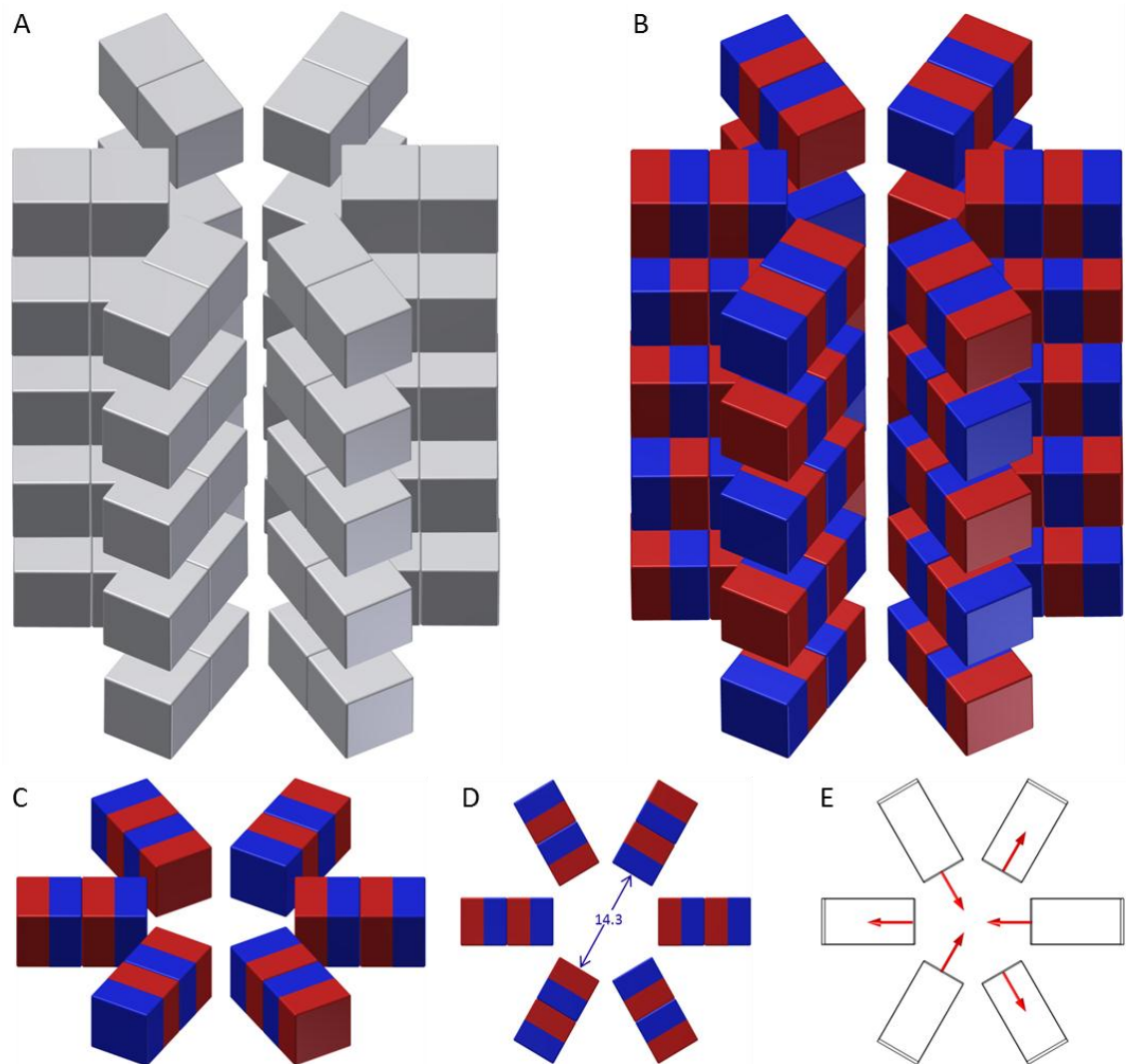


Figure 5.19: (A) 3D model of the HMS. (B) Each level consisted of 6 block magnets organised in a hexapole configuration. (C) Top view (xy plane) of the magnetic system and (D) magnetization directions.

This configuration aimed to achieve a magnetic field gradient as high as possible, and the use of the hexapole configuration allow to obtain a $|\nabla \vec{B}|$ of 150 mT/mm within the sorting device (see section 5.4.2).

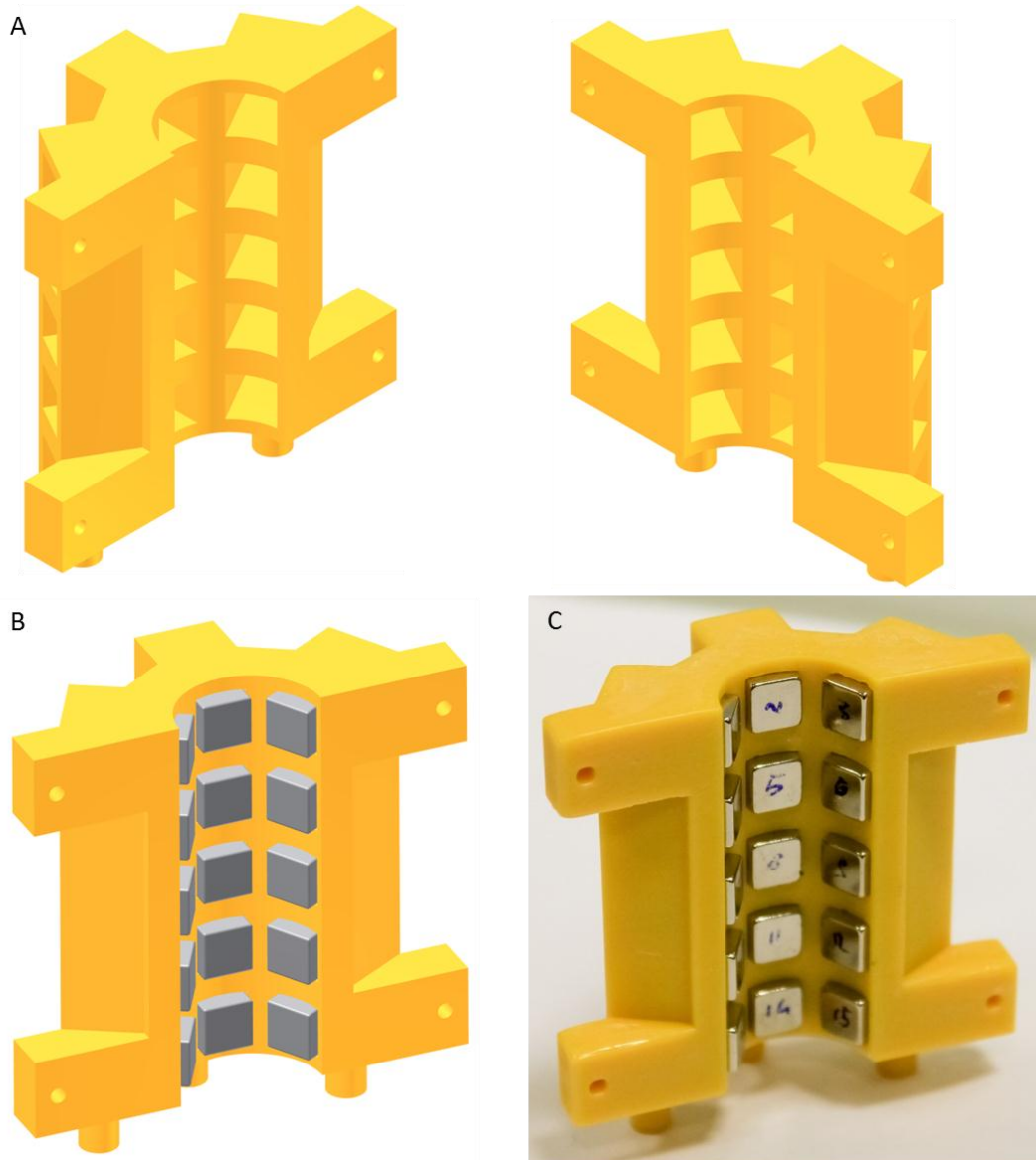


Figure 5.20: (A) 3D model of the support for the HMS. (B) Block magnets placed into one part of the support. (C) Picture of one half of the support.

5.4.1 Magnetic system support: design and manufacturing

To hold in place the 30 block magnets, a support was designed and manufactured. The support for the HMS was made of two parts, each with 15 slots to insert the block magnets. The slots ran through the entire thickness of the support to facilitate the assembling and adjustment of the system. The magnets were not permanently fixed, but just wedged in the slots, which permitted the correction of their position to allocate sorting devices of different external diameters (Figure 5.20).

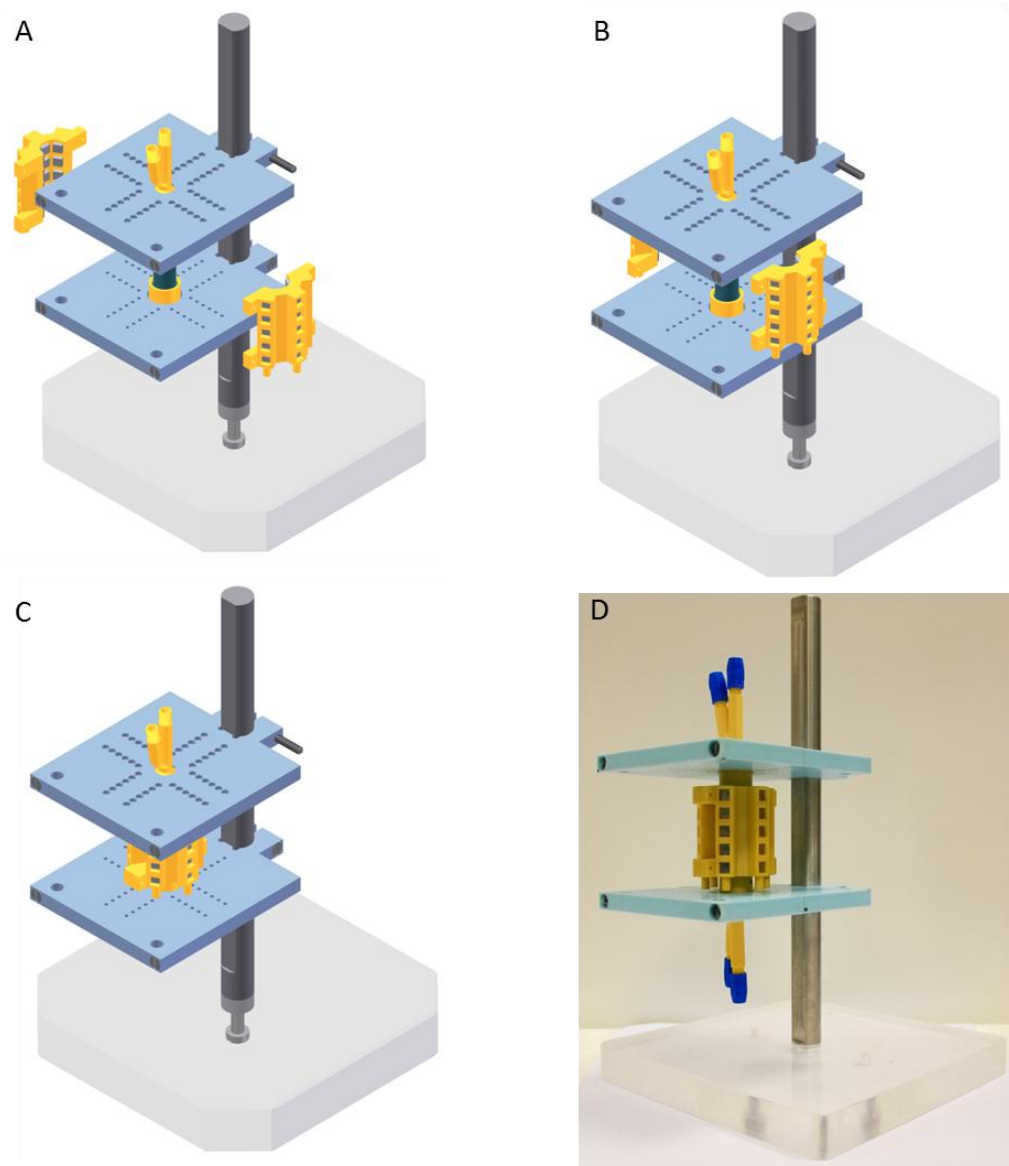


Figure 5.21: (A) 3D models of the HMS and the sorting device. (B) Magnetic system slid into the device support once the sorting device was placed in position. (C) The two halves of the magnetic system in place around the sorting device. (D) Picture of the HMS and the sorting device.

Stereolithography was used to manufacture the HMS support. The position of the magnets was adjusted to be tangential to the exterior surface of the sorting device. Once the magnets were in position within the support, the two parts of the HMS were placed around the sorting device. The magnetic system did not have a fastening mechanism; the two parts were kept in place by the attractive magnetic force.

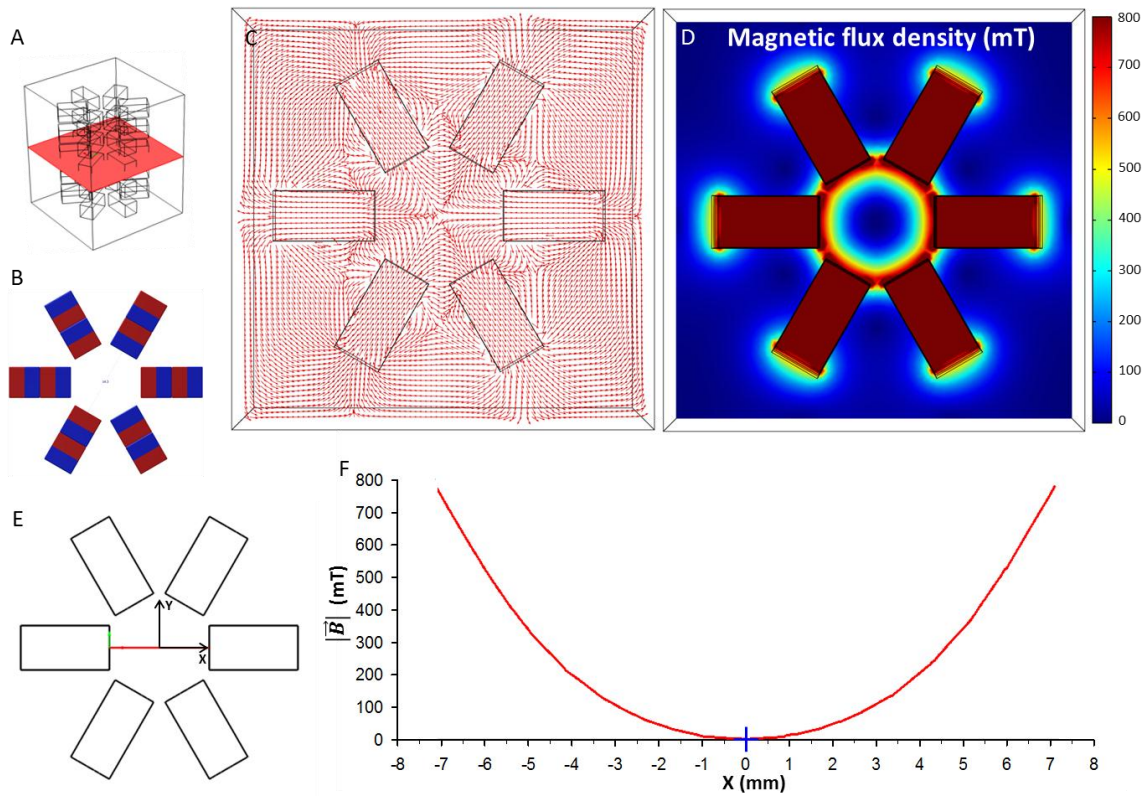


Figure 5.22: Numerical simulation of the magnetic flux density generated by the HMS. (A) Position of the horizontal mid-plane; (B) magnet arrangement and polarity. (C) Red arrows (normalised vectors) show the direction of \vec{B} and (D) colour map was the value of $|\vec{B}|$ (in mT) over the plane. (E) Line across the system along mid-plane; central point of the system represented in blue; (F) plot of $|\vec{B}|$ on the horizontal line (simulation details in Appendix D – Figure D.1).

5.4.2 Numerical simulation of the magnetic flux density

The field generated by the HMS was modelled using COMSOL Multiphysics 4.3b. The $|\vec{B}|$ and the direction of \vec{B} were modelled over the horizontal mid-plane (Figure 5.22C and D). Due to the hexapole configuration of the magnetic system, field generated within the system was radially symmetrical. As for the previous simulations, the $|\vec{B}|$ generated by the HMS was modelled along two lines drawn on the mid-plane. The first line was drawn between two opposite magnets (Figure 5.22E), and the $|\vec{B}|$ along this line was plotted (Figure 5.22F). The graph shows that $|\vec{B}|$ decreases from 770 mT ($X=-7$) to 1 mT in the centre of the magnetic system ($X=0$).

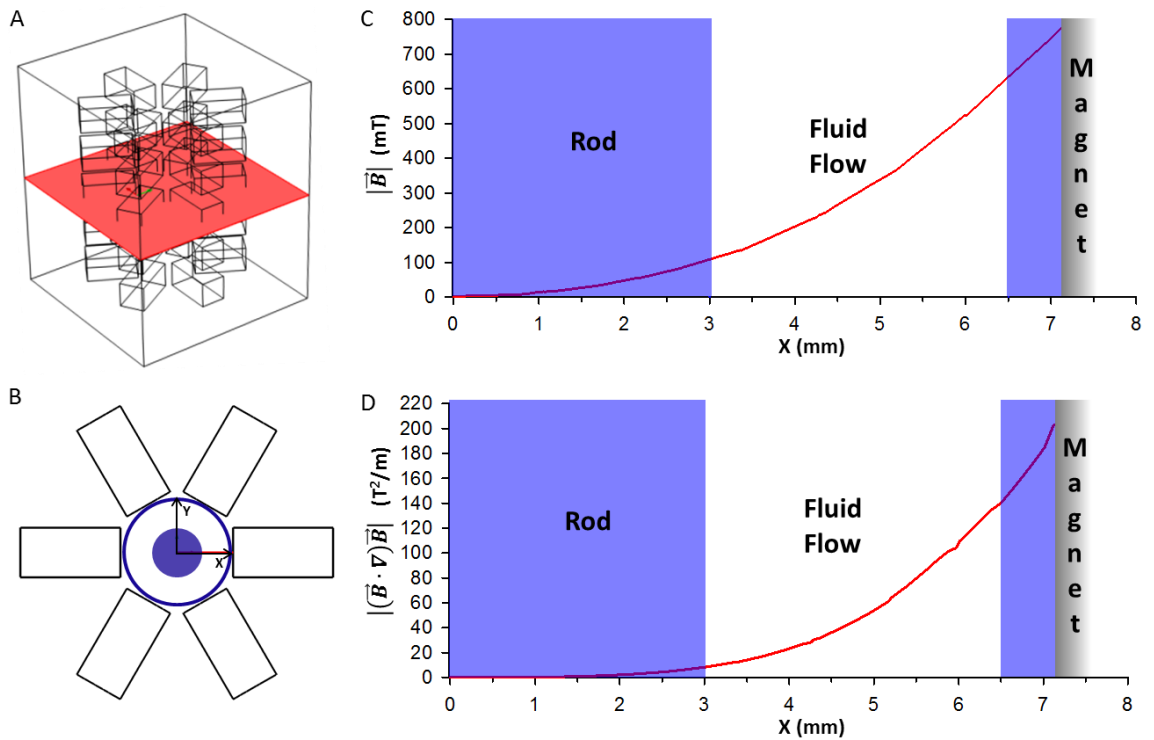


Figure 5.23: Numerical simulation of $|\vec{B}|$ and $|(\vec{B} \cdot \nabla)\vec{B}|$ generated by the QMS ver.2. (A) Horizontal mid-plane; (B) line drawn between the centre point and the magnet surface; (C) plot of $|\vec{B}|$ along the line. (D) Plot of $|(\vec{B} \cdot \nabla)\vec{B}|$ along the line. Simulation details in Appendix D – Figure D.1).

A second line was drawn along the same mid-plane, between the centre of the system and the block magnet surface (Figure 5.23B). Figure 5.23C shows $|\vec{B}|$ along the line, with the position of the sorting device indicated by two vertical blue lines. At the beginning ($X=3$) $|\vec{B}|$ had a value of 110 mT, increasing to 640 mT ($X=6.5$). This change in $|\vec{B}|$ creates a gradient $|\nabla\vec{B}|$ of 150 mT/mm. As for the previous magnetic systems, $(\vec{B} \cdot \nabla)\vec{B}$ was modelled along the same line, and $|(\vec{B} \cdot \nabla)\vec{B}|$ was plotted in Figure 5.23D.

At the beginning of the area of interest ($X=3$), $|(\vec{B} \cdot \nabla)\vec{B}|$ had a value of 8 T²/m, which increased to 142 T²/m ($X=6.5$). In Appendix D (Figure D.2 / Figure D.3) the various components of \vec{B} and $(\vec{B} \cdot \nabla)\vec{B}$ along the lines analysed were plotted. Moreover, in Appendix B (Figure B.3) $|(\vec{B} \cdot \nabla)\vec{B}|$ was modelled along the entire length of the HMS, revealing variations in correspondence of the edge of the magnets.

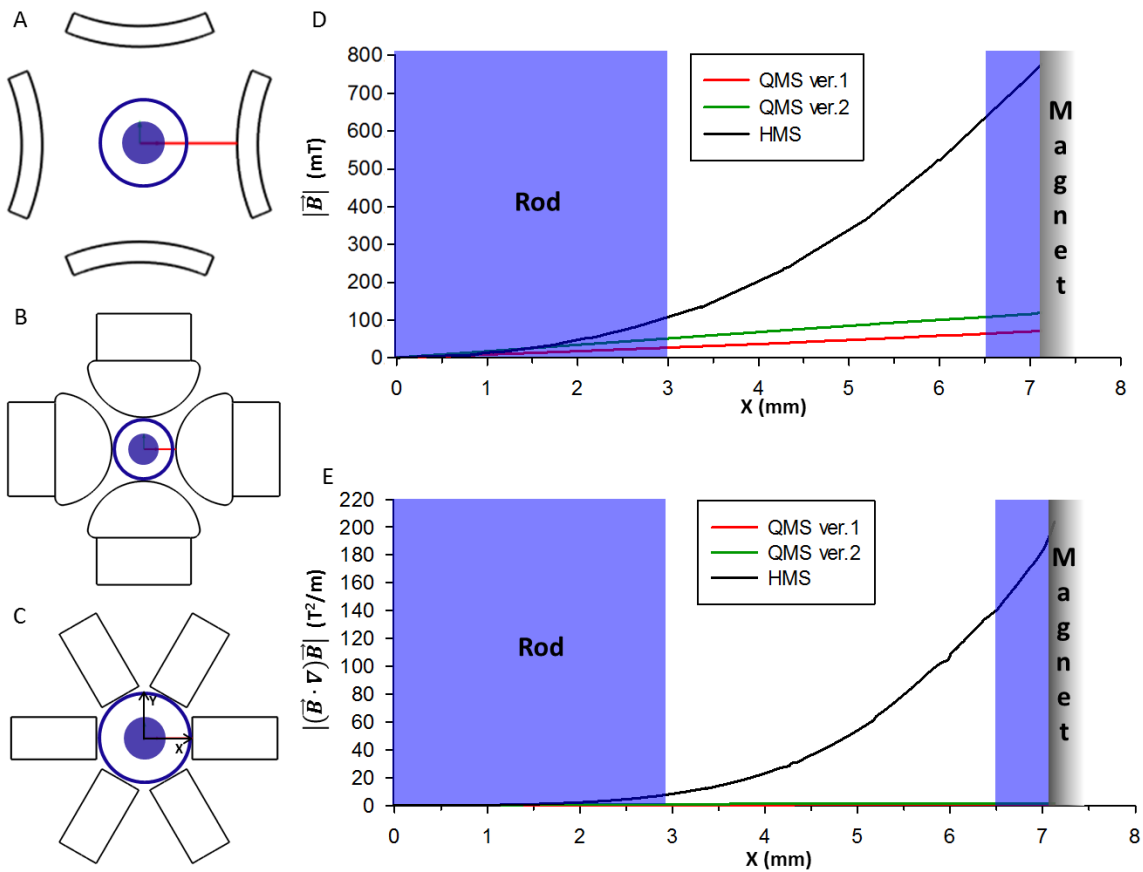


Figure 5.24: Comparison among magnetic systems. (A, B, C) Cut lines drawn between the centre of the magnetic systems ($X=0$) and the surface of the magnetic element on the horizontal mid-planes of the magnetic systems. Drawings not in scale. (D) $|\vec{B}|$ and (E) $|(\vec{B} \cdot \nabla)\vec{B}|$ generated by the QMS ver.1, the QMS ver.2 and the HMS represented by red, green and black lines respectively. The plots stop after the region of interest delimited by blue vertical lines.

5.5 Summary

In this study, three magnetic systems were developed: the QMS ver.1, the QMS ver.2 and the HMS. All the systems used neodymium permanent magnets (NdFeB).

The QMS ver.1 was made up of 12 arc magnets (grade N42) arranged on three levels. The magnets were kept in place by 8 magnet holders screwed into the sorting device support. This solution made the assembling/disassembling procedure laborious.

Table 5.1: Summary table reporting the values of $|\vec{B}|$ and $|(\vec{B} \cdot \nabla)\vec{B}|$ at the beginning ($X=3.5$) and the end ($X=6.5$) of the segment of interest (within the device); and the $|\nabla\vec{B}|$ along the same segment.

	$ \vec{B} $ [mT]	$ \nabla\vec{B} $ [mT/mm]	$ (\vec{B} \cdot \nabla)\vec{B} $ [T ² /m]
QMS ver. 1	27 – 64	10	0.26 – 0.78
QMS ver. 1	52 – 110	16	0.88 – 1.7
HMS	110 – 640	150	8 - 142

The QMS ver.2 consisted of 4 block neodymium magnets (grade N52) each placed behind half rod obtained from mild steel. The magnetic system had a stainless steel support that simplified the assembling procedure around the sorting device.

The HMS consisted of 60 cubic neodymium magnets (grade 52) organised in groups of two, forming 30 block magnets. The block magnets were organised on 5 levels and each level had 6 magnets arranged in a hexapole configuration. The support for the magnetic system was built using stereolithography and made up of two halves, which were placed around the sorting device.

Using COMSOL Multiphysics 4.3b software, \vec{B} and $(\vec{B} \cdot \nabla)\vec{B}$ generated by the magnetic systems within the sorting device were modelled. $(\vec{B} \cdot \nabla)\vec{B}$ defined the magnetic force (\vec{F}_m) experienced by paramagnetic particles in the presence of the magnetic field according to the equation (5.3). To validate the data from the numerical simulations, a set of experimental measurements of \vec{B} generated within a simplified magnetic system were performed. The modelled and experimental data agreed on both $|\vec{B}|$ and direction of \vec{B} along defined cut lines.

Figure 5.24 compares the three magnetic systems, showing the variations of $|\vec{B}|$ and $|(\vec{B} \cdot \nabla)\vec{B}|$ along the cut line. Table 5.1 summarizes the values of $|\vec{B}|$ and $|(\vec{B} \cdot \nabla)\vec{B}|$ obtained at the beginning ($X=3.5$) and at the end ($X=6.5$) of the region of interest in each magnetic systems. The values of $|\nabla\vec{B}|$ created by each system along the cut line (within the region of interest) were also shown.

In section 2.3.3, a number of immunomagnetic cell separation devices were described, in particular the QMS developed by Chalmers and co-workers. The latest version for this device was producing a maximum $|\vec{B}|$ of 1.37 T with a $|\nabla\vec{B}|$ of 179 mT/mm. As reported in Table 5.1, the values of $|\vec{B}|$ and $|\nabla\vec{B}|$ produced by the first two magnetic systems developed, were far from the values reported in Chalmers work despite sharing the same

magnets arrangement (quadrupole). Changing shape and arrangement (hexapole) of the permanent magnets used, the magnetic system (HMS) produced a maximum $|\vec{B}|$ of 800 mT. Moreover, the values of $|\vec{B}|$ and $|\nabla\vec{B}|$ in the region of interest (within the sorting device), were considerably higher than that produced by previous versions.

Within the device, the $|\vec{B}|$ ranged between 110 mT and 640 mT, creating a $|\nabla\vec{B}|$ of 150 mT/mm. This value was lower than the one produced by Chalmers device, but in the same order of magnitude.

The QMS ver.1, the QMS ver.2 and the HMS were tested experimentally (see Chapter 7) using MG63 cells labelled with paramagnetic beads. The HMS was found to be the most suitable for this study and used to sort SSCs from HBSMCs.

Chapter 6

Cell Magnetisation

The sorting device developed in this study used the expression level of a specific marker on a cell surface as a separation parameter. To sort SSCs, the antigen used was the STRO-1 which was the best known SSC marker [72]. To make the target cells susceptible to an external magnetic field, functionalised superparamagnetic bead were bind to the target cell surface. The bead functionalisation protocol and cell labelling protocol were investigated. The magnetic susceptibility of a labelled cell (χ_c) was estimated experimentally, and this value was used in numerical simulations. The simulations modelled cell trajectories in order to find the optimum flow rate value for cell sorting experiments.

6.1 Magnetic bead

In Chapter 5 the working principle of the sorting device was described. Within the device immunomagnetically labelled cells experienced a magnetic force and consequently changed their position. The magnetic field acts on the immunomagnetic labels attached to the cells surface. These labels increase the average magnetic susceptibility of the labelled cells. Magnetic susceptibility (χ) was a dimensionless proportionality constant that described how a given material was susceptible to an applied magnetic field. As shown in Chapter 3, χ was a parameter that discriminates between target and non-target cells. The magnetic susceptibility of an immunomagnetically labelled cell was defined as χ_c and the magnetic susceptibility of a magnetic bead as χ_b . The χ_c of a cell was influenced by the number, volume and χ_b of magnetic bead bind to the cell surface. The number of superparamagnetic bead bind to a cell depends mostly on the expression level of the surface antigen chosen as marker for the sorting experiment.

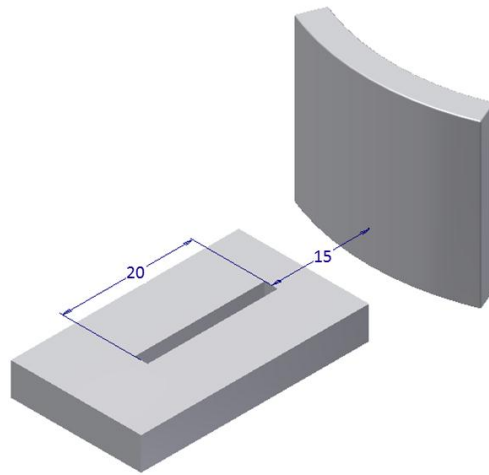


Figure 6.1: 3D model of the experimental setup used to estimate χ_p ; PDMS channel and arc segment neodymium magnet. All measurements were in millimetres.

For the aim of this study, high values of χ_c were desirable because they would result in higher cell mobility, all conditions equal. To achieve high χ_c , magnetic beads with high values of χ_b were needed. Due to the structural differences between MACS and the sorting device developed in this study, it was not possible to use the magnetic microbeads ($\phi 50$ nm - Miltenyi Biotec, Germany) used in the standard MACS procedure. As described in section 2.1, the MACS column was packed with ferromagnetic spheres forming a matrix within the column. This structure created a local high gradient magnetic field. The MACS magnetic microbeads were optimised to operate in these conditions.

The sorting device consisted of an open annulus (see Chapter 4), and the field generated by the magnetic system used was not suitable for the use of MACS magnetic microbeads. Experiments were performed flowing labelled MG63 cells with MACS magnetic microbeads through the sorting device, resulting in less than 5% of STRO-1 positive cells recovered in the device positive fraction. Two categories of magnetic bead were commercially available at the time of this study: ferromagnetic bead and superparamagnetic bead. The main difference between these was that ferromagnetic beads retained their magnetism after exposure to a magnetic field, while paramagnetic beads did not. In this study, superparamagnetic beads were chosen because, unlike ferromagnetic beads, they did not form clumps. The paramagnetic beads, with high values of χ_b , were superparamagnetic beads. Therefore, several kinds of superparamagnetic beads were tested in order to find those with the highest possible χ_b .

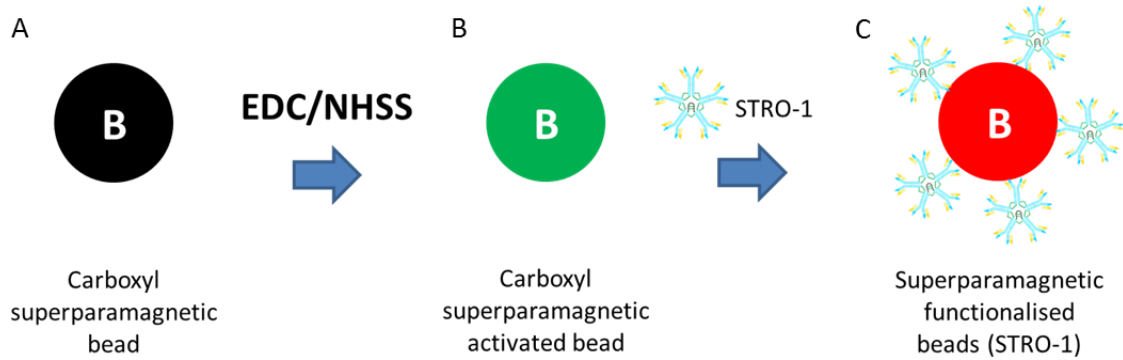


Figure 6.2: Diagram of bead functionalisation procedure. (A) Carboxyl superparamagnetic bead. (B) Carboxyl superparamagnetic activated bead. (C) Superparamagnetic functionalised (STRO-1) bead. The chemical reactions on the beads surface were described in Appendix F (Figure F.1).

6.1.1 Experimental estimation of bead magnetic susceptibility

A set of experiments was designed to estimate the values of χ_b for several brands of bead. The experimental setup included a PDMS channel (2 mm x 2 mm x 20 mm) and an arc segment neodymium magnet (Figure 6.1). The magnet was placed 15 mm from the end of the channel and \vec{B} (magnetic flux density) along the channel was measured with a non-commercial Gaussmeter (see Section 5.2.2). These measurements allowed the estimation of $\nabla\vec{B}$ along the channel. The distance between the end of the channel and the magnet was optimised to ensure the entire length of channel sat in an area where the Gaussmeter did not saturate. The setup was then placed under the stereoscopic microscope and the channel filled with 80 μl of PBS with 1 μl of bead suspension placed at the beginning of the channel (opposite to the magnet). The time for the bead to move the length of the channel was recorded. The measurements were performed several times ($n=6$) for each bead to ensure a reliable value. The velocity of the bead was calculated to estimate the bead magnetic susceptibility.

Several types of superparamagnetic bead (purchased from different companies) were investigated. Two types of superparamagnetic bead obtained the highest values of χ_b , CM-08-10 (0.82 μm - $\chi_b=1.3*10^{-3}$) and CM-025-10 (0.34 μm - $\chi_b=1.1*10^{-3}$), both purchased from Spherotech, Inc. (USA) and were used for cell labelling. The following Sections illustrate further tests performed with the suitable bead (equations used in Appendix E).

6.2 Cell labelling

Both CM-08-10 (0.82 μm) and CM-025-10 (0.34 μm) were carboxyl superparamagnetic bead: with carboxylic acid groups (COOH) on their surface.

SSC were sorted using a cell surface antigen expressed by stromal elements in the human BM [73], called STRO-1 - the best known SSCs marker [72]. A STRO-1 positive fraction of BM was heterogeneous in that it contains a variety of cell types thought to include SSCs. BM mononuclear cells sorted on the basis of STRO-1 expression were capable of establishing an adherent stromal layer *in vitro*, consisting of a number of phenotypically distinct stromal cell types, including fibroblasts, smooth muscle cells, and adipocytes [20].

6.2.1 Superparamagnetic bead functionalisation

The most common method to bind proteins to carboxyl bead (or other substrates), was the carbodiimide coupling. Carbodiimide coupling covalently bind carboxylic acids (COOH) to the primary amines (NH_2) of the proteins. N-(3-Dimethylaminopropyl)-N'-ethylcarbodiimide hydrochloride (EDC) was used as a coupling agent. EDC reacts with the carboxylic acid groups on the bead surface to form an amine-reactive active intermediate (*O*-acylisourea intermediate). EDC did not become part of the bond, and was considered a zero-length carboxyl-to-amine crosslinker. The *O*-acylisourea intermediate undergoes rapid hydrolysis; therefore it was unstable in aqueous solution. To increase the efficiency of the coupling reaction, N-Hydroxysulfosuccinimide sodium salt (NHSS or Sulfo-NHS) was added to the activation solution. The addition of NHSS converted the unstable *O*-acylisourea intermediate to amine-reactive NHSS ester allowing the conjugation to primary amines [74]. The carboxyl superparamagnetic bead (Figure 6.2A) were suspended in the activation solution and incubated for two hours at room temperature. After this procedure the beads surface was activated (Figure 6.2B) and ready to bind to the STRO-1 antibodies. After several PBS washes mouse monoclonal IgM anti-human STRO-1 primary antibodies (Hybridoma) was added to the bead suspension and incubated overnight at 4°C (Figure 6.2C). The end product was functionalised bead (detailed protocol in Appendix F).

6.2.1.1 Negative and positive controls

To verify that the STRO-1 antibodies were bound to the bead surface, a set of control experiments were performed using fluorescent secondary antibodies (goat polyclonal IgG anti-mouse IgM Alexa Flour 488 conjugated). Secondary antibodies bind the tail regions

(Fragment crystallisable region – Fc region) of the primary antibodies. The tail regions were constant within the same animal class. A secondary antibody (labelled with fluorescent tags) binds all the primary antibodies within the same animal class. The binding of STRO-1 antibodies to the bead surface would be proven if the bead became fluorescent after incubation with the Alexa 488 fluorescent antibodies. CM-08-10 superparamagnetic bead were used in these experiments. Three samples were prepared:

- 1 – un-activated bead incubated with fluorescent antibodies (Figure 6.3A);
- 2 - activated bead (incubated with EDC/NHSS but not with STRO-1 antibodies) incubated with fluorescent antibodies (Figure 6.3B);
- 3 - functionalised bead (incubated with EDC/NHSS and with STRO-1 antibodies) incubated with fluorescent antibodies (Figure 6.3C).

After two PBS washes, the samples were analysed using a flow cytometer (Guava EasyCyte Mini - Merck Millipore, Germany) and observed in bright field and fluorescence light. The flow cytometer data revealed that the fluorescent antibodies did not interact with neither the bare bead nor the activated bead (Figure 6.3D and E), but did bind to the STRO-1 antibodies on the surface of the functionalised bead. The entire population of functionalised bead became fluorescent (Figure 6.3F), proving the robustness of the functionalisation protocol. The fluorescence microscopy (Axiovert 200, ZEISS - Germany) investigation revealed no fluorescence activity in the negative controls (Figure 6.3L and M), while it recorded fluorescence signals in the sample of functionalised bead incubated with fluorescent antibodies (Figure 6.3N).

In conclusion, fluorescence activity was given by the presence of the STRO-1 antibodies on the bead surface and not from false positive. Similar experiments were performed with functionalised bead kept at 4°C for 7 and 14 days and then incubated with Alexa 488 fluorescent antibodies. The results were similar to the ones shown in Figure 6.3F, highlighting the possibility to keep functionalised bead (at controlled temperature) for a longer period of time

6.2.1.2 STRO-1 antibody titration

Once the functionalisation protocol to bind STRO-1 antibodies to the bead surface was established, a set of antibody titration experiments were performed in order to determine the optimal STRO-1 concentration. The STRO-1 antibodies used were produced by a mouse hybridoma cell line (Bone and Joint group) and they were stored at -80°C in stock aliquots. The titration experiment consisted of functionalising six bead samples (CM-08-10) using different dilutions of STRO-1 antibodies. Once functionalised, the bead were incubated with the Alexa 488 fluorescent antibodies (Figure 6.4A) and then analysed using

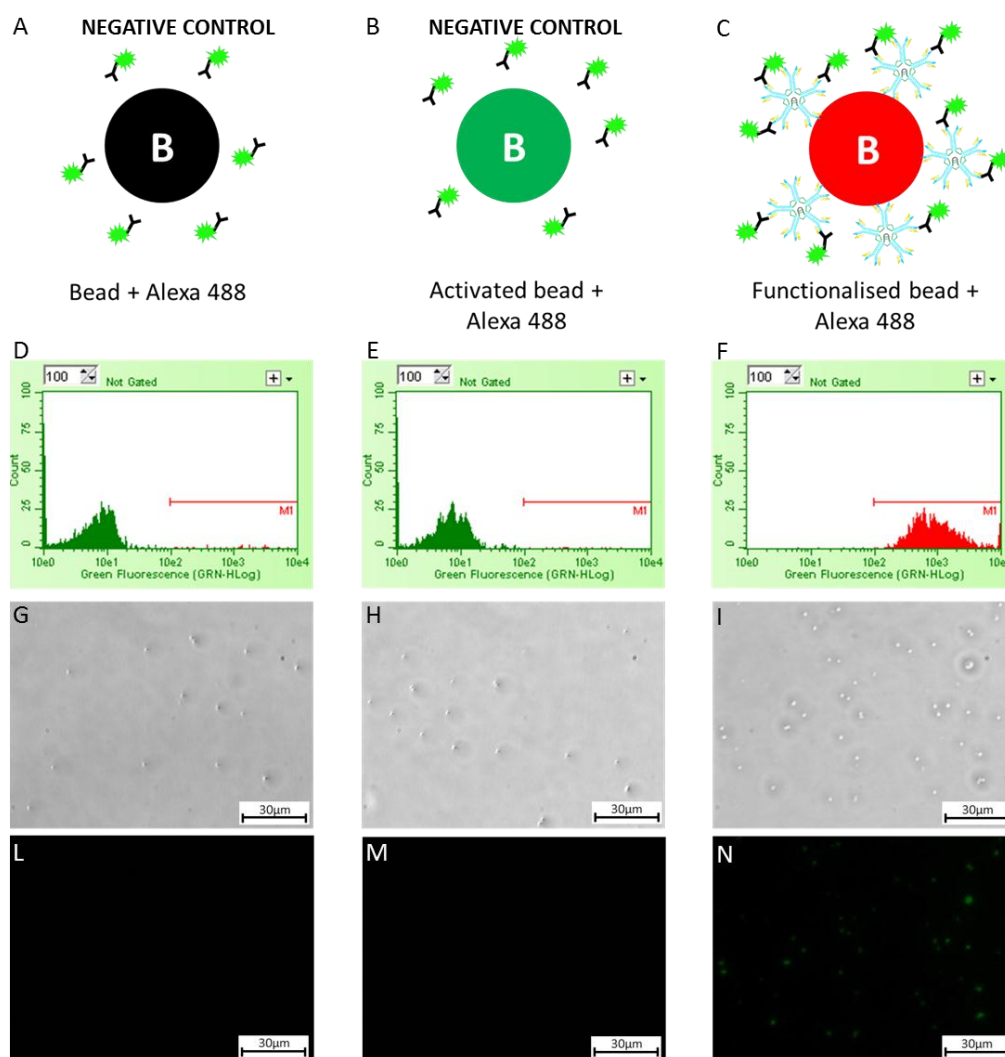


Figure 6.3: Diagrams of the negative controls and the experiment. (A) Fluorescent antibodies (Alexa 488) were incubated with bare bead, (B) activated bead and (C) functionalised bead respectively. (D,E) Flow cytometry histograms showing no fluorescence activity for the controls and (F) fluorescence signal for the experiment. (G,H,I) Bright field photomicroscopy of the three samples. (L,M) Fluorescence microscopy (FITC; Ex/Em (nm): 495/519) revealed no signals of fluorescence in the negative controls, (N) while signals of fluorescent bead were registered in the experiment. Scale bars represented 30 μm .

the flow cytometer. The percentage of fluorescent bead per sample represented the functionalisation efficiency for each dilution. The STRO-1 antibodies concentrations tested were: pure (1:1), 10 times dilution (1:10), 100 times dilution (1:100), 200 times dilution (1:200), 500 times dilution (1:500), 1000 times dilution (1:1000). The histograms in Figure 6.4 show the percentage of fluorescent bead for each STRO-1 antibody dilution. The results showed that $\sim 98\%$ of the bead population was labelled with Alexa 488 when using the pure stock hybridoma aliquot concentration of STRO-1 antibodies.

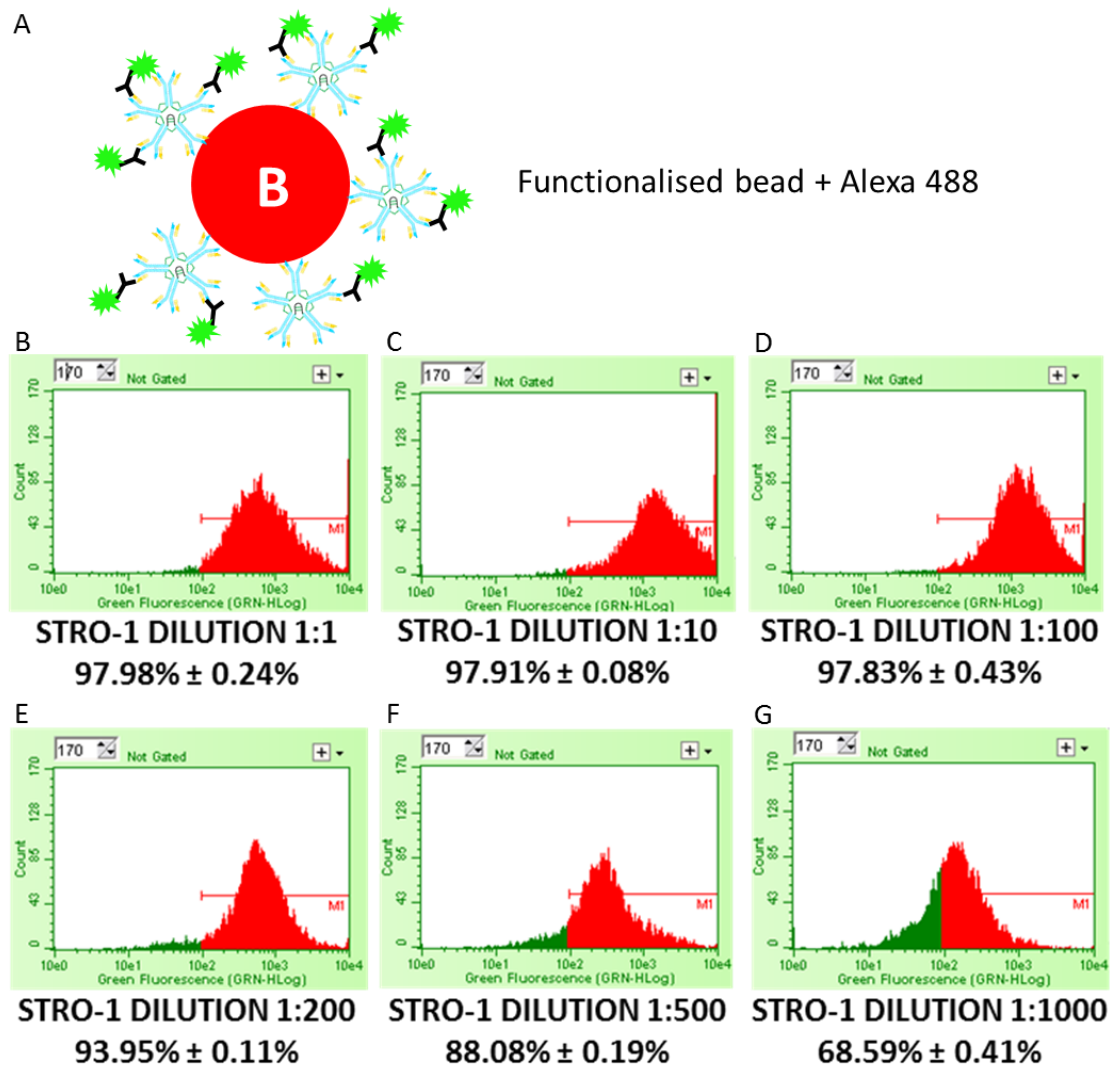


Figure 6.4: (A) Fluorescent antibodies (Alexa 488) were incubated with six bead samples functionalised using different STRO-1 antibodies dilutions. (B) Flow cytometry histograms and percentages of fluorescent bead for samples functionalised using 1:1, (C) 1:10, (D) 1:100, (E) 1:200, (F) 1:500 and (G) 1:1000 dilutions of the STRO-1 antibodies (threshold set accordingly to negative control).

According to section 6.2.1.1, Alexa 488 fluorescent antibodies label just functionalised beads (so beads with STRO-1 antibodies on the surface); see negative controls (Figure 6.3D and E). This meant that ~98% of beads were functionalised with STRO-1 antibodies (because Alexa 488 would not label non-functionalised beads). That percentage did not change significantly until a 200 times dilution (~94%) of the STRO-1 antibodies was used. In conclusion, a 100 times dilution of the STRO-1 antibodies was chosen to functionalise the superparamagnetic beads.

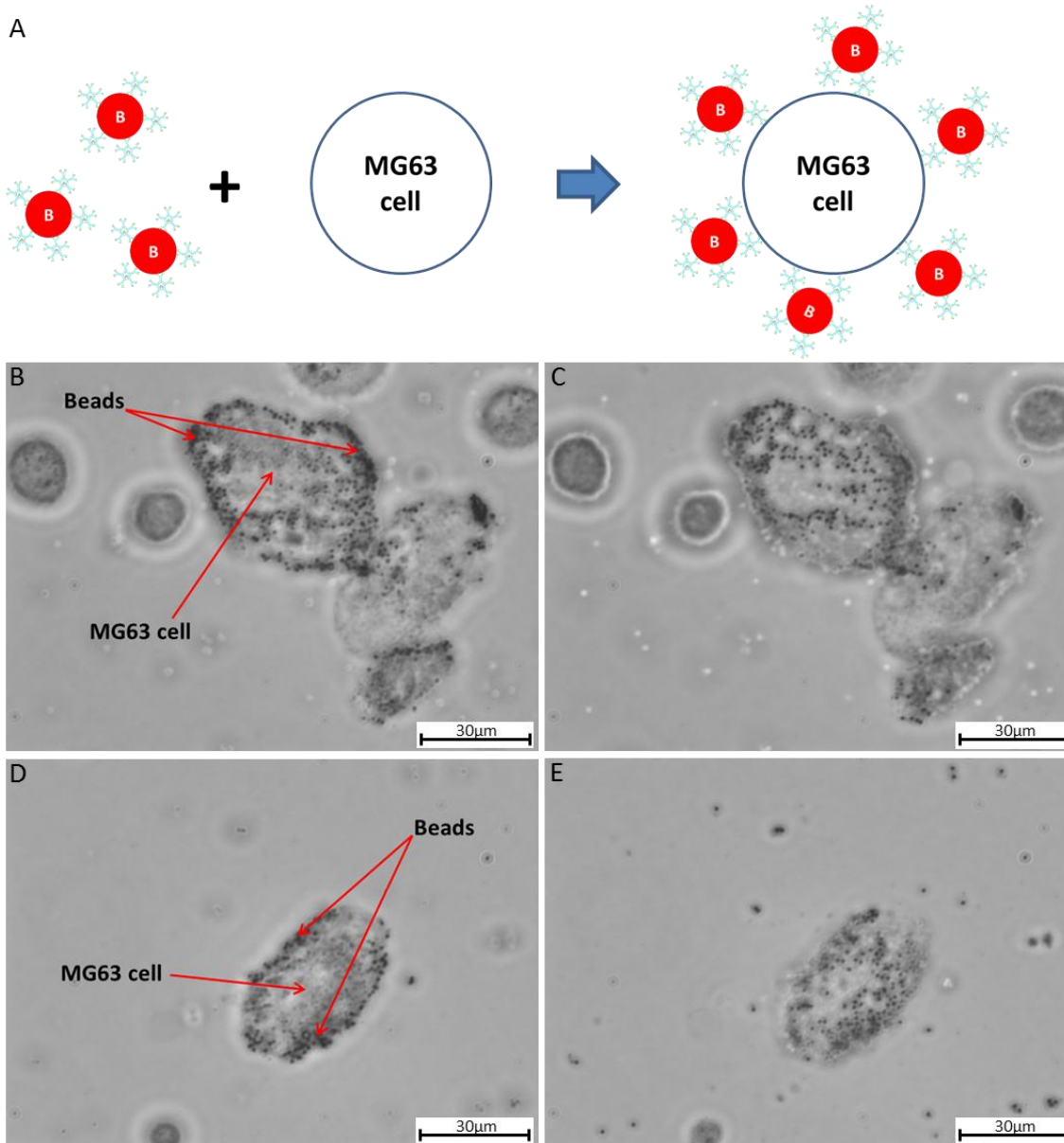


Figure 6.5: (A) Diagram of the cell labelling protocol; MG63 cells (fixed with Ethanol) were incubated with functionalised bead. (B, C and D, E) Bright field photomicroscopy of labelled cells at different focal planes. Scale bars represented 30 µm.

6.2.2 Cell labelling protocol

Once the efficiency of the bead functionalisation protocol was determined, it was necessary to investigate the cell labelling process. To test the cell labelling protocol, MG63 cells were used to mimic the SSCs behaviour. MG63 cells express STRO-1 in a percentage around 60 - 70%. MG63 cells were suspended in blocking buffer (3% goat serum) and kept at 4°C for 15 min. After a few PBS washes the functionalised beads were added to the cell suspension and kept at 4 °C for 30 min.

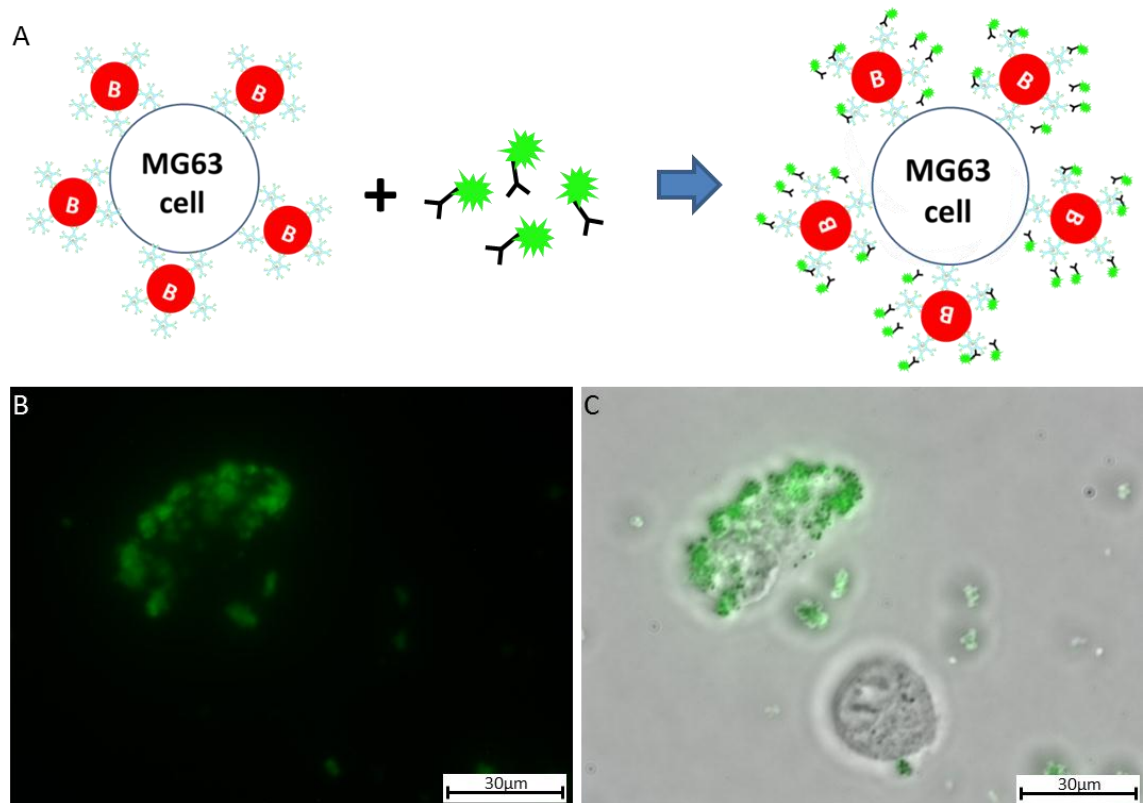


Figure 6.6: (A) Diagram of the control experiment; labelled MG63 cells were incubated with fluorescent antibodies (Alexa 488). (B) Fluorescence microscopy (FITC; Ex/Em (nm): 495/519) of labelled cells; all the beads were fluorescent. (C) Overlying bright field photomicroscopy. Scale bars represented 30 μm .

A few PBS washes more and the cells were labelled and ready to be used (Figure 6.5A) in the sorting device (detailed protocol in Appendix F). Figure 6.5 shows MG63 cells labelled with CM-08-10 beads. The pictures were taken at different focal planes and show how the beads decorate the surface of a MG63 cells. Estimations of minimum number of beads needed for a labelled cell to be sorted and the magnetic force acting on a labelled cell were calculated in Appendix M. In order to further confirm that the beads labelled the cells through STRO-1 antibodies and not through non-specific binding, a control experiment was performed. As demonstrated in 6.2.1.1, the fluorescent secondary antibody Alexa 488 binds to the STRO-1 antibodies on the bead surface. Labelled MG63 cells were incubated with the fluorescent antibodies Alexa 488 at 4 °C for 30 min (Figure 6.6A), and after a few washes they were observed under fluorescence light.

Since all the beads on the MG63 cells were fluorescent (Figure 6.6), it was confirmed that the bead labelled the cells through STRO-1 antibodies and not through non-specific bonding.

6.3 Experimental estimation of labelled cells magnetic susceptibility

The magnetic susceptibility of labelled cells (χ_c) was a key parameter to ensure the effectiveness of the external magnetic field and the consequent efficacy of the sorting strategy. The experimental setup used to estimate the χ_b of commercial superparamagnetic bead was unsuitable to assess the value of χ_c . Therefore, a purpose-built microfluidic device was designed and manufactured just to estimate the value of χ_c .

6.3.1 Microfluidic device for magnetic susceptibility estimation

The microfluidic device used to estimate the value of χ_c consisted of a double adhesive tape (3M™, USA) 0.3 mm thick placed between two PMMA layers (1.5 mm thick). The top PMMA layer had input and output holes to access the channels cut in the middle layer. The channels had different geometries and dimensions. The two long edges of the device were covered with a thin layer of epoxy glue; therefore the input/output holes were the only access points to the channels. A support for the microfluidic device was manufactured using a stereolithography machine with a number of slots to accommodate magnets. The bottom of the support was designed to allow the use of an inverted microscope (Figure 6.7).

The magnets were four cubic neodymium magnets (NdFeB), grade N52 purchased from K&J Magnetics, Inc.® (USA). The support had to keep the magnets and the device horizontal mid-planes aligned, so that the only significant component of the \vec{F}_m experienced by a labelled cell flowing through the channels was the horizontal X component. This feature of the experimental system guaranteed that the cells would only move towards the magnets without influence from the vertical component of \vec{F}_m .

6.3.2 Labelled cell magnetic susceptibility calculation

To estimate the value of χ_c for a labelled cell, the information needed is:

- 1 - the time for a labelled cell to cover a known distance;
- 2 - the relative position of that distance to the magnet;
- 3 - the values of \vec{B} and $(\vec{B} \cdot \nabla)\vec{B}$ along the distance covered.

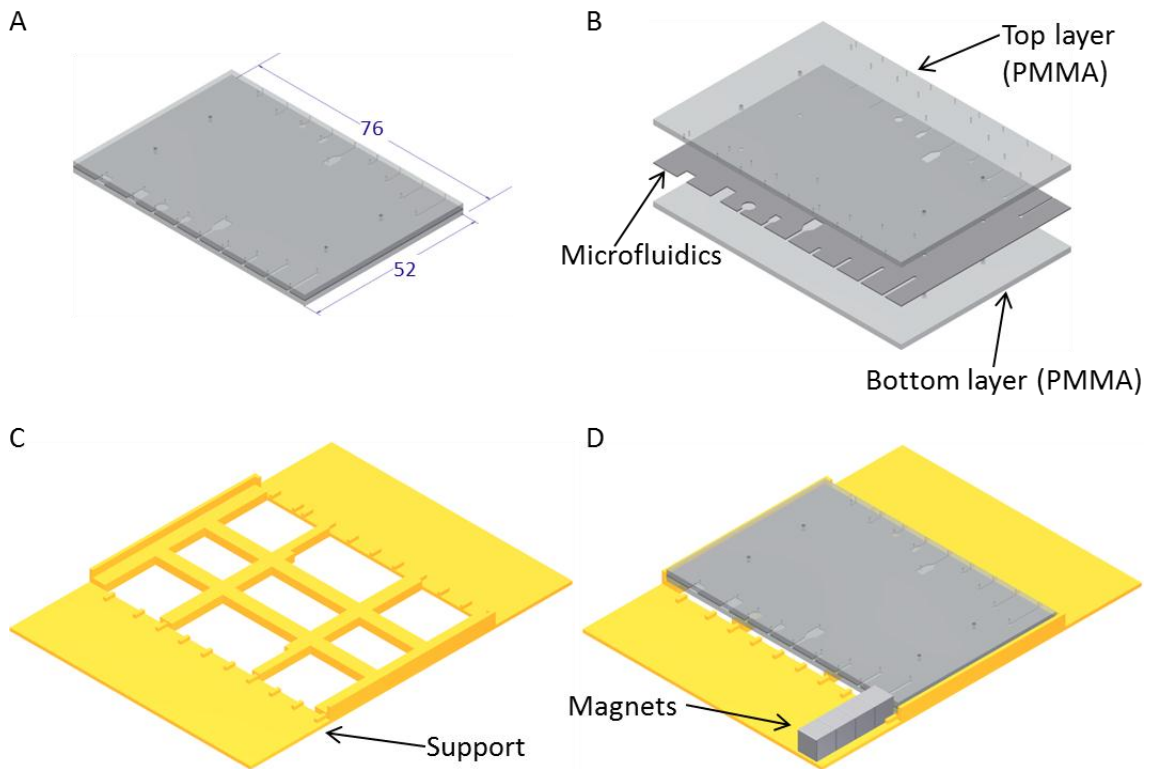


Figure 6.7: (A) 3D models of the microfluidic device used to estimate χ_c ; (B) exploded view. (C) Stereolithography built support and (D) experimental setup. All the measurements were in millimetres.

The method used to estimate χ_c was as follows: one of the microfluidic channels was filled with MACS buffer (PBS + 0.5% BSA + 2 mM EDTA); 1 μl of labelled cell suspension was pipetted at the beginning of the channel through the input hole (far away from the magnet); the microfluidic device was placed under an inverted optical microscope and the magnet was placed in position. The time for a labelled cell to cover a known distance was recorded. 30 labelled cells were observed and the corresponding times recorded. The segment of the channel observed was placed at a known distance from the magnet. The experiments were recorded with a digital camera placed in one of the eyepieces of the microscope. MG63 cells labelled with CM-08-10 (0.82 μm) and CM-025-10 (0.34 μm) were used to estimate χ_c (Figure 6.8A and B). \vec{B} and $(\vec{B} \cdot \nabla)\vec{B}$ along the channel were modelled by numerical simulation (all the numerical simulations in this chapter were performed with COMSOL Multiphysics 4.3b software). A cut line was drawn on the horizontal middle cut plane (Figure 6.8D and E) and \vec{B} and $(\vec{B} \cdot \nabla)\vec{B}$ plotted (Figure 6.8F - H). According to the position of the magnets, the only significant components of \vec{B} and $(\vec{B} \cdot \nabla)\vec{B}$ along the channel were the X components, which had negative values (Figure 6.8F and H).

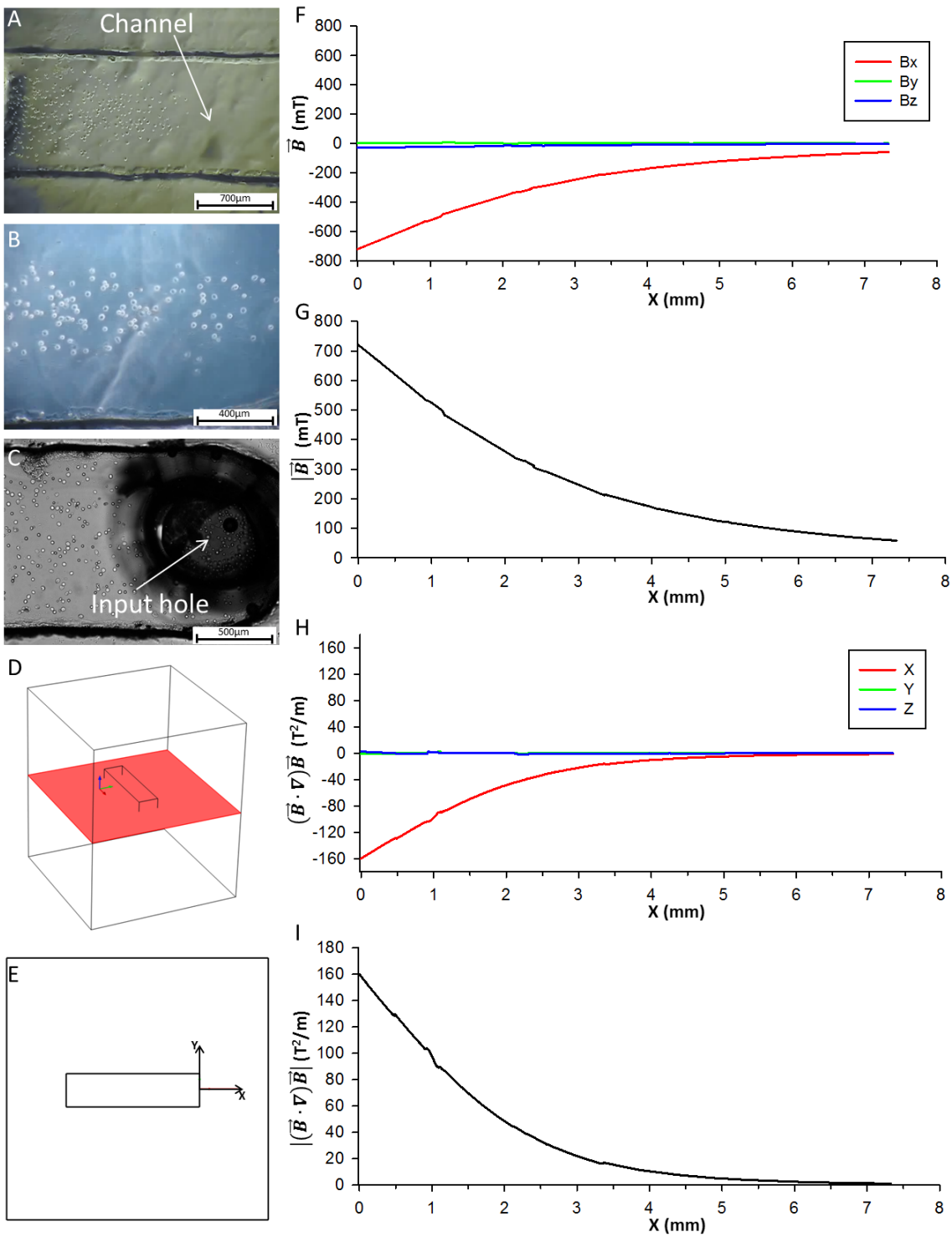


Figure 6.8: (A,B) Frames extracted from the videos recorded during the χ_c estimation experiments at different magnifications. (C) Photomicroscopy of MG63 cells in the channel and in the input hole. (D) Horizontal mid-plane and (E) cut line along which \vec{B} and $(\vec{B} \cdot \nabla)\vec{B}$ were modelled. (F) Plot of $\vec{B}(B_x, B_y, B_z)$ and (G) $|\vec{B}|$ along the cut line. (H) Plot of $(\vec{B} \cdot \nabla)\vec{B}$ and (I) $|(\vec{B} \cdot \nabla)\vec{B}|$ along the cut line.

This meant that \vec{B} and $(\vec{B} \cdot \nabla)\vec{B}$ were pointing in the opposite direction compared to the X axis chosen in the model. $(\vec{B} \cdot \nabla)\vec{B}$ defined the direction of the magnetic force (\vec{F}_m) experienced by a labelled cell, which in this case was attracted towards the magnet. Cells labelled with CM-08-10 beads had a higher χ_c than the CM-025-10 beads. Therefore, these latter bead were not used any further. The χ_c of a MG63 cell labelled with CM-08-10 was estimated to be $3.292 * 10^{-5} \pm 0.24 * 10^{-5}$ (see Appendix G).

6.4 Sample and buffer input flow rates ratio modelling

Numerical simulations were performed to establish the optimum flow rates to be used in the sorting experiments. The key concept of the sorting device was that unlabeled cells ($\chi_c = 0$) must remain close to the central rod and be collected in the non-target output, while the labelled cells ($\chi_c \neq 0$) must be directed to the target output. As unlabeled cells did not experience \vec{F}_m theoretically they should follow the direction of the inner stream in which they were suspended. We investigated the input flow rates needed to achieve this condition through numerical simulations. At first, numerical simulations were performed to investigate the optimum ratio between the sample input flow rate and the buffer input flow rate. Simulations were run along the vertical cut plane shown in Figure 6.9A, and due to the geometrical symmetry of the system (Figure 6.9B) they were performed on just half of the cut plane. With a ratio between the sample flow rate (Q_S) and the buffer flow rate (Q_B) of 1:4 two situations were modelled: outputs unregulated (boundary condition $P=0$ Pa) (Figure 6.9C); and equal flow rates for the two outputs (Figure 6.9D). Setting the flow rates of the two outputs to equal values ensured the inner stream (and the particles suspended in it) exited in the non-target output only (simulation details in Appendix H – Figure H.1). Several ratios ($Q_S:Q_B$) of sample input flow rate and buffer input flow rate were modelled. For the ratios 2:1 and 1:1, part of the sample flow exited in the target output, which was undesirable (Figure 6.9 E - F). For lower ratios, the sample flow became more and more constrained by the buffer flow. However, using ratios of 1:2 and 1:3, the buffer flow did not provide a sufficient containment of the sample flow (Figure 6.9 G - H). As said at the beginning of the Section, this was a key condition for the correct operation of the device; and the maximum $Q_S:Q_B$ ratio to fulfil that condition was 1:4 (Figure 6.9I). The final $Q_S:Q_B$ ratio modelled was 1:10. This ratio constrained the sample flow close to the central rod even more than the 1:4 ratio, ensuring that the sample flow exited in the non-target output.

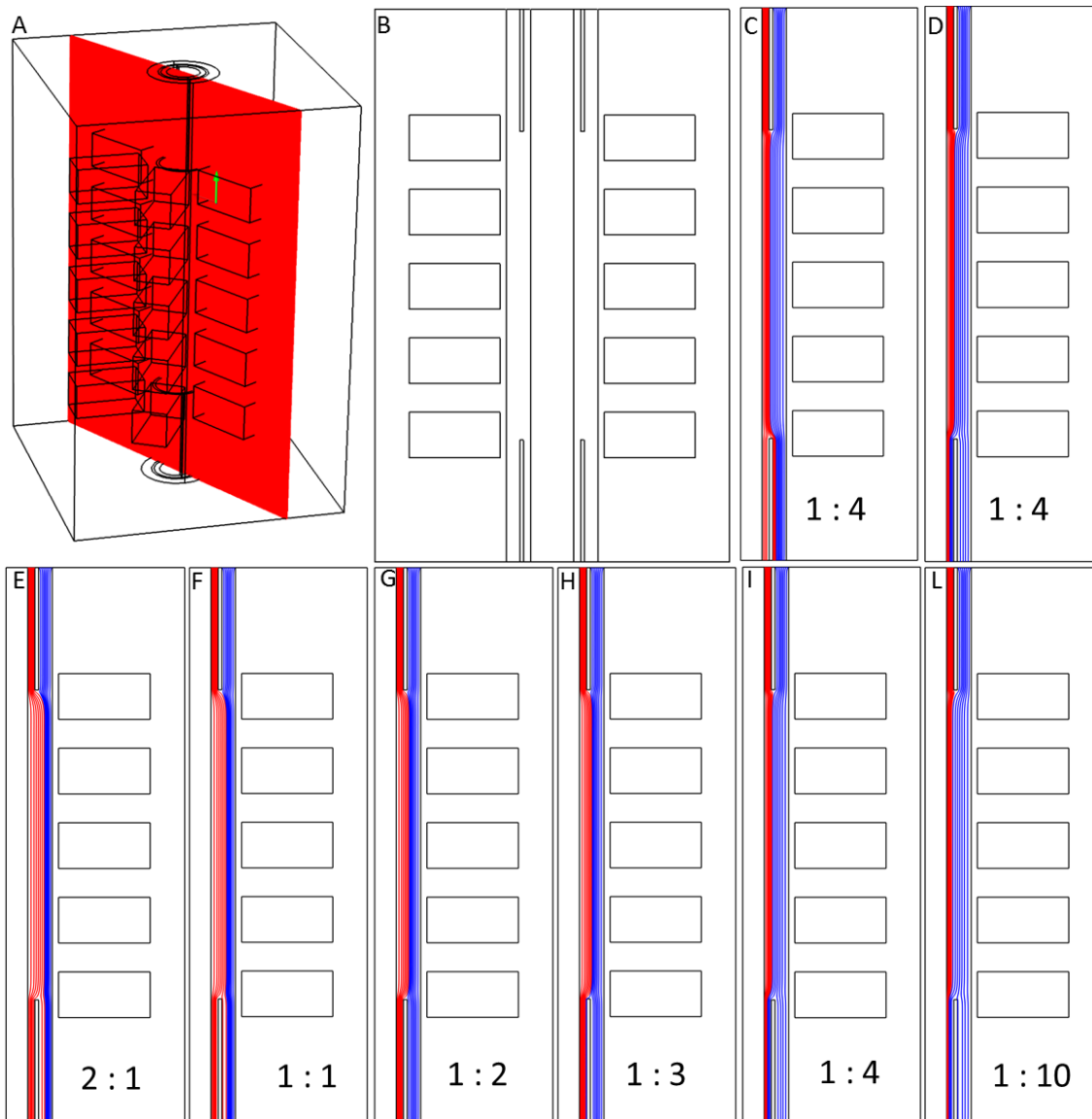


Figure 6.9: (A) Vertical mid-plane. (B) Section of the sorting device (without manifolds) and magnetic system. (C) Due to the geometrical symmetry, just half of the system was modelled (sample flow in red, buffer flow in blue): outputs unregulated, (D) equal flow rates for the two outputs. (E - L) Velocity field streamlines representing a parameter sweep for different flow rate ratios (simulation details in Appendix H – Figure H.1).

However, to ensure a high throughput for the sorting device and a moderate duration of the experiment, the sample flow rate should be as high as possible. In conclusion, the $Q_S:Q_B$ ratio used in the further numerical simulation was 1:4.

The input flow rate ratio was investigated using 3D numerical simulation including the input and output manifolds in the simulation. The velocity field streamlines of the flow within the sorting device were shown in Figure 6.10A.

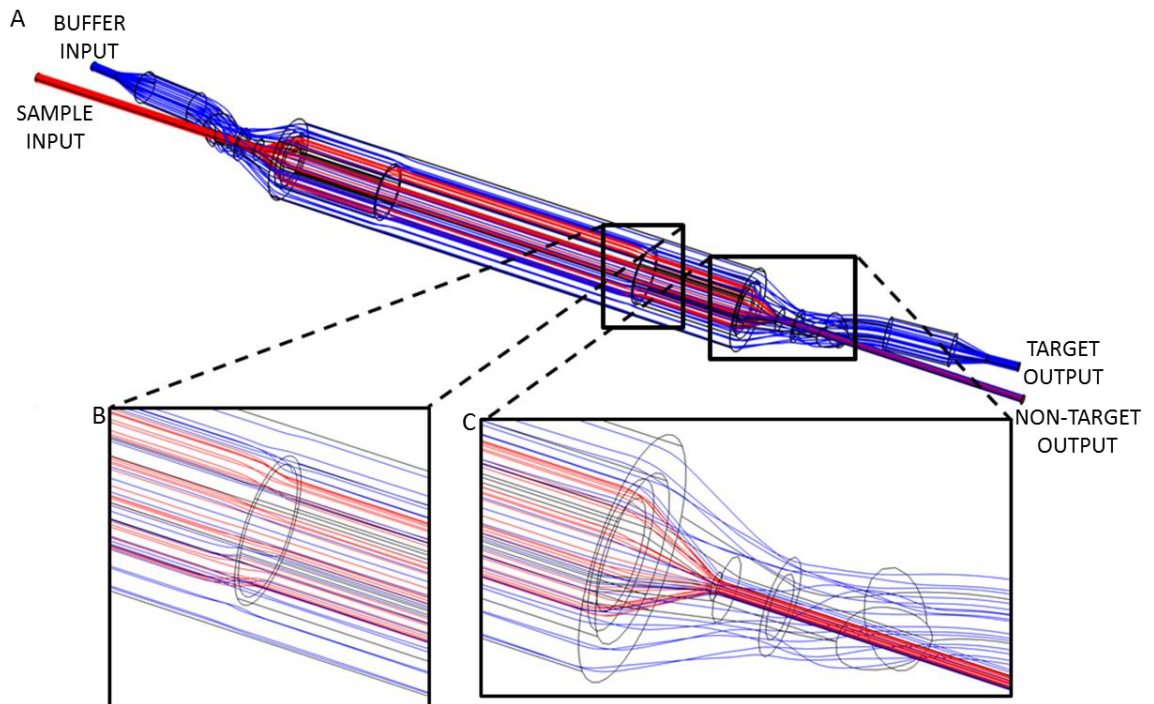


Figure 6.10: (A) Velocity field streamlines of the flow within the sorting device using a ratio between the two flow rates of 1:4. The lines in red and blues represented the sample flow and buffer flow, respectively. (B) Details of the flow at the beginning of the outlet manifold (C) and in correspondence to the separate outputs (simulation details in Appendix H – Figure H.2).

The result described above was confirmed. With a $Q_S:Q_B$ ratio of 1:4, the sample flow (in red) exited only into the non-target output (simulation details Appendix H).

6.5 Particle tracking: 2D numerical simulation

6.5.1 Unlabelled cells

The result described in Section 6.4 was further confirmed by a 3D particle tracking numerical simulation that modelled unlabelled cell trajectories within the sorting device (Figure 6.11) (simulation details Appendix H – Figure H.3). The numerical simulations demonstrated that unlabelled cells followed the direction of the inner stream in which they were suspended.

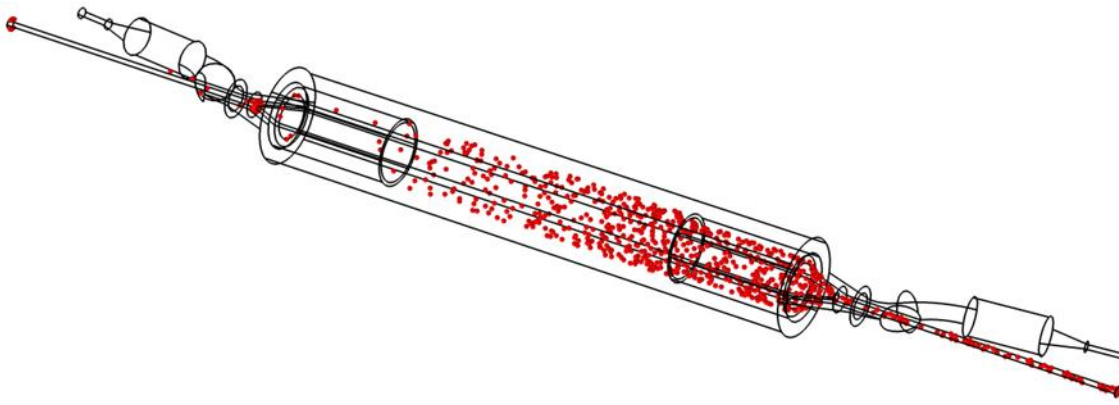


Figure 6.11: Particle trajectories for unlabelled cells (ratio between the two flow rate of 1:4) (simulation details in Appendix H – Figure H.3).

6.5.2 Labelled cells

Once the behaviour of unlabeled cells within the sorting device was modelled, numerical simulations were implemented to investigate the trajectories of labelled cells exposed to a magnetic field (simulation details Appendix H – Figure H.4). The magnetic system used in these simulations was the hexapole magnetic system (see Section 5.4) and the magnetic susceptibility bestowed on labelled cell was the experimentally estimated χ_c (see Section 6.3.2). Hence, a parametric sweep of the total flow rate ($Q_T = Q_S + Q_B$) was performed. Simulations were done using the ratio 1:4 between the Q_S and Q_B and boundary conditions of equal flow rates for the two outputs. This combination kept the non-target cells close to the central rod so that they would not be collected into the target output. The values of the modelled Q_T ranged from 10 ml/min to 2 ml/min in steps of 0.5 ml/min. The values of Q_T at the two ends of the range, were not significant and Figure 6.12 shows simulations for $Q_T=6$ ml/min to $Q_T=4$ ml/min. As per simulations in Figure 6.9, the particle trajectory was modelled on a vertical cut plane for half of the sorting device due to the symmetry of the system.

Figure 6.12 shows the trajectories of a labelled cell (with magnetic susceptibility χ_c) released in the middle of the sample input for several values of Q_T . 4.5 ml/min was found to be the maximum Q_T that allowed the labelled cell to be collected in the target output with a $Q_S:Q_B$ ratio of 1:4. It was desirable to use a Q_T as high as possible to limit the duration of the experiment and achieve a high throughput. Under these conditions, the velocity field within the sorting device was modelled (Figure 6.13A) and the velocity of the labelled cell was investigated. The horizontal (v_x) and vertical (v_y) components of the cell velocity were plotted along the length of the sorting device.

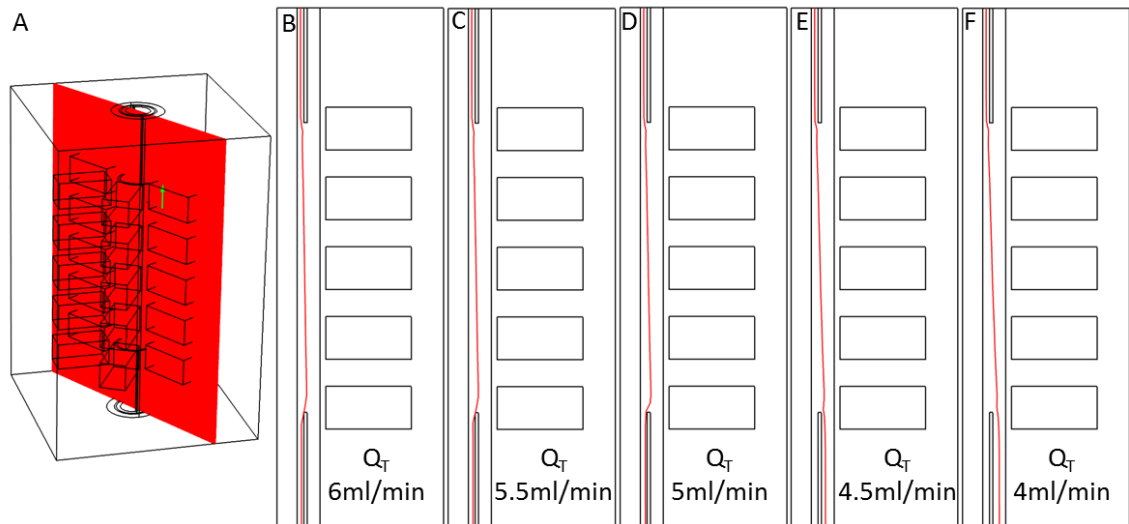


Figure 6.12: (A) Vertical mid-plane. (B, C, D) Trajectory of a single labelled cell modelled using a range of Q_T with a fixed ratio between Q_S and Q_B of 1:4. The labelled cell in the sample input and collected in the non-target output or (E, F) in the target output according to the Q_T used (simulation details in Appendix H – Figure H.4).

On the same graph the Euclidean norm of the velocity ($v_n = \sqrt{v_x^2 + v_y^2}$) was shown (Figure 6.13D). In Figure 6.13C a table summarising the parameters used in the numerical simulations, including χ_c estimated experimentally and used to model the labelled cell; the value of Q_T which was found to be suitable for cell sorting; and the average values of v_x , v_y and v_n obtained from the numerical simulation. The above simulations were modelled in the best possible situation along the vertical cut plane along the centre of the magnets. Along the mid-plane chosen (Figure 6.12A), the labelled cells experienced higher values of $\overrightarrow{F_m}$ compared to other positions within the system; this increased the horizontal velocity of the labelled cell, resulting in a higher vertical velocity. The trajectory of a single cell released in the middle of the sample input was also modelled.

6.6 Particle tracking: 3D numerical simulation

In order to obtain the best Q_T for the sorting experiments (a value as close as possible to real-life) the particle tracking simulation was refined. A 3D numerical simulation was implemented to investigate the trajectories of labelled cells within the sorting device (just the flow within the tube was modelled) surrounded by the hexapole magnetic system (Section 5.4) (as per 2D simulations).

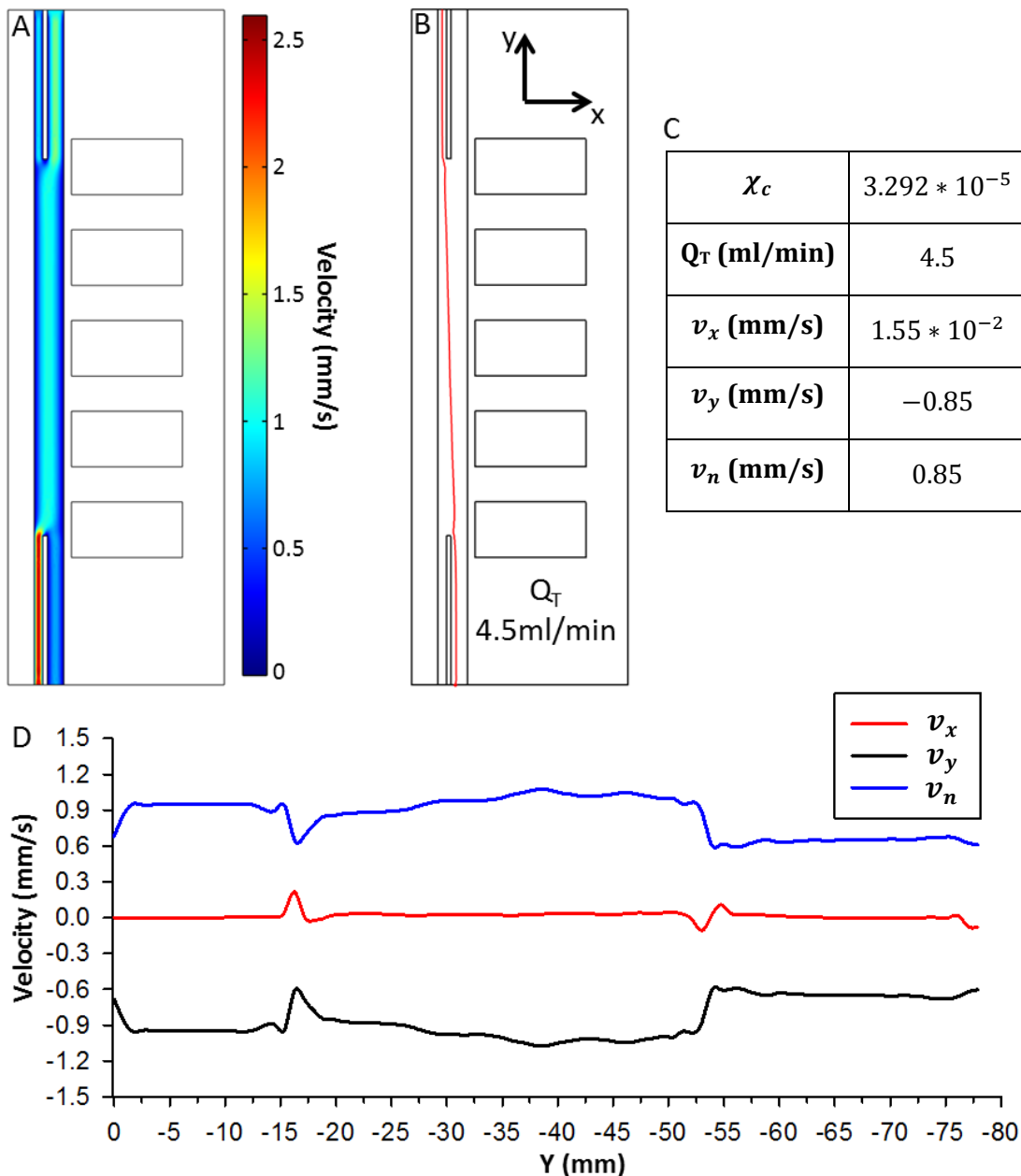


Figure 6.13: (A) Magnitude of the flow velocity. (B) Trajectory of labelled cell within the sorting device ($Q_T = 4.5 \text{ ml/min}$). (C) Table summarizing the simulation parameters. (D) Plot of the cell velocity along the sorting device.

1000 labelled cells (with magnetic susceptibility χ_c) were released into the sample input, while the 2D simulation modelled the trajectory of a single labelled cell. Again, a parameter sweep was performed to investigate cell trajectories for different values of Q_T . The values of Q_T ranged from 4.5 ml/min (value obtained from the 2D simulation) to 2 ml/min in 0.5 ml/min steps. The ratio between Q_S and Q_B was kept constant at 1:4 (simulation details in Appendix H – Figure H.5).

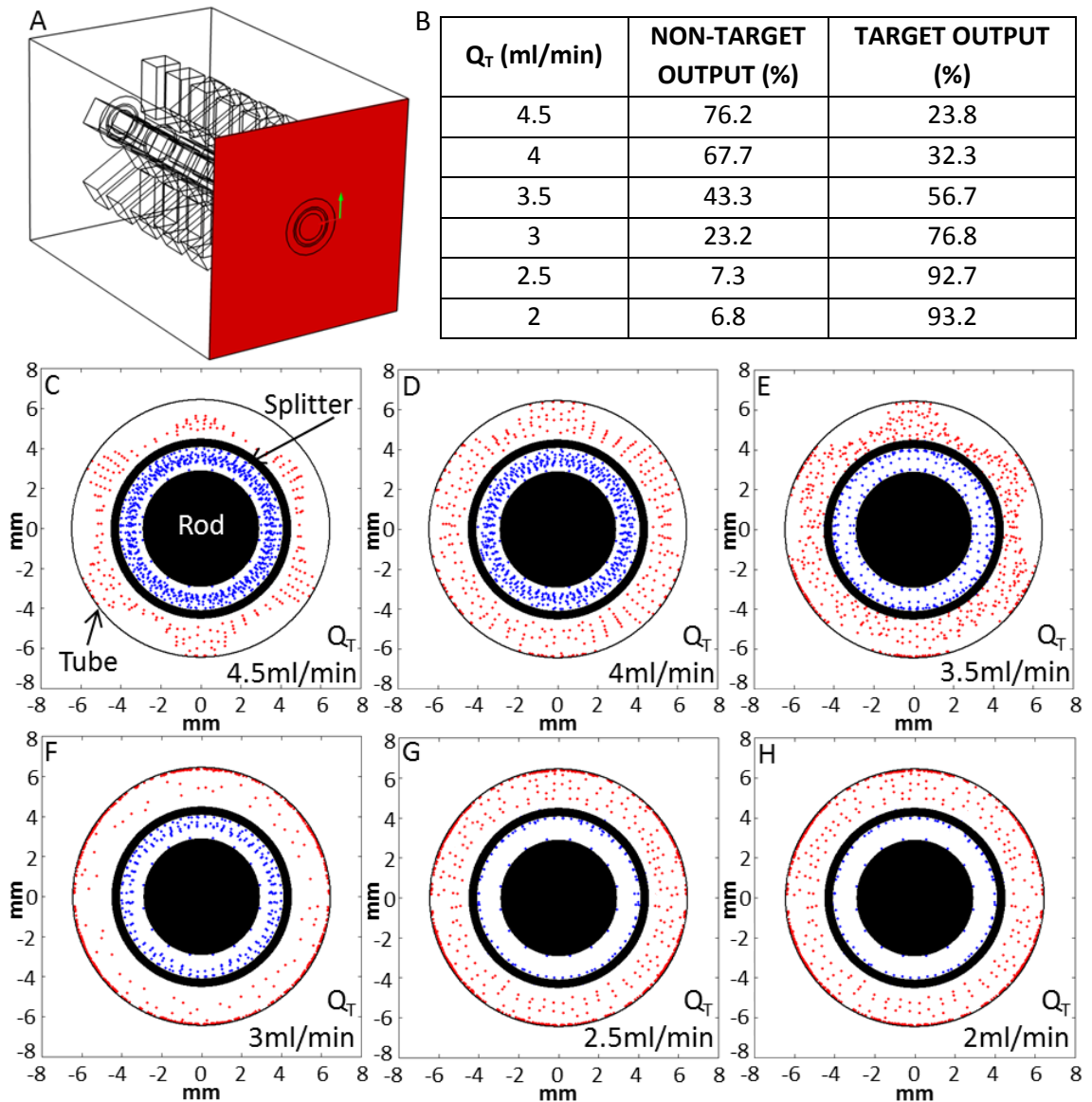


Figure 6.14: (A) Plane where the cells final positions ($t=150$ s) were projected. (B) Summarizing table of the percentages of cells recovered in each output for the values of Q_T investigated. (C – H) Projections on the plane of the cells positions at $t=150$ s under several Q_T values. All the cells had identical magnetic susceptibility χ_c . The Matlab script allowed to represent the cells collected into the target and non-target outputs by red and blue dots respectively.

All the simulations were performed using the experimental value of χ_c as previously used in the 2D simulations. Once the numerical simulations were completed, the position of each cell at the final time point ($t=150$ s) was projected on the plane shown in Figure 6.14A, and exported to Matlab (MathWorks, Cambridge, UK) for plotting. Figure 6.14 shows the final positions ($t=150$ s) of the labelled cells within the sorting device for different values of Q_T .

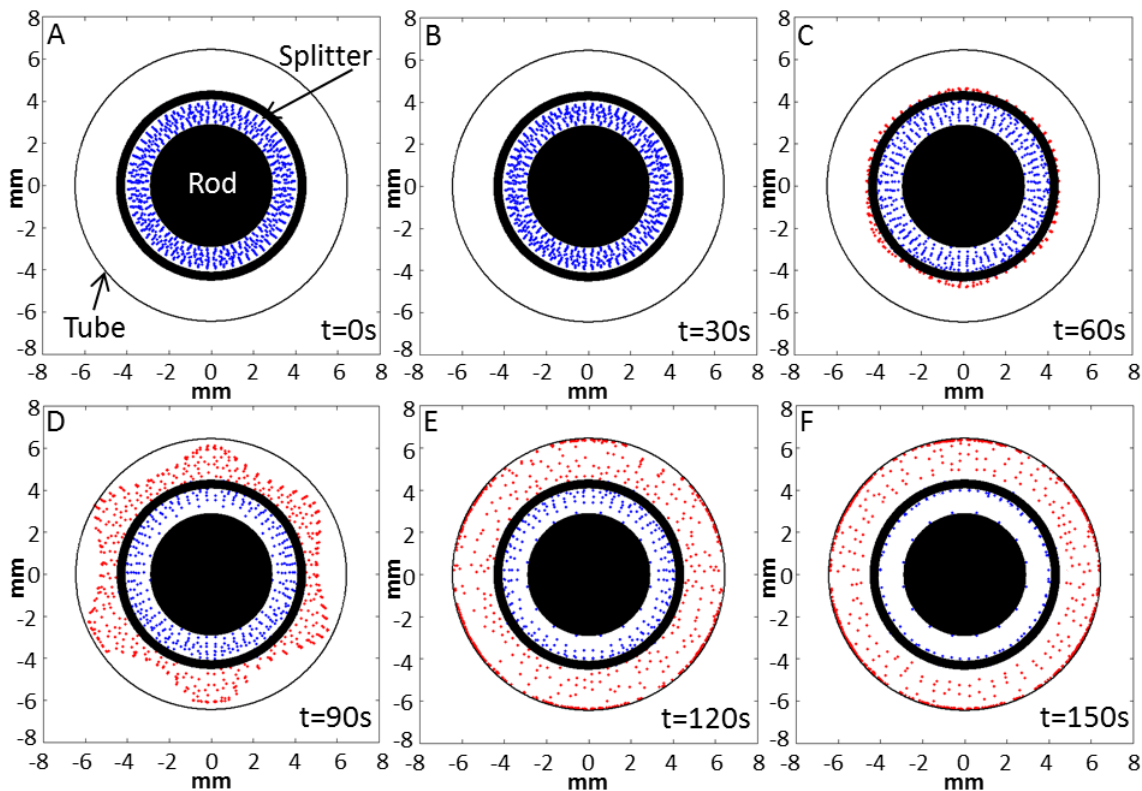


Figure 6.15: (A - F) Projections on the plane (Figure 6.14A) of the cells positions at different time points, between $t=0$ s and $t=150$ s (residence time), at a fixed flow rate ($Q_T = 2.5$ ml/min – $Q_S:Q_B = 1:4$). The Matlab script allowed to represent the cells collected into the target and non-target outputs by red and blue dots respectively

In each plot the structure of the sorting device was shown in black (from the center: rod, manifold defining the two outputs and the internal wall of the tube). The percentage of labelled cells collected into the target output was calculated for each Q_T investigated (Figure 6.14B).

The optimum value of Q_T corresponded to the highest percentage of cells collected in the target output. In the simulations the best recovery efficiencies were obtained with $Q_T=2$ ml/min (Figure 6.14H). However, the difference between the best (93.2%) and the second best (92.7%) recovery efficiencies was not significant, and since a higher values of Q_T was desirable, a value of $Q_T=2.5$ ml/min was chosen (Figure 6.14G). Cell trajectories under this flow condition were investigated extensively as shown in Figure 6.15. Using the same Matlab script as previously used, the positions of the cells within the sorting device at different time points were plotted. Figure 6.15D shows the flower shaped structure formed by the cells in response to the F_m generated by the neodymium magnets. The 3D particle tracking simulation using $Q_T = 2.5$ ml/min was shown in Figure 6.16, with the magnetic system and the flow within the sorting device outlined in grey.

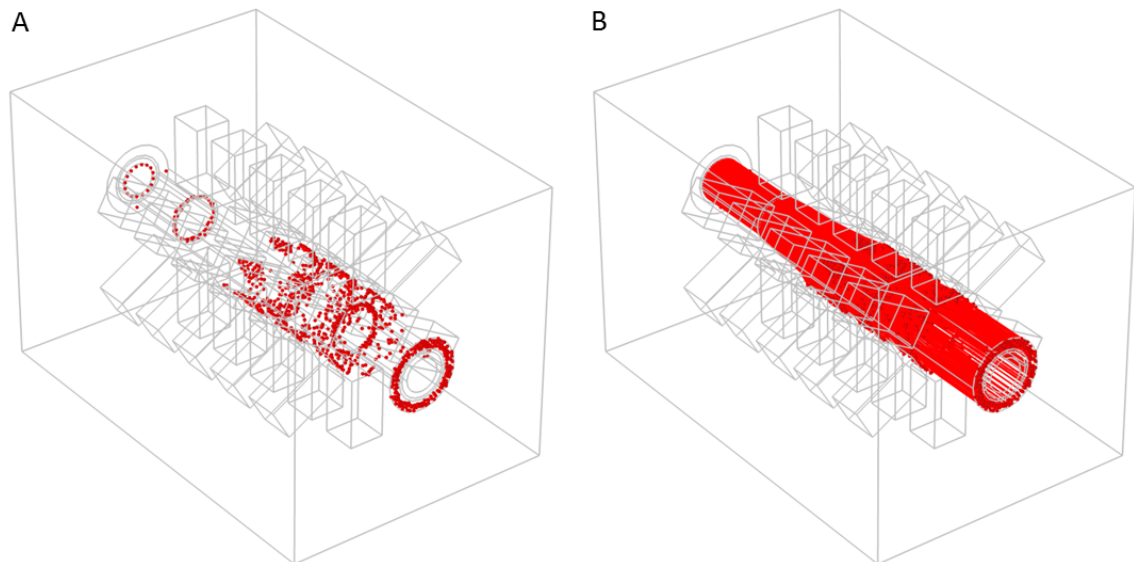


Figure 6.16: (A) Final positions of the labelled cells, $t=150$ s and (B) trajectories of the labelled cells within the sorting device (simulation details in Appendix H – Figure H.5).

As shown in Figure 6.14G, even with the optimum flow conditions, the percentage of cells collected into the target output never achieved 100%. This was because the numerical simulation assumed an uniform distribution of the cells into the sample input, which lead to simulation artefacts resulting in some cells remaining trapped along the system manifold.

Figure 6.17B details the effects of a uniform distribution of cells at the entrance of the sorting device: at $t=0$ the cells were released at the beginning of the tube and started to flow through the sorting device; the line of cells closest to the central rod did not move from the initial position; nor did the last line of cells adjacent to the internal part of the manifold, which after travelling for a few millimetres remained attached to the manifold surface. Figure 6.17C shows several cells trapped at the edge of the output manifold (highlighted by blue arrows), again not contributing to the cells collected in the target output. In real-life these cells would be probably exit from one of the two outputs.

In Figure 6.17 C another group of trapped cells was shown attached to the internal wall of the sorting device (cells highlighted by green arrows). Those cells were initially positioned far away from the central rod, and hence had to cover a short horizontal distance before collection at the target output. Because of their short path, these cells hit the internal wall and get trapped, whilst the cells starting closer to the central rod travelled to the bottom of the tube and were collected in the target output (Figure 6.17A). Once the trajectories of the labelled cells within the sorting device were defined, the flow velocity field and the average cell velocity were investigated under the same conditions ($Q_T=2.5$ ml/min).

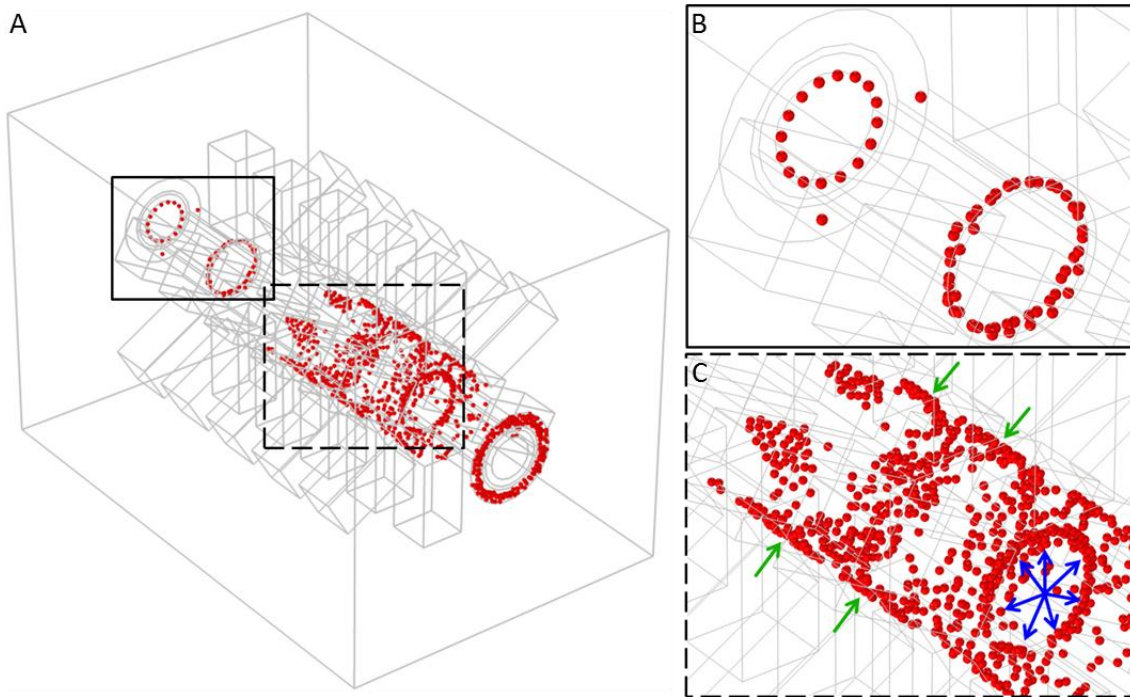
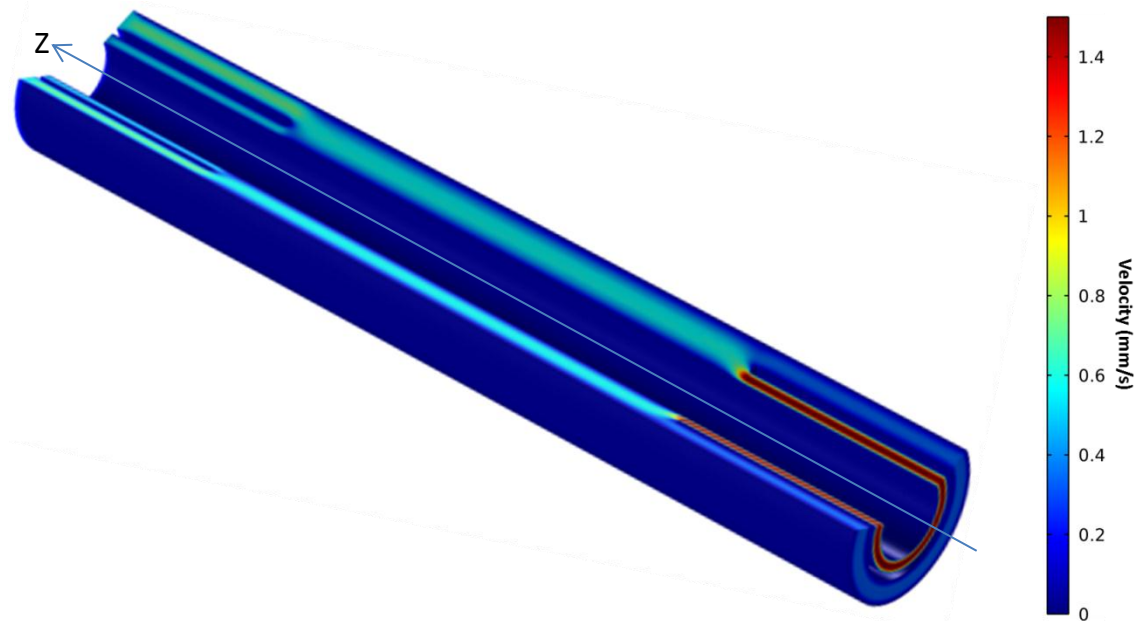


Figure 6.17: (A) Final positions of the labelled cells within the sorting device. (B) Detail of cells trapped onto the internal surface of the input manifold. (C) Detail of cells trapped onto the internal surface of the tube (highlighted by green arrows) and the internal surface of the output manifold (highlighted by blue arrows).

Figure 6.18 shows the velocity field within the sorting device, together with a table summarising the parameters used and the cell velocity obtained.

The trajectories of 1000 cells were modelled at six time points: $t=0$ s, 30 s, 60 s, 90 s, 120 s and 150 s. For each cell, the three components (v_x v_y v_z) of the cell velocity was known at each time point. 6000 values (6 time points * 1000 cells) were averaged and the modulus of these figures were calculated for each velocity component. The average v_x v_y v_z of a cell flowing within the device was thus obtained. The average also included the velocity values for cells adhering to the tube walls (with zero velocity).



χ_c	Q_T (ml/min)	Q_S (ml/min)	Q_B (ml/min)	$ v_x $ (mm/s)	$ v_y $ (mm/s)	$ v_z $ (mm/s)
$3.29 \cdot 10^{-5}$	2.5	0.5	2	$5.55 \cdot 10^{-3}$	$1.11 \cdot 10^{-2}$	0.515

Figure 6.18: Flow velocity magnitude within the sorting device ($Q_T = 2.5$ ml/min); table summarising parameters used and cells velocity values obtained.

6.7 Summary

The principle of the sorting device was to focus the target cells into a dedicated output using an external magnetic field. To do so, target cells had to respond to the magnetic field. The magnetic susceptibility was a dimensionless proportionality constant indicating how a material was susceptible to an applied magnetic field, and to increase this value, target cells were labelled with superparamagnetic beads. The superparamagnetic beads CM-08-10 ($0.82 \mu\text{m}$; Spherotech, Inc. USA) were found the most suitable for the aim of the study, with an experimentally estimated magnetic susceptibility (χ_b) of $1.3 \cdot 10^{-3}$.

To use these beads to label target cells, it was necessary to immobilise antibodies on the bead that bind the antigens expressed on target cells. To sort skeletal stem cells (SSCs), the antigen used was the STRO-1 which was the best known SSCs marker.

Carbodiimide coupling was used to bind STRO-1 antibodies to the carboxyl bead surface using EDC/NHSS as coupling agent. The functionalisation efficiency was tested with negative and positive experimental controls. Once functionalised, the superparamagnetic beads were incubated with MG63 cells to mimic the behaviour of the SSCs.

The magnetic susceptibility of labelled cells (χ_c) was a key parameter for the sorting, and was estimated experimentally. A purpose built microfluidic device (Figure 6.7) was designed and manufactured to estimate χ_c .

Numerical simulations were used to model the trajectories of unlabelled cells within the sorting device. The optimum ratio between Q_S and Q_B was found to be 1:4 and this ratio ensured that the unlabelled cells remained close to the central rod and could be collected in the non-target output. The value of χ_c was used to model the trajectory of a labelled cells within the sorting device with the hexapole magnetic system. The ratio between Q_S and Q_B was kept constant at 1:4 and a parametric sweep of Q_T was performed. The maximum value of Q_T that ensured that the labelled cells were collected in the target output was 4.5 ml/min. This value was obtained from a 2D numerical simulation of the best condition (cut plane through the middle of the magnets). For a more accurate values of Q_T (to be used experimentally) a 3D numerical simulation was designed. The same value of χ_c was used and the trajectories of 1000 labelled cells released into the sample input were modelled at several time points for different values of Q_T . The final position of the cells within the sorting device was plotted in Matlab and the percentages of labelled cells collected into the target output for each value of Q_T was calculated. The optimum value of Q_T was found to be 2.5 ml/min. The numerical simulation generated two artefacts (see Section 6.4.3) but the value of Q_T obtained provided a starting figure for the experimental investigation of the optimum flow regime for the sorting experiments.

Chapter 7

Sorting Device Testing

In Chapter 6 the experimental estimation of the labelled cell magnetic susceptibility (χ_c) was described. Numerical simulations were designed to model cell trajectory within the device, in order to find the optimum flow rate for cell sorting. In this chapter experiments were performed to test multiple versions of the sorting device (see Chapter 4) and combination with magnetic systems (see Chapter 5). Preliminary experiments were performed using polystyrene beads to mimic cell behaviour. Later, cell sorting experiments (using MG63 cell line) were conducted on four sorting device + magnetic system combinations. Lastly, performance of the final sorting device was compared to that of conventional MACS.

7.1 Experimental setup and protocol

The experimental setup consisted of: two syringe pumps (Harvard Apparatus – 11 Plus, USA), plastic syringes, tubing (Omnifit No:12946291), valves (Omnifit No:001101), the magnetic system and the sorting device. Setup simplicity and small size allowed us to perform cell sorting experiments (particularly when using primary cells) within a laminar flow cabinet, providing a quasi-sterile experimental environment (Figure 7.1). The sorting device working principle was described in section 5.1. The sorting device was incubated in PBS + 0.1% BSA overnight when possible, or at least one hour before the start of the experiment. The sorting device was fastened to the device support and before each experiment was washed by flushing with 10% sodium hypochlorite, MilliQ water, ethanol (90%) and finally rinsing with MilliQ water. This washing step was commonly used to clean and sterilized a microfluidic device prior to utilisation with live cells [75]. The system was then filled with buffer. Two buffers were used for sorting experiments. The first, used to perform experiments with polystyrene beads composed of: PBS + 0.1% glycolic acid

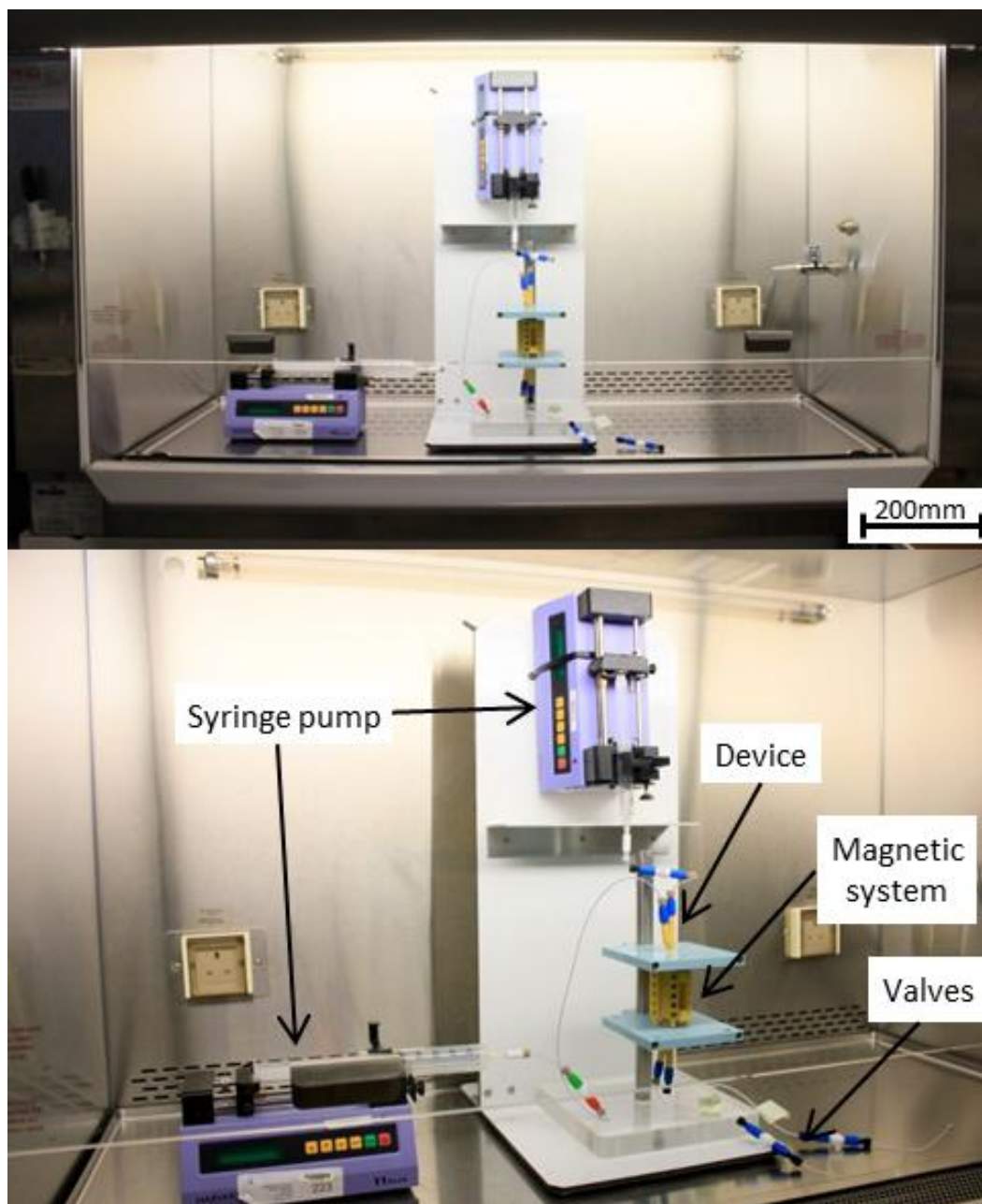


Figure 7.1: (A) Picture of the experimental setup in a laminar flow hood. (B) The setup consisted of: two syringe pumps (Harvard Apparatus – 11 Plus, USA), plastic syringes, tubing (Omnifit No:12946291), valves (Omnifit No:001101), the magnetic system and the sorting device.

ethoxylate 4-nonylphenyl ether (GAENE) + 1% bovine serum albumin (BSA). The second buffer was used to perform sorting experiments with cells and comprised PBS + 2 mM EDTA + 25 mM HEPES + 1% BSA + 0.1% Pluronic F-68 + 5% Dextran T70. Addition of Pluronic F-68 to the buffer helped to prevent the cell bursting during the sorting procedure [76,77].

Dextran was a large molecular weight polysaccharide ($T_{70} = 70,000\text{Da}$), and its addition to the buffer increases buoyancy, reducing cell sedimentation [75].

The two syringe pumps were set to operate at the desired buffer and sample flow rates. The system was flushed with buffer whilst adjusting output valves to ensure equal output flow rates at the positive and negative fractions outputs.

After checking for leakages, the magnetic system was mounted around the device and the sorting procedure initiated. The positive and negative fractions were recovered in two separate tubes (50 ml) and then analysed by a flow cytometer (Guava EasyCyte Mini - Merck Millipore, Germany). At the end of each experiment, the system was purged with MilliQ water and washed as previously described.

7.2 Preliminary experiments

In this section, the sorting device was tested using non-magnetic polystyrene beads and unlabelled cells. No magnetic system was used. The aim of these studies was to investigate two phenomena; cross-contamination and the reasons behind missing cell fraction. Finally, the results obtained using three generations of sorting device were compared.

7.2.1 Cross-contamination

As described in Section 6.4, the key concept of the sorting device was that unlabelled cells ($\chi_c = 0$) must remain close to the central rod and be collected in the non-target output, while labelled cells ($\chi_c \neq 0$) must be directed to the target output. When this condition was not satisfied, *cross-contamination* occurs.

In Chapter 6 numerical simulations were used to assess the optimum sample and buffer input flow rate ratio ($Q_S:Q_B$); calculated to be 1:4. To validate this result, bench experiments were performed, testing several $Q_S:Q_B$ ratios. The aim of the experiments was to keep the sample flow rate as high as possible to maximize throughput. To investigate whether unlabelled cells remained close to the central rod, non-magnetic polystyrene beads ($\emptyset 10 \mu\text{m}$) were used to mimic the behaviour of unlabelled cells. At this stage of device testing, the incongruence between beads and cells size was neglected. The beads were suspended in buffer at a concentration of 200,000 beads/ml to create the original sample. Sorting device version 1 (ver. 1 - see Section 4.3), without any magnetic system, was tested with several $Q_S:Q_B$ ratios, ranging from 1:1 to 1:40.

Table 7.1: Table summarising the cross-contamination experiments (mean values $n=3 \pm SD$) performed with the sorting device ver.1.

Cross-contamination experiments – Sorting device ver.1

INPUT FLOW RATE ($\mu\text{l}/\text{min}$)			TARGET OUTPUT (%)	NON-TARGET OUTPUT (%)
$Q_S:Q_B$	BUFFER (Q_B)	SAMPLE (Q_S)		
1:1	2000	2000	29.50 \pm 5.78	32.83 \pm 7.82
1:2	2000	1000	18.57 \pm 4.94	45.20 \pm 7.91
1:3	2000	700	11.31 \pm 4.13	61.31 \pm 6.69
1:4	2000	500	5.97 \pm 1.98	70.06 \pm 5.34
1:10	2000	200	3.92 \pm 0.82	74.61 \pm 7.93
1:20	2000	100	2.84 \pm 0.81	77.54 \pm 6.95
1:40	2000	50	1.66 \pm 0.79	77.31 \pm 7.02

The buffer input flow rate (Q_B) was fixed at 2000 $\mu\text{l}/\text{min}$, and the sample input flow rate (Q_S) was modified to investigate the $Q_S:Q_B$ ratios of interest. According to the numerical simulations (section 6.4), Q_B must be always higher than Q_S , and the maximum total flow rate (Q_T) must never be higher than 4.5 ml/min. Each condition was tested in triplicate. Samples recovered from the target and non-target outputs were analysed by FACS and compared to the beads solution used as original sample.

Table 7.1 shows Q_S and Q_B values alongside several ratios investigated. For each condition the average percentage of beads recovered in the target and non-target outputs were reported +/- standard deviation ($n=3$). The sum of the percentages of beads recovered from both outputs was not 100%. This will be discussed later in the chapter (see Section 7.2.2). Below are discussed the percentages of beads recovered from the target output.

In Table 7.1, with a $Q_S:Q_B$ ratio of 1:1, 1:2 and 1:3 the percentages of beads recovered in the target output ranged from $\sim 30\%$ to $\sim 11\%$, respectively indicating high cross-contamination. Only when the ratio was lowered to 1:4 did the recovery percentage decrease below 10% ($\sim 6\%$). $Q_S:Q_B$ ratios of 1:10, 1:20 and 1:40 further reduced recovery in the target output to $\sim 4\%$, $\sim 3\%$ and $\sim 2\%$, respectively.

As the aim of this study was to sort cells with high-throughput, it was paramount that Q_S remains as high as feasibly possible. However, a balance must be struck with sorted fraction purity.

According to the results showed in Table 7.1, a significant number of beads moved from the original internal stream (close to the central rod) into output stream designed for target particles.

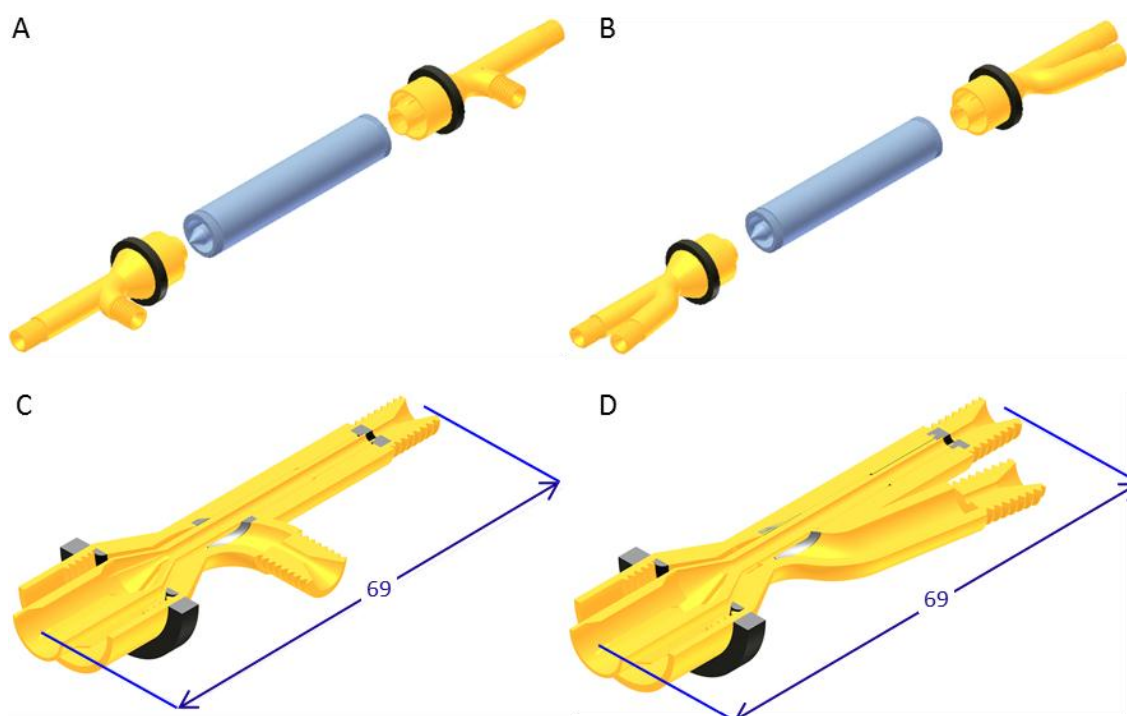


Figure 7.2: (A) 3D models of the sorting device ver.1 and (B) ver.2. (C) Horizontal section of the input/output manifolds ver.1 and (D) ver.2. All measurements were in millimetres.

To tackle cross-contamination, changes to the input/output manifolds were made, leading to the design of sorting device version 2 (ver. 2) (Figure 7.2B).

Sorting device ver. 2, with the exception of manifolds, shared all other components with the first version (see section 4.6). Manifold ver.1 and manifold ver.2 were shown in Figure 7.2.

Table 7.2: Table summarising the cross-contamination experiments (mean values $n=3$) performed with the sorting device ver.2.

Cross-contamination experiments – Sorting device ver.2

INPUT FLOW RATE ($\mu\text{l}/\text{min}$)			TARGET OUTPUT (%)	NON-TARGET OUTPUT (%)
$Q_S:Q_B$	BUFFER (Q_B)	SAMPLE (Q_S)		
1:1	2000	2000	18.71 \pm 3.73	44.13 \pm 7.62
1:2	2000	1000	11.29 \pm 3.13	49.11 \pm 7.31
1:3	2000	700	5.31 \pm 2.13	61.92 \pm 5.19
1:4	2000	500	1.07 \pm 0.37	70.93 \pm 4.14
1:10	2000	200	0.92 \pm 0.35	76.21 \pm 6.93
1:20	2000	100	0.81 \pm 0.31	77.94 \pm 6.15
1:40	2000	50	0.61 \pm 0.23	77.71 \pm 7.22

Table 7.3: Comparative table of the cross-contamination experiments performed with the sorting device ver.1 and the sorting device ver.2.

Cross-contamination experiments – Sorting device ver.1 vs Sorting device ver.2

FLOW RATE ($\mu\text{l}/\text{min}$)			TARGET OUTPUT (%)		NON-TARGET OUTPUT (%)	
$Q_S:Q_B$	BUFFER (Q_B)	SAMPLE (Q_S)	DEV VER.1	DEV VER.2	DEV VER.1	DEV VER.2
1:1	2000	2000	29.50 \pm 5.78	18.71 \pm 3.73	32.83 \pm 7.82	44.13 \pm 7.62
1:2	2000	1000	18.57 \pm 4.94	11.29 \pm 3.13	45.20 \pm 7.91	49.11 \pm 7.31
1:3	2000	700	11.31 \pm 4.13	5.31 \pm 2.13	61.31 \pm 6.69	61.92 \pm 5.19
1:4	2000	500	5.97 \pm 1.98	1.07 \pm 0.37	70.06 \pm 5.34	70.93 \pm 4.14
1:10	2000	200	3.92 \pm 0.82	0.92 \pm 0.35	74.61 \pm 7.93	76.21 \pm 6.93
1:20	2000	100	2.84 \pm 0.81	0.81 \pm 0.31	77.54 \pm 6.95	77.94 \pm 6.15
1:40	2000	50	1.66 \pm 0.79	0.61 \pm 0.23	77.31 \pm 7.02	77.71 \pm 7.22

Cross-contamination experiments were performed with sorting device ver. 2 using the same parameters. Each condition was tested in triplicate.

Table 7.2 shows the results of cross-contamination studies for each $Q_S:Q_B$ ratio. The first two $Q_S:Q_B$ ratios investigated resulted in more than 10% of the bead population being recovered in the target output. Recovery percentages decreased from \sim 5% to \sim 1% at ratios ranging from 1:4 to 1:40. In particular the last three ratios (1:10, 1:20 and 1:40) achieved a cross-contamination lower than 1%.

Table 7.3 shows a comparison between the performances of the sorting device ver.1 and ver.2.

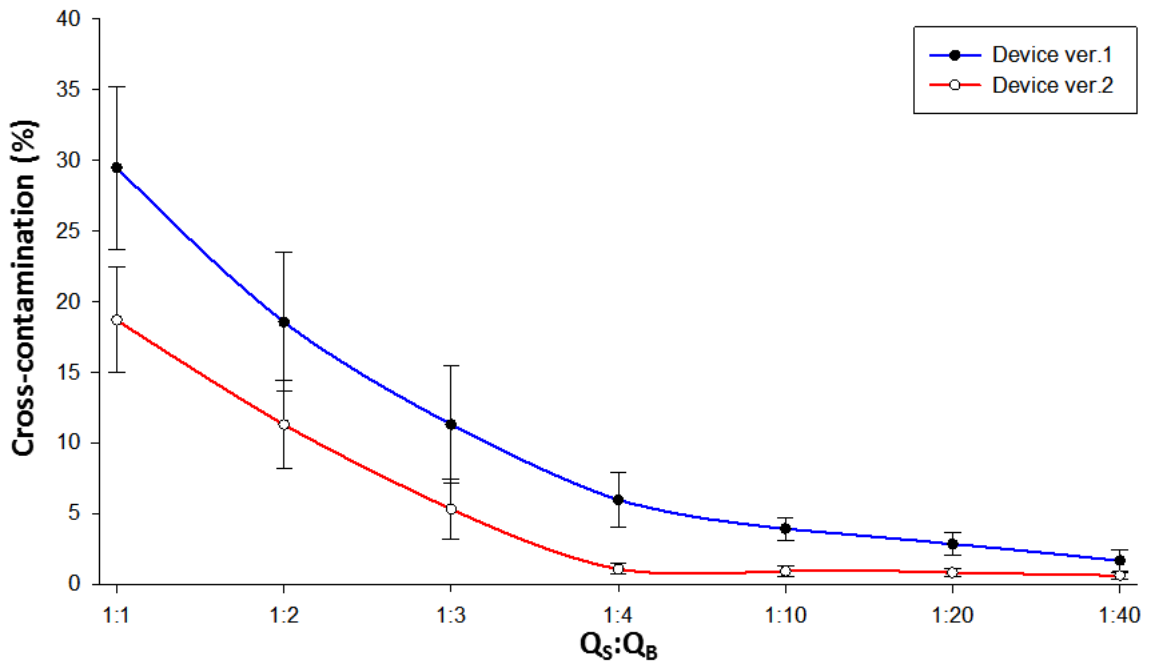


Figure 7.3: Plots of the cross-contamination percentages (mean values $n=3 \pm SD$) recorded using the sorting device ver.1 (blue line) and the sorting device ver.2 (red line) across the range of $Q_S:Q_B$ ratios investigated.

Sorting device ver.2 achieved lower recovery percentages within the target output across the entire range of $Q_S:Q_B$ ratios investigated.

In particular, the cross-contamination levels recorded at 1:10, 1:20 and 1:40 were lower than 1%, while the 1:4 ratio was 1.07%. A representation of the improvement achieved by the sorting device ver.2 in terms of cross-contamination percentages was shown in Figure 7.3.

In conclusion, sorting device ver.2 improved the cross-contamination performance across the entire range of $Q_S:Q_B$ ratios investigated with respect to the ver.1, due to the use of ver.2 input/output manifolds.

The choice of optimum $Q_S:Q_B$ ratio to be used in cell sorting experiments must be a compromise between low level cross-contamination (to guarantee an adequate level of purity of target cell populations) and device throughput. This parameter controls sorting experiment duration, which should be as short as possible. Considering cross-contamination levels achieved by sorting device ver.2, $Q_S:Q_B$ ratio 1:4 was the best compromise between throughput and purity and hence was used for all further cell sorting experiments.

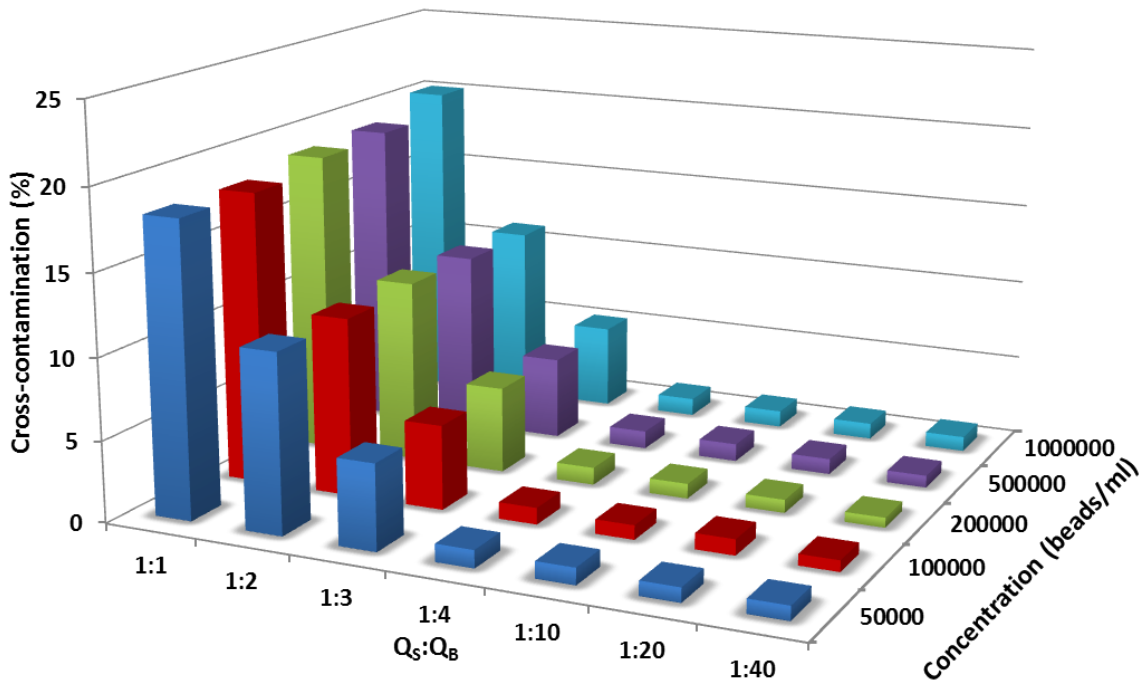


Figure 7.4: 3D bar chart of the cross-contamination percentages (mean values $n=3$) recorded using the sorting device ver.2 across the range of $Q_S:Q_B$ ratios investigated using different sample concentrations.

7.2.1.1 Cross-contamination and sample concentration relationship

Cross-contamination experiments described in Section 7.2.1 were performed using a sample concentration of 200,000 beads/ml. The relationship between cross-contamination and sample concentration was investigated and the results were reported in this section. All the experiments described in this section were performed using sorting device ver.2. The sample concentrations used in this set of experiments ranged between 50,000 beads/ml and 1,000,000 beads/ml.

In Figure 7.4, a 3D bar chart shows the percentages of cross-contamination using different sample concentrations across the entire range of $Q_S:Q_B$ ratios investigated. Each condition was tested in triplicate. The graph in Figure 7.4 reveals that cross-contamination percentages were independent of sample concentration. This occurred across the entire range of $Q_S:Q_B$ ratios investigated.

Results led to the conclusion that sample concentration had minor influence on the percentages of beads recovered in the target output.

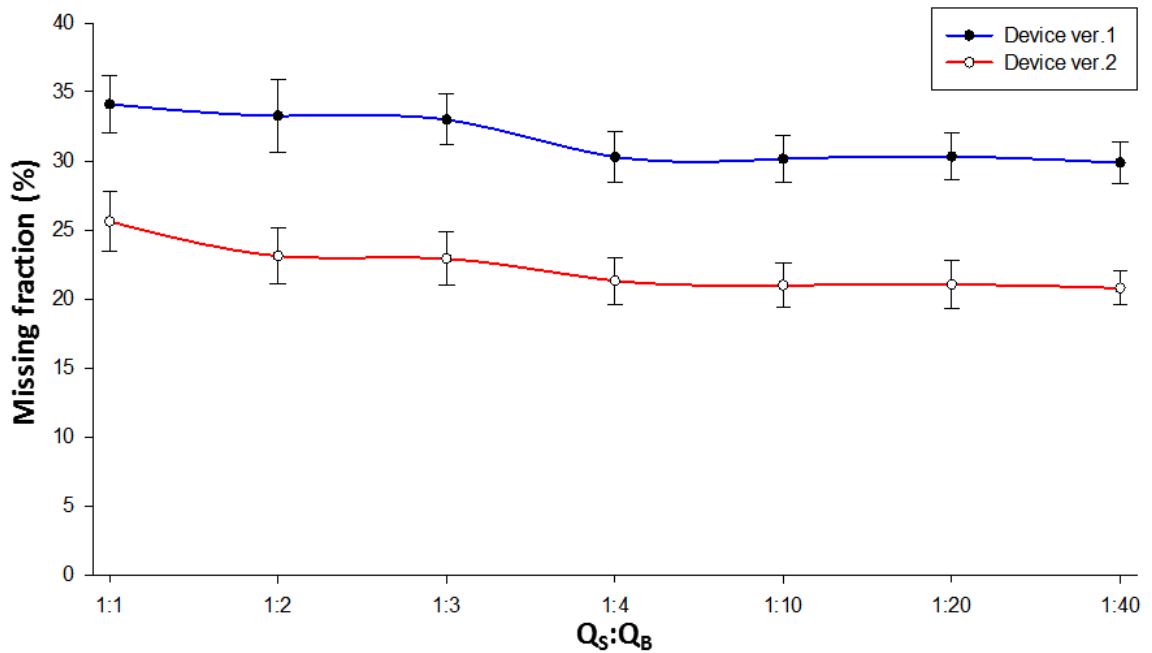


Figure 7.5: Missing cell fraction percentages (mean values $n=3$) recorded using the sorting device ver.1 (blue line) and the sorting device ver.2 (red line) across the range of $Q_S:Q_B$ ratios investigated.

7.2.2 Missing cells

According to data shown in Table 7.3 the sum of beads collected in the two outputs did not add up to 100% and between 20% and 40% of the original number of beads were missing. After each experiment the missing fraction of beads was partially recovered by purging the system (~85% of the missing fraction of beads was recovered). This issue needed to be addressed, particularly from the perspective of using the sorting device with live cells.

To investigate further, a set of experiments with MG63 cells was conducted. Few parameters were altered compared to previous experiments. The buffer comprised PBS + 2 mM EDTA + 25 mM HEPES + 1% BSA + 0.1% Pluronic F-68 + 5% Dextran.

The sample comprised an MG63 cell suspension (in the same buffer) with a concentration of 500,000 cells/ml. Experiments were performed with sorting device ver.1 and ver.2 across the entire range of $Q_S:Q_B$ ratios, to investigate the relationship between $Q_S:Q_B$ ratio and missing cell fraction. Each condition was investigated in triplicate.

Before each experiment, a sample was taken from the initial cell solution. After each experiment, the samples recovered from both outputs were analysed with a flow cytometer, to assess cell density. Knowing the volume of the recovered sample it was possible to estimate the number of cells recovered and subtract this number from the number of cells in the initial sample suspension, calculating the missing cell fraction.

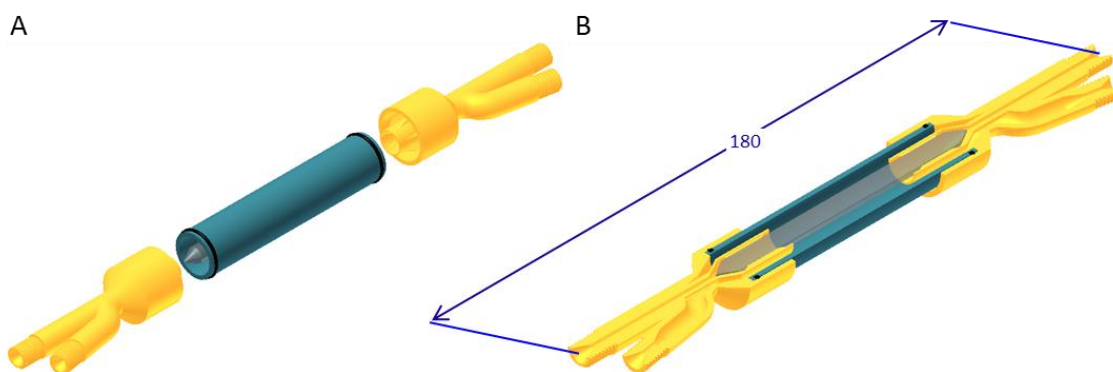


Figure 7.6: (A) 3D models of the sorting device ver.3.4. (B) Horizontal section of the sorting device ver.3.4. All measurements were in millimetres.

Figure 7.5 shows the missing cell fraction percentages obtained from testing sorting devices ver.1 and ver.2 across the entire range of $Q_S:Q_B$ ratios.

Data from both devices did not vary significantly across the range of $Q_S:Q_B$ ratios investigated. A decrement lower than 5% was observed in the data obtained from the range of $Q_S:Q_B$ ratio investigated. The data suggested that the $Q_S:Q_B$ ratio had minimal influence on the missing cell fraction. However, the missing cell fraction obtained using sorting device ver.2 (red line) was lower than that with sorting device ver.1 (blue line) across the entire range of $Q_S:Q_B$ ratios investigated (Figure 7.5). Although the missing cell fractions using device ver.2 were lower than those for the previous version, the missing cell fraction was ~23%, depending on the $Q_S:Q_B$ ratios used (21% using 1:4).

To further investigate the missing cell fraction, the internal surfaces of the device were analysed. Samples of all the components of the device were observed using a scanning electron microscope (SEM) (see Section 4.6.1). After these analyses, all the materials and building techniques were changed, leading to third generation devices (see Section 4.7). Sorting device ver.3.4 was the first version to solve the leakage issues due to these new building techniques used, and was therefore the first device of the third generation to be tested (Figure 7.6).

The missing cell fraction experiments were performed using device ver.3.4 with the same buffer and sample concentrations (experimental protocol in Section 7.1). Experiments over all previous $Q_S:Q_B$ ratios were conducted and each condition was tested in triplicate. The samples confirmed negligible influence on missing cell fractions (Figure 7.7 – green line). The average values ranged between 15% and 11% without a clear trend.

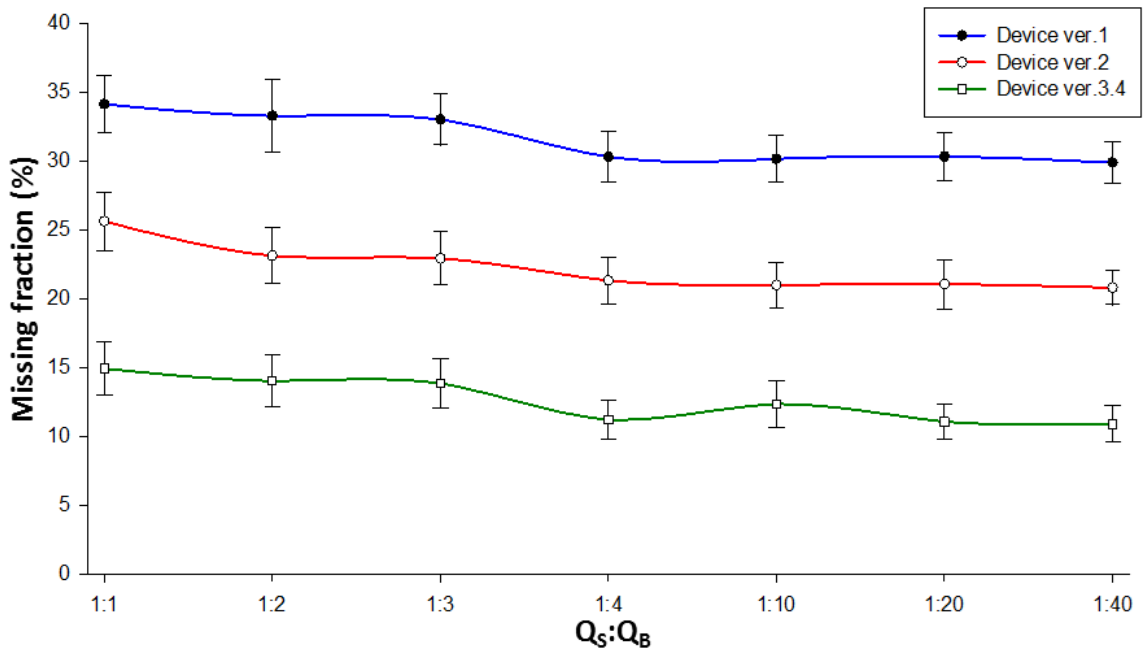


Figure 7.7: Missing cell fraction recorded (mean values $n=3$) using the sorting device ver.1 (blue line), the sorting device ver.2 (red line) and the sorting device ver.3.4 (green line) across the range of $Q_S:Q_B$ ratios investigated.

7.2.2.1 Missing cell fraction and surface treatments

The missing cell fractions obtained from sorting device ver.3.4 were around 11% ($Q_S:Q_B$ ratios 1:4). To improve this result, several surface treatment strategies were employed (see Appendix I). The most successful approach was to coat the device internal surface with poly(L-lysine)-graft-poly(ethylene glycol) (PLL-g-PEG).

Experiments were conducted with PLL-g-PEG-coated sorting device ver.3.4. The same experimental protocol as previous experiments was used (sample concentration of 500,000 MG63 cell/ml) and the entire range of $Q_S:Q_B$ ratios was tested in triplicate.

Figure 7.8 shows the average percentages of missing cell for each $Q_S:Q_B$ ratio used. PLL-g-PEG-coated sorting device ver.3.4 achieved lower missing cell fractions compared to the uncoated device (ver.3.4), with values ranging between 8% and 7% (7.03% for $Q_S:Q_B$ =ratio 1:4), without any detectable trend.

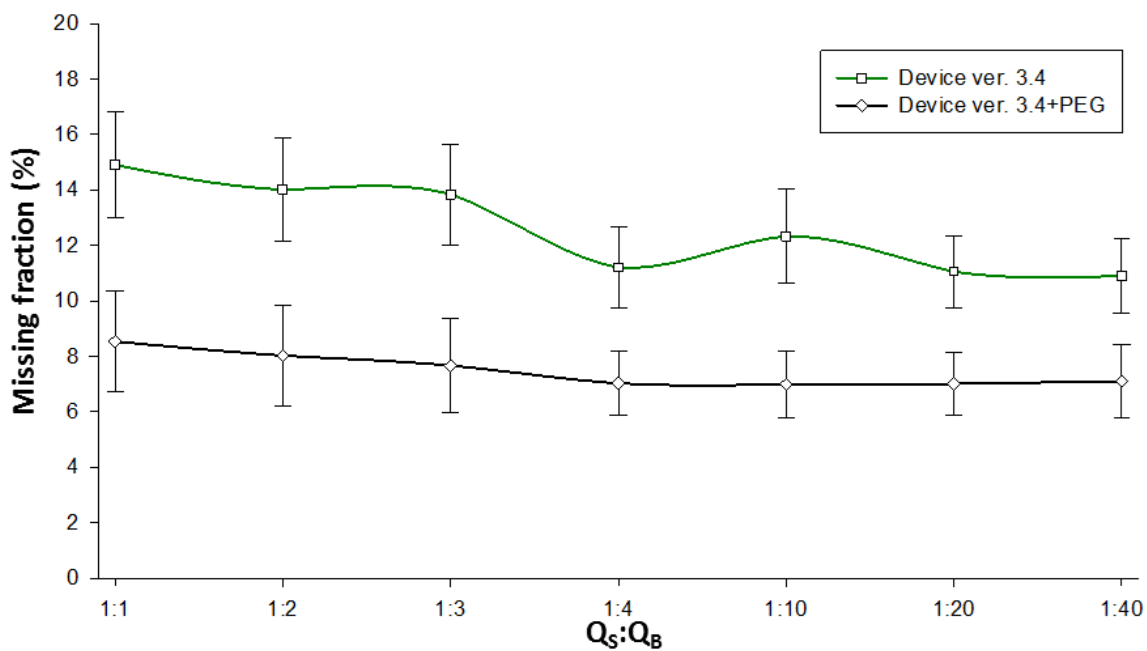


Figure 7.8: Missing cell fraction recorded (mean values $n=3$) using the sorting device ver.3.4 (green line) and the sorting device ver.3.4 coated with PLL-g-PEG (black line) across the range of $Q_S:Q_B$ ratios investigated.

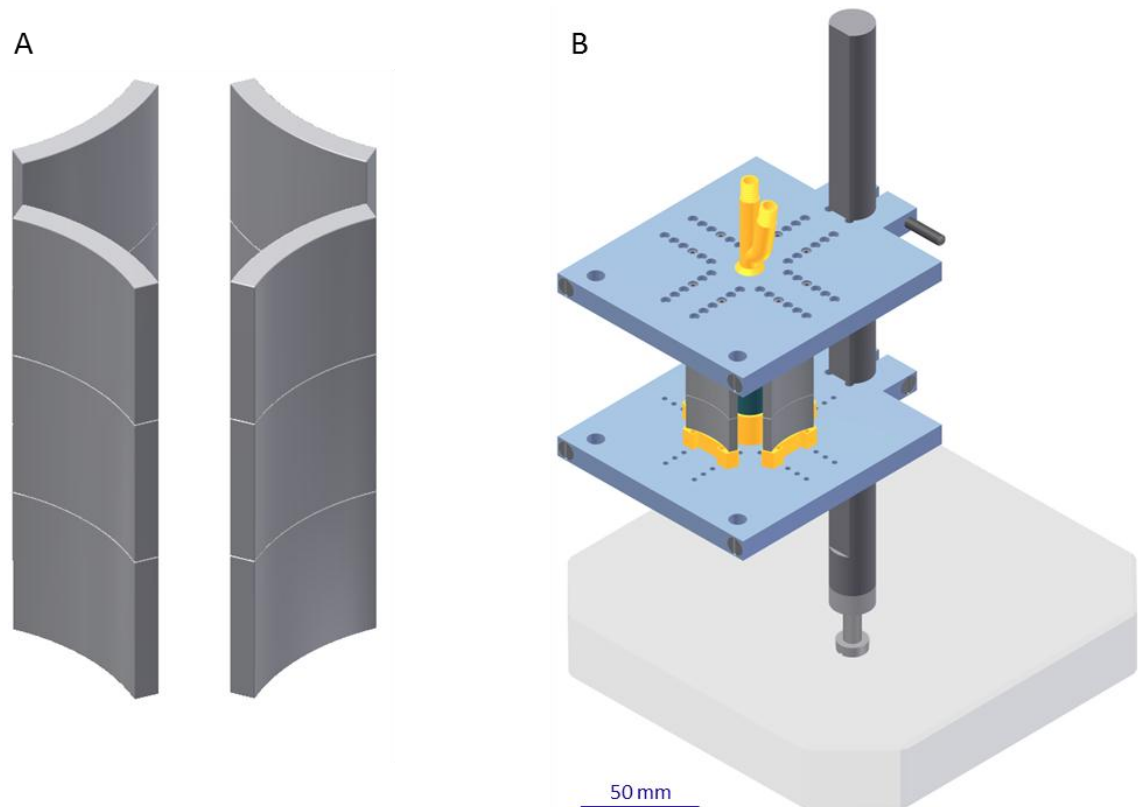


Figure 7.9: (A) 3D models of the QMS ver.1 and (B) the experimental setup with the sorting device ver.3.4 surrounded by the QMS ver.1.

7.3 Sorting experiments: device ver.3.4 + QMS ver.1

In Section 7.2 the sorting devices were tested with non-magnetic beads and unlabelled MG63 cells to investigate cross-contamination and missing cell phenomena. The results of these experiments established that sorting device ver.3.4 was the most suited to achieve the aim of the study. This section describes the sorting capability of ver.3.4 coupled with the quadrupole magnetic system ver.1 (QMS ver.1 – see Section 5.2). Figure 7.9 shows the QMS ver.1 and the experimental setup.

7.3.1 Bead mobility

The first step was to investigate the ability of the sorting device ver.3.4 + QMS ver.1 to direct magnetic beads toward the target output. Green fluorescent (480/520) carboxyl polystyrene beads ($\varnothing 10 \mu\text{m}$ - Bangs Laboratories, Inc.TM, USA) labelled with ferromagnetic nanoparticles ($\varnothing 30 \text{ nm}$ - TurboBeads[®], Switzerland) by streptavidin-biotin binding were employed for these studies (see Appendix L).

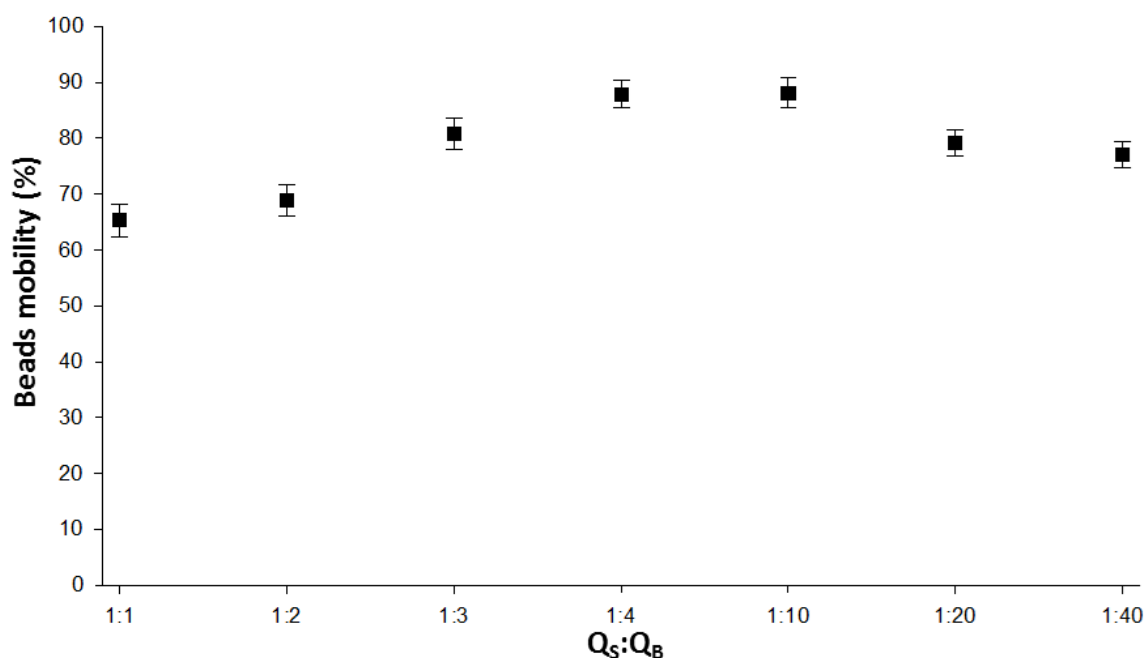


Figure 7.10: Plots of the percentages (mean values $n=3$) of magnetically labelled beads recovered in the target output using the sorting device ver.3.4 + QMS ver.1.

Magnetically labelled beads were suspended in buffer at a concentration of 500,000 beads/ml (initial sample). Buffer and the $Q_S:Q_B$ ratios were the same as those used in previous cross-contamination experiments (see Section 7.2.1): PBS + 0.1% GAENE + 1% BSA; Q_B was fixed at 2000 $\mu\text{l}/\text{min}$ and Q_S varied.

The initial sample comprised magnetically labelled beads so the theoretical result was to recover 100% in the target output. Each condition was tested in triplicate and the recovered samples were analysed by flow cytometry. The percentage of beads recovered in the target output with respect to the total loaded, was called *bead mobility* and plotted in Figure 7.10. The percentages of beads recovered in the target output ranged between ~65% and ~90% across the entire range of $Q_S:Q_B$ ratios investigated. The highest values were recorded with $Q_S:Q_B$ ratios of 1:4 and 1:10 (~88%), with the recovery percentages decreasing at ratios 1:20 and 1:40.

Before drawing any conclusions, a second set of experiments were conducted using the same setup (sorting device ver.3.4 + QMS ver.1) in order to investigate the capacity of the system to move labelled beads when mixed with unlabelled beads, and the results were reported below.

7.3.2 Bead sorting

Prior to testing the device with live cells, sorting experiments were performed using mixed bead populations to mimic the cell population. The aim of the experiments was to find the optimum $Q_S:Q_B$ ratio for further cell sorting experiments.

After each sorting experiment, samples to be analysed included the initial sample (original), the sample collected from the non-target output (negative fraction) and the sample collected from the target output (positive fraction). To create the original sample (5×10^6 beads dissolved in buffer at a concentration of 0.5×10^6 beads/ml), polystyrene orange fluorescent (540/560) beads ($\varnothing 10 \mu\text{m}$ - Bangs Laboratories, Inc.TM, USA) (non-target beads) were mixed with the green fluorescent (480/520) carboxyl polystyrene beads ($\varnothing 10 \mu\text{m}$ - Bangs Laboratories, Inc.TM, USA) labelled with magnetic nanoparticles ($\varnothing 30 \text{nm}$ - TurboBeads[®], Switzerland) (target beads – previously defined as magnetically labelled beads) at a ratio of 1:1.

The experimental setup and parameters used (buffer, original sample concentration) were the same as those in previous experiments; the entire range of $Q_S:Q_B$ ratios were tested in triplicate ($n=3$).

Positive and negative fractions were analysed by flow cytometry, measuring sample beads (beads/ μl) and the percentages of target and non-target beads. The number of target and non-target beads recovered from each fraction was then calculated. In Table 7.4 the average number of target and non-target beads recovered from the positive and negative fractions were reported, together with the percentages that these numbers represented with respect to the total number of beads in the original sample (2.5×10^6 target beads and 2.5×10^6 non-target beads).

Table 7.4: Table summarising the beads sorting experiments (mean values $n=3 \pm SD$) performed with the sorting device ver.3.4+QMS ver.1. Target beads (in orange) and non-target beads (in blue) percentages of the original bead population recovered from the negative and positive fraction of the sorting device

FLOW RATE ($\mu\text{l}/\text{min}$)			NEGATIVE FRACTION				POSITIVE FRACTION			
			TARGET		NON-TARGET		TARGET		NON-TARGET	
$Q_S:Q_B$	BUFFER (Q_B)	SAMPLE (Q_S)	BEADS	%	BEADS	%	BEADS	%	BEADS	%
1:1	2000	2000	833360	33.33 \pm 4.13	1799373	71.97 \pm 5.02	1366657	54.66 \pm 4.01	400620	16.02 \pm 3.11
1:2	2000	1000	720940	28.83 \pm 3.92	1955371	78.21 \pm 5.12	1479081	59.16 \pm 5.10	244640	9.78 \pm 2.01
1:3	2000	700	447923	17.91 \pm 3.02	2083189	83.32 \pm 5.03	1752072	70.08 \pm 5.01	116820	4.6 \pm 1.43
1:4	2000	500	282932	11.31 \pm 2.86	2173363	86.93 \pm 5.08	1917069	76.68 \pm 4.26	26620	1.06 \pm 0.45
1:10	2000	200	283360	11.33 \pm 2.91	2178229	87.13 \pm 5.24	1916621	76.66 \pm 4.85	21780	0.87 \pm 0.22
1:20	2000	100	303820	12.15 \pm 2.72	2179122	87.16 \pm 5.13	1896177	75.84 \pm 4.72	20900	0.83 \pm 0.39
1:40	2000	50	281380	11.25 \pm 2.83	2179760	87.19 \pm 5.09	1918641	76.74 \pm 4.66	20240	0.81 \pm 0.27

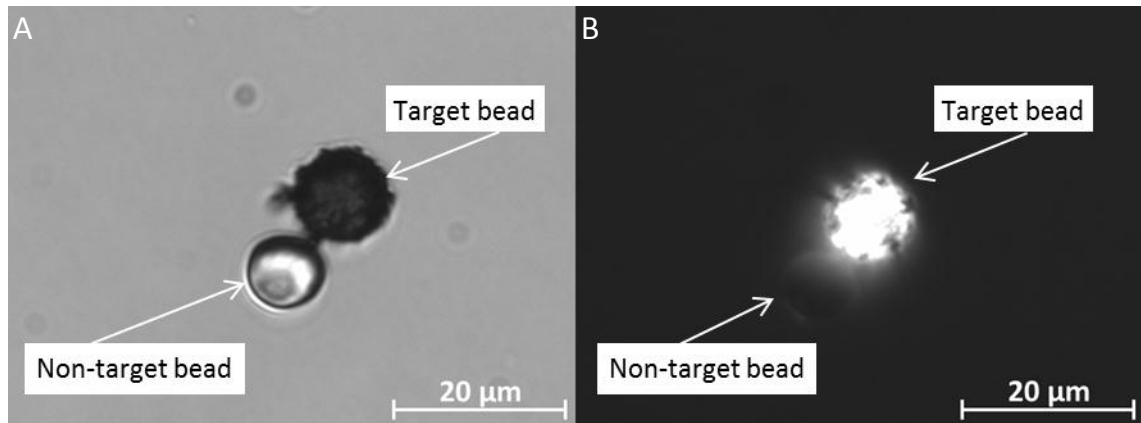


Figure 7.11: (A) Photomicroscopy of a target and non-target bead in bright field and (B) in fluorescence light (FITC filter – bright bead was the target bead).

$Q_S:Q_B$ ratios 1:1 and 1:2 led to $\sim 30\%$ recovery of the initial target bead population in the negative fraction. These results were in agreement with the results obtained in previous sorting experiments (bead mobility; see Section 7.2.1 – Figure 7.10). The best compromise between performance and throughput was achieved using $Q_S:Q_B$ ratio 1:4. At this ratio the device sorted $\sim 11\%$ of the original target bead into the non-target output. This result agreed with the bead mobility experiments (see Section 7.2.1 – Figure 7.10). In the positive fraction, $\sim 1\%$ of the original non-target bead population was found, supporting the results obtained with cross-contamination experiments conducted at the same $Q_S:Q_B$ ratio (see Section 7.2.1 – Figure 7.3). Although slightly improved performance was obtained testing $Q_S:Q_B$ ratios of 1:10, 1:20 and 1:40, the best compromise between performance and device throughput remained at 1:4. Table 7.4 shows that $\sim 12\%$ of the original bead population went missing; as expected from previous experiences (see Section 7.2.2).

The presence of target beads in the device's negative fraction was reduced with decreasing of the $Q_S:Q_B$ ratios. However, the smallest percentage recorded was $\sim 11\%$: this could be caused by the low magnitude values of the magnetic force (\vec{F}_m) yielded by the QMS ver.1 used in the sorting experiments (see Section 5.2.1).

Furthermore, the magnetic susceptibility (χ_p) of the magnetically labelled beads (not quantified) could be heterogeneous. This second hypothesis was confirmed by microscopy investigation of the original mixed bead population. Figure 7.11 shows bright field and fluorescence images of one non-target and one target bead. In Figure 7.11A, the visible magnetically labelled bead (target bead), and the magnetic nanoparticles ($\varnothing 30$ nm - TurboBeads®, Switzerland) were recognisable. However, Figure 7.11B shows the non-uniform magnetic nanoparticles coating on the bead surface.

The fluorescence image clearly shows uncoated areas of the bead surface. Differences in extent of the magnetic nanoparticle coating may have caused variation in the target beads' magnetic susceptibility.

7.3.3 MG63 cell sorting

This Section describes the tests performed on the sorting device ver.3.4 (PEG coated) + QMS ver.1 using MG63 cells in place of HBMSCs, which were the ultimate aim of the study. Approximately 60% to 70% of MG63 cells express STRO-1, and they were used to optimise the cell labelling protocol with functionalised superparamagnetic beads (see Section 6.2.2).

7.3.3.1 Experimental setup

MG63 cells labelled with functionalised superparamagnetic beads were suspended in buffer (PBS + 2 mM EDTA + 25 mM HEPES + 1% BSA + 0.1% Pluronic F-68 + 5% Dextran T70) at a final concentration of 500,000 cells/ml. In addition, the sorting device was immersed in a solution of PBS + 0.1% BSA overnight. The experimental protocol used was described in section 7.1 [75].

Before each sorting experiment, an aliquot was withdrawn from the original unsorted sample. After the experiment, cells collected from the negative and positive fraction outputs were washed five times with PBS (to detach most of the beads bound to the cells' surface) and fixed through suspension in ethanol (95%). The same treatment was implemented on the original sample aliquot. Two-step immunostaining was performed on each sample. Firstly, fixed cells were incubated with mouse monoclonal IgM anti-human STRO-1 primary antibody (Hybridoma) and secondly, with fluorescent secondary antibodies (Alexa Fluor 488 conjugated goat polyclonal IgG anti-mouse IgM). In order to measure the percentage of STRO-1+ cells in each fraction, output samples were analysed by flow cytometry (in triplicate).

Flow cytometry measured cell density (cells/ μ l) for each sample analysed, and the number of cells collected in each fraction (original sample included) was estimated. Figures obtained from the negative and positive fractions were compared with those from the original sample.

7.3.3.2 Results

After each sorting experiment, two aspects were investigated including purity and cell recovery.

Purity describes the percentage of STRO-1+ cells in each fraction. The desired result was to recover a pure 100% STRO-1+ cell population in the positive fraction.

Cell recovery referred to the total number of cells collected from each fraction in relation to the total number of cells loaded in the original sample. The desired result was to recover the entire loaded STRO-1+ cell population in the positive fraction.

According to the results shown in Table 7.4 (see Section 7.3.2) the optimum $Q_S:Q_B$ ratio was 1:4. However, this set of experiments was performed with live cells, so once again the entire range of $Q_S:Q_B$ ratios was investigated (each condition in triplicate).

The results of the tests performed with MG63 cells were shown in two tables: Table 7.5 summarises the purity values achieved and Table 7.6 summarises the cell recovery efficiency.

Table 7.5 shows the percentage of STRO-1+ (in orange) and STRO-1- cells (in blue) found in the original sample. The STRO-1+ cell population consistently comprised ~68% of the whole cell population across the entire set of experiments. In the same table, the percentage of STRO-1+ and STRO-1- cells recovered from the negative and positive fractions of the sorting device were reported. Regarding data from the positive fraction, the percentage of STRO-1+ cells ranged between ~80% and ~89%, with the highest value corresponding to $Q_S:Q_B$ ratio 1:4. Similar percentages of STRO-1+ cells were obtained using $Q_S:Q_B$ ratios of 1:10, 1:20 and 1:40.

For a better understanding of the results achieved by the sorting device in terms of purity, the increase was calculated as the percentage of STRO-1+ cells in the positive fraction minus percentage of STRO-1+ cells in the original sample and plotted in Figure 7.12.

Table 7.5: Percentages (mean values $n=9 \pm SD$) of STRO-1+ cells (in orange) and the STRO-1- cells (in blue) recovered from the negative and positive fraction of the sorting device (device ver.3.4 PEG coated + QMS ver.1). The sorting experiments were performed using MG63 cells across the entire range of $Q_S:Q_B$ ratios.

PURITY - Sorting device ver.3.4 (PEG coated) + QMS ver.1								
FLOW RATE ($\mu\text{l}/\text{min}$)			ORIGINAL		NEGATIVE FRACTION		POSITIVE FRACTION	
$Q_S:Q_B$	BUFFER (Q_B)	SAMPLE (Q_S)	STRO-1+ (%)	STRO-1- (%)	STRO-1+ (%)	STRO-1- (%)	STRO-1+ (%)	STRO-1- (%)
1:1	2000	2000	68.12 \pm 2.13	31.88 \pm 2.13	61.33 \pm 2.63	38.67 \pm 2.63	79.89 \pm 2.73	20.14 \pm 2.73
1:2	2000	1000	67.36 \pm 2.73	32.64 \pm 2.73	58.51 \pm 2.51	41.49 \pm 2.51	82.28 \pm 2.33	17.72 \pm 2.33
1:3	2000	700	67.19 \pm 2.84	32.81 \pm 2.84	57.37 \pm 2.23	42.63 \pm 2.23	84.36 \pm 3.01	15.64 \pm 3.01
1:4	2000	500	68.84 \pm 3.14	31.16 \pm 3.14	54.73 \pm 2.19	45.27 \pm 2.19	88.98 \pm 3.13	11.02 \pm 3.13
1:10	2000	200	68.01 \pm 1.91	31.99 \pm 1.91	52.81 \pm 2.94	47.19 \pm 2.94	88.97 \pm 4.01	12.03 \pm 4.01
1:20	2000	100	67.94 \pm 2.02	32.06 \pm 2.02	52.14 \pm 2.82	47.86 \pm 2.82	88.55 \pm 2.93	11.45 \pm 2.93
1:40	2000	50	68.66 \pm 2.41	31.34 \pm 2.41	51.86 \pm 2.02	48.14 \pm 2.02	87.83 \pm 2.87	12.17 \pm 2.87

Table 7.6: Table summarising MG63 cell sorting experiments (mean values $n=9 \pm SD$). Total numbers of cells and numbers of STRO-1+ cells in the original sample, positive and negative fractions (after sorting with device ver.3.4 PEG coated + QMS ver.1) were reported. Percentages of the initial STRO-1+ cells number collected in the negative and positive fractions reported in red.

CELL RECOVERY EFFICIENCY - Sorting device ver.3.4 (PEG coated) + QMS ver.1										
FLOW RATE ($\mu\text{l}/\text{min}$)			ORIGINAL		NEGATIVE FRACTION			POSITIVE FRACTION		
$Q_S:Q_B$	BUFFER (Q_B)	SAMPLE (Q_S)	Total (10^6)	STRO-1+ cells (10^6)	Total (10^6)	STRO-1+ cells		Total (10^6)	STRO-1+ cells	
						Number (10^6)	%		Number (10^6)	%
1:1	2000	2000	4.87 \pm 0.23	3.32 \pm 0.26	4.21 \pm 0.27	2.58 \pm 0.28	77.83 \pm 8.54	0.32 \pm 0.02	0.25 \pm 0.02	7.71 \pm 0.76
1:2	2000	1000	4.91 \pm 0.15	3.31 \pm 0.24	4.08 \pm 0.19	2.38 \pm 0.22	72.18 \pm 6.60	0.39 \pm 0.04	0.32 \pm 0.04	9.70 \pm 1.30
1:3	2000	700	5.02 \pm 0.11	3.37 \pm 0.22	3.87 \pm 0.14	2.22 \pm 0.17	65.82 \pm 5.03	0.35 \pm 0.01	0.29 \pm 0.02	8.75 \pm 0.57
1:4	2000	500	4.95 \pm 0.13	3.41 \pm 0.25	3.79 \pm 0.17	2.07 \pm 0.18	60.87 \pm 5.27	0.41 \pm 0.02	0.36 \pm 0.03	10.71 \pm 0.92
1:10	2000	200	4.97 \pm 0.15	3.38 \pm 0.20	3.81 \pm 0.18	2.01 \pm 0.21	59.52 \pm 6.28	0.45 \pm 0.03	0.40 \pm 0.04	11.84 \pm 1.36
1:20	2000	100	5.07 \pm 0.14	3.44 \pm 0.20	3.75 \pm 0.19	1.95 \pm 0.21	56.76 \pm 6.10	0.47 \pm 0.01	0.41 \pm 0.02	12.08 \pm 0.66
1:40	2000	50	4.98 \pm 0.12	3.42 \pm 0.20	3.87 \pm 0.18	2.00 \pm 0.17	58.69 \pm 5.12	0.38 \pm 0.04	0.33 \pm 0.04	9.76 \pm 1.38

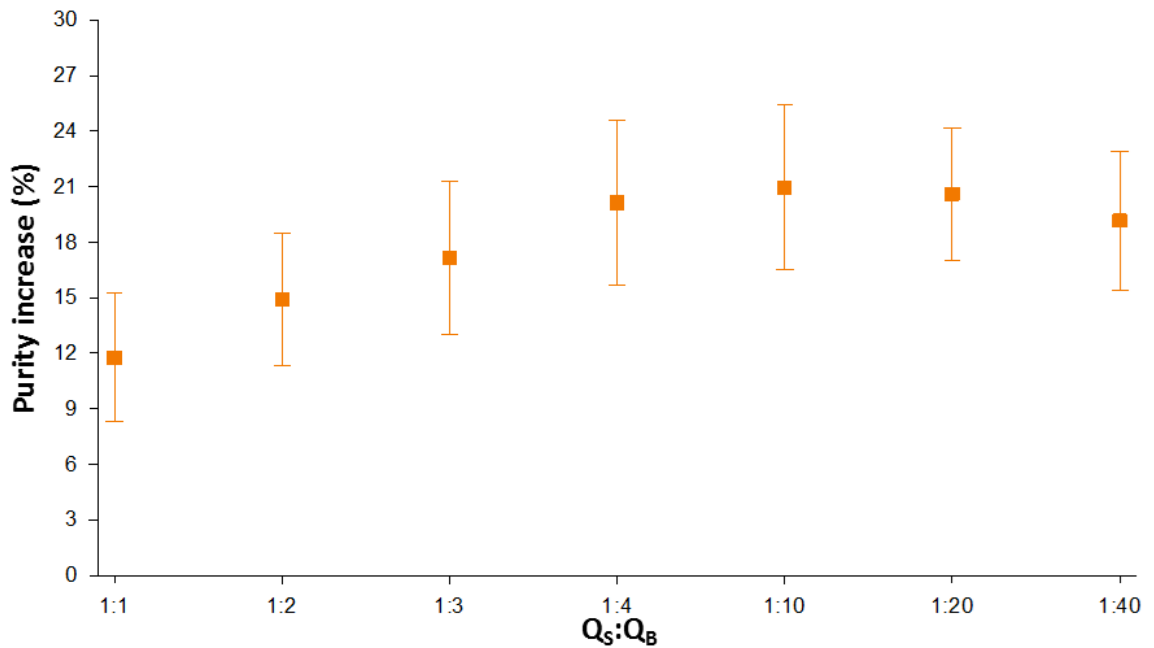


Figure 7.12: Purity increases (defined as the difference between the percentage of STRO-1+ cells in the positive fraction and percentage of STRO-1+ cells in the original sample) in the cell population recovered from the positive fraction of the device ver.3.4 PEG coated + QMS ver.1 across the range of $Q_S:Q_B$ ratios tested (mean values $n=9 \pm SD$).

In Figure 7.12 purity increases (in percentages) were shown. The sorting device increased the percentage of STRO-1+ cells (collected in the positive fraction) between ~12% and ~21% compared to percentages in the original sample. The maximum increment was recorded using $Q_S:Q_B$ ratio 1:10, while the second highest was achieved using ratio 1:4. The difference between these two ratios was not significant.

In the negative fraction, high percentages of STRO-1+ cells were found, with values ranging between ~52% and ~61%.

Across the entire set of experiments, cell populations recovered from the negative fraction presented higher percentages of STRO-1+ cells than those of STRO-1- cells.

Table 7.6 shows the total number of cells present within the original samples, negative fractions and positive fractions. These figures support data obtained from the set of experiments performed in section 7.2.1.1, where reasons behind the missing cell fraction were investigated. The sum of the total number of cells recovered from the two device fractions was lower than the original number of cells loaded; between ~7% and ~16% lower across the range of $Q_S:Q_B$ ratios investigated.

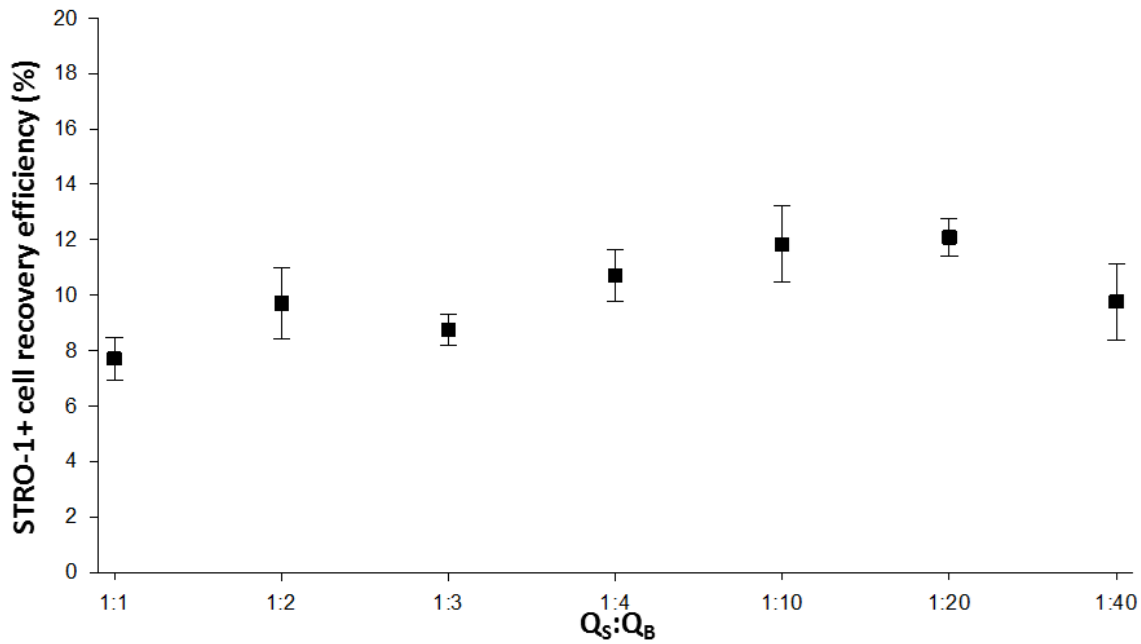


Figure 7.13: STRO-1+ cells recovery efficiency in the positive fraction of the device ver.3.4 PEG coated + QMS ver.1 across the range of $Q_S:Q_B$ ratios tested. Percentages of the initial STRO-1+ cells number collected in the positive fraction were plotted (mean values $n=9 \pm SD$).

The second aspect investigated was STRO-1+ cell recovery efficiency. In Table 7.6 it was evident that the majority of STRO-1+ cells were collected in the negative fraction of the sorting device across the entire range of $Q_S:Q_B$ ratios used. Percentages ranging from ~77% to ~59% of the loaded STRO-1+ cell sample were collected in the negative fraction of the device. These percentages represented the number of STRO-1+ cells not sorted by the device.

Table 7.6 also reports the number of STRO-1+ cells recovered in the positive fraction; these percentages never went beyond 12% of the initial STRO-1+ cell number. This data represented the STRO-1+ cell recovery efficiency and was plotted in Figure 7.13. The highest efficiencies were achieved using a $Q_S:Q_B$ ratio of 1:20. However, the difference between this ratio and 1:4 and 1:10 was not significant.

Overall, the percentage of STRO-1+ cells sorted by the device was not close to the desirable 100% of STRO-1+ cells recovered. The cause of miss-sorting was to be found in the low $|\vec{F}_m|$ as a consequence of the insufficient values of $|\vec{B}|$ and $|\nabla\vec{B}|$ produced by the QMS ver.1 used in this set of experiments. The values of $|\vec{B}|$ were ranging between 27 mT and 64 mT (within the device) producing a $|\nabla\vec{B}|$ of 10 mT/mm (see section 5.5). These values were far from the ones described in literature (Chalmers' device in particular) as described in section 2.3.3.

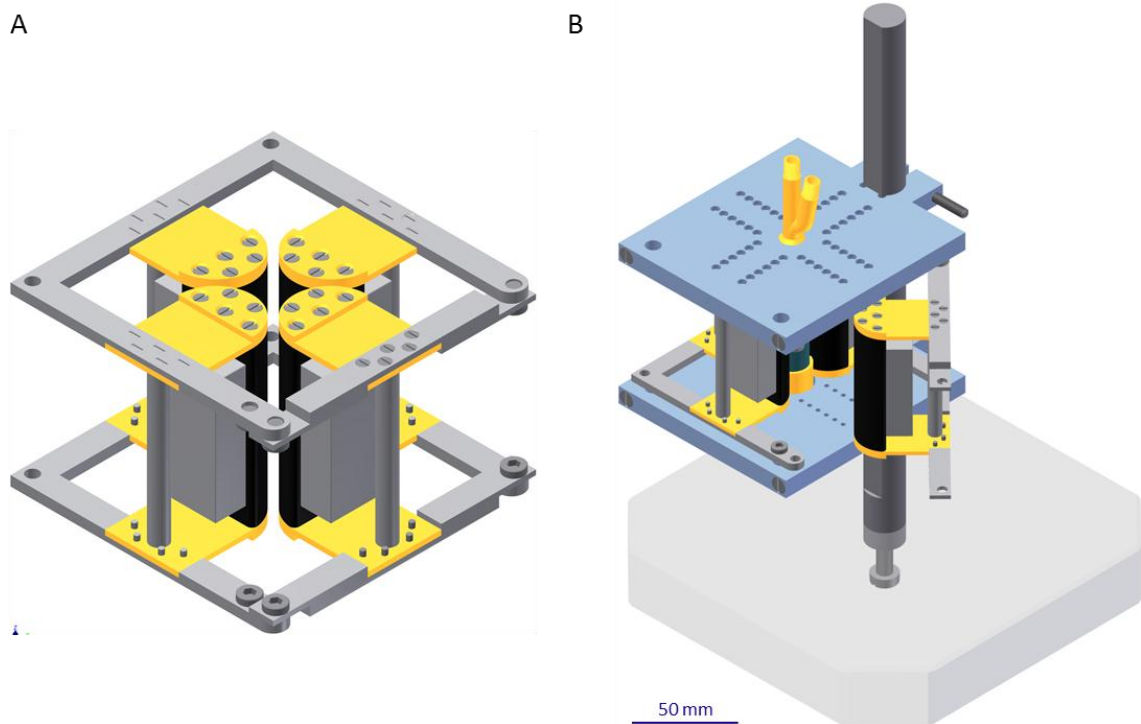


Figure 7.14: (A) 3D models of the QMS ver.2 and (B) the experimental setup with the sorting device ver.3.4 (PEG coated) surrounded by the QMS ver.2.

7.4 MG63 cell sorting: device ver.3.4 + QMS ver.2

The results obtained through testing device ver.3.4 + QMS ver.1 were far from the aim of this study. As Table 7.6 summarises, the QMS ver.1 only sorted $\sim 10\%$ of the initial number of STRO-1+ cells loaded into the device.

To address this problem and improve the sorting capacity of device ver.3.4, QMS ver.2 was designed and manufactured (see Section 5.3). Figure 7.14 shows QMS ver.2 and the experimental setup with sorting device ver.3.4.

The sorting capability of device ver.3.4 (PEG coated) + QMS ver.2 was tested directly with MG63 cells, using the same experimental protocol, buffer, sample concentration and assessment technique (flow cytometry) within previous experiments (see Section 7.3.3.1). Moreover, the entire range of $Q_S:Q_B$ ratios was again tested (each condition in triplicate), and the purity and cell recovery investigated. Table 7.7 reports the percentage of STRO-1+ (in orange) and STRO-1- cells (in blue) present in the original samples, and both the negative and positive outputs.

Table 7.7: Percentages (mean values $n=9 \pm SD$) of STRO-1+ cells (in orange) and the STRO-1- cells (in blue) recovered from the negative and positive fraction of the sorting device (device ver.3.4 PEG coated + QMS ver.2). The sorting experiments were performed using MG63 cells across the entire range of $Q_S:Q_B$ ratios.

PURITY - Sorting device ver.3.4 (PEG coated) + QMS ver.1								
FLOW RATE ($\mu\text{l}/\text{min}$)			ORIGINAL		NEGATIVE FRACTION		POSITIVE FRACTION	
$Q_S:Q_B$	BUFFER (Q_B)	SAMPLE (Q_S)	STRO-1+ (%)	STRO-1- (%)	STRO-1+ (%)	STRO-1- (%)	STRO-1+ (%)	STRO-1- (%)
1:1	2000	2000	69.15 \pm 2.11	30.85 \pm 2.11	57.31 \pm 2.83	42.69 \pm 2.83	83.11 \pm 2.63	16.89 \pm 2.63
1:2	2000	1000	69.39 \pm 2.53	30.61 \pm 2.53	55.55 \pm 2.51	44.45 \pm 2.51	85.27 \pm 2.02	14.73 \pm 2.02
1:3	2000	700	70.18 \pm 2.85	29.82 \pm 2.85	51.27 \pm 2.03	48.73 \pm 2.03	86.30 \pm 2.36	13.70 \pm 2.36
1:4	2000	500	66.81 \pm 3.18	33.19 \pm 3.18	49.73 \pm 2.19	50.27 \pm 2.19	90.01 \pm 1.84	9.99 \pm 1.84
1:10	2000	200	69.03 \pm 1.99	30.97 \pm 1.99	48.83 \pm 2.74	51.17 \pm 2.74	89.95 \pm 3.01	10.05 \pm 3.01
1:20	2000	100	68.92 \pm 2.07	31.08 \pm 2.07	47.91 \pm 1.82	52.09 \pm 1.82	89.55 \pm 2.13	10.45 \pm 2.13
1:40	2000	50	68.96 \pm 2.21	31.04 \pm 2.21	48.03 \pm 2.01	51.97 \pm 2.01	87.99 \pm 2.77	12.01 \pm 2.77

Table 7.8: Table summarising the MG63 cell sorting experiments (mean values $n=9 \pm SD$). Total numbers of cells and numbers of STRO-1+ cells in the original sample, positive and negative fractions (after sorting with device ver.3.4 PEG coated + QMS ver.2) were reported. Moreover, the percentages of the initial STRO-1+ cells number collected in the negative and positive fractions were reported (in red).

CELL RECOVERY EFFICIENCY - Sorting device ver.3.4 (PEG coated) + QMS ver.2										
FLOW RATE ($\mu\text{l}/\text{min}$)			ORIGINAL		NEGATIVE FRACTION			POSITIVE FRACTION		
$Q_S:Q_B$	BUFFER (Q_B)	SAMPLE (Q_S)	Total (10^6)	STRO-1+ cells (10^6)	Total (10^6)	STRO-1+ cells		Total (10^6)	STRO-1+ cells	
						Number (10^6)	%		Number (10^6)	%
1:1	2000	2000	4.97 \pm 0.21	3.44 \pm 0.25	3.91 \pm 0.23	2.24 \pm 0.25	65.20 \pm 7.24	0.47 \pm 0.08	0.39 \pm 0.08	11.36 \pm 2.35
1:2	2000	1000	4.94 \pm 0.17	3.43 \pm 0.25	3.82 \pm 0.21	2.12 \pm 0.22	61.90 \pm 6.35	0.52 \pm 0.06	0.44 \pm 0.06	12.93 \pm 1.83
1:3	2000	700	4.99 \pm 0.10	3.50 \pm 0.21	3.64 \pm 0.13	1.87 \pm 0.14	53.29 \pm 4.09	0.57 \pm 0.05	0.49 \pm 0.06	14.04 \pm 1.65
1:4	2000	500	4.91 \pm 0.11	3.28 \pm 0.23	3.51 \pm 0.17	1.74 \pm 0.16	53.21 \pm 5.03	0.61 \pm 0.04	0.55 \pm 0.05	16.74 \pm 1.46
1:10	2000	200	4.96 \pm 0.14	3.42 \pm 0.20	3.48 \pm 0.22	1.70 \pm 0.21	49.63 \pm 6.10	0.62 \pm 0.04	0.56 \pm 0.05	16.28 \pm 1.63
1:20	2000	100	5.02 \pm 0.18	3.46 \pm 0.23	3.61 \pm 0.16	1.73 \pm 0.14	49.99 \pm 4.20	0.60 \pm 0.04	0.54 \pm 0.05	15.53 \pm 1.43
1:40	2000	50	4.98 \pm 0.13	3.43 \pm 0.20	3.47 \pm 0.19	1.67 \pm 0.16	48.53 \pm 4.80	0.59 \pm 0.09	0.52 \pm 0.10	15.12 \pm 2.85

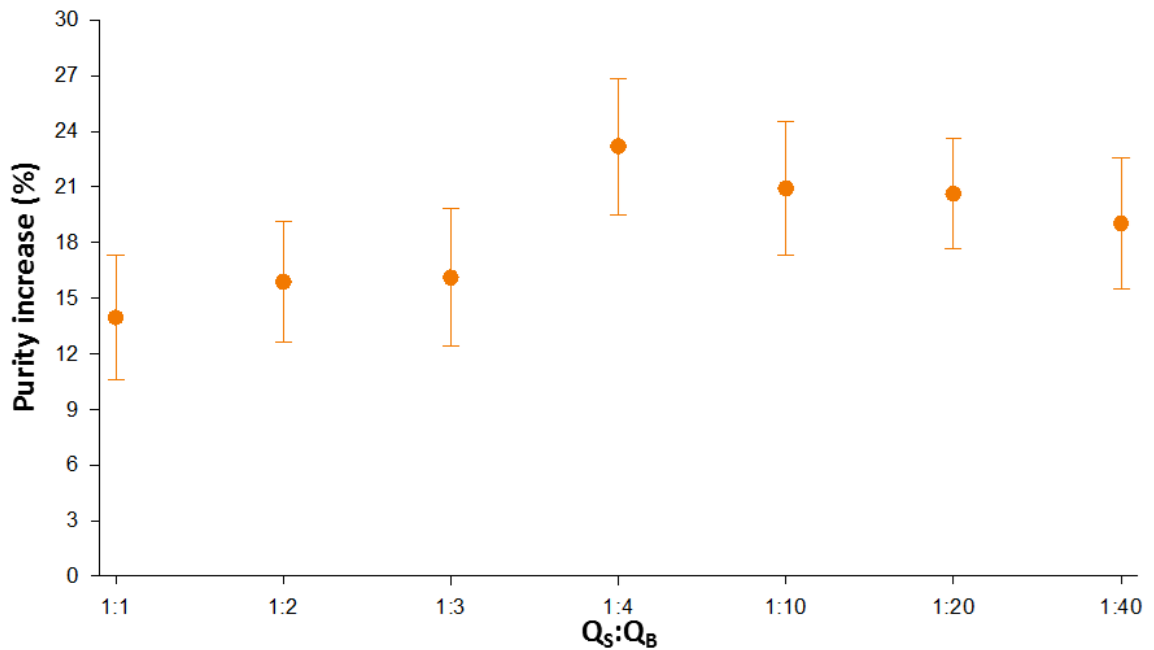


Figure 7.15: Purity increases (defined as the difference between the percentage of STRO-1+ cells in the positive fraction and percentage of STRO-1+ cells in the original sample) in the cell population recovered from the positive fraction of the device ver.3.4 PEG coated + QMS ver.2 across the range of $Q_S:Q_B$ ratios tested (mean values $n=9 \pm SD$).

As with the previous set of experiments, the STRO-1+ cell population represented ~68% to 70% of the whole cell population.

Analysis of the cell populations recovered from the positive fraction revealed that the percentage of STRO-1+ cells ranged between ~83% ($Q_S:Q_B$ ratio 1:1) and ~90% ($Q_S:Q_B$ ratio 1:4). The purity increases (defined in section 9.3.3.2) achieved by sorting device ver.3.4 (PEG coated) + QMS ver.2 were plotted in Figure 7.15. The device increased the percentage of STRO-1+ cells recovered in the positive fraction; values ranging between ~14% and ~23% (across the range of $Q_S:Q_B$ ratios used) compared to percentages in the original sample. The highest purity was achieved with $Q_S:Q_B$ ratio 1:4.

However, purity increases achieved using QMS ver.2 were not significantly different from those obtained with QMS ver.1 (comparison among all the magnetic system tests was shown in Section 7.7). Analysing retrieved cell populations from the negative fraction revealed high percentages of STRO-1+ cells across the entire range of $Q_S:Q_B$ ratios investigated, with values ranging between ~48% and ~57% (Table 7.7).

Recovery efficiency was investigated with QMS ver.2, similar to previous investigation with QMS ver.1.

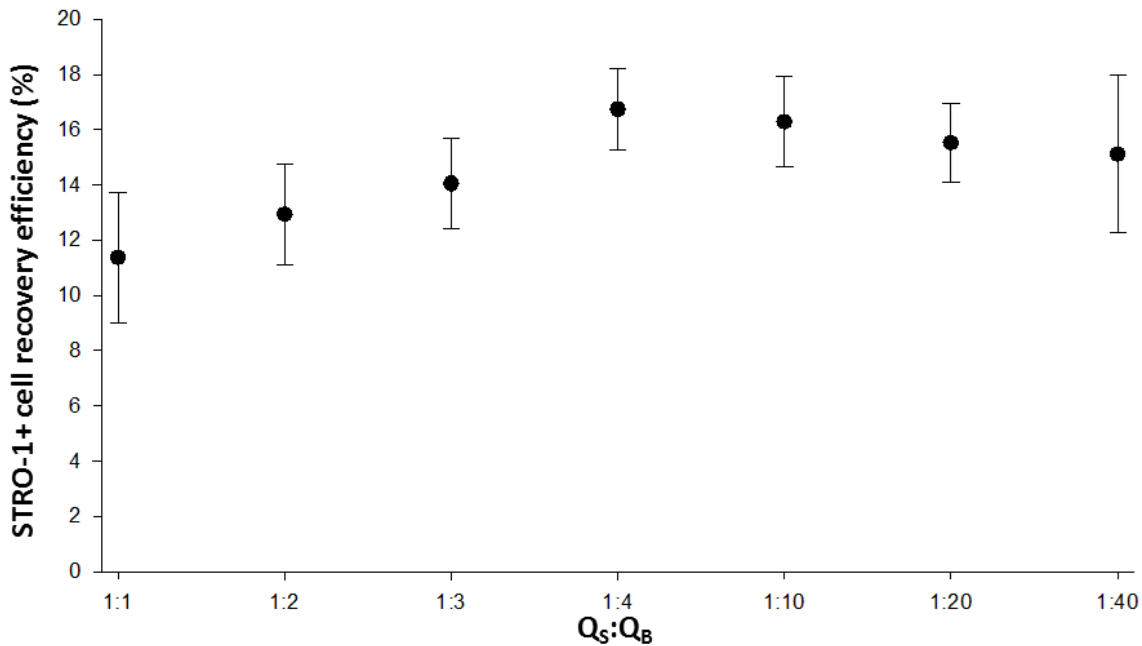


Figure 7.16: STRO-1+ cells recovery efficiency in the positive fraction of the device ver.3.4 PEG coated + QMS ver.2 across the range of $Q_S:Q_B$ ratios tested. Percentages of the initial STRO-1+ cells number collected in the positive fraction were plotted (mean values $n=9 \pm$ SD).

Table 7.8 reports the total number of cells retrieved from negative and positive fractions with $\sim 13\%$ of the cells present in the original sample missing. The STRO-1+ cell recovery efficiency was also investigated, comparing the number of STRO-1+ cells in the original samples with the number of STRO-1+ cells recovered in the negative and positive fractions.

Once again the majority of STRO-1+ cells was collected in the negative fraction across the entire range of $Q_S:Q_B$ ratios used. Percentages between $\sim 65\%$ to $\sim 48\%$ of the initial STRO-1+ cells loaded were retrieved from the negative fraction. This meant that almost half of the initial number of STRO-1+ cells was not sorted, and consequently discarded.

Analysis of cell populations collected in the positive fraction revealed percentages ranging between $\sim 11\%$ ($Q_S:Q_B$ ratio 1:1) and $\sim 17\%$ ($Q_S:Q_B$ ratio 1:4) of the initial STRO-1+ cell number were correctly sorted by the device.

In Figure 7.16, STRO-1+ cell recovery efficiency of sorting device ver.3.4 (PEG coated) + QMS ver.2 was plotted. The highest STRO-1+ cell recovery efficiency ($\sim 17\%$) was obtained using $Q_S:Q_B$ ratio 1:4. However, similar to QMS ver.1, the STRO-1+ cell recovery efficiency obtained using the QMS ver.2 was far from the desired 100% of STRO-1+ cells recovered.

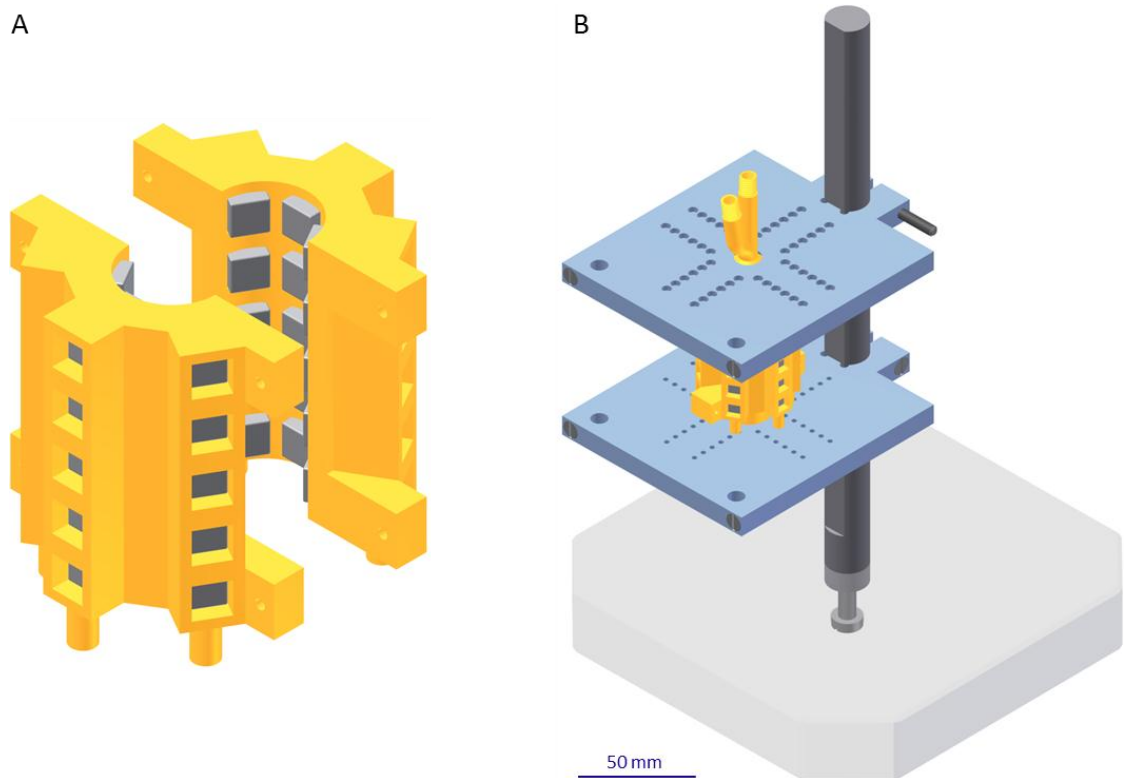


Figure 7.17: (A) 3D models of the HMS and (B) the experimental setup with the sorting device ver.3.4 (PEG coated) surrounded by the HMS.

7.5 MG63 cell sorting: device ver.3.4 + HMS

To improve the device sort capacity, a radical change to the magnetic system was adopted. The quadrupole geometry used in the previous two systems was replaced with a hexapole configuration. The hexapole magnetic system (HMS) comprised 60 cubic neodymium magnets (NdFeB) of grade N52 arranged as shown in Figure 7.17 (see Section 5.4).

This configuration aimed to achieve a magnetic field gradient as high as possible, and the use of the hexapole configuration allow to obtain a $|\nabla B|$ of 120 mT/mm within the sorting device. This value was considerably lower than that obtained by Chalmers and co-workers [16] (see section 2.3.3) but in the same order of magnitude. The HMS was tested with the same sorting device used to test the first two magnetic systems: PEG-coated sorting device ver.3.4. The same experimental protocol, buffer and sample concentration (500,000 MG63 cells/ml with a total number of 5×10^6 MG63 cells per sample) and assessment technique (flow cytometry) were implemented (see Section 7.3.3.1). Sorting device ver.3.4 (PEG coated) + HMS was tested over the whole range of $Q_S:Q_B$ ratios previously investigated. Cell populations retrieved from the negative and positive fractions were analysed and

compared with the cell populations present within the original samples. The HMS sorting capability was evaluated in terms of purity and recovery efficiency. The percentages of STRO-1+ (in orange) and STRO-1- cells (in blue) in the original sample, negative and positive fractions were reported in Table 7.9.

The STRO-1+ cell fraction within the original sample ranged between ~65% and ~70% of the entire cell population.

The analysis of cell populations recovered from the positive fraction revealed that the highest percentage of STRO-1+ cells was achieved using $Q_S:Q_B$ ratio 1:4 (~93%). Other $Q_S:Q_B$ ratios investigated achieved STRO-1+ cell percentages ranging between ~85% and ~93%.

Purity increases (defined in section 9.3.3.2) achieved by sorting device ver.3.4 (PEG coated) + HMS were plotted in Figure 7.18. Cell populations recovered from the positive fraction presented higher percentages of STRO-1+ cells than percentages in the original samples (across the range of $Q_S:Q_B$ ratios used). Purity increases ranged from ~17% to ~28% ($Q_S:Q_B$ ratio 1:4), thus being significantly higher than those obtained using the two QMS system (comparison among all the magnetic systems tested was shown in Section 7.7).

Table 7.9: Percentages (mean values $n=9 \pm SD$) of STRO-1+ cells (in orange) and the STRO-1- cells (in blue) recovered from the negative and positive fraction of the sorting device (device ver.3.4 PEG coated + HMS). The sorting experiments were performed using MG63 cells across the entire range of $Q_S:Q_B$ ratios.

PURITY - Sorting device ver.3.4 (PEG coated) + HMS								
FLOW RATE ($\mu\text{l}/\text{min}$)			ORIGINAL		NEGATIVE FRACTION		POSITIVE FRACTION	
$Q_S:Q_B$	BUFFER (Q_B)	SAMPLE (Q_S)	STRO-1+ (%)	STRO-1- (%)	STRO-1+ (%)	STRO-1- (%)	STRO-1+ (%)	STRO-1- (%)
1:1	2000	2000	67.84 \pm 2.22	32.16 \pm 2.22	49.67 \pm 2.98	50.33 \pm 2.98	85.69 \pm 2.94	14.31 \pm 2.94
1:2	2000	1000	68.91 \pm 2.01	31.09 \pm 2.01	46.51 \pm 2.81	53.49 \pm 2.81	87.32 \pm 2.72	12.68 \pm 2.72
1:3	2000	700	66.17 \pm 2.71	33.83 \pm 2.71	44.31 \pm 2.23	55.69 \pm 2.23	90.54 \pm 2.06	9.46 \pm 2.06
1:4	2000	500	65.11 \pm 2.73	34.89 \pm 2.73	41.03 \pm 2.09	58.97 \pm 2.09	93.13 \pm 1.91	6.87 \pm 1.91
1:10	2000	200	69.36 \pm 2.91	30.64 \pm 2.91	41.64 \pm 2.79	58.36 \pm 2.79	92.81 \pm 2.01	7.19 \pm 2.01
1:20	2000	100	68.04 \pm 2.81	31.96 \pm 2.81	41.31 \pm 2.11	58.69 \pm 2.11	92.95 \pm 2.63	7.05 \pm 2.63
1:40	2000	50	69.94 \pm 2.29	30.06 \pm 2.29	41.02 \pm 2.08	58.98 \pm 2.08	93.02 \pm 2.47	6.98 \pm 2.47

Table 7.10: Table summarising MG63 cell sorting experiments (mean values $n=9 \pm SD$). Total numbers of cells and numbers of STRO-1+ cells in the original sample, positive and negative fractions (after sorting with device ver.3.4 PEG coated + HMS) were reported. Percentages of the initial STRO-1+ cells number collected in the negative and positive fractions were reported (in red).

CELL RECOVERY EFFICIENCY - Sorting device ver.3.4 (PEG coated) + HMS										
FLOW RATE ($\mu\text{l}/\text{min}$)			ORIGINAL		NEGATIVE FRACTION			POSITIVE FRACTION		
$Q_S:Q_B$	BUFFER (Q_B)	SAMPLE (Q_S)	Total (10^6)	STRO-1+ cells (10^6)	Total (10^6)	STRO-1+ cells		Total (10^6)	STRO-1+ cells	
						Number (10^6)	%		Number (10^6)	%
1:1	2000	2000	4.99 \pm 0.20	3.38 \pm 0.25	3.51 \pm 0.21	1.74 \pm 0.21	51.50 \pm 6.35	0.71 \pm 0.07	0.61 \pm 0.08	17.97 \pm 2.45
1:2	2000	1000	4.92 \pm 0.16	3.39 \pm 0.21	3.32 \pm 0.22	1.54 \pm 0.20	45.54 \pm 5.95	0.77 \pm 0.09	0.67 \pm 0.10	19.83 \pm 3.00
1:3	2000	700	4.91 \pm 0.11	3.25 \pm 0.21	3.24 \pm 0.12	1.43 \pm 0.13	44.19 \pm 3.94	0.89 \pm 0.06	0.80 \pm 0.07	24.80 \pm 2.27
1:4	2000	500	4.98 \pm 0.13	3.24 \pm 0.22	3.17 \pm 0.13	1.30 \pm 0.12	40.11 \pm 3.77	1.13 \pm 0.04	1.05 \pm 0.06	32.45 \pm 1.84
1:10	2000	200	4.99 \pm 0.11	3.46 \pm 0.22	3.19 \pm 0.17	1.33 \pm 0.16	38.38 \pm 4.75	1.12 \pm 0.05	1.04 \pm 0.07	30.03 \pm 2.02
1:20	2000	100	4.98 \pm 0.15	3.39 \pm 0.25	3.18 \pm 0.21	1.31 \pm 0.16	38.77 \pm 4.67	1.13 \pm 0.06	1.05 \pm 0.09	30.99 \pm 2.57
1:40	2000	50	4.93 \pm 0.14	3.45 \pm 0.21	3.20 \pm 0.20	1.31 \pm 0.15	38.07 \pm 4.43	1.11 \pm 0.04	1.03 \pm 0.06	29.94 \pm 1.90

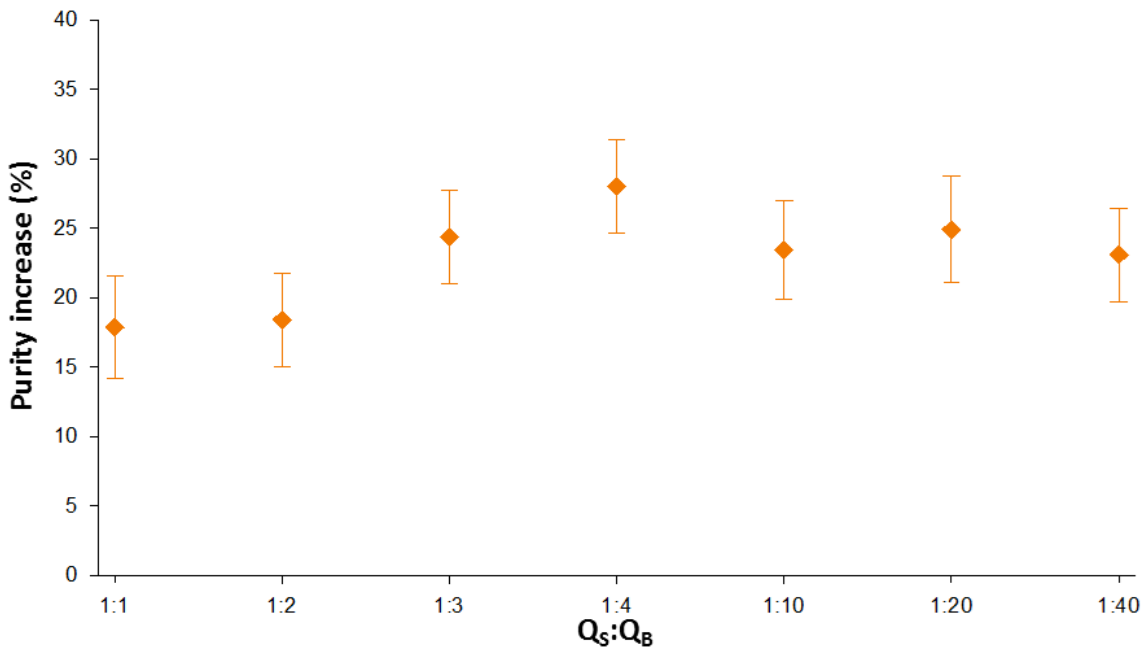


Figure 7.18: Purity increases in the cell population recovered from the positive fraction of the device ver.3.4 PEG coated + HMS across the range of $Q_S:Q_B$ ratios tested (mean values $n=9 \pm SD$).

In cell populations recovered from the negative fraction the percentage of STRO-1+ cells ranged from ~41% to ~49%, indicating that the majority comprised STRO-1- cells, even if by a little.

Table 7.10 shows the total number of cells retrieved from the negative and positive fractions. As observed previously, ~12% of initial number of cells was missing (see Section 7.2.1.1).

The most substantial improvement recorded testing the sorting device ver.3.4 (PEG coated) + HMS was STRO-1+ cell recovery efficiency. The percentage of original STRO-1+ cells collected in the positive fraction varied from ~18% to ~32% (Table 7.10), with the best results obtained using $Q_S:Q_B$ ratio 1:4. No significant differences were observed in the STRO-1+ cell recovery efficiency obtained using lower $Q_S:Q_B$ ratios (Figure 7.19), but as previously stated, the use of high Q_S values was desirable.

The negative fraction still contained the majority of initial loaded number of STRO-1+ cells, with percentages ranging between ~38% and ~51% across the range of $Q_S:Q_B$ investigated. These percentages represented the number of miss-sorted STRO-1+ cells, and they were considerably higher than those collected in the positive fraction.

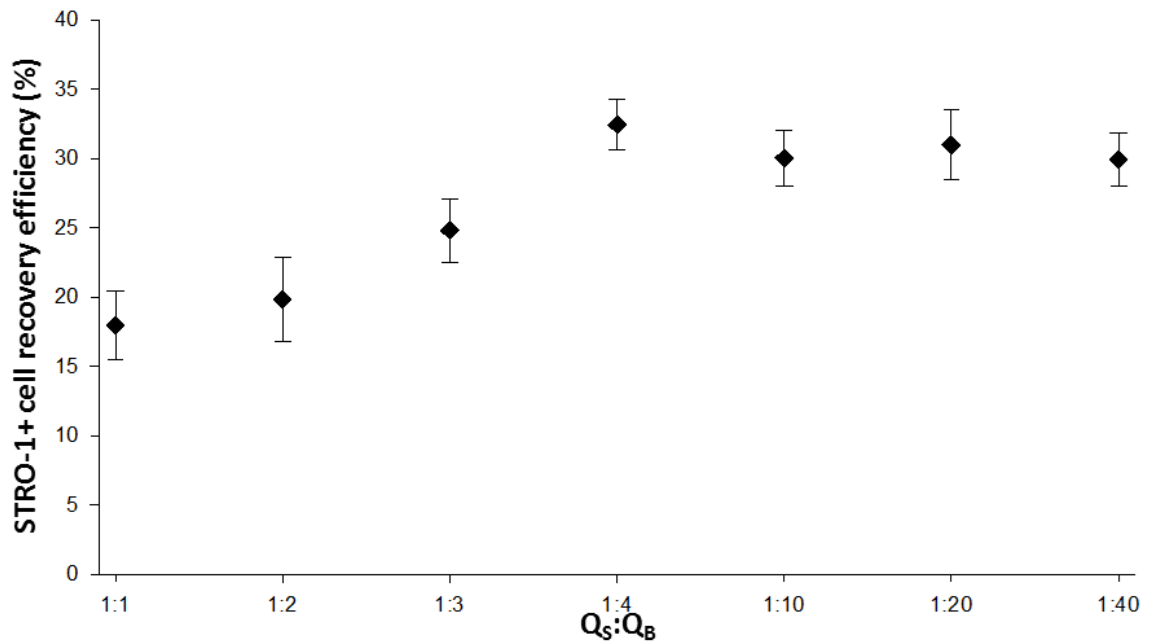


Figure 7.19: STRO-1+ cells recovery efficiency in the positive fraction of the device ver.3.4 PEG coated + HMS across the range of $Q_S:Q_B$ ratios tested. Percentages of the initial STRO-1+ cells number collected in the positive fraction were plotted (mean values $n=9 \pm SD$).

7.6 MG63 cell sorting: device ver.3.5 + HMS

To further improve the performance of the sorting device, one final version was designed and manufactured; sorting device ver.3.5. This version shared all its components with the sorting device ver.3.4, with exception of the tube (see Section 4.7.2). Figure 7.20 compares the two devices.

The difference between the two versions was the external diameter of the tube; 16.6 mm for ver.3.4 (Figure 7.20A) and 14.3 mm for ver.3.5 (Figure 7.20C). Due to the HMS design, reduction in the tube external diameter meant that the magnets which were tangential to the tube's external surface and positioned opposite to each other, were 14.3 mm away from one another instead of 16.6 mm.

The two HMS magnet configurations were modelled in COMSOL Multiphysics 4.3b. The $|\vec{B}|$ and the $|(\vec{B} \cdot \nabla)\vec{B}|$ generated by them were modelled over the horizontal mid-plane (Figure 7.20E), and compared along the cut line drawn on that same horizontal mid-plane (Figure 7.20F). In Figure 7.20G the $|\vec{B}|$ generated by the HMS when used with device ver.3.4 (red line) and ver.3.5 (black line) were plotted. The area of interest (within the device) was defined by two vertical lines.

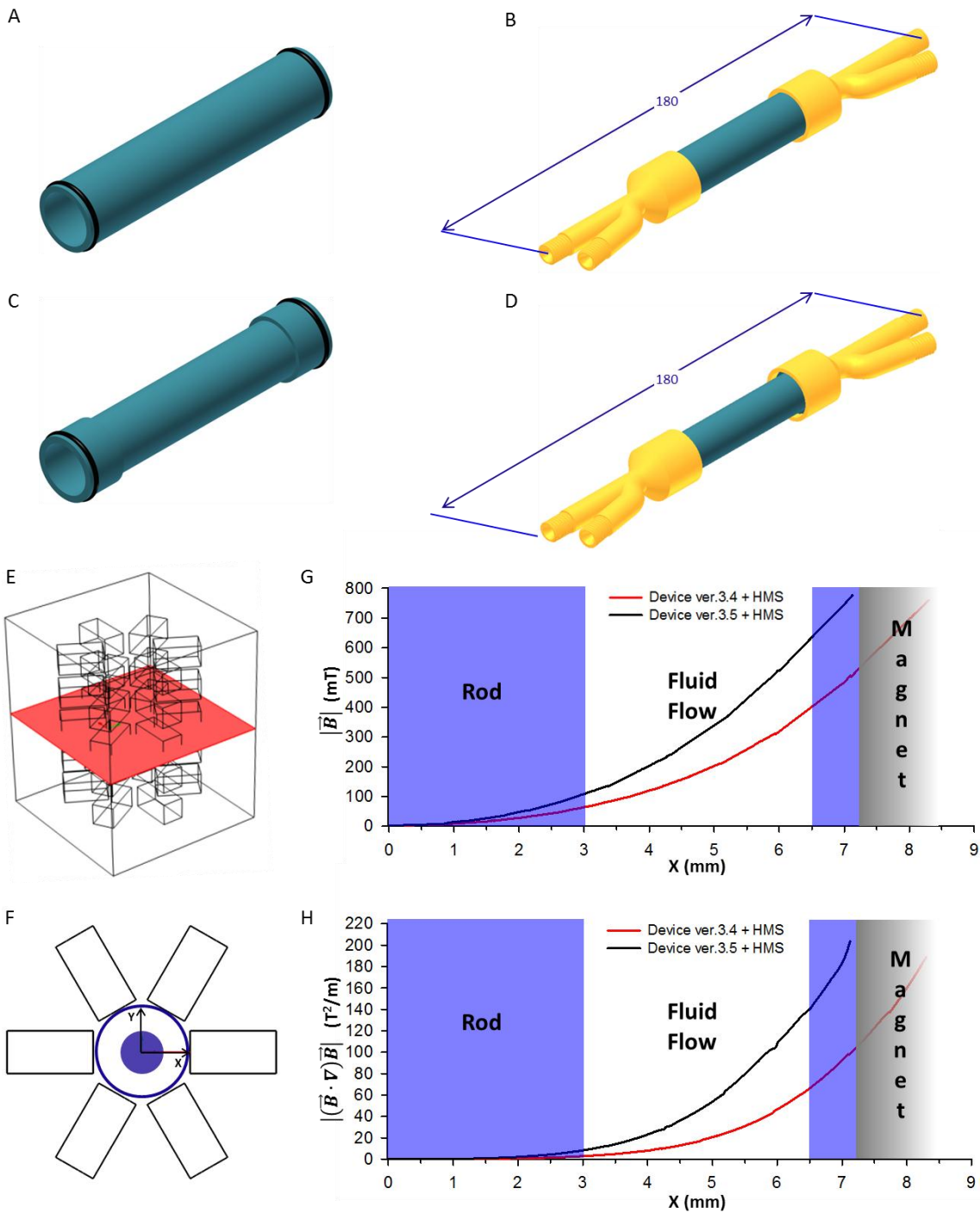


Figure 7.20: (A) 3D models of the tube used in (B) the sorting device ver.3.4. (C) 3D models of the tube (D) used in the sorting device ver.3.5. (E) Horizontal mid-plane of the HMS; (F) cut line drawn between the centre point and the magnet surface. (G) Plot of $|\vec{B}|$ generated by the device ver.3.4 + HMS (red line) and the device ver.3.5 + HMS (black line) along the cut line. (H) Plot of $|(\vec{B} \cdot \nabla)\vec{B}|$ generated by the device ver.3.4 + HMS (red line) and the device ver.3.5 + HMS (black line) along the cut line.

As a consequence of distance reductions between the magnets, the $|\vec{B}|$ and the $|(\vec{B} \cdot \nabla)\vec{B}|$ (double magnitude at $X=6.5$ mm) generated by device ver.3.5 + HMS were a factor of two higher than those generated by the previous configuration.

The lines in the two plots (Figure 7.20G and H) did not have the same length because the cut lines along which $|\vec{B}|$ and $|(\vec{B} \cdot \nabla)\vec{B}|$ were modelled had different lengths, in particular: 7.15 mm and 8.3 mm for ver.3.5 and ver. 3.4 respectively. The increase of $|(\vec{B} \cdot \nabla)\vec{B}|$ represented a proportional increase in $|\vec{F}_m|$.

The device ver.3.5 + HMS allowed to obtain a $|\nabla\vec{B}|$ of 150 mT/mm within the sorting device. This value was in the same order of magnitude than that achieved by Chalmers and co-workers (179 mT/mm) [16] (see section 2.3.3).

After numerical simulations, MG63 cell sorting experiments were conducted on sorting device ver.3.5 + HMS under the same conditions used to test other magnetic systems (experimental protocol, buffer, sample concentration). Once again the entire range of $Q_S:Q_B$ ratios was investigated to compare the performances (purity and recovery efficiency) of ver.3.5 + HMS with the previous magnetic systems. As performed for all the other versions, prior to sorting experiments, the internal surface of ver.3.5 was PEG coated (see Section 7.2.1.1).

Table 7.11 shows the percentage of STRO-1+ cells in the original sample, and negative and positive fractions. The initial STRO-1+ cell percentages did not vary significantly compared with those in other experiments performed; the STRO-1+ cell fraction represented ~65% to 70% of the whole cell population.

The positive fraction contained STRO-1+ cell percentages ranging between ~86% and ~96% ($Q_S:Q_B$ ratio 1:4). Purity increases achieved by sorting device ver.3.5 (PEG coated) + HMS across the entire range of $Q_S:Q_B$ ratios examined were reported in Figure 7.21.

Table 7.11: Percentages (mean values n=9 ±SD) of STRO-1+ cells (in orange) and the STRO-1- cells (in blue) recovered from the negative and positive fraction of the sorting device (device ver.3.5 PEG coated + HMS). The sorting experiments were performed using MG63 cells across the entire range of Q_S:Q_B ratios.

PURITY - Sorting device ver.3.5 (PEG coated) + HMS								
FLOW RATE (μl/min)			ORIGINAL		NEGATIVE FRACTION		POSITIVE FRACTION	
Q _S :Q _B	BUFFER (Q _B)	SAMPLE (Q _S)	STRO-1+ (%)	STRO-1- (%)	STRO-1+ (%)	STRO-1- (%)	STRO-1+ (%)	STRO-1- (%)
1:1	2000	2000	67.13±2.20	32.87±2.20	38.46±2.91	61.54±2.91	85.91±2.36	14.09±2.36
1:2	2000	1000	69.91±2.12	30.09±2.12	36.99±2.01	63.01±2.01	89.87±2.70	10.13±2.70
1:3	2000	700	66.89±2.77	33.11±2.77	35.12±2.13	64.88±2.13	91.39±2.26	8.61±2.26
1:4	2000	500	65.26±2.23	34.74±2.23	33.76±2.03	66.24±2.03	95.67±1.92	4.33±1.92
1:10	2000	200	66.01±2.76	33.99±2.76	33.65±2.99	66.35±2.99	94.01±1.84	5.99±1.84
1:20	2000	100	65.51±2.83	34.49±2.83	32.88±2.81	67.12±2.81	90.36±2.03	9.64±2.03
1:40	2000	50	66.37±2.19	33.63±2.19	32.91±2.38	67.09±2.38	91.02±1.47	8.98±1.47

Table 7.12: Table summarising MG63 cell sorting experiments (mean values n=9 ±SD). Total numbers of cells and numbers of STRO-1+ cells in the original sample, positive and negative fractions (after sorting with device ver.3.5 PEG coated + HMS) were reported. Percentages of initial STRO-1+ cells number collected in the negative and positive fractions reported in red.

CELL RECOVERY EFFICIENCY - Sorting device ver.3.5 (PEG coated) + HMS										
FLOW RATE (μl/min)			ORIGINAL		NEGATIVE FRACTION			POSITIVE FRACTION		
Q _S :Q _B	BUFFER (Q _B)	SAMPLE (Q _S)	Total (10 ⁶)	STRO-1+ cells (10 ⁶)	Total (10 ⁶)	STRO-1+ cells		Total (10 ⁶)	STRO-1+ cells	
						Number (10 ⁶)	%		Number (10 ⁶)	%
1:1	2000	2000	4.98±0.21	3.34±0.25	3.13±0.22	1.20±0.18	36.00±5.44	1.19±0.06	1.02±0.08	30.58±2.42
1:2	2000	1000	4.97±0.18	3.47±0.23	3.02±0.23	1.12±0.15	32.15±4.33	1.34±0.10	1.20±0.13	34.66±3.70
1:3	2000	700	4.94±0.13	3.30±0.23	2.81±0.14	0.99±0.11	29.86±3.39	1.45±0.07	1.32±0.10	40.10±2.97
1:4	2000	500	4.99±0.11	3.26±0.18	2.74±0.12	0.92±0.10	28.40±3.03	1.65±0.04	1.58 ±0.07	48.47±2.17
1:10	2000	200	4.98±0.14	3.29±0.23	2.76±0.15	0.93±0.14	28.25±4.18	1.62±0.05	1.52±0.08	46.33±2.36
1:20	2000	100	4.94±0.17	3.24±0.25	2.72±0.18	0.89±0.14	27.63±4.34	1.64±0.06	1.48±0.09	45.79±2.74
1:40	2000	50	4.95±0.16	3.28±0.22	2.81±0.18	0.92±0.13	28.15±4.08	1.65±0.05	1.50±0.07	45.71±2.14

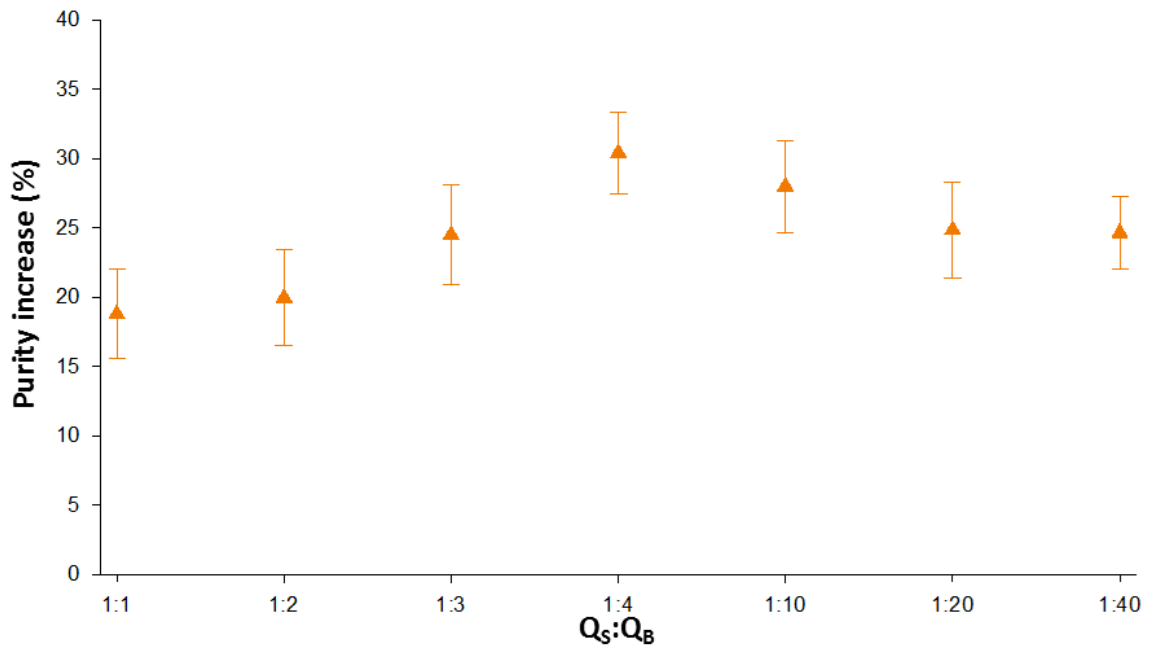


Figure 7.21: Purity increases in the cell population recovered from the positive fraction of the device ver.3.5 PEG coated + HMS across the range of $Q_S:Q_B$ ratios tested (mean values $n=9 \pm SD$).

The highest purity increase (~30%) was recorded using $Q_S:Q_B$ ratio 1:4, followed closely by that obtained using 1:10 (with no significant difference).

In the negative fraction, STRO-1⁻ cells represented the majority of the cell population. However, the presence of STRO-1⁺ cells was still recorded, with percentages between ~38% and ~33% depending on the $Q_S:Q_B$ ratio used. Sorting device ver.3.5 (PEG coated) + HMS achieved the highest purity increases of all the tested magnetic systems.

An improved result was achieved with regards to STRO-1⁺ cell recovery efficiency. Table 7.12 reports the number of STRO-1⁺ cells recovered from each fraction and the percentage of original STRO-1⁺ cells collected in the negative and positive fractions. For the first time, STRO-1⁺ cells collected in the positive fraction were higher than those collected in the negative fraction. In particular, the percentage of initial STRO-1⁺ cells recovered in the positive fraction ranged between ~30% and ~48%. The STRO-1⁺ cell recovery efficiency achieved by sorting device ver.3.5 (PEG coated) + HMS was shown in Figure 7.22. The graph shows an increase in percentage of STRO-1⁺ cells recovered over the $Q_S:Q_B$ ratios investigated.

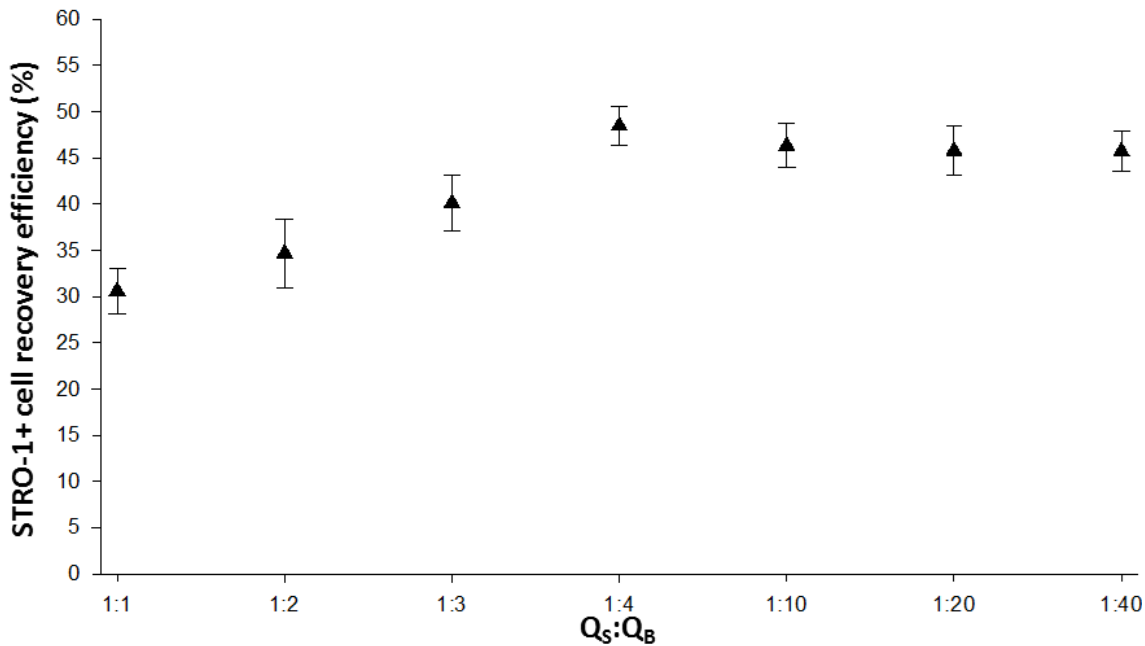


Figure 7.22: STRO-1+ cells recovery efficiency in the positive fraction of the device ver.3.5 PEG coated + HMS across the range of $Q_S:Q_B$ ratios tested. Percentages of the initial STRO-1+ cells collected in the positive fraction were plotted (mean values $n=9 \pm SD$).

The STRO-1+ cell recovery efficiency reached its maximum value at $Q_S:Q_B$ ratio 1:4. However, analyses of cell populations recovered from the negative fraction, showed that ~30% of the initial STRO-1+ cell number was still not sorted correctly.

7.7 Comparison among magnetic systems and analysis

In this chapter four sorting device + magnetic system combinations were tested:

- sorting device ver.3.4 + QMS ver.1
- sorting device ver.3.4 + HMS
- sorting device ver.3.4 + QMS ver.2
- sorting device ver.3.5 + HMS

MG63 cell sorting experiments were conducted on the above combinations using constant experimental parameters (protocol, buffer, sample concentration and number of cells examined) across the entire range of $Q_S:Q_B$ ratios (from 1:1 to 1:40). Each ratio was tested in triplicate. All sorting devices were PEG coated. The sort capacity of each combination was assessed in terms of purity and cell recovery. Figure 7.23 summarizes the purity increases recorded during MG63 cell sorting experiments performed with device + magnetic system combinations tested.

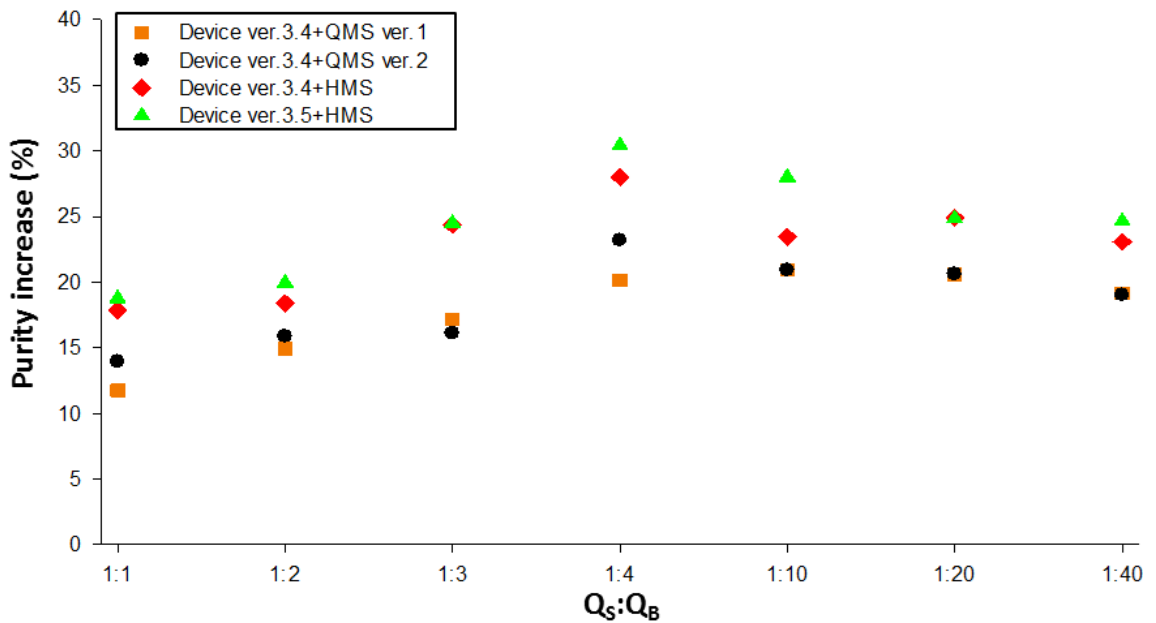


Figure 7.23: Purity increases the cell population recovered from the positive fractions of all the sorting device + magnetic system combinations across the range of Q_S:Q_B ratios tested (mean values n=9).

Purity increases followed comparable trends across Q_S:Q_B ratios examined. The highest purity increases were achieved using Q_S:Q_B ratios of 1:4 and lower. Sorting device ver.3.5 + HMS achieved the highest purity increase of all the systems tested. In particular, using a Q_S:Q_B ratio of 1:4 (buffer flow rate=2000 μl/min; sample flow rate=500 μl/min), the cell population collected from the positive fraction resulted in approximately 96% of STRO-1+ cells and approximately 4% of STRO-1- cells, achieving a purity increase of ~30%.

Contamination of the positive fraction with STRO-1- cells was a consequence of two phenomena including cross-contamination and cell clumping. As observed in preliminary tests performed with sorting device ver.3.4, in the case of Q_S:Q_B ratio 1:4, ~1% of unlabelled cells were found in the positive fraction (see Section 7.2.1). The remaining percentage of STRO-1- cells found in the positive fraction could be a consequence of cell clumping. The sorting step of the experimental protocol lasted for 20 min (~5 × 10⁶ MG63 cells suspended in 10 ml and processed with sample flow rate of 500 μl/min). During this time, labelled (STRO-1+) and unlabelled cells (STRO-1-) could potentially clump together. In such a case, the entire clump of cells (indiscriminately formed by labelled and unlabelled cells) would be influenced by the magnetic field applied and would be deflected within the device towards the positive fraction output.

In Figure 7.24 the STRO-1+ cell recovery efficiency achieved by sorting device + magnetic systems combinations tested were reported.

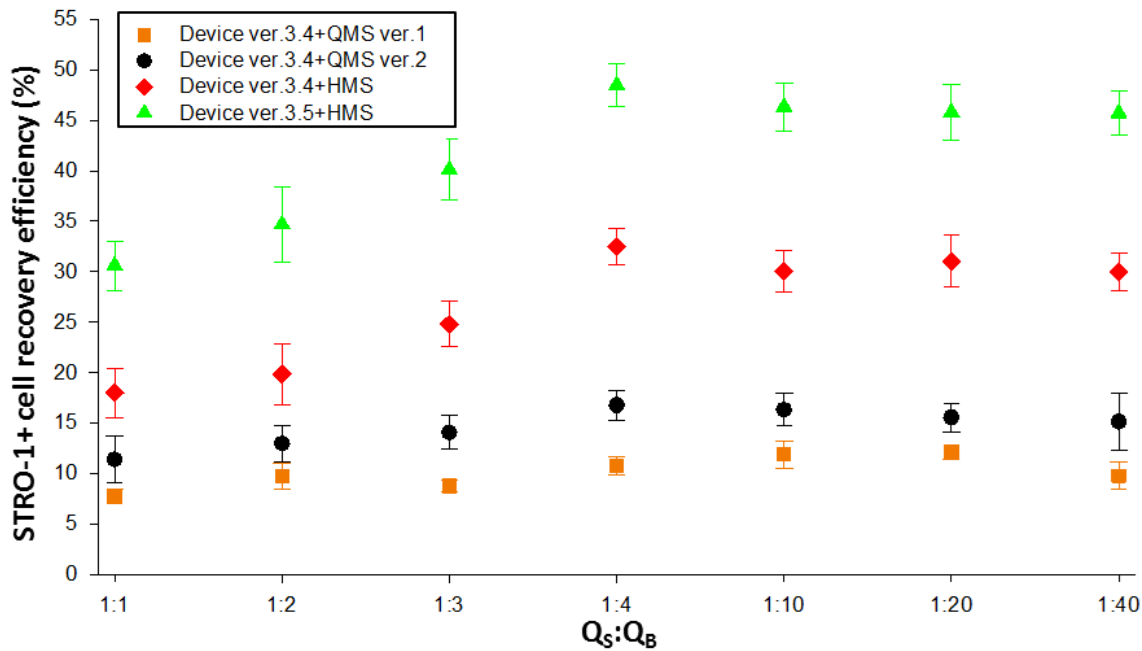


Figure 7.24: STRO-1+ cells recovery efficiency in the positive fractions of all the sorting device + magnetic system combinations across the range of $Q_S:Q_B$ ratios tested. Percentages of the initial STRO-1+ cells number collected in the positive fractions were plotted (mean values $n=9 \pm SD$).

Cell recovery efficiency increased with each new magnetic system, and reached the highest results with sorting device ver.3.5 + HMS. Once again, $Q_S:Q_B$ ratio 1:4 was the optimum compromise between performance and throughput. When $Q_S:Q_B$ ratio 1:4 was used, in the positive fraction of sorting device ver.3.5 + HMS ~48% of original STRO-1+ cells were recovered.

Table 7.12 shows that a significant percentage (~28%) of the initial STRO-1+ cells were missorted and collected in the negative fraction.

A likely explanation for the presence of STRO-1+ cells in the negative fraction was discordance between the fluorescence thresholds of the flow cytometer and the sorting device (see Appendix M). Flow cytometry analysis involved a two-step immunostaining process, resulting in fluorescently tagged cells expressing STRO-1. The flow cytometer recorded fluorescent signals of fluorescently tagged cells, classifying them as STRO-1+ cells. Similarly, in the sorting experiments the cells were immunomagnetically labelled according to their expression of STRO-1. However, STRO-1 expression might not be sufficiently high enough to bind an adequate number of superparamagnetic beads on the cell surface leaving the cell insensitive to the applied magnetic field within the device. In such a case, the cell would not be sorted by the device, but STRO-1 cell expression would

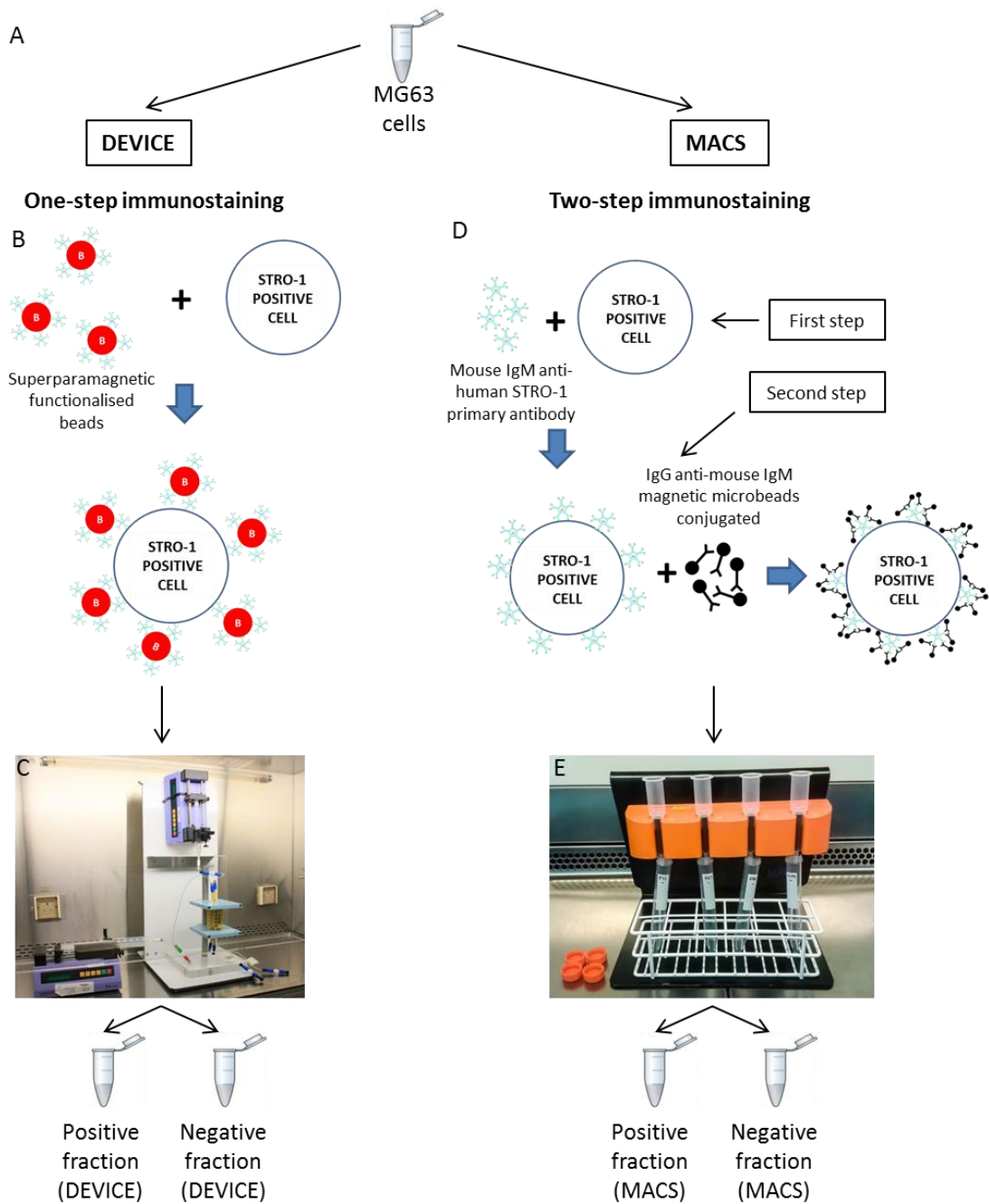


Figure 7.25: (A) The cell sample was divided in two. (B) Half was processed with a one-step immunostaining and (C) processed with the sorting device. (D) The second part was processed with a two-step immunostaining and (E) processed with traditional MACS.

lead to the emission of a fluorescent signal sufficiently strong enough to reach the flow cytometer threshold, and thus the cell would be recognised as STRO-1+. To summarise, the best sorting capacity was achieved using the sorting device ver.3.5 (PEG coated) + HMS, with the optimum $Q_S:Q_B$ ratio 1:4 (buffer flow rate=2000 $\mu\text{l}/\text{min}$; sample flow rate=500 $\mu\text{l}/\text{min}$). Sorting device ver.3.5 (PEG coated) + HMS with these parameters was used for all further testing.

7.8 Sorting device ver.3.5 + HMS vs MACS

Once defined the optimum flow regime ($Q_s:Q_B$ ratio 1:4) to be used during the cell sorting experiments, the sorting performance of device ver.3.5 + HMS was compared to the standard cell sorting technique MACS (Figure 7.25). This device + magnetic system combination (device ver.3.5 + HMS) was called ***continuous flow magnetic sorter (CFMS)***. The two methods were tested using the MG63 cell line ($\sim 5 \times 10^6$ MG63 cells diluted in 10 ml of buffer) similar to previous experiments. The test was performed in triplicate.

7.8.1 Experiment design

MG63 cells to be processed by MACS were incubated with mouse monoclonal IgM anti-human STRO-1 primary antibody (Hybridoma) for 30 min at 4°C; the suspension was mixed every 10 min. After three washes with MACS buffer (PBS + 0.5% BSA + 2 EDTA), HBMSCs were incubated with rat polyclonal IgG anti-mouse IgM magnetic microbeads conjugated ($\varnothing 50$ nm - Miltenyi Biotec, Germany) for 30 min at 4 °C; the suspension was mixed every 10 min (Figure 7.25). After three washes with MACS buffer the cells were run through the MACS column and the positive (containing STRO-1+ cells) and negative (containing STRO-1- cells) fractions were recovered (detailed protocol in Appendix N)

MG63 cells to be processed by the sorting device ver.3.5 + HMS were incubated with CM-08-10 ($\varnothing 0.82$ μm - Spherotech, Inc, USA) superparamagnetic beads functionalised with mouse monoclonal IgM anti-human STRO-1 primary antibody (Hybridoma) (see Section 6.2.1) for 30 min at 4 °C; the suspension was mixed every 10 min (Figure 7.25).

After two washes with MACS buffer, MG63 cells were run through sorting device ver.3.5 + HMS (buffer flow rate=2000 $\mu\text{l}/\text{min}$; sample flow rate=500 $\mu\text{l}/\text{min}$) and the positive (containing STRO-1+ cells) and negative (containing STRO-1- cells) fractions were recovered (experimental protocol in section 7.1).

7.8.2 Results

Cell populations recovered from the negative and positive fractions of the sorting device and MACS were analysed by flow cytometry, providing the percentage of STRO-1+ cells and the cell density (cells/ μl) in each sample (three reading were taken from each sample). These were compared to the original sample, used as a baseline.

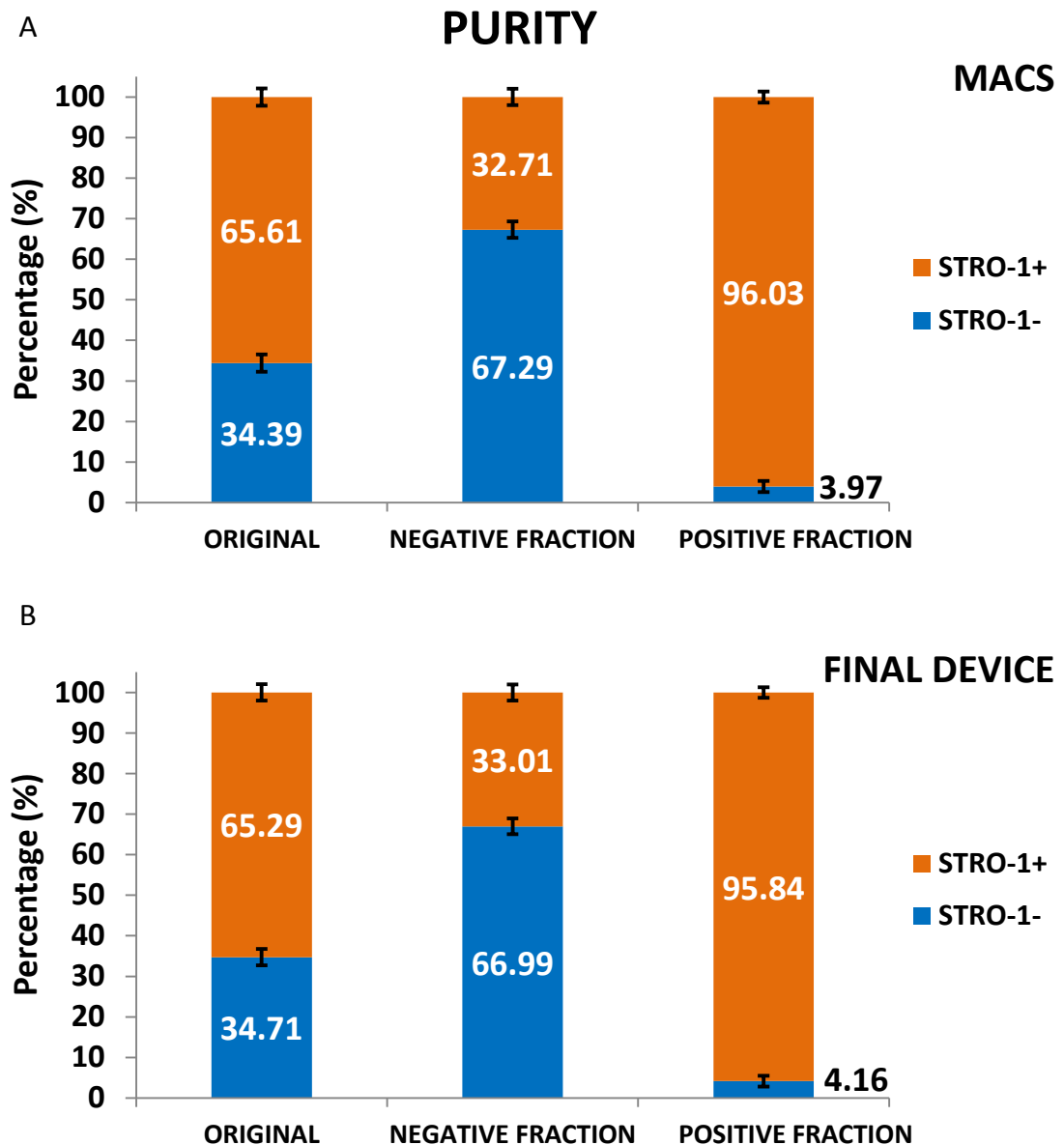


Figure 7.26: (A) Bar chart reporting the composition of the original sample, negative fraction and positive fraction recovered from MACS and (B) final device. Results expressed as mean \pm SD, $n = 9$.

7.8.2.1 Purity

Figure 7.26 shows bar charts detailing the average values of purity achieved by MACS (Figure 7.26A) and the device (Figure 7.26B) after the sorting experiments. Analysis of the original sample used in this set of experiments revealed that $\sim 65\%$ of the MG63 cell population expressed STRO-1 antigen. The composition of the cell populations recovered from MACS and the sorting device negative fractions were almost identical. Approximately 33% of the cell population retrieved from both negative fractions consisted of STRO-1+ cells.

The cell population collected from the positive fractions of both MACS and the sorting device were very similar too, resulting in approximately 96% STRO-1+ cells and ~4% STRO-1- cells.

The standard sorting technique MACS and the final device achieved comparable results in terms of purity of the sorted cell populations, with a purity increase of approximately 30% compared to the original sample.

7.8.2.2 Cell recovery efficiency

According to flow cytometry analyses, the number of cells present in each fraction of both the sorting device and MACS was calculated and compared with the original number of cells. Figure 7.27A reports the average number of cells recovered in the negative and positive fractions of the two methods after sorting. The initial cell number for each experiment was approximately 5×10^6 MG63 cells.

MACS recovered 3.64×10^6 cells (STRO-1+ and STRO-1-) in the negative fraction and 0.92×10^6 cells in the positive fraction. As shown in Figure 7.27A, the numbers of MG63 cells recovered in the sorting device negative and positive fractions were significantly different compared to those retrieved from MACS. In particular, comparing the cell populations recovered from the positive fractions of the two techniques, the sorting device recovered $\sim 0.7 \times 10^6$ cells more than MACS.

Considering only STRO-1+ cells recovered from MACS and the sorting device, it was possible to calculate the STRO-1+ cell recovery efficiency achieved by the two techniques. Figure 7.27B shows the average number of STRO-1+ cells recovered in each fraction of the two methods. Comparing these data with the original number of STRO-1+ cells, the recovery efficiency of MACS and the sorting device was calculated.

Figure 7.27C reports the percentage of the original number of STRO-1+ cells recovered in each fraction. The final sorting device sorted ~48% of the initial STRO-1+ cell population, compared to 27% found in the positive fraction following MACS. This meant that the sorting device recovered almost twice the number of STRO-1+ cells present in the original sample compared with conventional MACS. Moreover, MACS recovered more STRO-1+ cells in the negative compared to the positive fraction, further highlighting the positive performance of the device.

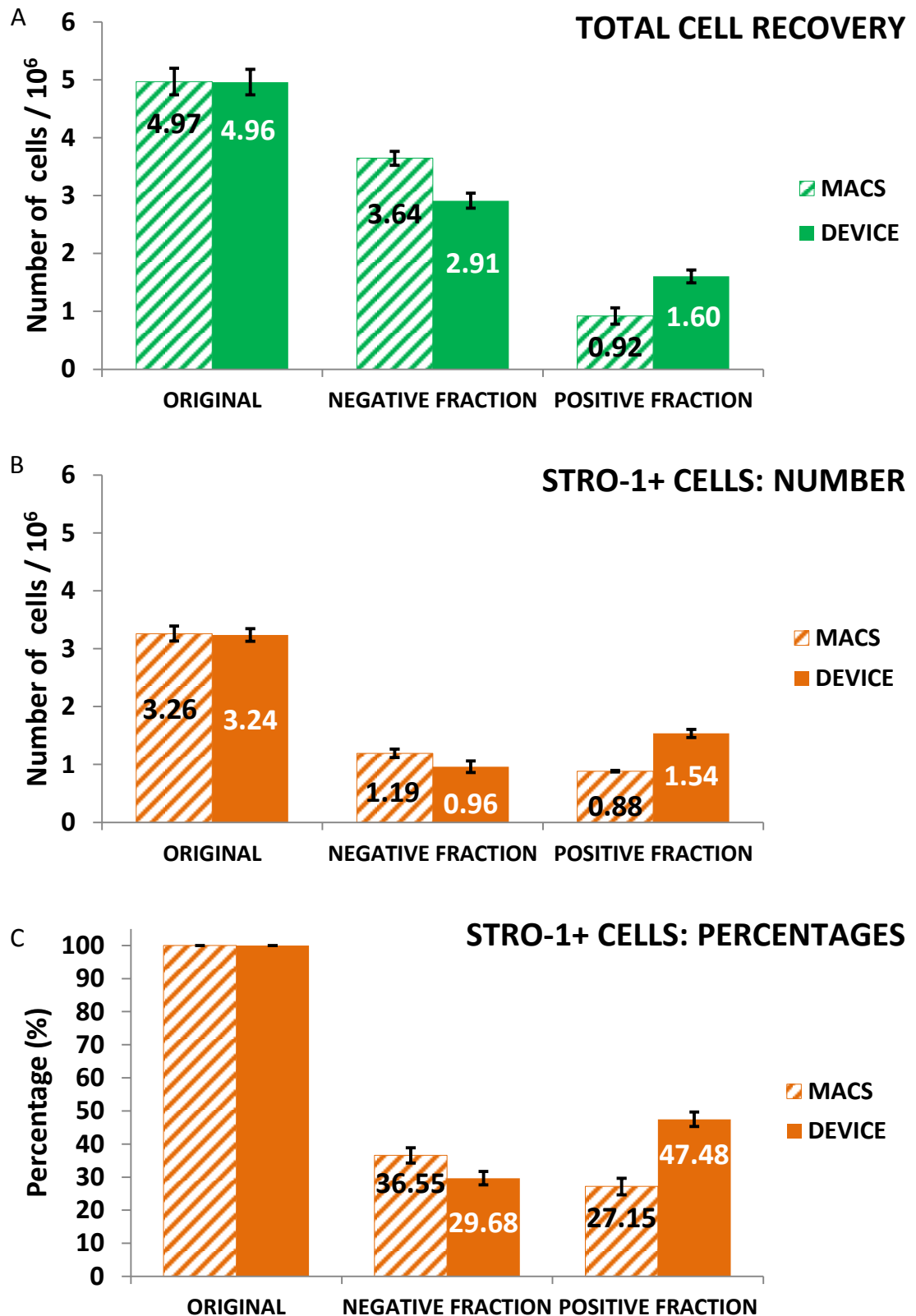


Figure 7.27: (A) Bar charts reporting the total number of cells in the original sample, negative fraction and positive fraction recovered from MACS and sorting device. (B) Number of STRO-1+ cells recovered from each fraction of the two techniques and (C) percentages these numbers represented compared with the original number. Results expressed as mean \pm SD and $n = 9$.

7.8.2.3 Summary

Flow cytometry analyses of cell populations recovered from the negative and positive fractions of both MACS and the sorting device, showed that a significant percentage of the initial number of STRO-1+ cells was not sorted correctly. STRO-1+ cells represented ~33% of the cell population recovered from the negative fractions of both techniques. Furthermore, ~4% of the cell population retrieved from the positive fractions of both MACS and the sorting device consisted of STRO-1- cells.

The presence of STRO-1+ cells in the device's negative fraction was discordance between the fluorescence thresholds of the flow cytometer and the sorting device as discussed in section 7.7. The presence of STRO-1- cells in the device's positive fraction was a consequence of two phenomena including cross-contamination and cell clumping (see section 7.7).

For MACS, a likely explanation for the presence of STRO-1-cells in the positive fractions (~4%) could be the working principle of the technique. MACS isolates STRO-1+ cells by trapping them within the column surrounded by a permanent magnet. The technique relies on washing to remove STRO-1- cells (unlabelled) from the column by rinsing it with MACS buffer, and then collecting the STRO-1- cells in the negative fraction. After this step, the MACS column was removed from the permanent magnet and a plunger was used to push the STRO-1+ cells (labelled) from the column collecting them in the positive fraction. The presence of STRO-1- cells in the positive fraction could be due to unspecific adhesion occurring within the MACS column, with a number of STRO-1- cells resisting the washing step and then being collected in the positive fraction.

Contamination of STRO-1+ cells in the negative fraction (~33%) could be due to several reasons. During the washing step of the MACS protocol, STRO-1+ cells trapped in the column could be mistakenly washed away with the STRO-1- cells and collected in the negative fraction. Another reason (in common with the sorting device) could be discordance between the fluorescence thresholds of the flow cytometer and MACS. STRO-1 expression might not be sufficiently high enough to ensure trapping of cells within the MACS column, but STRO-1 cell expression would lead to the emission of a fluorescent signal sufficiently strong enough to reach the flow cytometer threshold, and thus the cell would be recognised as STRO-1+.

7.9 Summary and considerations

Three generations of sorting devices and three magnetic systems were developed during this study. In this chapter, the sorting devices were tested using polystyrene beads and the MG63 cell line to mimic the behaviour of HBMSCs. Each version, manufactured with different designs or materials, improved different aspects of the previous sorting device. Sorting device ver.3.4 obtained the best results in terms of cross-contamination and missing cell fraction, and was chosen to be further tested, coupled up with different magnetic systems.

Combinations of sorting device ver.3.4 with QMS ver.1, QMS ver.2 and HMS were tested using MG63 cells which express STRO-1 in 60% to 70% of the population. The MG63 cell population was immunomagnetically labelled with functionalized superparamagnetic beads according to STRO-1 expression. Cell sorting experiments were conducted using a range of $Q_S:Q_B$ ratios between 1:1 to 1:40.

The sorting capabilities of each combination were compared and the best performances resulted from sorting device ver.3.4 coupled with the HMS.

One minor design change was applied to sorting device ver.3.4 to further improve its performance. Sorting device ver.3.5 was hence created, with a smaller external diameter of the tube. This modification moved the magnets 14.3 mm away from one another instead of 16.6 mm. This displacement led to a significant increase in the $|\vec{B}|$ and $|(\vec{B} \cdot \nabla)\vec{B}|$ generated, which in turn resulted in a proportional increase of $|\vec{F}_m|$. As a consequence of these enhanced performances, sorting device ver.3.5 coupled with the HMS was called continuous flow magnetic sorter (CFMS) and used for all the primary cell sorting experiments. Cell sorting tests conducted on the CFMS established that an optimum $Q_S:Q_B$ ratio to be used was 1:4. With this setting, the CFMS achieved a purity increase of $\sim 30\%$ compared to the original sample and recovered $\sim 49\%$ of the STRO-1+ cells present in the original sample.

The data obtained from these experimental investigations agree with the numerical simulations performed in Chapter 6, where the trajectory of labelled cells within the sorting device was simulated. One thousand particles with the same χ_c were modelled to flow through sorting device ver.3.5 + HMS, using a range of $Q_S:Q_B$ ratios. The best results were obtained using $Q_S:Q_B$ ratio 1:4. Nonetheless, the numerical simulation suggested that $\sim 92\%$ of the original number of particles would be collected in the positive fraction, while the CFMS collected just $\sim 49\%$ of the STRO-1+ cells present in the original sample.

This significant discrepancy could be due to non-uniform STRO-1 expression on MG63 cell populations used in these experiments. While in the modelled system, the particles all had the same value of χ_c , in the life experiments STRO-1+ cells did not. This meant that a cell could have had a STRO-1 expression high enough to be recognized as STRO-1+ by flow cytometry analysis but not high enough to bind an adequate number of superparamagnetic beads on the cell surface to be successfully sorted by the device (~400 beads/cell – see Appendix M).

Lastly, the CFMS was compared to the standard sorting technique MACS using MG63 cells. The purity obtained by the CFMS (~80%) was not significantly different from that obtained using MACS. However, the CFMS recovered ~47% of STRO-1+ cells present in the original sample, compared to ~27% recovered by MACS. The CFMS achieved recovery efficiency ~74% higher than MACS.

This meant recover almost double number of target cells. In the case of SSCs isolation from HBMSCs, a greater initial number of STRO-1+ cells would be beneficial to *in vitro* expansion because would reduce both culturing period and passage number prior to utilisation within tissue engineering strategies. Reduced passage number was especially important as serial *in vitro* passage have been shown repeatedly to result in the emergence of a dominating fibroblastic phenotype [78].

Chapter 8

Human Bone Marrow Stromal Cell Characterisation

The aim of this study was to examine the differentiation potential of isolated human bone marrow stromal cells (HBMSCs) under different *in vitro* conditions including basal and osteogenic media. Alkaline Phosphatase (ALP) expression was used to assess any differences between basal and osteogenic cultures. HBMSCs and STRO-1 positive cells were cultured under basal and osteogenic conditions and the ALP expression within the cells investigated. ALP was an enzyme that was produced in bone during skeletal development and was a well-documented, although non-specific *in vitro* marker for osteogenesis [79]. Alkaline phosphatase expression was investigated using well-known histological, biochemical and molecular analysis [80]. This would provide baseline data for comparison with isolated cell fractions using developed microfluidic strategies in this programme of work.

8.1 Materials and Methods

8.1.1 Bone marrow samples

HBMSCs were isolated from samples obtained from a haematologically normal (absence of blood related diseases) patient, undergoing routine total hip replacement surgery. Samples were used with patient consent under the approval of the Southampton Hospital Ethics Committee (LREC 194/99). HBMSCs were isolated by disaggregation, following mixing of the marrow sample in 10 ml of α -MEM (modified Eagle's Medium alpha) within a 50 ml falcon tube. This process was repeated five times to provide a final volume of 50 ml, or until the trabecular bone appeared white (fully washed of bone marrow). The

suspension was centrifuged at room temperature for 4mins at 1,100 rpm and suspended in 20 ml media, before filtration through a 40 µm sieve to remove blood clots and bone fragments. The filtrate was made up to 50 ml and divided between two tubes containing 20 ml Lymphoprep™.

The cell suspension was centrifuged at 1,100 rpm for 40 min at 18°C with the centrifuge brake off. The buffered cell suspension layer located immediately above the Lymphoprep™ was transferred to a fresh tube, washed with media and seeded (220 cells/cm²) into culture flasks. Cells were cultured in α-MEM, 10% fetal calf serum (FCS), Penicillin (100 U/ml) and Streptomycin (0.1 mg/ml) (P/S) at 37°C. The media was changed twice weekly.

8.1.2 Cell cultures conditions

HBMSCs were seeded into four individual T75 flasks and four separate six well plates at a seeding density of 220 cells/cm². HBMSCs were cultured under basal conditions (α-MEM, 10% FCS, P/S) for 11 days. The cell population was either cultured under osteogenic conditions (α-MEM, 10% FCS, P/S, 10 nM Dexamethasone and 100 µM Ascorbate-2-Phosphate) or under basal conditions, both for 14 days. Media was changed twice per week.

8.2 Alkaline Phosphatase Activity

Alkaline phosphatase activity was examined after 7 and 14 days from the start of differentiation. At each time point, cells seeded in plates were fixed using 95% ethanol for ALP staining, or 0.6 ml 0.05% Triton X-100 was added per well to facilitate cell lysis for biochemical analysis. Cells grown in flasks were harvested (Trizol step) for RNA (ribonucleic acid) isolation. ALP activity was determined using both histological and biochemical analysis.

8.2.1 Histological analysis

For ALP histological analysis, cells were fixed with 95% ethanol for 10 min and then rinsed using PBS. *ALP staining* was performed by adding 600 µL/well of ALP staining solution (0.4 ml Naphthol AS-MX phosphate alkaline solution, 9.6 ml of distilled water and 2.4 mg of fast Violet salt just prior to use).

The plates were incubated in the dark at 37 °C for 30 min and the reaction stopped by rinsing the wells with distilled water. ALP staining provides a qualitative measurement of ALP expression with cells expressing ALP activity presenting with a strong purple/red stain.

8.2.2 Biochemical analysis

ALP biochemical assay was performed as follows: a solution of 0.05% of Triton was added to cells (600 µL/well), which were lysed by three freezing/thaw and disaggregation cycles. Lysed cells were incubated for a recorded period of time in 90 µL of ALP buffer (40 mg Phosphate Substrate, 10 ml 2-AMP alkaline buffer solution, 20 ml distilled water). The reaction was terminated by the addition of 100 µl of 1 M Sodium Hydroxide into each well. The plate was read on ELx800 spectrophotometer at 415 nm.

PicoGreen double-stranded DNA (dsDNA) quantification assay was performed to determine the amount of DNA within each sample. PicoGreen dsDNA quantitative reagent was an ultra-sensitive fluorescent nucleic acid stain that allows quantitation of dsDNA in solution. Fluorescence was read on a FLx800 cytofluor microplate reader. ALP assay results were corrected for sample DNA content and incubation time.

8.2.3 Molecular analysis

Full details of the cell RNA isolation and cDNA preparation protocol were detailed in Appendix N. For RNA isolation, in brief, cells seeded in flasks were washed with PBS, treated with Trizol and frozen at -80 °C.

RNA isolation was performed using the RNeasy Plus Mini Kit (Qiagen) according to manufacturer's instructions (see Appendix N).

Synthesis of double-stranded Complementary Deoxyribonucleic Acid (cDNA) was performed using 1 µg of RNA reverse transcribed using the VILO cDNA Synthesis kit (Invitrogen) according to manufacturer's instructions (see Appendix N).

8.2.4 Real Time Polymerase Chain Reaction (RT-PCR)

RT-PCR was performed using SYBR green to monitor DNA synthesis, SYBR green, a dye that binds dsDNA but not to single-stranded DNA (ssDNA). SYBR green displays low fluorescence in the absence of dsDNA and high fluorescence in the presence of dsDNA.

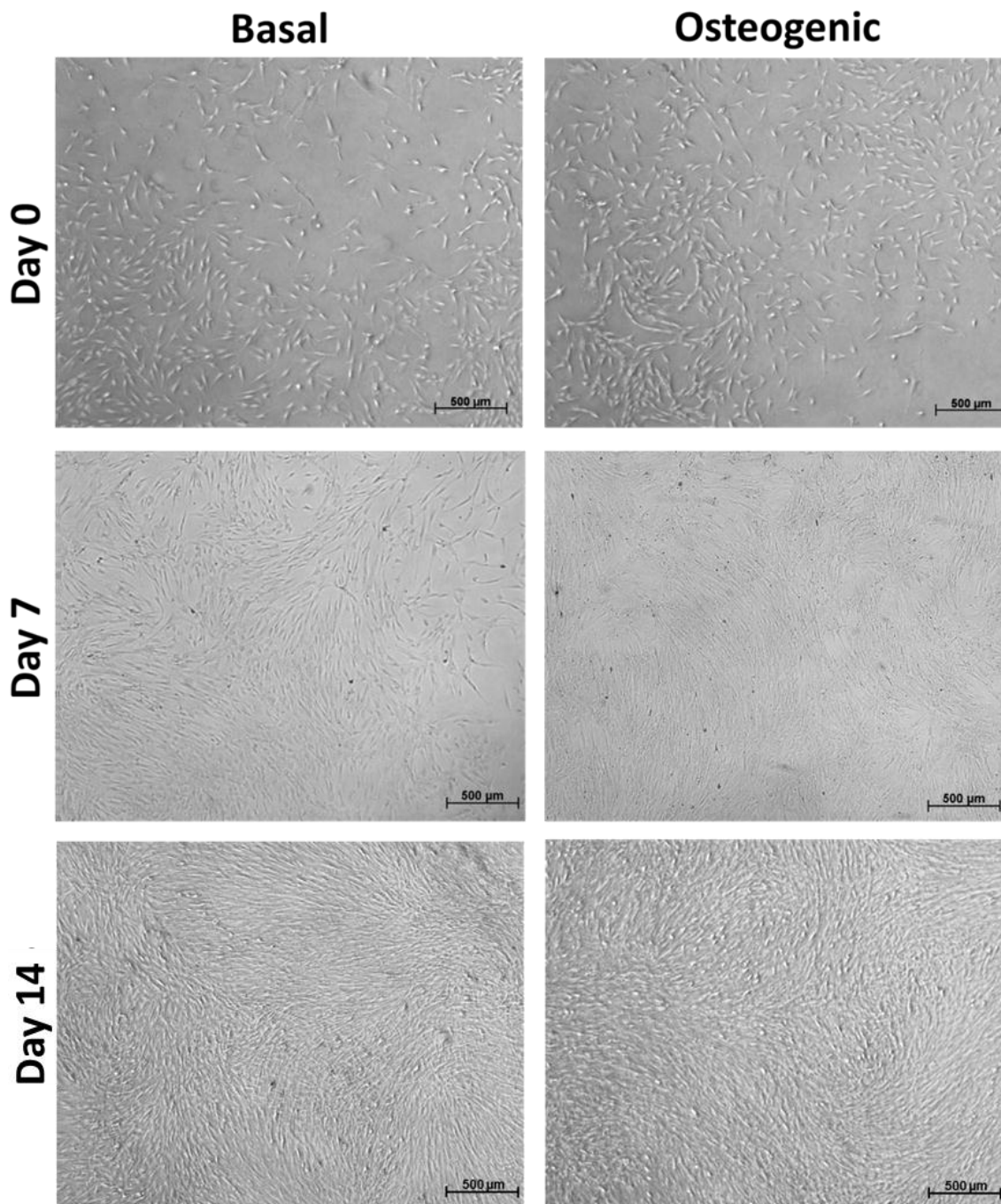


Figure 8.1: Photomicroscopy of HBMSCs in basal and osteogenic media at day 0, day 7 and day 14 from the start of differentiation (11 days after seeding). Scale bars represented 500 µm.

However as SYBR green was not DNA specific quality checks were confirmed by analysis of melt temperature. The expression values were normalised for each gene for the basal condition (which was the reference sample). In this experiment, the basal sample was set as reference. Each reaction was performed in duplicate. RT-PCR was performed using a 96 well plate. Reaction consisted of 12.5 µl of 2xSYBR green master mix, 2.5 µl of 5 µM forward primer, 2.5 µl of 5 µM reverse primer, 6.5 µl of ultra-pure water and 1 µl of cDNA.

The total volume was 25 μ l per well. The assignment of one or more housekeeping genes was necessary, which were assumed to be uniformly and constantly expressed in all samples, as well as in the reference samples. The expression of test samples was then compared to that in the reference sample [81].

Table 8.1: List of real time primers used in this study with sequences (Developed by Dr Rahul Tare, Bone and Joint Research Group).

Primers	Sequences	
	Forward	Reverse
B-actin	ggcatcctcaccctgaagta	aggtgtggtgccagatttc
Runx2	gtagatggacctcggaacc	gaggcggtcagagaacaac
ALP	ggaactcctgacccttgacc	tcctgttcagctcgtactgc
Col1a1	gagtgtctgtcccgtctgc	tttcttggtcgggtgggtg
Osteocalcin	ggcagcgaggtagtgaagag	ctcacacacctccctcct

8.3 Results

Figure 8.1 shows primary (Passage 0) HBMSCs in basal and osteogenic conditions at day 0, day 7 and day 14. Good cell growth was observed in basal and osteogenic conditions.

8.3.1 Histological and Biochemical Analysis

The ALP staining procedure was performed at day 7 and day 14. Figure 8.2A shows an overview of a 6 wells plate stained for ALP. The first and the second rows were seeded with HBMSCs cultured under basal and osteogenic condition, respectively. As can be seen in Figure 8.2, extensive and enhanced ALP expression was observed at day 7 in osteogenic (Figure 8.2C) compared to basal samples (Figure 8.2B). Similar results were obtained for HBMSCs cultured for 14 days and examined for ALP expression with higher ALP expression evident in osteogenic samples compared to basal samples (Figure 8.2E).

Both ALP analysis and ALP Specific Activity highlighted a lower level of ALP activity for HBMSCs cells cultured under basal conditions than those grown under osteogenic conditions for both time points examined. Figure 8.3 and Figure 8.4 show the results of these two assays, illustrating extensive and significantly enhanced alkaline phosphatase expression in osteogenic conditions compared to basal conditions.

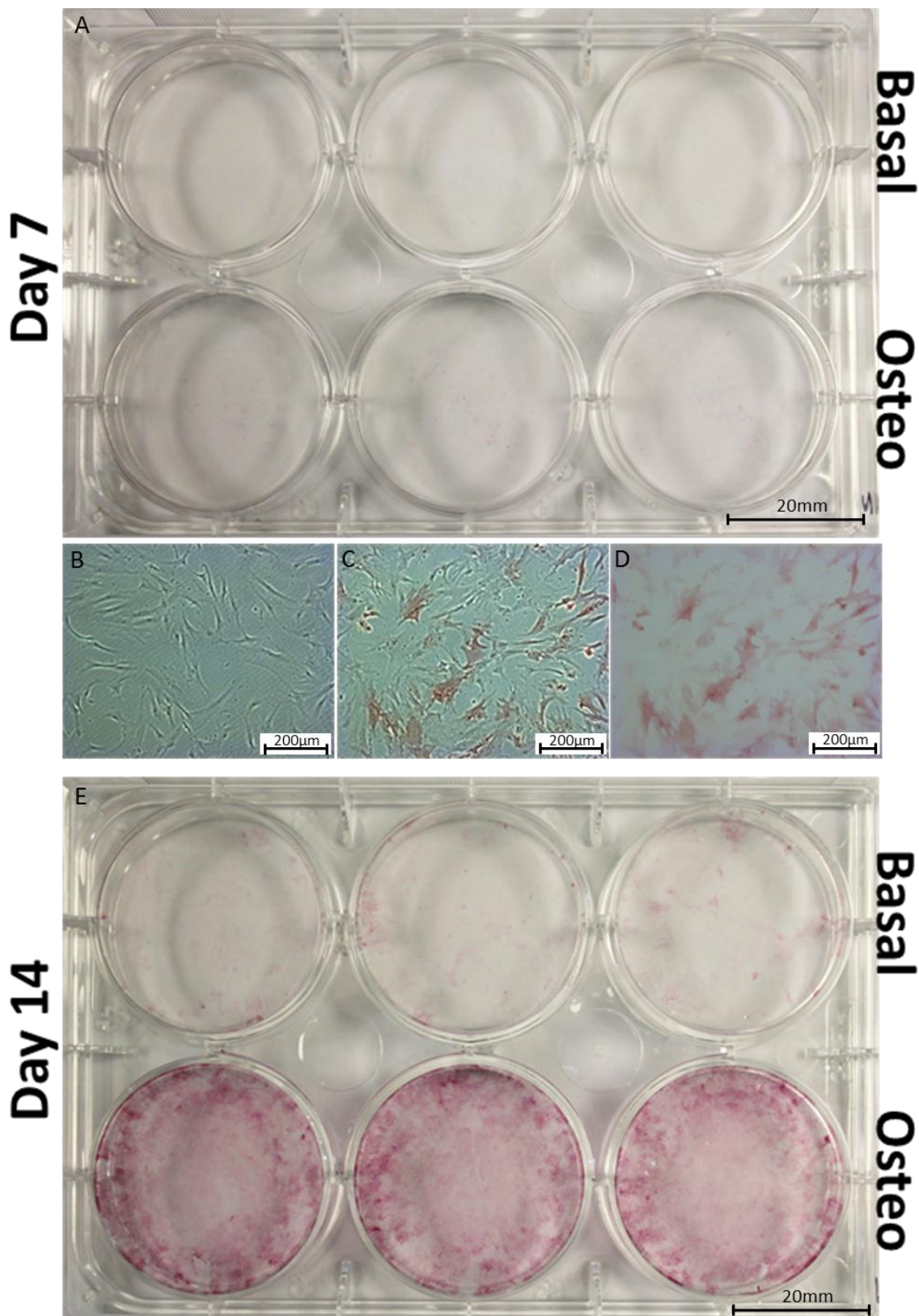


Figure 8.2: (A) ALP staining at day 7 and (E) day 14 for Basal and Osteogenic samples. (B) Photomicroscopy of HBMSCs under basal condition a day 7. (C) Photomicroscopy of HBMSCs maintained in osteogenic conditions at day 7 and (D) through a H/DIC (Differential Interference Contrast) filter. Samples were run in triplicate. Scale bars represented 20 mm and 200 µm.

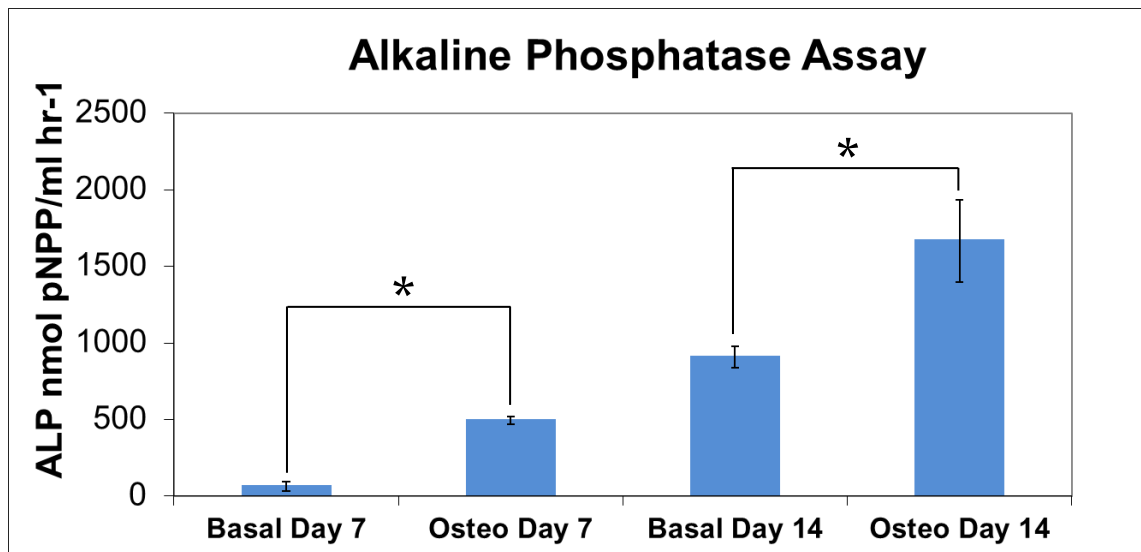


Figure 8.3: ALP assay performed for HBMSCs after 7 days and 14 days of differentiation under basal and osteogenic conditions. Results expressed as mean \pm SD and $n = 3$. * $P < 0.05$ calculated using t -test.

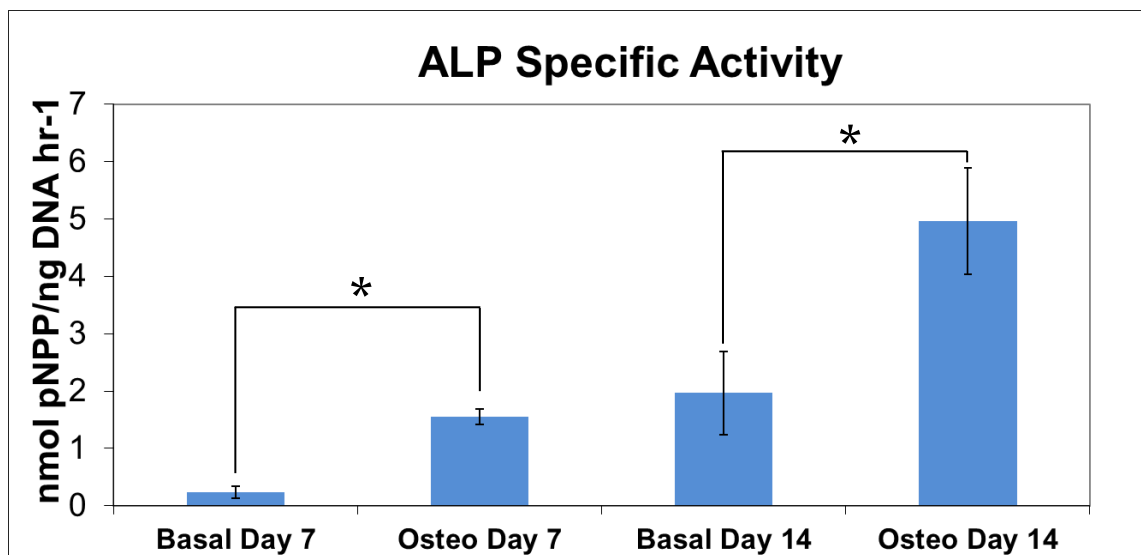


Figure 8.4: ALP Specific Activity for HBMSCs after 7 days and 14 days of differentiation under basal and osteogenic condition (incubation time 40 min). Results expressed as mean \pm SD and $n = 3$. * $P < 0.05$ calculated using t -test.

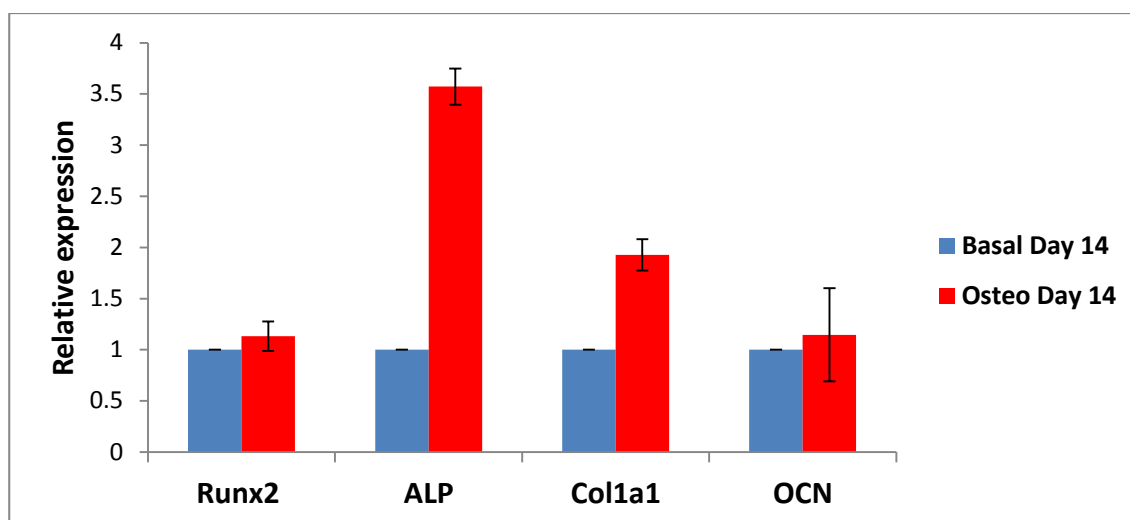


Figure 8.5: Real time PCR quantification for HBMSCs cultured under basal and osteogenic conditions for 14 days (n=2). The values were normalised for the basal condition for each gene. Results expressed as average \pm SD and n = 2.

8.3.2 Molecular Analysis

Real time PCR was employed to assess transcriptional differences in gene expression profiles between cells cultured under basal and osteogenic conditions after 14 days. β -actin was used as housekeeping gene, with Runx2 and ALP as early osteogenic genes, Col1a1 and Osteocalcin as late stage genes. The RT-PCR reaction was performed in duplicate for each sample and each primer.

Runx2 expression exhibited a modest difference between cultures in basal and osteogenic condition (Figure 8.5). However, osteogenic samples showed significantly enhanced ALP expression and strong Col1a1 expression compared with basal samples.

No significant differences were observed in osteocalcin expression between cultures maintained in basal and osteogenic conditions. This was likely a consequence of the short culture period employed (Osteocalcin was expressed late in differentiation) and absence of vitamin D in the culture medium.

8.4 STRO-1 positive cells characterisation

HBMSCs were isolated from samples obtained from a haematologically normal (absence of blood related diseases) patient, undergoing routine total hip replacement surgery.

To sort SSCs, the antigen used was the STRO-1 a routinely used SSC marker. The STRO-1 positive (STRO-1+) fraction was isolated using MACS (see Appendix N) and cultured under basal conditions for 10 days to expand the STRO-1+ cell population isolated.

After this period, the cell population was trypsinised (P0→P1) and split into two subpopulations which were seeded (220 cells/cm²) and cultured under basal and osteogenic conditions for 21 days, respectively. Media was changed twice weekly throughout the culture period. Samples were analysed after 7, 14 and 21 days from the start of differentiation. Photomicroscopy of Passage 1 STRO-1+ cells in basal and osteogenic media were taken at each time point (Figure 8.6). Cells seeded in plates were fixed in 95% ethanol for ALP staining at days 7, 14 and 21.

Results obtained demonstrate enhanced expression of ALP in cells maintained under osteogenic conditions, at each time points compared to the basal conditions. ALP expression at 7 days was relatively modest in the osteogenic samples but still higher compared to the basal sample (Figure 8.7). RT-PCR was used to investigate transcriptional differences in gene expression profiles between cells cultured under basal and osteogenic conditions for the three time points. The real time primers used in this study were reported in Table 8.1. As in the previous study, β -actin was used as housekeeping gene, with Runx2 and ALP as early osteogenic genes, Col1a1 and Osteocalcin as late stage genes. The RT-PCR reaction was performed in duplicate for each sample and each primer. The values in Figure 8.8 were normalised for the expression obtained from the sample under basal conditions at day 7 for each gene. Only Runx2 expression was noted to be higher in osteogenic samples in comparison to basal cultures (Figure 8.8A).

No significant differences were observed in Runx2 expression over time in basal or osteogenic cultures. In contrast, marked differences were observed in ALP expression between cells maintained in basal compared to osteogenic conditions with enhanced expression following culture in osteogenic conditions.

On the other hand, an important difference was observed in the ALP expression between the two conditions. Osteogenic samples showed higher ALP expression than the basal sample in particular at day 14, where the ALP expression in the osteogenic sample was almost four times higher than in the other culture condition.

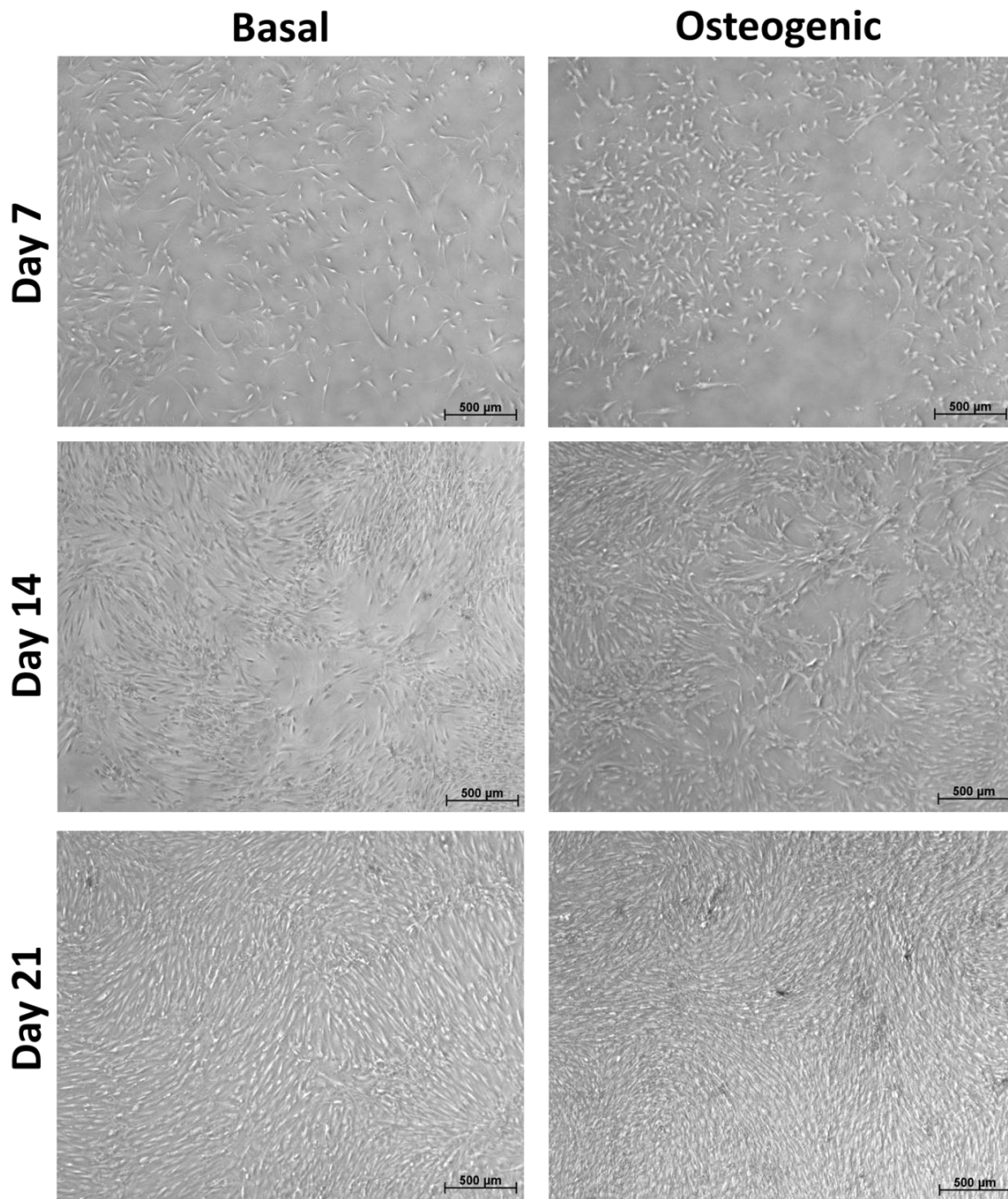


Figure 8.6: Photomicroscopy of P1 STRO-1+ cells in basal and osteogenic media at day 7, day 14 and day 21 from the start of differentiation (10 days from the seeding operation). Scale bars represented 500 μm.

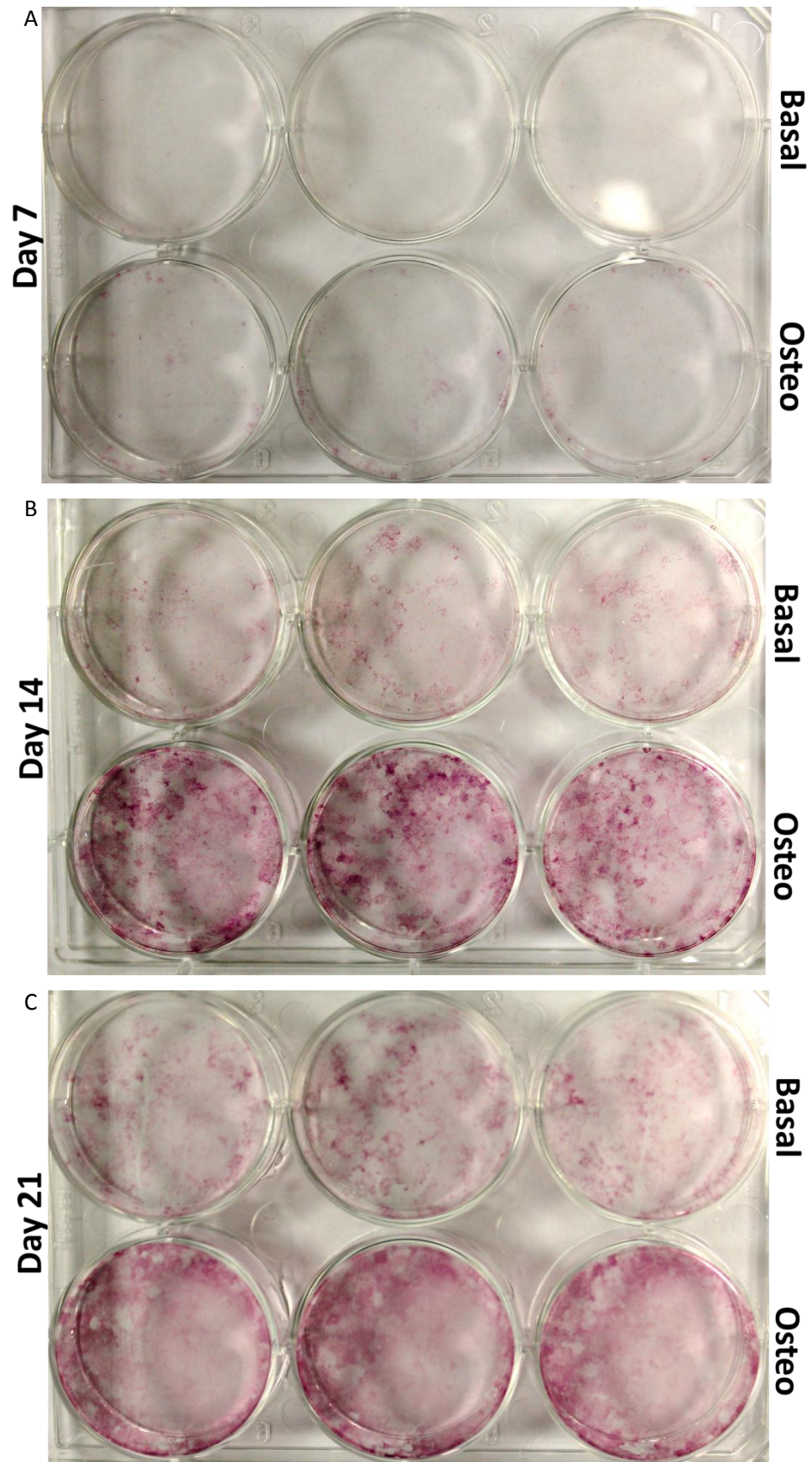


Figure 8.7: (A) ALP staining at day 7, (B) day 14 and (C) day 21 for Basal and Osteogenic samples. Samples were run in triplicate.

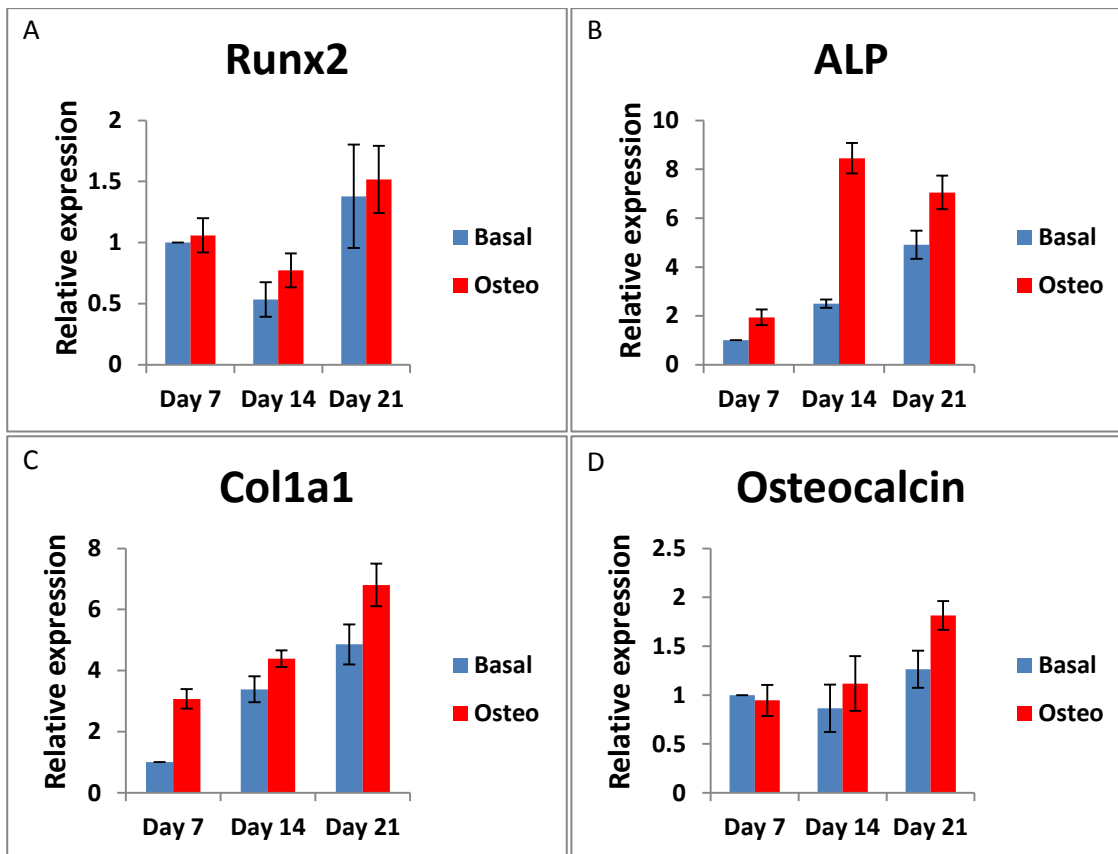


Figure 8.8: RT-PCR quantification for STRO-1+ cells cultured under basal and osteogenic conditions for 21 days. The values were normalised for the condition basal at day 7 for each gene. Results expressed as average \pm SD and $n = 2$.

Col1a1 and Osteocalcin exhibited higher expressions in samples under osteogenic condition compared with basal samples. In particular in the third time point, where the difference between the two conditions was more evident according to the late stage nature of the genes in question. The molecular analyses confirmed the well know differentiation ability of the STRO-1+ [82].

8.5 Conclusion

In this chapter the isolation, differentiation and characterisation of HBMSCs and STRO-1+ cells was examined.

Primary HBMSCs, which comprise the heterogeneous population of cultured TCP adherent cells isolated from BM, were isolated from samples obtained from a haematologically normal (absence of blood related diseases) patient, undergoing routine total hip replacement surgery, and cultured under basal condition for 11 days [20]. ALP expression investigated at two time points (day 7 and day 14) using histological and biochemical analysis demonstrated significantly higher ALP expression in cell populations maintained under osteogenic conditions. Moreover, RT-PCR confirmed the histological and biochemical data sets.

STRO-1+ cells were isolated from HBMSCs using traditional sorting technique (MACS), cultured under the same conditions as unsorted HBMSCs (basal and osteogenic) and characterised after 7, 14 and 21 days of differentiation (this study was performed at Passage 1). The results revealed a higher expression of ALP in the osteogenic cultures in both histological and molecular analysis, revealing a further stage in the osteogenesis process [80].

The analyses performed on the HBMSCs and STRO-1+ cell populations, revealed a higher differentiation potential expressed by the STRO-1+ cells. Both cell populations were split and cultured under basal and osteogenic conditions. The HBMSCs cultured under osteogenic conditions exhibited an ALP expression (at day 14) ~3.5 fold greater than in basal culture. Under the same circumstances the STRO-1+ cells cultured under osteogenic conditions exhibited an ALP expression ~4 fold greater than in basal culture.

Overall, the STRO-1 cell population exhibited greater differences in the genes expression (across the entire range of genes investigated) between samples cultured under basal and osteogenic conditions compared with the HBMSC cell population, revealing a higher differentiation potential. These results were expected and highlighted a higher differentiation potential of the STRO-1+ cell fraction compare to the HBMSCs [83,84]. The STRO-1+ cell fraction of BM (although heterogeneous), was capable of establishing an adherent proliferative cell layer in vitro with colony-forming unit-fibroblastic (CFU-F) potential, a prerequisite of SSCs. The higher differentiation potential expressed by the STRO-1+ cell population was strategic for tissue engineering strategies.

Chapter 9

Device characterisation and comparison with MACS

In Chapter 8 the differentiation potential of isolated cells under different *in vitro* conditions was examined. HBMSCs and STRO-1 positive cells were cultured under basal and osteogenic conditions and ALP expression examined. The STRO-1+ cell fraction was isolated from the HBMSC population using a standard cell sorting technique - MACS. This chapter describes the isolation of STRO-1+ cells from BM samples using both a MACS approach as well as a sorting device developed in this study. The performances of the two techniques were compared to evaluate purity and recovery efficiency of the sorted cells. The STRO-1+ cells isolated with the two techniques were cultured under basal and osteogenic conditions and characterised using histological and molecular analyses.

9.1 Experiment design

Tests were run to investigate the sort capacity of the developed device in comparison to the application of MACS. Three BM samples obtained from haematologically normal patients were processed. STRO-1+ cells were isolated from each sample using both techniques. The experiment was implemented in three steps: 1) STRO-1+ cell isolation using sort strategies; 2) negative and positive fractions analysis and 3) STRO-1+ cells differentiation and characterisation.

9.1.1 STRO-1 positive cells sorting

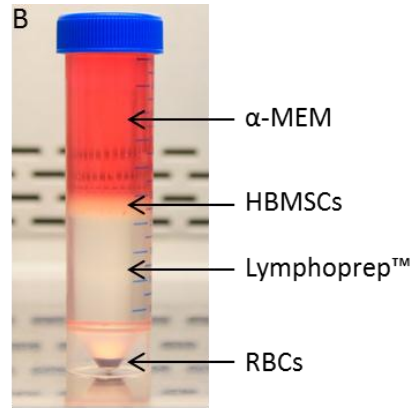
The BM samples (Figure 9.1A) were processed using the methods described in Section 8.1.1. HBMSCs were isolated from each BM sample using density gradient centrifugation (Figure 9.1B).

HBMSCs isolations from bone marrow sample



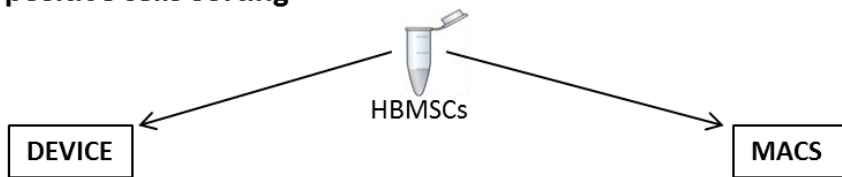
A Bone marrow sample

Density gradient centrifugation



STRO-1 positive cells sorting

C



HBMSCs + Functionalised beads

HBMSCs + STRO-1 antibodies + MACS beads

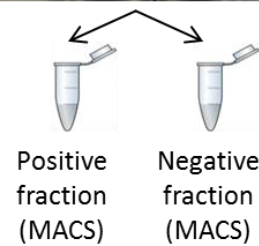
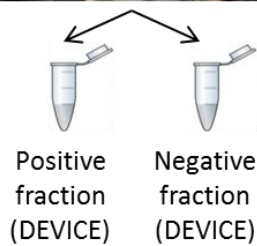
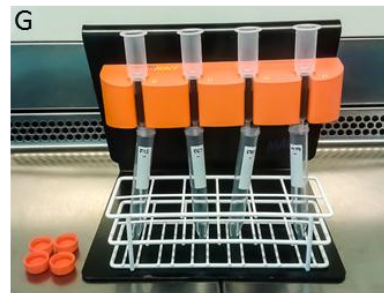
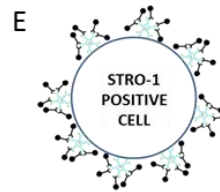
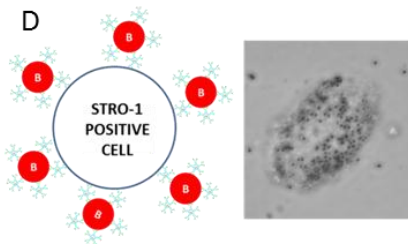


Figure 9.1: (A) Bone marrow sample. (B) HBMSCs were isolated using density gradient centrifugation. (C) HBMSC populations were divided in two to enable processing with the sort device and MACS. (D) HBMSCs were labelled with functionalised beads and (F) processed through the device. (E) HBMSCs labelled with MACS beads (two-step process) and (G) treated with MACS.

The HBMSCs were suspended in blocking buffer (PBS + 0.5% BSA + 2 mM EDTA + 3% goat serum) and incubated for 15 min at 4 °C. The HBMSCs population was then divided in two to be processed with the MACS and the sorting device (Figure 9.1C).

The HBMSCs to be treated with the sorting device were incubated with CM-08-10 (\varnothing 0.82 μ m - Spherotech, Inc, USA) superparamagnetic beads functionalised with mouse monoclonal IgM anti-human STRO-1 primary antibody (Hybridoma) (see Section 6.2.1) for 30 min at 4 °C; the suspension was mixed every 10 min (Figure 9.1D). After two washes with MACS buffer (PBS + 0.5% BSA + 2 mM EDTA), the cells were run through the sorting device (ver. 3.5 using the hexapole magnetic system to create the magnetic field) and the positive (containing STRO-1+ cells) and negative (containing STRO-1- cells) fractions were recovered (Figure 9.1F). The sample concentration used was 10^6 cells/ml and the flow rates used were 2000 μ l/min for the buffer input and 500 μ l/min for the sample input (see Section 7.1 for experimental details). The experimental protocol lasted 85 min, excluding the isolation of HBMSCs from the BM sample and the application of blocking buffer.

The HBMSCs to be treated with the MACS were incubated with mouse monoclonal IgM anti-human STRO-1 primary antibody (Hybridoma) for 30 min at 4 °C; the suspension was mixed every 10 min. After three washes with MACS buffer, the HBMSCs were incubated with rat polyclonal IgG anti-mouse IgM magnetic microbeads conjugated (\varnothing 50 nm - Miltenyi Biotec, Germany) for 30 min at 4 °C; the suspension was mixed every 10 min (Figure 9.1E). After three washes with MACS buffer the cells were run through the MACS column and the positive (containing STRO-1+ cells) and negative (containing STRO-1- cells) fractions were recovered (Figure 9.1G). The experimental protocol lasted 110 min excluding the isolation of HBMSCs from the BM sample and the application of blocking buffer (see section 2.1).

At the end of each experiment, 4 aliquots were collected: i) positive fraction (DEVICE), ii) negative fraction (DEVICE), iii) positive fraction (MACS) and, iv) negative fraction (MACS).

9.1.2 Negative and positive fraction analysis

In order to compare the isolation ability of the MACS and the sorting device, it was paramount to determine the purity of the negative and positive fractions recovered using each technique. To do so, the percentage of STRO-1+ cells in each sample was quantified. A sample from each fraction (including the original unsorted sample: HBMSCs suspension) was collected (Figure 9.2A).

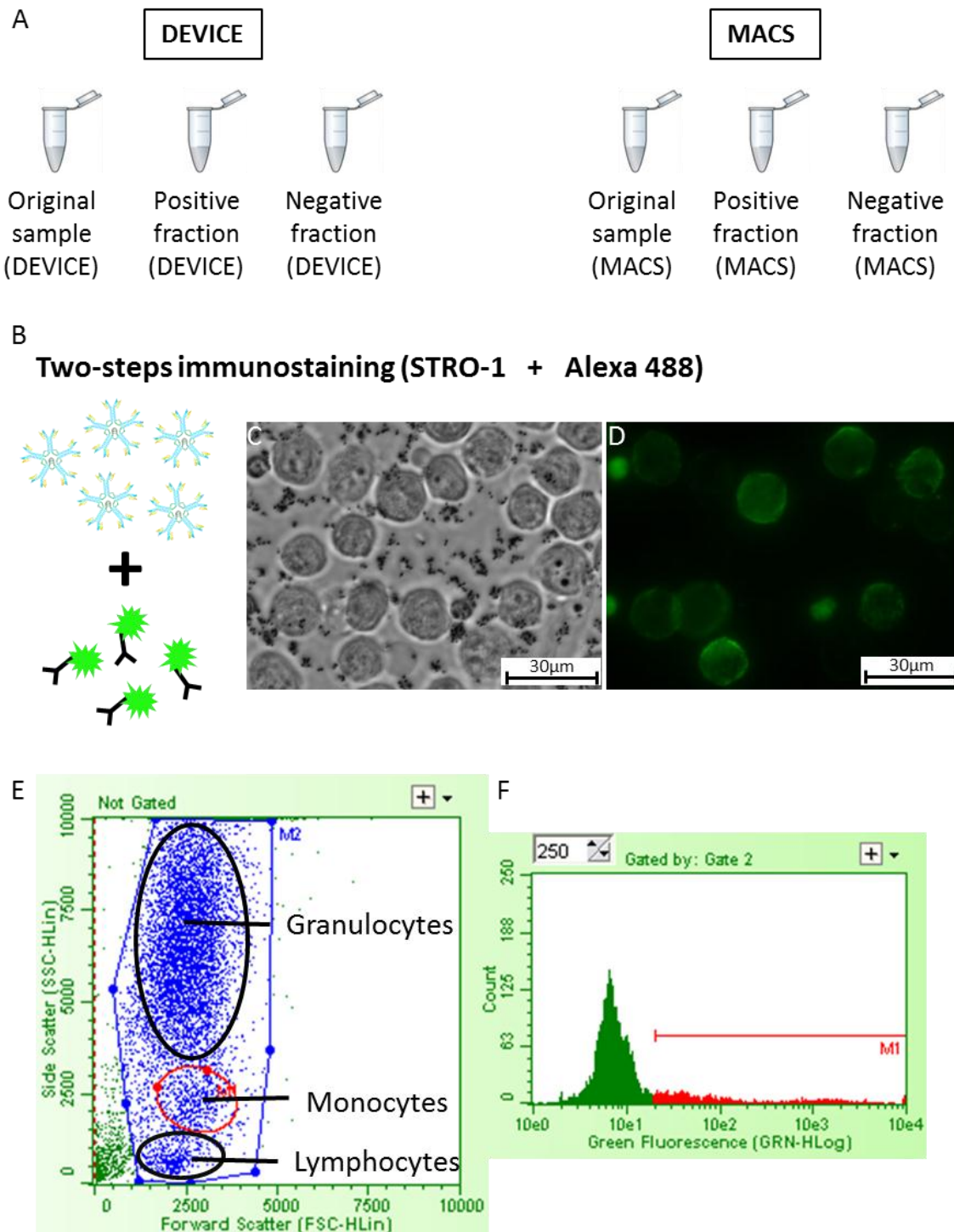


Figure 9.2: (A) Samples collected from each fraction. (B) Sample for immunostaining (STRO-1 + Alexa Fluor 488). (C) Bright field and (D) fluorescence microscopy of HBMSCs collected from the positive fraction (DEVICE). (E) Flow cytometry scatter plot and (F) histogram of HBMSCs immunostained for STRO-1 expression; only the monocytes (red circle) were gated to derive the histogram plots. Scale bars represented 30 μm .

The samples were washed five times with PBS, to enable detachment of most of the beads from the cell surface (Figure 9.2C) and fixed by suspension in ethanol (95%). Then a two-step immunostaining process was performed on each sample to determine STRO-1 expression. The fixed cells were incubated with STRO-1 primary antibody and then with a fluorescent secondary antibody (goat polyclonal IgG anti-mouse IgM Alexa Fluor 488 conjugated) (Figure 9.2B).

Figure 9.2C bright field image of HBMSCs collected from the positive fraction (DEVICE) following immunostaining. Superparamagnetic beads can be observed (even after several washes) although the beads were in suspension and were not bound to the cell surface due to the washing step. The same sample observed under fluorescence microscopy confirmed the presence of STRO-1+ cells (Figure 9.2D). Although the functionalised beads in solution were also bound by the fluorescent secondary antibodies, the beads were not visible in the captured images as the level of brightness was set to illustrate fluorescent cells only.

To determine the percentage of STRO-1+ cells in each aliquot, samples were analysed using a flow cytometer (Guava EasyCyte Mini - Merck Millipore, Germany).

Analysis revealed the percentage of STRO-1+ cells in the original sample and the percentage of STRO-1+ cells in the negative and positive fraction following isolation by MACS or with the sorting device.

Figure 9.2E shows a flow cytometry scatter plot of HBMSCs stained for STRO-1 expression. Three main groups of cells were recognisable: granulocyte, monocyte and lymphocyte fractions. For this study, only the monocytes were gated and contributed to the recorded percentages of STRO-1+ cells. Figure 9.2F shows a fluorescence intensity histogram of the gated monocyte population in the sample. A fluorescent intensity threshold (red line in Figure 9.2F) was set to define the minimum fluorescent intensity required to demonstrate a STRO-1+ cell. The threshold was set according to the appropriate negative control not shown in the figure.

9.1.3 Cell differentiation and characterisation

Following sorting of the cell fractions, the *in vitro* differentiation potential of the cells recovered from the positive fraction (DEVICE) (Figure 9.3A) and positive fraction (MACS) (Figure 9.3B) was investigated. The two cell populations were seeded separately and cultured under basal conditions (α -MEM, 10% FCS, P/S) for 10 days. Each sample was then divided (P0→P1) in half and cultured under both basal and osteogenic conditions (α -MEM, 10% FCS, P/S, 10 nM Dexamethasone and 100 μ M Ascorbate-2-Phosphate).

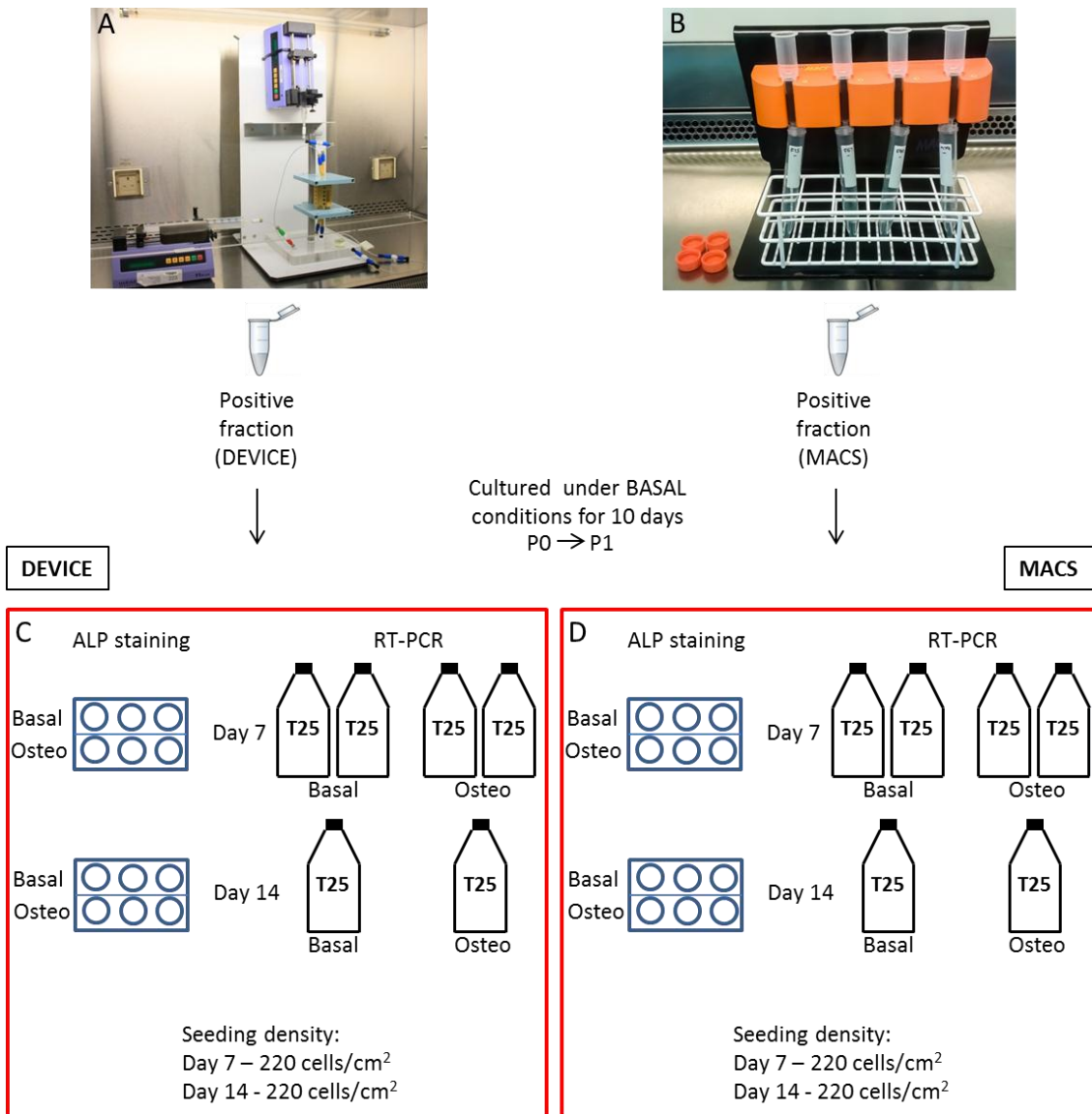


Figure 9.3: (A) The positive fraction (DEVICE) and (B) the positive fraction (MACS) were cultured in basal media for 10 days and then each cell populations was seeded (P0→P1) in six wells plates and flasks as illustrated in C and D.

Table 9.1: List of real time primers used in this study and corresponding sequence (Developed by Dr Rahul Tare, Bone and Joint Research Group).

Primers	Sequences	
	Forward	Reverse
B-actin	ggcatcctcaccctgaagta	aggtgtggtgccagatttc
Runx2	gtagatggacctcggaacc	gaggcggtcagagaacaac
ALP	ggaactcctgacccttgacc	tcctgtcagctcgactgc
Col1a1	gagtgtgtcccgtctgc	tttcttggtcggtgggtg
Osteocalcin	ggcagcgaggtagtgaagag	ctcacacacctccctcct

The media was changed twice weekly. Time points for this study were 7 and 14 days from the start of differentiation. The two cell populations were seeded as detailed in Figure 9.3C and D. At each time point histological (ALP staining) and molecular (RT-PCR) analyses were performed (see Section 8.2).

9.2 Results

The sorting capacity and efficiency of the MACS and device were compared, analysing samples from the positive and negative fractions recovered from the sorting device and the MACS. Thereafter, the differentiation potential of the two cell populations was investigated.

9.2.1 Negative and positive fraction analysis: results

The HBMSCs isolated from the BM sample were divided in two, to be processed using the MACS and sorting device. Before the sorting experiments, two samples from the original HBMSCs suspensions were collected to assess the initial percentages of STRO-1+ cells and STRO-1 negative (STRO-1-) cells present, and thus provide baseline data. Following sorting, samples were collected from: the negative fraction (DEVICE), positive fraction (DEVICE), negative fraction (MACS), positive fraction (MACS).

The performances of MACS and device were compared according to:

- purity of the negative fraction;
- purity of the positive fraction;
- recovery efficiency of the negative fraction;
- recovery efficiency of the positive fraction.

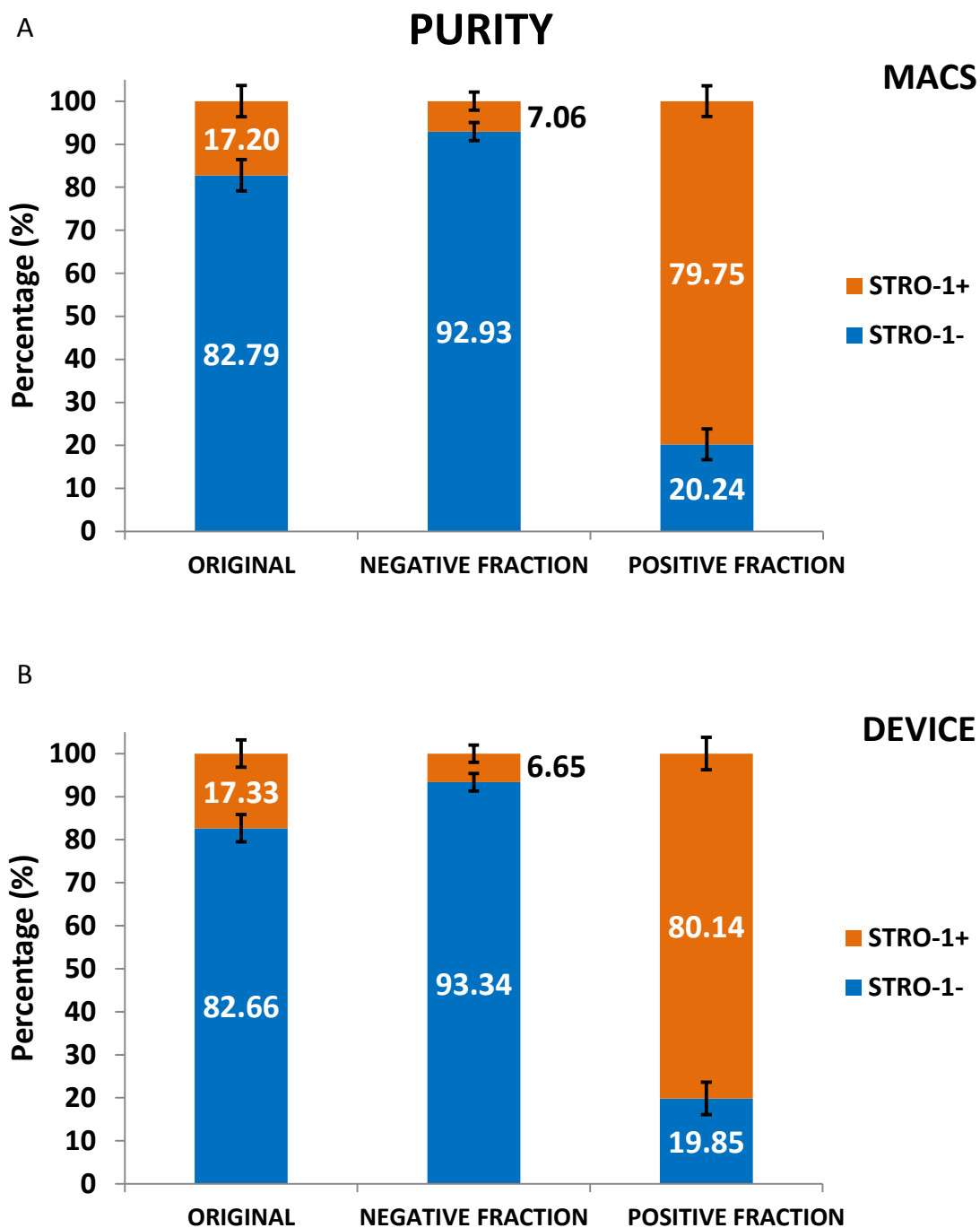


Figure 9.4: (A) Bar chart illustrating the composition of the original sample, negative fraction and positive fraction recovered from MACS and (B) sorting device. Results expressed as mean \pm SD and from $n = 9$.

To measure these parameters, the six samples collected were immunostained to determine STRO-1 expression and analysed using a flow cytometer (three readings for each sample) as described in Section 9.1.2.

9.2.1.1 Purity

The desired outcome from the sorting experiment was to collect 100% of STRO-1⁻ cells in the negative fraction and 100% of STRO-1⁺ cells in the positive fraction.

The performances of the MACS and the sorting device were assessed in comparison to the known initial percentages of the STRO-1⁺ and STRO-1⁻ cells present in the original samples. Figure 9.4 shows bar charts detailing the average values of purity achieved by the MACS (Figure 9.4A) and the device (Figure 9.4B) after the sorting experiments.

The charts summarise the purity percentages resulting from the three BM samples processed with the MACS and the device. For each sorting technique, three replicate measurements per each BM sample were obtained from the original samples (total of nine values), the positive fractions (nine values) and the negative fractions (nine values).

The analysis of the original samples revealed that ~17% of the HBMSCs population expressed STRO-1 antigen (STRO-1⁺ cells). This percentage remained consistent ($\pm 3\%$) across the three BM samples.

The composition of the cell populations in the negative fractions collected from MACS and device were almost identical, with ~93% STRO-1⁻ cells and ~7% of STRO-1⁺ cells. As the ideal outcome was to collect only STRO-1⁻ cells in the negative fraction, the presence of STRO-1⁺ cells in the samples remains an area for further improvement.

The negative fraction could be contaminated with STRO-1⁺ cells as a result of various reasons including the accidental removal of STRO-1⁺ cells from the MACS column during the washing step of the protocol resulting in cross contamination.

For the sorting device, a likely explanation for the contamination was the discordance between the fluorescence threshold of the flow cytometer and the sorting device, as discussed in section 7.7.

The cell population collected from the positive fractions of both MACS and device resulted in approximately 80% of STRO-1⁺ cells and approximately 20% of STRO-1⁻ cells. As in the negative fractions, some contamination of labelled and non-labelled cells was observed.

In the case of MACS, once again the impurity in the positive fraction was likely a consequence of the intrinsic working principle of the technique. The MACS isolates the STRO-1⁺ cells by trapping them within the column surrounded by a permanent magnet.

The technique relies on the washing step of the protocol to remove the STRO-1⁻ cells from the column by rinsing in MACS buffer, and then collecting the STRO-1⁻ cells in the negative fraction. The 20% of STRO-1⁻ cells consistently found in the positive fraction was evidence that unspecific contact occurred within the MACS column, with a number of STRO-1⁻ cells resisting the washing step and then being collected in the positive fraction.

Table 9.2: Summary of purity achieved by MACS and the sorting device. The first row indicates the composition of the original samples (orange STRO-1+ cells; blues STRO-1- cells); the following rows the composition of the negative and positive fractions collected from MACS and sorting device after the sorting protocol.

	PURITY (%)			
	MACS		DEVICE	
ORIGINAL	17.20±3.6	82.79±3.6	17.33±3.2	82.66±3.2
NEGATIVE FRACTION	7.06±2.1	92.93±2.1	6.65±2	93.35±2
POSITIVE FRACTION	79.75±3.5	20.24±3.5	80.15±3.7	19.85±3.7

In the case of the device, the reasons of the contamination of the positive fraction with STRO-1- cells could have been a consequence of cell clumping. The sorting step of the experimental protocol typically lasted for 40 min (considering $\sim 20 \times 10^6$ HBMSCs to be processed with a sample concentration of 10^6 cells/ml and a sample flow rate of 500 $\mu\text{l}/\text{min}$).

This length of time could favour cell clumping, and labelled (STRO-1+) and unlabelled cells (STRO-1-) could potentially clump together. In such a case, the entire clump of cells would be influenced by the magnetic field applied and would be collected into the device positive fraction output. To limit this phenomenon a reduction of the sorting time would be required. This could be achieved by increasing the sample concentration or increasing the sample input flow rate. However, the first solution was undesirable: increasing the sample concentration and consequently decreasing the sample volume would increase the possibility of clumping. The second solution would be possible by increasing the magnetic force experienced by the magnetically labelled cells, but only after a modification of the magnetic system. The purity values obtained by MACS and sorting device were summarised in Table 9.2.

9.2.1.2 Recovery Efficiency

The second parameter investigated to compare MACS and the sorting device was the recovery efficiency. The flow cytometer measured the cell density for each sample analysed; knowing the volume of each fraction collected from the two techniques it was possible to estimate the number of cells in each fraction (including the number of cells in the original sample).

Figure 9.5 shows bar charts reporting the average number of cells recovered in the negative and positive fractions of MACS (Figure 9.5A) and sorting device (Figure 9.5B) after the sorting experiments. As per the purity analysis, the values of recovery efficiency plotted resulted from the 3 BM sample processed with the MACS and the device. For each sorting technique, 3 replicate measurements (with the flow cytometer) per each BM sample were obtained from the original samples (total of 9 values), the positive fractions (9 values) and the negative fraction (9 values).

In Figure 9.5 the number of cells in each sample was reported. The first bar in each graph represented the number of HBMSCs in the original samples, which was approximately 20×10^6 for the MACS and 18.9×10^6 for the sorting device. The other bars report the number of cells recovered respectively from the negative and positive fractions. Both MACS and sorting device collected circa 16×10^6 cells (15.34×10^6 for MACS and 15.99×10^6 for device) in the negative fraction. The most significant difference was observed in the positive fractions: the MACS collected 1.21×10^6 cells, while the device collected 2.54×10^6 cells. The device recovered more than twice the amount of cells in the positive fraction compared to the MACS with the same purity. Considering the two fractions together, the MACS recovered 16.55×10^6 cells; thus 3.53×10^6 cells (approximately 17.5% of the original number of cells) were not collected in either fraction and remained in the MACS columns. To investigate this aspect, the used MACS columns were purged twice with MACS buffer and the liquid recovered subsequently analysed. Even after the purging only 19.7% of the missing cells were found. This was due to a poor efficiency in removing trapped cells from the MACS columns during the step with the plunger.

In contrast, the sorting device collected all the cells processed, minus 400,000 cells (approximately 2.5% of the original number of cells). The aim of this study was to assess the number of STRO-1+ cells sorted by the MACS and the device. The recovery efficiency was defined as the ratio between the number of STRO-1+ cells recovered from the positive fraction compared to the number of STRO-1+ cells present in the original sample. The bar chart in Figure 9.6A reports the numbers of STRO-1+ cells in the original sample, negative fraction and positive fraction of MACS and sorting device. The number of STRO-1+ cells in the original samples of the two techniques was similar (3.45×10^6 for the MACS and 3.27×10^6 for the sorting device). The same was observed for the negative fractions of the two techniques (1.08×10^6 for the MACS and 1.06×10^6 for the sorting device). Both techniques incorrectly sorted circa 10^6 STRO-1+ cells, which were collected in the negative fraction and were consequently discarded. The difference between MACS and the sorting device was clearer on analysis of the positive fraction.

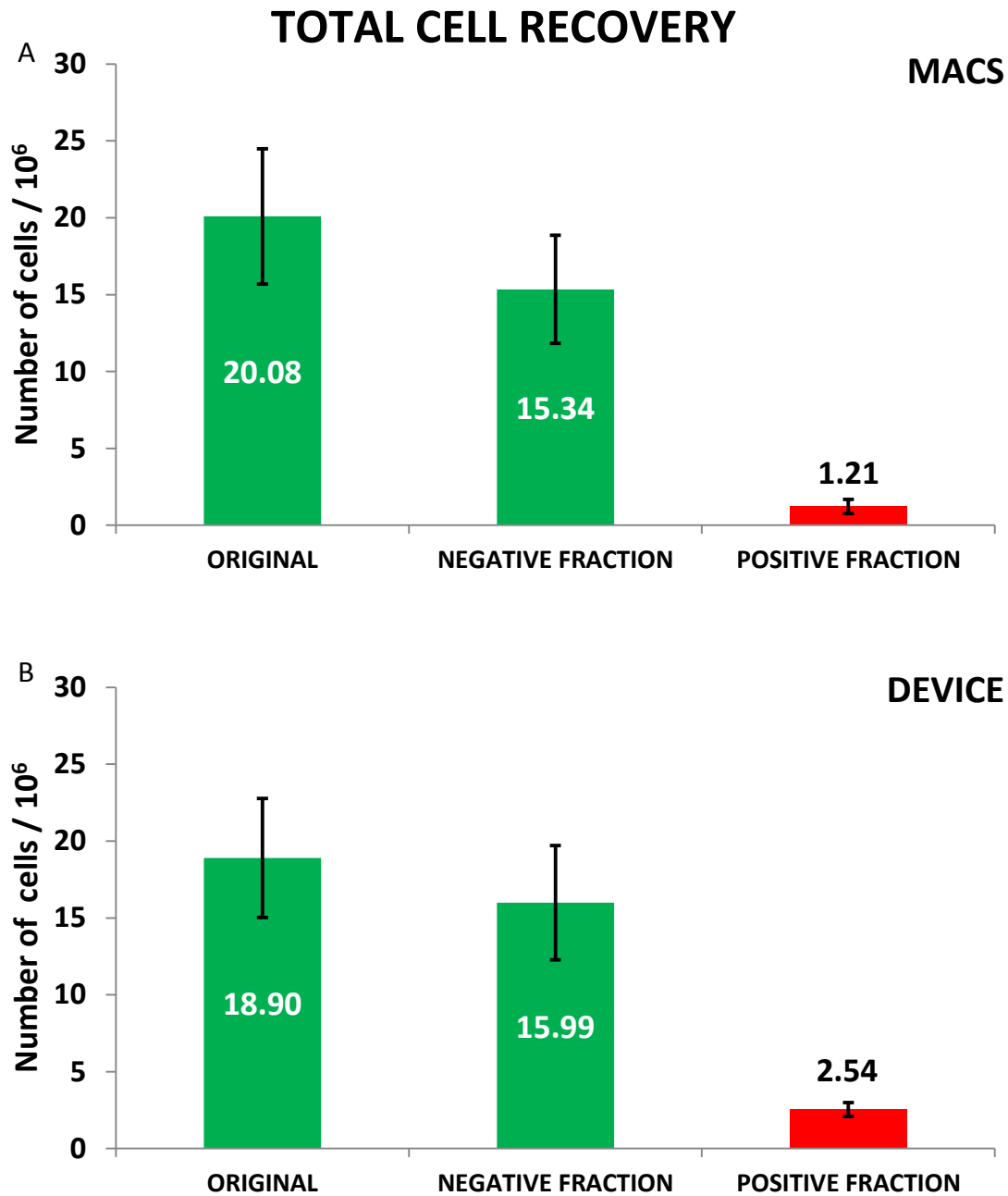


Figure 9.5: (A) Bar charts illustrating the total number of cells in the original sample, negative fraction and positive fraction recovered from MACS and (B) sorting device. The device collected more than twice the amount of cells in the positive fraction (in red) compared to the MACS with equal purity. Results expressed as mean \pm SD and $n = 9$.

While the purity obtained by MACS and the sorting device was comparable (Figure 9.4), the number of STRO-1+ cells recovered from the positive fraction of the device (2.04×10^6 STRO-1+ cells) was more than twice what observed in the positive fraction of the MACS (0.97×10^6 STRO-1+ cells).

Table 9.3: Summary table of recovery efficiency for MACS and sorting device (mean values $n=3 \pm SD$). In red the total number (in million) of cells recovered from the positive fractions of the two techniques. In blue the percentages of STRO-1+ cells contained in the original samples recovered from the positive fractions of the two techniques.

	RECOVERY EFFICIENCY (million cells)					
	MACS			DEVICE		
	Total	STRO-1+ cells		Total	STRO-1+ cells	
ORIGINAL	20.08±4.4	3.45±0.7	100%	18.90±3.8	3.27±0.6	100%
NEGATIVE FRACTION	15.34±3.5	1.08±0.3	31.36%±9.3%	15.99±3.7	1.06±0.3	32.41%±9.8%
POSITIVE FRACTION	1.21±0.4	0.97±0.04	28.12%±1.2%	2.54±0.4	2.04±0.09	62.38%±2.9%

As a further drawback, the MACS recovered less STRO-1+ cells in the positive fraction (0.97×10^6) than in the negative fraction (1.08×10^6).

Given the number of STRO-1+ cells in the original samples, the recovery efficiency of the two techniques was calculated (Figure 9.6B). The MACS recovered approximately 28% of the STRO-1+ cells present in the original sample. The sorting device recovered more than twice as many cells, isolating approximately 62% of the original STRO-1+ cell population.

Finally, the current studies indicate that from the available STRO-1+ cells recovered in the negative and positive fractions of the MACS, approximately 40% of the original number of STRO-1+ cells were not recovered by MACS. In contrast, only approximately 6% of cells were not collected by the sorting device. As reported previously in this Section, a possible explanation of the percentage of STRO-1+ cells not recovered during the MACS protocol could be found in the working principle of the MACS itself. According to the recovery efficiency results, it was possible that a significant percentage of STRO-1+ cells remained inside the MACS columns. To investigate this aspect, the used MACS columns were purged (twice) and the liquid recovered was analysed. Analysis indicated 13% of the STRO-1+ cells missing were recovered. The recovery efficiency achieved with the sorting device was more than double (62.38% vs 28.12%) that of a conventional MACS system, and exhibited equivalent purity (approximately 80% of STRO-1+ cells recovered in the positive fraction). Table 9.3 summarises the recovery efficiency values obtained by MACS and sorting device, considering both the total amount of cells recovered and the number of STRO-1+ cells recovered in each fractions.

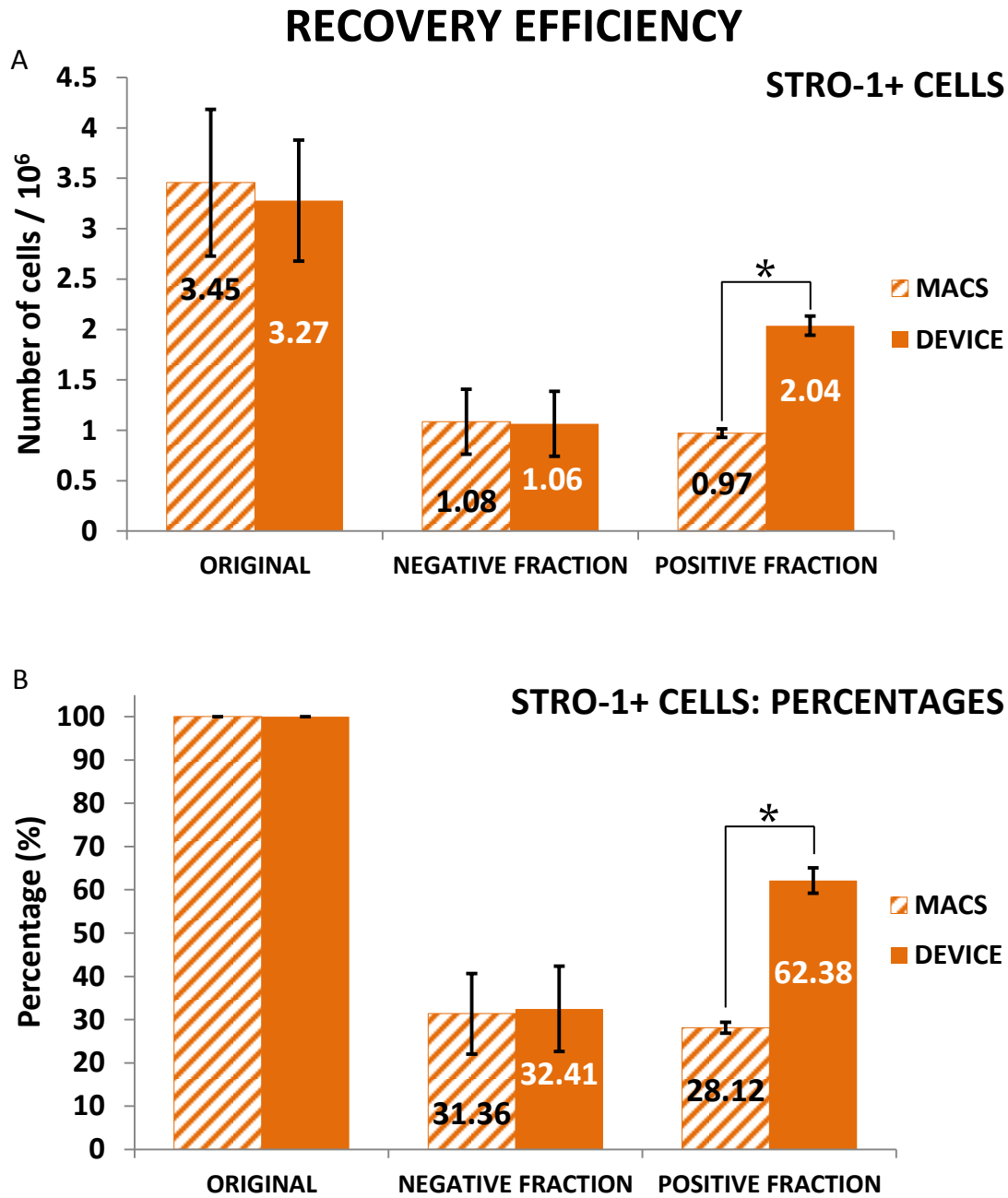


Figure 9.6: (A) The number of STRO-1+ cells in the original sample, negative fraction and positive fraction recovered from MACS and sorting device. (B) Percentages of STRO-1+ cells in negative and positive fractions recovered with MACS and sorting device. Results expressed as mean \pm SD and $n = 9$. * $P < 0.05$ calculated using t -test.

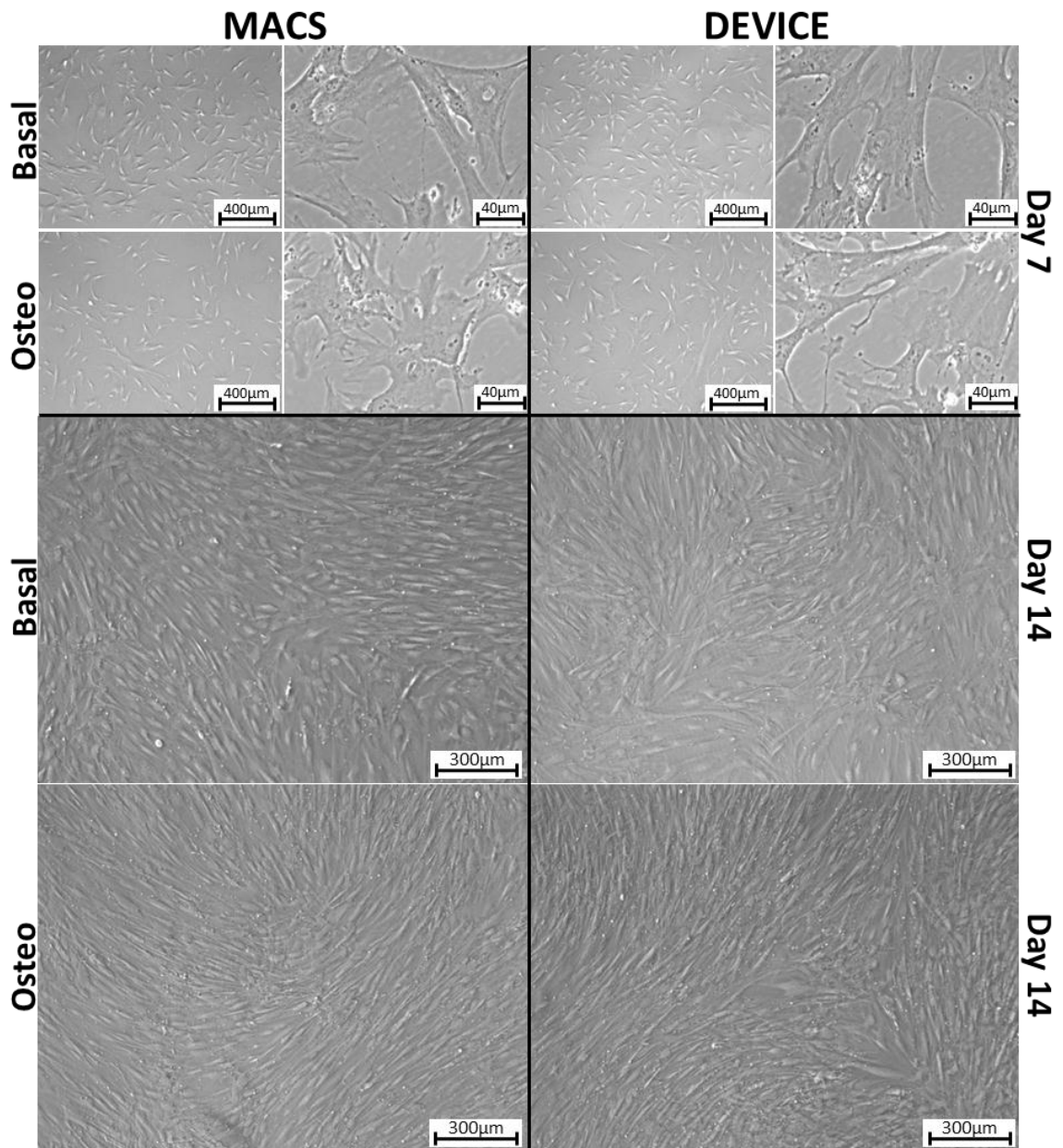


Figure 9.7: Photomicroscopy of P1 STRO-1+ cells sorted with the MACS and the sorting device under basal and osteogenic conditions at day 7 and day 14 from the start of differentiation (10 days from the seeding operation).

9.2.2 Cell differentiation and characterisation: results

As described in paragraph 9.1.3, the cells recovered from the positive fractions of both MACS and sorting device were seeded in separate flasks and after 10 days of culture under basal condition, each cell populations was divided in two and the differentiation process (under basal and osteo conditions) initiated. After the first media change, there were no evidence of superparamagnetic beads in the cell cultures.

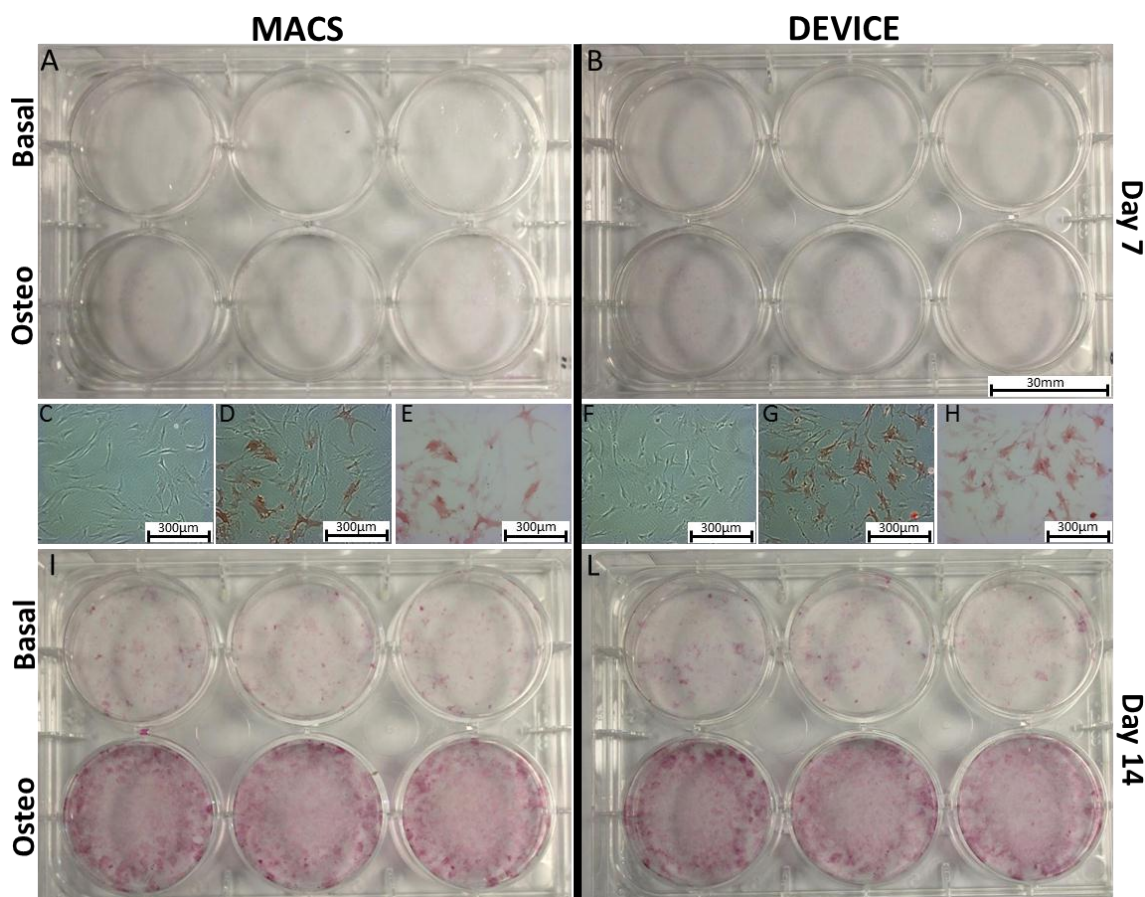


Figure 9.8: ALP staining of the STRO-1+ cell populations sorted with MACS and sorting device cultured under basal and osteogenic conditions. (A, B) ALP staining performed after 7 days. (C, F) Photomicroscopy of the cell populations cultured under basal conditions at day 7. (D, G) Photomicroscopy of the cell populations cultured under osteogenic condition at day 7 and (E, H) through a H/DIC (Differential Interference Contrast) filter. The procedure was implemented in triplicate (incubation time 30 min).

The experimental scheme was shown in Figure 9.3. Pictures of the cell cultures were taken at each time point of the study (after 7 and 14 days). Figure 9.7 shows the cell population sorted with the MACS and with the sorting device, cultured under basal and osteogenic conditions. At each time point the ALP expression of the cell populations was investigated by histological (ALP staining) analysis. Figure 9.8 shows the results of the ALP staining performed on the STRO-1+ cells isolated with MACS and sorting device, under basal and osteogenic conditions after 7 days and 14 day from the start of the differentiation.

The ALP staining was performed in triplicate (three wells per condition) on each of the three BM sample used in the study. The results shown in Figure 9.8 refer to one representative BM sample (see Appendix O). After 7 days (first time point) of differentiation, the differences between basal and osteogenic samples in both MACS and

sorting device cultures were not immediately visible (Figure 9.8A, B). However, photomicroscopy analysis revealed that both the MACS (Figure 9.8D, E) and the device (Figure 9.8G, H) cell populations expressed ALP under osteogenic conditions, unlike the samples cultured under basal conditions, which after 7 days did not express ALP (Figure 9.8C, F).

After 14 days (second time point), the differences between basal and osteogenic samples were clearly visible in both cell cultures (Figure 9.8I, L). As shown in Figure 9.8 no significant difference were observed between the cell populations sorted using the MACS and sorting device; both showed differentiation potential under osteogenic conditions.

Cell populations sorted through conventional MACS and through the novel sorting device were assessed by molecular analysis following 7 and 14 days *in vitro* culture as monolayers in either basal or osteogenic medium. β -actin was used as housekeeping gene, Runx2 and ALP were employed to represent early osteogenic genes, and Col1a1 and Osteocalcin as late stage genes (Table 9.1). Triplicate samples were assessed per gene, per patient sample.

Figure 9.9 demonstrates the gene expression observed for each sample, comparing those sorted with MACS (blue bars) to those sorted with the sorting device (red bars). The values refer to the three BM samples used in this study and were normalised for against Day 7 basal sample (MACS). A significant difference was observed in Runx2 expression between cultures maintained under basal and osteogenic condition at day 7. Runx2 expression within basal samples showed an ~ 3 fold increase compared to osteogenic samples. However, expression was observed to plateau by day 14. At both time points no significant differences in gene expression were recorded between samples sorted with MACS or the sorting device (Figure 9.9A).

ALP expression within osteogenic samples showed >2 fold increase ALP expression compared to basal samples at day 7. Moreover, ALP expression in osteogenic samples was approximately 5 fold greater than in basal culture at day 14 (Figure 9.9B).

Col1a1 exhibited higher expression under osteogenic conditions compared to basal samples at day 7. However, this increase was not observed after 14 days (Figure 9.9C).

Osteocalcin expression was not significantly different between cultures under basal and osteogenic conditions (Figure 9.9D). This may be due to an insufficient culture period, since Osteocalcin was expressed in late differentiation of bone cell cultures.

RT-PCR analysis revealed a significant difference in ALP expression between basal and osteogenic samples. This result was expected due to the nature of the enzyme ALP, which was a well-known *in vitro* marker for osteogenesis [79].

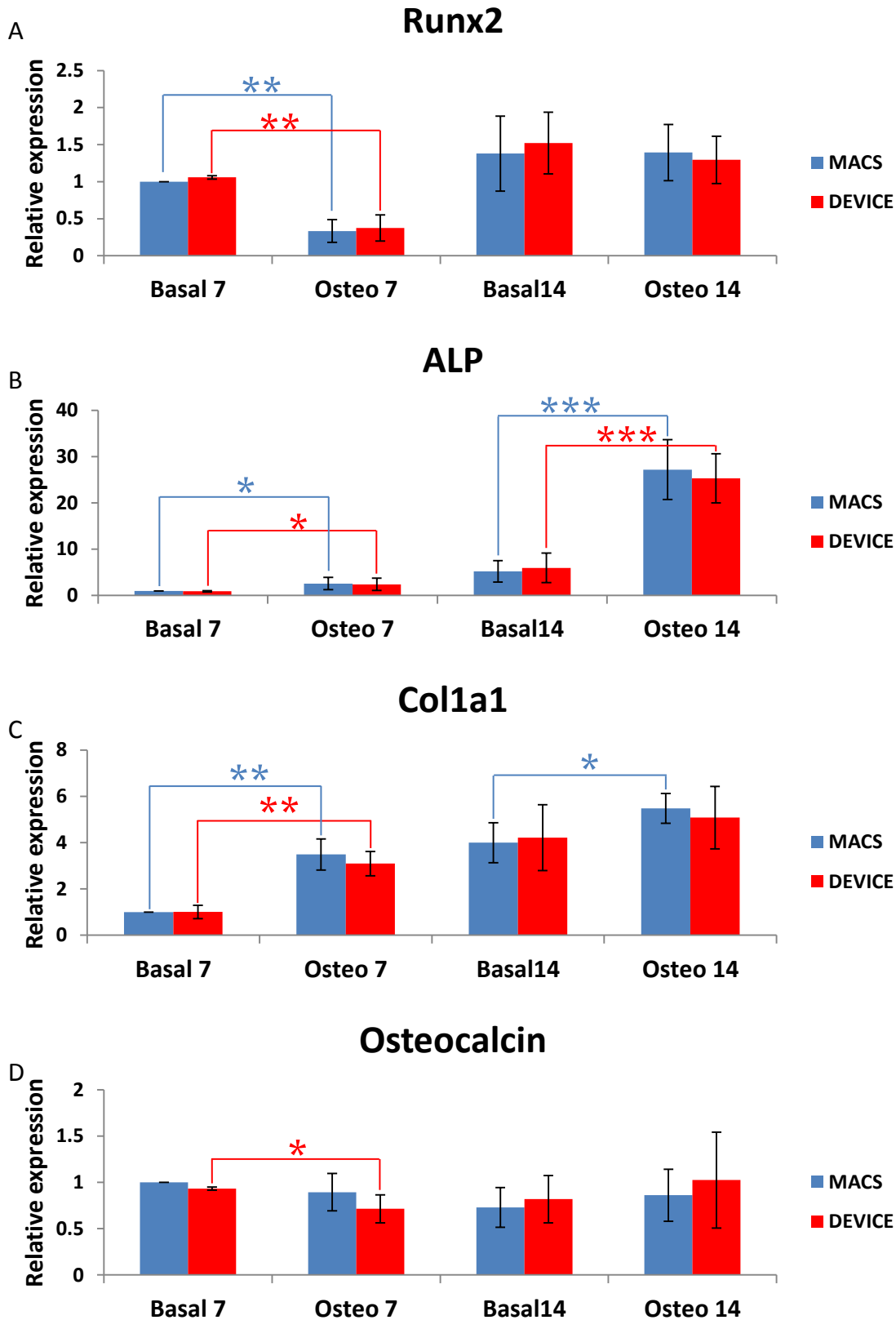


Figure 9.9: RT-PCR quantification for STRO-1+ cells isolated with MACS (blue bars) and sorting device (red bars) cultured under basal and osteogenic conditions for 14 days. The values were normalised against the condition basal 7 (MACS) sample for each gene. Results expressed as mean \pm SD and $n = 9$. * $P < 0.05$; ** $P < 0.005$; *** $P < 0.001$ calculated using Mann-Whitney test.

9.3 Conclusion

In this chapter three BM samples were processed to isolate the STRO-1+ cells using both MACS and the developed sorting device. The performances of the two techniques were compared using two parameters: purity and recovery efficiency of the sorted cells.

From the use of flow cytometry analyses, the purity of the positive fractions collected from both techniques was estimated. In both positive fractions, ~80% of the cell population consisted in STRO-1+ cells.

The recovery efficiency was investigated and interestingly, the sorting device achieved a greater than two fold recovery efficiency compared to the MACS device with a recovery of ~62% of the STRO-1+ cells contained in the original solution compared with ~28% achieved by the MACS.

To examine the differentiation potential of STRO-1+ cells isolated through MACS and sorting device, the two cell populations were cultured under different *in vitro* conditions including basal and osteogenic media.

ALP expression was used to assess any differences between basal and osteogenic cultures and between the two cell populations (isolated with MACS and sorting device). The ALP expression was investigated at day 7 and day 14 through ALP staining. The analyses showed a higher ALP expression in the osteogenic samples compared to the basal samples; and showed no significant differences between the cell populations sorted with the two techniques.

Cell populations sorted through MACS and sorting device were assessed by molecular analysis (RT-PCR) at the two time points. The most significant differences were found in the ALP expression within osteogenic samples (both MACS and DEVICE), which showed >2 fold increase in ALP expression compared to basal samples at day 7. Moreover, ALP expression in osteogenic samples was ~5 fold greater than in basal culture at day 14. Expression differences in all genes at each time point between samples sorted with conventional MACS and the sorting device were not significant. In conclusion, the STRO-1+ cell population sorted with the developed device had the same differentiation capability of the ones isolated with conventional MACS. The sorting device recovered more than twice STRO-1+ cells (~62%) compared to the MACS with equal purity (~80%). Further, during the sorting experiments, the device ver.3.5 + HMS processed ~9 x 10³ cells/s.

In terms of throughput, the sorting device ver.3.5 + HMS achieved better performances compared to some of the size-based and affinity-based sorting device discussed in Chapter 2.

For example, the device developed by Liu *et al.* [85] in 2013 used a label-free size-based separation with hydrodynamics as a sorting method, with a throughput of 333 cells/s. A similar device was developed by Choi *et al.* [10] in 2012 achieving a throughput of 277 cells/s. Critically, from the current study prospective, the device (size-based, label free) developed in 2013 by Lee *et al.* [8] to process whole blood for the CTCs isolation, stands out for the high purity and recovery and in particular for the cell throughput achieved. The cell throughput was recorded at 1.8×10^6 cells/s, significantly higher than the throughput of the sorting device developed in this study.

The affinity-based sorting devices discussed in Chapter 2 included the devices developed by Green *et al.* [86] and Li *et al.* [87], both performing negative selection with throughputs of 125 cells/s and 69 cells/s respectively. Results significantly lower than the one achieved by the sorting device ver.3.5 + HMS, which processed $\sim 9 \times 10^3$ cells/s.

In the same group (affinity-based), the device developed in 2013 by Yoon *et al.* [6] processed 1ml of whole blood in one hour, isolating CTCs in 20 out of 20 samples of whole blood obtained from patients affected by breast, lung and pancreatic cancer. The ability to process 1ml of whole blood in one hour implies a throughput of several orders of magnitude higher than obtained by the device developed in this study.

In terms of purity and recovery efficiency, the sorting device ver.3.5 + HMS achieved better results than the affinity-based sorting device developed by Kralj *et al.* [88] in 2012 which recovered only 40% of the MCF-7 spiked in blood; or the size-based device developed by Mach *et al.* [89] in 2011 which recovered 10-20% of the MCF-7 spiked in diluted blood with a purity of 40-10%.

However, the size-based sorting device developed by Lee *et al.* [8] which reached higher cell throughput than the device developed in this study, achieved also remarkable recovery (99%) and purity (88%).

The sorting device ver.3.5 + HMS was compared with microfluidic devices using the same sorting method: immunomagnetic labelling. The device developed by Moore *et al.* [65] in 2013 achieved slightly better purity and recovery than the sorting device ver.3.5 + HMS, but a significant difference was recorded in the throughput of the two devices. The device developed by Moore *et al.* processed 550 cell/s, which was far from the $\sim 9 \times 10^3$ cells/s processed by the sorting device + HMS.

In the same group, the device developed in 2013 by Ozkumur *et al.* [15] reached important results in terms of sort capacity. The authors tested the device with SKBR3 breast cancer cells spiked in blood achieving a recovery of 98% with a remarkable throughput of 10^7 cells/s. Moreover, the device was tested with cancer blood samples isolating CTCs from 36 of the 42 samples tested (all the device discussed here were listed in Table 2.1).

In summary, the device (sorting device ver. 3.5 with hexapole magnetic system (HMS)) developed in this program of work demonstrated a higher capacity for greater bulk isolation enabling enrichment of higher cell numbers within the initial cell populations with respect to the commonly used MACS technique. A greater initial STRO-1+ cell number was beneficial to *in vitro* expansion because would reduce both culturing period and passage number prior to utilisation within tissue engineering strategies. Reduced passage number was especially important as serial *in vitro* passage have been shown repeatedly to result in the emergence of a dominating fibroblastic phenotype [78]. The device ultimately allows for superior bulk cell isolation permitting shorter *in vitro* proliferation and differentiation periods for the production of desired cell populations to be used within regenerative medicine.

However, several aspects need further investigation to achieve high level of recovery efficiency and purity of the sorted cell population to improve the performances of the sorting device.

Chapter 10

Conclusion and Discussion

The system developed in this study employed immunomagnetic cell separation to sort SSCs from HBMSCs according to expression of the surface marker STRO-1. To make target cells susceptible to an external magnetic field, superparamagnetic beads were functionalised with STRO-1 antibodies and bound to the target cell surface. The magnetic susceptibility of a labelled cell (χ_c) was initially estimated experimentally with a separate purpose-built microfluidic device.

The sorting system developed in this study comprised two parts including the sorting device and the magnetic system. Three generations of sorting device with different designs, building techniques and materials were projected and manufactured (see Chapter 4). Preliminary experiments using polystyrene beads and the MG63 cell line were conducted on each device, establishing the optimised sorting device ver.3.4. A minor modifications of this device (reduction in the tube's external diameter) generated a final device labelled as ver.3.5 which was later used in comparison to conventional MACS for sorting of STRO-1+ sub-populations from HBMSCs.

To generate the external magnetic field, three magnetic systems were designed and manufactured including QMS ver.1, QMS ver.2 and HMS. Numerical simulations were implemented to established the magnetic flux density \vec{B} generated along with $(\vec{B} \cdot \nabla)\vec{B}$, which was the only spatial variable in the equation, to find the magnetic force \vec{F}_m experienced by a labelled cell within the sorting device (see Chapter 5). The HMS generated the highest values of \vec{B} and $(\vec{B} \cdot \nabla)\vec{B}$, and coupled with the sorting device ver.3.5, was used in a 3D numerical simulation to model cell trajectory (with magnetic susceptibility χ_c). This simulation calculated values for sample and buffer flow rates alongside their optimum ratio, $Q_s:Q_b$ (sample flow rate : buffer flow rate).

The sorting device ver.3.4 was coupled with each of the magnetic systems developed. MG63 cell sorting experiments were conducted with each combination (sorting device +

magnetic system), to assess sorting performance. All combinations were tested with several $Q_S:Q_B$ ratios ranging from 1:1 to 1:40. Increases in purity and recovery efficiency were recorded and compared for each combination. The device ver.3.4 with the HMS achieved the best performance compared to the other magnetic systems. This result was coherent with numerical simulations, which supported the HMS as the optimum magnetic system for the aim of this study. Moreover, ver.3.4 was further improved following reduction of the tube's external diameter (ver.3.5) in combination with the HMS. This combination, called continuous flow magnetic sorter (CFMS), achieved the best sorting performance of all the other combinations using a $Q_S:Q_B$ ratio of 1:4 (buffer flow rate: 2000 $\mu\text{l}/\text{min}$; sample flow rate: 500 $\mu\text{l}/\text{min}$) (see Section 7.7).

Sorting performance of the continuous flow magnetic sorter (CFMS) was compared with that of conventional MACS using MG63 cells. Starting from equal percentages ($\sim 65\%$) of STRO-1+ cells present in the original sample, both MACS and the sorting device achieved a purity of $\sim 96\%$ STRO-1+ cells in the positive fraction. However, recovery efficiency between the two techniques was significantly different, with the sorting device recovering $\sim 47\%$ of the STRO-1+ cells suspended in the original solution compared with $\sim 27\%$ in conventional MACS. The recovery efficiency achieved by the sorting device was almost double that achieved by conventional MACS (see Section 7.8).

The last stage of the study compared sorting of SSCs from HBMSCs using the CFMS and conventional MACS. As observed in previous experiments the two techniques achieved comparable levels of purity within the positive fractions ($\sim 80\%$). However, the CFMS achieved a greater than two fold recovery efficiency compared to the MACS device, recovering $\sim 62\%$ of the STRO-1+ cells suspended within the original solution compared with $\sim 28\%$ achieved by conventional MACS (see Chapter 9). Moreover, the CFMS was designed to sort under continuous flow ($\sim 9 \times 10^3$ cells/s) rather than individual batch sorting with conventional MACS, offering greater bulk isolation.

A greater seeding STRO-1+ cell population was beneficial for *in vitro* expansion because this would reduce both culture period and passage number prior to utilisation within tissue engineering strategies. Reduced passage number was especially important as serial *in vitro* passage have been shown repeatedly to result in the emergence of a dominating fibroblastic phenotype [78]. Following the sorting procedure, *in vitro* differentiation potential of cells recovered from the positive fraction of the CFMS and conventional MACS was investigated. Recovered cell populations were divided in half and cultured under both basal and osteogenic conditions. After 7 and 14 days, histological (ALP staining) and molecular (RT-PCR) analyses were performed on each of the four groups (basal macs, osteo macs, basal device, and osteo device). Both analyses revealed significant differences

between cell populations cultured under basal and osteogenic conditions, irrespective of the sorting technique used.

10.1 Discussion

Numerical simulations (see Chapter 5) were designed to model the trajectory of a labelled cell within the CFMS (sorting device ver.3.5 + HMS). Interestingly, the numerical simulations identified $Q_S:Q_B$ ratio 1:4 as the optimum balance between sorting performance and device throughput. Experimental testing also demonstrated that $Q_S:Q_B$ ratio 1:4 was optimum (see Chapter 7).

However, in the numerical simulation, 1,000 labelled cells (all having magnetic susceptibility χ_c – experimentally estimated) were suspended in the original sample and ~92% were correctly sorted and recovered in the positive fraction. In terms of recovery efficiency there was a discrepancy between the modelled and experimental data. The sorting device only recovered ~62% of STRO-1+ cells (labelled cells) suspended in the original solution. However, this was significantly higher than that of conventional MACS which achieved only ~28%. This discrepancy could have several reasons, the main reason being non-uniform STRO-1 expression. In the numerical simulation, all the labelled cells had the same magnetic susceptibility χ_c . In the experimental situation, this was not the case. The labelled cells' magnetic susceptibility was dependent on the number of functionalised superparamagnetic beads attached to the cells' surface. This number was dependent on STRO-1 expression level of each cell, and if <400 beads were bound (see Appendix I), the cell would not exhibit sufficient susceptibility to the magnetic field to be sorted.

Purity achieved by the CFMS (~80%) was comparable to MACS. Consequently, STRO-1-cells (~20%) were present within the positive fraction. The most likely reason was to be found in the adherent nature of HBMSCs. With the current experimental settings (sample flow rate: 500 $\mu\text{l}/\text{min}$, sample concentration: $\sim 1 \times 10^6$ cells/ml), processing a typical sized HBMSC population ($\sim 20 \times 10^6$ cells) would take 40 min. In this time period, HBMSCs could potentially clump together indiscriminately. In this eventuality, the entire clump of cells could experience a magnetic force (due to the applied magnetic field) deflecting the clump towards the positive fraction output.

Table 10.1: Table comparing the performances of the most efficient microfluidic cell sorting devices with the CFMS developed in this study. The sorting devices were divided in three main categories: affinity-based (in blue), size-based (in red) and immunomagnetic (in black). The values in bold referred to experiments with primary cells (in the case of CFMS, HBMSCs from patients). The highlighted row reported the details form CFMS tests.

AUTOR	YEAR	GROUP	METHOD	PURITY	RECOVERY	FLOW RATE	THROUGHPUT	PARTICLES	REF
Yoon et al.	2013	Affinity-based	Positive selection (EpCAM)	-	3-5cells→73% 10-20→94.2% 100→87.3%	1 ml/h	-	MCF-7 in whole blood	[6]
					20 of 20			CTCs from whole blood	
Stott et al.	2010	Affinity-based	Positive selection (EpCAM)	-	91%	1.2 ml/h	-	PC3 from whole blood	[5]
					14 of 15 S			CTCs from whole blood	
Lee et al.	2013	Size-based	Hydrodynamic (label-free)	88% 97.4%	99%	6 ml/h	1.8×10^6 cells/s	MCF-7 from whole blood	[8]
Hou et al.	2013	Size-based	Hydrodynamic (label-free)	-	>85%	3 ml/h	-	MCF-7 in blood (20% hematocrit)	[12]
					20 of 20 S			CTCs from blood	
Ozkumur et al.	2013	Immunomagnetic	Positive selection (EpCAM)	-	98% 89%	8 ml/h	10^7 cells/s	SKBR3, PC3-9 in blood	[15]
					36 of 42 S			CTCs from whole blood	
Yang et al.	2009	Immunomagnetic	Negative selection (CD45)	-	82.7% 99.9%Deplation	-	10^7 cells/s	Cancer cells from PBL	[63]
					20 of 26 S			CTCs from buffy coat	
CFMS	2014	Immunomagnetic	Positive selection (STRO-1)	80%	62.38%	30 ml/h	9×10^3 cells/s	SSCs from HBMSCs	

Table 10.1 compared the performances of the most efficient microfluidic cell sorting devices with the CFMS developed in this study. The sorting devices described in Chapter 2 were divided in three main categories: affinity-based, size-based and immunomagnetic.

The affinity-based isolation devices used non-covalent bonds between molecules immobilized on a surface and an antigen expressed on the target cell membrane. To increase the functionalised surface area within the device, specific features (such as posts) were created. The application of specific geometries increased the possibility of contact and bonding between target cells and a functionalized surface.

The devices developed by Yoon *et al.* [6] and Stott *et al.* [5] used this technique to isolate rare cells. Both these devices successfully isolated CTCs from whole blood demonstrating high working flow rate and recovery efficiency. However, although representing a great potential for diagnosis purposes, the devices belonging to this category had a communal limitation. When the dimensions of target and non-target cells were similar, the possibility of non-specific binding was high, resulting in low purity of the captured cells. In addition, negative selection performed with this technique could cause the blockage of the device due to the large number of background cells compared with target cells. For these reasons the devices developed by Yoon *et al.* [6] and Stott *et al.* [5] could not be used for purposes similar to the one described in this manuscript.

Size-based cell separation devices used the size difference between target and background cells as separation parameter. There were numerous methods to exploit the physical characteristics of target cells, including hydrodynamics, filtration, dielectrophoresis, acoustophoresis, magnetophoresis and deformability. Both devices reported in Table 10.1 under this category used hydrodynamic forces to isolate target cells. Hydrodynamic force based devices offered a label-free process providing a simple low cost sample preparation procedure. Moreover, these devices operated at high flow rate (in the order of tens ml per hour) with throughput in the order of thousands of cells per second. In particular, the device developed by Lee *et al.* [8] was used to isolate MCF-7 cells from whole blood, achieving a purity of 99% and recovery over 90%. Moreover, this device had a working throughput of 1.8×10^6 cells/s.

In 2013 Hou *et al.* [12] developed a device using the same principle to isolate rare cells in diluted blood (20% hematocrit). The authors isolated CTCs from all the blood samples from cancer patients tested (20 out of 20), with recovery efficiency over 85%. Both devices, although achieving remarkable performances, had few drawbacks. To perform the separation the hydrodynamic forces within the devices had to be finely controlled, involving the dilution of the samples in buffer with known properties. In addition, the size overlapping of target and background cells was a limitation of all the devices relying on

physical parameters to perform cell separation. As for the affinity-based category, devices relying on size difference between target and non-target cells, were unsuitable for any applications involving cell types with similar dimensions.

Finally, the immunomagnetic cell sorting devices did not rely on physical properties of target cells, but used antibodies conjugated to magnetic nanoparticles in order to target specific cell membrane antigens. Cells expressing the specific surface marker were labelled and manipulated by applying an external magnetic field. These devices did not rely on physical cell characteristics, and were ideal to separate target cells from background cells with comparable dimensions.

The devices better representing this category were the CTC-iChip developed by Ozkumur *et al.* [15] and the QMS developed by Chalmers and co-workers [63]. The CTC-iChip was used to isolate CTCs from whole blood. It used a flow rate of 8 ml/h, resulting in a throughput of 10^7 cells/s. The device was tested with blood samples from cancer patients, isolating CTCs in 36 of the 42 samples tested. Moreover, it was tested with SKBR3 and PC3-9 cells spiked in blood and in this occasion achieved a recovery efficiency ranging between 89% and 98%.

Chalmers and co-workers published a number of papers on cell isolation using the QMS. In particular Yang *et al.* [63] in 2009 used the QMS to deplete PBL population and isolate cancer cells. Using a throughput of 10^7 cells/s, the authors depleted 99.9% of the non-target cells, recovering 82.7% of the cancer cell spiked in the PBL population. The QMS device was also commercialised by the company IKOTECH (USA) [66], featuring purity of sorted cells in the range of 96% and throughput of 10^7 cells/sec.

The CTC-iChip and the QMS used the same principle of the CFMS developed in this study. As from Table 10.1, the CFMS working flow rate was 30 ml/h, but the throughput was considerably lower (9×10^3 cells/s) than that reported for the other two devices.

However, results presented for the CFMS were preliminary results, with possibility of improvements as described in section 10.2. Moreover, to date neither the CTC-iChip nor the QMS were used to isolate SSCs from HBMSCs. The CFMS performances in terms of purity and recovery were lower than that reported for the CTC-iChip and the QMS. However, as for the FACS, which performances were not compared with the CFMS ones, the IKOTECH device was more expensive to buy and maintain. In addition, both FACS and IKOTECH device needed trained personnel to be operated.

On the other hand, the CFMS were built using rapid prototyping techniques (3D printing and stereolithography), and the final aim was to develop a functional, compact, easy to use and to maintain sorting platform for researchers' everyday uses. Moreover, the hexapole

configuration elected to be the definitive magnets arrangement was developed using inexpensive permanent magnets.

10.2 Further work

One drawback to the current system was cell clumping prior to loading. To limit the presence of STRO-1- cells in the positive fraction and increase homogeneity, a reduced sorting time would be required. This could be achieved through two strategies, 1) increasing the sample concentration, or 2) increasing the sample input flow rate. However, increasing the sample concentration would increase the possibility of cell clumping. The second strategy would reduce experimental time limiting the possibility of clumps forming. To increase the sample input flow rate whilst conserving sorting performance, increased magnetic force \vec{F}_m experienced by labeled cells was required. \vec{F}_m depends on two main parameters including magnetic susceptibility χ_c of labelled cells and the variable $(\vec{B} \cdot \nabla)\vec{B}$ generated by the magnetic system used. χ_c could be increased by adhering more superparamagnetic beads to the cell surface through targeting a second SSC surface marker to STRO-1, such as CD105 or CD146. Increased $(\vec{B} \cdot \nabla)\vec{B}$ can be generated by redesigning the HMS, rearranging the neodymium magnets' position or using different magnet geometry to maximise the gradient of the magnetic field. An increase of either χ_c or $(\vec{B} \cdot \nabla)\vec{B}$ or both would allow increased sample input flow rate, resulting in reduced experiment duration. Moreover, these modifications would make the sorting device more sensitive, lowering the detection threshold (minimum number of superparamagnetic beads needed on the cell surface to be deflected) and allowing for higher recovery efficiency.

In the context of reducing cell clumping during experiments, a system for agitation of the cell suspension immediately prior to loading would be of great benefit. Replacement of the sample syringe pump with a peristaltic pump would allow for continuous loading from a cell reservoir that can be separately agitated to avoid cell sedimentation and clumping. There were several methods to agitate the cell reservoir such as magnetic stirring. For increased loading accuracy, rather than implement a peristaltic pump, a pressure pump could be used. The pressure pump would allow fine adjustment of the sample input flow rate through smaller computer controlled increments. A drawback to this approach however, would be increased device setup complexity.

The $|\nabla\vec{B}|$ generated by the CFMS was 150 mT/mm, in the same range of values of the ones generated by the QMS (179 mT/mm). Once reduced the cell clumping and increased χ_c by targeting multiples SSCs markers, the CFMS performances could be in the same order of magnitude of the QMS developed by Chalmers and co-workers and the IKOTECH device.

The CFMS successfully isolated SSCs from HBMSCs with the same purity of conventional MACS (~80%). In addition, the CFMS sorting procedure was 25 min shorter than the conventional MACS procedure (85 min for CFMS and 110 min for MACS). This because of the one-step immunostaining procedure needed for cell sorting with CFMS compared with the two-steps immunostaining necessary for MACS. This peculiarity also reduced the reagent consumption (secondary antibodies not necessary with the CFMS). Moreover, the CFMS recovered ~62% of the STRO-1+ cells suspended within the original solution compared with ~28% achieved by conventional MACS, demonstrating a recovery efficiency more than double compared with MACS.

This aspect was particularly important for tissue engineering strategies. The use of SSCs in regenerative medicine was related on the cell expansion process. Several approaches were developed to optimise this procedure as described in section 1.1.3. Perform cell isolation with CFMS instead of MACS, meant starting the cell expansion process with more than double the number of STRO-1+ cells with the same purity. A greater seeding STRO-1+ cell population would be beneficial for *in vitro* expansion because this would reduce both culture period and passage number prior to utilisation within tissue engineering strategies.

Moreover, reduced passage number was especially important as serial *in vitro* passage have been shown to result in the emergence of a dominating fibroblastic phenotype [78], nullifying differentiation strategies in process. For these reasons, the CFMS would be beneficial for research purposes, representing a functional, easy to use and to maintain sorting platform for researchers' everyday uses.

References

- [1] W.a.N.I. National Joint Registry for England.
- [2] S. Talukdar, Q.T. Nguyen, A.C. Chen, R.L. Sah, S.C. Kundu, Effect of initial cell seeding density on 3D-engineered silk fibroin scaffolds for articular cartilage tissue engineering, *Biomaterials* 32 (2011) 8927-8937.
- [3] L.A. Herzenberg, R.G. Sweet, L.A. Herzenberg, Fluorescence-Activated Cell Sorting, *Scientific American* 234 (1976) 108-117.
- [4] S. Nagrath, L.V. Sequist, S. Maheswaran, D.W. Bell, D. Irimia, L. Ulkus, M.R. Smith, E.L. Kwak, S. Digumarthy, A. Muzikansky, P. Ryan, U.J. Balis, R.G. Tompkins, D.A. Haber, M. Toner, Isolation of rare circulating tumour cells in cancer patients by microchip technology, *Nature* 450 (2007) 1235-U1210.
- [5] S.L. Stott, C.H. Hsu, D.I. Tsukrov, M. Yu, D.T. Miyamoto, B.A. Waltman, S.M. Rothenberg, A.M. Shah, M.E. Smas, G.K. Korir, F.P. Floyd, A.J. Gilman, J.B. Lord, D. Winokur, S. Springer, D. Irimia, S. Nagrath, L.V. Sequist, R.J. Lee, K.J. Isselbacher, S. Maheswaran, D.A. Haber, M. Toner, Isolation of circulating tumor cells using a microvortex-generating herringbone-chip, *Proceedings of the National Academy of Sciences of the United States of America* 107 (2010) 18392-18397.
- [6] H.J. Yoon, T.H. Kim, Z. Zhang, E. Azizi, T.M. Pham, C. Paoletti, J. Lin, N. Ramnath, M.S. Wicha, D.F. Hayes, D.M. Simeone, S. Nagrath, Sensitive capture of circulating tumour cells by functionalized graphene oxide nanosheets, *Nature Nanotechnology* 8 (2013) 735-741.
- [7] W. Sheng, T. Chen, R. Kamath, X. Xiong, W. Tan, Z.H. Fan, Aptamer-Enabled Efficient Isolation of Cancer Cells from Whole Blood Using a Microfluidic Device, *Analytical Chemistry* 84 (2012) 4199-4206.
- [8] M.G. Lee, J.H. Shin, C.Y. Bae, S. Choi, J.-K. Park, Label-Free Cancer Cell Separation from Human Whole Blood Using Inertial Microfluidics at Low Shear Stress, *Analytical Chemistry* 85 (2013) 6213-6218.
- [9] K.-A. Hyun, K. Kwon, H. Han, S.-I. Kim, H.-I. Jung, Microfluidic flow fractionation device for label-free isolation of circulating tumor cells (CTCs) from breast cancer patients, *Biosensors and Bioelectronics* 40 (2013) 206-212.

- [10] S. Choi, J.M. Karp, R. Karnik, Cell sorting by deterministic cell rolling, *Lab on a Chip* 12 (2012) 1427-1430.
- [11] S. Zheng, H. Lin, B. Lu, A. Williams, R. Datar, R. Cote, Y.-C. Tai, 3D microfilter device for viable circulating tumor cell (CTC) enrichment from blood, *Biomedical Microdevices* 13 (2011) 203-213.
- [12] H.W. Hou, M.E. Warkiani, B.L. Khoo, Z.R. Li, R.A. Soo, D.S.W. Tan, W.T. Lim, J. Han, A.A.S. Bhagat, C.T. Lim, Isolation and retrieval of circulating tumor cells using centrifugal forces, *Scientific Reports* 3 (2013).
- [13] S. Shim, K. Stemke-Hale, A.M. Tsimberidou, J. Noshari, T.E. Anderson, P.R.C. Gascoyne, Antibody-independent isolation of circulating tumor cells by continuous-flow dielectrophoresis, *Biomicrofluidics* 7 (2013) -.
- [14] J.H. Kang, S. Krause, H. Tobin, A. Mammoto, M. Kanapathipillai, D.E. Ingber, A combined micromagnetic-microfluidic device for rapid capture and culture of rare circulating tumor cells, *Lab on a Chip* 12 (2012) 2175-2181.
- [15] E. Ozkumur, A.M. Shah, J.C. Ciciliano, B.L. Emmink, D.T. Miyamoto, E. Brachtel, M. Yu, P.I. Chen, B. Morgan, J. Trautwein, A. Kimura, S. Sengupta, S.L. Stott, N.M. Karabacak, T.A. Barber, J.R. Walsh, K. Smith, P.S. Spuhler, J.P. Sullivan, R.J. Lee, D.T. Ting, X. Luo, A.T. Shaw, A. Bardia, L.V. Sequist, D.N. Louis, S. Maheswaran, R. Kapur, D.A. Haber, M. Toner, Inertial Focusing for Tumor Antigen-Dependent and -Independent Sorting of Rare Circulating Tumor Cells, *Science Translational Medicine* 5 (2013).
- [16] M. Hoyos, K.E. McCloskey, L.R. Moore, M. Nakamura, B.J. Bolwell, J.J. Chalmers, M. Zborowski, Pulse-injection studies of blood progenitor cells in a quadrupole magnet flow sorter, *Separation Science and Technology* 37 (2002) 745-767.
- [17] M.J. Dalby, N. Gadegaard, R. Tare, A. Andar, M.O. Riehle, P. Herzyk, C.D.W. Wilkinson, R.O.C. Oreffo, The control of human mesenchymal cell differentiation using nanoscale symmetry and disorder, *Nat Mater* 6 (2007) 997-1003.
- [18] A.I. Caplan, S.P. Bruder, Mesenchymal stem cells: building blocks for molecular medicine in the 21st century, *Trends in Molecular Medicine* 7 (2001) 259-264.
- [19] P. Augustsson, C. Magnusson, M. Nordin, H. Lilja, T. Laurell, Microfluidic, Label-Free Enrichment of Prostate Cancer Cells in Blood Based on Acoustophoresis, *Analytical Chemistry* 84 (2012) 7954-7962.
- [20] S. Gronthos, S.E. Graves, S. Ohta, P.J. Simmons, The STRO-1+ fraction of adult human bone marrow contains the osteogenic precursors, *Blood* 84 (1994) 4164-4173.

- [21] J.I. Dawson, J. Kanczler, R. Tare, M. Kassem, R.O.C. Oreffo, Concise Review: Bridging the Gap: Bone Regeneration Using Skeletal Stem Cell-Based Strategies—Where Are We Now?, *STEM CELLS* 32 (2014) 35-44.
- [22] B. Philippe, S. Luc, P.B. Valerie, R. Jerome, B.R. Alessandra, C. Louis, Culture and Use of Mesenchymal Stromal Cells in Phase I and II Clinical Trials, *Stem Cells Int* 2010 (2010) 503593.
- [23] M. Owen, A.J. Friedenstein, Stromal stem cells: marrow-derived osteogenic precursors, *Ciba Found Symp* 136 (1988) 42-60.
- [24] M. Dominici, K. Le Blanc, I. Mueller, I. Slaper-Cortenbach, F. Marini, D. Krause, R. Deans, A. Keating, D. Prockop, E. Horwitz, Minimal criteria for defining multipotent mesenchymal stromal cells. The International Society for Cellular Therapy position statement, *Cytotherapy* 8 (2006) 315-317.
- [25] R.S. Tare, J.C. Babister, J. Kanczler, R.O.C. Oreffo, Skeletal stem cells: Phenotype, biology and environmental niches informing tissue regeneration, *Molecular and Cellular Endocrinology* 288 (2008) 11-21.
- [26] J. Ma, S.K. Both, F. Yang, F.-Z. Cui, J. Pan, G.J. Meijer, J.A. Jansen, J.J.P. van den Beucken, Concise Review: Cell-Based Strategies in Bone Tissue Engineering and Regenerative Medicine, *Stem Cells Translational Medicine* 3 (2014) 98-107.
- [27] P. Hernigou, A. Poignard, O. Manicom, G. Mathieu, H. Rouard, The use of percutaneous autologous bone marrow transplantation in nonunion and avascular necrosis of bone, *Journal of Bone and Joint Surgery-British Volume* 87B (2005) 896-902.
- [28] S. Durdu, A.R. Akar, M. Arat, T. Sancak, N.T. Eren, U. Ozyurda, Autologous bone-marrow mononuclear cell implantation for patients with Rutherford grade II-III thromboangiitis obliterans, *Journal of Vascular Surgery* 44 732-739.
- [29] K. Stenderup, J. Justesen, C. Clausen, M. Kassem, Aging is associated with decreased maximal life span and accelerated senescence of bone marrow stromal cells, *Bone* 33 (2003) 919-926.
- [30] A. Mizukami, M.D. Orellana, S.R. Caruso, K.D. Prata, D.T. Covas, K. Swiech, Efficient expansion of mesenchymal stromal cells in a disposable fixed bed culture system, *Biotechnology Progress* 29 (2013) 568-572.
- [31] J. Kim, J. Kang, J. Park, Y. Choi, K. Choi, K. Park, D. Baek, S. Seong, H.-K. Min, H. Kim, Biological characterization of long-term cultured human mesenchymal stem cells, *Archives of Pharmacal Research* 32 (2009) 117-126.
- [32] K. Lee, E.A. Silva, D.J. Mooney, Growth factor delivery-based tissue engineering: general approaches and a review of recent developments, *Journal of the Royal Society Interface* 8 (2011) 153-170.

- [33] M.P. Lutolf, J.A. Hubbell, Synthetic biomaterials as instructive extracellular microenvironments for morphogenesis in tissue engineering, *Nature Biotechnology* 23 (2005) 47-55.
- [34] J.F. Connolly, R. Guse, J. Tiedeman, R. Dehne, AUTOLOGOUS MARROW INJECTION AS A SUBSTITUTE FOR OPERATIVE GRAFTING OF TIBIAL NONUNIONS, *Clinical Orthopaedics and Related Research* (1991) 259-270.
- [35] H. Kitoh, M. Kawasumi, H. Kaneko, N. Ishiguro, Differential effects of culture-expanded bone marrow cells on the regeneration of bone between the femoral and the tibial lengthenings, *Journal of pediatric orthopedics* 29 (2009) 643-649.
- [36] A. Bongso, C.Y. Fong, G.S.L. Peh, K. Gauthaman, Separation of SSEA-4 and TRA-1-60 Labelled Undifferentiated Human Embryonic Stem Cells from A Heterogeneous Cell Population Using Magnetic-Activated Cell Sorting (MACS) and Fluorescence-Activated Cell Sorting (FACS), *Stem Cell Reviews and Reports* 5 (2009) 72-80.
- [37] A. Willasch, S. Eing, G. Weber, S. Kuci, G. Schneider, J. Soerensen, A. Jarisch, E. Rettinger, U. Koehl, T. Klingebiel, H. Kreyenberg, P. Bader, Enrichment of cell subpopulations applying automated MACS technique: purity, recovery and applicability for PCR-based chimerism analysis, *Bone Marrow Transplantation* 45 (2010) 181-189.
- [38] S. Miltenyi, W. Muller, W. Weichel, A. Radbruch, High-Gradient Magnetic Cell-Separation with Macs, *Cytometry* 11 (1990) 231-238.
- [39] S.G. Withers, G.Y. Yang, J.R. Rich, M. Gilbert, W.W. Wakarchuk, Y. Feng, Fluorescence Activated Cell Sorting as a General Ultra-High-Throughput Screening Method for Directed Evolution of Glycosyltransferases, *Journal of the American Chemical Society* 132 (2010) 10570-10577.
- [40] L.A. Herzenberg, D. Parks, B. Sahaf, O. Perez, M. Roederer, The history and future of the fluorescence activated cell sorter and flow cytometry: A view from Stanford, *Clinical Chemistry* 48 (2002) 1819-1827.
- [41] A.Y. Fu, C. Spence, A. Scherer, F.H. Arnold, S.R. Quake, A microfabricated fluorescence-activated cell sorter, *Nature Biotechnology* 17 (1999) 1109-1111.
- [42] J. Seidl, R. Knuechel, L.A. Kunz-Schughart, Evaluation of membrane physiology following fluorescence activated or magnetic cell separation, *Cytometry* 36 (1999) 102-111.
- [43] J.M. Cooper, D. Wlodkowic, S. Faley, M. Zagnoni, J.P. Wikswo, Microfluidic Single-Cell Array Cytometry for the Analysis of Tumor Apoptosis, *Analytical Chemistry* 81 (2009) 5517-5523.

- [44] D. Wlodkovic, J.M. Cooper, Tumors on chips: oncology meets microfluidics, *Current Opinion in Chemical Biology* 14 (2010) 556-567.
- [45] H. Andersson, A. van den Berg, Microfluidic devices for cellomics: a review, *Sensors and Actuators B-Chemical* 92 (2003) 315-325.
- [46] J.P. Gleghorn, E.D. Pratt, D. Denning, H. Liu, N.H. Bander, S.T. Tagawa, D.M. Nanus, P.A. Giannakakou, B.J. Kirby, Capture of circulating tumor cells from whole blood of prostate cancer patients using geometrically enhanced differential immunocapture (GEDI) and a prostate-specific antibody, *Lab on a Chip* 10 (2010) 27-29.
- [47] Y. Dong, A.M. Skelley, K.D. Merdek, K.M. Sprott, C. Jiang, W.E. Pierceall, J. Lin, M. Stocum, W.P. Carney, D.A. Smirnov, Microfluidics and Circulating Tumor Cells, *The Journal of molecular diagnostics : JMD* 15 (2013) 149-157.
- [48] Y. Gao, W. Li, D. Pappas, Recent advances in microfluidic cell separations, *Analyst* 138 (2013) 4714-4721.
- [49] S.K. Arya, B. Lim, A.R.A. Rahman, Enrichment, detection and clinical significance of circulating tumor cells, *Lab on a Chip* 13 (2013) 1995-2027.
- [50] A.E. Saliba, L. Saias, E. Psychari, N. Minc, D. Simon, F.C. Bidard, C. Mathiot, J.Y. Pierga, V. Fraissier, J. Salamero, V. Saada, F. Farace, P. Vielh, L. Malaquin, J.L. Viovy, Microfluidic sorting and multimodal typing of cancer cells in self-assembled magnetic arrays, *Proceedings of the National Academy of Sciences of the United States of America* 107 (2010) 14524-14529.
- [51] J.A. Laure Saias, Laurent Malaquin and Jean-Louis Viovy, Design, modeling and characterization of microfluidic architectures for high flow rate, small footprint microfluidic systems, *Lab on a Chip* (2010).
- [52] M.S. Kim, T.S. Sim, Y.J. Kim, S.S. Kim, H. Jeong, J.-M. Park, H.-S. Moon, S.I. Kim, O. Gurel, S.S. Lee, J.-G. Lee, J.C. Park, SSA-MOA: a novel CTC isolation platform using selective size amplification (SSA) and a multi-obstacle architecture (MOA) filter, *Lab on a Chip* 12 (2012) 2874-2880.
- [53] M.X. Lin, K.-A. Hyun, H.-S. Moon, T.S. Sim, J.-G. Lee, J.C. Park, S.S. Lee, H.-I. Jung, Continuous labeling of circulating tumor cells with microbeads using a vortex micromixer for highly selective isolation, *Biosensors and Bioelectronics* 40 (2013) 63-67.
- [54] J.-M. Park, J.-Y. Lee, J.-G. Lee, H. Jeong, J.-M. Oh, Y.J. Kim, D. Park, M.S. Kim, H.J. Lee, J.H. Oh, S.S. Lee, W.-Y. Lee, N. Huh, Highly Efficient Assay of Circulating Tumor Cells by Selective Sedimentation with a Density Gradient Medium and Microfiltration from Whole Blood, *Analytical Chemistry* 84 (2012) 7400-7407.

- [55] J. Autebert, B. Coudert, F.-C. Bidard, J.-Y. Pierga, S. Descroix, L. Malaquin, J.-L. Viovy, Microfluidic: An innovative tool for efficient cell sorting, *Methods* 57 (2012) 297-307.
- [56] S.C. Hur, N.K. Henderson-MacLennan, E.R.B. McCabe, D. Di Carlo, Deformability-based cell classification and enrichment using inertial microfluidics, *Lab on a Chip* 11 (2011) 912-920.
- [57] Y.Y. Huang, K. Hoshino, P. Chen, C.H. Wu, N. Lane, M. Huebschman, H.Y. Liu, K. Sokolov, J.W. Uhr, E.P. Frenkel, J.X.J. Zhang, Immunomagnetic nanoscreening of circulating tumor cells with a motion controlled microfluidic system, *Biomedical Microdevices* 15 (2013) 673-681.
- [58] B.D. Plouffe, M. Mahalanabis, L.H. Lewis, C.M. Klapperich, S.K. Murthy, Clinically Relevant Microfluidic Magnetophoretic Isolation of Rare-Cell Populations for Diagnostic and Therapeutic Monitoring Applications, *Analytical Chemistry* 84 (2012) 1336-1344.
- [59] M. Zborowski, L.R. Moore, P.S. Williams, J.J. Chalmers, SEPARATIONS BASED ON MAGNETOPHORETIC MOBILITY, *Separation Science and Technology* 37 (2002) 3611-3633.
- [60] M. Zborowski, P.S. Williams, L. Sun, L.R. Moore, J.J. Chalmers, Cylindrical Splitt and Quadrupole Magnetic Field in Application to Continuous-Flow Magnetic Cell Sorting, *Journal of Liquid Chromatography & Related Technologies* 20 (1997) 2887-2905.
- [61] L.P. Sun, M. Zborowski, L.R. Moore, J.J. Chalmers, Continuous, flow-through immunomagnetic cell sorting in a quadrupole field, *Cytometry* 33 (1998) 469-475.
- [62] X. Tong, Y. Xiong, M. Zborowski, S.S. Farag, J.J. Chalmers, A novel high throughput immunomagnetic cell sorting system for potential clinical scale depletion of T cells for allogeneic stem cell transplantation, *Experimental Hematology* 35 (2007) 1613-1622.
- [63] L.Y. Yang, J.C. Lang, P. Balasubramanian, K.R. Jatana, D. Schuller, A. Agrawal, M. Zborowski, J.J. Chalmers, Optimization of an Enrichment Process for Circulating Tumor Cells From the Blood of Head and Neck Cancer Patients Through Depletion of Normal Cells, *Biotechnology and Bioengineering* 102 (2009) 521-534.
- [64] F. Shen, H. Hwang, Y.K. Hahn, J.-K. Park, Label-Free Cell Separation Using a Tunable Magnetophoretic Repulsion Force, *Analytical Chemistry* 84 (2012) 3075-3081.
- [65] L.R. Moore, F. Nehl, J. Dorn, J.J. Chalmers, M. Zborowski, Open Gradient Magnetic Red Blood Cell Sorter Evaluation on Model Cell Mixtures, *Ieee Transactions on Magnetics* 49 (2013) 309-315.

- [66] Website: <http://www.ikotech.com/technology/ikotech-qms/>.
- [67] W.S. Urs Häfeli, Joachim Teller, Maciej Zborowski, Scientific and clinical applications of magnetic carriers, Plenum Press, New York, 1997.
- [68] S.S. Shevkoplyas, A.C. Siegel, R.M. Westervelt, M.G. Prentiss, G.M. Whitesides, The force acting on a superparamagnetic bead due to an applied magnetic field, *Lab on a Chip* 7 (2007) 1294-1302.
- [69] M. Zborowski, L.P. Sun, L.R. Moore, P.S. Williams, J.J. Chalmers, Continuous cell separation using novel magnetic quadrupole flow sorter, *Journal of Magnetism and Magnetic Materials* 194 (1999) 224-230.
- [70] H. Morgan, and Green, N., , AC Electrokinetics: colloids and nanoparticles., Research Studies Press,, 2003.
- [71] P.S. J. Berthier, *Microfluidics for Biotechnology* (2nd Edition), Artech House (2009).
- [72] H.X. Ning, G.T. Lin, T. Lue, C.S. Lin, Mesenchymal stem cell marker Stro-1 is a 75kd endothelial antigen, *Biochemical and Biophysical Research Communications* 413 (2011) 353-357.
- [73] P.J. Simmons, B. Torokstorb, Identification of Stromal Cell Precursors in Human Bone-Marrow by a Novel Monoclonal-Antibody, Stro-1, *Blood* 78 (1991) 55-62.
- [74] N.T.K. Thanh, L.A.W. Green, Functionalisation of nanoparticles for biomedical applications, *Nano Today* 5 (2010) 213-230.
- [75] R.S.W. Thomas, P.D. Mitchell, R.O.C. Oreffo, H. Morgan, Trapping single human osteoblast-like cells from a heterogeneous population using a dielectrophoretic microfluidic device, *Biomicrofluidics* 4 (2010) 022806.
- [76] Z. Zhang, M. Al-Rubeai, C.R. Thomas, Effect of Pluronic F-68 on the mechanical properties of mammalian cells, *Enzyme and Microbial Technology* 14 (1992) 980-983.
- [77] S. Shim, P. Gascoyne, J. Noshari, K.S. Hale, Dynamic physical properties of dissociated tumor cells revealed by dielectrophoretic field-flow fractionation, *Integrative Biology* 3 (2011) 850-862.
- [78] G. Huang, Q. Zheng, J. Sun, C. Guo, J. Yang, R. Chen, Y. Xu, G. Wang, D. Shen, Z. Pan, J. Jin, J. Wang, Stabilization of cellular properties and differentiation mutipotent of human mesenchymal stem cells transduced with hTERT gene in a long-term culture, *Journal of Cellular Biochemistry* 103 (2008) 1256-1269.
- [79] Y.J. Kim, M.H. Lee, J.M. Wozney, J.Y. Cho, H.M. Ryoo, Bone morphogenetic protein-2-induced alkaline phosphatase expression is stimulated by Dlx5 and repressed by Msx2, *Journal of Biological Chemistry* 279 (2004) 50773-50780.

- [80] R. Tare, P. Mitchell, J. Kanczler, R.C. Oreffo, Isolation, Differentiation, and Characterisation of Skeletal Stem Cells from Human Bone Marrow In Vitro and In Vivo, in: M.H. Helfrich, S.H. Ralston (Eds.), *Bone Research Protocols*, Humana Press, 2012, pp. 83-99.
- [81] T.D. Schmittgen, K.J. Livak, Analyzing real-time PCR data by the comparative CT method, *Nat. Protocols* 3 (2008) 1101-1108.
- [82] R.S. Tare, J. Kanczler, A. Aarvold, A.M.H. Jones, D.G. Dunlop, R.O.C. Oreffo, Skeletal stem cells and bone regeneration: translational strategies from bench to clinic, *Proceedings of the Institution of Mechanical Engineers Part H-Journal of Engineering in Medicine* 224 (2010) 1455-1470.
- [83] I.C. Gay, S. Chen, M. MacDougall, Isolation and characterization of multipotent human periodontal ligament stem cells, *Orthodontics & Craniofacial Research* 10 (2007) 149-160.
- [84] J. van den Dolder, J.A. Jansen, Enrichment of osteogenic cell populations from rat bone marrow stroma, *Biomaterials* 28 (2007) 249-255.
- [85] Z.B. Liu, F. Huang, J.H. Du, W.L. Shu, H.T. Feng, X.P. Xu, Y. Chen, Rapid isolation of cancer cells using microfluidic deterministic lateral displacement structure, *Biomicrofluidics* 7 (2013).
- [86] J.V. Green, S.K. Murthy, Microfluidic enrichment of a target cell type from a heterogenous suspension by adhesion-based negative selection, *Lab on a Chip* 9 (2009) 2245-2248.
- [87] P. Li, Y. Gao, D. Pappas, Negative Enrichment of Target Cells by Microfluidic Affinity Chromatography, *Analytical Chemistry* 83 (2011) 7863-7869.
- [88] J.G. Kralj, C. Arya, A. Tona, T.P. Forbes, M.S. Munson, L. Sorbara, S. Srivastava, S.P. Forry, A simple packed bed device for antibody labelled rare cell capture from whole blood, *Lab on a Chip* 12 (2012) 4972-4975.
- [89] A.J. Mach, J.H. Kim, A. Arshi, S.C. Hur, D. Di Carlo, Automated cellular sample preparation using a Centrifuge-on-a-Chip, *Lab on a Chip* 11 (2011) 2827-2834.
- [90] Website: <https://www.lifetechnologies.com/it/en/home/life-science/protein-biology/protein-biology-learning-center/protein-biology-resource-library/pierce-protein-methods/carbodiimide-crosslinker-chemistry.html>.
- [91] H. Hardelauf, J. Sisnaiske, A.A. Taghipour-Anvari, P. Jacob, E. Drabiniok, U. Marggraf, J.-P. Frimat, J.G. Hengstler, A. Neyer, C. van Thriel, J. West, High fidelity neuronal networks formed by plasma masking with a bilayer membrane: analysis of neurodegenerative and neuroprotective processes, *Lab on a Chip* 11 (2011) 2763-2771.

-
- [92] A. Azioune, M. Storch, M. Bornens, M. They, M. Piel, Simple and rapid process for single cell micro-patterning, *Lab on a Chip* 9 (2009) 1640-1642.
- [93] S. Lee, J. Vörös, An Aqueous-Based Surface Modification of Poly(dimethylsiloxane) with Poly(ethylene glycol) to Prevent Biofouling, *Langmuir* 21 (2005) 11957-11962.
- [94] E. Antoniou, M. Tsianou, Solution properties of dextran in water and in formamide, *Journal of Applied Polymer Science* 125 (2012) 1681-1692.

LIST OF APPENDICES

APPENDIX A – QMS ver.1

APPENDIX B – Magnetic field measurements

APPENDIX C – QMS ver.2

APPENDIX D – HMS

APPENDIX E - Superparamagnetic bead susceptibility calculation

APPENDIX F – Superparamagnetic beads functionalisation protocol

APPENDIX G – Cell magnetic susceptibility calculation

APPENDIX H – Particle tracing simulation details

APPENDIX I – Surface treatments

APPENDIX L - Carboxyl polystyrene beads coating protocol

APPENDIX M – Sorting device threshold

APPENDIX N – Protocols

APPENDIX O – ALP staining

APPENDIX P – Technical Drawings

APPENDIX A – QMS ver.1

In this appendix, the numerical simulation details regarding the QMS ver.1 were reported, including the meshing setting and the solver used (Figure A.1). In addition, the all the components of \vec{B} and $(\vec{B} \cdot \nabla)\vec{B}$ were plotted along two cut lines (Figure A.2 and Figure A.3).

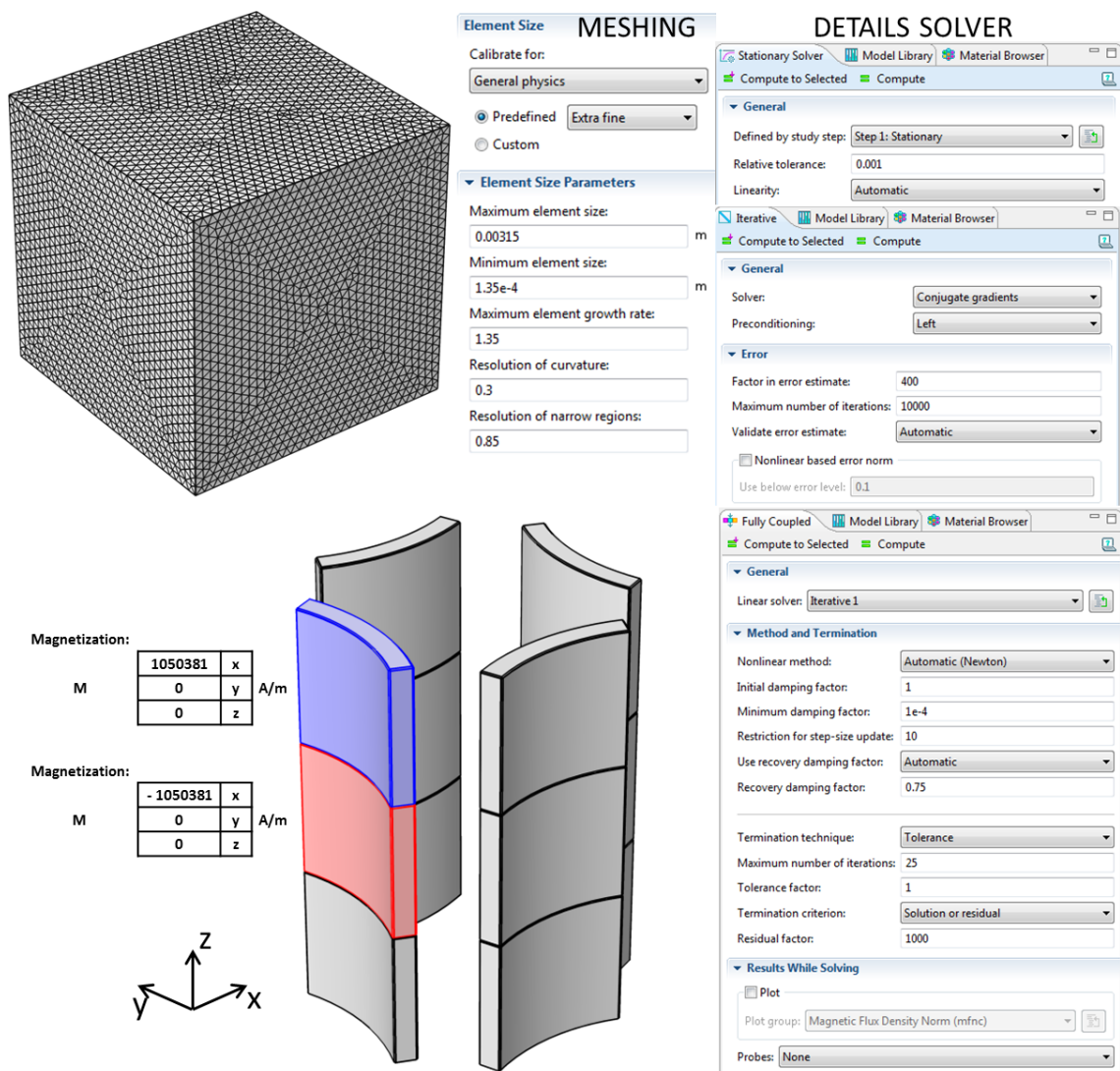


Figure A.1: Simulation details (Section 5.2.1 – Figure 5.5 / Figure 5.6). The 12 arc magnets were merged within the block (air).

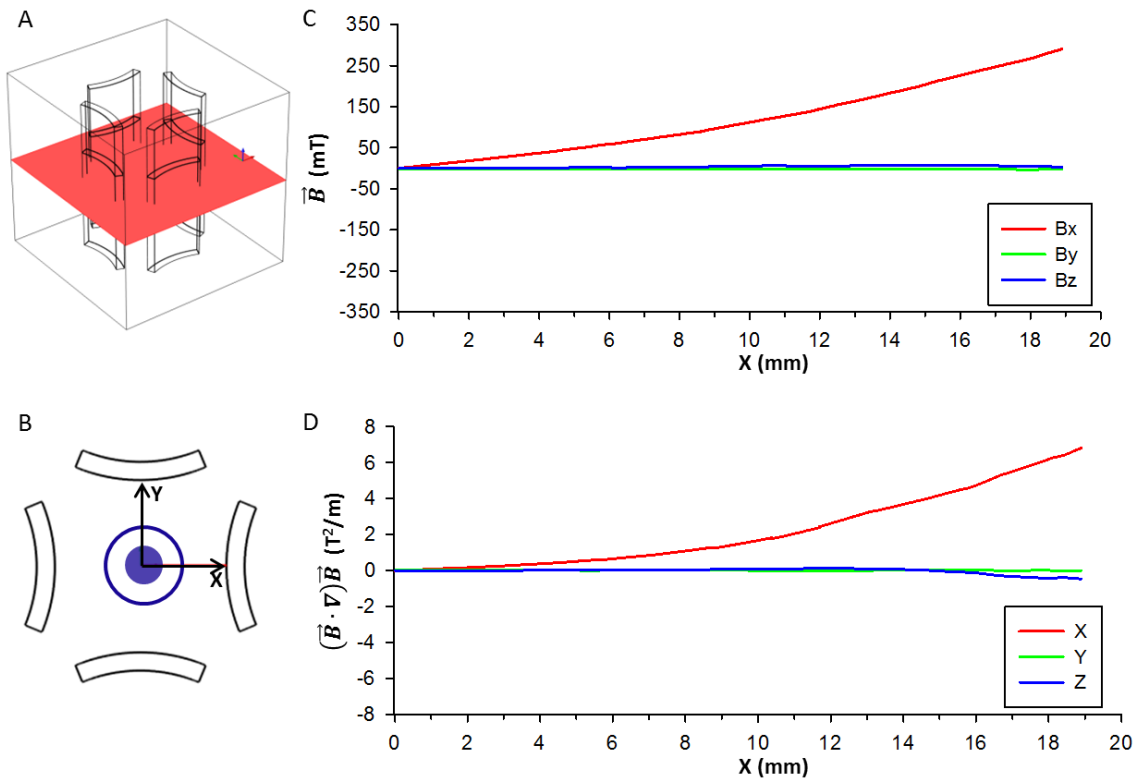


Figure A.2: Magnetic system horizontal middle cut plane (A); cut line drawn on the horizontal cut plane (B). Plot of \vec{B} along the cut line (C); plot of $(\vec{B} \cdot \nabla)\vec{B}$ along the cut line (D).

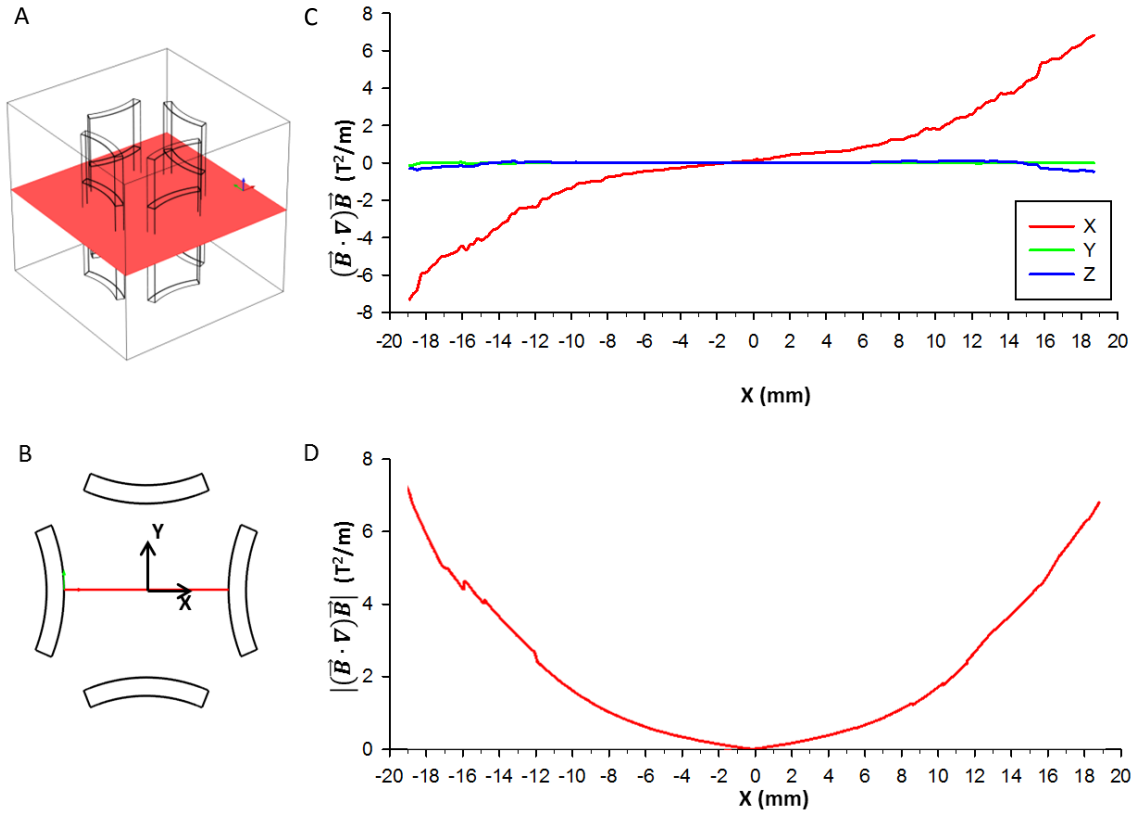


Figure A.3: Magnetic system horizontal middle cut plane (A); cut line drawn on the horizontal cut plane (B). Plot of $(\vec{B} \cdot \nabla)\vec{B}$ along the cut line (C); plot of $|(\vec{B} \cdot \nabla)\vec{B}|$ along the cut line (D).

APPENDIX B – MAGNETIC FIELD MEASUREMENTS

In this appendix, the experimental magnetic field measurements were described along with the Matlab code used to process and plot the data. In particular, plots of \vec{B} and $(\vec{B} \cdot \nabla)\vec{B}$ were shown in Figure B.2. Figure B.3 described $|(\vec{B} \cdot \nabla)\vec{B}|$ along two vertical cut lines, emphasising how the values of $|(\vec{B} \cdot \nabla)\vec{B}|$ changed along the length of the HMS.

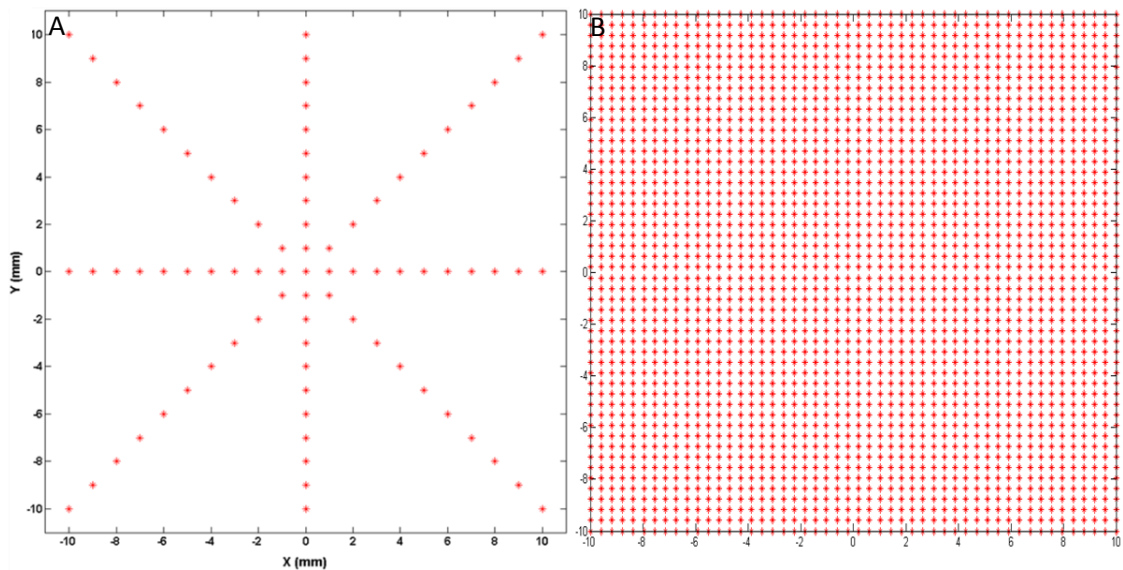


Figure B.1: 80 points within an area of 20 mm x 20 mm at the centre of the system where measurements of B_x and B_y were performed (A). For each of these points I had a value of B_x and a value of B_y . Using cubic interpolation I obtain an array covering the entire analysed surface (B), so I had a value of B_x and a value of B_y for each of the points in figure B.

$$\text{Segment D (Figure 5.11F): } |\vec{B}| = \sqrt{(B_x)^2 + (B_y)^2} = \sqrt{(0.05)^2 + (0)^2} = 0.05 \text{ T}$$

$$\text{Segment E (Figure 5.11G): } |\vec{B}| = \sqrt{(B_x)^2 + (B_y)^2} = \sqrt{(0.049)^2 + (0.049)^2} = 0.0693 \text{ T}$$

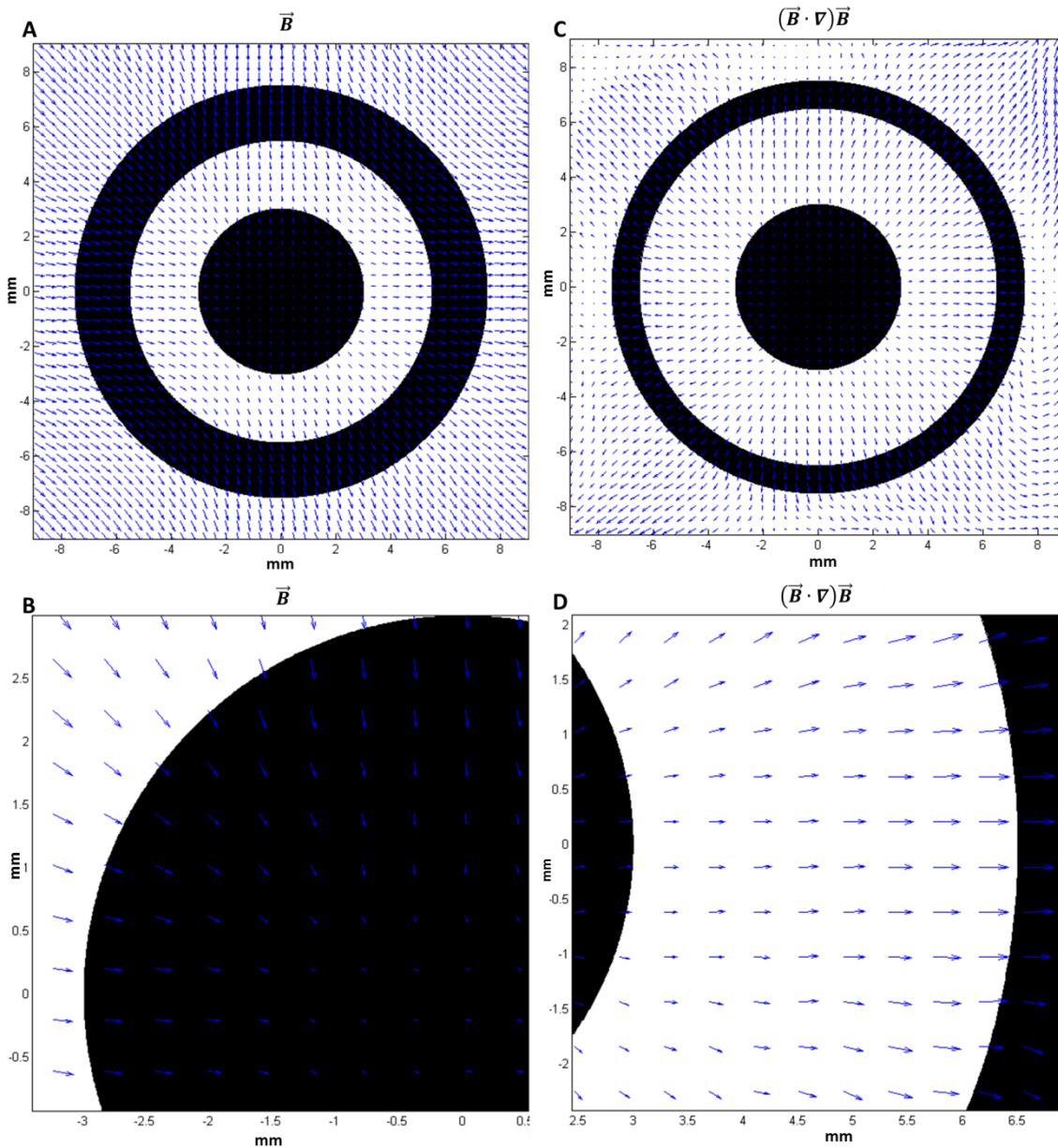


Figure B.2: (A) Proportional vectors representing the direction of \vec{B} according to the experimental measurements and (B) detail. (C) Proportional vectors representing the direction of $(\vec{B} \cdot \nabla)\vec{B}$ according to the experimental measurements and (D) detail.

MATLAB CODE

Matlab code to obtain the grid in Figure 0.1B:

```
xlin = linspace(min(x),max(x),50);
ylin = linspace(min(y),max(y),50);
[X,Y] = meshgrid(xlin,ylin);
```

Matlab code for the cubic interpolation of the B_x and B_y measured over the entire grid:

```
Bx =(griddata(x,y,bx,X,Y,'cubic'));
```

`By = -(griddata(x,y,by,X,Y,'cubic'));`

Matlab code to plot the vectors describing the direction of \vec{B} (Figure B.2A):

`quiver(X,Y,Bx,By)`

Matlab code to plot the vectors describing the direction of $(\vec{B} \cdot \nabla)\vec{B}$ (Figure B.2C):

```
[Bxx,Bxy]=gradient(Bx);
[Byx,Byy]=gradient(By);
C1=Bx.*Bxx+By.*Bxy;
C2=Bx.*Byx+By.*Byy;
quiver(X,Y,C1,C2)
```

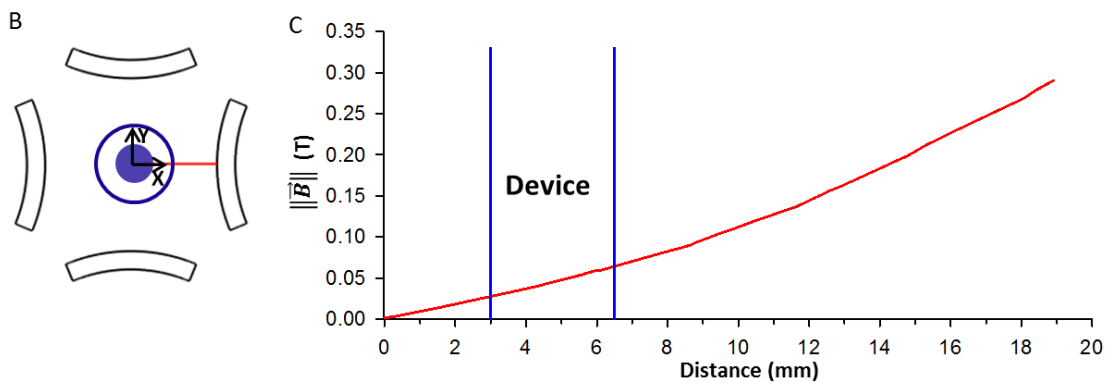
$$(\vec{B} \cdot \nabla)\vec{B} = \left(B_x \frac{\partial B_x}{\partial x} + B_y \frac{\partial B_x}{\partial y}, B_x \frac{\partial B_y}{\partial x} + B_y \frac{\partial B_y}{\partial y} \right)$$

COMSOL SIMULATIONS

$$\vec{F}_m = \frac{V_p \Delta \chi}{\mu_0} (\vec{B} \cdot \nabla)\vec{B} = \frac{V_p \Delta \chi}{\mu_0} \begin{bmatrix} B_x \frac{\partial B_x}{\partial x} + B_y \frac{\partial B_x}{\partial y} + B_z \frac{\partial B_x}{\partial z} \\ B_x \frac{\partial B_y}{\partial x} + B_y \frac{\partial B_y}{\partial y} + B_z \frac{\partial B_y}{\partial z} \\ B_x \frac{\partial B_z}{\partial x} + B_y \frac{\partial B_z}{\partial y} + B_z \frac{\partial B_z}{\partial z} \end{bmatrix}$$

Magnitude of $\vec{B} = |\vec{B}| = \sqrt{(B_x)^2 + (B_y)^2 + (B_z)^2}$

So in all the plots (like the one below) the simulation calculated $|\vec{B}|$ for each point along the line (in figure B) and plot the value in the graph. So it plots the values of magnitude of vector $\vec{B}(B_x, B_y, B_z)$ along the line (so in this case B_x was relevant).



Magnitude of $(\vec{B} \cdot \nabla)\vec{B}$:

$$|(\vec{B} \cdot \nabla)\vec{B}| =$$

$$\sqrt{\left(B_x \frac{\partial B_x}{\partial x} + B_y \frac{\partial B_x}{\partial y} + B_z \frac{\partial B_x}{\partial z}\right)^2 + \left(B_x \frac{\partial B_y}{\partial x} + B_y \frac{\partial B_y}{\partial y} + B_z \frac{\partial B_y}{\partial z}\right)^2 + \left(B_x \frac{\partial B_z}{\partial x} + B_y \frac{\partial B_z}{\partial y} + B_z \frac{\partial B_z}{\partial z}\right)^2}$$

COMSOL

$$B_x \frac{\partial B_x}{\partial x} + B_y \frac{\partial B_x}{\partial y} + B_z \frac{\partial B_x}{\partial z} = \text{mfnc.Bx*d(mfnc.Bx,x)} + \text{mfnc.By*d(mfnc.Bx,y)} + \text{mfnc.Bz*d(mfnc.Bx,z)}$$

$$B_x \frac{\partial B_y}{\partial x} + B_y \frac{\partial B_y}{\partial y} + B_z \frac{\partial B_y}{\partial z} = \text{mfnc.Bx*d(mfnc.By,x)} + \text{mfnc.By*d(mfnc.By,y)} + \text{mfnc.Bz*d(mfnc.By,z)}$$

$$B_x \frac{\partial B_z}{\partial x} + B_y \frac{\partial B_z}{\partial y} + B_z \frac{\partial B_z}{\partial z} = \text{mfnc.Bx*d(mfnc.Bz,x)} + \text{mfnc.By*d(mfnc.Bz,y)} + \text{mfnc.Bz*d(mfnc.Bz,z)}$$

$$|(\vec{B} \cdot \nabla)\vec{B}| =$$

$$\text{sqrt}((\text{mfnc.Bx*d(mfnc.Bx,x)} + \text{mfnc.By*d(mfnc.Bx,y)} + \text{mfnc.Bz*d(mfnc.Bx,z)})^2 + (\text{mfnc.Bx*d(mfnc.By,x)} + \text{mfnc.By*d(mfnc.By,y)} + \text{mfnc.Bz*d(mfnc.By,z)})^2 + (\text{mfnc.Bx*d(mfnc.Bz,x)} + \text{mfnc.By*d(mfnc.Bz,y)} + \text{mfnc.Bz*d(mfnc.Bz,z)})^2)$$

HEXAPOLE MAGNETIC SYSTEM (HMS)

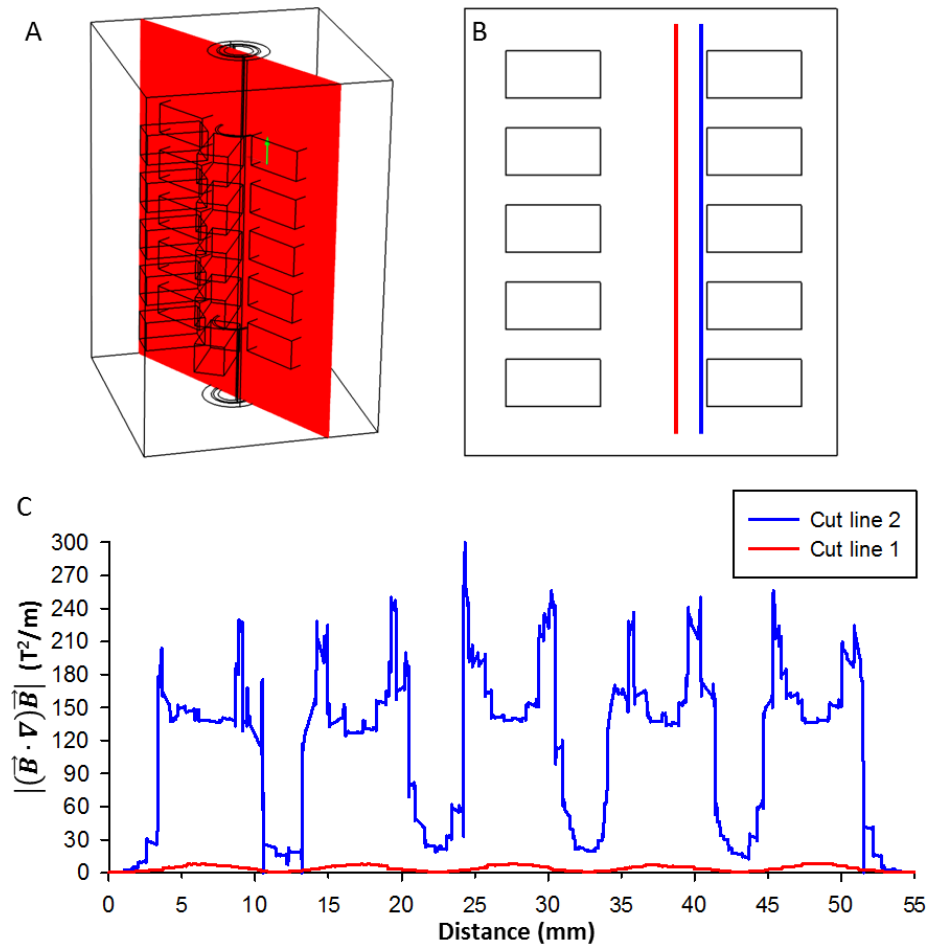


Figure B.3: (A) Horizontal mid-plane. (B) Vertical cut lines next to the central rod (in red) and next to the internal wall of the sorting device (in blue). (C) Magnitude of $|(\vec{B} \cdot \nabla)\vec{B}|$ along the two vertical cut lanes.

Figure B.3 shows the values of $|(\vec{B} \cdot \nabla)\vec{B}|$ vertical cut lanes. The first (in red) next to the central rod, the second next to the internal wall of the sorting device. $|(\vec{B} \cdot \nabla)\vec{B}|$ along the two cut lanes was significantly different. Moreover, $|(\vec{B} \cdot \nabla)\vec{B}|$ along each cut lane oscillated significantly in response to the structure of the magnetic system (HMS) surrounding the sorting device. This variation in magnitude was evident along cut line 2 (Figure B.3C). Along this line $|(\vec{B} \cdot \nabla)\vec{B}|$ oscillated between an average value of $150 \text{ T}^2/\text{m}$ and an average value $20 \text{ T}^2/\text{m}$ in correspondence of magnets and space between magnets respectively. Along cut line 2 peaks in the values of $|(\vec{B} \cdot \nabla)\vec{B}|$ were shown in correspondence to the edges of the magnets. The variation along the cut line 1 was less evident (between $9 \text{ T}^2/\text{m}$ and $1 \text{ T}^2/\text{m}$). This meant that a labelled cell experienced different values of $|(\vec{B} \cdot \nabla)\vec{B}|$ during its travel through the device.

APPENDIX C – QMS ver.2

In this appendix, the numerical simulation details regarding the QMS ver.2 were reported, including the meshing setting and the solver used (Figure C.1). Figure C.2 reported a colour map $|\vec{B}|$ over the horizontal mid-plane highlighting the effect of the half rod mild steel pieces on the magnetic field generated. In addition, the all the components of \vec{B} and $(\vec{B} \cdot \nabla)\vec{B}$ were plotted along two cut lines (Figure C.3 and Figure C.4).

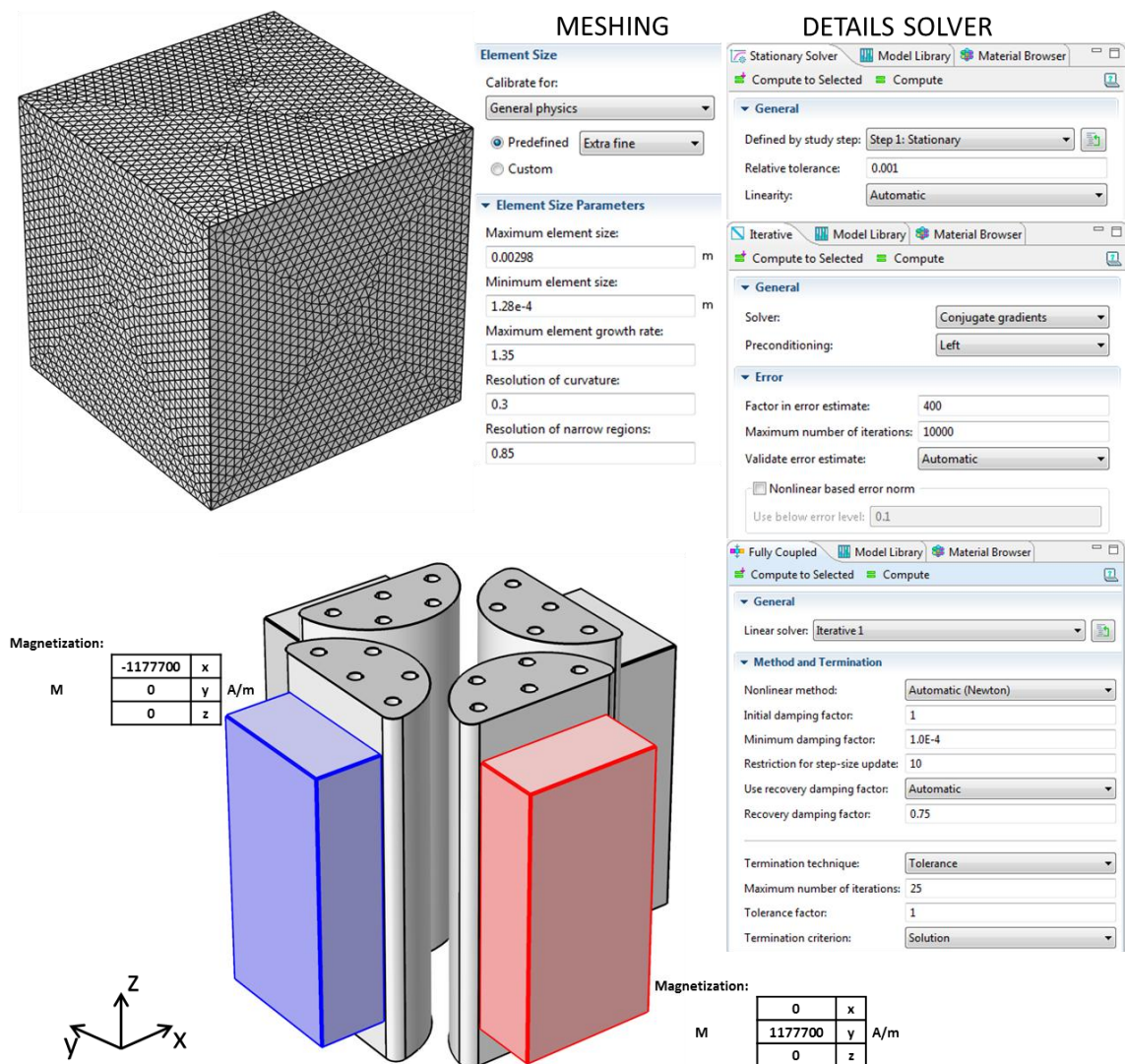


Figure C.1: Simulation details (Section 5.3.2 – Figure 5.15 / Figure 5.16). The magnets and the half rod mild steel pieces were merged within the block (air).

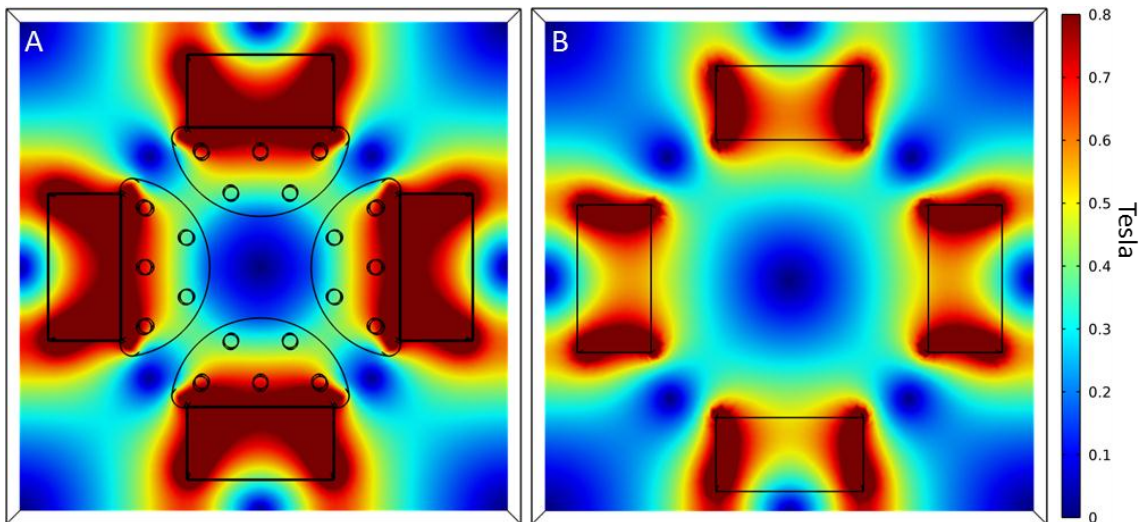


Figure C.2: (A) Colour map of $|\vec{B}|$ over the horizontal mid-plane for QMS ver.2 with and (B) without the half rod mild steel pieces (Section 5.3.2). Meshing and solver details were the same of previous simulation (Figure 2.1).

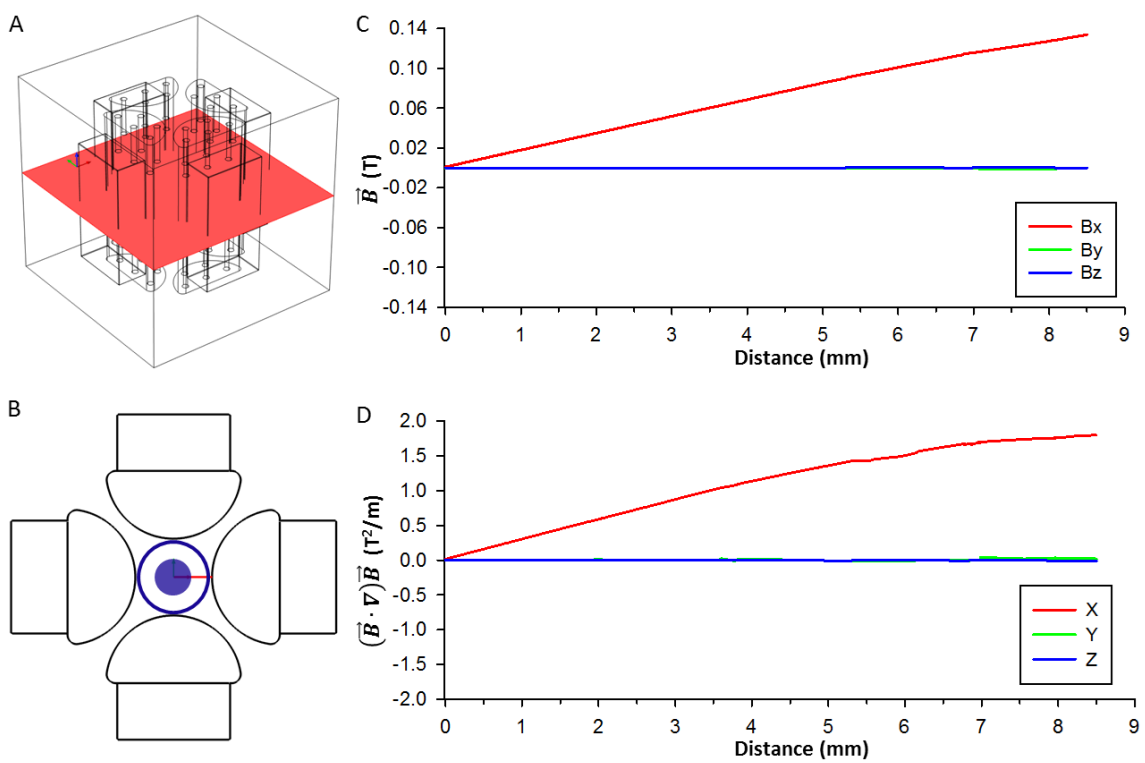


Figure C.3: (A) Magnetic system horizontal middle cut plane; (B) cut line drawn on the horizontal cut plane. (C) Plot of \vec{B} along the cut line; (D) plot of $(\vec{B} \cdot \nabla)\vec{B}$ along the cut line.

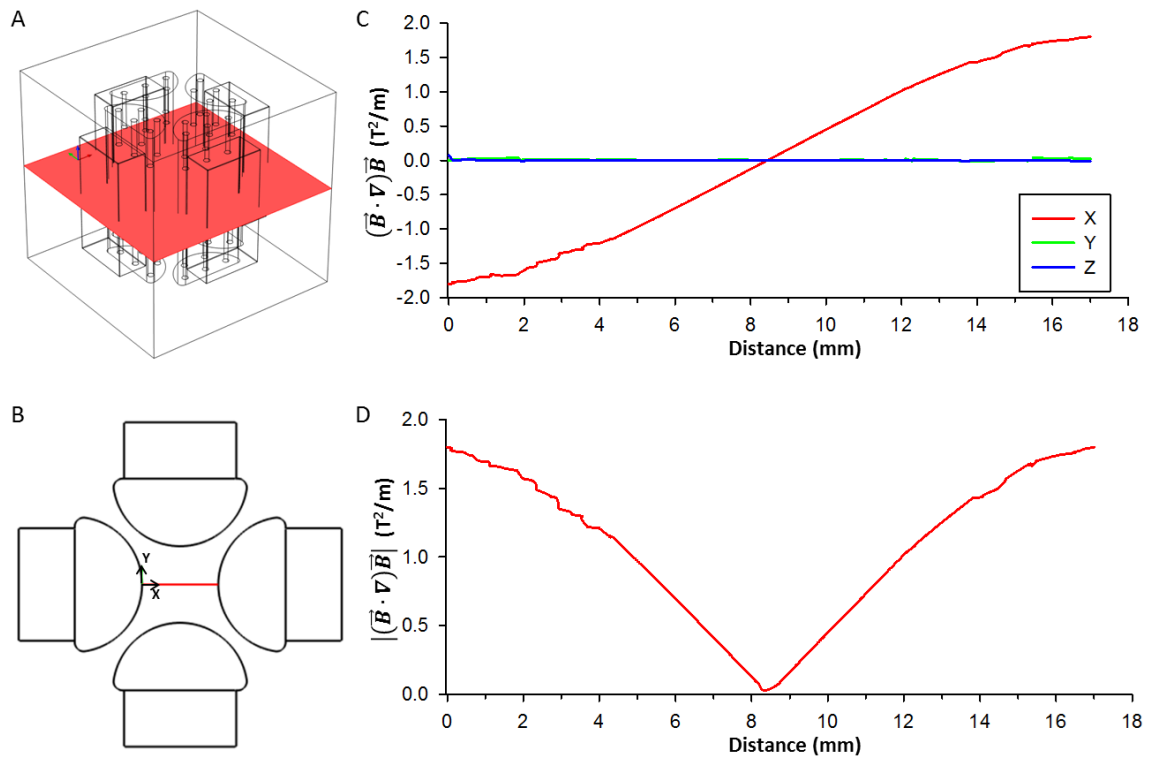


Figure C.4: (A) Magnetic system horizontal middle cut plane; (B) cut line drawn on the horizontal cut plane. (C) Plot of $(\vec{B} \cdot \nabla)\vec{B}$ along the cut line; (D) plot of $|(\vec{B} \cdot \nabla)\vec{B}|$ along the cut line.

APPENDIX D – HMS

In this appendix, the numerical simulation details regarding the HMS were reported, including the meshing setting and the solver used (Figure D.1). In addition, the all the components of \vec{B} and $(\vec{B} \cdot \nabla)\vec{B}$ were plotted along two cut lines (Figure D.2 and Figure D.3).

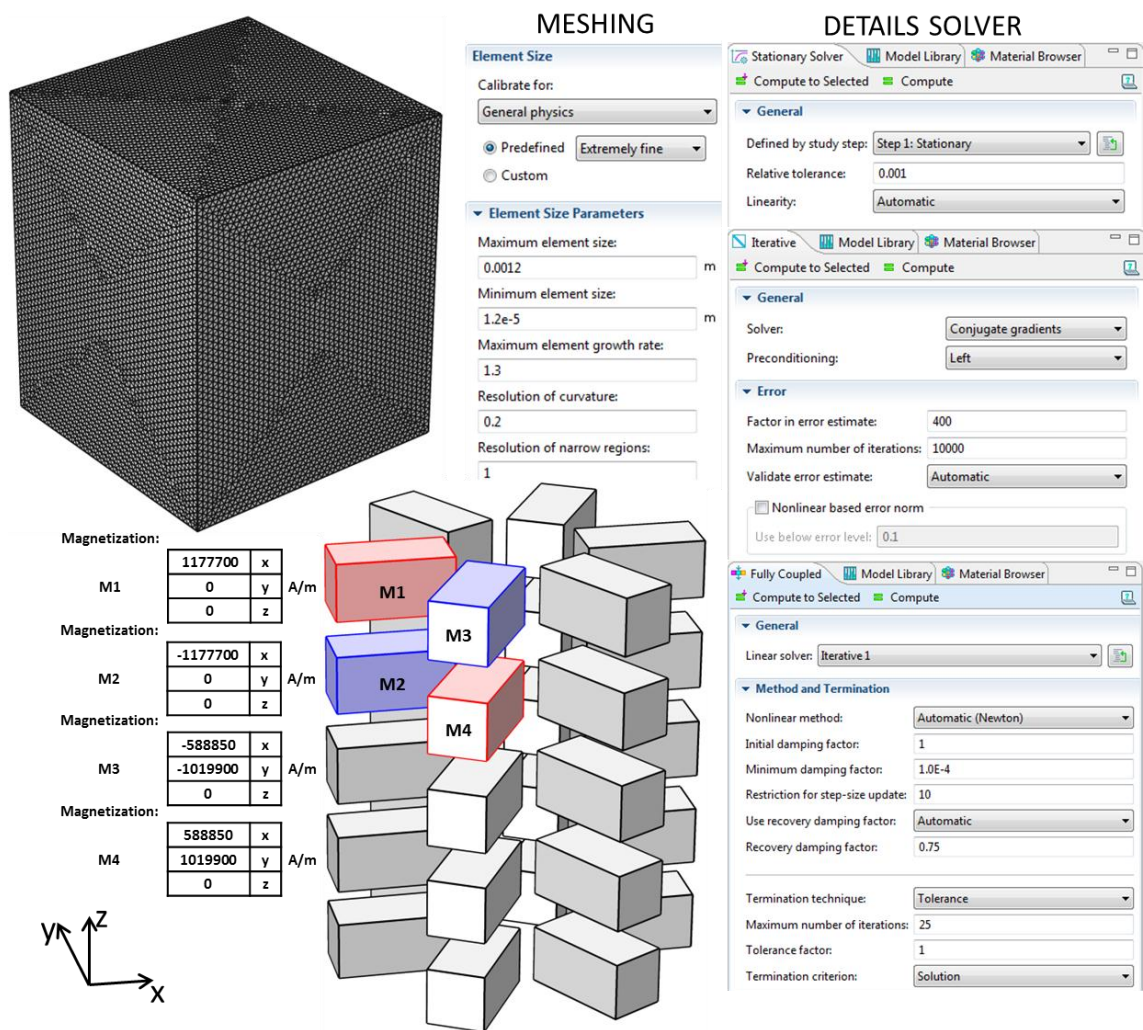


Figure D.1: Simulation details (Section 5.4.2 – Figure 5.21 / Figure 5.22). The magnets and the half rod mild steel pieces were merged within the block (air).

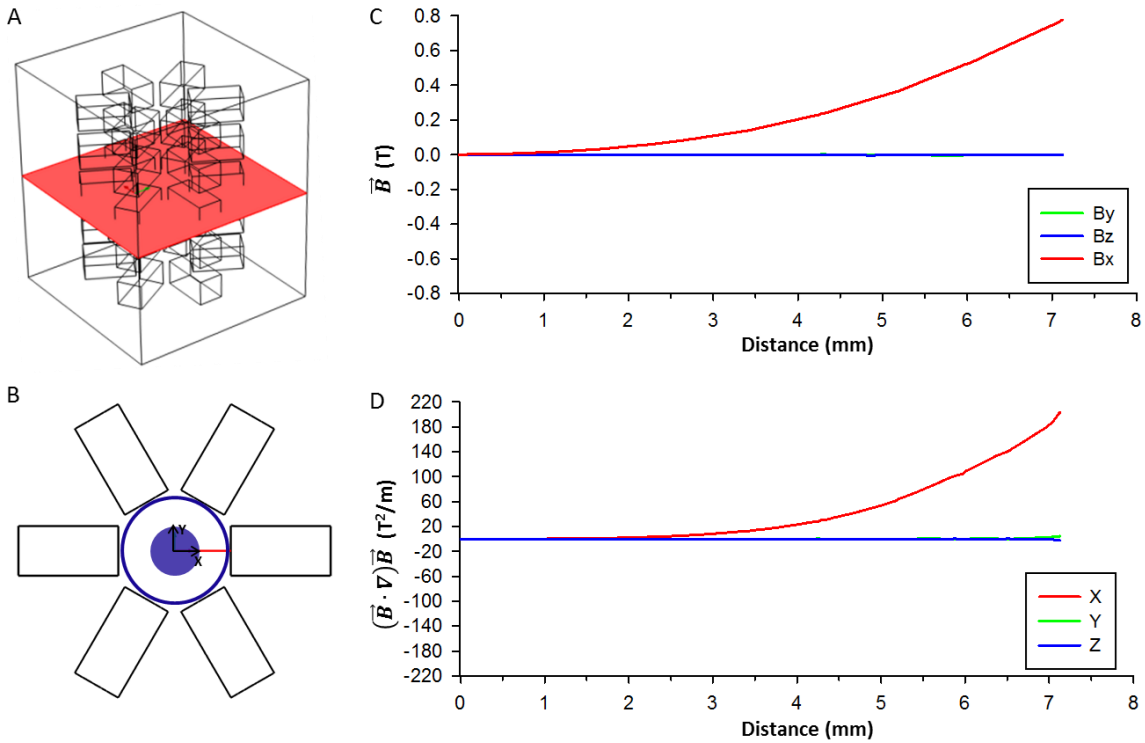


Figure D.2: (A) Magnetic system horizontal middle cut plane; (B) cut line drawn on the horizontal cut plane. (C) Plot of \vec{B} along the cut line; (D) plot of $(\vec{B} \cdot \nabla)\vec{B}$ along the cut line.

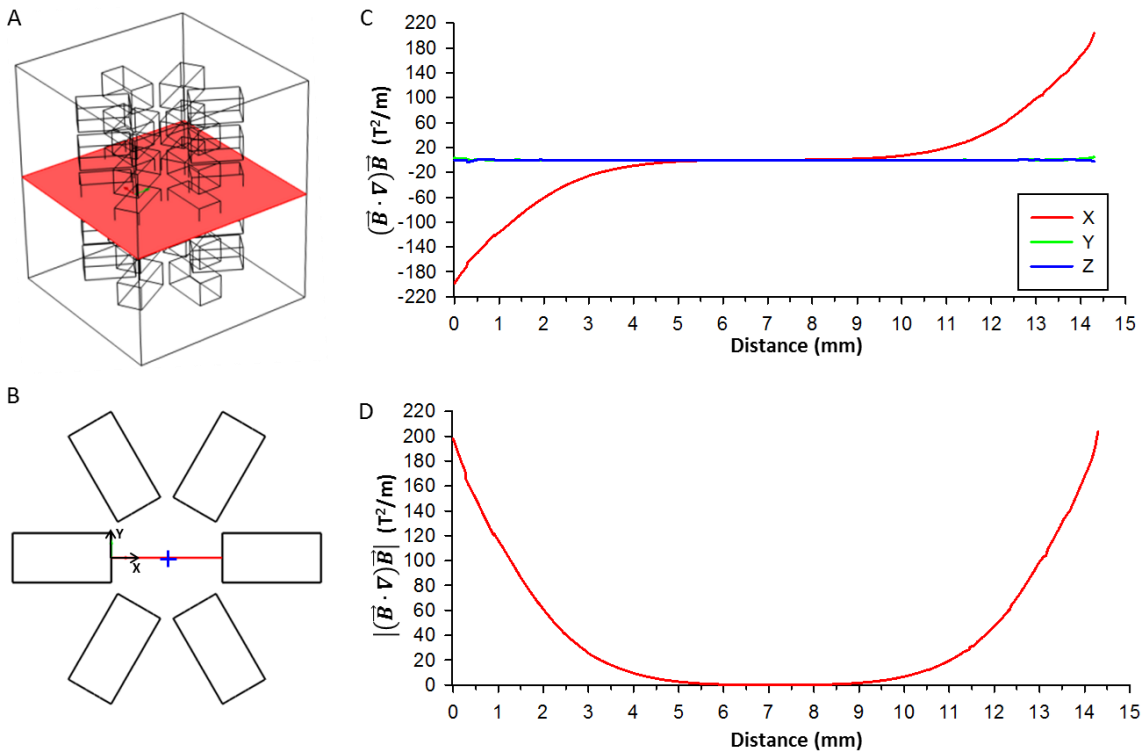


Figure D.3: (A) Magnetic system horizontal middle cut plane; (B) cut line drawn on the horizontal cut plane. (C) Plot of $(\vec{B} \cdot \nabla)\vec{B}$ along the cut line; (D) plot of $|(\vec{B} \cdot \nabla)\vec{B}|$ along the cut line.

APPENDIX E

In this appendix, the equations used to calculate the magnetic susceptibility of superparamagnetic beads were reported.

SUPERPARAMAGNETIC BEAD SUSCEPTIBILITY CALCULATION (χ_b)

$$\vec{F}_m = V_b \Delta\chi \frac{|\nabla \vec{B}^2|}{2\mu_0} \left[\frac{\text{m}^3 \frac{\text{N}^2}{\text{A}^2 \text{m}^3}}{\frac{\text{N}}{\text{A}^2}} \right] = [\text{N}]$$

$$v_b = \frac{\vec{F}_m}{f} = \frac{V_b \Delta\chi}{12\mu_0 \eta r_b \pi} |\nabla \vec{B}^2| \left[\frac{\text{N}}{\frac{\text{Ns}}{\text{m}^2} \text{m}} = \frac{\text{m}}{\text{s}} \right]$$

$$\chi_b = \frac{12\pi v_b \eta \mu_0 r_b}{V_b |\nabla \vec{B}^2|} + \chi_w \left[\frac{\frac{\text{m Ns N}}{\text{s m}^2 \text{A}^2} \text{m}}{\text{m}^3 \frac{\text{N}^2}{\text{A}^2 \text{m}^3}} \right] = []$$

\vec{F}_m magnetic force

η dynamic viscosity water = $1.002 * 10^{-3}$ [Ns/m²]

r_b the radius of the bead [m]

v_b was the average bead velocity (experimental) [m/s]

$\Delta\chi$ difference in magnetic susceptibility $\chi_b - \chi_w$ ($\chi_w = -9.035 * 10^{-6}$)

μ_0 was the magnetic permeability of free space = $4\pi * 10^{-7}$ [N/A²]

V_b bead volume [m³]

f friction coefficient

For each type of superparamagnetic bead, the travelling times along the channel were recorded, the average velocity calculated and the χ_p values estimated.

APPENDIX F

CARBOXYL BEAD FUNCTIONALISATION PROTOCOL

2.9 mg of N-Hydroxysulfosuccinimide sodium salt were suspended in 1 ml of PBS (pH 6), then 7.8 mg of N-(3-Dimethylaminopropyl)-N'-ethylcarbodiimide hydrochloride (EDC) were added. The solutions were added to the beads (surface COOH) and left on the bench at RT for 2 hours (or use the rotating arm to avoid sedimentation). The beads were washed three times with PBS (spin down 13000 rpm for 3 min). The sample was centrifuged, the supernatant discarded and 0.5 ml of PBS (pH 8) and antibodies (STRO-1 antibodies from Bone and Joint group. Dilution 1:100) were added to each sample. The beads suspension was left at 4 °C overnight on a 3D shaker, then washed three times with PBS (spin down 13000 rpm for 3 min), suspended in PBS and kept at 4 °C.

The chemical reactions on the beads surface were described in Figure F.1.

CELL LABELLING PROTOCOL

2 ml of blocking buffer (PBS + 0.5% BSA + 2 mM EDTA + 3% goat serum) were added to the cell suspension and incubated at 4 °C for 15 min. The cells were washed three times with MACS buffer (PBS + 0.5% BSA + 2 mM EDTA) and suspended in PBS. The functionalised beads were added to the cell suspension and incubated at 4 °C for 30 min on a 3D shaker. The cells were washed three times with MACS buffer (PBS + 0.5% BSA + 2 mM EDTA).

NUMBER OF BEAD PER BM SAMPLE

The approach was to incubate the HBMSCs isolated from a BM sample with a sufficient number of functionalised beads to cover the entire surface of the cells expressing STRO-1. This method overestimates the number of beads needed; a STRO-1+ cell would not be completely covered with functionalised beads (as from Figure 6.5). The number of HBMSCs isolated from a BM sample was $\sim 20 \times 10^6$, and $\sim 17\%$ of the cell population consisted in STRO-1+ cells. Approximating a cell to a sphere ($\varnothing 20 \mu\text{m}$) the cell surface was estimated ($\sim 1200 \mu\text{m}^2$), and the number of beads needed to cover the entire cell surfaces was calculated. In the case of the CM-08-10 ($\varnothing 0.82 \mu\text{m}$) beads used in this study, the number of beads per cell was ~ 2300 . This number was an overestimate (in the labelled cells suspension, a significant number of free beads was found); therefore the calculation was done considering just 10% of the HBMSCs population to be STRO-1+ (2×10^6 cells per BM sample).

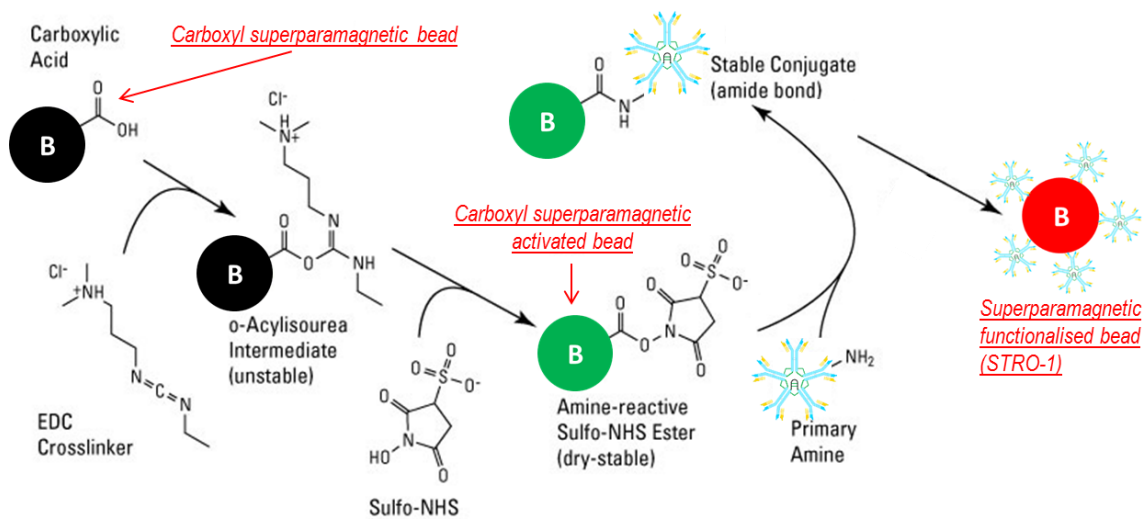


Figure F.1: Carboxyl superparamagnetic beads functionalization protocol [90]. Carbodiimide coupling covalently bind carboxylic acids (COOH) to the primary amines (NH₂) of the proteins. N-(3-Dimethylaminopropyl)-N'-ethylcarbodiimide hydrochloride (EDC) was used as a coupling agent. EDC reacts with the carboxylic acid groups on the bead surface to form an amine-reactive active intermediate (*O*-acylisourea intermediate). To increase the efficiency of the coupling reaction, N-Hydroxysulfosuccinimide sodium salt (NHSS or Sulfo-NHS) was added to the activation solution. The addition of NHSS converted the unstable *O*-acylisourea intermediate to amine-reactive NHSS ester allowing the conjugation to primary amines [74].

In this circumstance the number of functionalised beads used to process each BM sample was $\sim 4.6 \times 10^9$. A bead suspension (10 ml tube with a concentration of 0.87×10^{11} bead/ml) was purchased from Spherotech, Inc. (USA) providing ~ 195 BM samples.

APPENDIX G

In this appendix, the equations and the numerical simulation used to calculate the magnetic susceptibility of a labelled cell were reported. In Figure G.1 the \vec{B} and $(\vec{B} \cdot \nabla)\vec{B}$ a labelled cells experienced during the magnetic susceptibility estimations were reported.

CELL MAGNETIC SUSCEPTIBILITY CALCULATION (χ_c)

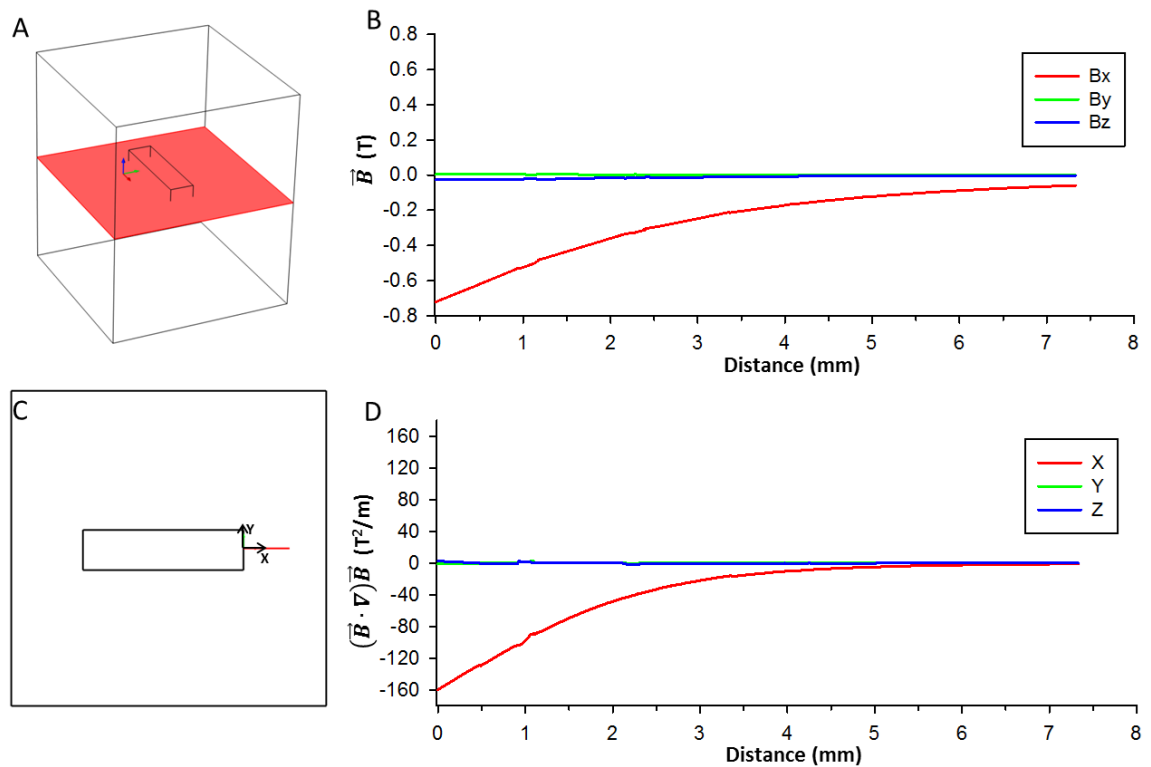


Figure G.1: (A) Horizontal mid-plane and (C) cut line along which \vec{B} and $(\vec{B} \cdot \nabla)\vec{B}$ were modelled. (B) Trend of the three components and Euclidian norm (blue line) of B along the cut line. (D) Trend of the three components and Euclidian norm (blue line) of $(B \cdot \nabla)B$ along the cut line.

The experimental setup (see Section 6.3 - Figure 6.7) used to estimate the magnetic susceptibility of a labelled cells (χ_c) was modelled. The values of B and $(B \cdot \nabla)B$ generated by the magnets along the channel used, were investigated through a numerical simulation. Once obtained the average time needed by a labelled cell to cover a known segment (as from Section 6.3.2, 30 labelled cells were observed), the average velocity was calculated ($2.41 \times 10^{-5} \pm 0.26 \times 10^{-5}$ [m/s]). At this point the relative position of that segment and the magnet was known; the values of $[(B \cdot \nabla)B]_0$ (value at the beginning of the segment –

far from the magnets) and $[(B \cdot \nabla)B]_1$ (value at the end of the segment – close from the magnets) were known. Combining equation (1) and (2) it was possible to obtain equation (3) which returned the value of χ_c .

$$\vec{F}_m = \frac{V_c \Delta\chi}{\mu_0} (\vec{B} \cdot \nabla) \vec{B} \left[\frac{\text{m}^3 \frac{\text{N}^2}{\text{A}^2 \text{m}^3}}{\frac{\text{N}}{\text{A}^2}} \right] = [\text{N}] \quad (1)$$

$$v_c = \frac{\vec{F}_m}{f} = \frac{V \Delta\chi}{6\mu_0 \eta r_c \pi} (\vec{B} \cdot \nabla) \vec{B} \left[\frac{\text{N}}{\frac{\text{Ns}}{\text{m}^2} \text{m}} = \frac{\text{m}}{\text{s}} \right] \quad (2)$$

$$\chi_c = \frac{6\pi v_c \eta \mu_0 r_c}{V_c \left[\frac{[(B \cdot \nabla)B]_0 + [(B \cdot \nabla)B]_1}{2} \right]} + \chi_w \left[\frac{\frac{\text{m Ns N}}{\text{s m}^2 \text{A}^2} \text{m}}{\frac{\text{m}^3 \frac{\text{N}^2}{\text{A}^2 \text{m}^3}}{\text{m}^2}} \right] = [] = 3.292 * 10^{-5} \pm 0.24 * 10^{-5} \quad (3)$$

$[(B \cdot \nabla)B]_0$ value beginning of the segment = 25 [T²/m]

$[(B \cdot \nabla)B]_1$ value end of the segment = 54 [T²/m]

F_m magnetic force

η dynamic viscosity water = $1.002 * 10^{-3}$ [Ns/m²]

r_c the radius of the cell = $10 * 10^{-6}$ [m]

v_c was the average cell velocity (experimental) = $2.41 * 10^{-5} \pm 0.26 * 10^{-5}$ [m/s]

$\Delta\chi$ difference in magnetic susceptibility $\chi_c - \chi_w$ ($\chi_w = -9.035 * 10^{-6}$)

μ_0 was the magnetic permeability of free space = $4\pi * 10^{-7}$ [N/A²]

V_c cell volume = $4.188 * 10^{-15}$ [m³]

f friction coefficient

APPENDIX H

In this appendix, the details (meshing, boundary conditions and solver) of all the particle tracing simulations were reported.

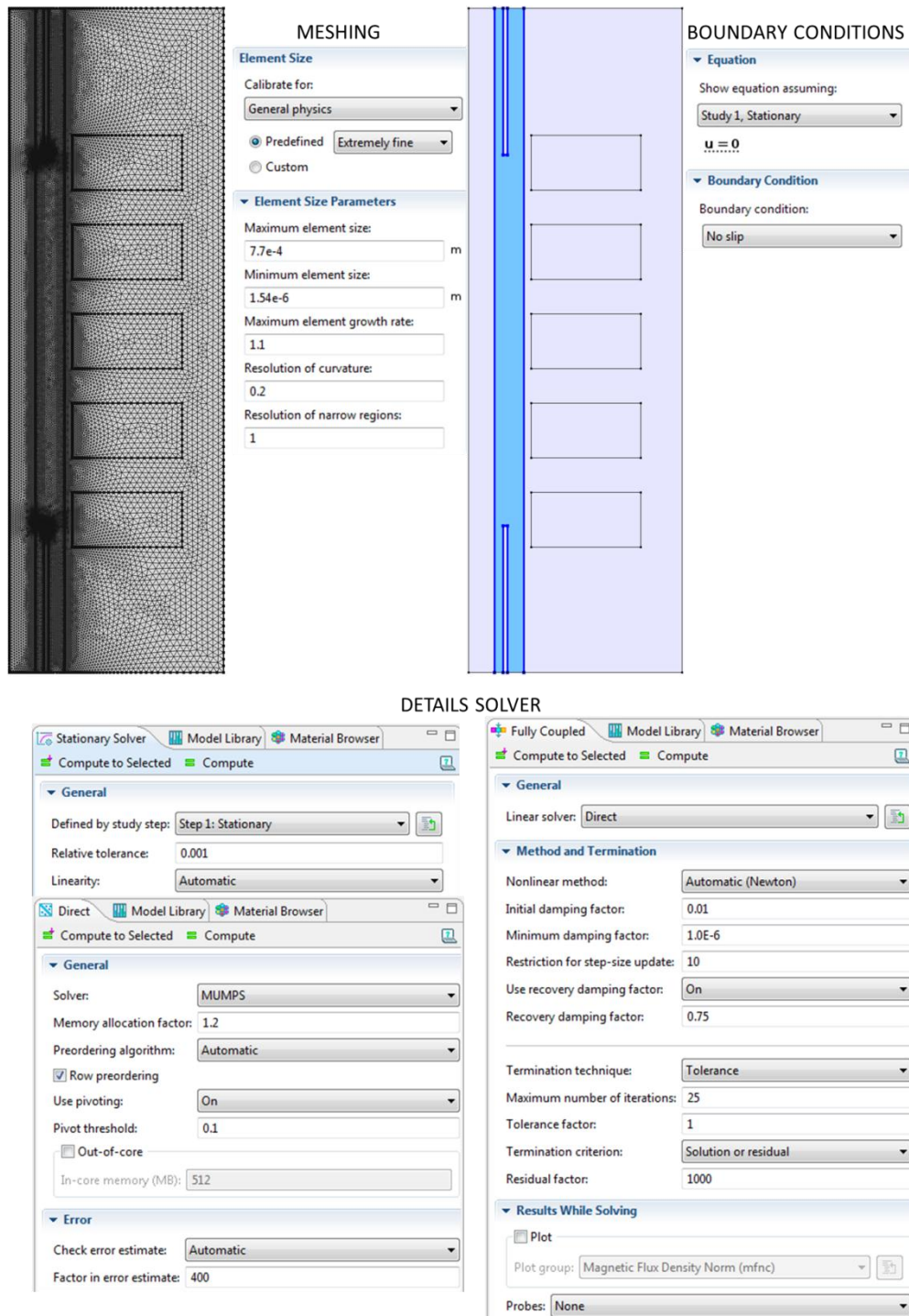


Figure H.1: Simulation details (Section 6.4 – Figure 6.9).

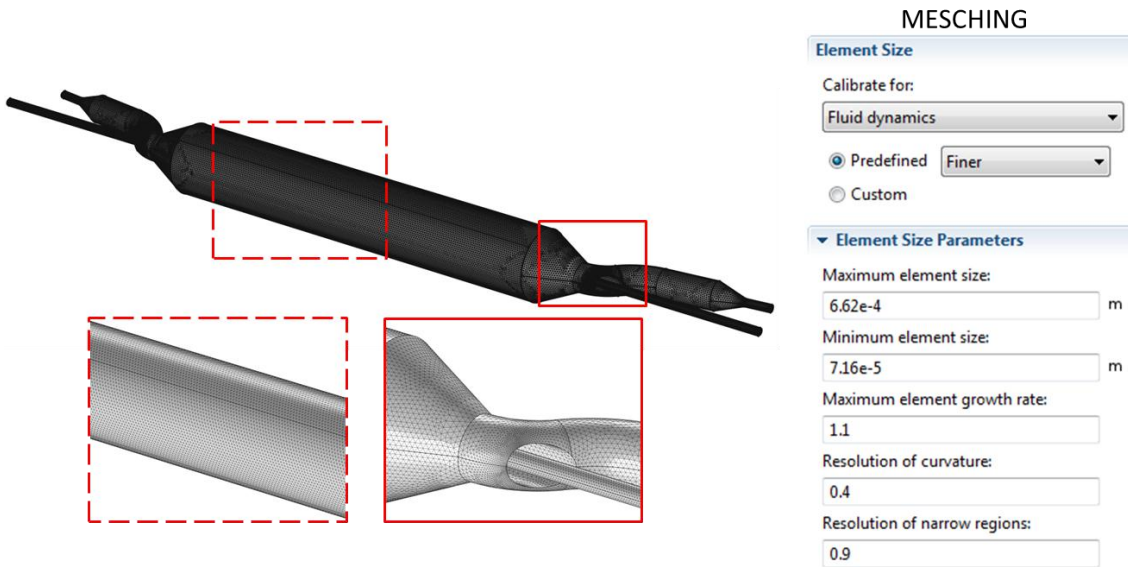


Figure H.2: Simulation details (Section 6.4 – Figure 6.10). The boundary conditions and the solver parameters were the same of the previous simulation (Figure H.1).

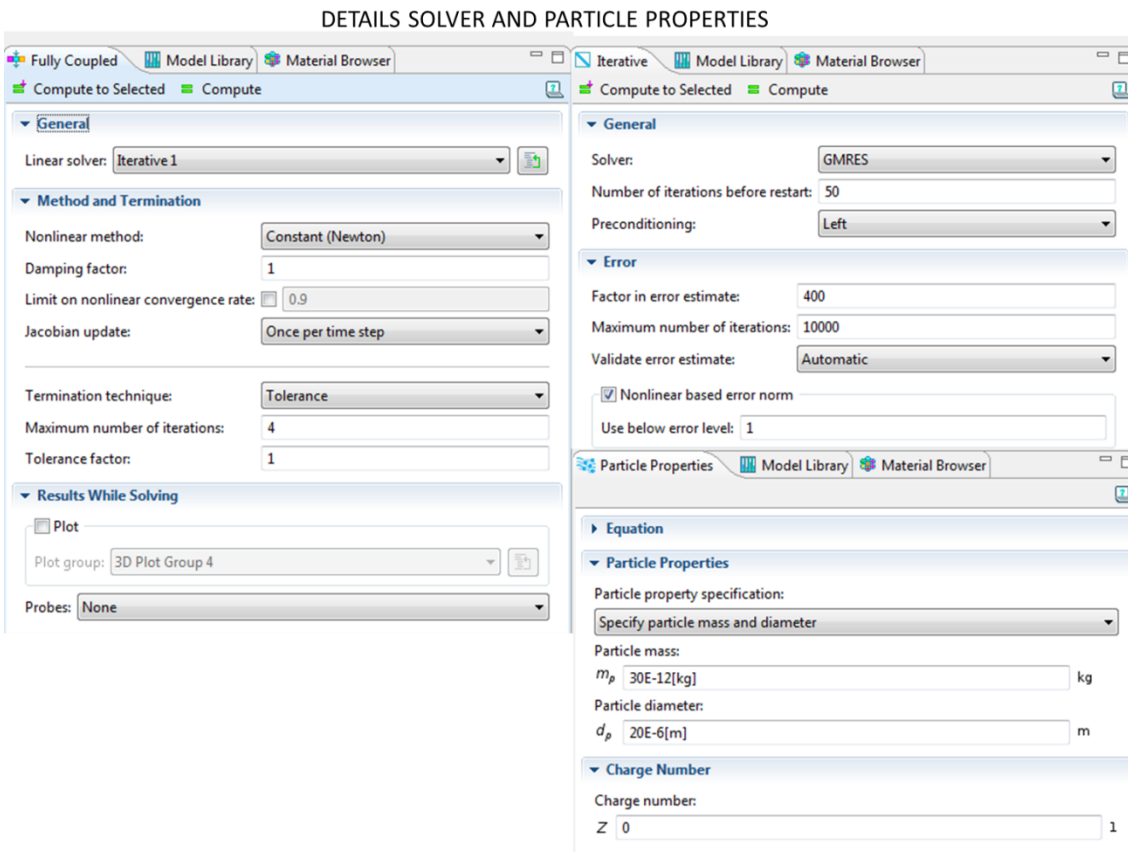


Figure H.3: Simulation details (Section 6.5 – Figure 6.11). Boundary conditions and meshing were the same of the previous simulation (Figure H.2).

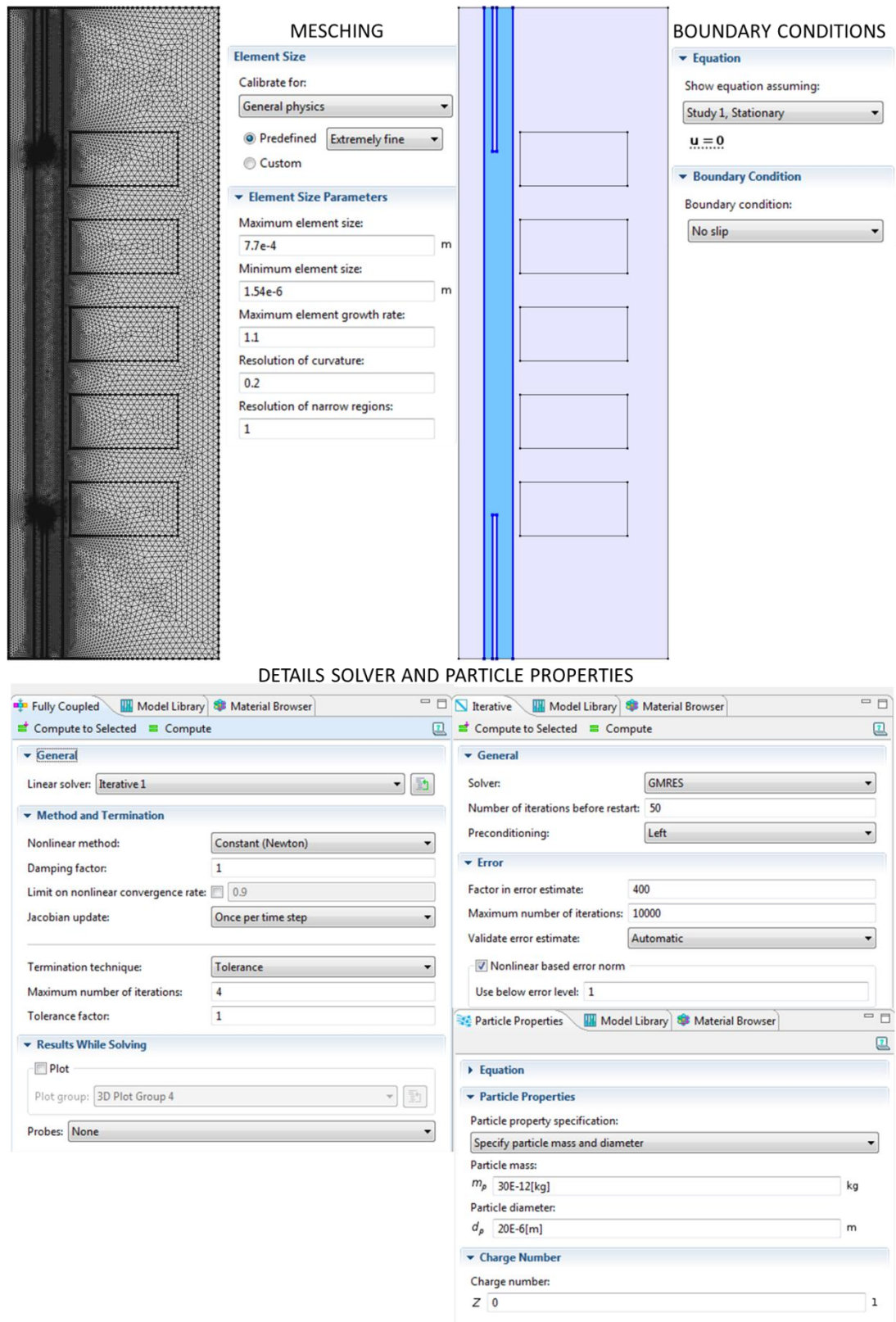


Figure H.4: Simulation details (Section 6.5.2 – Figure 6.12). Labelled cell magnetic susceptibility ($\chi_c = 3.292 * 10^{-5} \pm 0.24 * 10^{-5}$).

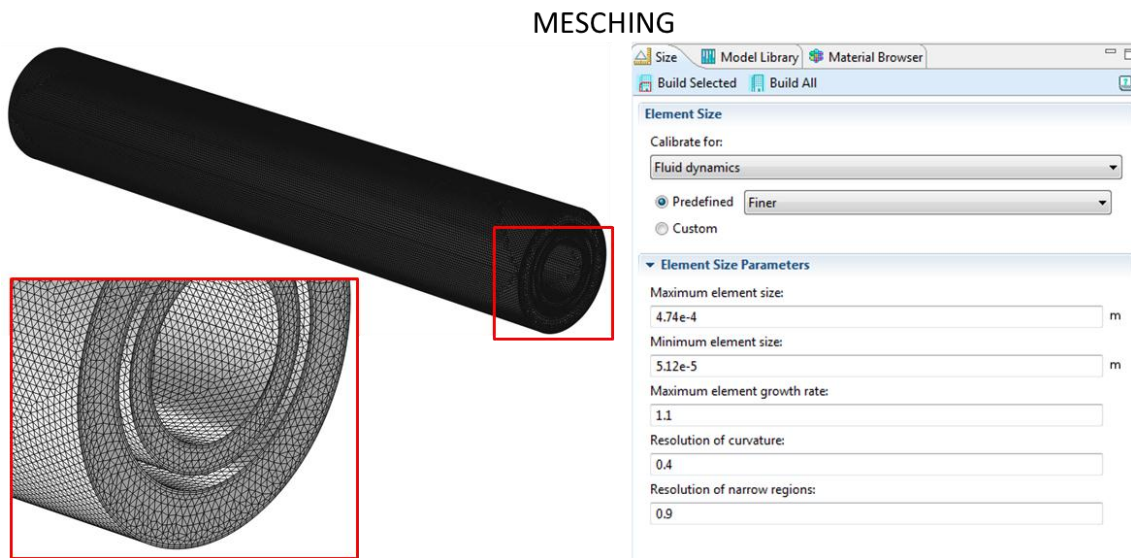


Figure H.5: Details of the simulations (Section 6.6 – Figure 6.16). The boundary conditions and the solver parameters were the same of the previous simulation (Figure H.4).

APPENDIX I

SURFACE TREATMENTS

The input/output manifold used in the sorting device ver.3.4 was machined using stereolithography. As observed (see Section 4.7.2), the internal surface of the manifold presented “steps” perpendicular to the building direction due to the machine resolution. In particular they presented a peak to peak distance of 50 μm (machine resolution) and a depth of $\sim 15 \mu\text{m}$.

Several cubic samples were built using the same technique, and a number of tests conducted on them (Figure I.1). According to the material (LS600 - EnvisionTEC) safety data sheet, the material used was soluble in organic solvents. Cubic samples of material were immersed in isopropanol and acetone for different amount of time (from 30 sec to 2 hours), but no changes were recorded on the sample surface. The increase of the time of exposure to 24 and 48 hours, ended with the formation of cracks on the samples surface.

The hypothesis of an internal coating with poly(L-lysine)-graft-poly(ethylene glycol) (PLL-g-PEG), which was used to prevent protein adsorption and thus cell adhesion [91,92], was investigated. In particular the PLL(20)-g[3.5]-PEG(2) was used purchased by Surface Solutions, Switzerland (PLL-*g*-PEG polymer with a 20 kDa PLL backbone, 2 kDa PEG side chains, and a grafting ratio, *g* -ratio of the number of lysine monomers to the number of PEG side chains- of 3.5). Figure I.2 shows the molecular structure of PLL-g-PEG. To coat the manifolds, tests were run on the cubic samples to optimise the coating protocol (the presence of the coating was checked measuring the contact angles before and after the treatment).

The protocol flowed for the surface coating with PLL-g-PEG was [91,92]:

- Dip the sample in ethanol (96%) for 15 min.
- Expose the sample to O₂ plasma for 1 min.
- Incubate the sample with 0.1 mg/ml of PLL(20)-g[3.5]-PEG(2) in 10 mM HEPES at RT for 1 hour.
- Wash with PBS and MilliQ water.
- Dry the sample and measure the contact angle.

To check the success of the coating procedure, the contact angle of the material was measured before and after the treatment. The surface to be coated presented waves due to the building technique used. Roughness influences the contact angle (increasing it) but the difference between the contact angle before and after the treatment should indicate the presence of a coating on the surface.

The expected contact angle of the PLL-g-PEG coated material was $\sim 35^\circ$ [93]. Due to the geometry of the manifold (there were no flat surfaces where to measure the contact angle), cubic material samples were used to test the protocol (Figure I.4).

In addition to the complete coating protocol, two negative controls were performed. The contact angle was measured before and after the dipping in PLL-g-PEG solutions and the plasma exposure (1 min). Each condition was tested six times.

In Figure I.3, bar charts reporting the results of the coating experiments were shown. The contact angle before any procedure was consistently $\sim 80^\circ$. After dip the sample in the PLL-g-PEG solutions for 1 hour (without expose it to the oxygen plasma treatment) the contact angle decreased to $\sim 68^\circ$.

After the sample exposure to oxygen plasma for 1 min (without dip the sample in the PLL-g-PEG solutions), the contact angle dropped to $\sim 8^\circ$. Finally, applying the complete protocol, the contact angle recorded was $\sim 38^\circ$, value close to the expected result. This confirmed that after the coating protocol, the surface was coated with PLL-g-PEG. Figure A.3 shows an example of the contact angle measurements before and after the coating protocol. The coating protocol was applied to all the components of the sorting device ver.3.4, which was tested as reported in Section 7.2.1.1.

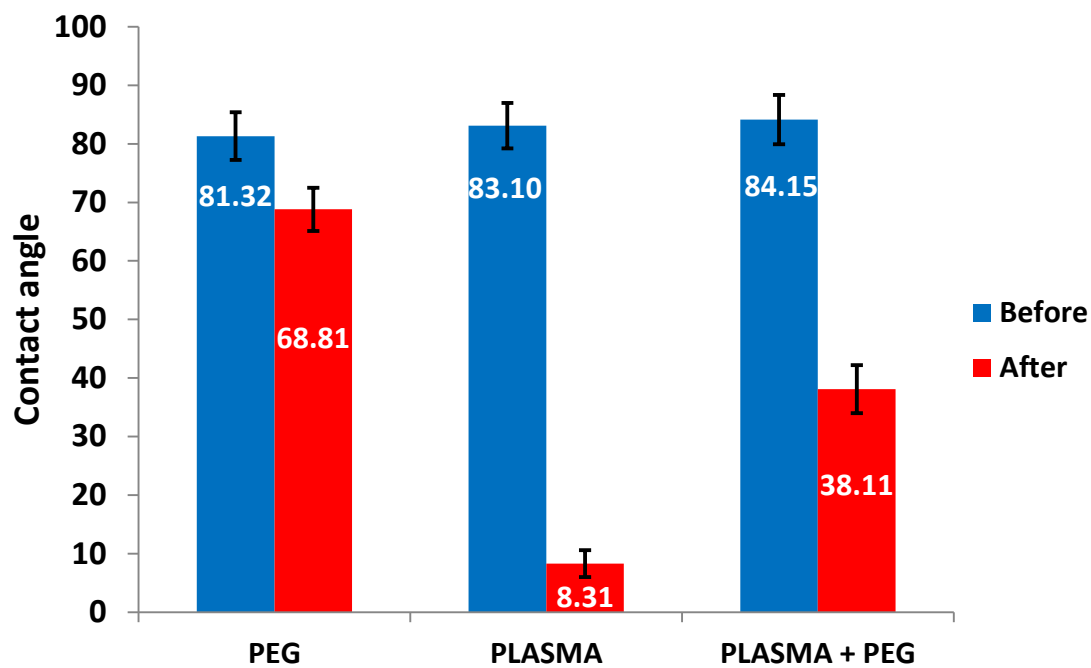


Figure I.3: Bar charts reporting the contact angles measured on material the cubic sample surface before and after the treatments. Results expressed as mean \pm SD and $n = 6$.

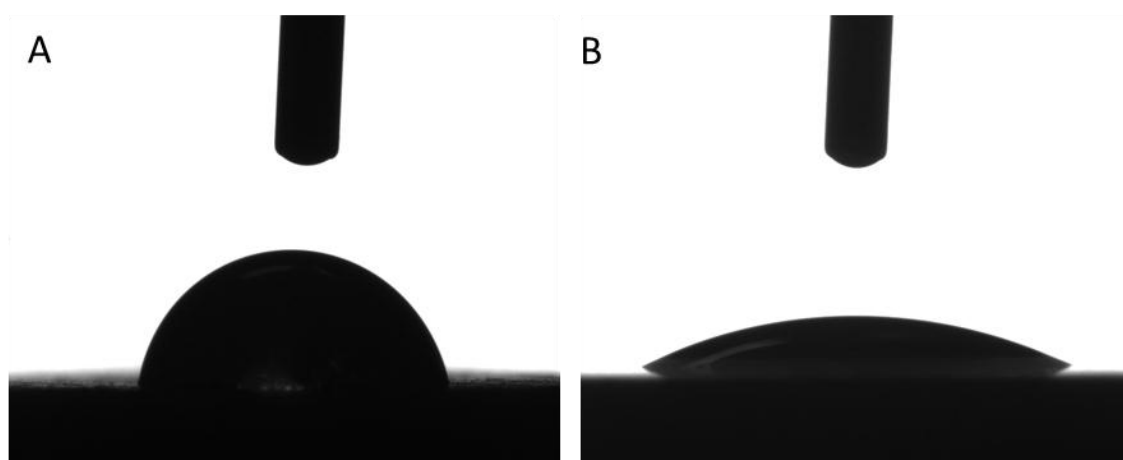


Figure I.4: Contact angle images before ($\sim 85^\circ$) and after ($\sim 32^\circ$) the PEG coating (the picture on the right was the lowest angle recorded).

APPENDIX L

In this appendix, the protocol followed to coat carboxyl polystyrene beads with ferromagnetic beads (TurboBeads) was reported.

STREPTAVIDIN FUNCTIONALISATION

To determine the quantity of streptavidin needed to coat the polystyrene beads, it was necessary to do some calculation.

Number of polyester beads (N_{pb}) = $2 * 10^6$

Bead surface (B_s) = $4\pi r^2 = 314.16 \mu\text{m}^2$

Total beads surface = $N_{pb} * B_s = 2 * 10^6 * 314.16 \mu\text{m}^2 \approx 6 * 10^8 \mu\text{m}^2 \rightarrow 6 * 10^{14} \text{nm}^2$

Streptavidin area = 20.25nm^2

Number of streptavidin molecules = Total beads surface / Streptavidin area = $2.96 * 10^{13}$

Molar quantity = $\frac{2.96 * 10^{13}}{\text{Avogadro constant}} = 4.9 * 10^{11} \text{mol}$

Streptavidin needed = $4.9 * 10^{11} \text{mol} * \text{Molecular weight} = 2.9 * 10^{-6} \text{g}$

To increase the speed of the reaction, 200 μg of streptavidin were dissolved in 1ml of PBS

COATING CARBOXYL BEADS WITH STREPTAVIDIN

MATERIALS

N-hydroxysuccinimide sodium salt (sulfo-NHS)

Streptavidin from *Streptomyces avidinii* (Streptavidin)

N-(3-Dimethylaminopropyl)-*N'*-Ethylcarbodiimide hydrochloride (EDC.HCl)

Ethanolamine

Tween 20 viscous liquid, polyoxyethylenesorbitan monolaurate

Bovine serum albumin (BSA)

2-(*N*-morpholino) ethanesulfonic acid (MES buffer)

PROTOCOL

The carboxyl polystyrene beads were washed in 100 μl of MES buffer twice. 7.8 mg of EDC.HCl and 2.9 mg of sulfo-NHS were dissolved in 1 ml of MES buffer. This solution

was added to the carboxyl polystyrene beads and left under slow tilt (using the rotating arm) for 120 min. The carboxyl polystyrene beads were washed with MES buffer (six times). 200 µg of streptavidin were dissolved in 1 ml of PBS, added to the carboxyl polystyrene beads and leave under slow tilt (using the rotating arm) for 120 min. Blocking step: 2 µl of Ethanolamine were added to the solution and left under slow tilt (using the rotating arm) for 20 min. The carboxyl polystyrene beads were washed with 200 µl of PBS + 0.05% of Tween (three times) and then suspended in 1.5 ml of PBS + 0.05% of Tween and leave under slow tilt (using the rotating arm) overnight. The carboxyl polystyrene beads were washed with 200 µl of PBS + 0.05% of Tween (three times) and stored in fridge in 1 ml of PBS + 0.05% of Tween.

LABELLING BIOTIN NANOBEADS TO CARBOXYL BEADS COATED WITH STREPTAVIDIN

TURBOBEADS

To determine the number of biotin nanobeads needed to label the carboxyl polystyrene beads, it was necessary to do some calculation.

$$\text{TurboBead section} = 4r^2 = 4 * (15\text{nm})^2 = 706.85 \text{ nm}^2$$

$$\text{Number of TurboBeads needed} = \text{Total beads surface} / \text{TurboBeads section} = 0.84 * 10^{12}$$

$$\text{Particle concentration} = 5 * 10^{13} \text{ particles/ml}$$

$$\text{Volume wanted} = 17 \text{ µl}$$

To ensure the completeness of the nanoparticle immobilization, ten times the required amount of TurboBeads was used.

PROTOCOL

After sonicate and mixed the TurboBeads tube, the wanted quantity of TurboBeads was put into an eppendorf (200 µl). The beads were separated using the magnet and the supernatant removed. The beads were washed (sonicate and mix) with 200 µl of PBS + 0.05% of Tween (three times). The beads were resuspend in 1 ml of PBS + 0.05% of Tween. Carboxyl polystyrene beads coated with streptavidin were added to the solution (the polystyrene beads were suspended in 1 ml of PBS + 0.05% of Tween, so we had with a volume of 2 ml). The solution was left to react under slow tilt (using the rotating arm) for 60 min. Beads were separated from the supernatant using the magnet. The coated beads were washed in PBS + 0.1% of BSA (two times) and resuspended 1 ml of PBS + 0.05% of Tween.

APPENDIX M

MINIMUM NUMBER OF BEADS (SORTING DEVICE THRESHOLD)

Estimation of the minimum number of superparamagnetic beads (CM-08-10) bind on the cell surface needed for a labelled cell to be sorted within the device.

- First method

The labelled cell was considering as a sphere with volume V_c (equation 1) and magnetic susceptibility χ_c (experimentally calculated). Each superparamagnetic bead was considered as a sphere with volume V_b (equation 2) and magnetic susceptibility χ_b . The idea was to calculate (equation 3) the number of beads needed to bestow the value of χ_c measured experimentally.

$$V_c = \frac{4}{3}\pi r_c^3 = 4.19 * 10^{-15} \text{ [m}^3\text{]} \quad (1)$$

$$V_b = \frac{4}{3}\pi r_b^3 = 2.89 * 10^{-19} \text{ [m}^3\text{]} \quad (2)$$

$$n = \frac{V_c \chi_c}{V_b \chi_b} = 367.42 \text{ [beads]} \quad (3)$$

V_c volume of the cell [m³]

V_b volume of the superparamagnetic bead [m³]

r_c radius of the cell = $10 * 10^{-6}$ [m]

r_b radius of the superparamagnetic bead = $0.41 * 10^{-6}$ [m]

χ_c magnetic susceptibility of a labelled cells(experimentally calculated) = $3.292 * 10^{-5}$

χ_b magnetic susceptibility of a superparamagnetic bead = $1.3 * 10^{-3}$

χ_w magnetic susceptibility water = $-9.035 * 10^{-6}$

- Second method

A second way to calculate the minimum number of superparamagnetic beads bind on a cell surface to be sorted, involved the hydrodynamic force \vec{F}_h .

Through numerical simulations and analytical calculations, the horizontal velocity ($v_c = 1.55 * 10^{-5}$ [m/s]) a labelled cells need to travel within the device to be sorted correctly. Knowing the dynamic viscosity of the buffer used ($\eta = 1.68 * 10^{-3}$ [Ns/m²]) [94], it was possible to calculate the \vec{F}_h a labelled cell was subjected, accordingly to equation 4 (assuming the horizontal component of the fluid velocity was zero).

$$\vec{F}_h = -6\pi\eta r_c \vec{v}_c = -490.84 * 10^{-14} \text{ [N]} \quad (4)$$

According to the Newton's law, the mass acceleration of a body was related to the resultant of the external forces acting upon it.

$$m \frac{d\vec{v}_p}{dt} = \vec{F}_h + \vec{F}_{mc} \quad (5)$$

Where \vec{F}_{mc} was the magnetic force applied on a magnetically labelled cell within the sorting device ver.3.5+HMS and was defined by equation (6) and m was the mass of the cell.

$$\vec{F}_{mc} = \frac{V_c \Delta\chi}{\mu_0} (\vec{B} \cdot \nabla) \vec{B} = \frac{V_c (\chi_c - \chi_w)}{\mu_0} (\vec{B} \cdot \nabla) \vec{B} \quad (6)$$

Where μ_0 was the magnetic permeability of free space.

Considering the inertial forces negligible in this case it was possible to write:

$$0 = \vec{F}_h + \vec{F}_{mc} \quad (7)$$

However, equation 7 could be written as follow:

$$0 = \vec{F}_h + n\vec{F}_{mb} \quad (8)$$

Where n was the number of superparamagnetic beads needed and \vec{F}_{mb} the magnetic force applied on a superparamagnetic bead within the sorting device ver.3.5+HMS. The condition needed for a labelled cell to be sorted correctly is:

$$n\overrightarrow{F_{mb}} > -\overrightarrow{F_h} \quad (9)$$

Through numerical simulation was possible to calculate a rough average of $(\vec{B} \cdot \nabla)\vec{B}$ experienced by a magnetic particle within the sorting device. With this information it was possible to calculate $\overrightarrow{F_{mb}}$ as follow:

$$\overrightarrow{F_{mb}} = \frac{V_b \Delta \chi}{\mu_0} (\vec{B} \cdot \nabla)\vec{B} = \frac{V_b (\chi_b - \chi_w)}{\mu_0} (\vec{B} \cdot \nabla)\vec{B} = 1.344 * 10^{-14} \text{ [N]} \quad (10)$$

The minimum number of superparamagnetic beads bind to the cell surface for this to be correctly sorted is:

$$n = \frac{-\overrightarrow{F_h}}{\overrightarrow{F_{mb}}} = 365.21 \text{ [beads]}$$

The results obtained with the two methods were comparable and considering the rough average of $(\vec{B} \cdot \nabla)\vec{B}$ (calculated in the best condition) we can asset that the minimum number of superparamagnetic beads bind on the cell surface for this to be correctly sorted was ~400 beads.

APPENDIX N

All the protocols described below were developed by the Bone and Joint Research Group.

MACS (Magnetically activated cell sorting) Stro-1 isolation

Virkon

a-MEM / 10% FCS / pen strep

Pastettes

15 ml tubes, rack

Stro1-hybridoma supernatant

MACS Rat a-mouse IgM Microbeads (TC fridge door, top, purple and white box 'MACS')

MACS magnet and column, plunger (TC cupboard)

Blocking buffer

17 ml a-MEM

2 ml AB Serum human (ready to use)

0.2 g BSA (TC fridge drawer)

1 ml FCS

Filter sterilise with 20 ml syringe

MACS buffer (the bottle needs to be de-gassed prior to each use. Use vacuum and pump in NTC for ~20min.)

1 L PBS

5 g BSA (TC fridge, takes long to dissolve) (0.5%)

0.74448g EDTA (disodium salt) (2 mM)

After last centrifugation of lymphoprep pour off supernatant and add 2ml blocking buffer

Leave for 30min in fridge

Get Stro-1-hybridoma supernatant ready Thaw and keep in fridge until ready

Take cells out, make up to 10 ml with MACS buffer (chilled), spin (1200 rpm for 5 min)

Re-suspend in all of Stro-1 hybridoma supernatant Incubate in fridge for 30 min., mix regularly.

Spin and wash in MACS buffer (chill) three times – up to 20ml, do cell count! (1200 rpm, 5 min.)

Re-suspend in 800 μ l (1×10^8 cells) (or 80 μ l per 10^7) MACS buffer.

Add 200 μ l of MACS Rat a-mouse IgM Microbeads (or 20 μ l per 10^7 cells). Mix and incubate 15 min (6-12C, or in fridge)

(Meanwhile get column/plunger and magnet from NTC (shelf above fridge))

Gently wash cells three times with MACS buffer (chilled)

Re-suspend pellet in 2 ml MACS buffer. Use 4 ml for 2×10^8 cells.

Proceed to magnetic separation.

Place column in magnetic holder, push in bracket.

Label 15 ml tube with -ve and +ve and place in rack underneath tube.

Fill column with 3 ml MACS buffer and let it go through

Add 2 ml cell suspension with pastette, (drips quite slowly)

Add 3 x 3 ml MACS buffer to wash out all -ve cells into 15 ml tube

Remove -ve tube. Take out column and place in +ve tube. Add 5 ml MACS buffer to column.

Place plunger at top of tube and press down firmly and swiftly to push +ve cells out.

Wash twice in a-MEM, 1200 rpm 5 min. Count cells again!

Re-suspend in a-MEM / 10% FCS / PS and plate out in T75/25. 37°C, 5% CO₂

Lymphoprep with Human Bone Marrow Cells

Prep marrow but wash cells twice in a-Mem before using sieve. After last spin add 25 ml of a-Mem (or 50 ml for copious amount of cells and more than one lymphoprep) for one lymphoprep. Re-suspend and filter through cell strainer. Get pastettes ready.

Lymphoprep (Axis shield) was always kept at RT and wrapped in foil to be protected from light.

20 ml Lymphoprep was used with 25 ml of cell suspension. If many cells use 2x25 ml cell suspension with 20 ml lymphoprep each.

Pour 20 ml of lymphoprep into fresh conical, use 3 ml pastette to add cell suspension very carefully to lymphoprep, build up layer on top of lymphoprep by holding pastette close to side of tube and releasing slow stream of suspension.

Spin at 2200 rpm (800 g) for 40 min. at 18 °C with **BREAKS OFF!** (will take at least 1 hr. to finish).

At end of spinning there should be a distinct layer of media at top with the mononuclear cell layer beneath (*BMMC – Bone Marrow mononuclear cells*) at interface with lymphoprep. (*buffy-coat*). All blood cells will be at bottom.

Use pastette to carefully remove all cells first and then media at top and transfer to new conical tube. Make up to 50 ml with media and pellet.

For Stro1-isolation re-suspend in 2 ml of blocking buffer and put in fridge for 15-30 min.

Proceed to stro1-isolation.

RNA Purification with RNeasy Plus Mini Kit

Add 350 μ l (<6 cm diam dish) or 600 μ l of RLT buffer to well, pipette up and down and transfer to RNase/DNase free tube with filter tip. Snap freeze and store at -80 °C or proceed to Isolation.

Transfer the homogenized lysate to a gDNA (purple) Eliminator spin column placed in a 2 ml collection tube (supplied). Centrifuge for 30 s at $\geq 8000 \times g$ ($\geq 10,000$ rpm). Discard the column, and save the flow-through.

Add 1 volume of 70% Ethanol to the flow-through and mix well by pipetting

Transfer up to 700 μ l of sample to spin column (pink) in collection tube. Centrifuge for 15 s at 10.000 rpm) Discard flow-through. If the sample volume exceeds 700 μ l, centrifuge successive aliquots in the same RNeasy spin column. Discard the flow-through after each centrifugation.

Add 700 μ l Buffer RW1 to spin column. Centrifuge for 15 s at 10.000rpm. Discard flow-through

Add 500 μ l Buffer RPE to spin column. Centrifuge 15 s at 10.000 rpm. Discard flow-through

Add 500 μ l Buffer RPE to spin column. Centrifuge for 2 min. at 10.000 rpm.

Place spin column in new 2 ml collection tube (supplied) and discard old collection tube with flow-through. Centrifuge full speed 1 min.

Place spin column in new 1.5 ml collection tube (supplied). Add 30-50 μ l RNase-free water directly to spin column membrane. Centrifuge for 1 min. at 10.000 rpm

Repeat step by adding a further 30-50 μ l RNase-free water or re-use eluate from previous step for higher concentration of RNA. Centrifuge 1 min. 10.000 rpm

Quantify the RNA on the nanodrop and store at -80 °C.

VILO Kit cDNA Synthesis

VILO RT Kit Protocol

1. Calculate RNA needed for reaction (150 ng – 500 ng(MAX)) (Should be the same amount for each sample in experiment) and make total volume of 7 μ l in PCR tubes.

For example for 500 ng

RNA Sample = 323 ng/ μ l on nanodrop

$500/323=1.55 \mu$ l of your stock RNA (make up to 7 μ l by adding 5.45 μ l of upH₂O)

2. If you were making cDNA for multiple samples, a master mix should be made:

	<u>1x</u>
VILO Reaction Mix	2 μ l
VILO 10X SuperScript	1 μ l

Aliquot _____ 3 μ l per tube containing 7 μ l of diluted RNA

Total Volume 10 μ l

DO NOT VORTEX, Mix by pipetting and briefly spin down using Minispin

3. Finally, place in thermocycler and run program “VILO RT”

Setup should be:

25°C for 10 mins

42 °C for 120 mins

85 °C for 5 mins

4 °C – HOLD

4. Conduct 1 in 5 dilution using upH₂O before qPCR (add 40 μ l up H₂O to the 10 μ l cDNA sample)

APPENDIX O

Figure O.1 reported the results of the ALP staining procedure performed on STRO-1+ cells isolated with conventional MACS and the developed device, under basal and osteogenic condition after 7 and 14 days of culture.

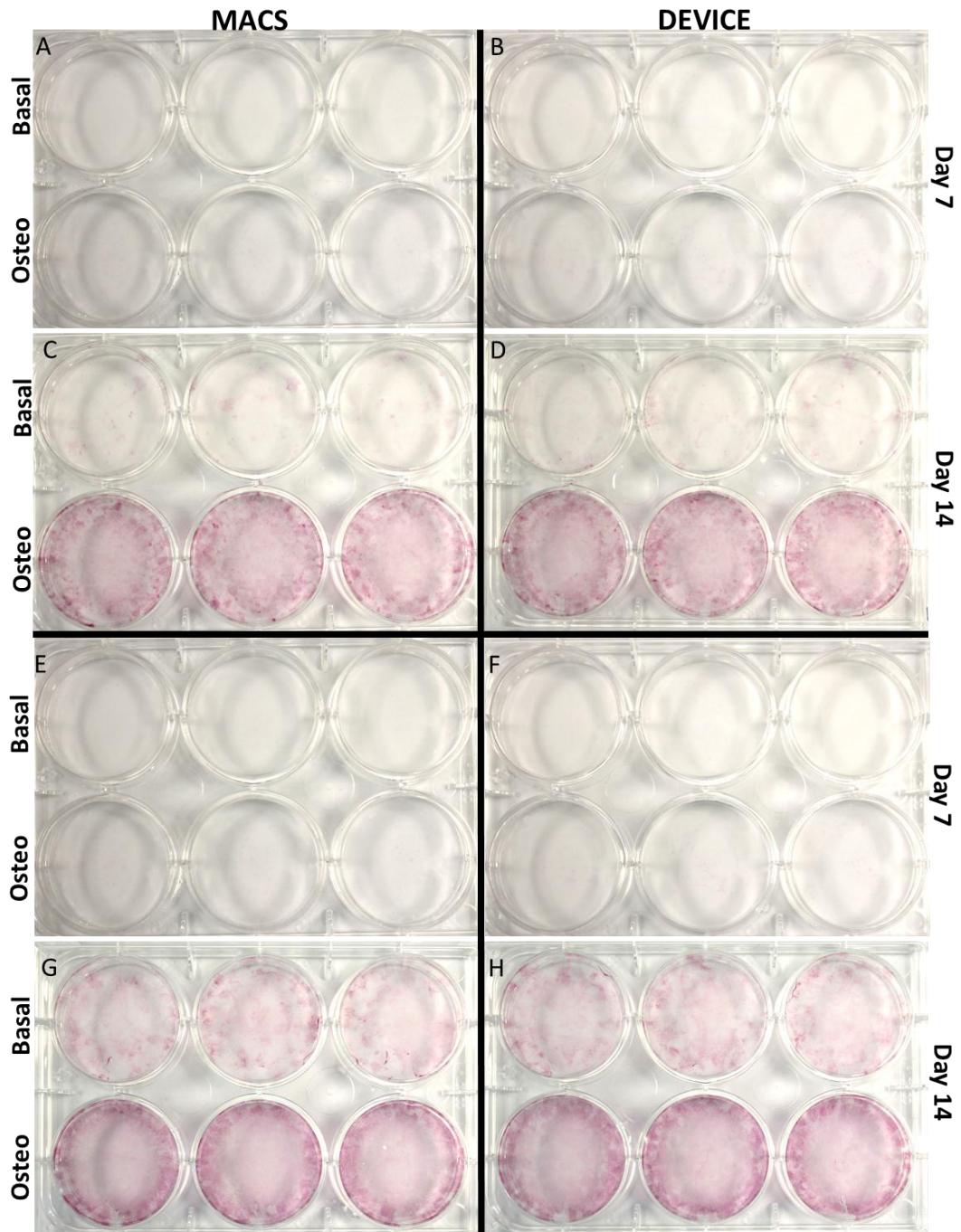
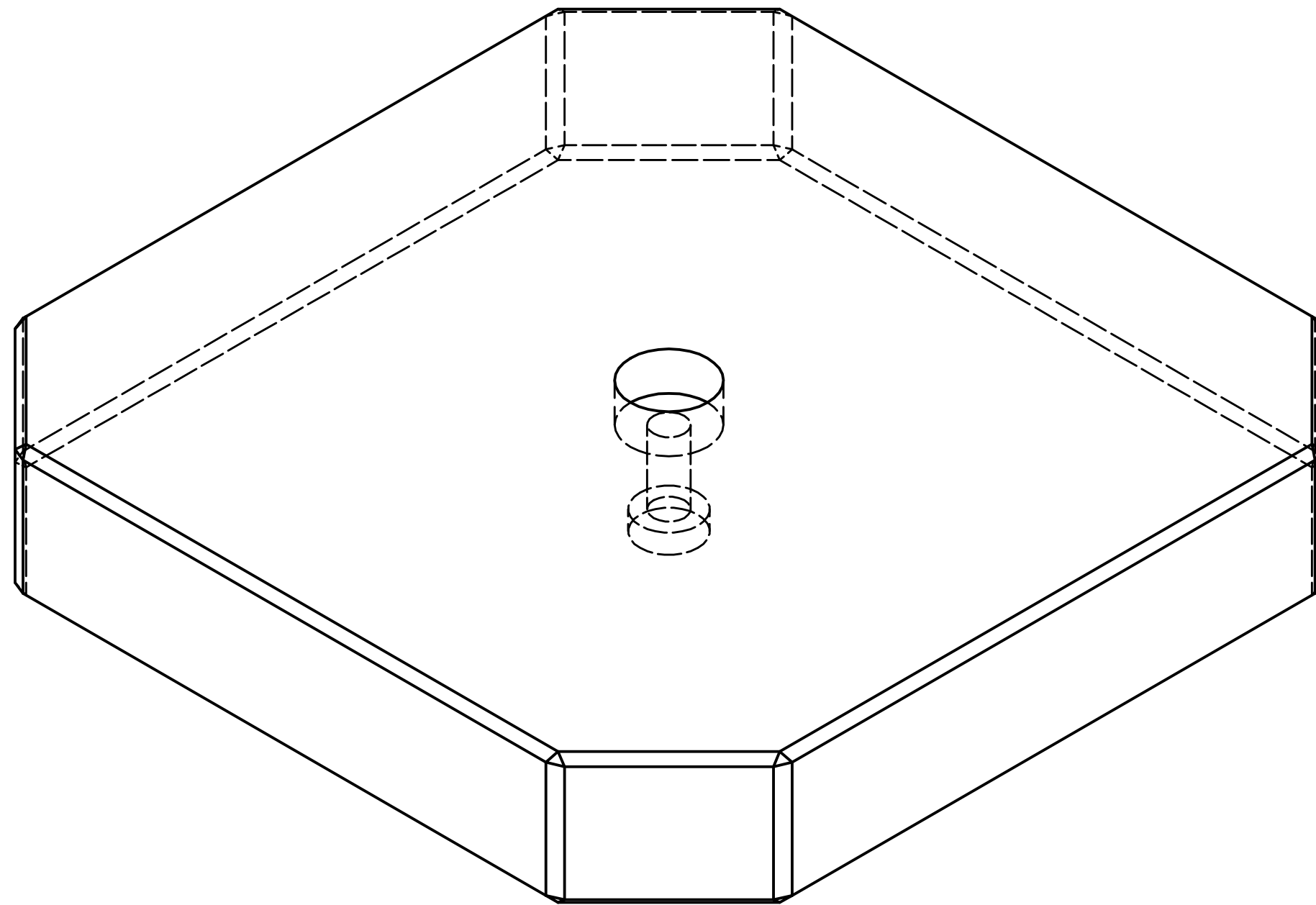


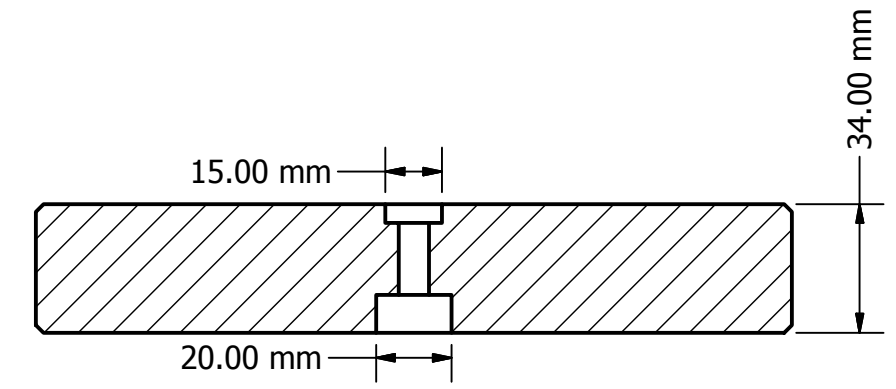
Figure O.1: (A, B, E, F) ALP staining of the STRO-1+ cell populations sorted from the other two BM sample analysed, with MACS and sorting device cultured under basal and osteogenic conditions. ALP staining performed after 7 days and (C, D, G, H) after 14 days. The procedure was implemented in triplicate (incubation time 30 min).

APPENDIX P

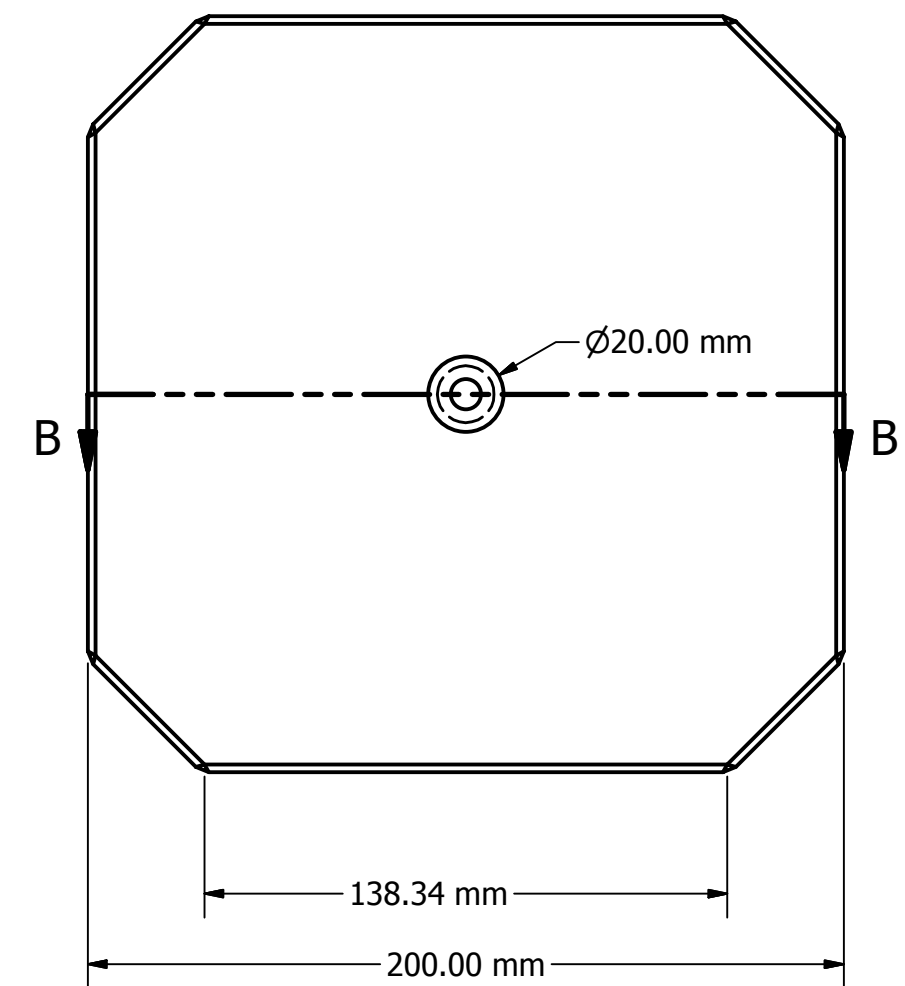
Technical drawings of all the components developed in this study were reported in the following pages.



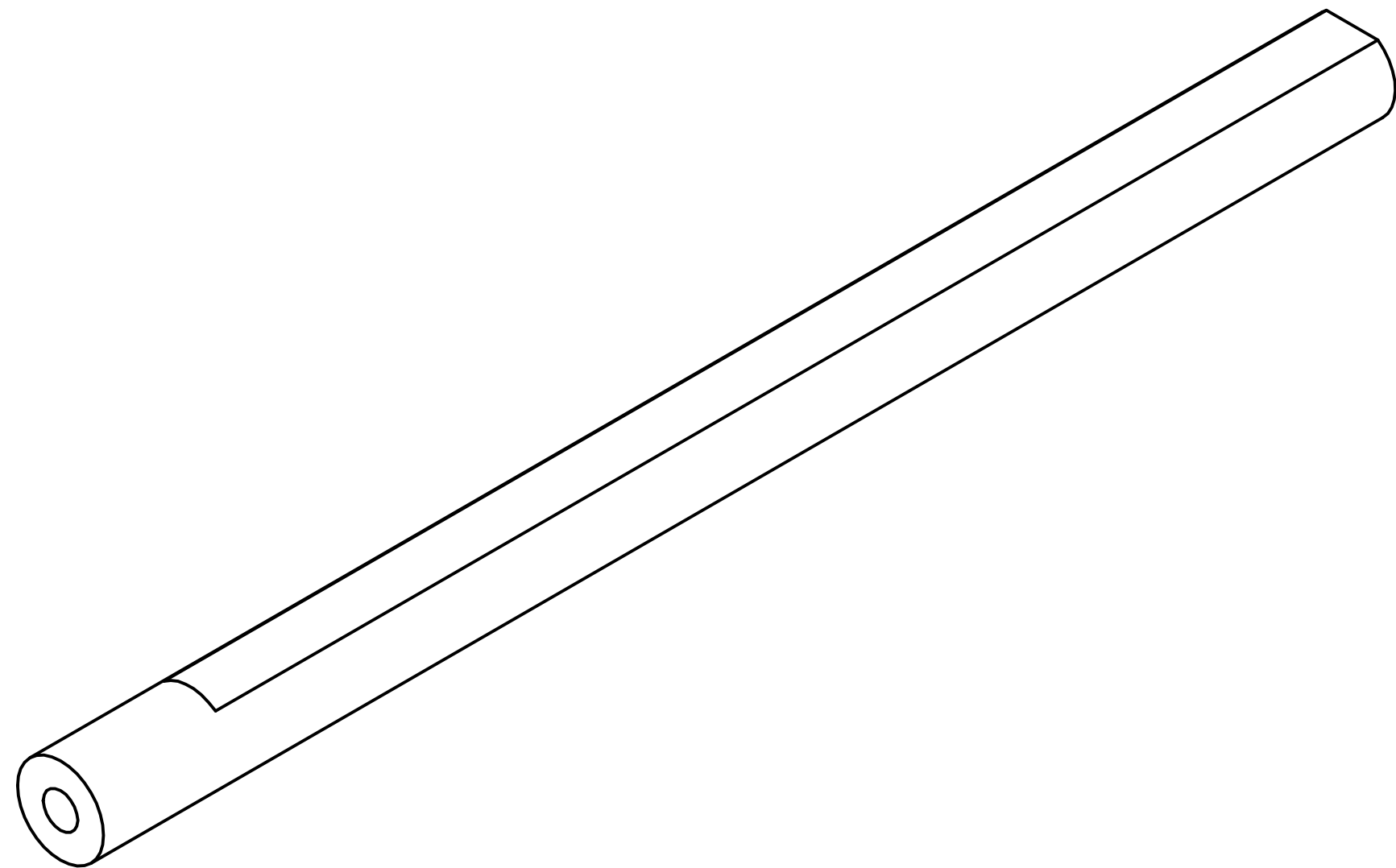
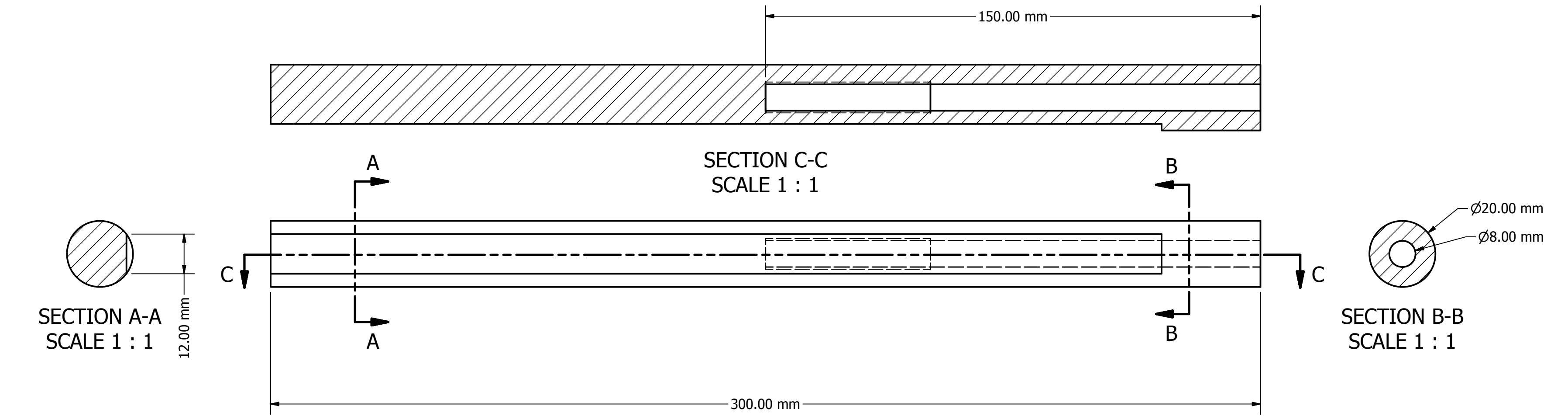
SCALE 1 : 1



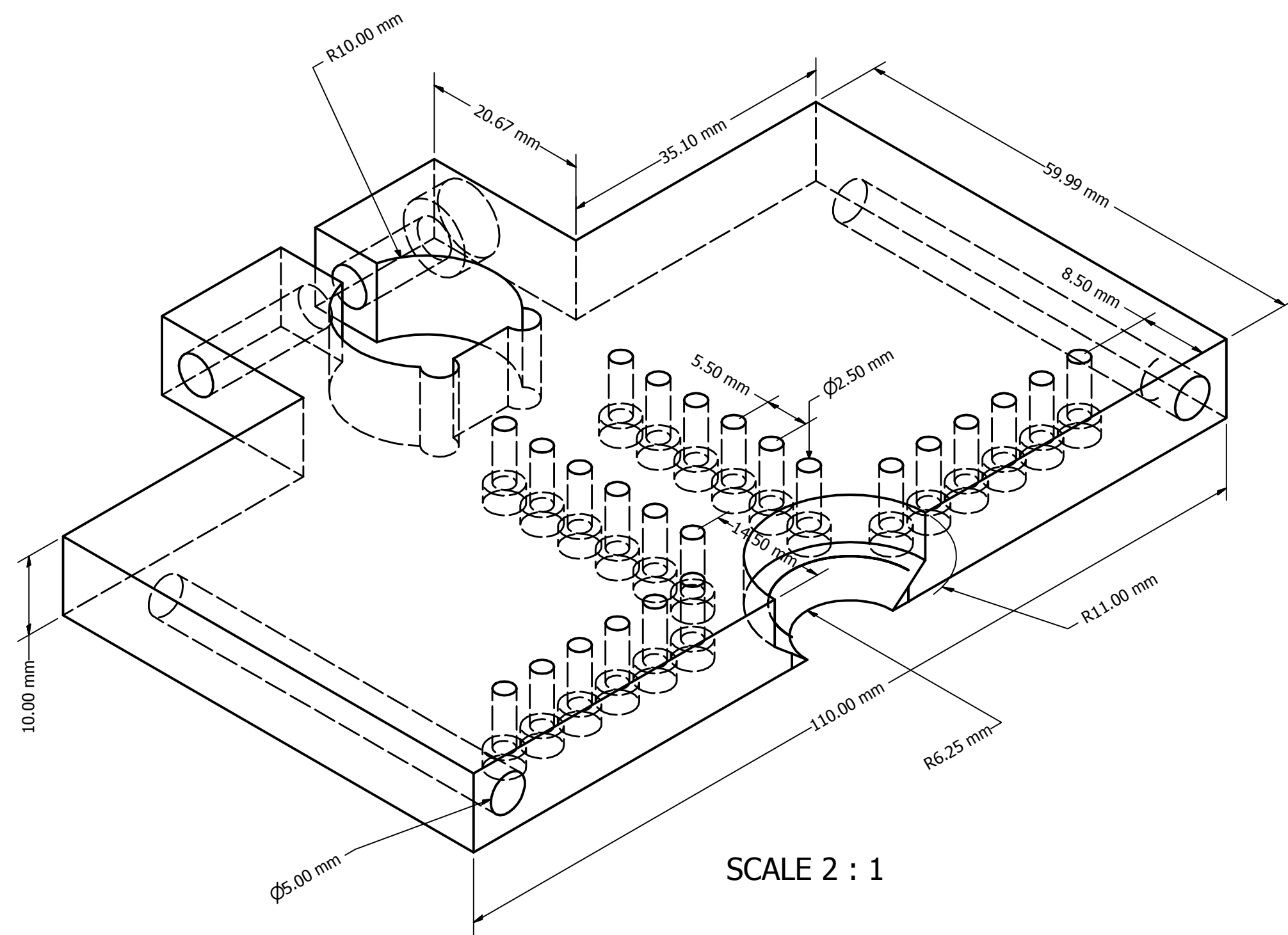
SECTION B-B
SCALE 1 / 2



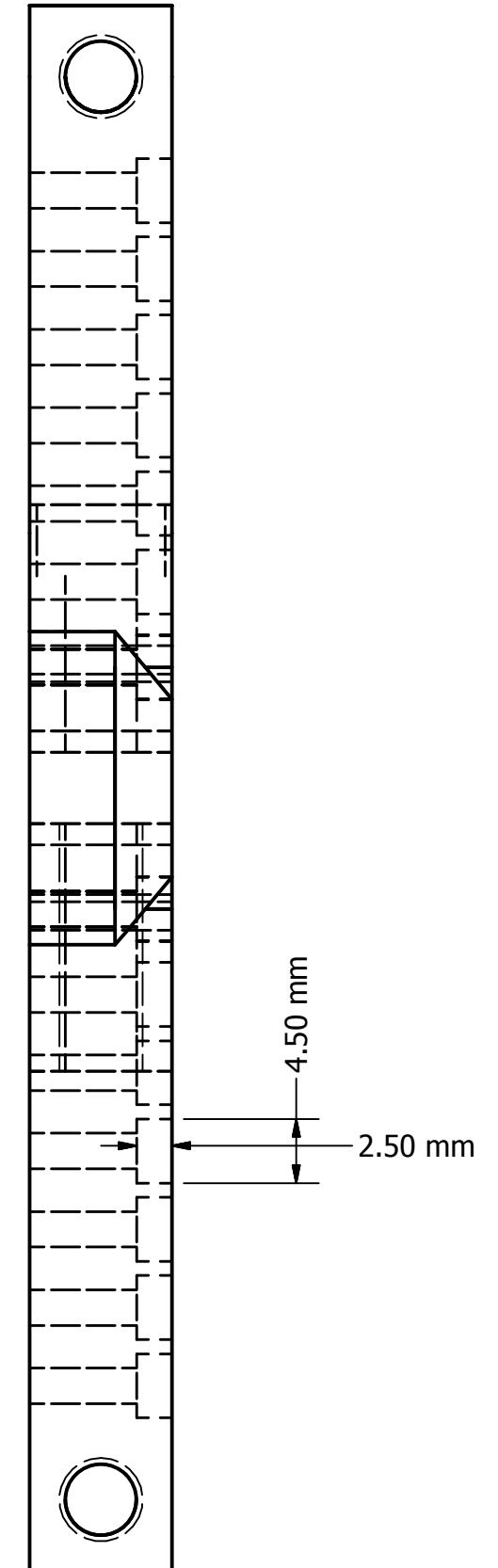
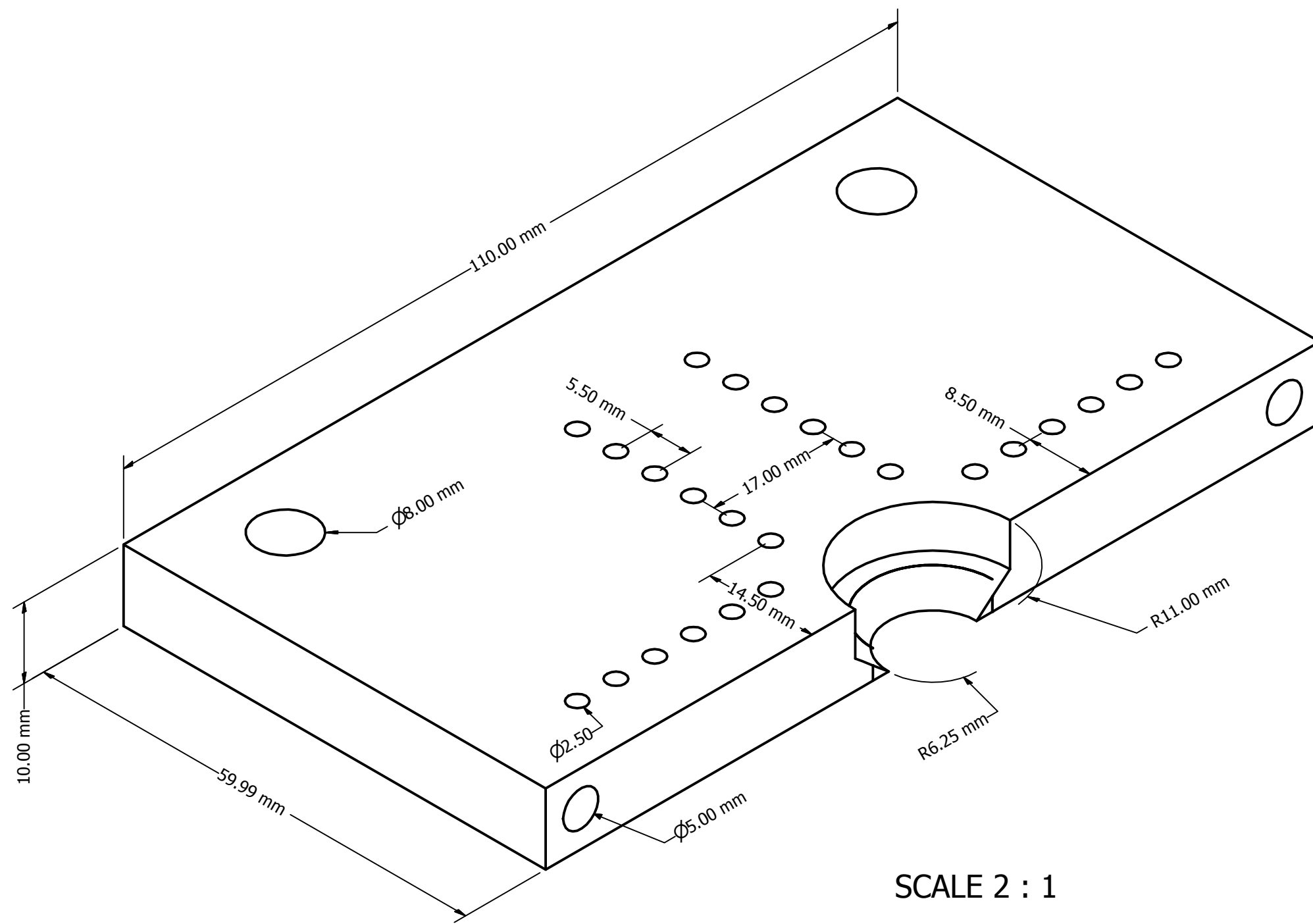
DRAWN	Marco Peca	04/09/2011	University of Southampton School of Electronic and Computer Science		
CHECKED			TITLE		
QA			BASE		
MFG					
APPROVED			SIZE	DWG NO	REV
			SCALE		SHEET 1 OF 1



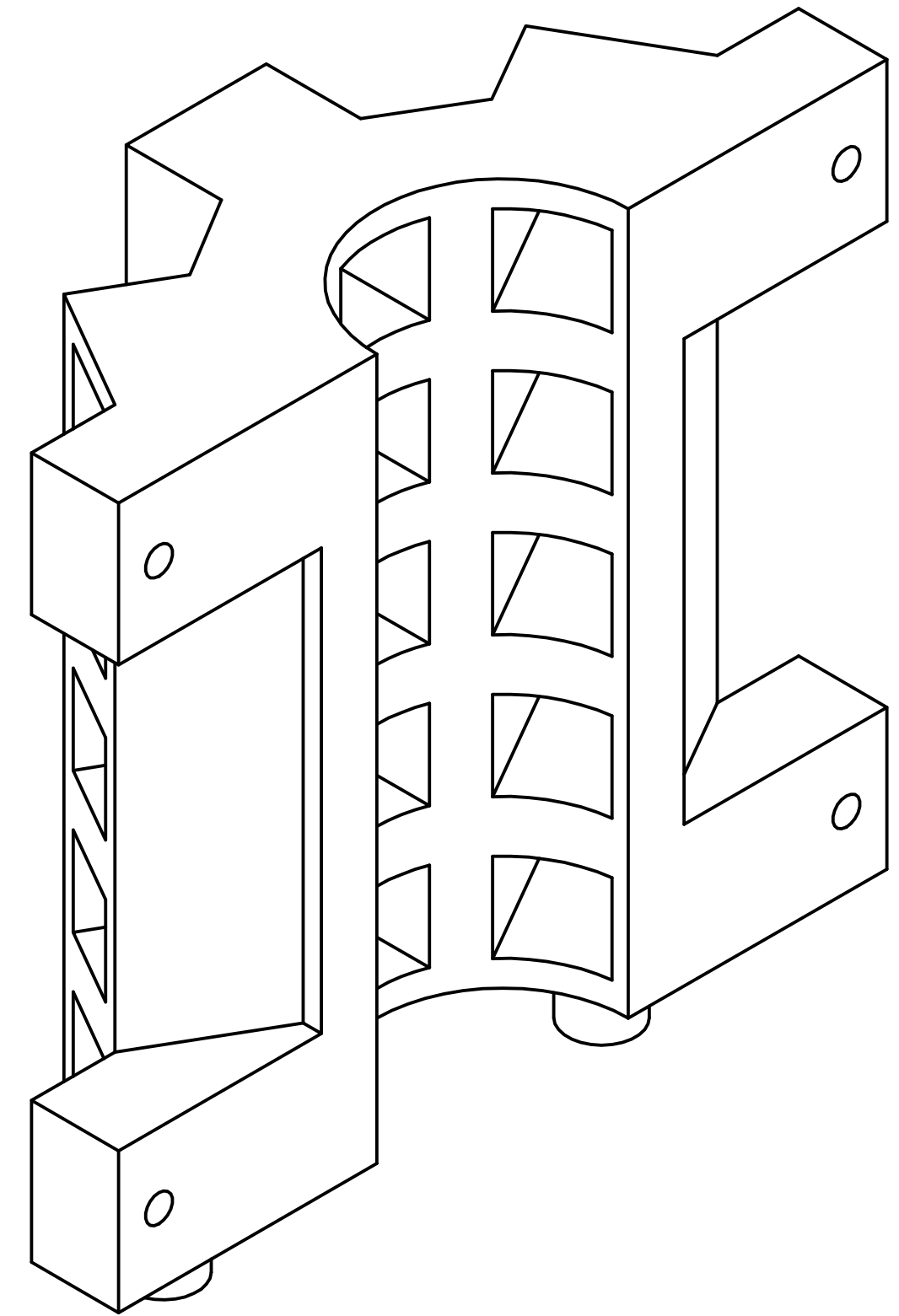
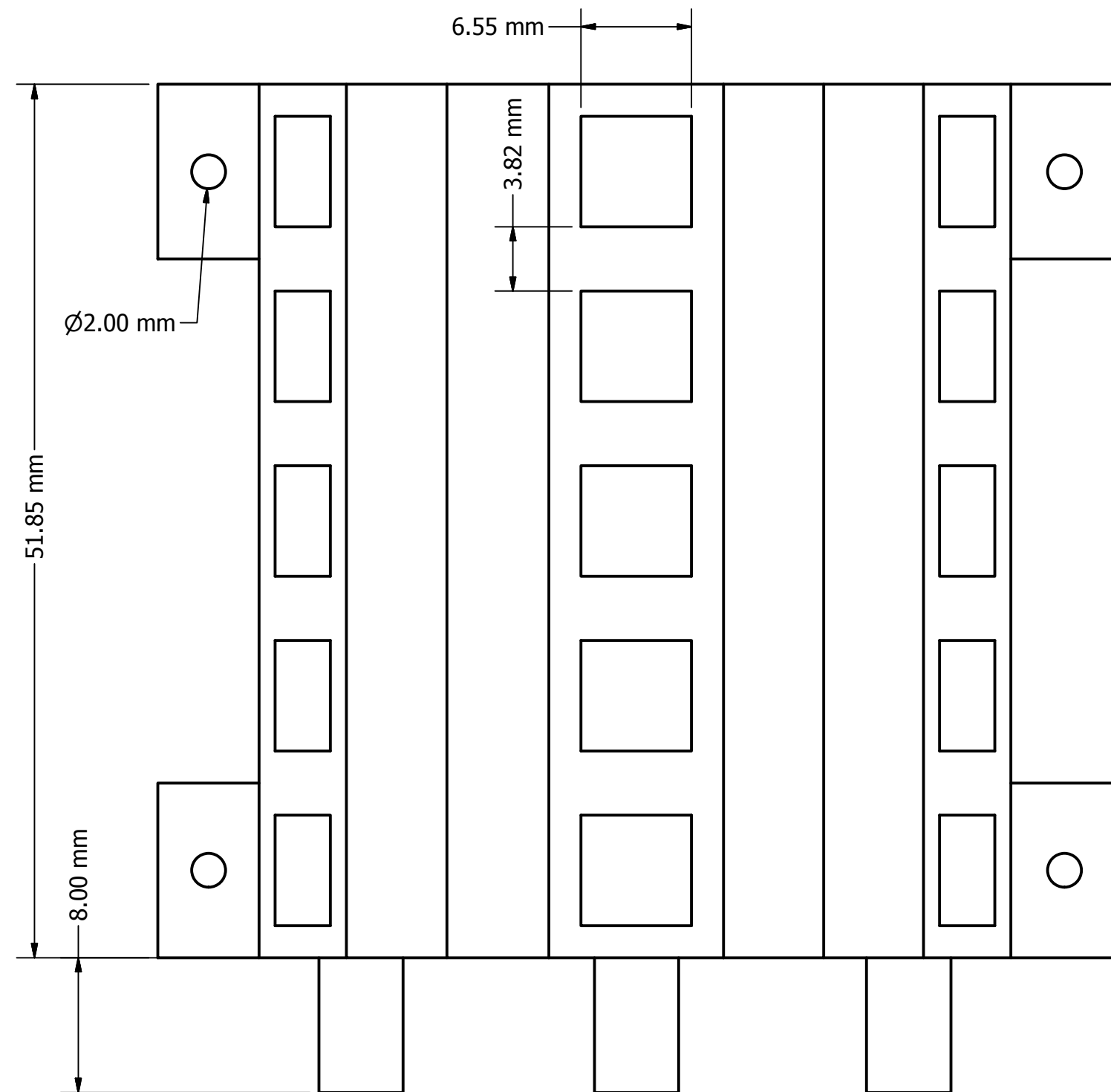
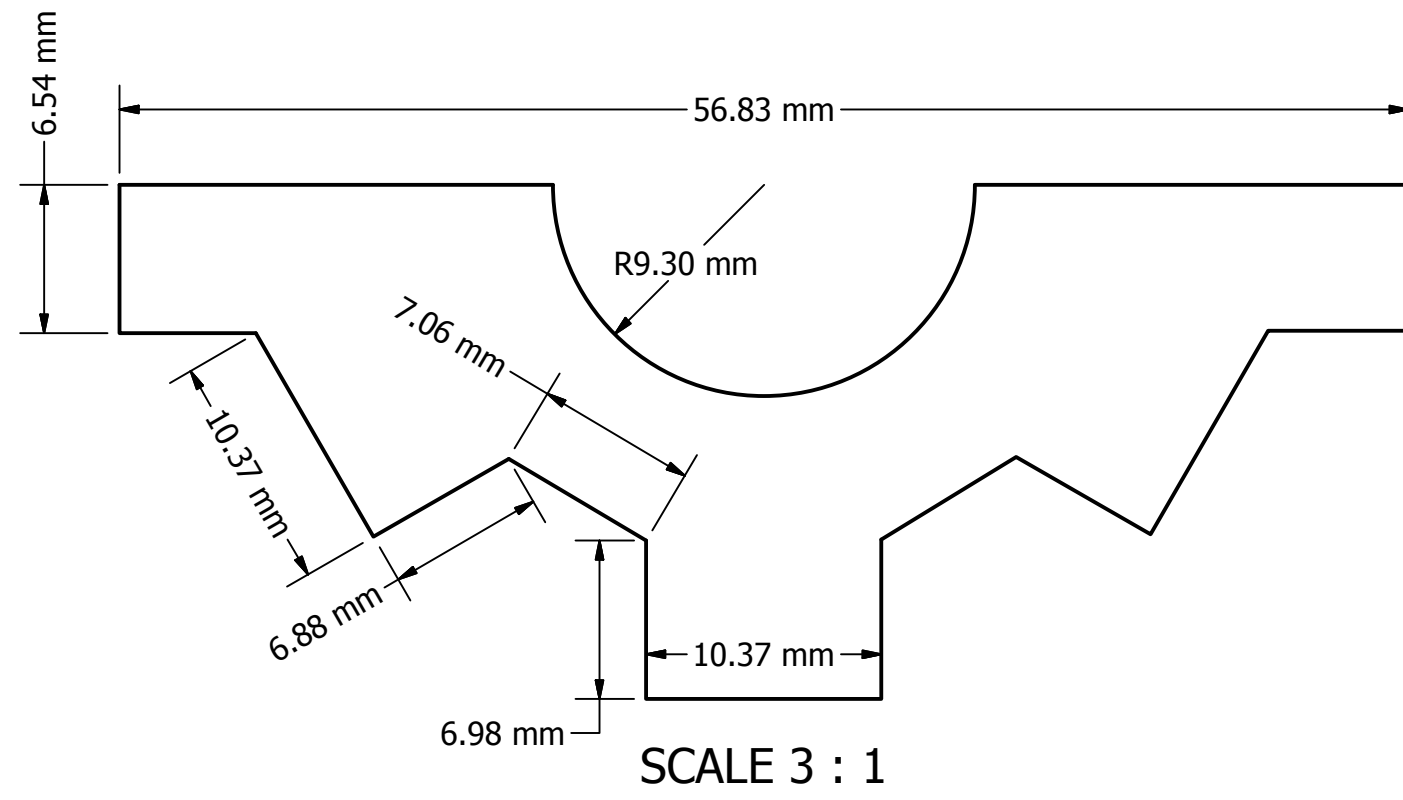
DRAWN Marco Peca	04/09/2011	University of Southampton School of Electronic and Computer Science		
CHECKED		TITLE		
QA		COLUMN		
MFG				
APPROVED		SIZE	DWG NO	REV
		SCALE	SHEET 1 OF 1	



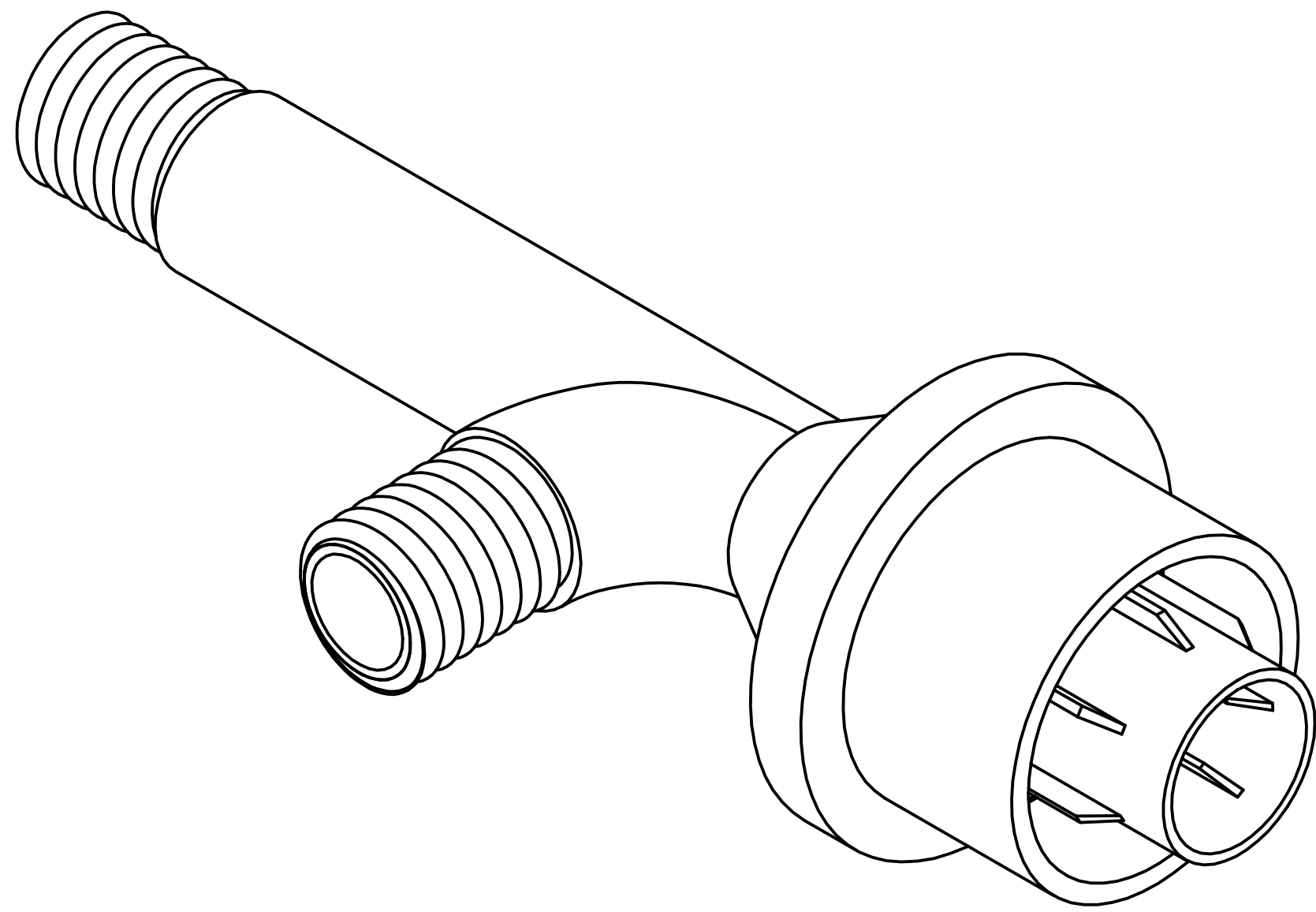
DRAWN Marco Peca	03/09/2011	University of Southampton School of Electronic and Computer Science		
CHECKED		TITLE		
QA		SUPPORT FIXED PART		
MFG				
APPROVED		SIZE	DWG NO	REV
		SCALE	SHEET 1 OF 1	



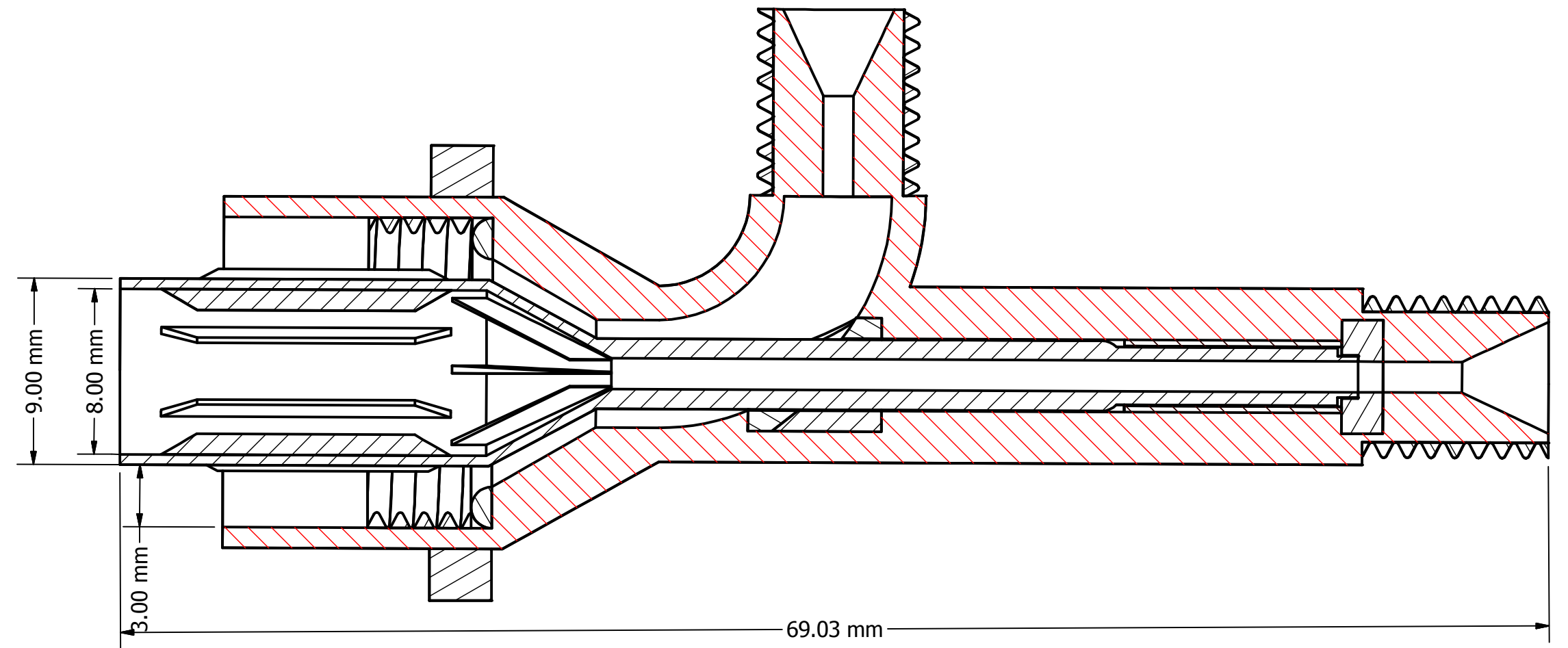
DRAWN	Marco Peca	03/09/2011	University of Southampton School of Electronic and Computer Science		
CHECKED			TITLE		
QA			SUPPORT SLIDING PART		
MFG					
APPROVED			SIZE	DWG NO	REV
			SCALE		SHEET 1 OF 1



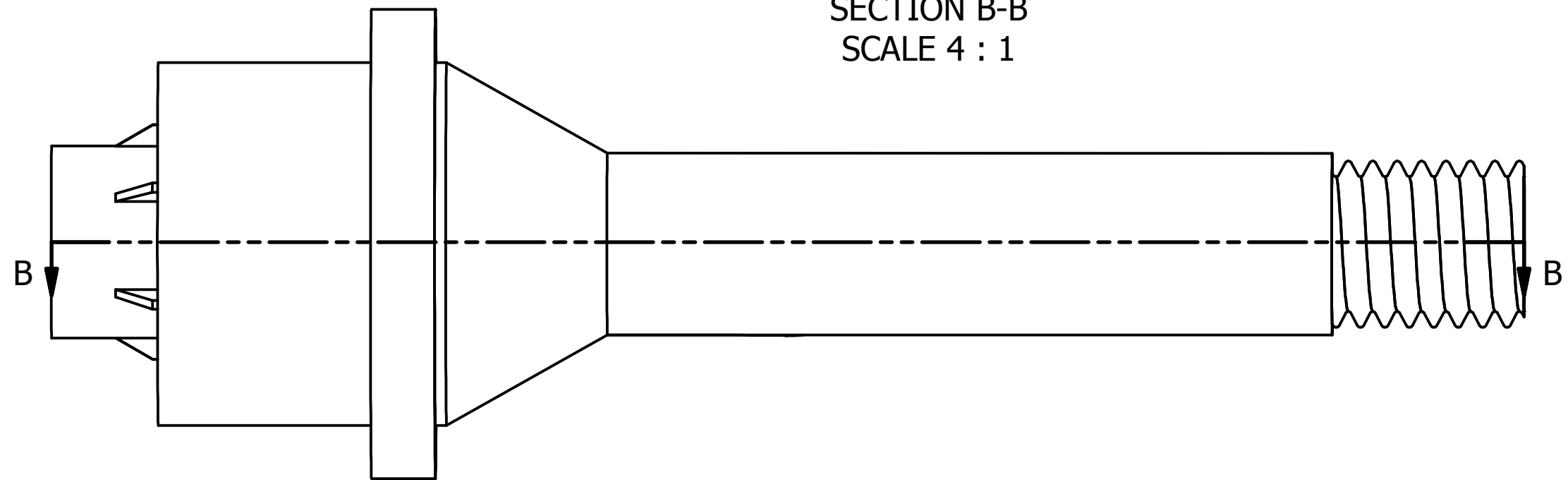
DRAWN	Marco Peca	03/09/2011	University of Southampton School of Electronic and Computer Science		
CHECKED			TITLE		
QA			SUPPORT MAGNETIC SYSTEM ver.3		
MFG			SIZE	DWG NO	REV
APPROVED			SCALE	SHEET 1 OF 1	



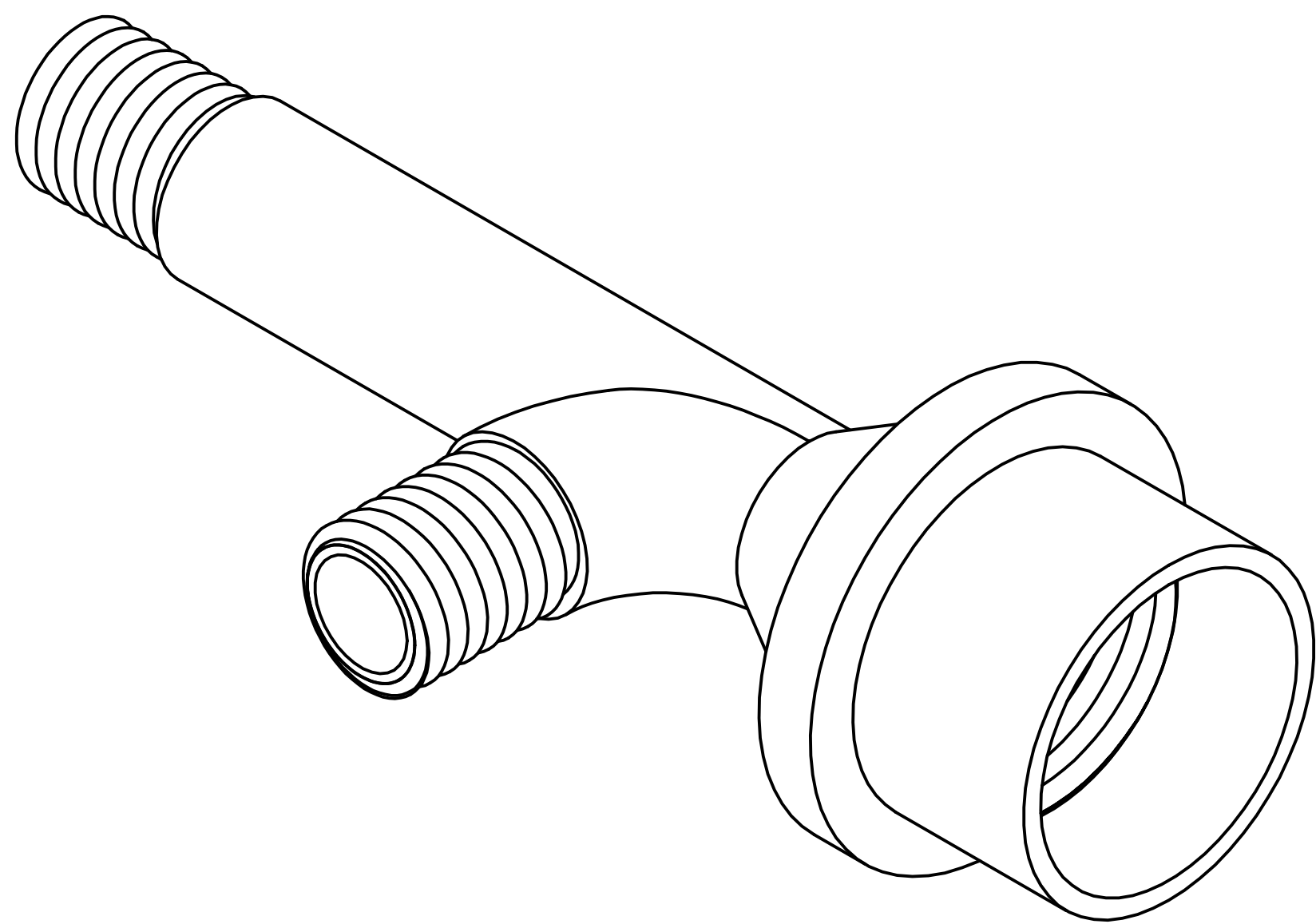
SCALE 4 : 1



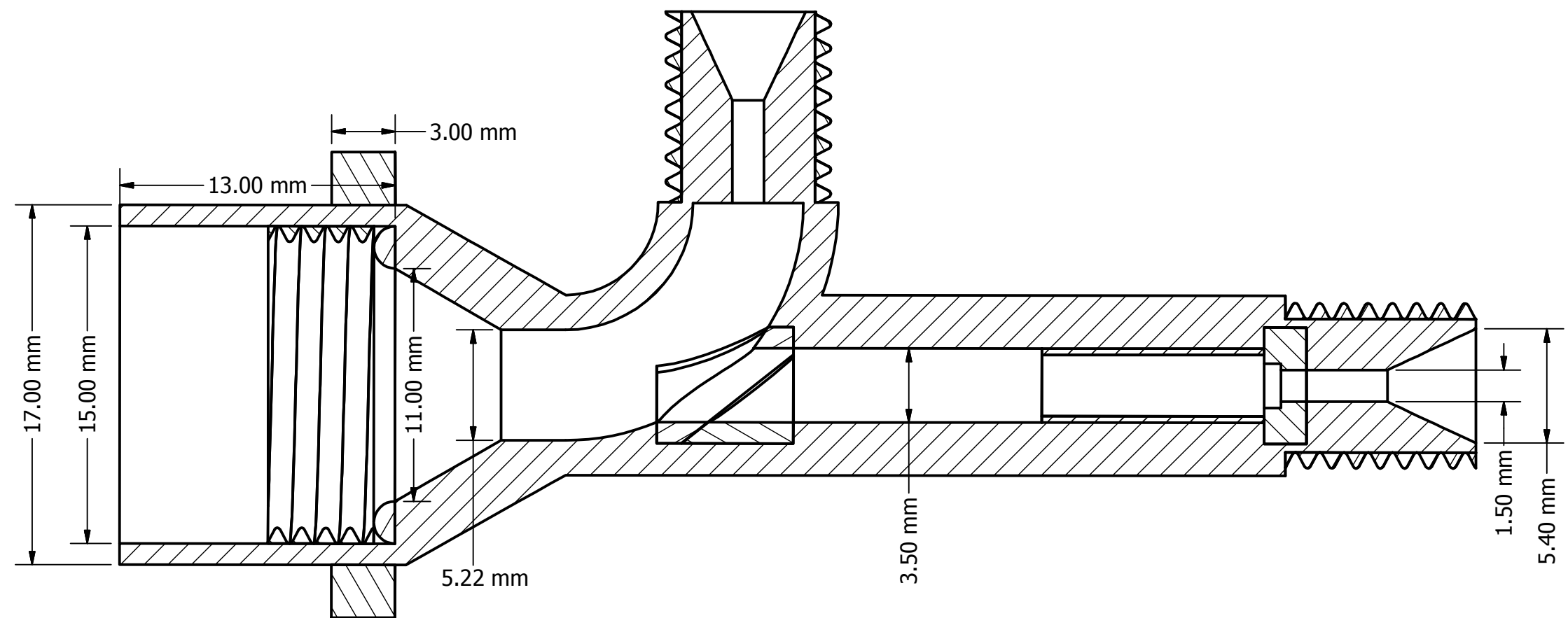
SECTION B-B
SCALE 4 : 1



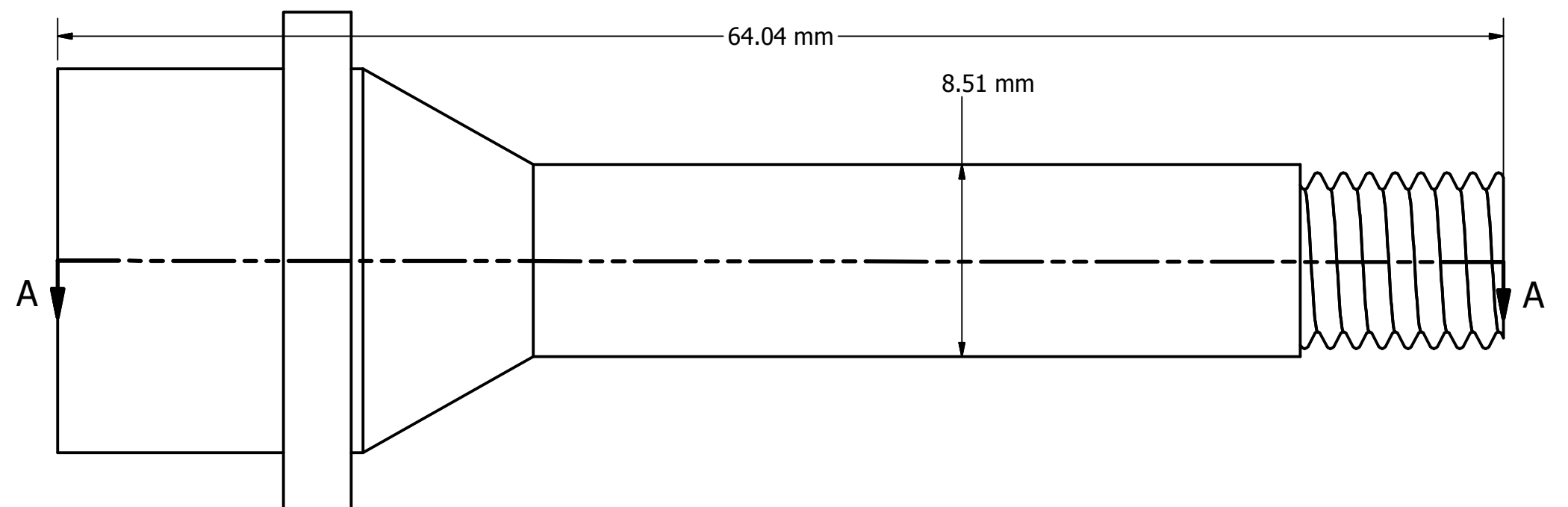
DRAWN	Marco Peca	03/09/2011	University of Southampton School of Electronic and Computer Science		
CHECKED			TITLE		
QA			MANIFOLD ver.1 - ASSEMBLY		
MFG			SIZE	DWG NO	REV
APPROVED			SCALE	SHEET 1 OF 1	



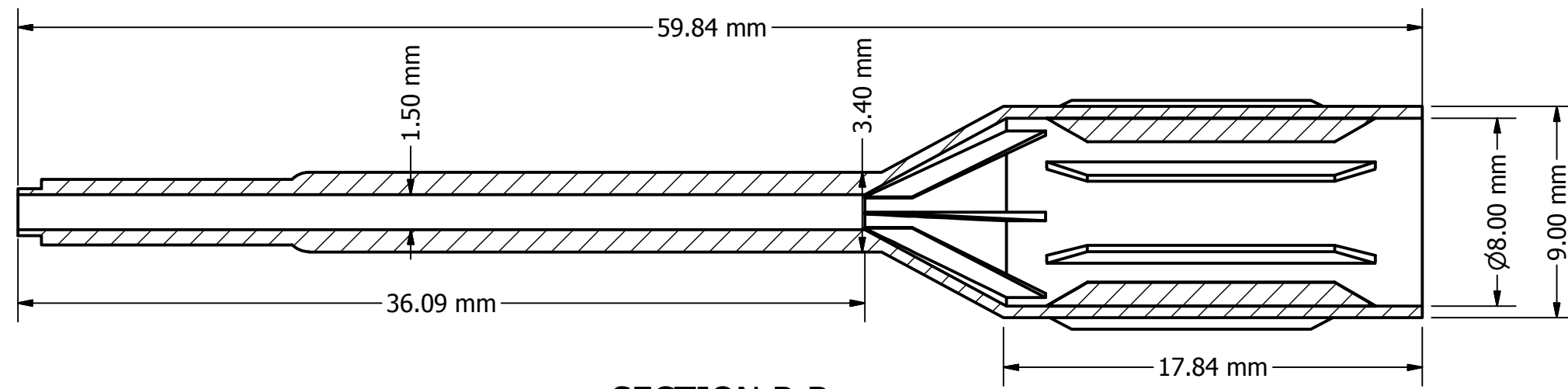
SCALE 4 : 1



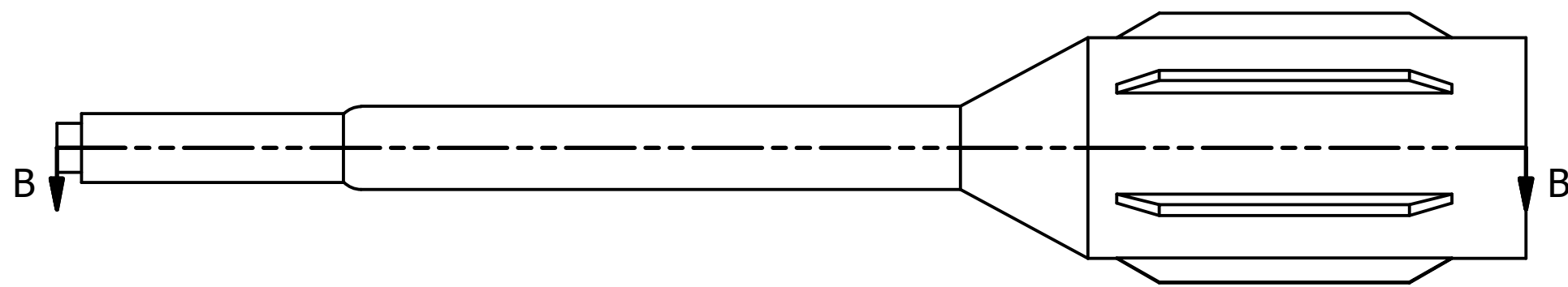
SECTION A-A
SCALE 4 : 1



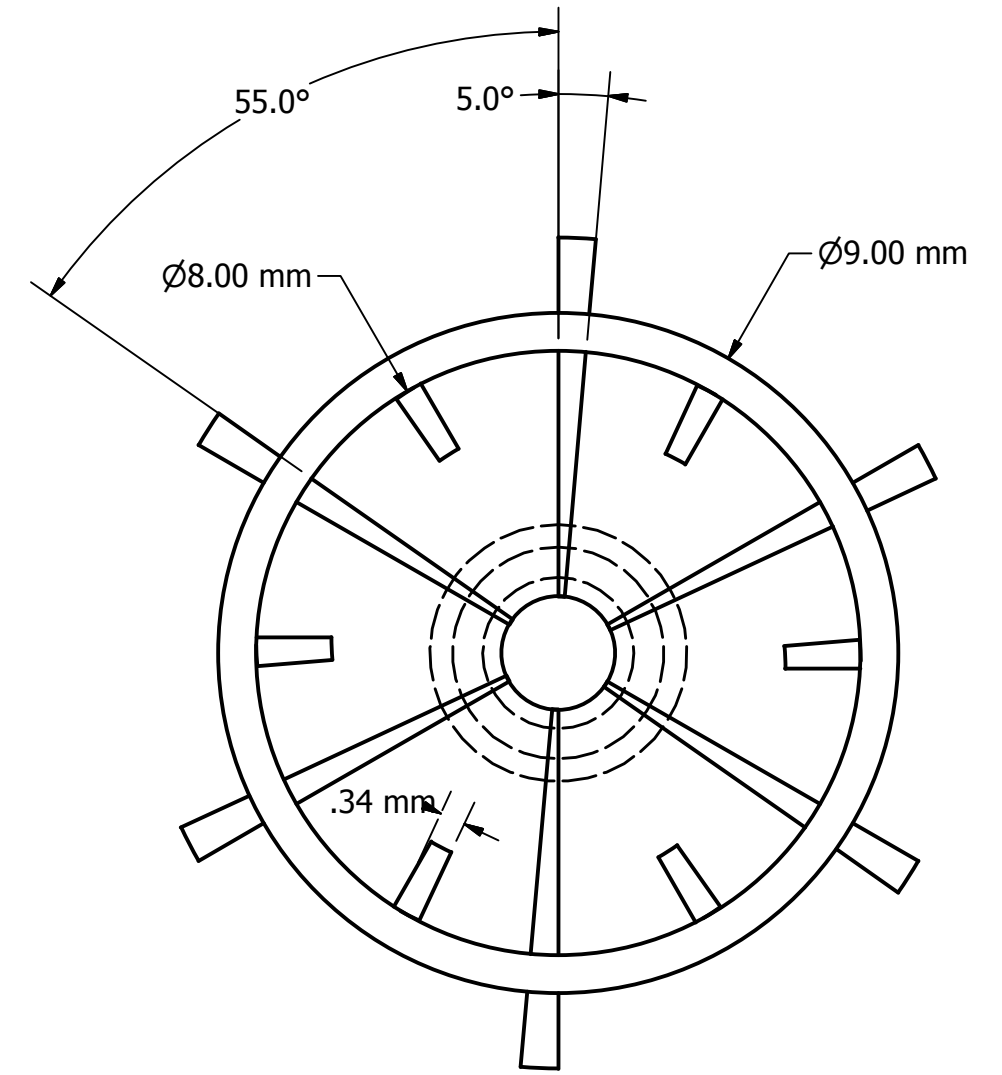
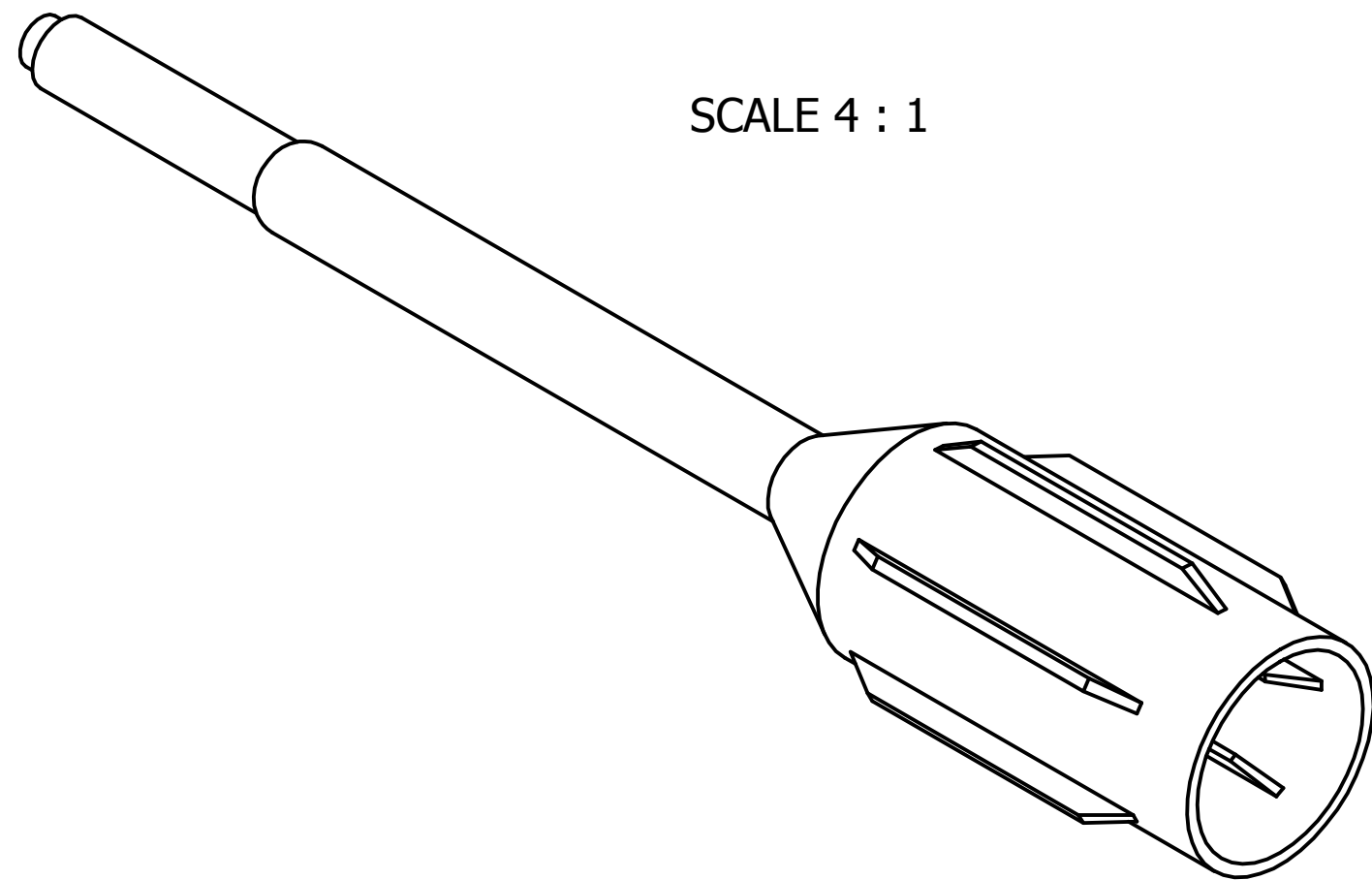
DRAWN	Marco Peca	03/09/2011	University of Southampton School of Electronic and Computer Science		
CHECKED			TITLE		
QA			MANIFOLD ver.1 - EXTERNAL PART		
MFG			SIZE	DWG NO	REV
APPROVED			SCALE	SHEET 1 OF 1	



SECTION B-B
SCALE 4 : 1

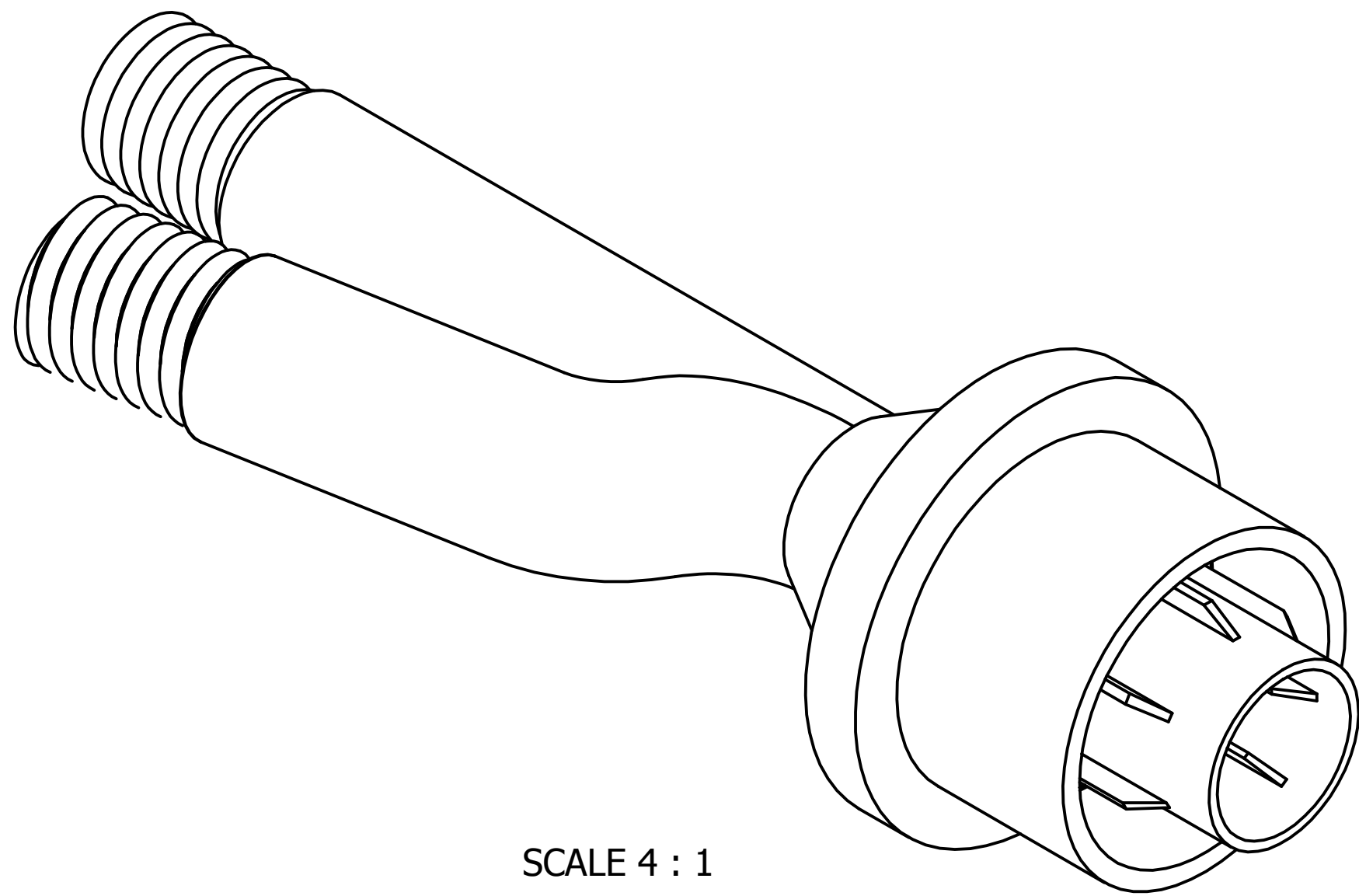


SCALE 4 : 1

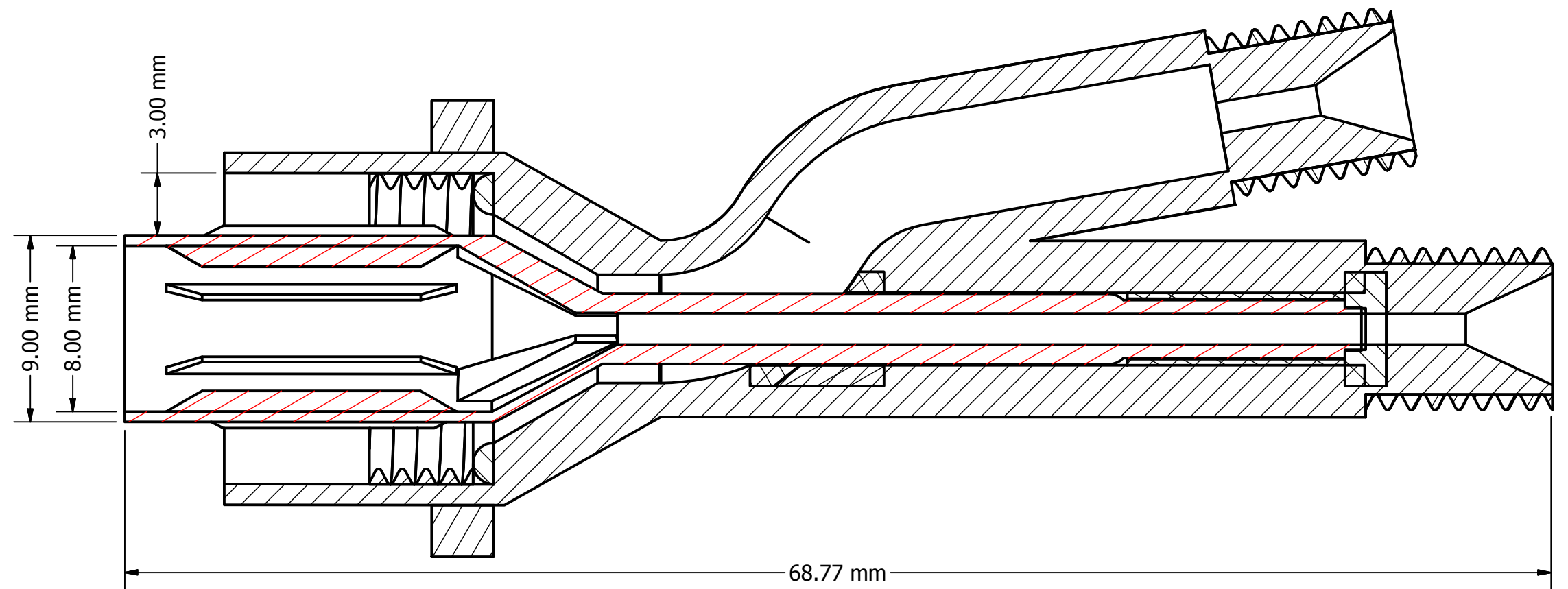


SCALE 10 : 1

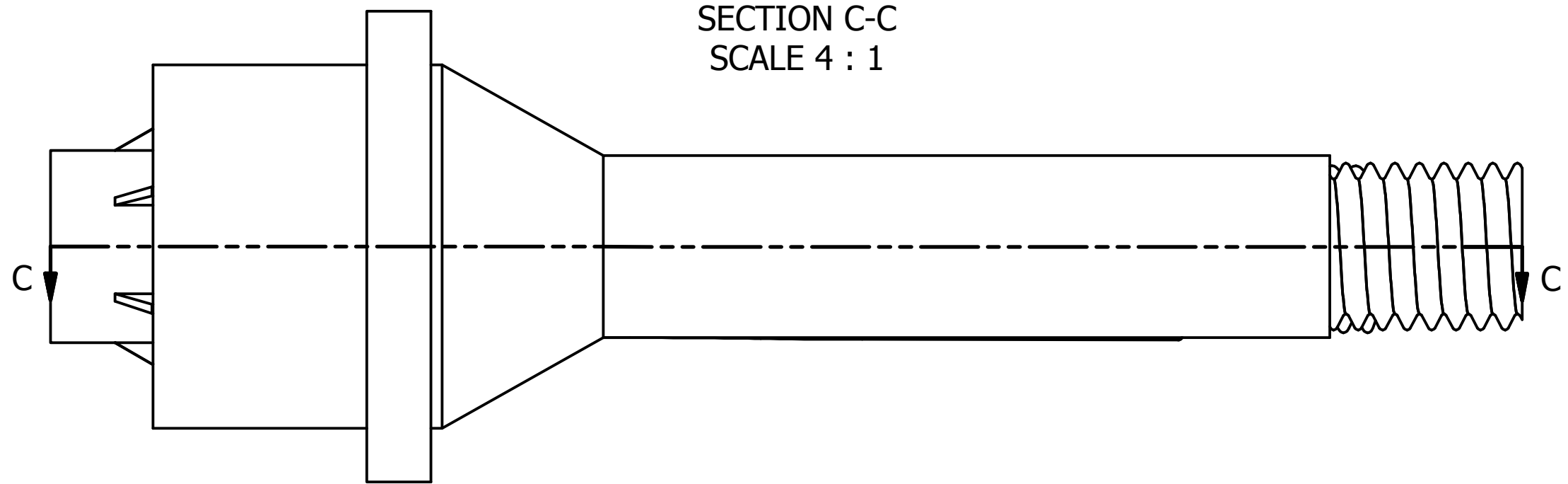
DRAWN	Marco Peca	03/09/2011	University of Southampton School of Electronic and Computer Science		
CHECKED			TITLE		
QA			MANIFOLD ver.1 - INTERNAL PART		
MFG			SIZE	DWG NO	REV
APPROVED			SCALE	SHEET 1 OF 1	



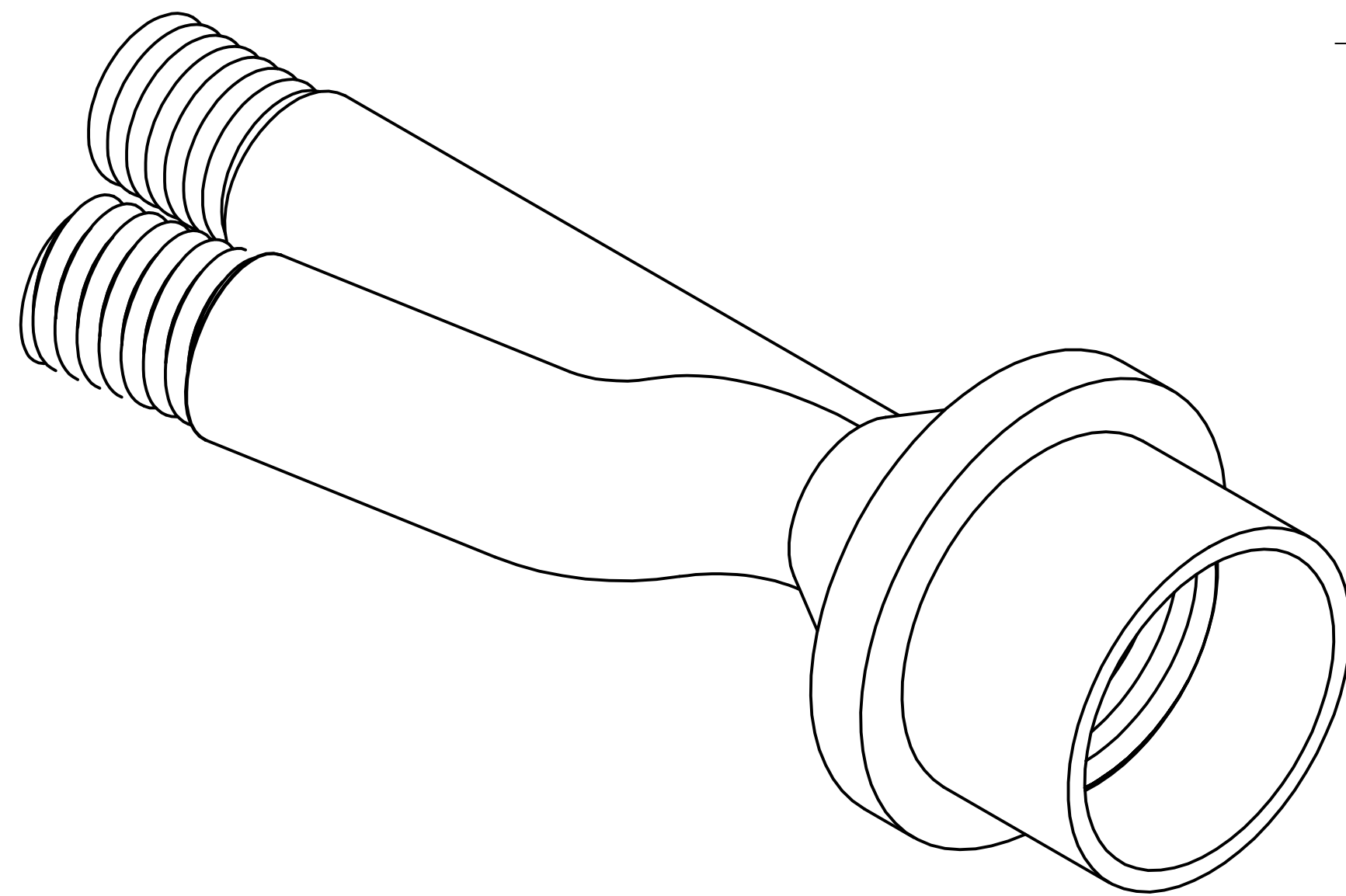
SCALE 4 : 1



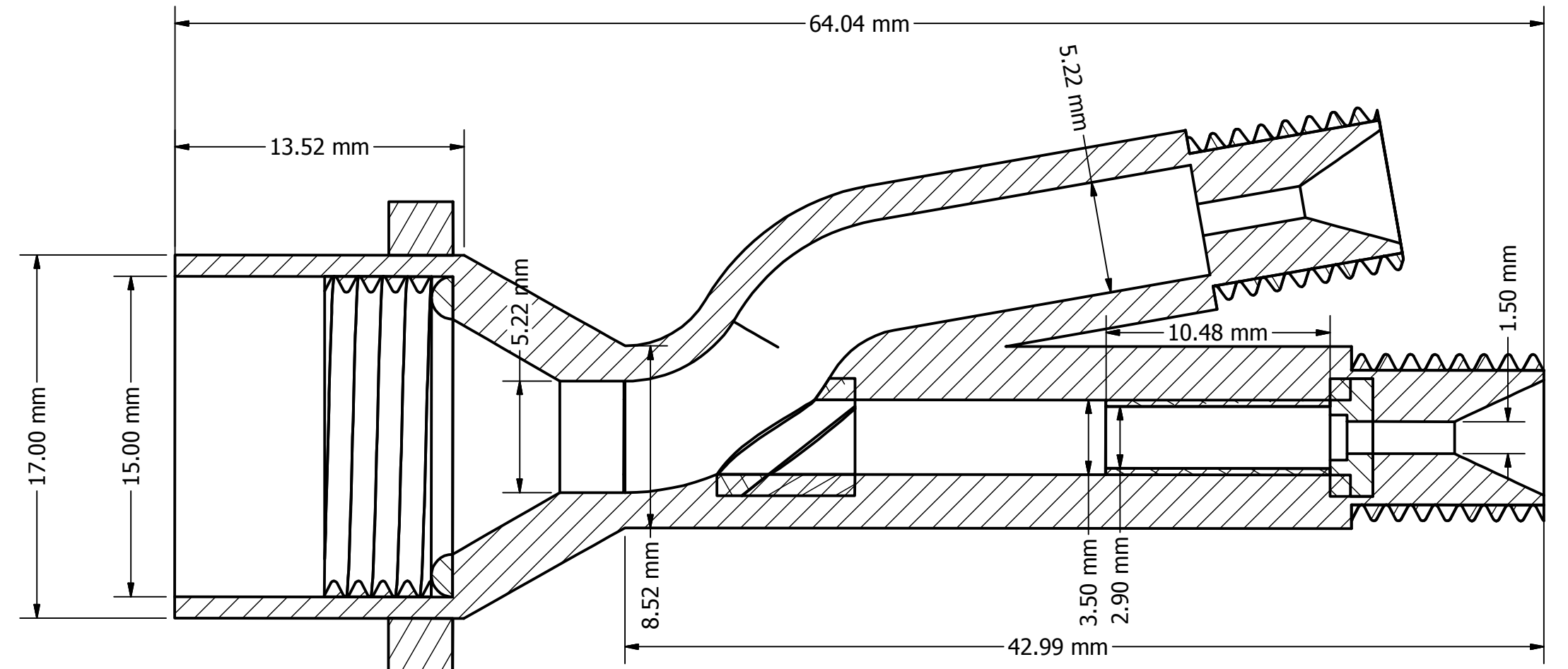
SECTION C-C
SCALE 4 : 1



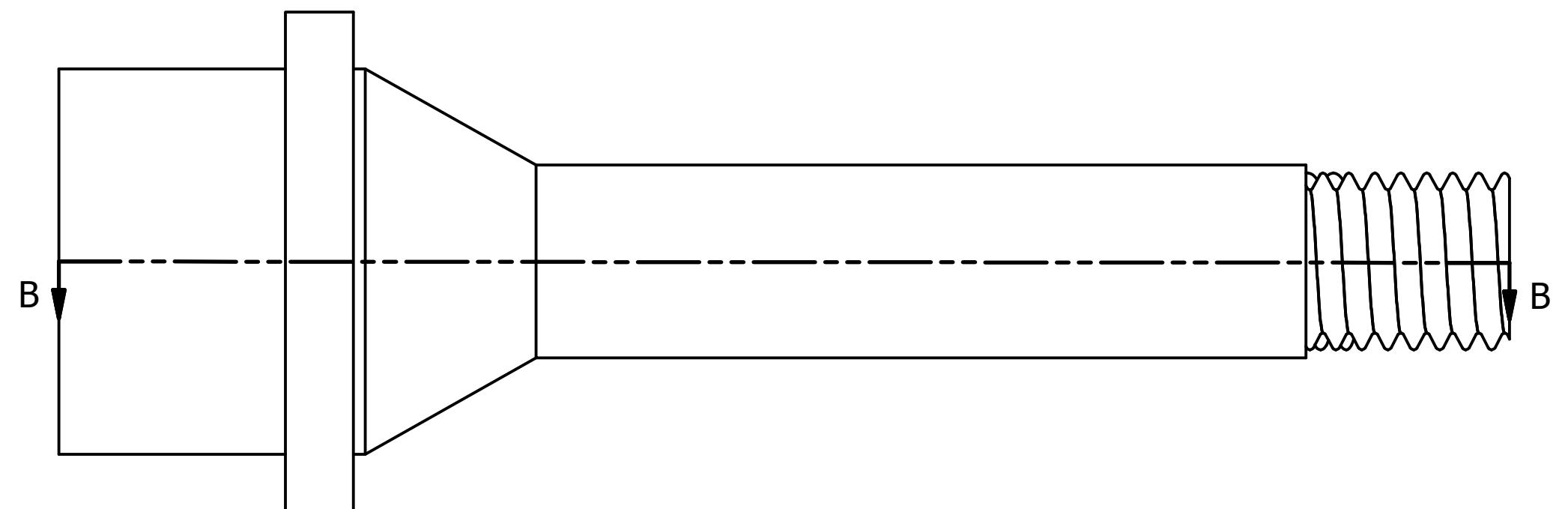
DRAWN	Marco Peca	03/09/2011	University of Southampton School of Electronic and Computer Science		
CHECKED			TITLE		
QA			MANIFOLD ver.2 - ASSEMBLY		
MFG			SIZE	DWG NO	REV
APPROVED			SCALE	SHEET 1 OF 1	



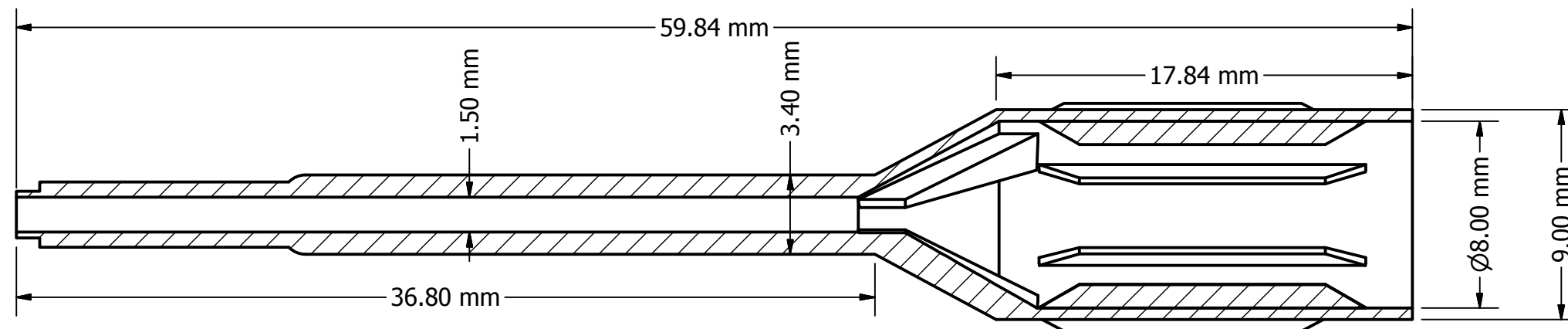
SCALE 4 : 1



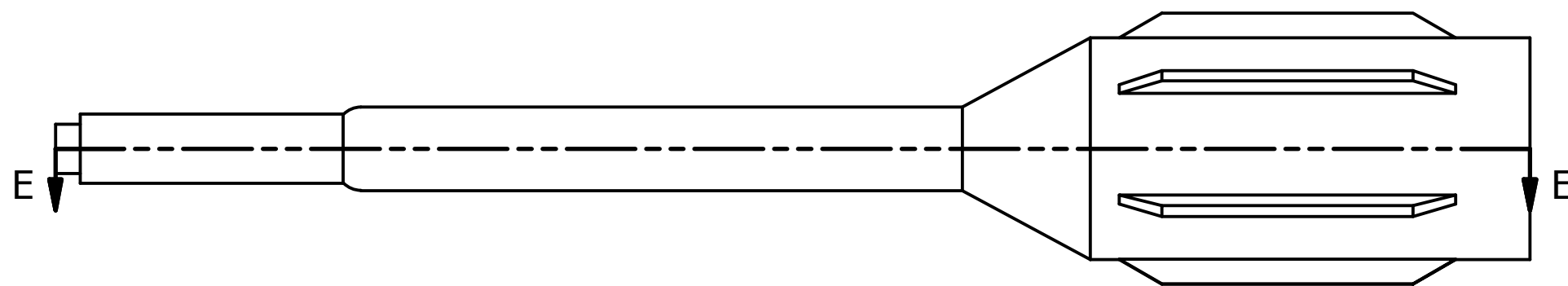
SECTION B-B
SCALE 4 : 1



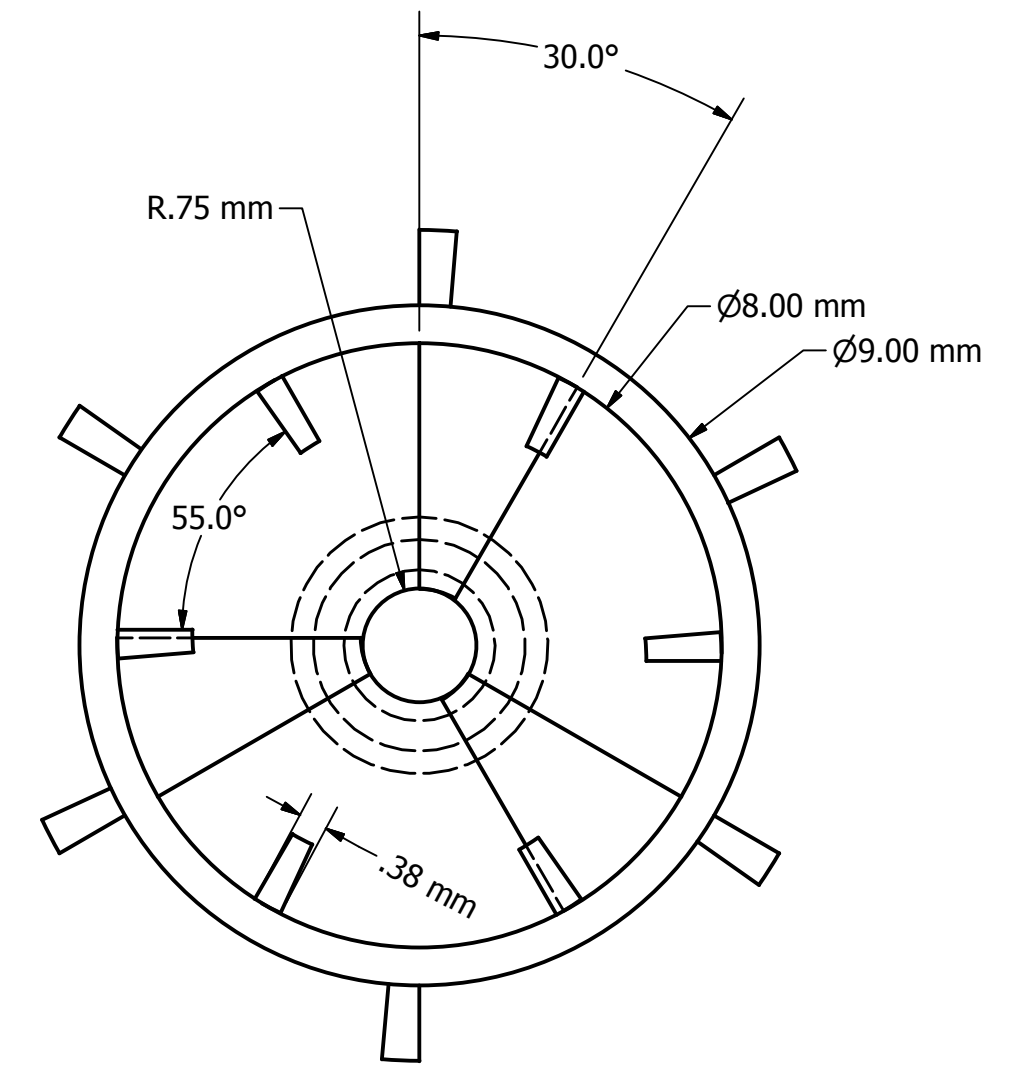
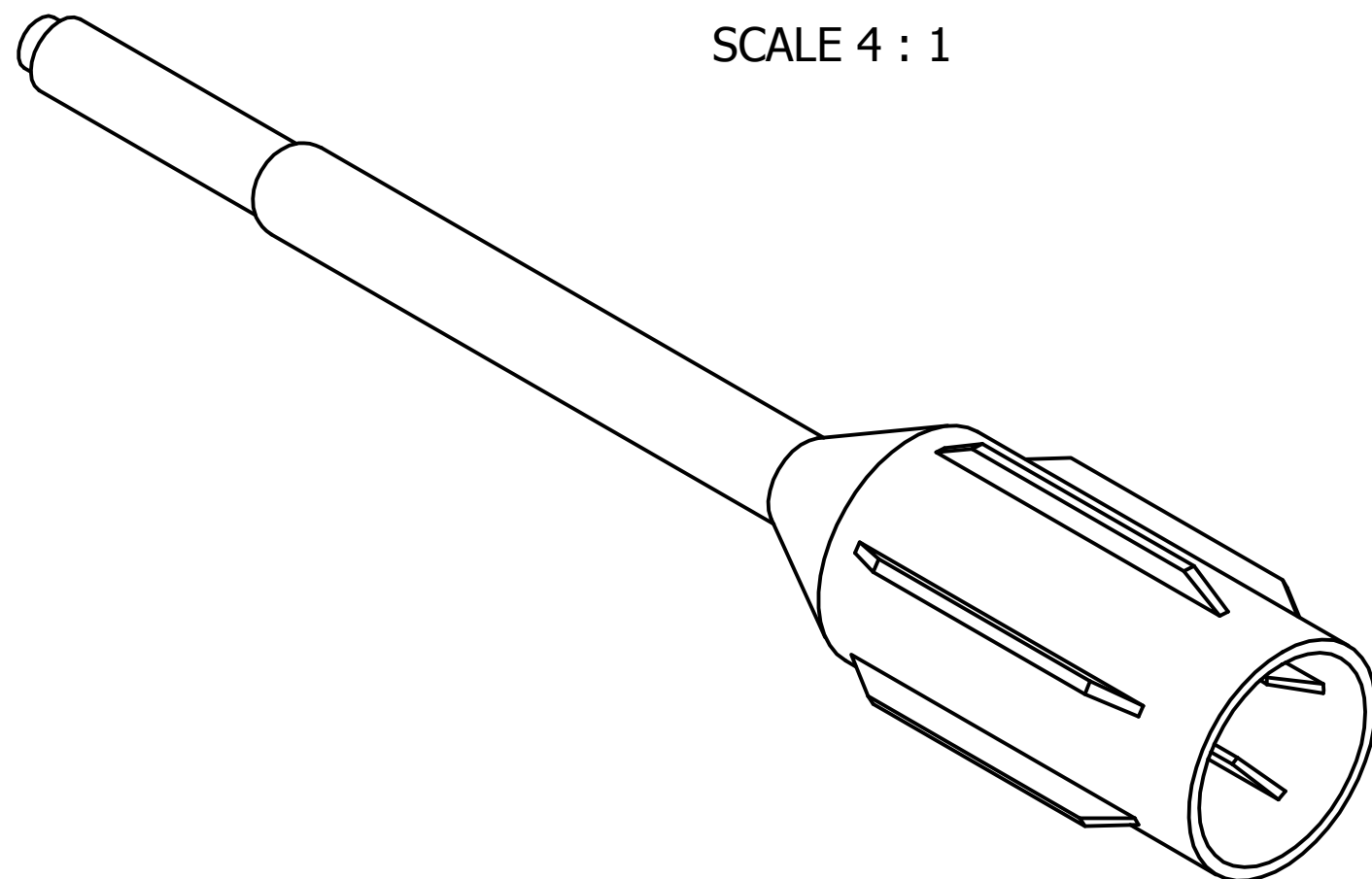
DRAWN	Marco Peca	03/09/2011	University of Southampton School of Electronic and Computer Science		
CHECKED			TITLE		
QA			MANIFOLD ver.2 - EXTERNAL PART		
MFG			SIZE	DWG NO	REV
APPROVED			SCALE	SHEET 1 OF 1	



SECTION E-E
SCALE 4 : 1

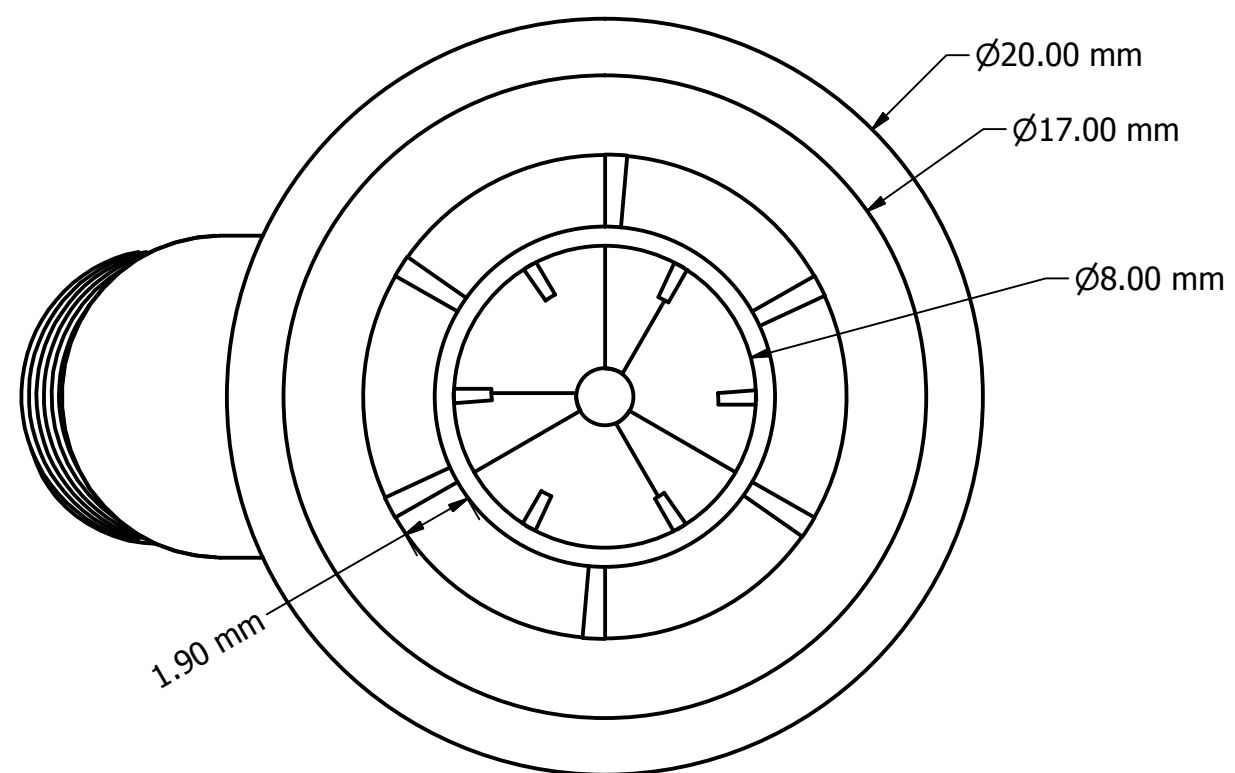


SCALE 4 : 1

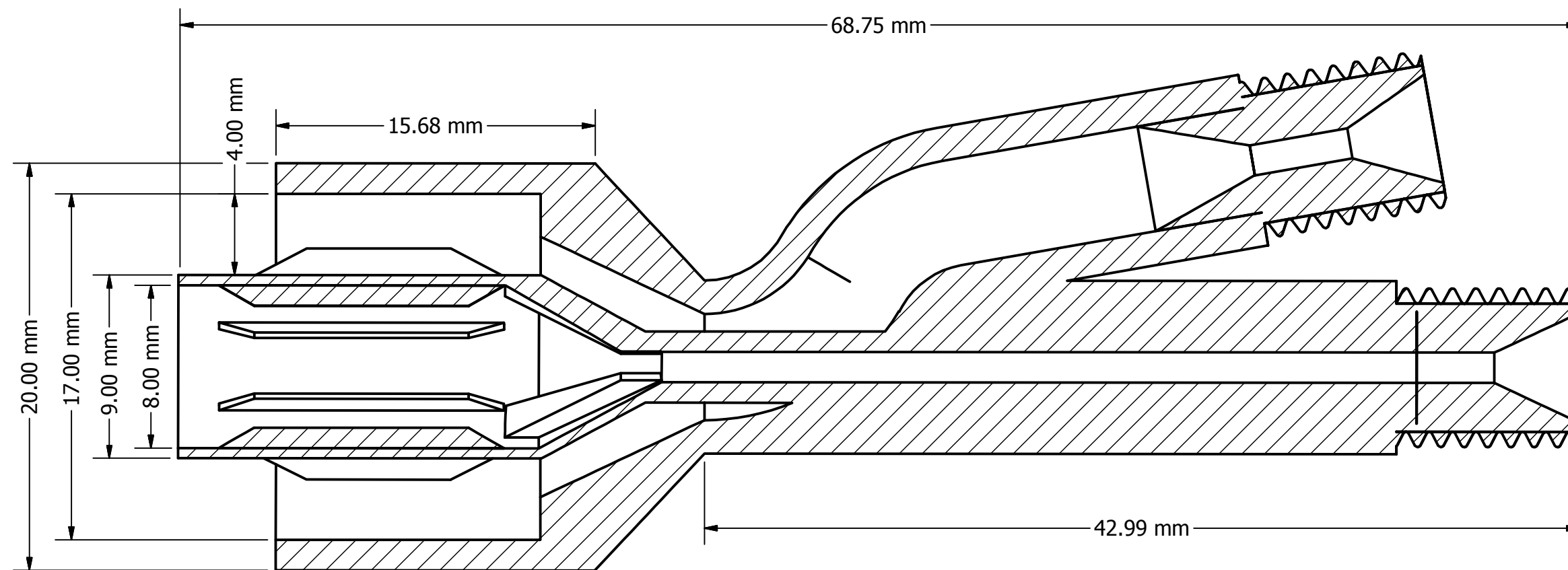


SCALE 10 : 1

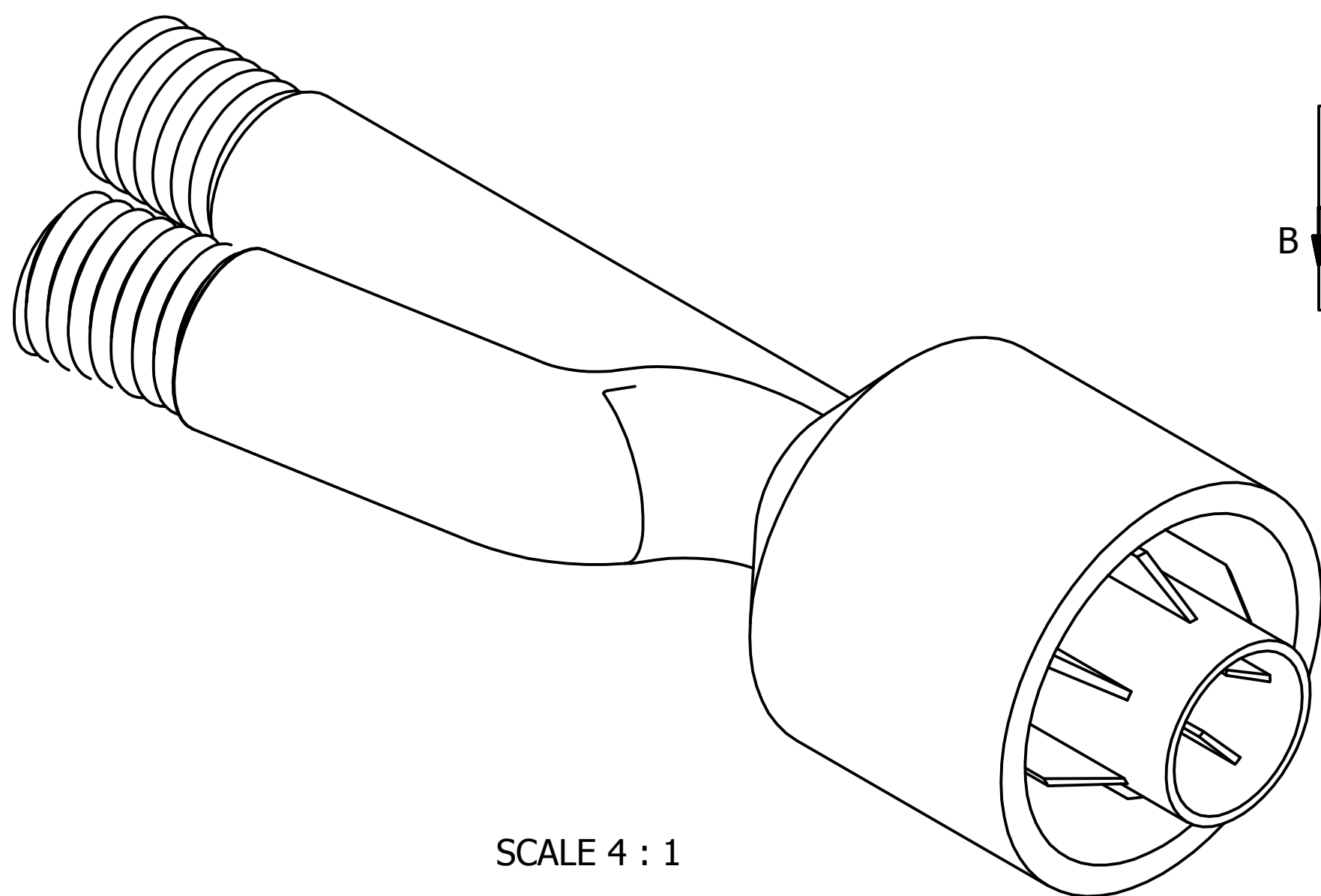
DRAWN	Marco Peca	03/09/2011	University of Southampton School of Electronic and Computer Science		
CHECKED			TITLE		
QA			MANIFOLD ver.2 - INTERNAL PART		
MFG			SIZE	DWG NO	REV
APPROVED			SCALE	SHEET 1 OF 1	



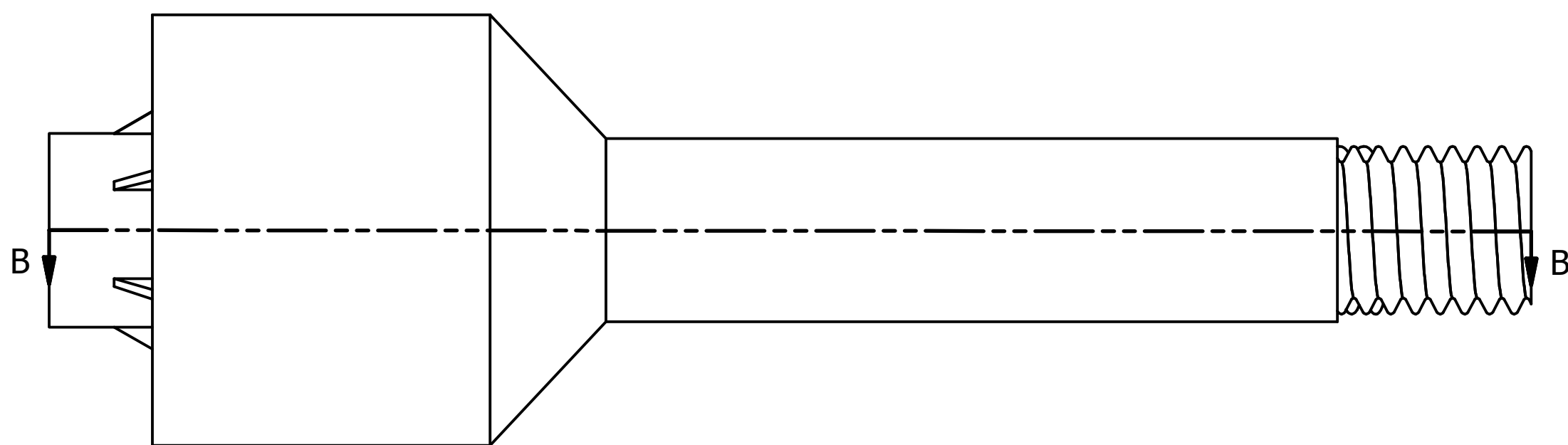
SCALE 5 : 1



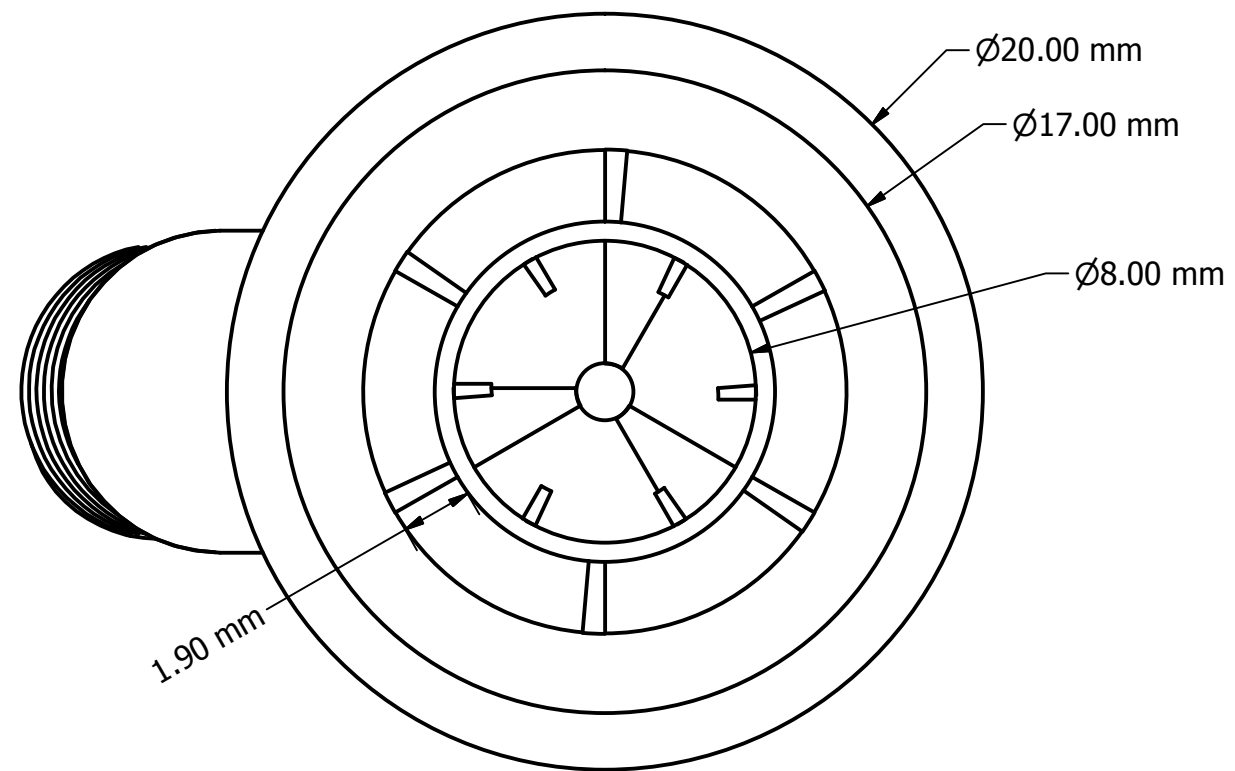
SECTION B-B
SCALE 4 : 1



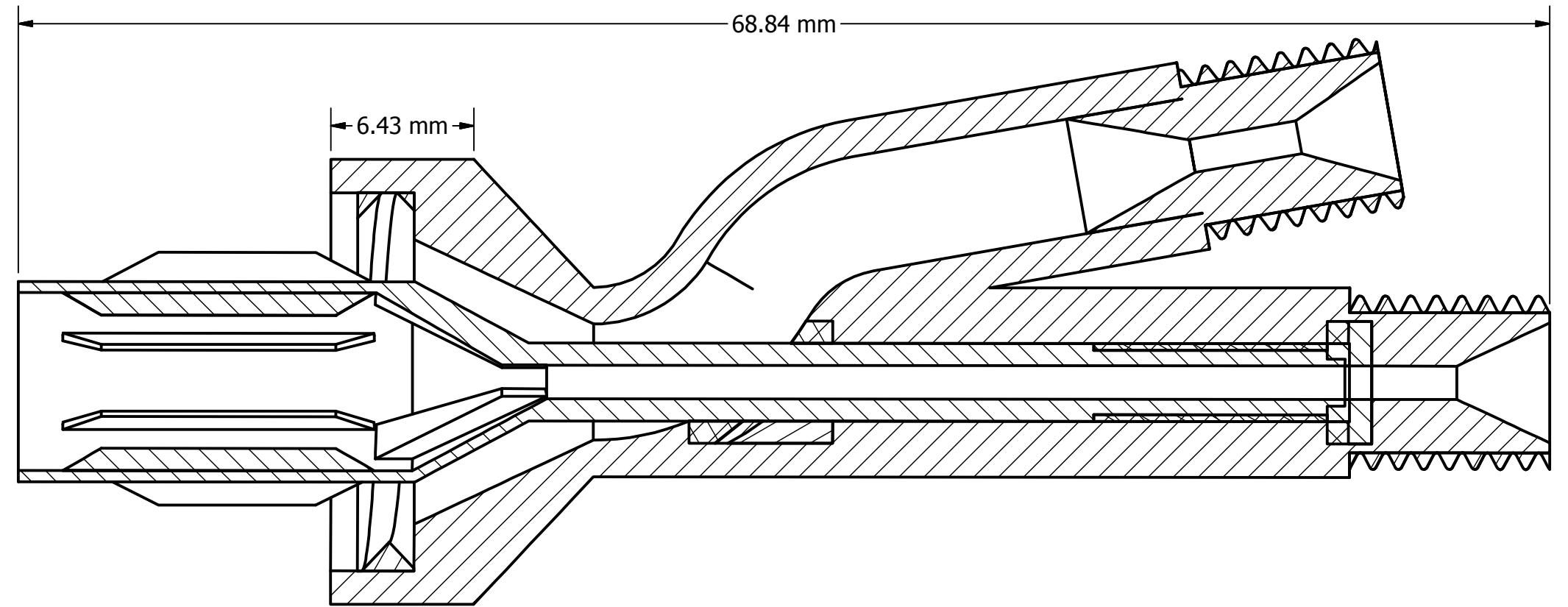
SCALE 4 : 1



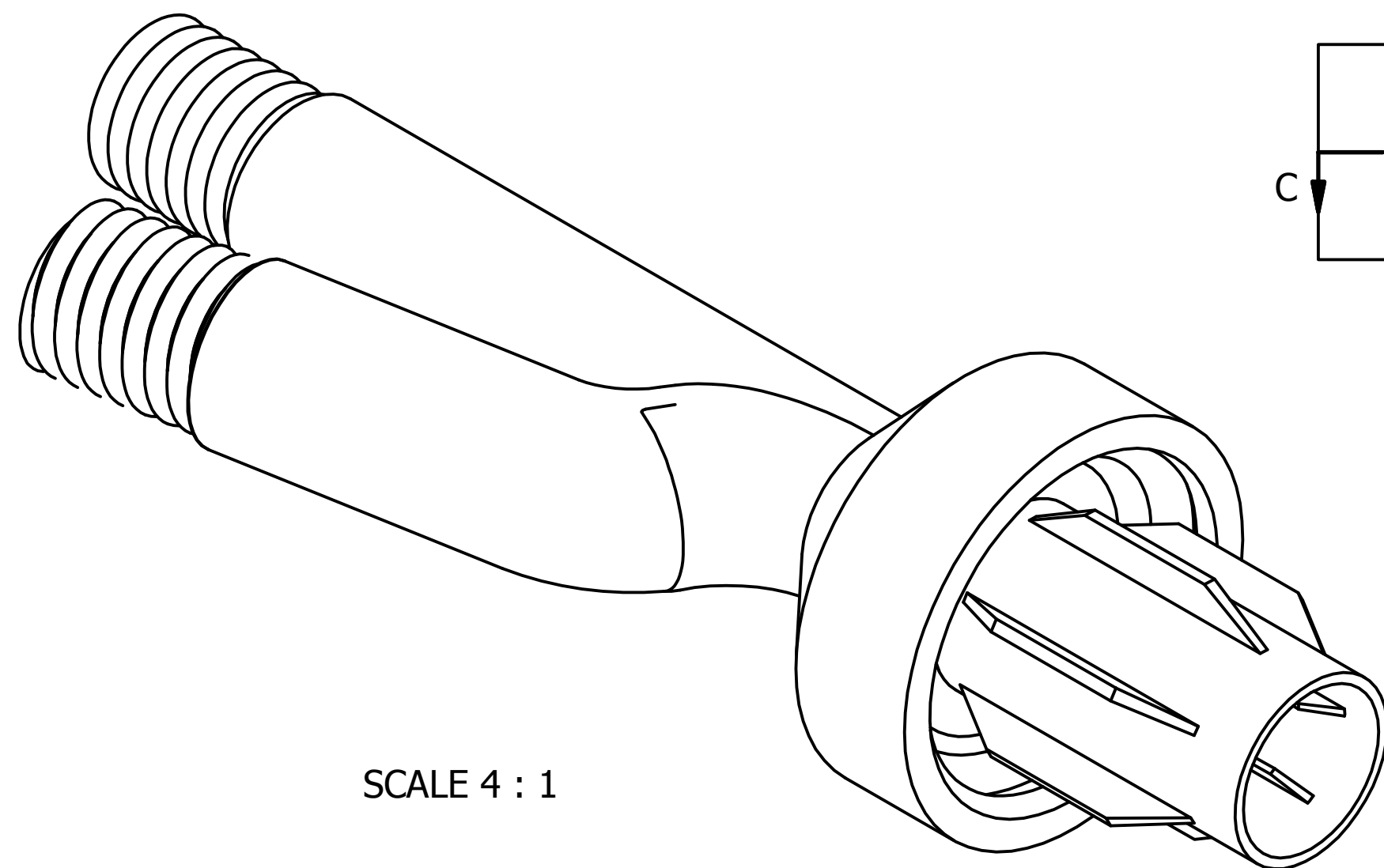
DRAWN	Marco Peca	09/12/2012	University of Southampton School of Electronic and Computer Science		
CHECKED			TITLE		
QA			MANIFOLD ver.3		
MFG			SIZE	DWG NO	REV
APPROVED			SCALE	SHEET 1 OF 1	



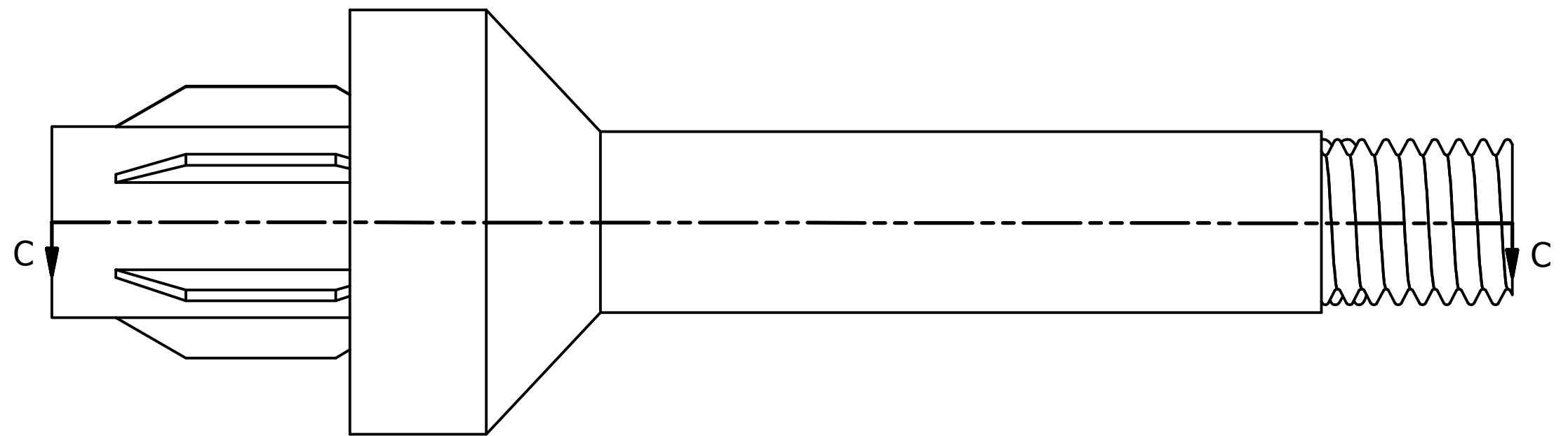
SCALE 5 : 1



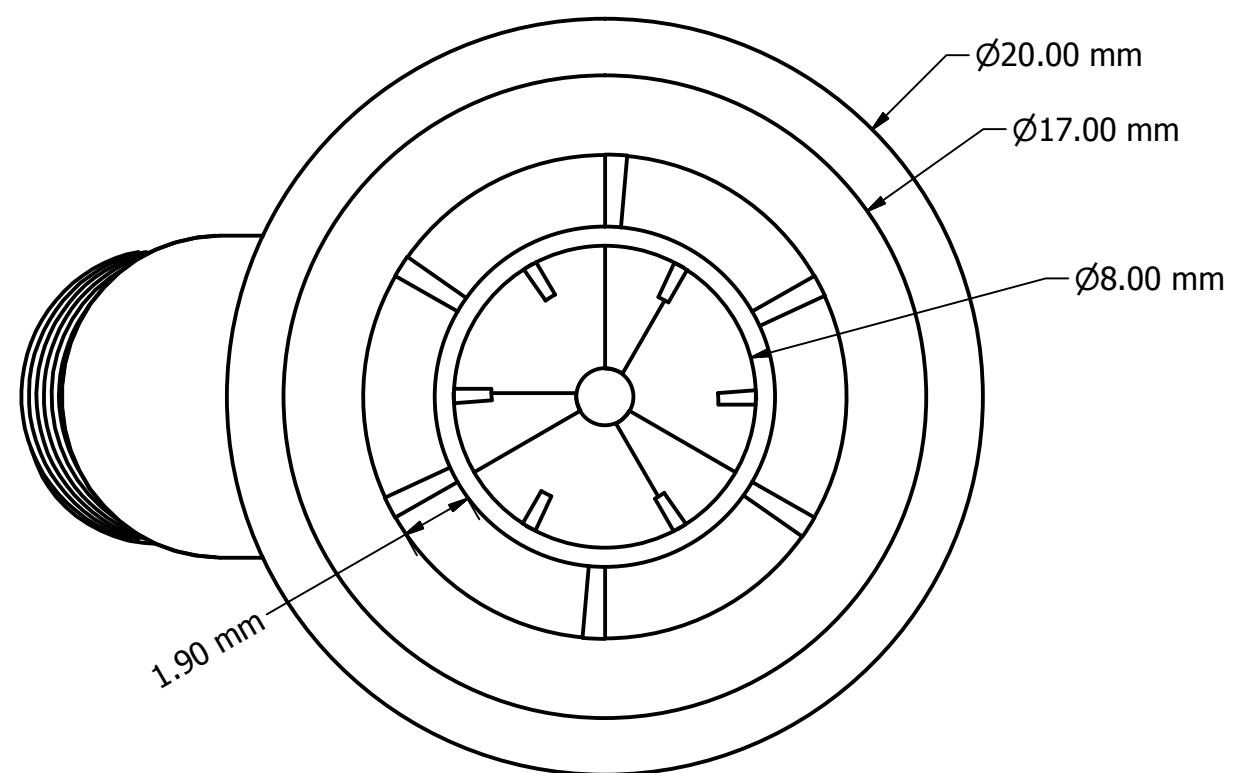
SECTION C-C
SCALE 4 : 1



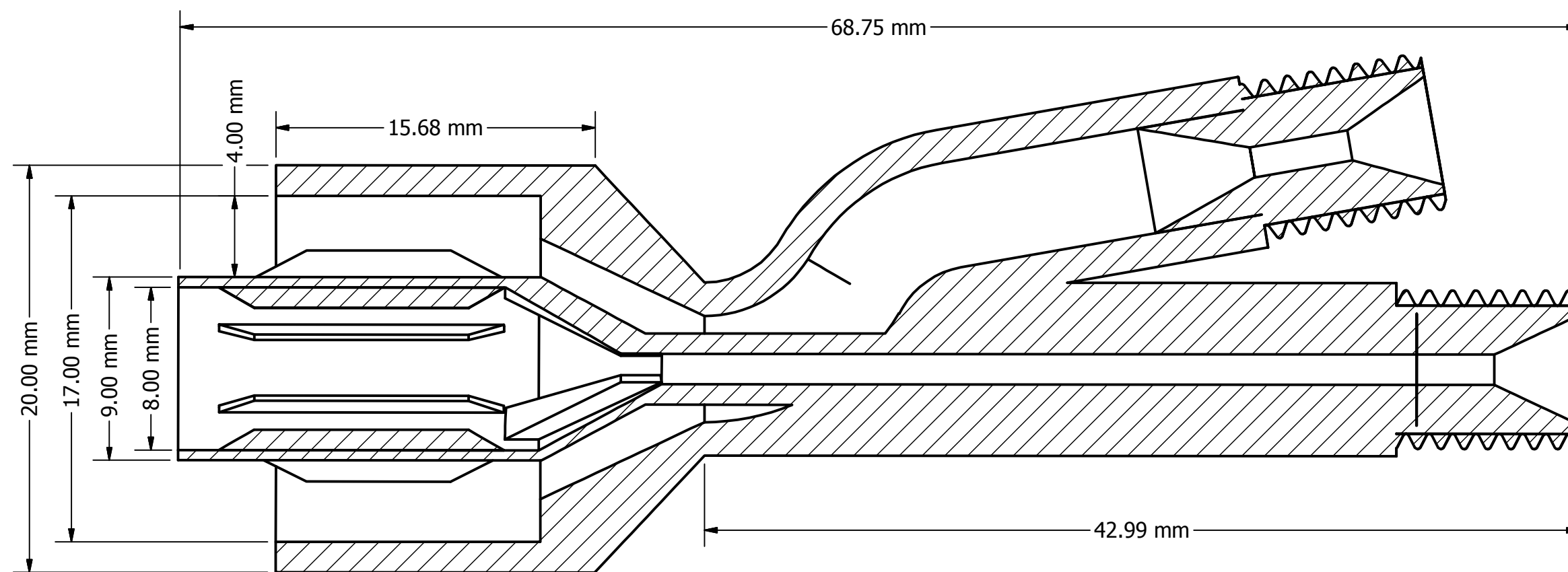
SCALE 4 : 1



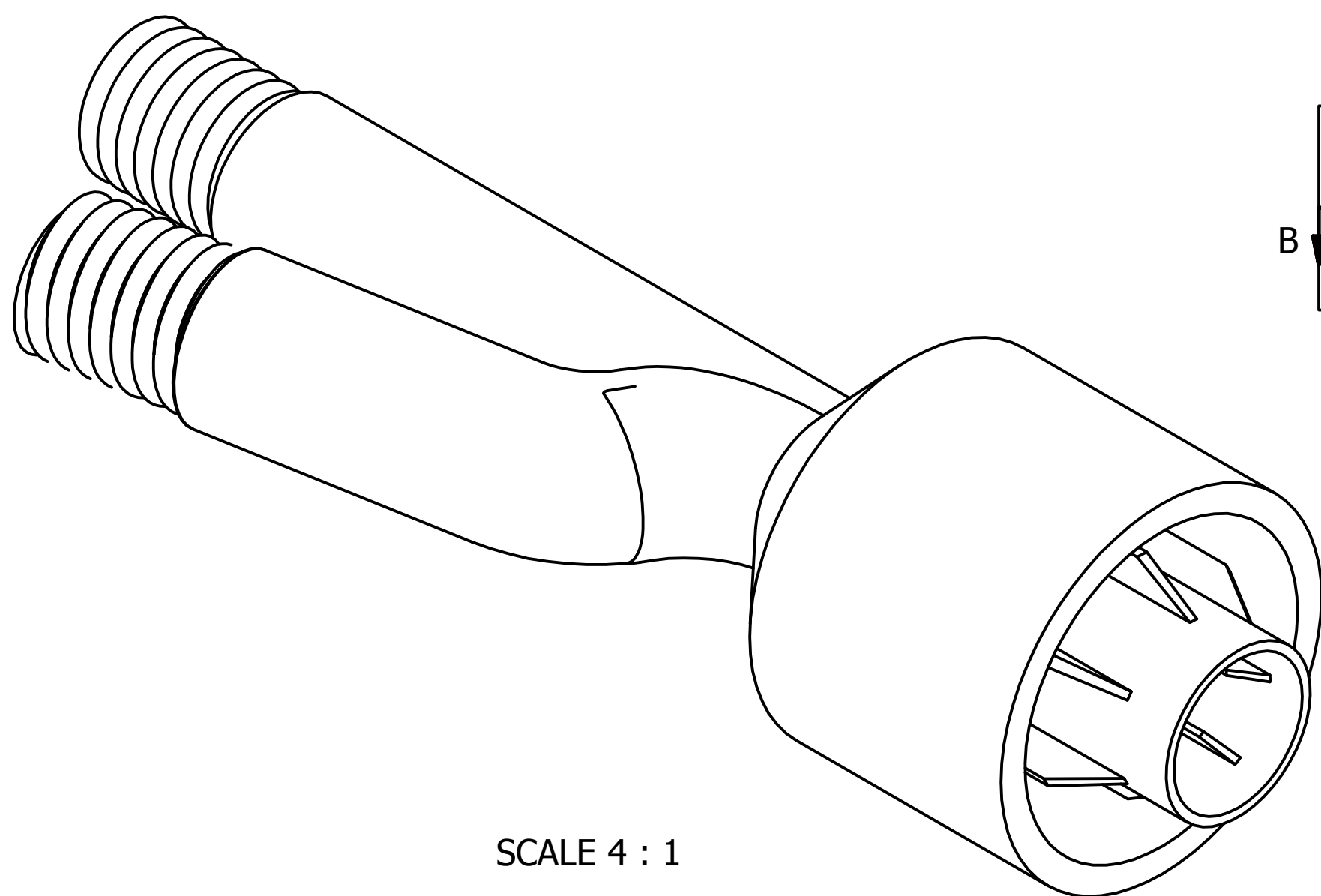
DRAWN	Marco Peca	03/09/2011	University of Southampton School of Electronic and Computer Science		
CHECKED			TITLE		
QA			MANIFOLD ver.3.2 & ver.3.3		
MFG					
APPROVED			SIZE	DWG NO	REV
			SCALE		SHEET 1 OF 1



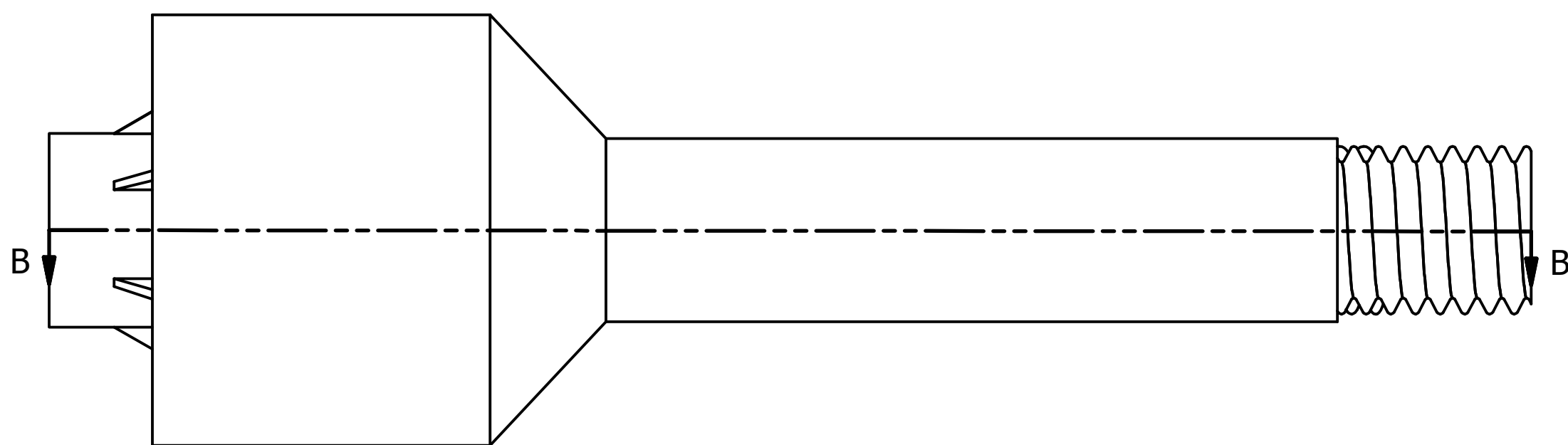
SCALE 5 : 1



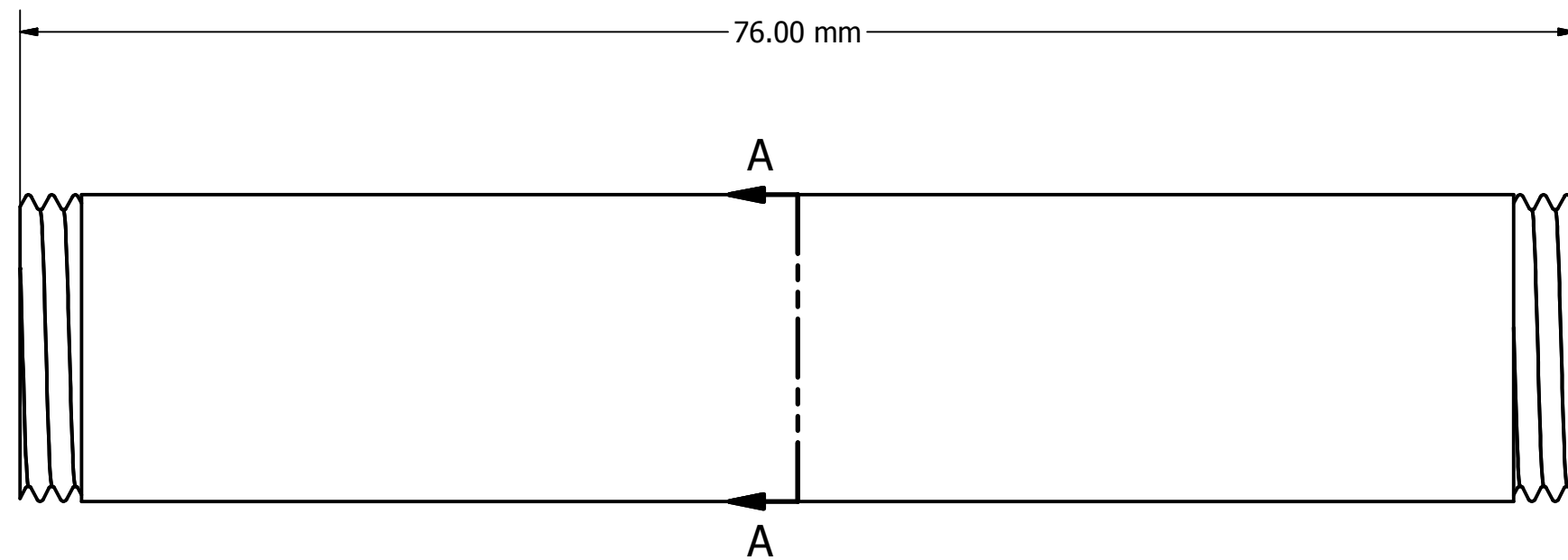
SECTION B-B
SCALE 4 : 1



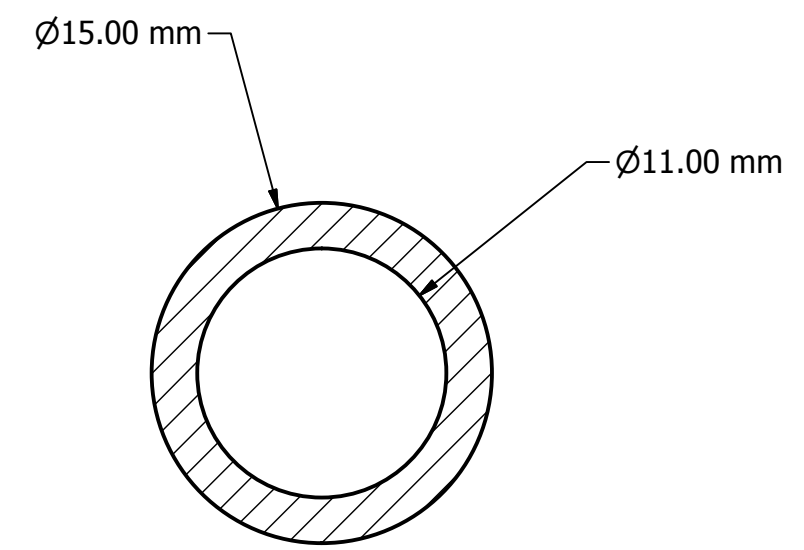
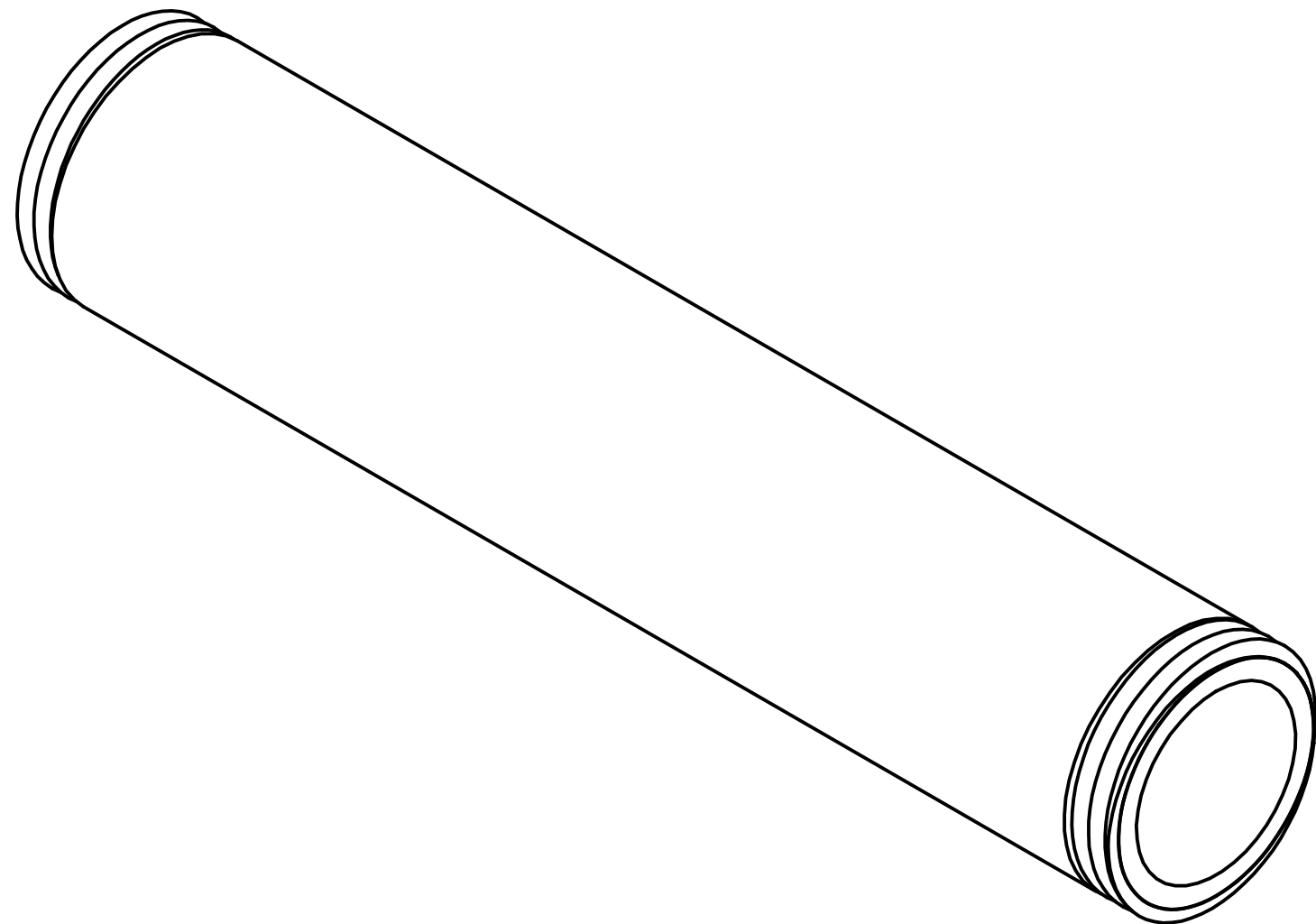
SCALE 4 : 1



DRAWN	Marco Peca	05/02/2013	University of Southampton School of Electronic and Computer Science		
CHECKED			TITLE		
QA			MANIFOLD ver.3.4		
MFG			SIZE	DWG NO	REV
APPROVED			SCALE	SHEET 1 OF 1	

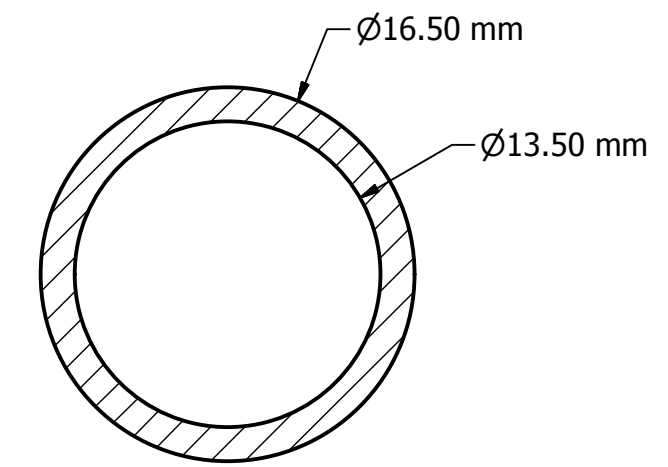
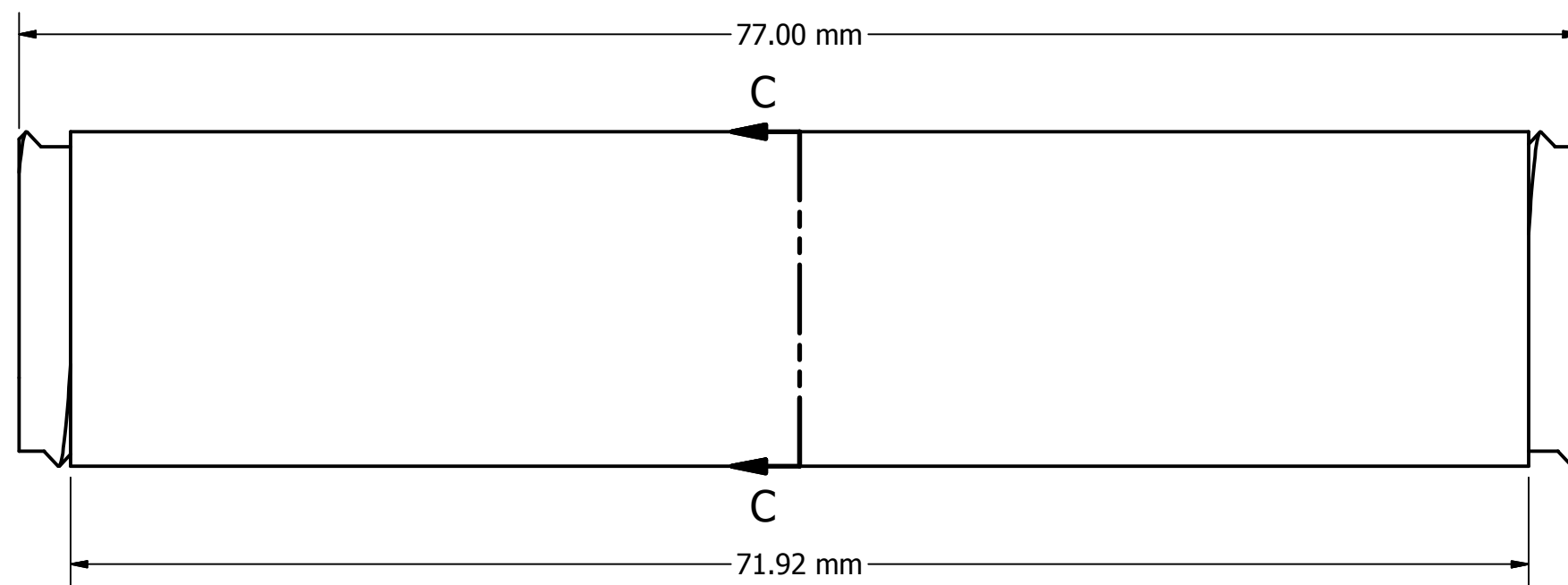


SCALE 3 : 1

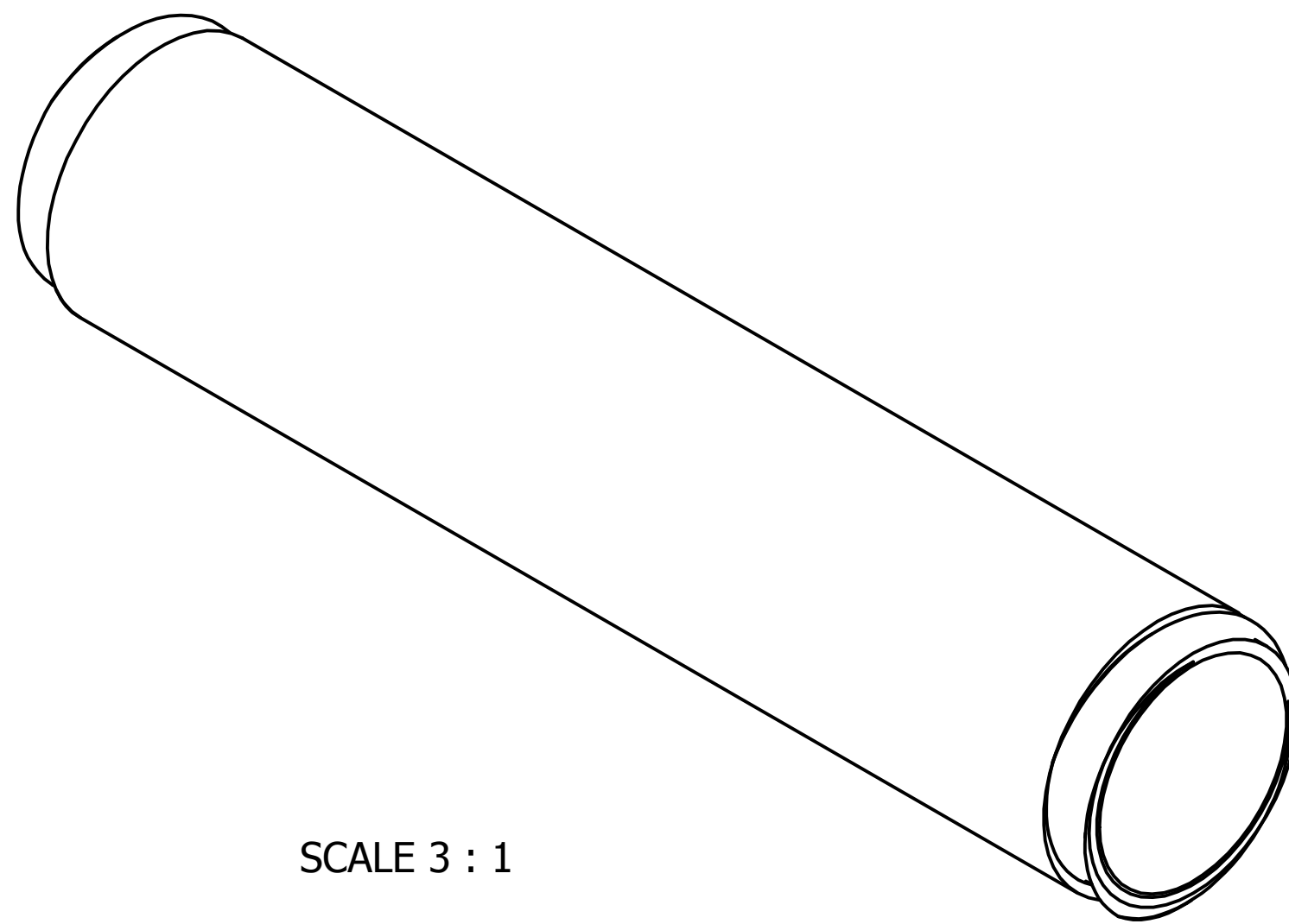


SECTION A-A
SCALE 3 : 1

DRAWN	Marco Peca	03/09/2011	University of Southampton School of Electronic and Computer Science		
CHECKED			TITLE		
QA			CYLINDER ver.1		
MFG					
APPROVED			SIZE	DWG NO	REV
			SCALE	SHEET 1 OF 1	

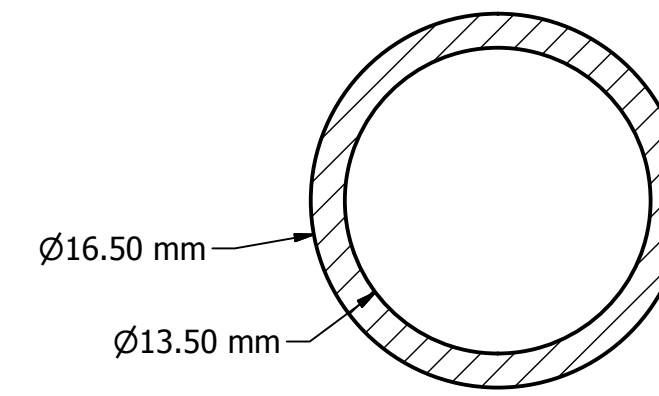
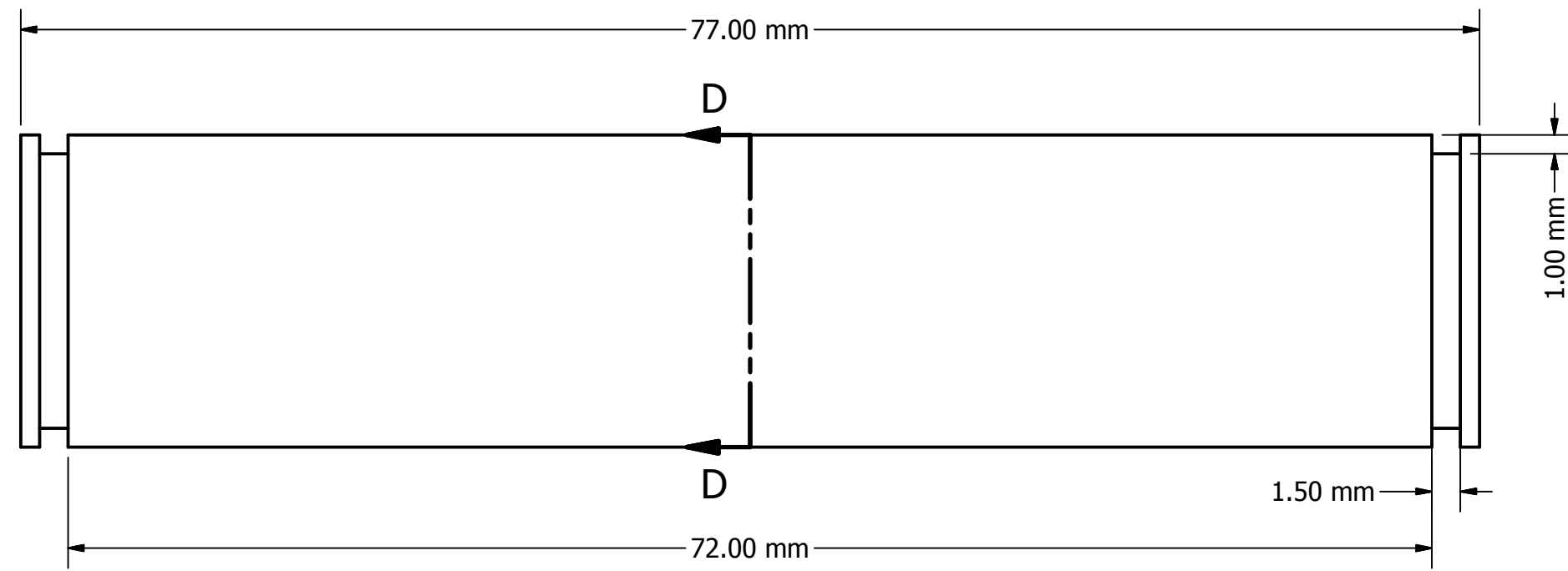


SECTION C-C
SCALE 3 : 1

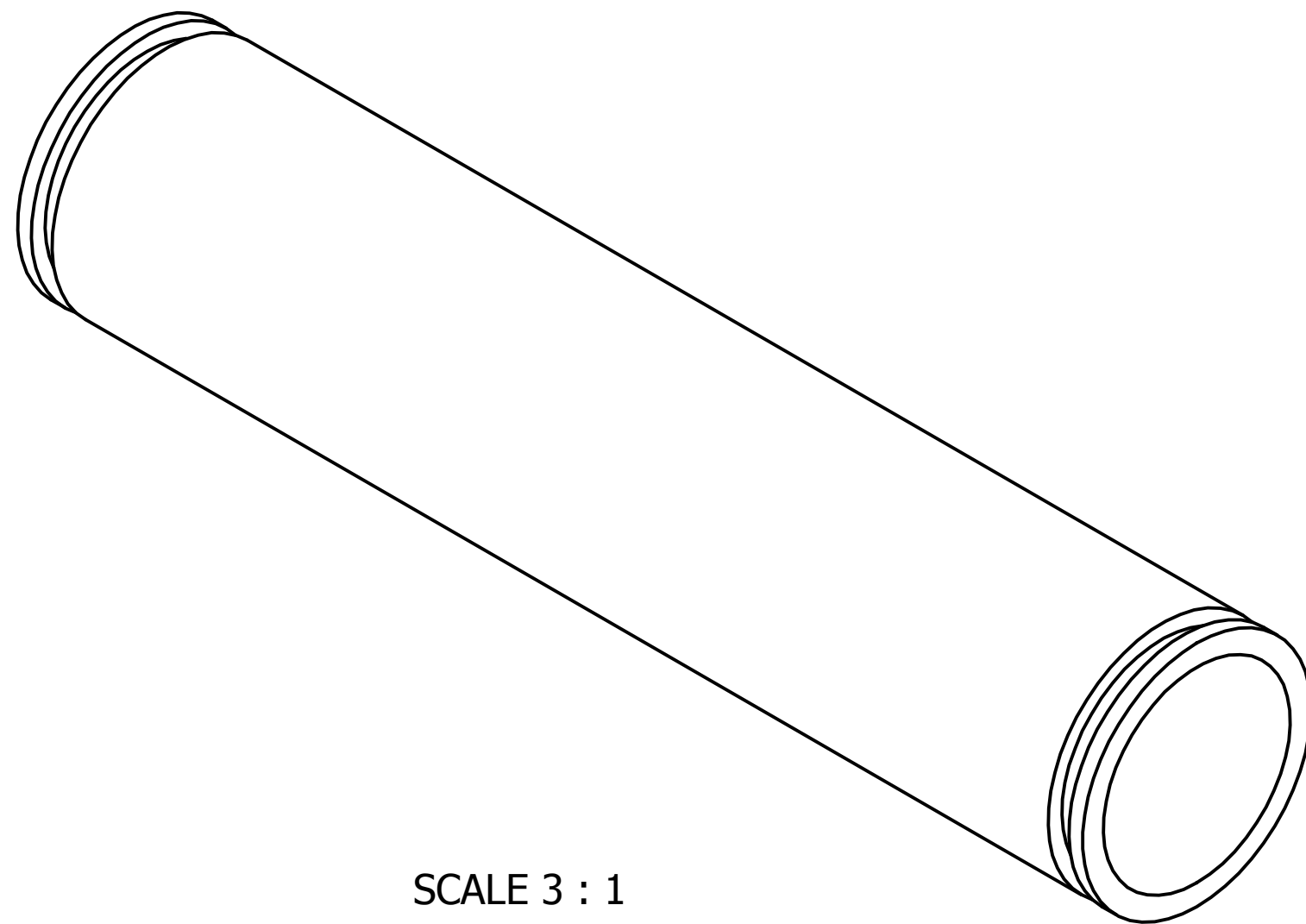


SCALE 3 : 1

DRAWN	Marco Peca	12/11/2012	University of Southampton School of Electronic and Computer Science		
CHECKED			TITLE		
QA			CYLINDER ver.3.2 & ver.3.3		
MFG					
APPROVED			SIZE	DWG NO	REV
			SCALE	SHEET 1 OF 1	

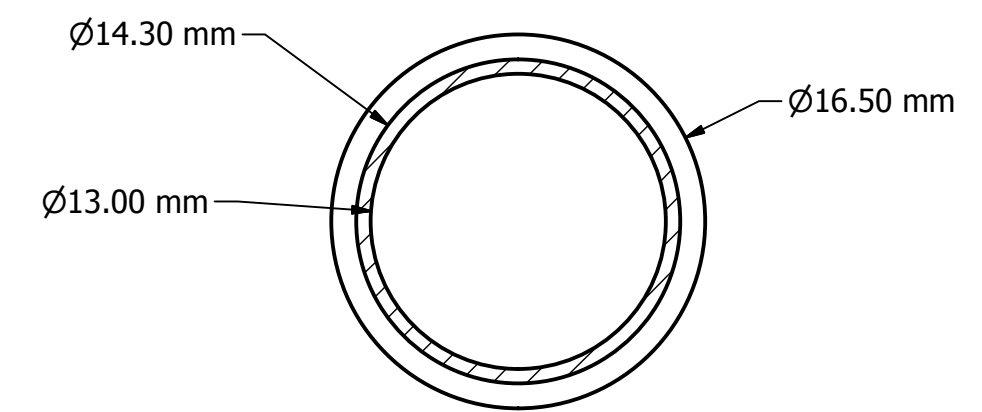
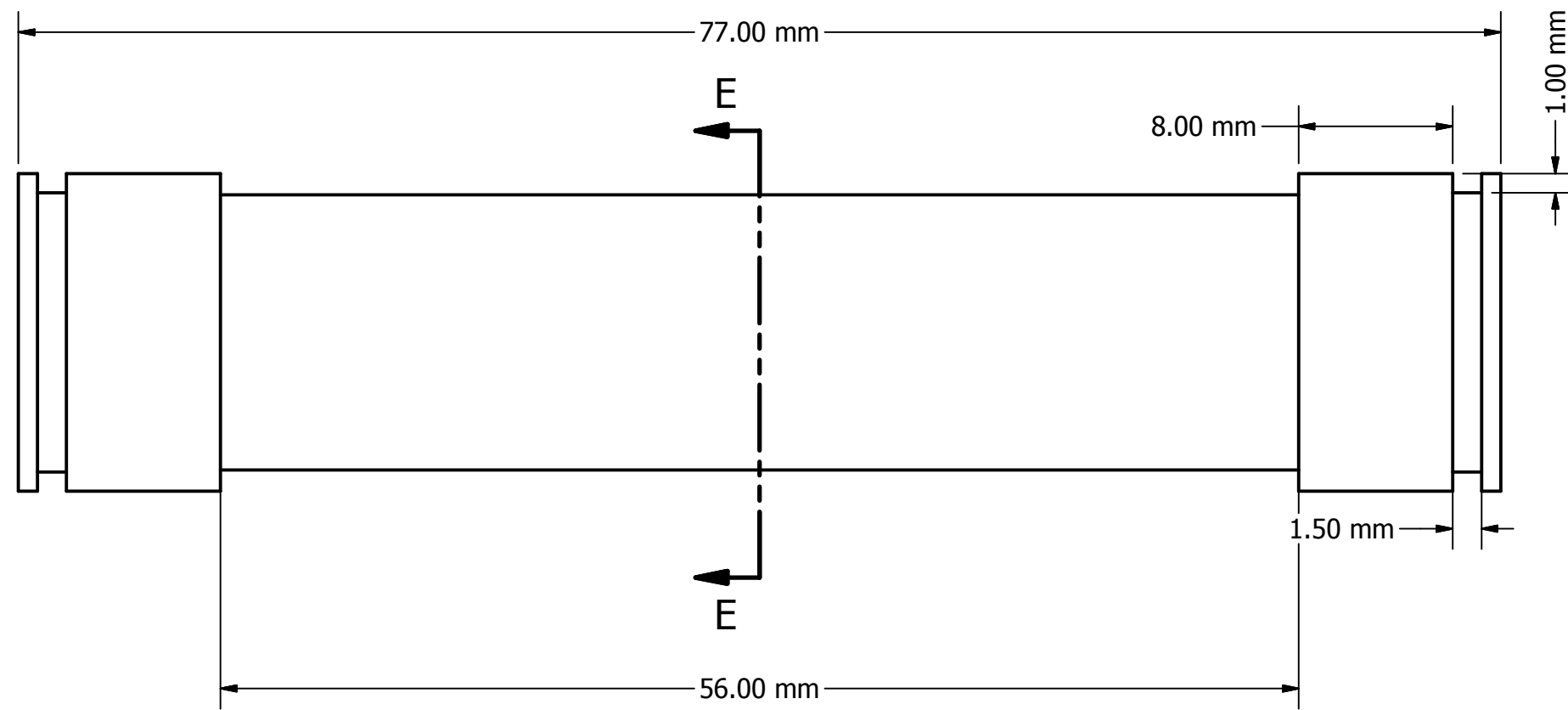


SECTION D-D
SCALE 3 : 1

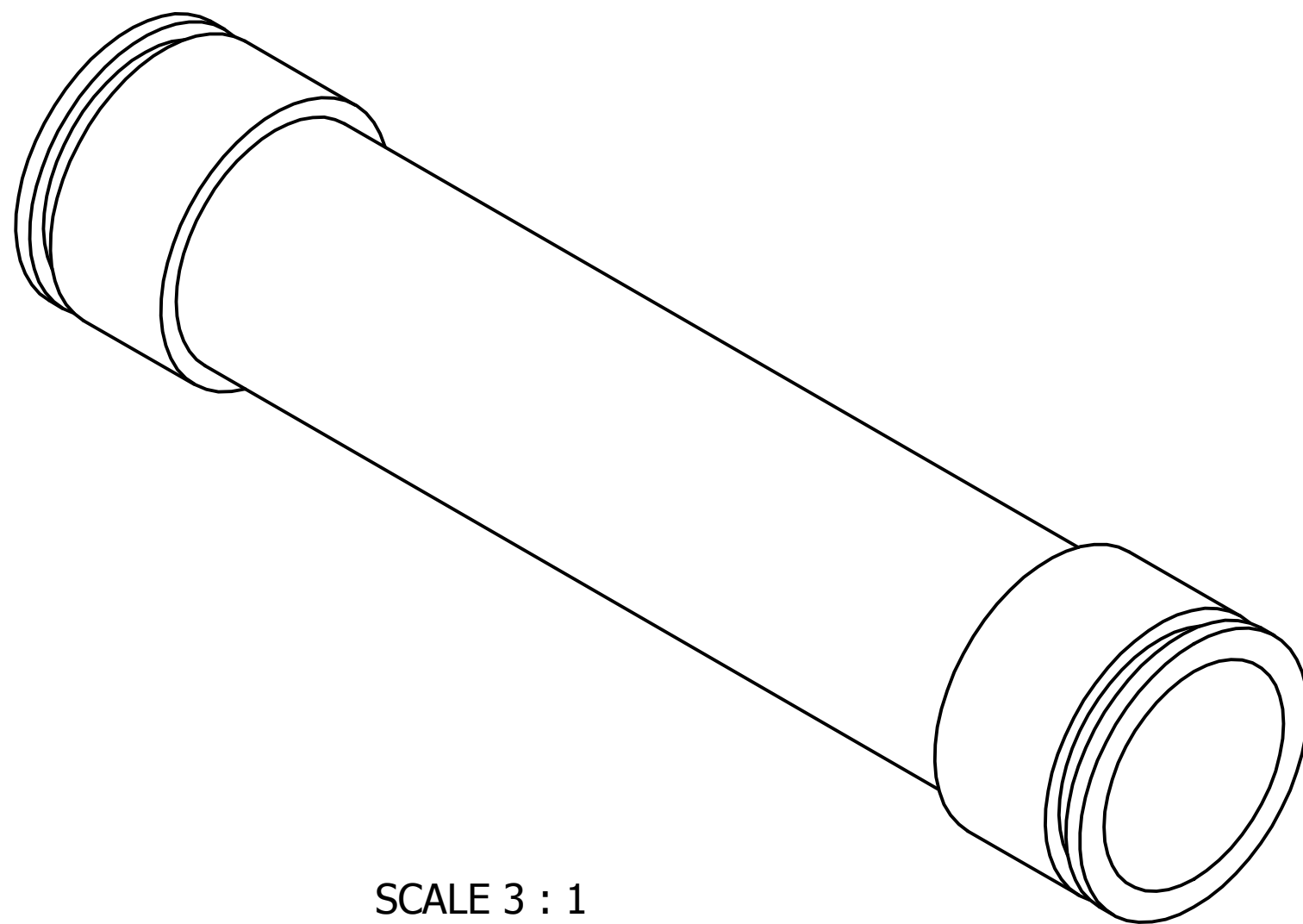


SCALE 3 : 1

DRAWN	Marco Peca	12/11/2012	University of Southampton School of Electronic and Computer Science		
CHECKED			TITLE		
QA			CYLINDER ver.3.4		
MFG					
APPROVED			SIZE	DWG NO	REV
			SCALE	SHEET 1 OF 1	

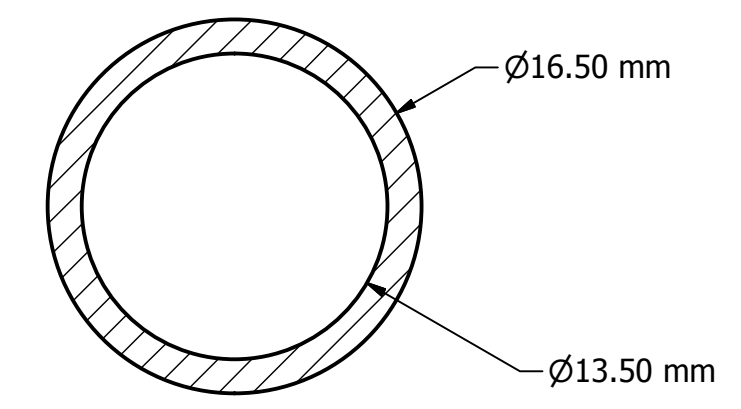
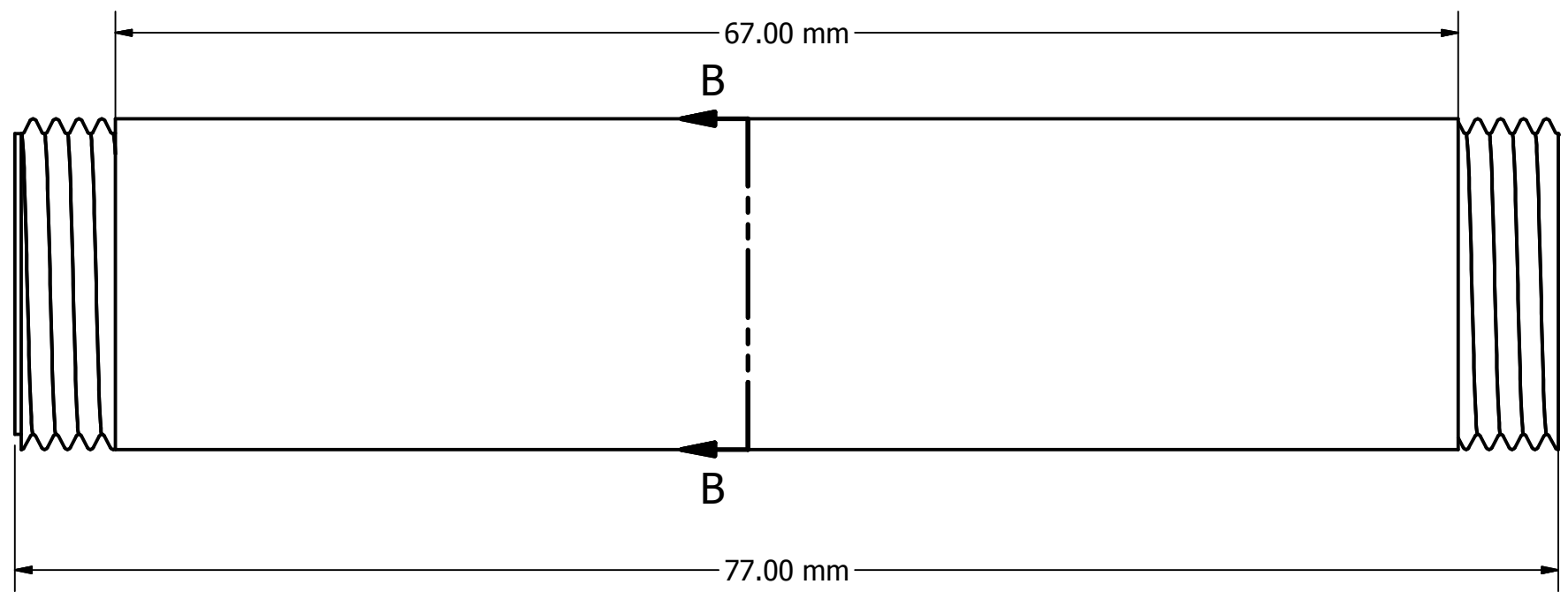


SECTION E-E
SCALE 3 : 1

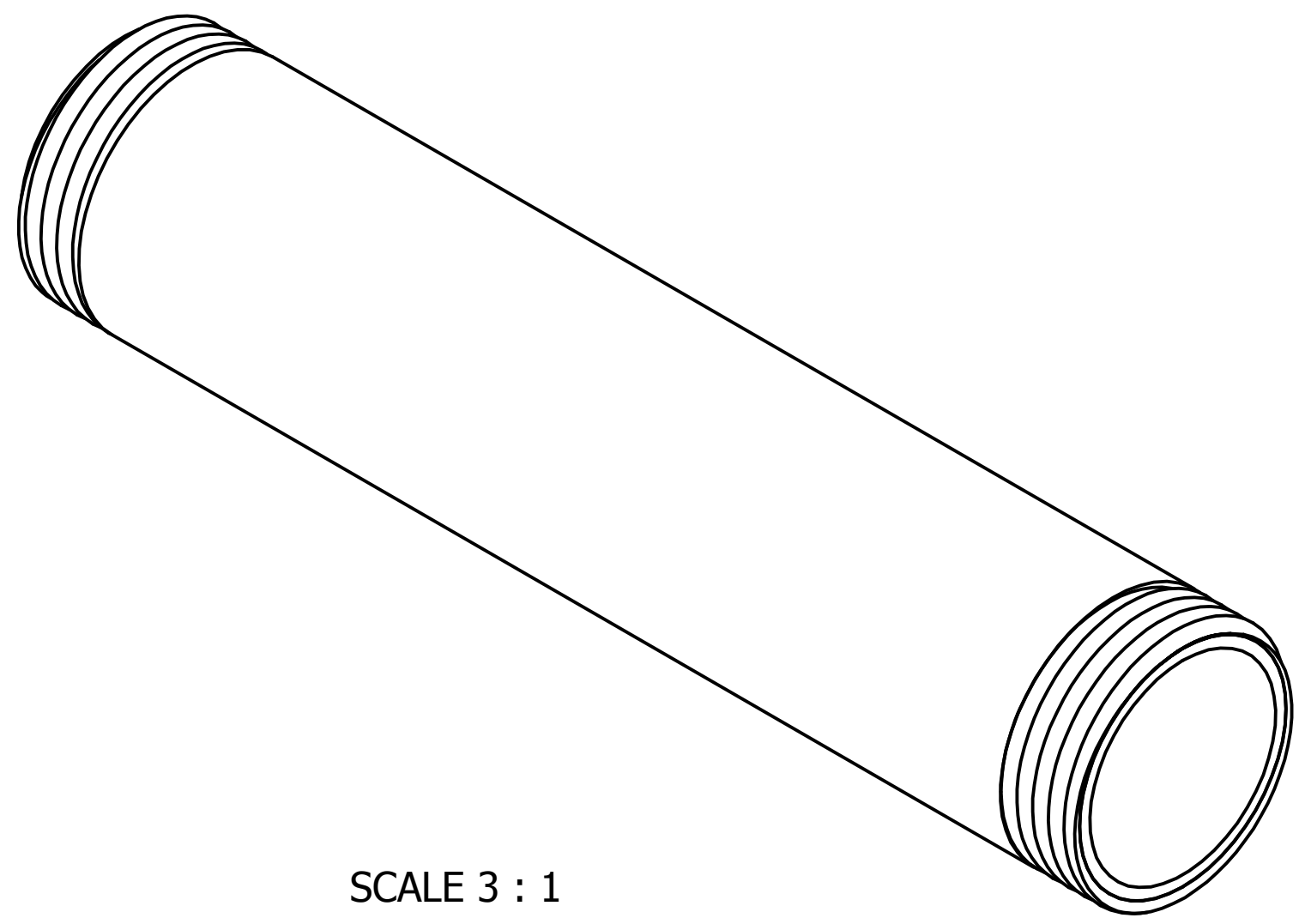


SCALE 3 : 1

DRAWN	Marco Peca	12/11/2012	University of Southampton School of Electronic and Computer Science		
CHECKED			TITLE		
QA			CYLINDER ver.3.5		
MFG			SIZE	DWG NO	REV
APPROVED			SCALE	SHEET 1 OF 1	



SECTION B-B
SCALE 3 : 1



SCALE 3 : 1

DRAWN	Marco Peca	03/09/2011	University of Southampton School of Electronic and Computer Science		
CHECKED			TITLE		
QA			CYLINDER ver.3		
MFG					
APPROVED			SIZE	DWG NO	REV
			SCALE	SHEET 1 OF 1	